Green Energy and Technology

Nabil Derbel · Quanmin Zhu *Editors*

Modeling, Identification and Control Methods in Renewable Energy Systems

Springer

Green Energy and Technology

More information about this series at http://www.springer.com/series/8059

Nabil Derbel • Quanmin Zhu
Editors

Modeling, Identification and Control Methods in Renewable Energy Systems

Springer

Editors
Nabil Derbel
Sfax Engineering School
University of Sfax
Sfax, Tunisia

Quanmin Zhu
University of the West of England
Bristol, UK

ISSN 1865-3529 ISSN 1865-3537 (electronic)
Green Energy and Technology
ISBN 978-981-13-1944-0 ISBN 978-981-13-1945-7 (eBook)
https://doi.org/10.1007/978-981-13-1945-7

Library of Congress Control Number: 2018964938

This Springer imprint is published by the registered company Springer Nature Singapore Pte Ltd.
The registered company address is: 152 Beach Road, #21-01/04 Gateway East, Singapore 189721, Singapore

Preface

This book entitled *Modeling, Identification and Control Methods in Renewable Energy Systems* consists of a representation of theoretical results related to renewable energy systems. It is not our intention to cover all renewable energy systems of recent control-related contributions, but the priority has been placed on the application of wind energy and solar energy with works related to their applications, such as vibration energy, converters, FPGA-based control, and MPPT techniques. Intelligent approaches such as fuzzy systems, neural networks, and genetic algorithm constitute powerful tools applied to the best work of these energy systems. This book is made of 17 invited chapters that have been written by leading researchers covering recent theoretical developments and applications of renewable energy systems.

The book presents theoretical explorations on several fundamental problems for several kinds of renewable energy systems. By integrating fresh concepts and state-of- the-art results to form systematic approaches for controlling these systems, fundamental theoretical approaches as well as practical framework have been established.

This book is intended for readers from a wide spectrum related to photovoltaic systems and wind energy systems. It is expected that readers require background knowledges to understand various concepts and results presented in this book. Moreover, this book provides not only theoretical results but also experimental case studies to highly motivate young students and researchers.

The book has been organized into the following chapters which are regrouped into three parts.

- The first part contains four chapters detailing fundamentals of photovoltaic systems. The first chapter of this part presents the modeling and performance analysis of a solar PV power system connected to a three phase. The second chapter is dedicated to the photovoltaic power prediction using recurrent neural networks. A comparison between two behavior MPPT techniques applied to photovoltaic systems has been given in Chap. 3. Chapter 4 is dedicated to discussion on cascaded boost converters for photovoltaic chains.

- The second part is dedicated to wind energy systems. It contains seven chapters. The fifth chapter applies the control of the power of a DFIG generator using the MPPT technique. Chapter 6 studies the ripple correlation on the optimal point determination in a medium power wind conversion system. Chapter 7 considers the control of wind turbine based on PMSG using pitch angle control. Chapter 8 consists to apply a nonlinear control of a variable speed wind energy conversion system-based PMSG. Chapter 9 is an application of the direct power control of a DFIG using sliding mode control approach. Chapter 10 presents a comparative study between PI and sliding mode control for the DFIG of a wind turbine. Chapter 11 is an emulation of wind turbine for stand-alone wind energy conversion systems.
- The third part is dedicated to tools for renewable energy systems. It is composed by six chapters. Chapter 12 starts this part by the vibration control by piezoelectric elements for renewable energy systems. Chapter 13 considers the feedback T-S fuzzy controller in a finite frequency for wind turbines. Chapter 14 considers an intelligent load frequency control in the presence of wind power generation. Chapter 15 proposes a fault tolerant control of switch power converter in WECS based on a DFIG. Finally, Chapters 16 and 17 consider FPGA-based control applied to a DFIG-based wind power system and to a PMSG on variable wind speed turbine.

We wish to express our sincere gratitude to colleagues who have contributed to this book. First of all, we are particularly indebted to our colleagues who have contributed their excellent research in order to bring valuable materials for graduate students, researchers, and practitioners. We greatly appreciate the contributors to this book for their patience and time taken to collaborate with us to finally complete this book. Next, particular thanks go to students and colleagues who helped engaging in the preparation and assisted us to improve this book. Finally, we would like to sincerely express our deepest gratitude to the Springer editorial staff for their continuous support, assistance, and significant improvement in the manuscript. Without their help, the book would not be published as scheduled.

Sfax, Tunisia — Nabil Derbel
Bristol, UK — Quanmin Zhu
May 2018

Contents

Chapter 1
Modeling and Performance Analysis of a Solar PV Power System Connected to a Three Phase Load Under Irradiation and Load Variations

Fatima-Ezzahra Tahiri, Khalid Chikh, and Mohamed Khafallah

Abstract This chapter describes a stand-alone solar photovoltaic system with a robust controllers which are Incremental Conductance and Perturb and Observe used to enhance the maximum power point tracking and stable output power under variations of solar irradiation, temperature and electrical loads. Indeed, to supply an alternative load with a sinusoidal line without harmonic distortion under weather conditions, algorithms techniques are used to control a DC-DC boost converter to generate the Maximum Power Point of the photovoltaic generator to alternative load via a PWM (Pulse Width Modulation) three phase inverter. The computer simulation results, in Matlab/Simulink environment, presented in this chapter validate the full PV system components and show that the photovoltaic simulation system can track the maximum power point accurately using the two maximum power point tracking techniques.

Keywords Photovoltaic system (PV) · Boost converter · Maximum power point tracking (MPPT) · Maximum power point (MPP) · Three phase inverter · Load variations · Weather conditions · Alternative load · Perturbation and observation (P&O) · Incremental conductance (INC)

F.-E. Tahiri (✉) · M. Khafallah
Energy and Electrical Systems Laboratory, Hassan II University ENSEM Casablanca, Casablanca, Morocco
e-mail: fatima-ezzahra.tahiri@ensem.ac.ma

K. Chikh
Engineering and Applied Technology Laboratory (LITA), High School of Technology, Sultan Moulay Slimane University, Béni Mellal, Morocco

N. Derbel, Q. Zhu (eds.), *Modeling, Identification and Control Methods in Renewable Energy Systems*, Green Energy and Technology,
https://doi.org/10.1007/978-981-13-1945-7_1

Nomenclature

I_{PV}: Solar cell current (A)
V_{PV}: Solar cell output voltage (V)
I_0: Diode saturation current (A)
R_S: Solar cell series resistance (Ω)
E_g: Energy band gap (eV)
n: Ideality factor (between 1 and 2)
q: Electron charge (1.6×10^{-19} C)
k: Boltzmann constant (1.38×10^{-23} J/K)
G: irradiance (W/m^2)
T: Cell temperature in Kelvin (K)
T_{ref}: Reference cell temperature (298.15 K)
I_L: Light generated current (A)
I_{cc}: Short circuit current (A)
V_{oc}: Open circuit voltage (V)
D: Duty cycle
V_S: Output voltage of the boost converter (V)
V_{PV}: Output voltage of the PV generator (V)
f_C: Cut-off frequency (Hz)
L_f: Filter inductor (H)
C_f: Filter capacitor (F)

1.1 Introduction

The solar photovoltaic system is one of the important renewable energy sources. It converts sunlight into electricity and offers many advantages such as the energy produced is not polluting, requiring little maintenance, most promising and inexhaustible (Jiang et al. 2005).

The basic device of a photovoltaic system is the photovoltaic cell. Cells may be grouped to form panels or modules. Panels can be grouped to form large photovoltaic arrays. The term array is usually employed to describe a photovoltaic panel (with several cells connected in series and/or parallel) or a group of panels (Bauer 2010).

However, the PV system still has relatively low conversion efficiency. Indeed, the power delivered by the PV module depends on the irradiance, temperature, and electrical loads and it has a maximum (MPP) at a certain working point. At the MPP (Maximum Power Point), the PV operates at its highest efficiency (Freeman 2010; Sera et al. 2006a,b; Suryakumari et al. 2013; Tahiri et al. 2016, 2017).

Therefore, to extract the maximum power under the different conditions stated earlier, a maximum power point tracking (MPPT) technique is used to control the fluctuating operating power point of the PV array via a DC-DC converter.

The MPPT controller can be realized based on different methods and algorithms. The most popular methods are known as Perturb and Observe (P&O) and Incremental Conductance (INC).

This chapter treats the deepened modeling of a whole photovoltaic system composed of a photovoltaic generator, power electronic components, filter and local loads.

This work is organized as follows: solar cell modeling and the simulation behavior of the PV module at different operating conditions will be presented and discussed in Sects. 1.2 and 1.3, respectively. In Sect. 1.4, the MPPT techniques are discussed and tested. Whereas in Sect. 1.5 the others components of the PV system are presented and the simulation results in Matlab/Simulink environment of the full PV power system are talked in order to evaluate its performance under different conditions. Eventually, conclusion is presented in Sect. 1.6.

1.2 Modeling of the Solar Cell

Solar cells consist of a p-n junction fabricated in thin wafer or layer of semiconductors (Kinjal et al. 2015), whose electrical characteristics differ very little from a diode represented by the equation of Shockly (Alsadi and Alsayid 2012). Thus the simplest equivalent circuit of a solar cell is a current source in parallel with a diode. The output of the current source is directly proportional to the light falling on the cell. For this research work, a model of moderate complexity was used. The circuit diagram for the solar cell is shown in Fig. 1.1 (Villalva et al. 2009; Walker and Geoffrey 2000).

Equations which describe the $I - V$ characteristics of the cell are: (Makhlouf et al. 2012)

$$I_{PV} = I_L - I_0 \left[\exp\left(\frac{q(V_{PV} + R_s I_{PV})}{nkT} \right) - 1 \right] \tag{1.1}$$

$$I_L(G, T) = I_{cc} \frac{G}{1000} [1 + a(T - T_{ref})] \tag{1.2}$$

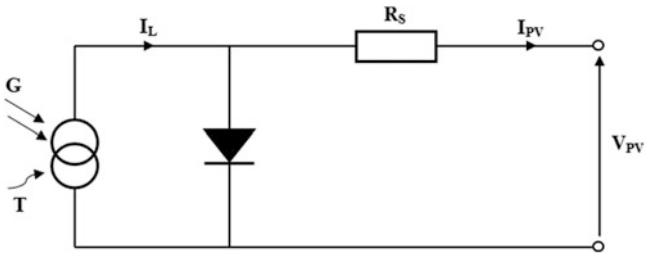

Fig. 1.1 Equivalent model of PV cell

$$I_0(T) = I_0(T_{ref}) \left(\frac{T}{T_{ref}}\right)^{\frac{3}{n}} \exp\left[\frac{qE_g}{nk}\left(\frac{1}{T_{ref}} - \frac{1}{T}\right)\right] \tag{1.3}$$

$$I_0(T_{ref}) = \frac{I_{cc}}{\exp\left(\frac{qV_{0C}}{nkT_{ref}}\right) - 1} \tag{1.4}$$

$$R_s = -\left.\frac{dP_{PV}}{dI_{PV}}\right|_{V_{0C}} - \frac{nkT_{ref}}{I_{cc}q \exp\left(\frac{qV_{0C}}{nkT_{ref}}\right)} \tag{1.5}$$

1.3 Photovoltaic Module

1.3.1 Photovoltaic Module Characteristics

BP SX 150 solar array PV module is chosen for a MATLAB simulation model. The module is made of 72 multicrystalline silicon solar cells in series and provides 150W of nominal maximum power. Table 1.1 shows its electrical specification take from datasheet (Datasheet, BP SX 150, 2002).

1.3.2 Photovoltaic Module Simulation

Figure 1.2 shows the modeling circuit of the PV module in environment Matlab/Simulink. The modeling of the PV is done applying the equations seen before, (1.1), (1.2), (1.3), (1.4) and (1.5). Note that the irradiance and temperature are the inputs of the system.

The $P - V_{PV}$ and $I_{PV} - V_{PV}$ characteristics at standard temperature condition are given in Figs. 1.3 and 1.4.

The characteristic $P - V_{PV}$ has only one maximum power point called MPP. Simulation results are identical to the values given by the datasheet.

Table 1.1 Electrical characteristics data of the BP SX 150 SOLAR AT 25 °C, 5AM, 1000 W/m^2

Maximum Power (Pmax)	150W
Voltage at Pmax (Vmp)	34.5V
Current at Pmax (Imp)	4.35A
Open-circuit voltage (Voc)	43.5V
Short-circuit current (Isc)	4.75A
(KI) Temperature coefficient of Isc	$(0.065 \pm 0.015)\%/°C$
(KV) Temperature coefficient of Voc	$-(160 \pm 20)$mV/ °C
NOCT	47± 2 °C

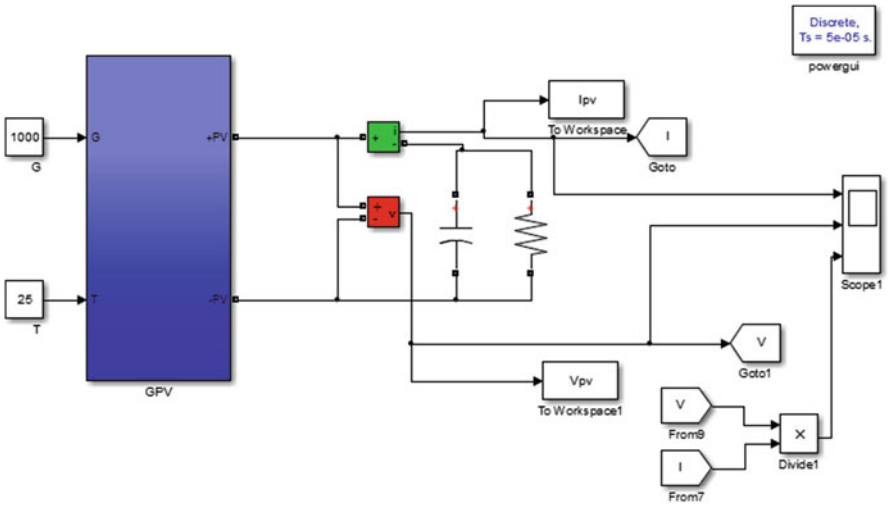

Fig. 1.2 PV Module Model in environment Matlab/Simulink

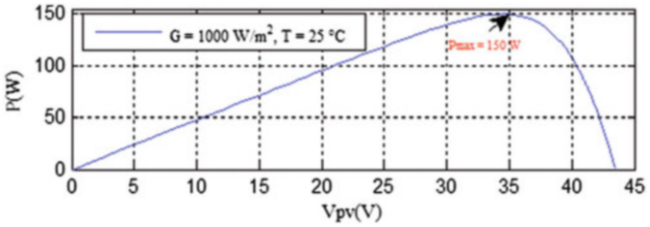

Fig. 1.3 Simulated $P - V_{PV}$ curve of BP SX 150S PV module (1 kW/m^2, 25 °C)

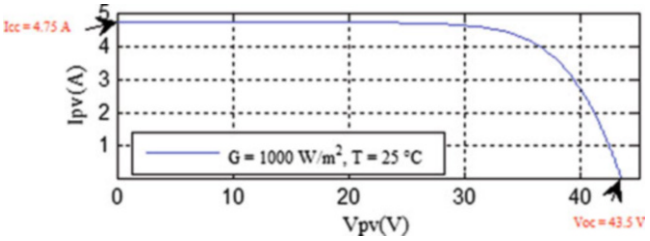

Fig. 1.4 Simulated $I_{PV} - V_{PV}$ curve of BP SX 150S PV module (1 kW/m^2, 25 °C)

1.3.3 *Effect of Changes in Parameters on the Characteristics of PV Module*

Figures 1.5 and 1.6 show the effect of irradiance variation (400, 500, 600, 700, 800, 900, 1000) W/m^2 at constant temperature (T = 25 °C) respectively on $I_{PV} - V_{PV}$ and $P - V_{PV}$ characteristics. As one can see in these figures, the module current and the MPP are proportional to the irradiation, while the open-circuit voltage changes slightly with irradiation (Ferchichi et al. 2016) (Yadav et al. 2016).

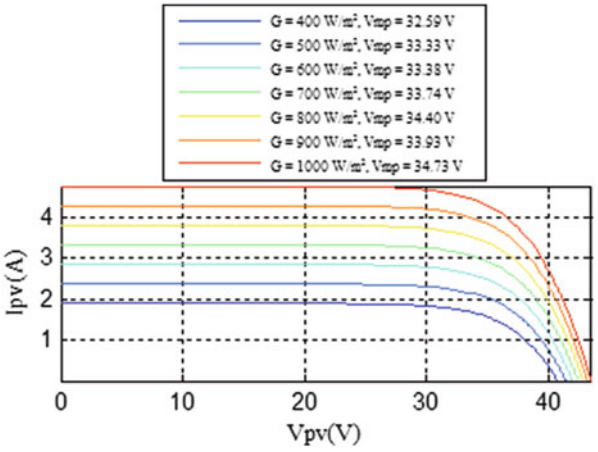

Fig. 1.5 Effect of the irradiation on $I_{PV} - V_{PV}$ characteristic of BP SX 150S PV module at $T = 25\,°C$

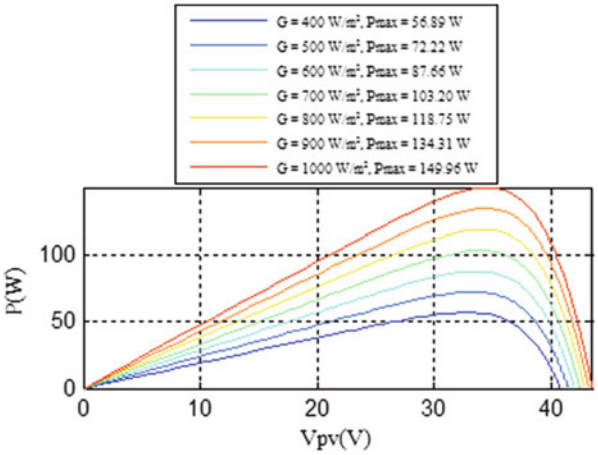

Fig. 1.6 Effect of the irradiation on $P - V_{PV}$ characteristic of BP SX 150S PV module at $T = 25\,°C$

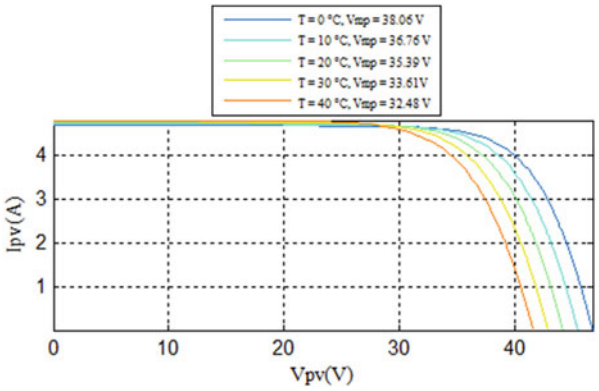

Fig. 1.7 Effect of the temperature on $I_{PV} - V_{PV}$ characteristic of BP SX 150S PV module at G = 1000 W/m^2

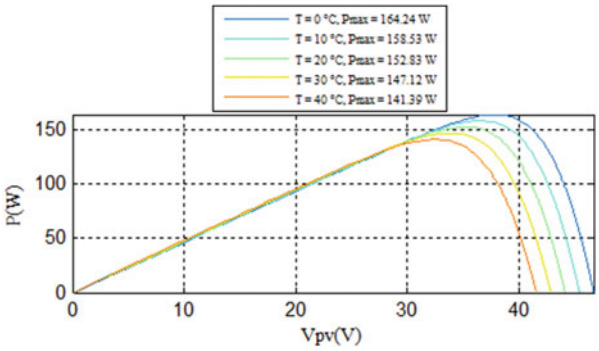

Fig. 1.8 Effect of the irradiation on $P - V_{PV}$ characteristic of BP SX 150S PV module at G = 1000 W/m^2

In Figs. 1.7 and 1.8 the simulation results are shown for different values of temperature (T = 25 °C, T = 50 °C, T = 75 °C) at constant irradiance (G = 1000 W/m^2) respectively on $I_{PV} - V_{PV}$ and $P - V_{PV}$ characteristics.

From Fig. 1.7 the generated power is gradually decreased and maximum power available more at low temperature. From Fig. 1.8 the current is constant up to some voltage and then it will decrease gradually.

Moreover, when a PV module is directly coupled to a load, the PV module's operating point depends strongly on the characteristics of the load (Fig. 1.9). In other term, the impedance of load dictates the operating condition of the PV module and only the optimal load, which passes through its characteristic MPP, allows extract the maximum power (Nemsi et al. 2013).

From Figs. 1.5, 1.6, 1.7, 1.8, and 1.9, we conclude that the MPP of the PV generator changes continuously under variations of solar irradiation, temperature

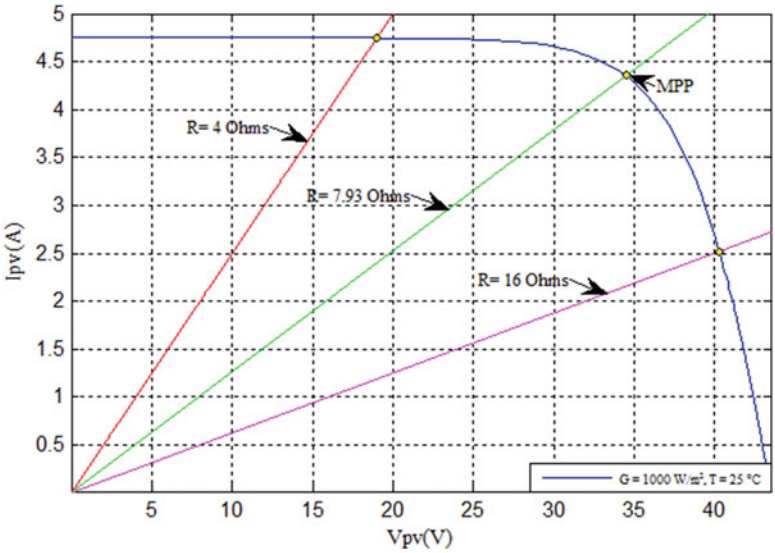

Fig. 1.9 $I_{PV} - V_{PV}$ curves of BP SX 150S PV module and various resistive loads Simulated with the MATLAB model (G = 1000 W/m^2, T = 25 °C)

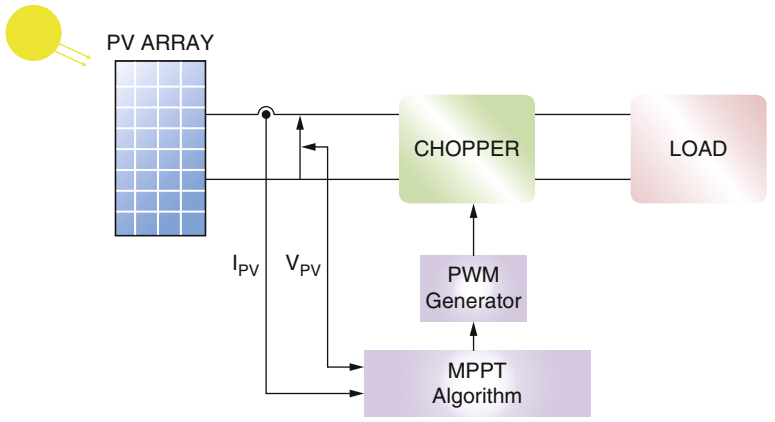

Fig. 1.10 Block diagram of a PV array connected to the load

and electrical loads. Therefore a MPPT technique is required to exploit the maximum power of the module and optimize the efficiency of PV cells.

1.4 Maximum Power Point Tracking (MPPT) Techniques

MPPT is an adaptive system used to control a static converter between the load and the PV panel (Fig. 1.10).

This converter is designed to fit every time the apparent impedance of the load to the impedance of PV field corresponding to the maximum power point. This method is based on the use of a search algorithm of maximum power of the photovoltaic panel curve (Mohssine et al. 2015). There are many different MPPT techniques available in the literature; the most largely used algorithms are described in the following sections.

1.4.1 Perturbation and Observation (P&O)

The most commonly used MPPT algorithm is the Perturb and Observe (P&O), due to its ease of implementation in its basic form. In Fig. 1.11, if the operating voltage

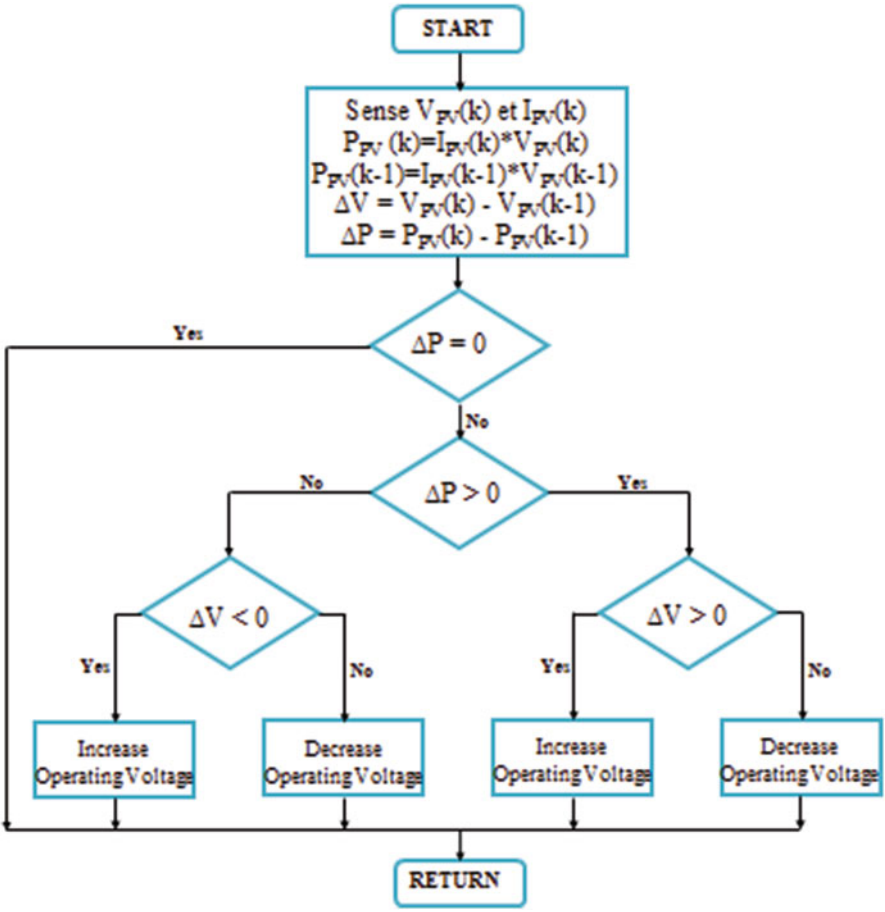

Fig. 1.11 Flowchart of the P&O MPPT method

of the PV array is perturbed in a given direction and $\frac{dP}{dV} > 0$, it is known that the perturbation moved the array's operating point toward the MPP. The P&O algorithm would then continue to perturb the PV array voltage in the same direction. If $\frac{dP}{dV} < 0$, then the change in operating point moved the PV array away from the MPP, and the P&O algorithm reverses the direction of the perturbation (Hohm and Ropp 2000).

The advantage of the P&O method is that it is easy to implement. However, it has some limitations, like oscillations around the MPP in steady state operation, slow response speed, and even tracking in wrong way under rapidly changing atmospheric conditions (Sera et al. 2006a).

1.4.2 Incremental Conductance (INC) Method

The incremental conductance uses the PV array's incremental conductance $\frac{dI}{dV}$ to compute the sign of $\frac{dP}{dV}$. It does this using an expression derived from the condition that, at the MPP, $\frac{dP}{dV} = 0$. Beginning with this condition, it is possible to show that, at the MPP $\frac{dI}{dV} + \frac{I}{V} = 0$. Thus, incremental conductance can determine that the MPPT has reached the MPP and stop perturbing the operating point. If this condition is not met, the direction in which the MPPT operating point must be perturbed can be calculated using the relationship between $\frac{dI}{dV}$ and $-\frac{I}{V}$ (Hohm and Ropp 2000)

The INC can track rapidly increasing and decreasing irradiance conditions with higher accuracy than P&O. However, because of noise and errors due to measurement and quantization, this method also can produce oscillations around the MPP; and it also can be confused in rapidly changing atmospheric conditions. Another disadvantage of this algorithm is the increased complexity when compared to perturb and observe. This increases computational time, and slows down the sampling frequency of the array voltage and current (Fig. 1.12) (Sera et al. 2006a).

1.4.3 Simulation Results

Figure 1.13 shows the modeling circuit of the PV system in Matlab/Simulink environment. The PV generator connected to a resistive load through a Boost converter controlled by two algorithms MPPT: P&O and INC.

To test the performance of the two algorithms (P&O and INC) in the same simulation conditions, we vary the irradiation, temperature and load as shown below.

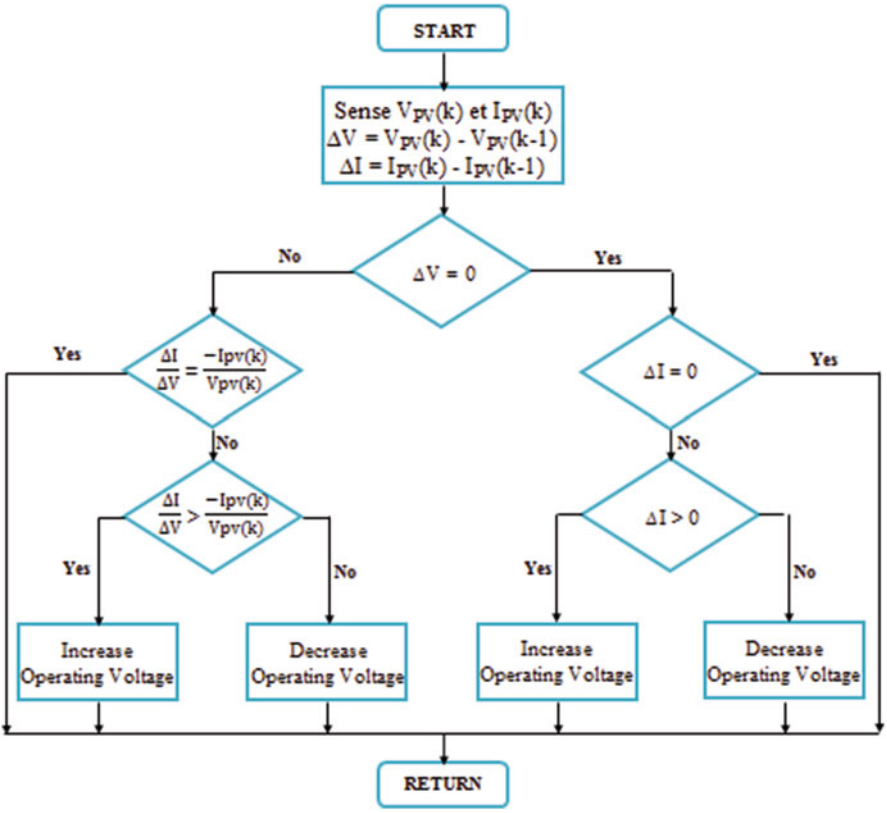

Fig. 1.12 Flowchart of the INC MPPT method

1.4.3.1 Variation of Irradiation

Figure 1.14 shows the convergence of the output power of the PV system to the MPP using P&O and INC commands under variation of irradiation as indicated in Fig. 1.15.

1.4.3.2 Temperature Variation

Figure 1.16 shows the convergence of the output power of the PV system to the MPP using P&O and INC commands under variation of temperature as indicated in Fig. 1.17.

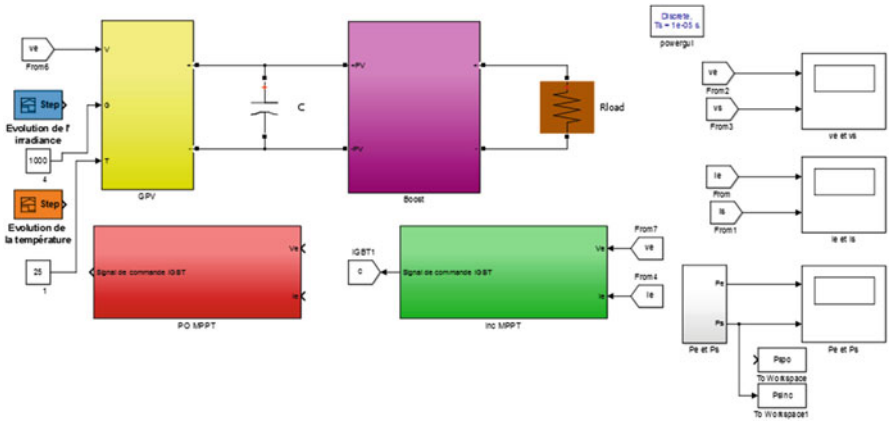

Fig. 1.13 PV system in environment Matlab/Simulink

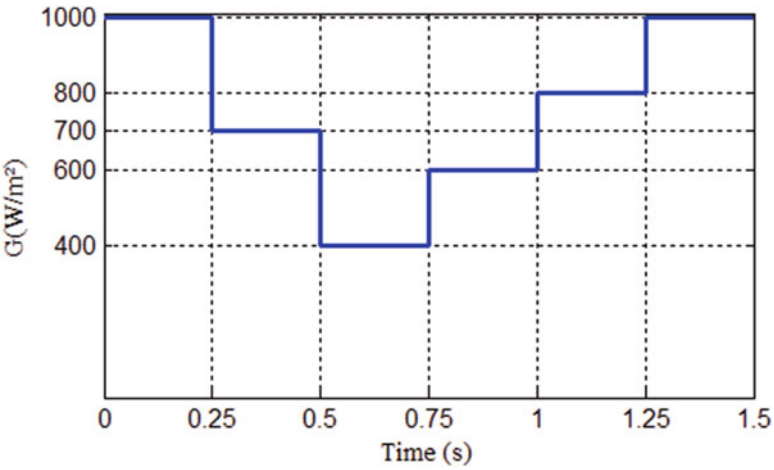

Fig. 1.14 Output power of the PV system verses time using P&O algorithm and INC algorithm at temperature 25 °C and different solar irradiation levels 1000, 800, 700, 600 and 400 W/m^2

1.4.3.3 Load Variation

Figures 1.18, 1.19 and 1.20 show the output power of the PV system respectively without MPPT algorithm, using INC command and using P&O command.

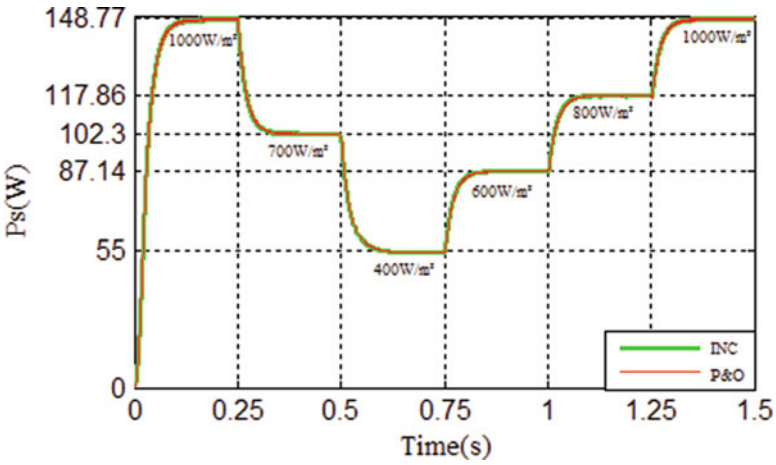

Fig. 1.15 Variation of solar irradiation

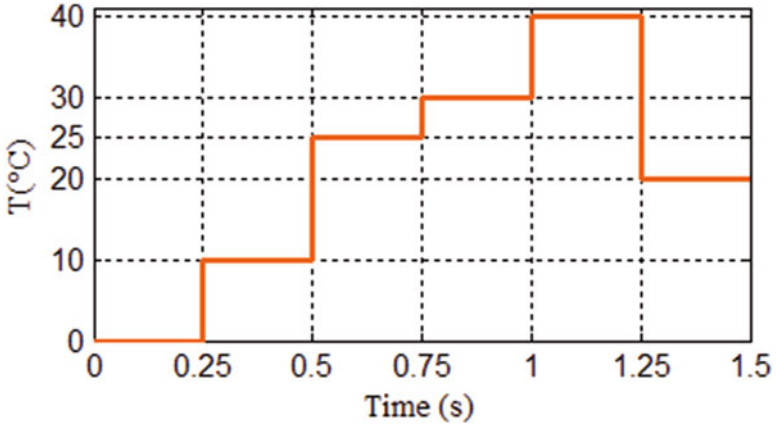

Fig. 1.16 Output power of the PV system verses time using P&O algorithm and INC algorithm at solar irradiation 1000 W/m^2 and different temperature levels 0, 10, 25, 30, 40 and 20 °C

1.5 The Full PV Power System

Figure 1.21 shows the simplified block structure of the investigated system. It contains a photovoltaic generator, power electronic components, filter and local loads.

The DC/DC converter with an MPPT (Maximum Power Point Tracker) connected to the solar array to optimize the PV output, a second DC/DC converter is connected to the output of this converter to increase the voltage received from the photovoltaic generator to the voltage level required by the voltage source inverter (VSI) via a LC filer.

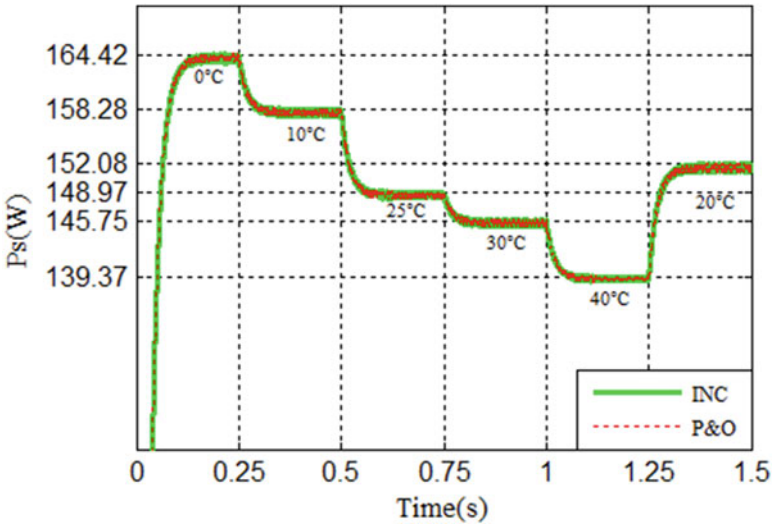

Fig. 1.17 Variation of temperature

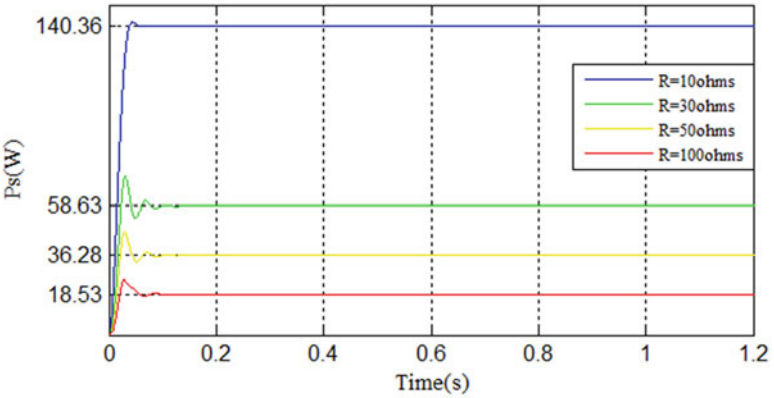

Fig. 1.18 Output power of the PV system verses time without MPPT algorithm at different value of resistive load 10Ω, 30Ω, 50Ω and 100Ω

1.5.1 DC Voltage Control

The continuous part of the PV system is presented in Fig. 1.22. The first DC/DC converter is a boost chopper circuit controlled by an MPPT algorithm for rise the low PV power to an optimal level under different weather conditions (Benkhelil and Gherbi 2012).

The second DC/DC converter is a boost which raises the input voltage to the voltage level demanded by the VSI and works with a fixed duty cycle (Bauer 2010).

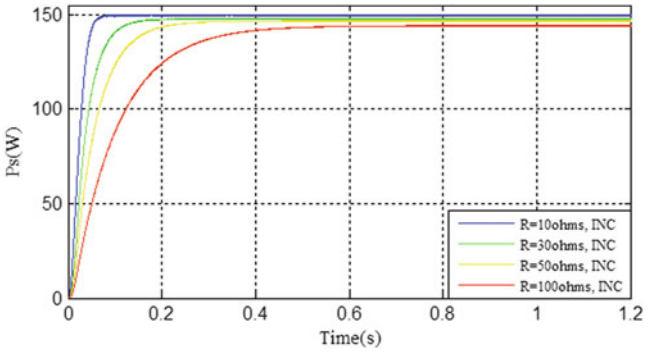

Fig. 1.19 Output power of the PV system verses time using INC algorithm at different value of resistive load 10, 30, 50 and 100 Ω

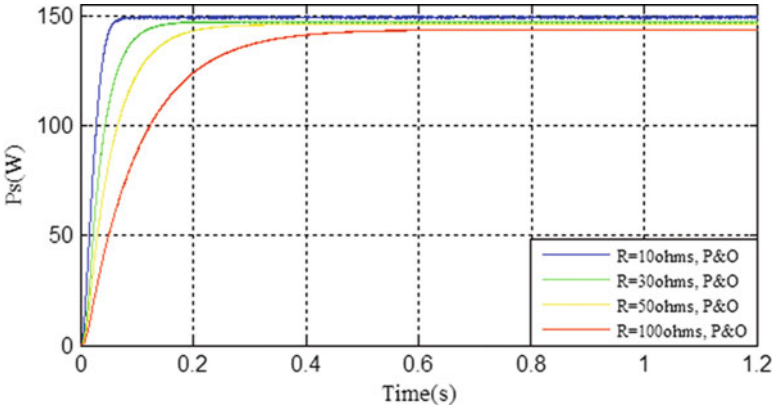

Fig. 1.20 Output power of the PV system verses time using P&O algorithm at different value of resistive load 10, 30, 50 and 100 Ω

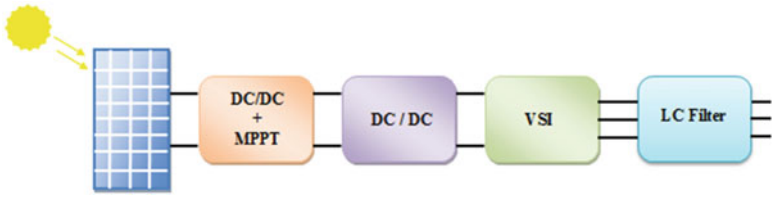

Fig. 1.21 Block diagram of the system

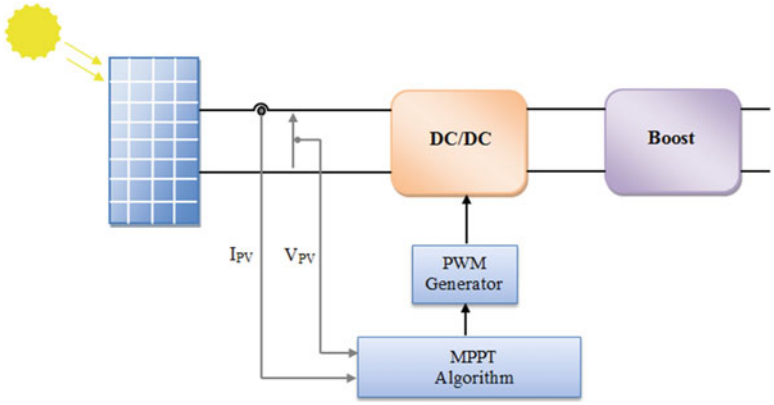

Fig. 1.22 DC voltage control

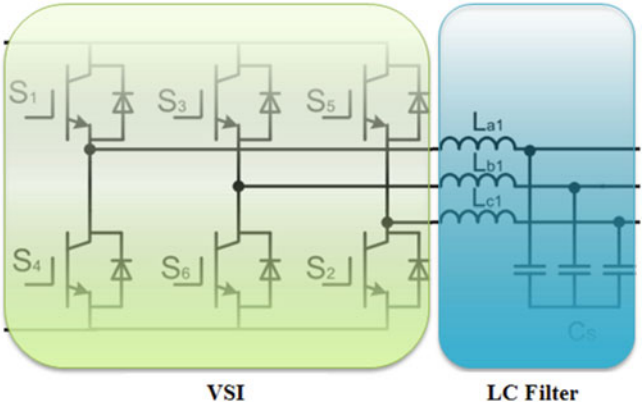

Fig. 1.23 Three-phase VSI

1.5.2 Voltage Source Inverter (VSI) Model

The VSI used in this work converts DC voltage to three-phase AC voltages. Figure 1.23 shows the detail circuit of the inverter. The power part of the inverter is composed of three arms consisting each one two switches. Each switch is composed of transistor (IGBT, MOSFET. . .) and of a diode coupled in parallel. The $L-C$ filter is connected to the inverter output, it's designed to reduce high order harmonics produced by the pulse-width modulation (PWM) inverters (Benadli et al. 2015).

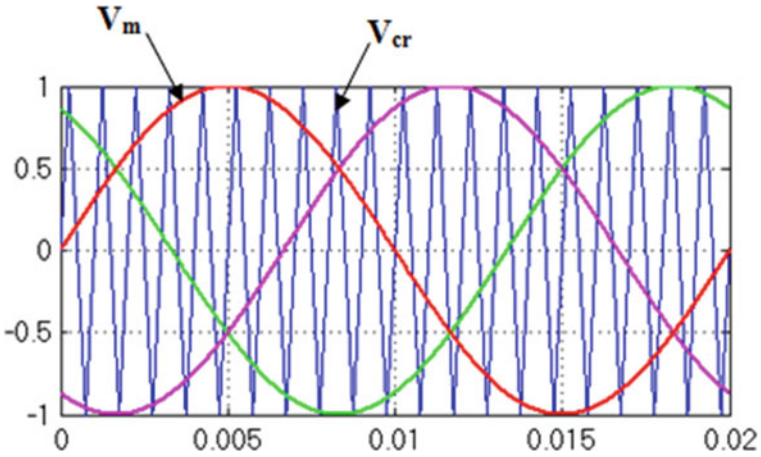

Fig. 1.24 Reference voltages and triangular wave carrier

1.5.3 PWM Control

A pulse width modulation (PWM) signal is a method for generating an analog signal using a digital source. A PWM signal consists of two main components that define its behavior: a duty cycle and a frequency. The interest of the PWM is to provide a variable DC voltage from a fixed DC voltage source. PWM provides a way to decrease the Total Harmonic Distortion (THD) of load current. The THD requirement can be met when the output of a PWM inverter is filtered since the unfiltered output of a PWM based inverted will have a relatively high distortion. There are different types of PWM schemes, the most used ones being sinusoidal PWM (SPWM), hysteresis PWM (HPWM), space vector modulation (SVM) and optimal PWM (Bratt 2011). The inverter switching, used in this studied system, is controlled by the SPWM. The high-frequency triangular carrier wave VCR is compared with a sinusoidal reference Vm of the desired frequency (shown in Fig. 1.24) to realize SPWM and generate the gating signal for the transistors (shown in Fig. 1.25).

1.6 *LC* Filter

The filter is an essential element after semiconductor converter. The filter reduces the effects caused by switching semiconductor devices on other devices. $L - C$ filter is one of the main existing harmonic filter topologies for three-phase inverters. It delivers a sinusoidal output current with THD less than 5% (Nordin et al. 2014). Consequently, the low-pass $L - C$ filter is designed so that the cut-off frequency, f_C is higher than the load current and voltage frequency and lower than the inverter switching frequency, based following equation:

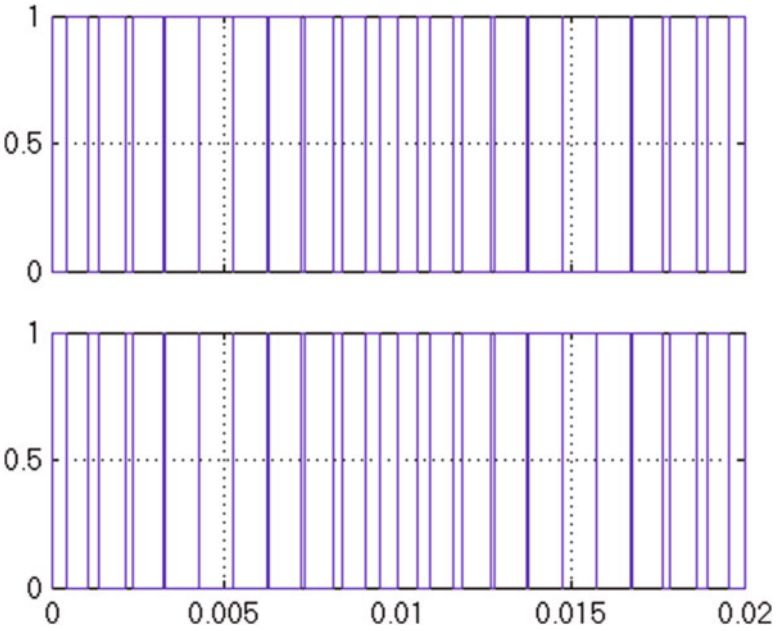

Fig. 1.25 Pulses generated to the first arm of inverter

$$f_C = \frac{1}{2\pi\sqrt{L_f C_f}} \tag{1.6}$$

1.6.1 Simulation Results

The power system is simulated in Matlab/Simulink power system toolbox software. In this work, the simulation model for the full PV power system components is designed (shown in Fig. 1.26).

A Perturbation and observation MPPT controller has been implemented in order to deliver the maximum power. The performance of the designed model is evaluated under changing weather conditions through the following case studies.

1.6.1.1 Case 1: Irradiation and Load Fixes

Figure 1.27 shows the simulation results of the power system model in stable weather conditions. In this case the resulting output line voltage is stable at 400 V.

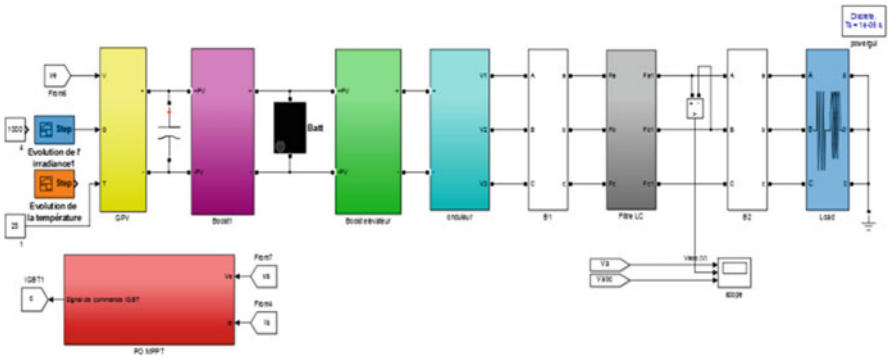

Fig. 1.26 Model for the full PV power system in Matlab/Simulink environment

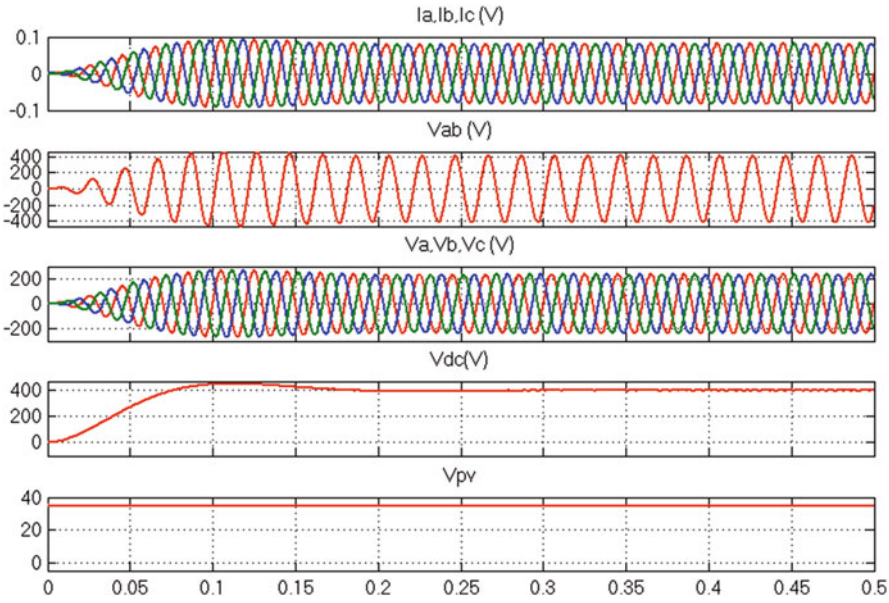

Fig. 1.27 PV system output voltage and current waveforms with a constant irradiation and load ($G = 1000\,W/m^2$ and $R = 3\,k\Omega$)

1.6.1.2 Case 2: Irradiation Variation

Figure 1.29 presents the simulation results of the power system model using P&O commands under irradiation variation as indicated in Fig. 1.28. The resulting output line and phase voltage remain constant.

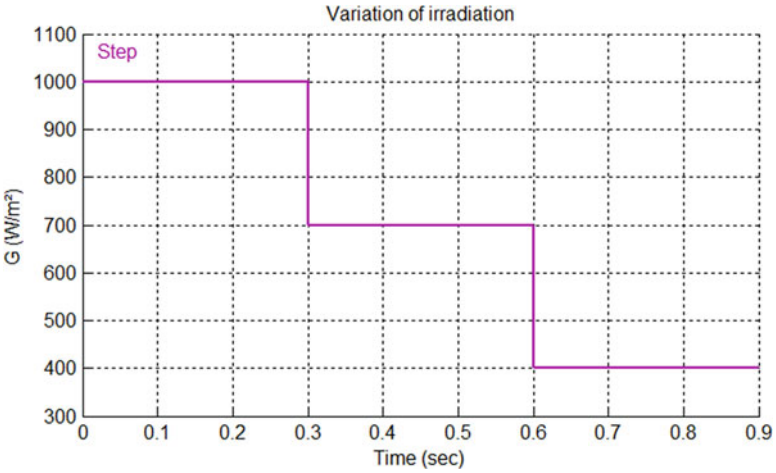

Fig. 1.28 Variation of irradiation

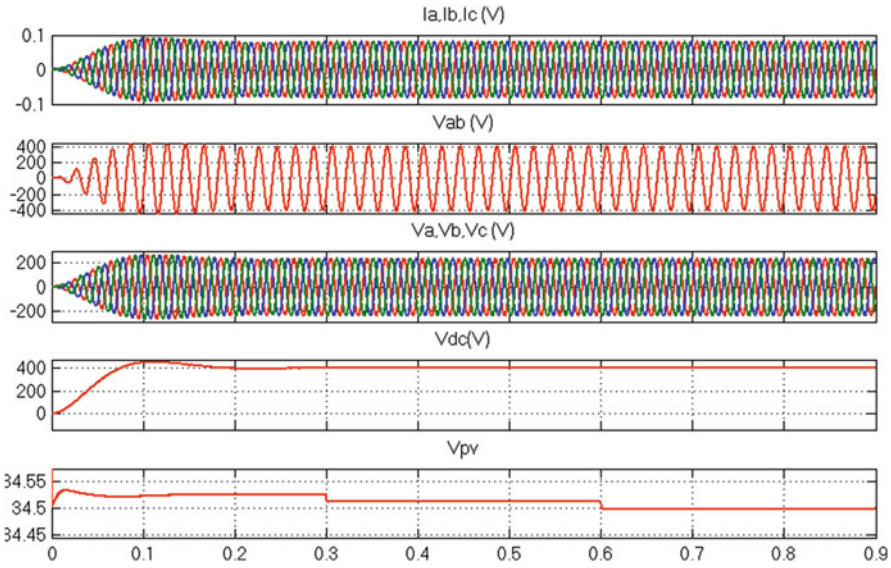

Fig. 1.29 PV system output voltage in case of irradiation variation

1.6.1.3 Case 3: Load Variation

Figure 1.30 presents the simulation presents of the power system model under load variation. For this case, the output current varies depending on the electrical load value and the output voltage remains constant in steady state after a fast dynamic state.

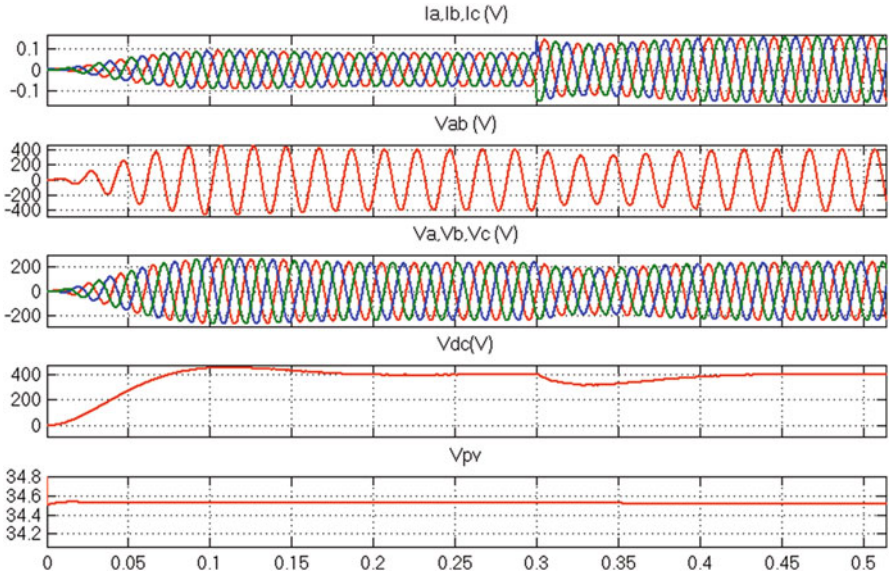

Fig. 1.30 PV system output voltage and current waveforms in case of load variation ($R = 3\,k\Omega$ before $t = 0.3$ s and $R = 5\,k\Omega$ after this time) and constant irradiation $G = 1000\,W/m^2$.

1.7 Conclusion

In this chapter, modeling of a stand-alone solar PV power system has been evaluated and validated under changing weather conditions and load variations through different cases in Matlab/Simulink environment. According to the results of the simulation, we conclude that:

- The PV generator performance deteriorates with increasing temperature, decreasing of solar irradiation and variation of the electrical load.
- The two MPPT algorithms (P&O and INC) make the output power of the PV system to be kept at the maximum when the irradiation and temperature varied and adjusts the PV generator to the load.
- The three phase voltage waveform, in the output inverter, remains constant in spite of irradiation or load variations.

References

Alsadi, S., & Alsayid, B. (2012). Maximum power point tracking simulation for photovoltaic systems using perturb and observe algorithm. *International Journal of Engineering and Innovative Technology (IJEIT), 2*(6), 83.

Bauer, J. (2010). Single phase voltage source inverter photovoltaic application. *ActaPolytechnica, 50*(4), 7–11.

Bellia, H., Youcef, R., & Fatima, M. (2014). A detailed modeling of photovoltaic module using MATLAB. *NRIAG Journal of Astronomy and Geophysics, 3*, 53–61.

Benadli, R., Khiari, B., & Sellami, A. (2015). Three-phase grid-connected photovoltaic system with maximum power point tracking technique based on voltage-oriented control and using sliding mode controller. In *6th International Renewable Energy Congress*, USA.

Benkhelil, E., & Gherbi, A. (2012). Modeling and simulation of grid-connected photovoltaic generation system. In *Revue des Energies Renouvelables SIENR'12 Ghardaïa*.

Bratt, J. (2011). *Grid connected PV inverters: Modeling and simulation*. Thesis, Faculty of San Diego State University.

Ferchichi, M., Zaidi, N., & Khedher, A. (2016). Comparative analysis for various control strategies based MPPT technique of photovoltaic system using DC-DC boost converter. In *17th International Conf. on Sciences and Techniques of Automatic control & computer engineering, STA'2016*, Sousse, Tunisia.

Freeman, D. (2010). *Introduction to photovoltaic systems maximum power point tracking*. Application Report, SLVA 446. Texas Instruments.

Hohm, D. P., & Ropp, M. E. (2000). Comparative study of maximum power point tracking algorithms using an experimental, programmable, maximum power point tracking test bed. In *Conference Record of the Twenty-Eighth IEEE Photovoltaic Specialists*, Anchorage, Alaska (pp. 1699–1702).

Jiang, J., Huang, T., Hsiao, Y., & Chen, C. (2005). Maximum power tracking for photovoltaic power systems. *Tamkang Journal of Science and Engineering, 8*(2), 147–153.

Kinjal, P., Shah, K. B., & Patel, G. R. (2015). Comparative Analysis of P&O and INC MPPT Algorithm for PV System. In *International Conference on Electrical, Electronics, Signals, Communication and Optimization (EESCO)*, Visakhapatnam, Andhrapradesh, India.

Makhlouf, M., Messai, F., & Benalla, H. (2012). Modeling and simulation of grid-connected photovoltaic distributed generation system. *Journal of Theoretical and Applied Information Technology, 45*(2), 378–386.

Mohssine, H., Kourchi, M., Bouhouch, H., & Debbagh, F. (2015). Perturb and observe (P&O) and incremental conductance (INC) MPPT algorithms for PV panels. *International Journal of Soft Computing and Engineering, 5*(2), 123–126.

Nemsi, S., Barazane, L., Diaf, S., & Malek, A. (2013). Comparative study between two maximum power point tracking (MPPT) techniques for photovoltaic system. *Revue des Energies Renouvelables, 16*(4), 773–782.

Nordin, A., Omar, A., & Zainuddin, H. (2014). Modeling and simulation of grid inverter in grid-connected photovoltaic system. *International Journal of Renewable Energy Research, 4*(4), 949–957.

Sera, D., Kerekes, T., Teodorescu, R., & Blaabjerg, F. (2006a). Improved MPPT algorithms for rapidly changing environmental conditions. In *12th International Conference on Power Electronics and Motion Control EPE-PEMC*, USA.

Sera, D., Kerekes, T., Teodorescu, R., & Blaabjerg, F. (2006b). Improved MPPT algorithms for rapidly changing environmental conditions. In *12th International Conference on Power Electronics and Motion Control EPE-PEMC*, USA.

Suryakumari, J., Sahiti, G., & Sudhakar, G. (2013). Analysis and simulation of perturb and observe MPPT technique. *International Journal of Engineering Research and Applications (IJERA), 3*(4), 1662–1668.

Tahiri, F. E., Chikh, K., Khafallah, M., & Saad, A. (2016). Comparative study between two Maximum Power Point Tracking techniques for Photovoltaic System. In *2nd International Conference on Electrical and Information Technologies ICEIT*, Tangier, Morocco.

Tahiri, F. E., Chikh, K., Khafallah, M., Saad, A., & Breuil, D. (2017). Modeling and performance analysis of a solar PV power system under irradiation and load variations. In *13th International Multi-conference on Systems, Signals and Devices SSD*, Marrakech, Morocco.

Villalva, M. G., Gazoli, J. R., & Ruppert, E. (2009). Modeling and circuit-based simulation of photovoltaic arrays. *Brazilian Journal of Power Electronics, 14*(1), 35–45.

Walker, G. (2000). Evaluating MPPT converter topologies using a Matab PV model. In *Innovation for Secure Power* (pp. 138–143). Brisbane: Queensland University of Technology.

Yadav, P., Bhargava, A., & Sharma, M. (2016). MPPT using soft computing technique with MLI in photovoltaic system. In *International Conference on Micro-Electronics and Telecommunication Engineering*, Ghaziabad, Uttarpradesh, India. IEEE.

Chapter 2
Photovoltaic Power Prediction Using Recurrent Neural Networks

Rim Ben Ammar and Abdelmajid Oualha

Abstract The intermittent characteristic of the photovoltaic power, due to the variability of the weather conditions, involves many problems in grid energy management. Therefore, the PV power forecasting becomes crucial to ensure grid stability and economic dispatch. Artificial neural network (ANN) techniques present alternative approaches to solve nonlinear problems in various areas. They can be trained and applied for prediction. A particular type of ANN namely the recurrent neural network (RNN) has shown powerful capabilities for PV power forecasting. The paper investigates and compares the efficiency of several RNN architectures specifically the modified Elman, Jordan and the hybrid model combining the latest topologies.

The useful data for prediction are acquired from the National Institute of Meteorology. The performance of these topologies is validated by calculating the Root Mean Squared Error, the Mean Absolute Error and the Correlation Factor. The results show that forecasting with the modified Elman outperforms the Jordan and the hybrid networks.

Keywords Artificial neural network · PV power · Forecasting · Prediction · Recurrent neural network · Elman · Jordan

2.1 Introduction

Over the recent years, photovoltaic systems have been progressively installed worldwide as a means of energy production. The intermittent characteristic of the photovoltaic power engenders many problems in grid management (Kou et al. 2013). Thus, PV system power prediction becomes highly recommended to guarantee the grid stability and facilitate the energy dispatching (Grazia De Giorgi

R. B. Ammar (✉) · A. Oualha
Sfax Engineering School, University of Sfax, Sfax, Tunisia
e-mail: abdelmajid.oualha@enis.rnu.tn

N. Derbel, Q. Zhu (eds.), *Modeling, Identification and Control Methods in Renewable Energy Systems*, Green Energy and Technology,
https://doi.org/10.1007/978-981-13-1945-7_2

et al. 2014). Various approaches are used to forecast the pv power production capacity. Physical prediction methods consist in establishing an equation related to the PV system characteristic and the weather data. However, it is limited to a particular weather condition and to a specific PV system (Pelland et al. 2013; Zhu et al. 2015). The artificial neural network presents another potential alternative for developing predictive models as it can solve complex non-linear relationships between input and output data.

There are two major categories of the neural network: the Feed-forward which transmits the data forward from input to output and the recurrent which disposes of a feedback loop where data can be fed back (Abdulkarim 2016).

In the present work, recurrent neural networks were used for short, medium and long term PV power forecasting. A comparative study between them is carried out.

The remaining of this paper was organized as follows. Section 2.2 provided the artificial neural network forecast models. Section 2.3 presented the recurrent neural network topologies. Section 2.4 defined the recurrent neural network training. The recurrent neural network evaluation was proven in Sect. 2.5. In Sect. 2.6, simulation results of the proposed forecasting approaches and their performances evaluation were discussed before drawing our major conclusion in Sect. 2.7.

2.2 Artificial Neural Network Forecast Models

An Artificial Neural Network (ANN) is an information processing paradigm that models operations of biological neural systems.

It consists of an interconnected processing elements (neurons) working in harmony to solve specific problems. The fundamental structure of an ANN includes an input, hidden and output layers. Figure 2.1 shows that the neuron involves two parts: the weights summation and the activation function. The weights summation defines the network inputs combination inside the neurone. The output of the network is related to the inputs through an activation function. The most commonly used activation function is the sigmoid one (Mellit 2009).

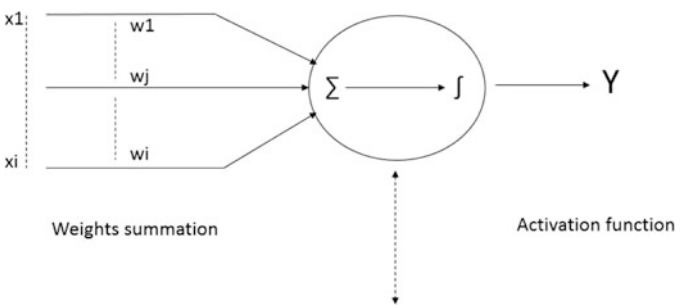

Fig. 2.1 The basic neuron

The ANN showed their notable capability in diverse applications like prediction. The ANN is able to learn the complex relationships between the output and the input after training. Different types of artificial neural networks have been used to solve the forecasting problems. The Radial Basis Function Neural Network (RBFNN) and the Back Propagation neural network (BPNN) are among the tools for the PV power prediction (Dragomir and Dragomirb 2014). Their combination with the wavelet transform leads to more accurate results (Mandal et al. 2012).

Two main types of artificial neural networks have been used for PV system power forecasting. These are the general regression neural network (GRNN) and the feed-forward back propagation (FFBP). A simulation test has shown that the FFBP outperforms the GRNN model (Saberian et al. 2014).

In Zhu et al. (2015), the authors confirm that the hybrid model formed by the ANN and the wavelet decomposition is recommended for PV power prediction.

A methodology based on ANN and the Analog Ensemble (AnEn) technique to procreate forecasts of the photovoltaic power based on weather and astronomical predictions have been presented in Cervone et al. (2017).

In Chow et al. (2012), the authors have used a classical ANN architecture model: multilayer perceptron (MLP) for short-term prediction. The input data are the solar azimuth angles, the solar elevation, the solar radiation data and the dry bulb temperature.

A hybrid method which combines the clear sky PV curves and the ANN called Physical Hybrid Artificial Neural Network (PHANN) have been used for PV system power prediction (Dolara et al. 2015).

The recurrent neural network RNN is another category of ANN.

This methodology is more efficient for PV power production prediction as it supplies feedback to the network. Actually, it provides a dynamic internal feedback loops to store information for later use and improve the learning efficiency. The recurrent neural network is able to deal with non linear prediction and guarantees a faster convergence. Thus, it is the best solution for problems that include dynamic changes over time and dependency on the past values time-series to predict those of the future. This is the case of the PV power forecasting (Mellit and Kalogirou 2008; Wang et al. 2016; Wysocki and Lawryn 2016). The major type of the feedback network is the partially recurrent networks. Among these topologies we can cite the Elman, Jordan and the combination between them.

2.3 Recurrent Neural Networks Topologies

2.3.1 The Modified Elman Neural Network

The modified Elman neural network was proposed by Pham and Liu based on its origin structure presented by Pham. The difference between them lies in the context neuron which has a self feed-back coefficient. The recurrent topology has not only classical layers namely input, hidden, and output, but also, a context layer. The

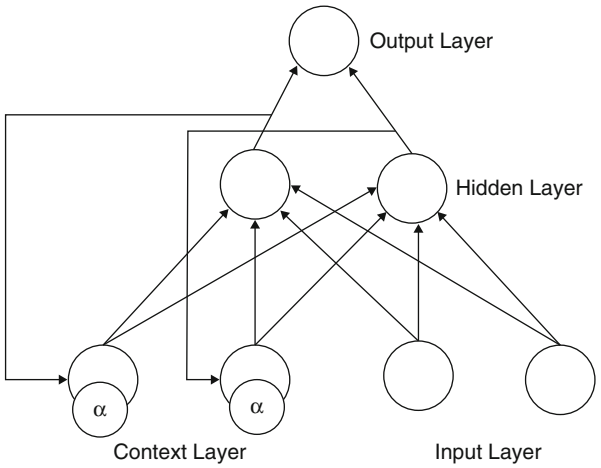

Fig. 2.2 The modified Elman network architecture

context unit is used to store a copy from the output of the hidden layer and from itself (Pham and Liu 1996).

The feedback path enables the modified ENN to perceive temporal and spatial patterns. Figure 2.2 shows the architecture of the modified Elman neural network. The hidden layer output is led for both, output and context layers.

The input layer and the context layer output are sent to the hidden layer input. The weights of the recurrent connections between hidden and context neurons are fixed to one. Hidden and context layers have the same number of neurons (RamaKrishna et al. 2014).

The mathematical model of the modified ENN is depicted in these expressions:

$$v_i(k) = \sum_{j=1}^{n} \omega_{ij}^{x}(k-1)x_j^c(k) + \omega_i^u(k-1)u(k) \tag{2.1}$$

$$x_i(k) = f(v_i) \tag{2.2}$$

$$x_j^c(k) = x_i(k-1) + \alpha x_j^c(k-1) \tag{2.3}$$

$$y(k) = \sum_{i=1}^{n} \omega_i^y(k-1)x_i(k) \tag{2.4}$$

Where n is the number of the context neurons which is equal to the number of the hidden neurons, u is the input of the modified Elman network, y is denoted as the output, v_i presents the total input of the ith hidden unit, x_i and x_j^c are the output of the ith hidden unit and the jth context unit, α is the self feed-back coefficient,

ω_{ij}^{x} designs the weights between context and hidden layers, ω_{i}^{u} defines the weights between input and hidden layers, ω_{i}^{y} characterizes the weights between hidden and output layers.

f is the sigmoid activation function for the hidden layer given by (2.5) (Wei et al. 2007).

$$f(x) = \frac{1}{1 + \exp(-x)} \tag{2.5}$$

For the output layer, the activation function is often taken as a linear function.

2.3.2 *The Jordan Neural Network*

Figure 2.3 shows The Jordan Neural Network (JNN) which was proposed by De Mulder et al. (2015). The JNN output, which is turned back, is stored in a context unit. Each unit receives a copy from the output neurons and from itself. Similar to the modified ENN, the context unit has a self feed-back coefficient which lies between 0 and 1. The output of the context layer is directly connected to the input of the hidden layer. Sigmoid and linear activation functions for the hidden and the output layers, respectively. The Output and context layers have the same number of neurons (Husaini et al. 2011).

The mathematical model of the JNN and the modified ENN differs only in the equation of the context layer which is described by the following expression:

$$x_{j}^{c}(k) = y(k-1) + \alpha x_{j}^{c}(k-1) \tag{2.6}$$

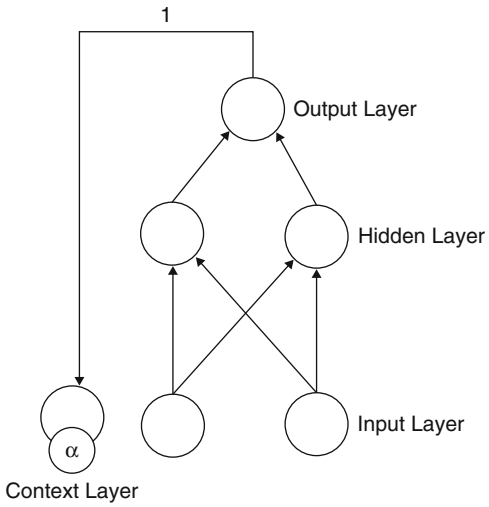

Fig. 2.3 The Jordan neural network architecture

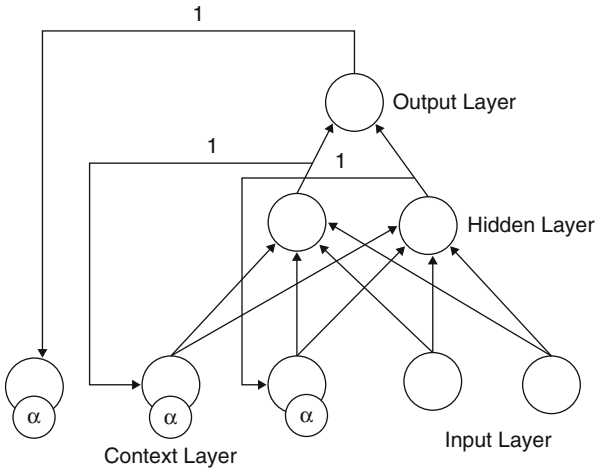

Fig. 2.4 The modified Elman-Jordan neural network architecture

Where x_j^c denotes the output of the jth context unit, y presents the output of the Jordan neural network and α is the self feed-back coefficient.

2.3.3 Hybrid Model: Modified Elman-Jordan Neural Network

The hybrid model is a combination of the modified ENN and the JNN. Figure 2.4 presents the architecture of this network. The output unit is led to the first context layer and the outputs of the hidden nodes are transmitted to the second context layer. The first and the second context units are presented by (2.6) and (2.3) respectively (RamaKrishna et al. 2014).

2.4 Recurrent Neural Network Training

One of the most important characteristics of the artificial neural networks is their ability of learning from patterns. ANN learning paradigms can be arranged as supervised and unsupervised learning. The supervised learning model, as shown in Fig. 2.5, acquires the existence of the desired output for a given set of inputs. It teaches the network the correct response for each sample. The weights are adjusted relying the error between the produced and the required outputs during the training. However, the unsupervised learning model identifes the pattern class information heuristically and does not require the knowledge of the desired outputs (Du and Swamy 2014; Sathya and Abraham 2013).

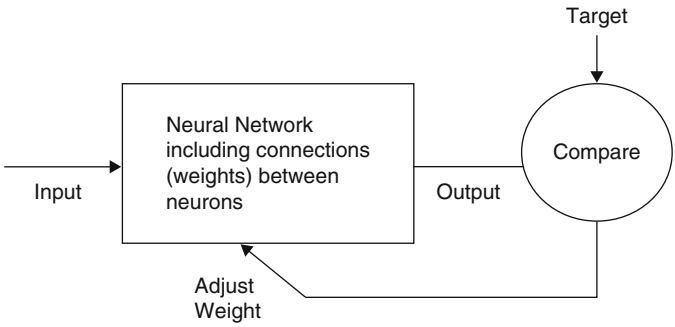

Fig. 2.5 Supervised learning

One of the most popular supervised training algorithms is the standard back propagation. It is used to compute the necessary weights corrections. The first step consists on making a random choice of the weights values of the network. After running, the network outputs are calculated and compared with the desired outputs. Then, the error from the desired and actual outputs is considered. This error is used to update the weights in a backward pass. The whole process is repeated until the error becomes negligible (Pham and Liu 1996).

The back propagation algorithm can be defined by the following expressions:

$$\Delta\omega_i^y(k) = \eta(y_d(k) - y(k))x_i(k) \tag{2.7}$$

$$\Delta\omega_i^u(k) = \eta(y_d(k) - y(k))\omega_i^y(k-1)f_{vi}u(k) \tag{2.8}$$

$$\Delta\omega_{ij}^x(k) = \eta(y_d(k) - y(k))\omega_i^y(k-1)f_{vi}x_j^c(k) \tag{2.9}$$

$$\Delta\omega_i^u(k) = \eta(y_d(k) - y(k))\omega_i^y(k-1)f_{vi}x_j^c(k) \tag{2.10}$$

$$f_{vi} = \frac{\partial f}{\partial v_i} = f(v_i)(1 - f(v_i)) = x_i(k)(1 - x_i(k)) \tag{2.11}$$

where $\Delta\omega_i^y$ presents the weight variation between hidden and output layers, $\Delta\omega_i^u$ characterizes the weight variation between input and hidden layers, $\Delta\omega_{ij}^x$ defines the weight variation between context and hidden layers, y_d is the desired output, y is the output of the network, x_i is the output of the ith hidden unit and v_i presents the total input of the ith hidden unit.

η determines the learning rate, which presents the weight updating step size. This learning rate should be large enough to fit the data well, but small enough to keep away from over-fitting.

It is to be noted that for recurrent neural networks, the learning algorithm is more complex, taking into account the historic of neurons. For this reason, we have used the standard back propagation algorithm dedicated for non recurrent neural

networks. Sometimes, this algorithm gives an unstable network. In this case, the procedure consists on applying the learning algorithm with other initial conditions and tests numerically the stability of the network.

2.5 Recurrent Neural Networks Design

This section detailed all the steps of the neural network design. The first step consisted in defining the number of the neurons in the different layers. In the second step, the necessary data for training and testing the recurrent architectures was presented. Finally, a test of the different topologies was performed using the neural performances evaluation.

2.5.1 Recurrent Neural Networks Design

The number of hidden layers that are necessary to ensure a satisfactory network performance has been a controversial topic. Due to the absence of a theoretical answer, heuristics processes have been assigned and generated that one hidden layer is enough to characterize the task because several hidden layers may produce undesired complexity to the problem (Gabriel 2014). Thus, for the prediction of the photovoltaic power, one hidden layer would be enough.

The modified Elman network has 2 neurons in the input, hidden and context layers and 1 neuron in the output layer. The Jordan network has 2 neurons in the input and hidden layers and 1 neuron in the context and output layers. The hybrid model has 2 neurons in the input and hidden layers, 3 neurons in the context layer and 1 neuron in the output layer.

2.5.2 Data Collection

Meteorological conditions, especially temperature and solar radiation, may affect PV power system efficiency. Thus, we put these two parameters as input data for the recurrent topologies.

The historical data, from 2012 to 2015, are collected from the National Institute of Meteorology. These data are related to the region of Sfax, Tunisia.

The historical data are divided into two categories: the data pertaining to the first 3 years were used for training, whereas, the observations of the last year were reserved for testing the different networks.

The historical data do not have the same magnitude. Thus, they should be normalized in the range of [0 1]. The following formula converts them to the same scale (Carcano et al. 2008).

$$x_{norm} = \frac{x - x_{\min}}{x - x_{\max}} \tag{2.12}$$

Where x_{norm} is the normalized value, x is the actual value, $x_{\max}$ and $x_{\min}$ are the maximum and minimum values.

2.6 Recurrent Neural Networks Evaluation

The connection weights were initially chosen as random numbers.The weights were updated during training using the standard back propagation process. When the error was low enough, the new weights were kept. These values were used for testing the networks.

There is a wide range of functions for neural network performance evaluation such as the Root Mean Squared Error (RMSE), Mean Absolute Error (MAE) and the Correlation Factor given by (2.12), (2.13), and (2.14) (Gabriel 2014; Mellit and Pavan 2010; Zhou et al. 2007).

$$RMSE = 100 \frac{1}{(y_{\max} - y_{\min})} \sqrt{\frac{1}{n} \sum_{i=1}^{n} (y - y_d)^2} \tag{2.13}$$

$$MAE = 100 \frac{1}{(y_{\max} - y_{\min})} \frac{1}{n} \sum_{i=1}^{n} |y - y_d| \tag{2.14}$$

$$R^2 = 100 \left(1 - \frac{\sum_{i=1}^{n} (y - y_d)^2}{\sum_{i=1}^{n} (y - \bar{Y})^2} \right) \tag{2.15}$$

where $y_{\max}$, $y_{\min}$ and $\bar{Y}$ present the maximum, minimum and mean value of the actual data, respectively. y and y_d are the measured and the predicted data.

2.7 Forecast Results and Discussion

The different topologies of the recurrent neural network used for forecasting are created in an m-file using MATLAB. There are three time horizons in the PV power prediction as shown in Fig. 2.6. Short term forecasting is aheived for one day to one week, medium term prediction for more than one weak to one month and long term forecasting for more than one month to one year (Yadav et al. 2015).

The photovoltaic panel used in simulation is SOLAREX-MSX60. Figure 2.7 presents the equivalent electrical circuit model of a PV cell: a current source parallel

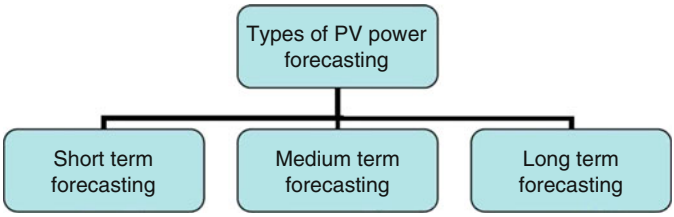

Fig. 2.6 Types of photovoltaic power forecasting

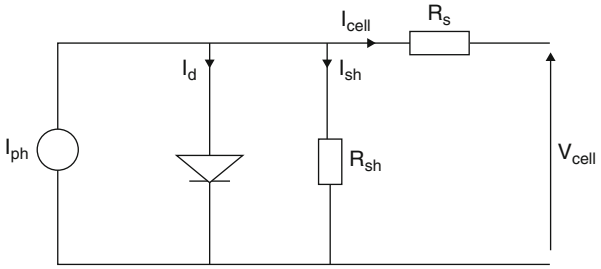

Fig. 2.7 PV cell Equivalent electrical circuit model

with one diode. R_s and R_{sh} are the shunt and the series resistances, respectively (Keles et al. 2013).

The current, the voltage and the power provided by the PV cell are formulated by (2.15), (2.16), (2.17) and (2.18) (Keles et al. 2013).

The cell temperature can be calculated from the Nominal Operating Cell Temperature (NOCT) and the air temperature using (2.19) (Babalola et al. 2014)

$$I_{cell} = I_r + \alpha \frac{G}{G_r}(T_c - T_{cr}) + \left(\frac{G}{G_r} - 1\right) I_{sc} \tag{2.16}$$

$$V_{cell} = -\beta(T_c - T_{cr}) - R_s \Delta(I) + V_r \tag{2.17}$$

$$\Delta(I) = \alpha \frac{G}{G_r}(T_c - T_{cr}) + \left(\frac{G}{G_r} - 1\right) I_{sc} \tag{2.18}$$

$$P = V_{cell} I_{cell} \tag{2.19}$$

$$T_c = T_a + (NOCT - 20)\frac{G}{800} \tag{2.20}$$

where, I_{cell} and V_{cell} are the cell current and voltage. I_r, V_r represent the reference current and voltage. G and G_r are the radiation and the reference radiation.

T_c and T_{cr} are the cell temperature and the reference cell temperature respectively. I_{sc} is the short circuit current. $\Delta(I)$ is the current variation. P is the

Table 2.1 Typical electrical characteristics of SOLAREX-MSX60

P_{max}	V_r	I_r	α	β	I_{sc}	R_s	NOCT
60	17.1 V	3.5	3×10^{-3}	73×10^{-3}	3.8	0.47	47 ± 2
W	V	A	mA/°C	mW/°C	V	Ω	

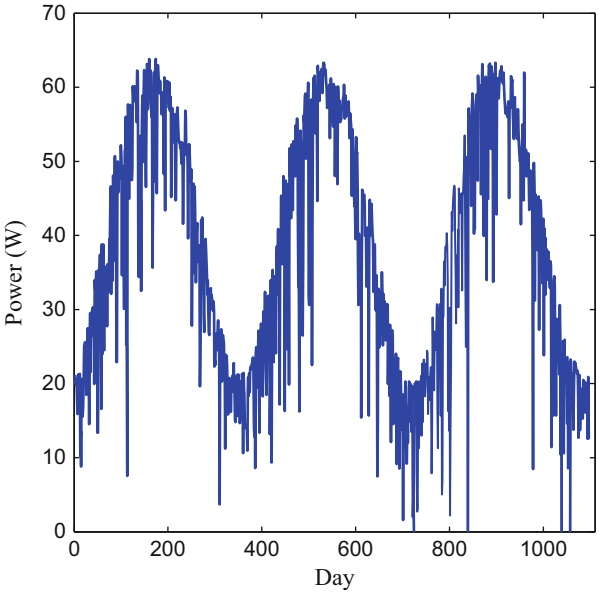

Fig. 2.8 Photovoltaic power

photovoltaic power. T_a defines the ambient temperature. α, β are the short circuit current and the open circuit voltage temperature coefficient.

The parameters of the photovoltaic panel, SOLAREX-MSX60, used in this study are depicted in Table 2.1 for a solar radiation of 1000 W/m^2 and the cell temperature is around 25 °C. These values correspond to G_r and T_{cr}, respectively.

The PV powers, during this period, are calculated using (2.1), (2.2), (2.3), (2.4) and (2.5). Figure 2.8 displays the daily photovoltaic powers of the different years, covering a period of 1097 days.

2.7.1 Short Term Photovoltaic Power Forecasting

2.7.1.1 Daily Forecasts

The curves of the measured and the forecasted power of the photovoltaic panel using the modified ENN, JNN and the hybrid model, are shown in Figs. 2.9, 2.11, and 2.13. From these graphical depictions, it is clear that the predictions are fairly

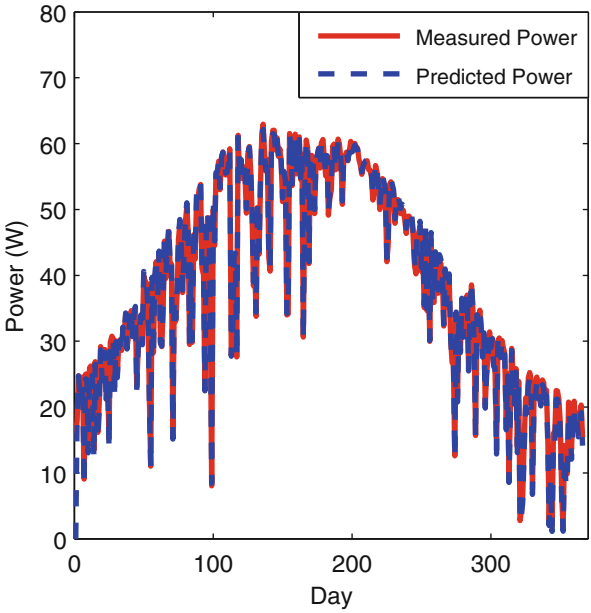

Fig. 2.9 Measured and predicted PV powers with the modified Elman network

close to the actual measurements. The average error of the modified ENN, illustrated in Fig. 2.10, doesn't exceed 2.5%. It is lower than the error of the JNN and the hybrid model displayed in Figs. 2.12 and 2.14, which is in the range of 4% and 6%. Thus the modified Elman network outperforms the other topologies.

To estimate the success of the different recurrent structures, three accuracy evaluators are introduced in Table 2.2 namely RMSE, MAE and the correlation factor, are calculated according to Eqs. (2.12), (2.13) and (2.14).

The lower values of the RMSE and MAE that do not exceed 2.6%, and the higher percentages of the correlation factor which are around 99%, show that a considerable accuracy level was reached by the feedback networks. Nevertheless, the modified ENN demonstrates better forecasting results with a high value of the correlation factor equal to 99.8% and low percentages of RMSE and MAE in the range of 1.3% and 1%. Therefore, it is more efficient for a daily PV power prediction.

2.7.1.2 Weekly Forecasts

In this part, the feedback networks were used for weekly forecasts. The curves of predicted and measured power, showed in Figs. 2.15, 2.16 and 2.17, demonstrate a good agreement between them.

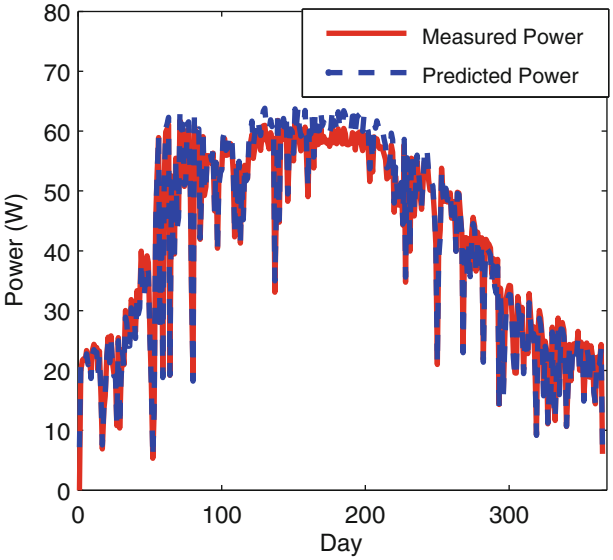

Fig. 2.10 Measured and predicted PV powers with the Jordan neural network

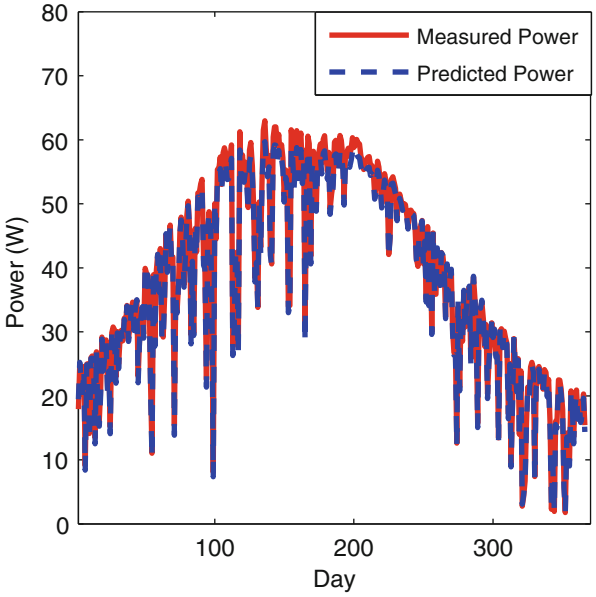

Fig. 2.11 Measured and predicted PV powers with the Hybrid neural network

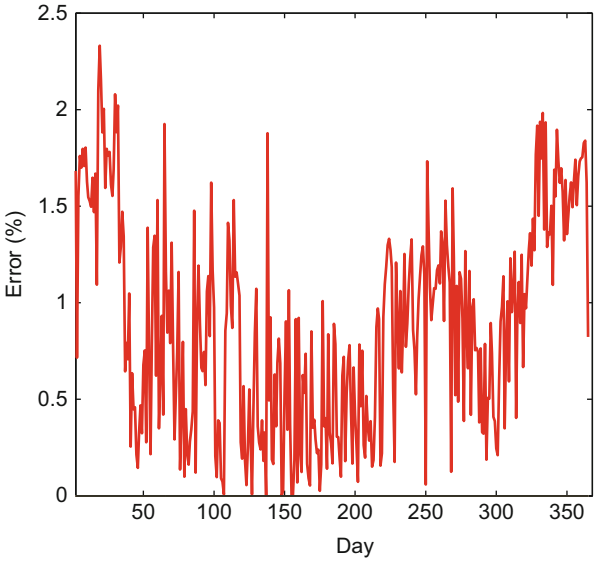

Fig. 2.12 Daily relative forecasting error with the modied Elman network

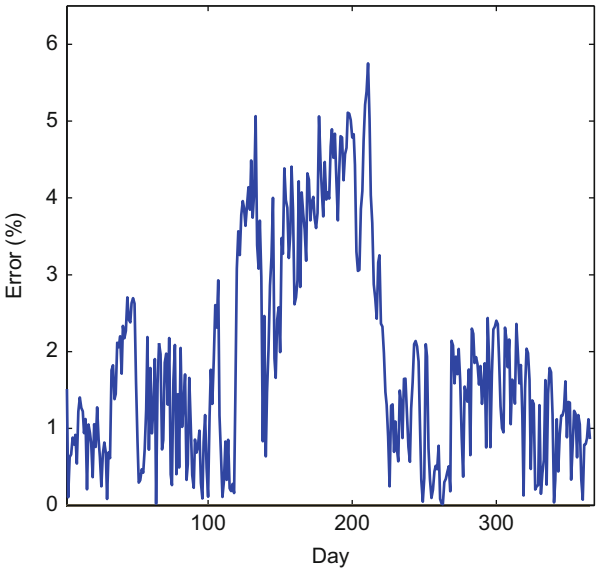

Fig. 2.13 Daily relative forecasting error with the Jordan neural network

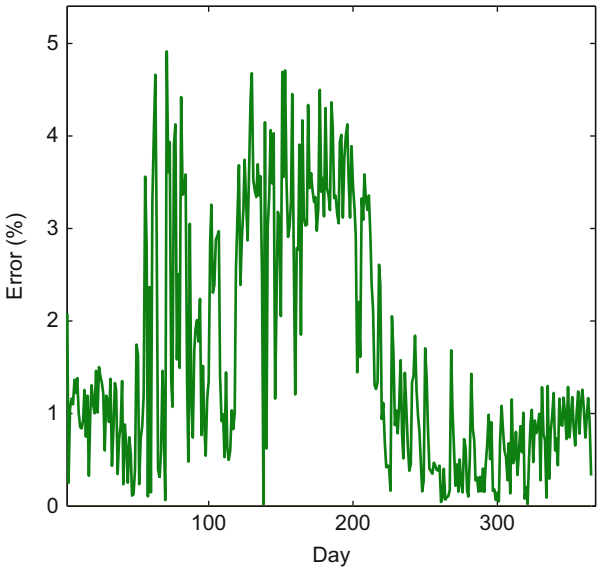

Fig. 2.14 Daily relative forecasting error with the Hybrid neural network

Table 2.2 Daily prediction accuracy evaluation

Accuracy-evaluators	Modified Elman	Jordan	Modified Elman-Jordan
RMSE %	1.3088	2.6358	2.3750
MAE %	1.0007	2.0904	1.8184
R^2 %	99.7962	99.1733	99.3288

In addition, the error rate presented in Fig. 2.18 was less than 9%, which highlighted the accuracy of the predictors.

Furthermore, as it can be seen in Table 2.3, the percentage of the correlation factor obtained from the modified Elman model is equal to 99.8%, the MAE value is only 1.16% and the RMSE value is around 2.1. These percentages are lower than those of the JNN, which are equal to 99.16%, 7.6% and 2.55%, respectively. Also, these rates are lower than those given by the hybrid model, which are equal to 99.43%, 16.41% and 2.3%. Thus, the modified ENN presents a high degree of accuracy for the weekly forecasts.

2.7.2 Medium Term Photovoltaic Power Forecasting: Monthly Forecasts

In the next stage of the study, medium term photovoltaic power forecasting is discussed. The recurrent networks were developed to forecast the monthly PV power. Just like the daily forecasts, the new weights generated after training were

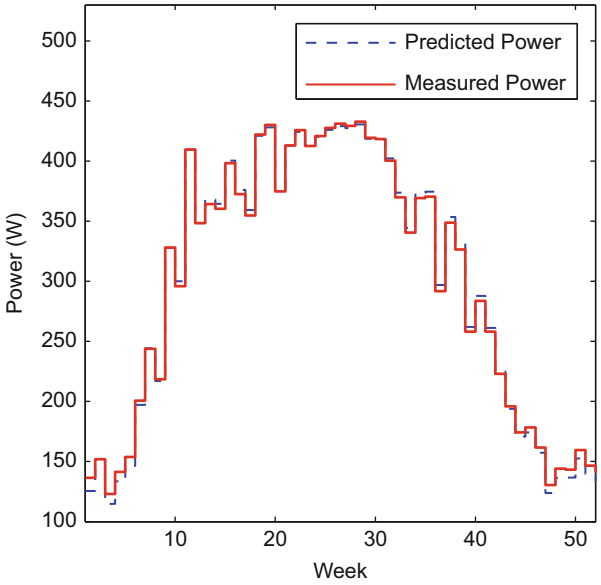

Fig. 2.15 Measured and predicted PV powers with the modified Elman network

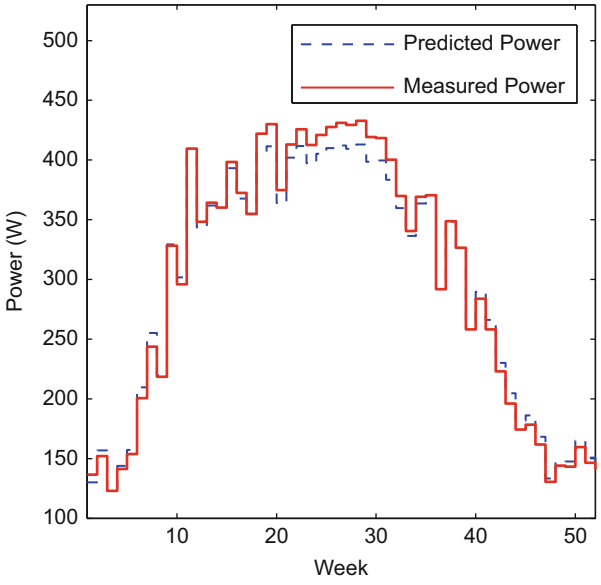

Fig. 2.16 Measured and predicted PV powers with the Jordan neural network

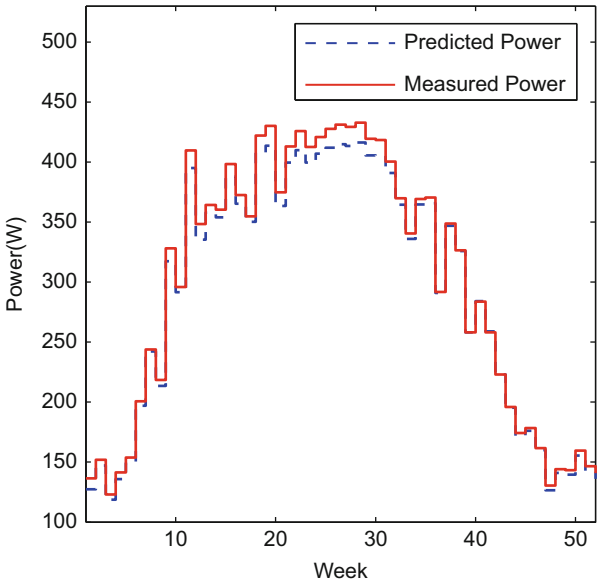

Fig. 2.17 Measured and predicted PV powers with the Hybrid neural network

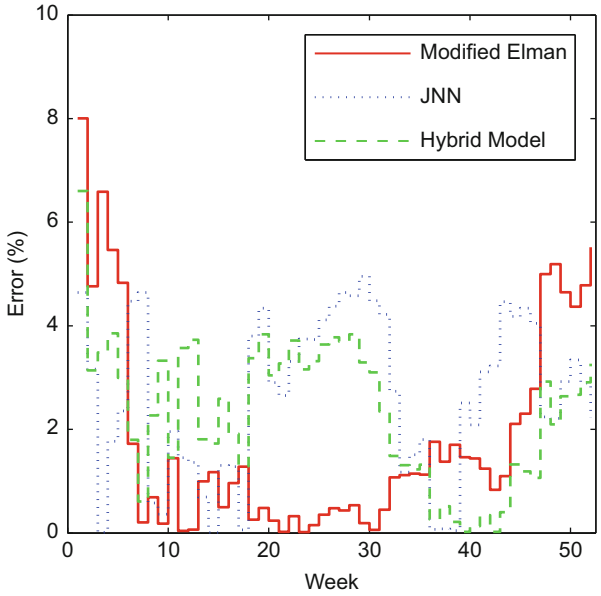

Fig. 2.18 Weekly relative forecasting error

Table 2.3 Weekly prediction accuracy evaluation

Accuracy-evaluators	Modified Elman	Jordan	Modified Elman-Jordan
RMSE%	phantom02.1341	phantom07.5934	16.4117
MAE%	phantom01.1686	phantom02.5540	phantom02.2921
R^2 %	99.8349	99.1631	99.3433

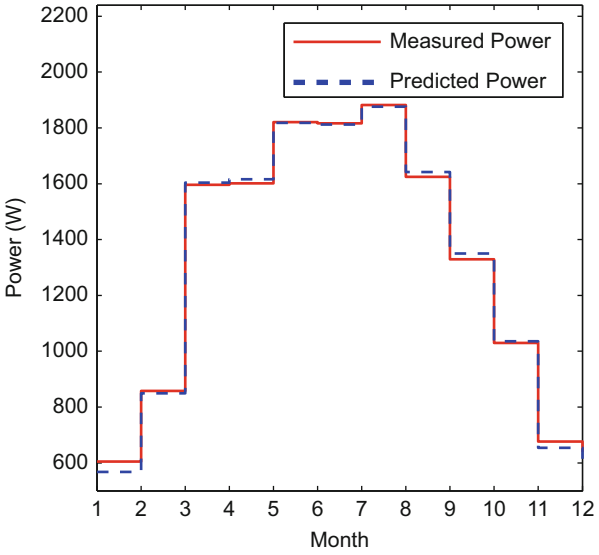

Fig. 2.19 Measured and predicted PV powers with the modified Elman network

used for testing the feedback networks. Figures 2.19, 2.20 and 2.21 show the comparison between the measured and the predicted data.

The curves presented in Fig. 2.22 indicate that the error rate does not exceed 7%. Similar to the daily and weekly predictions, these monthly prognoses seem to be closer to their measured values.

The Several statistical error measures are detailed in table IV. For the modified Elman network, the determination coefficient R^2 is found to be 99.8%; it is higher than 99.2% and 99.3% for the Jordan and the Hybrid networks, respectively. In addition, the RMSE and MAE rates are equal to 1.09% and 1.16%. These values are lower than 3.8% and 2.5% achieved by Jordan network. Also, they are much lower than 8.3% and 2.4% of the hybrid model. All these results confirm that the best predictions are obtained by the modified ENN.

The Monthly average error is smaller than the weekly one. For the modified Elman network, the maximum of error in weekly forecasts is 8%. In the monthly forecasts, the value becomes in the range of 6%. Also, for the Jordan network the maximum of error is reduced from 4.95% to 4.7%. Similarly, the hybrid model recorded a rate decrease from 6.6% to 4.2%. Thus, the forecasting accuracy increases as the forecasting interval is reduced (Table. 2.4).

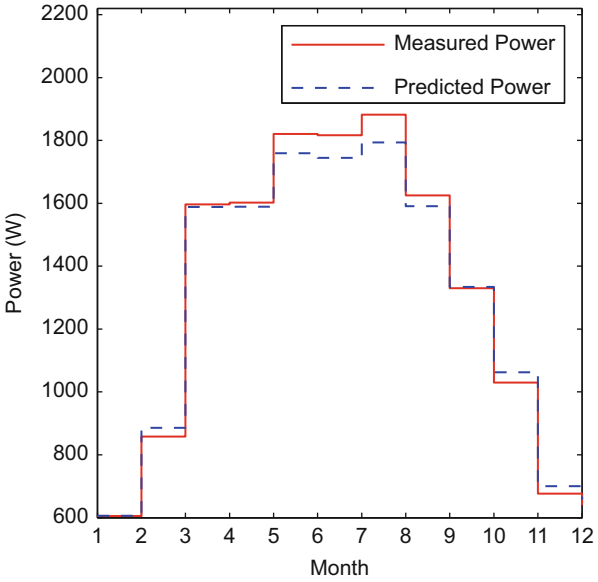

Fig. 2.20 Measured and predicted PV powers with the Jordan neural network

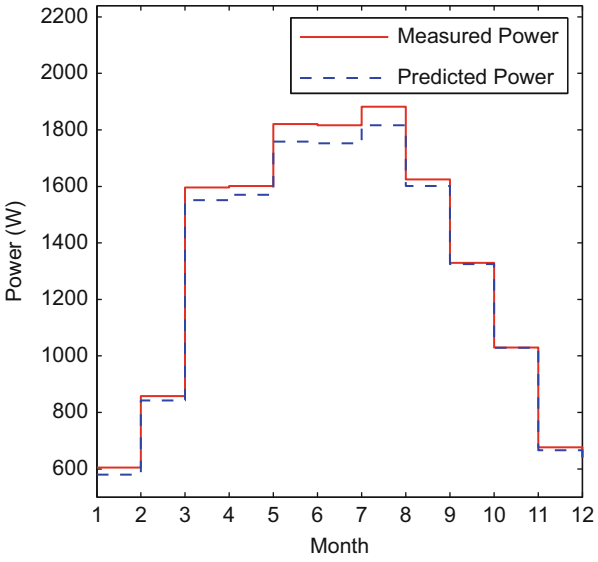

Fig. 2.21 Measured and predicted PV powers with the Hybrid neural network

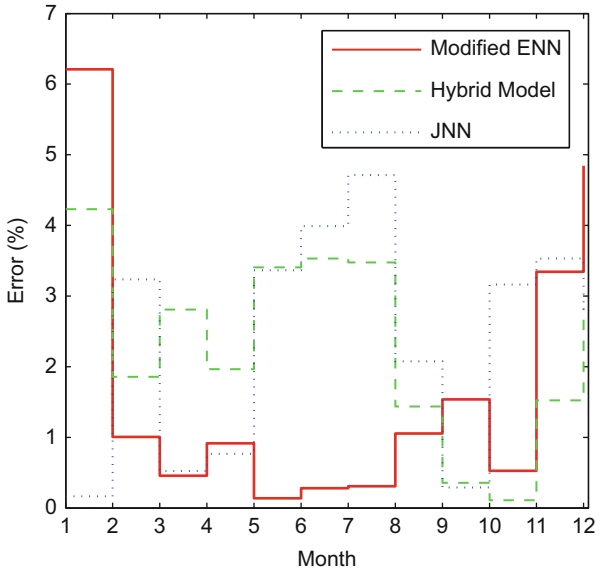

Fig. 2.22 Monthly relative forecasting error

Table 2.4 Monthly prediction accuracy evaluation

Accuracy-evaluators	Modified Elman	Jordan	Modified Elman-Jordan
RMSE %	1.0901	3.8489	8.2965
MAE %	1.1620	2.5019	2.3950
R^2 %	99.8526	99.2340	99.3732

Table 2.5 Yearly prediction accuracy evaluation

Accuracy evaluators	Modified Elman	Jordan	Modified Elman-Jordan
RMSE %	0.3115	1.0998	2.3708
MAE %	0.3115	1.0998	2.3708
R^2 %	99.9990	99.9879	99.9438

2.7.3 Long Term Photovoltaic Power Forecasting: Yearly Forecasts

Finally, long term photovoltaic power forecasting is introduced. The feedback neural networks were also used to try to forecast the yearly photovoltaic power output.

The statistical test between measured and predicted powers is summarized in Table 2.5. This table shows a good statistical behavior for our predictions with a correlation factor of around 99%. For the Jordan network the RMSE and MAE percentages do not exceed 1.1%. In the hybrid model, the average error of the MAE

and RMSE is equal to 2.3%. It can be noticed for the modified Elman network, the MAE is less than 0.4%. Therefore, this proposed network shows superior forecasting performance over the Jordan and the hybrid models.

2.8 Conclusion

The effective analysis of the different topologies of recurrent neural network proposed in this paper for short, medium and long term photovoltaic power forecasting, proved its accuracy with a high correlation factor rate about 99%. The validity of the proposed RNN architectures is confirmed by comparing the predicted and the measured powers. The average of MAPE, RMSE, which do not exceed 2.2%, acquired by the modified Elman neural network is much lower than those obtained with the JNN and the Hybrid models. Hence, the modified ENN shows a higher level of performance to forecast PV system power output. Therefore, it is more efficient when context units are fed from the hidden layer instead of the output layer. Also, the combination between the Jordan network and the modified Elman network induces more complexity on the network without yielding more accuracy than the modified Elman topology. The feedback networks present more accurate results as the forecasting interval is reduced. In fact, the recorded rates of the RMSE and MAE for the monthly forecasts are of smaller values compared to the weekly forecasts.

In conclusion, it can be deduced that the recurrent topologies can be easily adopted for forecasting the PV power and could be widely used for an efficient planning of the renewable systems utilization.

References

Abdulkarim, S. A. (2016). Time series prediction with simple recurrent neural networks. *Bayero Journal of Pure and Applied Sciences, 9*, 19–24.

Babalola, O. S., Komolafe, O. A., Jegede, O. O., & Ayoola, M. A. (2014). Photovoltaic generating system parameter sizing for building. *Journal of Energy Technologies and Policy, 4*, 65–73.

Casaca de Rocha Vaz, A. G. (2014). *Photovoltaic forecasting with artificial neural networks*. Ph.D. Thesis, Faculty of Sciences, University of Lisboa.

Carcano, E. C., Bartolinia, P., Musellib, M., & Piroddic, L. (2008). Jordan recurrent neural network versus IHACRES in modelling daily stream flows. *Journal of Hydrology, 362*, 291–307. Elsevier.

Cervone, G., Harding, L. C., Alessandrini, S., & Monache, L. D. (2017). Short term photovoltaic power forecasting using artificial neural networks and an analog ensemble. *Renewable Energy, 108*, 274–286.

Chow, S. K. H., Lee, E. W. M., & Li, D. H. W. (2012). Short-term prediction of photovoltaic energy generation by intelligent approach. *Energy Build, 55*, 660–667.

De Giorgi, M. G., Maria, C. P., & Malvoni, M. (2014). Photovoltaic power forecasting using statistical methods: Impact of weather data. *IET Science Measurement and Technology, 8*, 90–97.

De Mulder, W., Bethard, S., & Moens, M. F. (2015). A survey on the application of recurrent neural networks to statistical language modeling. *Computer Speech & Language*, 30, 61–98.

Dolara, A., Grimaccia, F., Leva, S., Mussetta, M., & Ogliari, E. (2015). A physical hybrid artificial neural network for short term forecasting of PV plant power output. *Energies, 8*, 1138–1153.

Dragomir, F., & Dragomirb, O. E. (2014). Forecasting of photovoltaic power generation by RBF neural networks. *Advanced Materials Research, 918*, 200–205.

Du, K. L., & Swamy, M. N. S. (2014). *Neural networks and statistical learning*. London/Heidelberg/New York/Dordrecht: Springer.

Husaini, N. A., Ghazali, R., Nawi, N. M., & Ismail, K. H. (2011). Jordan Pi-Sigma neural network for temperature prediction. *Communications in Computer and Information Science, 151*, 547–558.

Keles, C., Alagoz, B. B., Akcin, M., Kaygusuz, A., & Karabiber, A. (2013). A photovoltaic system model for matlab/simulink simulations. In *4th International Conference on Power Engineering, Energy and Electrical Drives*.

Kou, J., Liu, J., Li, Q., Fang, W., Chen, Z., Liu, L., & Guan, T. (2013). Photovoltaic power forecasting based on artificial neural network and meteorological data. In *TENCON 2013 – 2013 IEEE Region 10 Conference, 31194* (pp. 1–4).

Pelland, S., Remund, J., Kleiss, J., Oozeki, T., & Brabandere, K. D. (2013). Photovoltaic and solar forecasting: State of the art. *IEA Intenatioanl Energy Agency, 14*, 1–36.

Mandal, P., Teja, S. S., Ui Haque, A., Meng, J., & Mineda, R. L. (2012). Forecasting power output of solar photovoltaic system using wavelet transform and artificial intelligence techniques. *Progress in Energy and Combustion Science, 12*, 332–337. Elsevier.

Mellit, A. (2009). Recurrent neural network-based forecasting of the daily electricity generation of a photovoltaic power system. In *EVER'09*, Monaco.

Mellit, A., & Kalogirou, S. A. (2008). Artificial intelligence techniques for photovoltaic applications. *Progress in Energy and Combustion Science, 34*, 574–632. Elsevier.

Mellit, A., & Pavan, A. M. (2010). 24-h forecast of solar irradiance using artificial neural network, application for performance prediction of a grid-connected PV plant at Trieste. *Solar Energy, 84*, 221–226. Elsevier.

Pham, D. T., & Liu, X. (1996). Training of Elman networks and dynamic system modelling. *International Journal of Systems Science, 27*, 221–226.

RamaKrishna, K., Ramam, V. A., & Rao, R. S. (2014). Mathematical neural network, MaNN. Models part IV, recurrent neural networks, RecNN. In bio-/chemical-tasks. *Journal of Applicable Chemistry*, *3*(6), 2209–2311.

Saberian, A., Hizam, H., Radzi, M. A. M., Abkadir, M. Z. A., & Mirzaei, M. (2014). Modelling and prediction of photovoltaic power output using artificial neural networks. *International Journal of Photoenergy, 2014,* 1–10.

Sathya, R., & Abraham, A. (2013). Comparison of supervised and unsupervised learning algorithms for pattern classification. *International Journal of Advanced Research in Artificial Intelligence, 2*(2), 34–38.

Wang, J., Wang, J., Fang, W., & Niu, H. (2016). Financial time series prediction using Elman recurrent random neural networks. *Computational Intelligence and Neuroscience, 2016*, 1–14.

Wei, G. H., Qian, F., Chun, L. Y., Du, W., & Wang, L. (2007). Identification and control of nonlinear systems by a dissimilation particle swarm optimization-based Elman neural network. *Nonlinear Analysis Real Word Applications, 9*, 1345–1360.

Wysocki, A., & Lawryn, C. M. (2016). Elman neural network for modeling and predictive control of delayed dynamic systems. *Archives of Control Sciences, 26*, 117–142.

Yadav, H. K., Pal, Y., & Tripathi, M. M. (2015). Photovoltaic power forecasting methods in smart power grid. In *Annual IEEE India Conference (INDICON)*, New Delhi.

Zhou, W., Yang, H., & Fang, Z. (2007). A novel model for photovoltaic array performance prediction. *Applied Energy, 84*, 1187–1198. Elsevier.

Zhu, H., Li, X.,Sun, Q., Nie, L., Yao, J., & Zhao, G. (2015). A power prediction method for photovoltaic power plant based on wavelet decomposition and artificial neural networks. *Energies, 9*, 11.

Chapter 3
A Comprehensive Comparison of Two Behavior MPPT Techniques, the Conventional (Incremental Conductance (INC)) and Intelligent (Fuzzy Logic Controller (FLC)) for Photovoltaic Systems

Aouatif Ibnelouad, Abdeljalil El Kari, Hassan Ayad, and Mostafa Mjahed

Abstract This chapter presents a detailed procedure to study and discuss the behavior of different maximum power point tracking (MPPT) techniques applied to PV systems. In this work, we presented a review on the state-of-the-art of photovoltaic System, DC/DC converter and power point tracking techniques such as conventional one incremental conductance (INC) and soft computing method fuzzy logic controller (FLC) are evaluated. The simulation results obtained are developed under software MATLAB/Simulink. Both methods (INC) and (FLC) are used with a boost DC/DC converter and a load. These results show that the fuzzy logic controller is better and faster than the conventional incremental conductance (INC) technique in both dynamic response and steady state in normal operation.

Keywords MPPT · PV modeling · Technique INC · Technique FLC · Boost DC/DC converter

3.1 Introduction

In recent years, a demand for electric power has been increasing as well as the constraints linked to its production, such as the effect of pollution and global warming, conduct research into the development of renewable energy sources.

A. Ibnelouad (✉) · A. El Kari · H. Ayad
Department of Applied Physics, Laboratory of Electrical Systems and Telecommunications, Faculty of Sciences and Technologies, Cadi Ayyad University, Marrakech, Morocco

M. Mjahed
Department of Mathematics and Systems, Royal School of Aeronautics, Marrakech, Morocco

N. Derbel, Q. Zhu (eds.), *Modeling, Identification and Control Methods in Renewable Energy Systems*, Green Energy and Technology,
https://doi.org/10.1007/978-981-13-1945-7_3

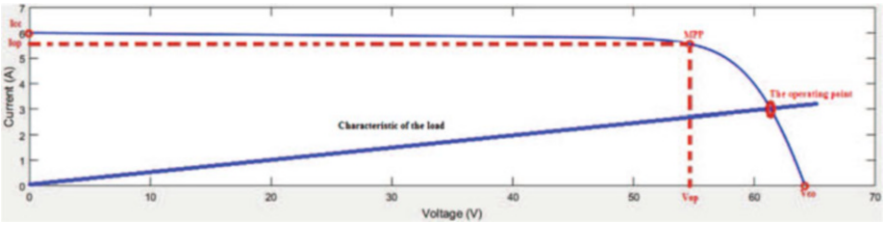

Fig. 3.1 Characteristic $I = f(V)$ of the photovoltaic panel

In this context, photovoltaic solar energy is one of the most important sources of renewable energy, which is an outcome to our problems of energy production. Moreover, this energy seems the most promising, non-polluting and inexhaustible.

Nevertheless, the production of this energy is nonlinear and it varies according to the luminous intensity and the temperature. Therefore, the operating point of the photovoltaic panel PV does not always coincide with the maximum power point (Fig. 3.1).

We use a mechanism that allows the search and tracking of the maximum power point tracking (MPPT) so that the maximum power is permanently generated (Azab 2008).

A MPPT is used for harvesting the maximum energy from the photovoltaic panel PV and transporting that energy to the load, on condition that using an appropriate duty cycle to configure the DC/DC converter. It is essential technique for optimal operation of the photovoltaic system. The principle of this control is based on the automatic variation of the duty cycle of the DC-DC converter, to the optimum value to maximize the power delivered by the PV panel. It used for matching the characteristics of the load with those of the solar panels. A DC/DC converter ensures to transferring maximum energy from photovoltaic panel PV to load. A DC/DC converter is the interface that regulates the adaptation between the photovoltaic panel PV and the load to ensure our load closer to the MPP.

As a result, several studies have focused on photovoltaic systems. They have tried to develop algorithms to extract the maximum energy converted by the panel and then allow an optimal operation of the system photovoltaic system (Zainudin and Mekhilef 2010). Since the 1970s, a significant number of MPPT control techniques have been developed, beginning with simple techniques such as MPPT controllers based on the feedback of voltage and current (Salas et al. 2006), to more efficient controllers using algorithms to calculate MPP of the PVG photovoltaic generator (photovoltaic panel PV), among the most used technique (Incremental conductance (INC)).

In recent years, more robust control techniques have been associated with the MPPT control such as fuzzy logic controller (FLC) in order to increase the efficiency of solar panels.

This chapter is ordered as follows. Section 3.2 describes the PV system modeling, and demonstrates basic operation principle equations for the PV system and differ-

ent connexion with load. A definition and details of calculations to demonstrate the operating principle of the converter DC/DC in its different state (continuous and discontinuous) are given in Sect. 3.3. A brief description of the considered MPPT (INC & FLC) system's architecture is provided in Sect. 3.4. Simulation results for the PV modeling and DC/DC Converter are addressed in Sect. 3.5. Analysis and discussions are illustrated in Sect. 3.6. Finally, conclusions are given in Sect. 3.7.

3.2 PV Systems

A photovoltaic (PV) system directly converts sunlight into electricity. The basic device of a PV system is the PV cell. Cells may be grouped to form panels or arrays (Villalva et al. 2009). These panels prove to be a source of electrical energy that is safe, reliable, maintenance-free and non-polluting. The majority of solar modules on the market today are backed by guarantees of more than 20 years, and they work well beyond that period.

Millions of systems have been installed worldwide, with different power ranging from a fraction of a watt to several megawatts. For many applications, electric solar systems are not only cost effective, but they can also be the least expensive option.

In this chapter, we will begin with the notion and characteristics of the sun and then the operating principle of the photovoltaic cells, thus, we present the different types of photovoltaic cells and their modeling. Finally, we will do a simulation for a direct connection of the photovoltaic generator.

3.2.1 How a PV Cell Works

A photovoltaic cell is a semiconductor diode whose $P - N$ junction is exposed to light (Moller 1993; Sedra et al. 2006). The PV cell produces an effect, which enables the solar energy to be converted directly into electrical energy by means of a semiconductor material carrying the electrical charges. It is broken down into two parts, the first one has an excess of electrons and the other an excess of so-called doped holes, respectively N-type and P-type, as illustrated in Fig. 3.2. When the radiation passes through the PV cell, the photons tear off electrons, which creates free electrons and holes. The electrons accumulate in the N layer, while the holes in the P layer. This gives rise to a potential difference and consequently the flow of a current between the two layers of the cell. The P-doped zone plays the role of the positive pole and the doped zone N plays the role of the negative pole. Subsequently, the growth of the intensity of light will cause the increase of the emission of photoelectrons in the PV material. An anti-reflective material generally covers PV cells so that they can absorb as much solar radiation as possible. In practice, the light absorbed by the solar cell will be the combination of direct solar radiation in addition to the scattered rays radiated from the surrounding surface (Kanji 2012).

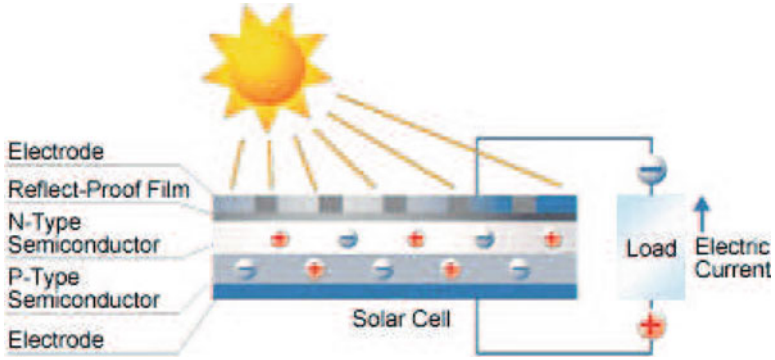

Fig. 3.2 Structure of a cell

Photovoltaic cells are made of several types of semiconductors using different manufacturing processes: Polycrystalline, Monocrystalline and Amorphous thin-film silicon.

1. Polycrystalline silicon: Polycrystalline silicon consists of several single crystals juxtaposed in different orientations giving the cell a mosaic appearance. It is the most widely used technology in the world market because of its good efficiency (about 15%) for controlled manufacturing costs.
2. Monocrystalline silicon: Monocrystalline silicon consists of a single crystal providing the cell with a perfect arrangement of atoms. It has a slightly higher yield than polycrystalline silicon (about 19%).
3. Amorphous thin-film silicon: The silicon is deposited in a thin layer on a glass plate or other flexible support. The irregular organization of its atoms gives it in part a poor semi-conduction.

3.2.2 Solar Panels

The PV cell is the basic unit of a solar panel, but it is intended to produce a small power of a few watts. The need for high power causes the necessity of gathering identical cells to form a module or a solar panel, in order to increase the power generated.

Figure 3.3 shows a typical PV cell assembly. The series connection of several solar cells makes it possible to easily increase the voltage, while the parallel connection leads to a summation of the currents while maintaining the voltage. Therefore, a series-parallel combination is used to obtain a PS with the desired characteristics, that is to say a desired voltage and current.

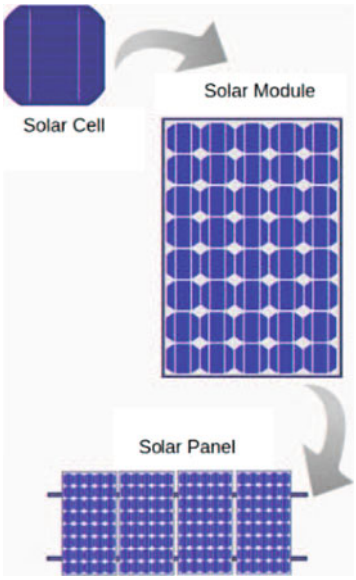

Fig. 3.3 Combination of the PV cell

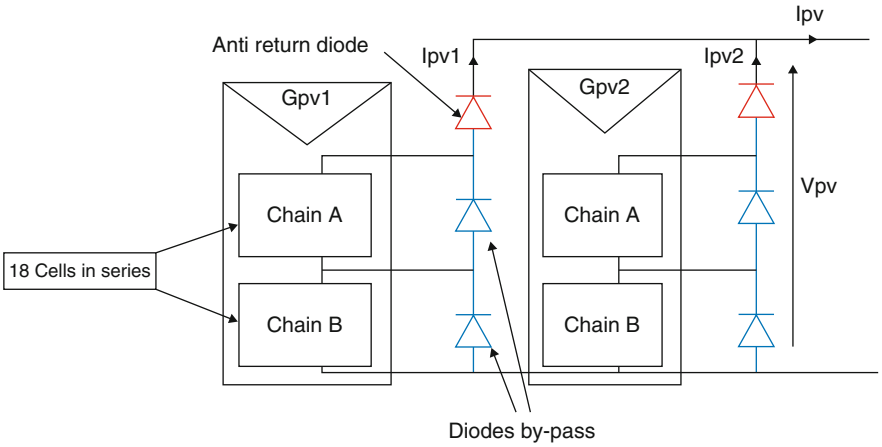

Fig. 3.4 Combination of two PV modules with their protective diodes

3.2.3 Protection of a PV Generator

In order to ensure a long service life for PV generators that tends towards 25 years, it is necessary to add some protections in order to avoid destructive failures resulting from the association of the cells in series and modules in parallel. Often we encounter the By-pass diodes and the anti-return diodes.

1. The anti-return diodes: Fig. 3.4 shows modules associated in series with anti-return diodes. Under the effect of the sun as long as the voltage produced by

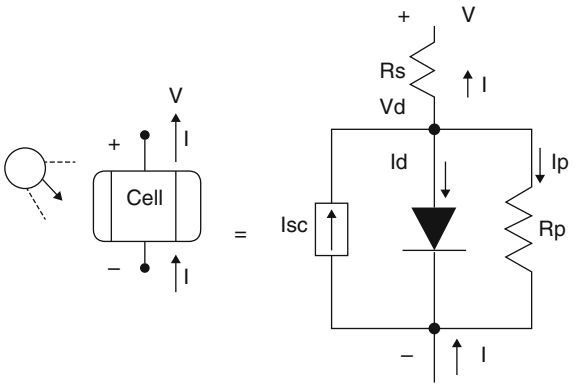

Fig. 3.5 Equivalent model of a GPV

the PV generator is higher than that of the battery, the battery charges. However, when the darkness occurs, no voltage is produced from the PV generator; the battery voltage would cause a current that would flow in the opposite direction through the panels, which can lead to the destruction of the PV generator. Hence, the use of the anti-return diodes will be beneficial to block the current flow and protect the PV generator.

2. By-pass diodes: These diodes are shown in Fig. 3.4. The Bypass diode is connected in parallel but in reverse polarity to a PV cell. In normal operation, each solar cell is directly biased and therefore the Bypass diode will be reverse biased and behaves as an open circuit. However, a cell is reverse biased due to a short circuit between the cells, the By-pass diode conducts while allowing the current to pass from the good solar cells to the external circuits. Then, the maximum inverse polarization across the low cell is reduced to about a voltage drop of a single diode, thereby limiting current, and attenuating hot spots.

3.2.4 Modeling of PV Devices

To be able to study and analyze the behavior of the cells during their operation, modulation of the PV cells is necessary. A PV cell is equivalent to a current generator to which we have added a diode in parallel, Fig. 3.5. The output of the current generator is directly proportional to the light falling on the cell. The current I from the cell is then written (Zagrouba et al. 2010).

3.2.4.1 Ideal PV Cell

Figure 3.6 shows the equivalent circuit of the ideal PV cell. The basic equation from the theory of semiconductors (Rauschenbach 1980; Villalva et al. 2009) that mathematically describes the $I - V$ characteristic of the ideal PV cell is:

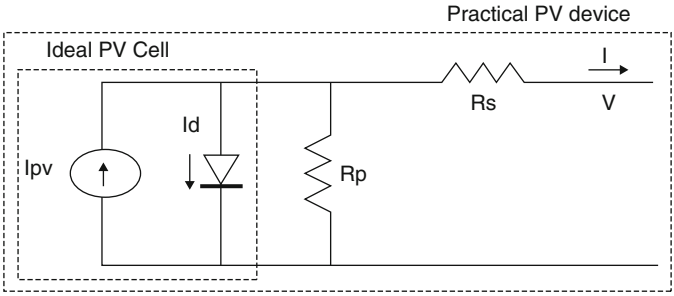

Fig. 3.6 Single-diode model pf the theoretical PV cell and equivalent circuit of a practical PV device including the series and parallel resistances (Villalva et al. 2009)

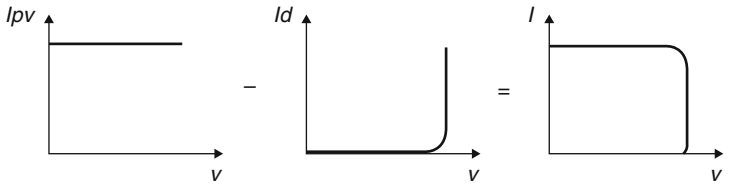

Fig. 3.7 Characteristic $I - V$ curve of the PV cell. The net cell current I is composed of the light-generated current I_{pv} and the diode current I_d (Villalva et al. 2009)

$$I = I_{pv,cell} - I_{0,cell}\left[\exp\left(\frac{qV}{aT}\right) - 1\right] \tag{3.1}$$

where:

- $I_{pv,cell}$ is the current generated by the incident light (it is directly proportional to the Sun irradiation).
- I_d is the Shockley diode equation.
- $I_{0,cell}$ is the reverse saturation or leakage current of the diode.
- q is the electron charge ($1.60217646 \times 10^{-19}$ C).
- k is the Boltzmann constant ($1.3806503 \times 10^{-23}$ J/K).
- T (in Kelvin) is the temperature of the $P - N$ junction.
- a is the diode ideality constant.

Figure 3.7 shows the $I - V$ curve originated from (3.1).

3.2.4.2 Modeling the PV Array

The basic equation (3.1) of the elementary PV cell does not represent the $I - V$ characteristic of a practical PV array. Practical arrays are composed of several connected PV cells and the observation of the characteristics at the terminals of the PV array requires the inclusion of additional parameters to the basic equation

(Rauschenbach 1980; Villalva et al. 2009).

$$I = I_{pv} - I_0 \left[\exp\left(\frac{V + R_s I}{a V_t} \right) - 1 \right] - \frac{V + R_s I}{R_p} \tag{3.2}$$

where:

- I_{pv} and I_0 are the photovoltaic (PV) and saturation currents of the array, respectively.
- $V_t = \dfrac{N_s k T}{q}$ is the thermal voltage of the array with Ns cells connected in series. Cells connected in parallel increase the current and cells connected in series provide greater output voltages. If the array is composed of parallel connections of cells the PV and saturation currents may be expressed as: $I_{pv} = N_p I_{pv,cell}$, $I_0 = N_p I_{0,cell}$.

In (3.2), R_s is the equivalent series resistance of the array and R_p is the equivalent parallel resistance. This equation originates the $I - V$ curve in Fig. 3.8, where three remarkable points are highlighted: short circuit (0, I_{sc}), MPP (V_{mp}, I_{mp}), and open circuit (V_{0c}, 0).

Equation (3.2) describes the single-diode model presented in Fig. 3.6. Some authors have proposed more sophisticated models that present better accuracy and serve for different purposes. For example, in Gow et al. (1999) and Hyvarinen et al. (2003) an extra diode is used to represent the effect of the recombination of carriers. A three-diode model is proposed in Nishioka et al. (2007) to include the influence of effects that are not considered by the previous models. For simplicity, the single diode model of Fig. 3.6 is studied in this paper. This model offers a good compromise between simplicity and accuracy (Carrero et al. 2007), and has been used by several authors in previous works, sometimes with simplifications but always with the basic structure composed of a current source and a parallel diode (Koutroulis et al. 2008; Xiao et al. 2004; Yi-Bo et al. 2008). The simplicity of the single-diode model with the method for adjusting the parameters and the improvements proposed in this paper make this model perfect for power electronics designers who are looking for an easy and effective model for the simulation of PV devices with power converters (Villalva et al. 2009).

All PV array datasheets bring basically the following information: the nominal open-circuit voltage ($V_{0c,n}$), the nominal short-circuit current ($I_{sc,n}$), the voltage at the MPP (V_{mp}), the current at the MPP (I_{mp}), the open-circuit voltage/temperature coefficient (K_v), the short circuit current/temperature coefficient (K_I), and the maximum experimental peak output power ($P_{max,e}$). This information is always provided with reference to the nominal condition or standard test conditions (STCs) of temperature and solar irradiation. Some manufacturers provide $I - V$ curves for several irradiation and temperature conditions. These curves make easier the adjustment and the validation of the desired mathematical $I - V$ equation. Fundamentally, this is all the information one can get from datasheets of PV arrays (Villalva et al. 2009).

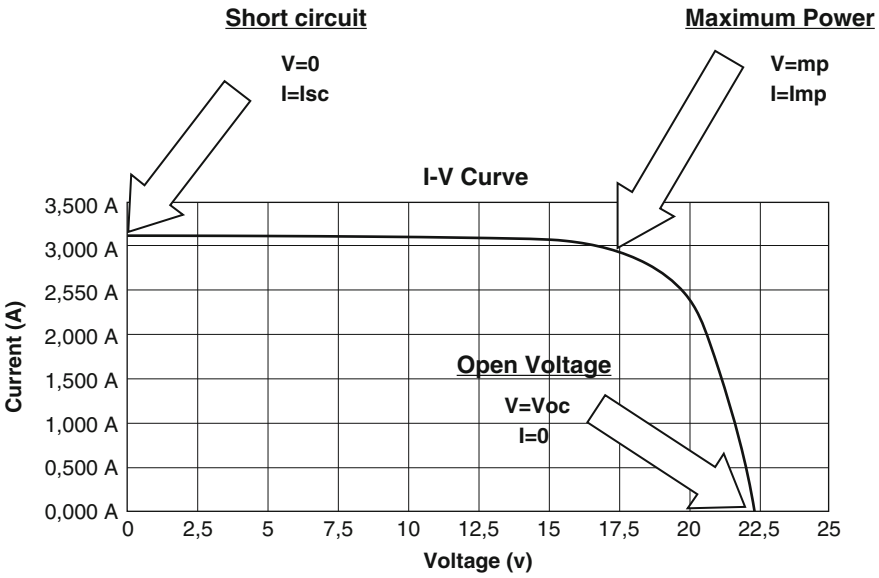

Fig. 3.8 Characteristic $I-V$ curve of a practical PV device and the three remarkable points: short circuit $(0, I_{sc})$, MPP (V_{mp}, I_{mp}), and open circuit $(V_{oc}, 0)$

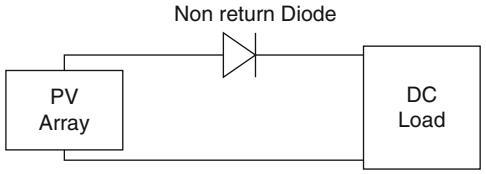

Fig. 3.9 Principle of a direct connection between a PV and a load

3.2.5 Connection (PV Generator-Charge)

3.2.5.1 Direct Connection

When connecting directly a load with a PV array without passing through another electrical device, it is in the case of a direct connection. In this case, the operating point of the PV array depends on the impedance of the load to which it is connected (Amarouayache 2014).

Figure 3.9 shows the principle of a direct connection between a PV and a load. In general, the power extracted from a PV generator directly connected to an application is often very far from the maximum power (MPP) that the PV generator can deliver, as shown in Fig. 3.9.

As shown in Fig. 3.10, a PV generator can be connected directly to three types of DC loads:

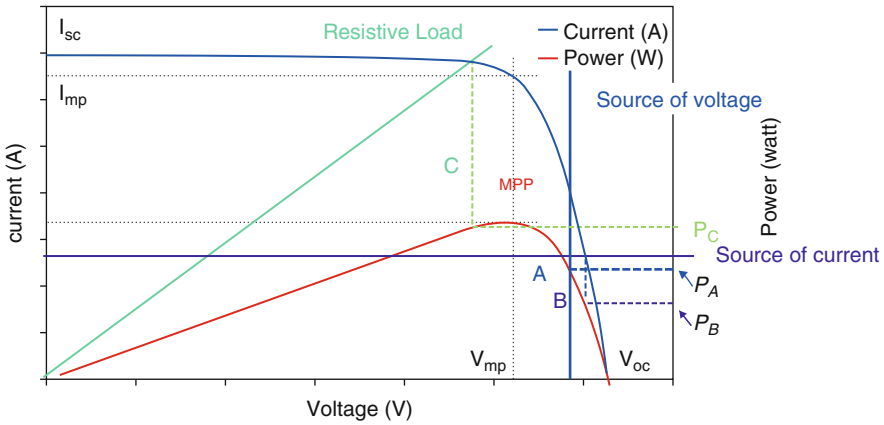

Fig. 3.10 Operating points of a GPV in direct connection, depending on the load

- Direct current source type load.
- DC source load.
- Purely resistive load.

Three respective operating points A, B, C can be identified providing power P_A, P_B and P_C. These scenarios show that the GPV is badly exploited and does not provide the maximum potential power. The difference being lost as dissipated heat in the generator.

3.3 DC/DC Converter

DC/DC converters convert DC power to another DC level (voltage/current to voltage/current). Their outputs are controlled by pulse width modulation (PWM) of the gate signals. Switching frequency of the gate signal, in most cases, is high and constant. In practice, their outputs are usually regulated by closed loop control. Output DC voltage level of DC/DC converters can be stepped up, stepped down, both stepped up and down, and inversed. In this project, we are specifically interested in study of buck converter according to the project specification.

3.3.1 Topologies of DC/DC Converters

DC/DC converters can be classified as non-isolated DC/DC converters and isolated DC/DC converters. Six most popular topologies of non-isolated DC/DC converters (also called classical type DC/DC converters) are as below. All of them are single-transistor converters. They are:

- Buck converter (step-down voltage only).
- Boost converter (step-up voltage only).
- Buck/Boost converter (inverse voltage, and step-up/step-down voltage).
- Cuk converter (inverse voltage, and step-up/step-down voltage).
- Zeta converter (step-up/step-down voltage).
- Sepic converter (step-up/step-down voltage).

There are four most popular topologies of isolated DC/DC converters. All of them are able to step-up or step-down voltage. They are:

- Fly back converter (single-transistor).
- Forward converter (single-transistor).
- Single-ended two-transistor forward converter.
- Phase shift full-bridge converter.

3.3.2 Applications of DC/DC Converters

The DC-DC converter products are used extensively for diverse applications in the healthcare (bio life science, dental, imaging, laboratory, medical), communications, computing, storage, business systems, test and measurement, instrumentation, and industrial equipment industries. They are used in electric motor drives, in Switch mode DC power supplies etc.

3.3.3 Comparison of Montages

Table 3.1 summarizes the voltage gains and the stresses on the switches of the different assemblies. For these converters, if more than one arrangement can be considered as an elevator, especially if the duty cycle is greater than 0.5, only the Boost system is lifted over the entire range of the duty cycle. For a cyclic ratio of 0.5, for example, the Boost has a double output voltage of the input voltage. Whereas

Table 3.1 Characteristics of continuous and discontinuous conduction systems

Converter	Voltage gain	V_{kmax} $\lvert V_{dmax}\rvert$	i_{kmax} $\lvert i_{Dmax}\rvert$	Current source
Boost	$\frac{1}{1-\alpha}$	$\frac{V_e}{1-\alpha}+\frac{\Delta V_s}{2}$	$\frac{I_s}{1-\alpha}+\frac{\alpha V_e}{2Lf}$	Continuous
Buck	α	V_e	$I_s+\frac{\alpha(1-\alpha)V_e}{2Lf}$	Discontinuous
Buck-Boost	$\frac{\alpha}{1-\alpha}$	$\frac{V_e}{1-\alpha}+\frac{\Delta V_s}{2}$	$\frac{I_s}{1-\alpha}+\frac{\alpha V_e}{2Lf}$	Discontinuous
Sepic	$\frac{\alpha}{1-\alpha}$	$\frac{V_e}{1-\alpha}+\frac{\Delta V_s+\Delta V_c}{2}$	$\frac{I_s}{1-\alpha}+\frac{\alpha V_e}{2f}\left(\frac{1}{L_1}+\frac{1}{L_2}\right)$	Continuous
Fly-Back	$\frac{m\alpha}{1-\alpha}$	$V_e+\frac{V_s}{m}$	$\frac{mI_s}{1-\alpha}+\frac{\alpha V_e}{2L_1 f}$	Continuous

for the other risers the output voltage for this value of the duty cycle is equal to the input voltage. It is only when the duty cycle is close to 1 that the other risers tend to resemble the Boost circuit (Naffouti 2012).

3.3.4 DC-DC Adaptation Circuit of Type BOOST

In order to have a higher DC voltage at the output necessary to supply the various loads directly or indirectly (through an inverter for example), a value which will be mentioned hereafter according to the study to be carried out later, which depends ontThe characteristic of the coupled load. Taking into account the economic constraints, this brings us to the use of a voltage-boosting DC/DC converter, this is the Boost chopper assembly (also called boost chopper or parallel chopper). This type of static converter makes it possible to convert a DC voltage into another DC voltage of higher value (Naffouti 2012).

In the following, we will study the operating of this structure in order to determining the relationships between the different electrical signals.

3.3.4.1 Operation of the Boost Chopper

Presentation of the Structure

The schematic diagram of a Boost chopper is given in the Fig. 3.11. This structure is composed mainly of an inductor L and two switches and D. Depending on the state of these two switches, two operating phases can be distinguished (Reza Reisi et al. 2013):

- The active phase when the switch is closed and the switch D is open. During this sequence, the current flowing through the inductor L will increase linearly and an energy is stored in L. The capacitor C supplies energy to the load R.

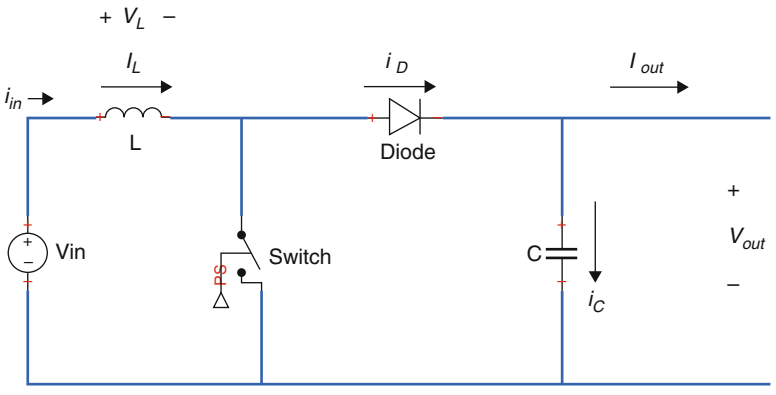

Fig. 3.11 Diagram of a boost converter DC/DC

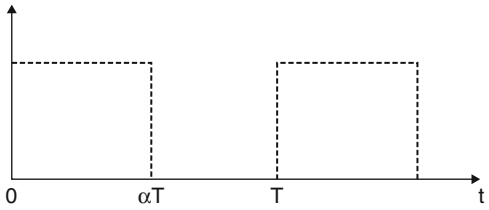

Fig. 3.12 Control signal of the switch T_r

- The freewheel phase when the switch is open, the switch D is closed. During this sequence, the energy stored in the inductance L is restored to the capacitor and to the charge R. During this phase, the fact that the inductance L is in series with the source of input voltage makes it possible to obtain a boosting circuit.

Figure 3.12 shows the pattern of the control signal applied to switch T_r. It is a rectangular signal of frequency f whose the duration is in the high state (duration of conduction of the switch T_r, denoted T_{ON}) is adjusted by the parameter α. This parameter, called the duty cycle, Is defined as the ratio between the duration of conduction of the switch T_r and the cutting period T of the latter: $\alpha = \frac{T_{ON}}{T}$, we have: $T = T_{ON} + T_{OFF}$, whither T_{OFF} Corresponds to the duration of blocking of the switch T_r.

The duration of conduction, T_{on} is between 0 and T therefore, the duty cycle is between 0 and 1. The duration of conduction and of blocking of the switch T_r can be expressed as a function of α and T:

- Duration of conduction: $T_{ON} = \alpha T$
- Blocking time: $T_{OFF} = (1 - \alpha)T$

In the following study, we will make the following assumptions:

- The supply voltage is continuous and constant.
- The value of the capacitor C is large enough so that the output voltage can be considered as continuous.
- The components are ideal.

Two conduction regimes can be distinguished:

- Continuous conduction, which corresponds to the case where the current through the inductance never vanishes.
- The discontinuous conduction, which corresponds to the case where the current passing through the inductance cancels before the next active phase.

Continuous Conduction

In the following, we explain the behavior of the structure as a function of these two conduction regimes. The main objective is to determine the relationships between the quantities electrical input and output of the converter as well as formulas for dimensioning the various components (Naffouti 2012).

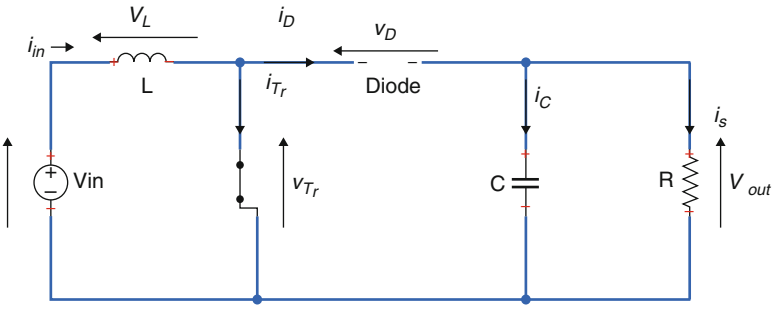

Fig. 3.13 Equivalent diagram of the Boost chopper during the active phase

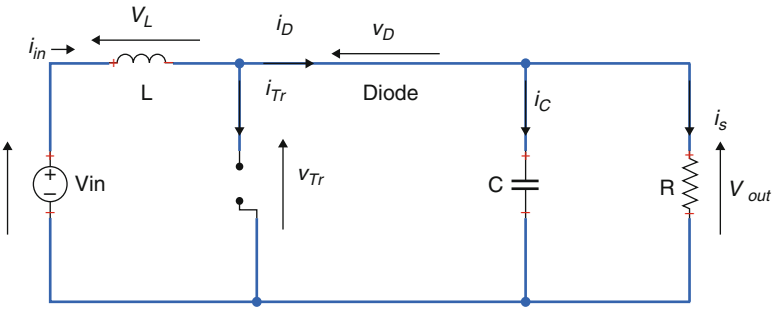

Fig. 3.14 Equivalent diagram of the Boost chopper during the freewheeling phase

Sequence 1: Active Phase: $0 < t < \alpha T$

At the instant $t = 0$, the switch is closed for a period αT. The voltage across the diode D is equal to $V_D = V_{Tr} - V_{out}$. Since the switch T_r is closed, we have $V_{Tr} = 0$, which implies that $V_D = -V_{out}$. The diode is thus blocked since $V_{out} > 0$. Under these conditions, we obtain the equivalent diagram of Fig. 3.13.

The voltage at the terminals of the inductance is then:

$$V_L = V_{in} = L\frac{di}{dt} \tag{3.3}$$

By solving this differential equation, we obtain the following expression, which expresses the evolution of the current flowing through the inductance:

$$i_L = \frac{V_{in}}{L}t + I_{Lmin} \tag{3.4}$$

Sequence 2: Freewheel Phase; $\alpha T < t < T$

At the instant $t = \alpha T$, the switch is opened for a duration $(1 - \alpha)T$. To ensure the continuity of the current, the diode D goes into conduction. We then obtain the equivalent diagram of Fig. 3.14.

The voltage at the terminals of the inductance is then:

$$V_L = V_{in} - V_{out} = L\frac{di_L}{dt} > 0 \tag{3.5}$$

By solving this differential equation, we obtain the following formula, which expresses the evolution of the current passing through the inductance:

$$i_L = \frac{V_{in} - V_{out}}{L}(t - \alpha T) + I_{Lmax} \tag{3.6}$$

Expressions of V_{out} and I_s

By definition:

$$\langle V_L \rangle = \frac{1}{T}\int_0^T V_L dt = \frac{1}{T}\int_0^{\alpha T} V_{in} dt + \frac{1}{T}\int_{\alpha T}^{T} (V_{in} - V_{out}) dt \tag{3.7}$$

Since the mean voltage at the terminals of a steady state, inductance is zero, we can write:

$$\langle V_L \rangle = \alpha T V_{in} + (1 - \alpha)(V_{in} - V_{out}) = 0 \tag{3.8}$$

Finally, we obtain the following relation:

$$V_{out} = \langle v_{out}(t) \rangle = \frac{V_{in}}{1 - \alpha} \tag{3.9}$$

The duty cycle α is between 0 and 1, so the output voltage V_s is necessarily higher than the input voltage V_{bat} (boosting circuit).

If we assume that the input current is perfectly continuous, we can write:

$$I_s = \langle i_s(t) \rangle = \frac{1}{T}\int_{\alpha T}^{T} I_{in} dt \tag{3.10}$$

which leads to:

$$I_s = I_{in}(1 - \alpha) \tag{3.11}$$

This expression clearly shows that the Boost chopper is a step-down device. With regard to these various expressions, it can be noted that the duty cycle α makes it possible to adjust the average output voltage (or mean output current) for a given average input voltage (respectively an average input current). It is therefore possible to adjust the average power transfer between the input and the output of the structure from the duty cycle α (Naffouti 2012).

The average power transfer is:

$$P = \langle p \rangle = (1 - \alpha) V_{out} I_{in} \tag{3.12}$$

Expression of ΔI_L:

The absolute ripple of the current i_L is defined by $\Delta I_L = I_{Lmax} - I_{Lmin}$. From the above relations, at $t = \alpha T$, we can write $I_{Lmax} = \frac{V_{in}}{L} \alpha T + I_{Lmin}$. We deduce the following expression of $\Delta I_L = \frac{\alpha V_{in}}{Lf}$. This expression shows that the current ripple decreases when the switching frequency f increases the value of the inductor L. As $V_{in} = (1 - \alpha) V_{out}$, we can write:

$$\Delta I_L = \frac{\alpha (1 - \alpha) V_{out}}{Lf} \tag{3.13}$$

By solving $\frac{d \Delta I_L}{dt} = 0$, it is found that the current ripple ΔI_L is maximum for $\alpha = \frac{1}{2}$. The dimensioning of the inductance L, from a given current ripple is carried out using the following inequality:

$$L \geq \frac{V_{out}}{4 f \Delta I_{Lmax}} \tag{3.14}$$

Voltage Ripple

To determine the expression of the voltage ripple ΔV_{out}, it is assumed that the current I_s is perfectly constant. We have the following relation: $i_c = C \frac{d V_{out}}{dt}$, and for $0 < t < \alpha T$: we have $i_c = -I_s$, then the resolution of this differential equation gives us:

$$V_{out} = -\frac{1}{C} I_s t + V_{outmax} \tag{3.15}$$

For $t = \alpha T$, we have:

$$V_{out}(\alpha T) = V_{outmin} = -\frac{1}{C} I_s \alpha T + V_{outmax} \tag{3.16}$$

Then, we have:

$$\Delta V_{out} = V_{outmax} - V_{outmin} = \frac{1}{C} I_s \alpha T \tag{3.17}$$

Finally:

$$\Delta V_{out} = \frac{\alpha V_{out}}{RCf} \tag{3.18}$$

This expression shows that the voltage ripple decreases when the switching frequency f or the value of the capacitor C increases.

The dimensioning of the capacitor C, starting from a given ripple voltage, is carried out using the following inequality:

$$C > \frac{\alpha_{max} V_{out}}{Rf \Delta V_{out}} \tag{3.19}$$

Waveforms of the Main Signals

The waveforms of the main signals are given in Fig. 3.15. From these waveforms, the mean and effective values of the currents flowing through the diode D and the switch T_r can be expressed. We can also deduce the maximum stresses in voltage and current from the switches. These relationships will be used when dimensioning the various components of the structure (Naffouti 2012).

- Average current flowing through diode D:

$$I_D = \langle i_D \rangle = I_s \tag{3.20}$$

- Efficient current flowing through diode D:

$$I_{Deff} = \sqrt{(1-\alpha)\left[\left(\frac{I_s}{1-\alpha}\right)^2 + \frac{\Delta I_L^2}{12}\right]} \tag{3.21}$$

- Average current flowing through the switch T_r:

$$I_{Tr} = \langle i_{Tr} \rangle = \frac{I_s}{1-\alpha} = I_{pv} \tag{3.22}$$

- Efficient current flowing through switch T:

$$I_{Deff} = \sqrt{\alpha\left[\left(\frac{I_s}{1-\alpha}\right)^2 + \frac{\Delta I_L^2}{12}\right]} \tag{3.23}$$

The voltage and current stresses on the controlled switch T_r and the diode D are the same.

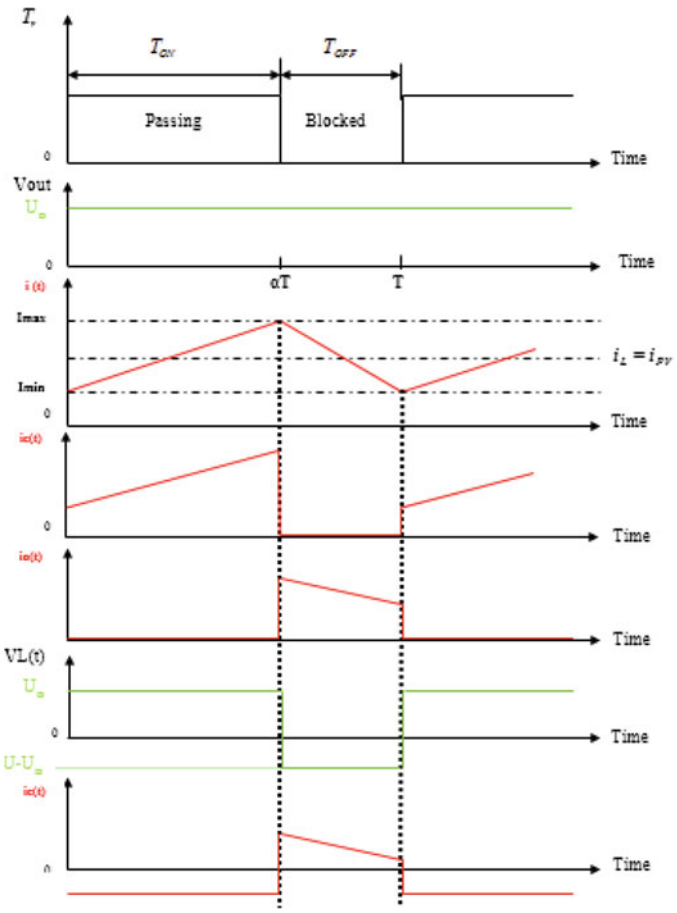

Fig. 3.15 The appearance of the voltages and currents in continuous conduction mode

- Maximum voltage constraints

$$V_{Trmax} = |v_{Dmax}| = v_{outmax} = \frac{V_{in}}{1-\alpha} + \frac{\Delta V_{out}}{2} \tag{3.24}$$

- Maximum current constraints

$$I_{Trmax} = i_{Dmax} = i_{Lmax} = \frac{I_s}{1-\alpha} + \frac{\Delta I_L}{2} \tag{3.25}$$

The dimensioning of the switching cell takes place in the worst case. To calculate the worst-case voltage and current constraints, we need to replace in the above expressions α by α_{max}.

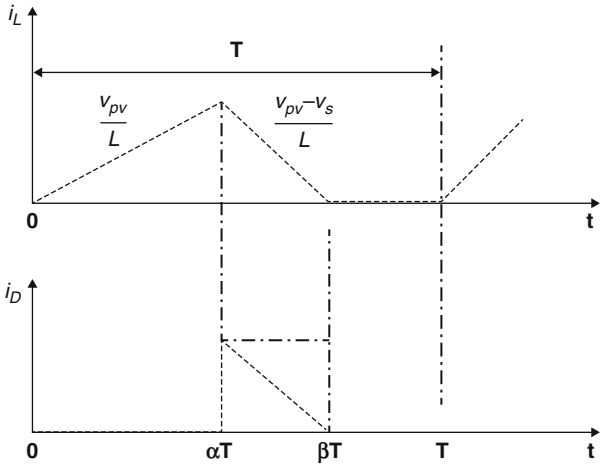

Fig. 3.16 Current flowing through the inductor in continuous conduction

Discontinuous Conduction

In discontinuous conduction, a phase is added during which the diode D does not conduct.

From the curve of i_L in Fig. 3.16, Δt can be deduced from the cancellation time of this current: for $\alpha T < t < \beta T$, $\Delta t = (\beta - \alpha)T$:

$$i_L(t) = \frac{V_{in} - V_{out}}{T}(t - \alpha T) + I_{L\alpha T} \tag{3.26}$$

and $i_L(\beta T) = 0$.

In addition, with $i_L(\alpha T) = \frac{V_{in}}{T}\alpha T$, we have: $\Delta t = \frac{V_{in}}{V_{in} - V_{out}}\alpha T$. The average output current is:

$$I_s = \langle i_s \rangle = \langle i_D \rangle = \frac{1}{T}\int_{\alpha T}^{\beta T} i_L(t)dt = \frac{1}{2} i_L(\alpha T)(\beta - \alpha) \tag{3.27}$$

which leads to:

$$I_s = \frac{\beta^2 V_{in}^2 T}{2L(V_{out} - V_{in})} \tag{3.28}$$

or else:

$$V_{out} = V_{in}\left(1 + \alpha^2 \frac{V_{in}}{2Lf I_s}\right) \tag{3.29}$$

In this operating mode, the output voltage is therefore load-dependent for a fixed duty cycle. This implies that, in discontinuous conduction, it is necessary to implement a control loop.

Power Available or Exchanged

$$P = \frac{1}{T}\int_0^T V_{out}\langle i_s(t)\rangle dt = \frac{\alpha^2 T}{2L} \times \frac{V_{out}V_{in}^2}{V_{out} - V_{in}} \tag{3.30}$$

Critical Conduction

This phase defines the limit between continuous and discontinuous regimes. For α_{limit}, we have: $\Delta t = (\beta - \alpha)T = (1 - \alpha)T$ that is to say $\beta T = T$.

$$\Delta t = \frac{V_{in}}{V_{out} - V_{in}}\alpha_{lim} T = (1 - \alpha_{lim})T \tag{3.31}$$

which ultimately gives us:

$$\alpha_{lim} = \frac{V_{out} - V_{in}}{V_{out}} \tag{3.32}$$

3.4 Maximum Power Point Tracking (MPPT) Techniques

As mentioned before, the temperature and the irradiation depend on the atmospheric conditions, which are not constant during the year and not even during a single day; they can vary rapidly due to fast changing conditions such as clouds. This causes the MPP to move constantly, depending on the irradiation and temperature conditions in Fig. 3.17. If the operating point is not close to the MPP, great power losses occur. Hence, it is essential to track the MPP in any conditions to assure that the maximum available power is obtained from the PV panel. In a modern solar power converter, this task is entrusted to the MPPT algorithms.

Maximum power point tracking (MPPT) aims to ensure that at any irradiation or temperature, maximum achievable power is extracted from the PV system. This is done by adjusting the duty cycle of the DC-DC converter, i.e. the converter's duty cycle is adjusted in a way that the operating point matches maximum point of P-V curve. MPPT is a very important problem in PV systems, since extraction of maximum achievable power from PV systems is of utmost importance. A MPPT system directs the operating point of PV system toward maximum power point (Rezaee Jordehi 2016). An efficient MPPT strategy must feature the following properties:

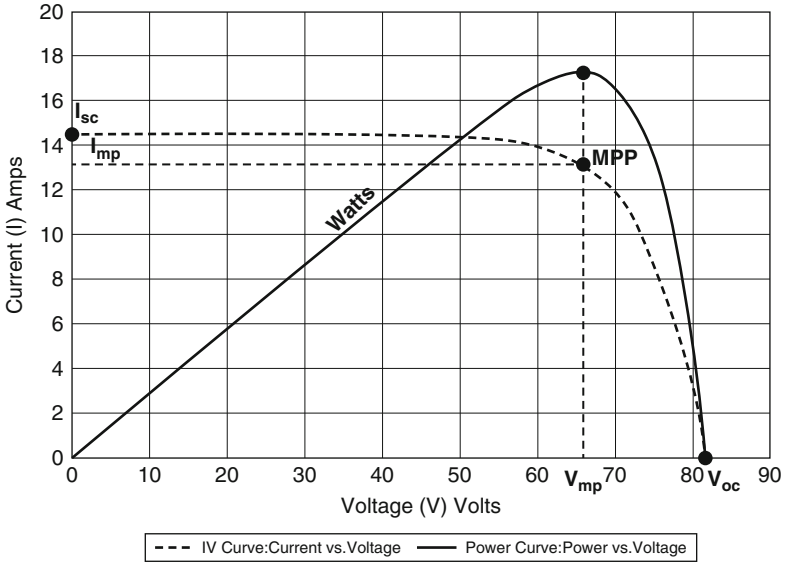

Fig. 3.17 Maximum power point (MPP)

- It should provide high accuracy and be able to find true global maximum power point (MPP). An accurate MPPT system results in a PV system with higher efficiency.
- It should have high tracking speed. Slow tracking speed results in reduction of extracted power and low efficiency of PV systems.
- It should be able to perform effectively both in uniform insolation conditions and partial shading conditions. In partial shading conditions, there are several local optima in $P - V$ curve, therefore finding the true global maximum power point is a challenging task.
- It should be system-independent, i.e. it should perform effectively for different PV systems.
- It should not be too complex. Simplicity is a merit.
- It should not oscillate around maximum power point.
- It should be able to effectively track maximum power point after sudden drastic changes in environmental conditions. Figure 3.17 illustrates the maximum power point (MPP) of the solar panel computed by the MPPT controller.

Several MPPT algorithms have been developed, it differ in many aspects such as required sensors, complexity, cost, range of effectiveness, convergence speed, correct tracking when irradiation and/or temperature change, hardware needed for the implementation or popularity, among others. The following algorithms are the most common:

In this chapter, two MPPT techniques have been selected for purpose of comparison; Incremental conductance (INC) and fuzzy logic controller (FLC).

3.4.1 *Incremental Conductance (INC) Technique*

The Incremental Conductance (INC) algorithm is based to know the variation of conductance of the photovoltaic generator, and the consequences on the position of the operating point by comparison at the MPP. Thus, the conductance of the photovoltaic module is defined by the relationship between the current and the voltage of the GPV as indicated below:

$$G = \frac{I_{pv}}{V_{pv}} \tag{3.33}$$

Therefore, an elementary variation (increment) of conductance can be defined by:

$$dG = \frac{\partial I_{pv}}{\partial V_{pv}} \tag{3.34}$$

On the other hand, the GPV power evolution by voltage gives the position of the operation point by to the MPP. When the power derivative is zero, it means MPP has been reached, if positive the operating point is to the left of the maximum, when negative, is on the right. Figure 3.18 shows the following conditions:

- Left of MPP: $\frac{\partial P_{pv}}{\partial V_{pv}} > 0$
- Right of MPP: $\frac{\partial P_{pv}}{\partial V_{pv}} < 0$
- At MPP: $\frac{\partial P_{pv}}{\partial V_{pv}} = 0$

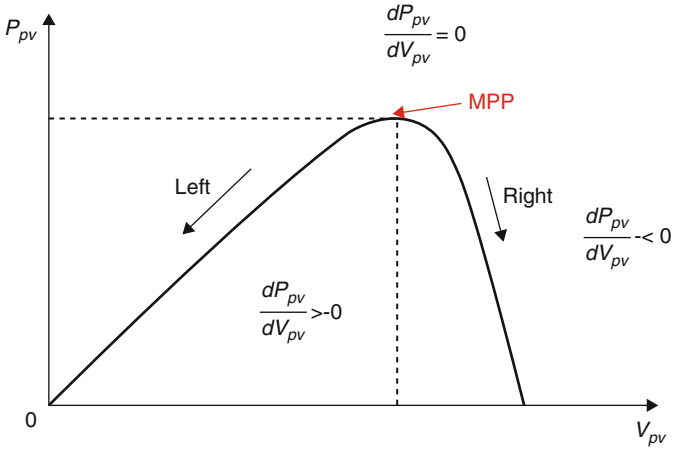

Fig. 3.18 The operation of incremental conductance method

The relationship between the conductance given by (3.33) and the derivative of the power $\frac{\partial P_{pv}}{\partial V_{pv}}$ can be described by the following equation:

$$\frac{\partial P_{pv}}{\partial V_{pv}} = \frac{\partial (I_{pv} V_{pv})}{\partial V_{pv}} = I_{pv} + V_{pv} \frac{\partial I_{pv}}{\partial V_{pv}} \simeq I_{pv} + V_{pv} \frac{\Delta I_{pv}}{\Delta V_{pv}} \tag{3.35}$$

Hence, we can write new conditions on the variation of conductance.

- Left of MPP: $\frac{\Delta I_{pv}}{\Delta V_{pv}} > -\frac{I_{pv}}{V_{pv}}$
- Right of MPP: $\frac{\Delta I_{pv}}{\Delta V_{pv}} < -\frac{I_{pv}}{V_{pv}}$
- At MPP: $\frac{\Delta I_{pv}}{\Delta V_{pv}} = -\frac{I_{pv}}{V_{pv}}$

The Maximum Power Point (MPP) can thus be tracked by comparing the instantaneous conductance $\frac{I_{pv}}{V_{pv}}$ to the incremental conductance $\frac{\Delta I_{pv}}{\Delta V_{pv}}$ (Abdelhak and Boubaker 2014), as illustrated by the algorithm of Fig. 3.19 (Abdelhak and Boubaker 2014; Verma et al. 2016).

3.4.2 MPPT Controller with Fuzzy Logic

The objective is to present a reminder of the fuzzy sets and a general overview on the fuzzy logic as well as its application for the optimization of a photovoltaic system. We first introduce some notions of fuzzy logic; we will limit ourselves to essential properties and then apply this optimization technique to maximize PV system performance.

The output power of the photovoltaic modules is influenced by the intensity of the solar radiation, the temperature and surface of the cells, as well as the charge. Therefore, to maximize the efficiency of the renewable energy system, it is necessary to continue the maximum power point (MPP) of the input source. We propose an MPPT control system based on the theory of fuzzy sets to improve the efficiency of PV energy conversion. The fuzzy algorithm based on the linguistic rules is applied to the control of the DC-DC converter (boost converter) for the MPPT.

3.4.2.1 Comparison Between Fuzzy Logic and Boolean Logic

Fuzzy logic is widespread instead of Booleen logic, which cannot explain most human reactions because the response cannot take only 0 or 1. On the other hand, fuzzy logic can take all values between 0 and 1, following Functions belonging.

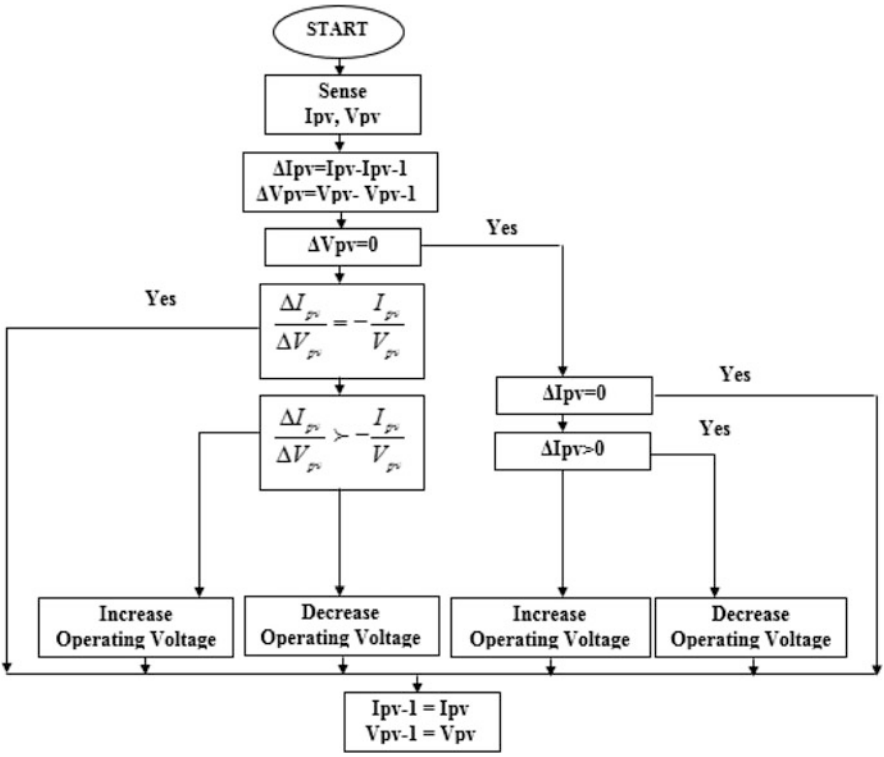

Fig. 3.19 State-flow chart of INC MPPT technique

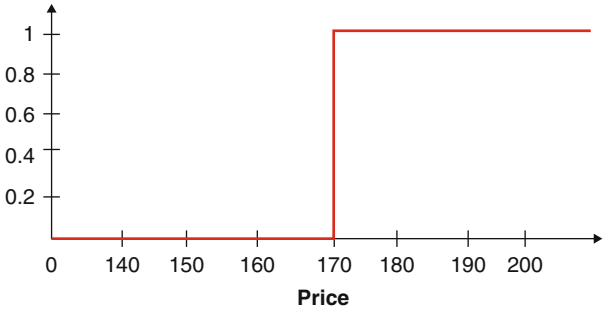

Fig. 3.20 Square membership functions

Example

Figure 3.20 shows the price of a product: expensive or not expensive in classical logic, we introduce a value "Threshold": below this value, the product will not be expensive and beyond it will be part of expensive. In fuzzy logic, we introduce

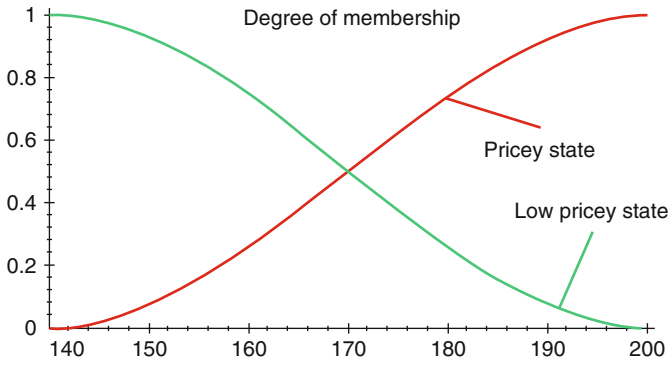

Fig. 3.21 Membership functions of price

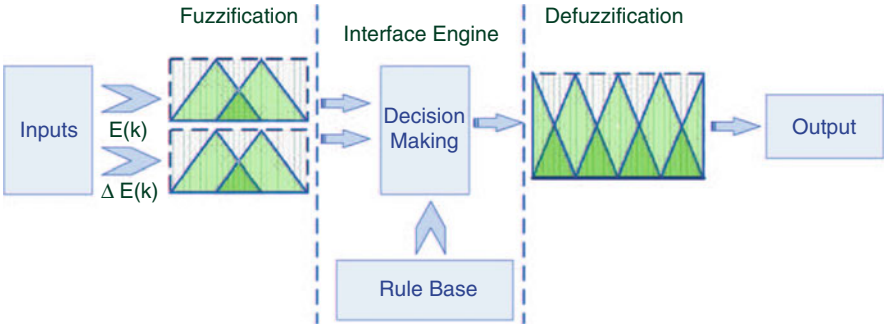

Fig. 3.22 FLC block diagram

membership functions, which define, according to the parameter (price), the degrees of belonging to each state. In this example, a product of 170 DH price will be 50% expensive and 50% cheap and another of 180 DH will be cheap to 20% and expensive to 80%. Figure 3.21 shows membership functions of price.

3.4.2.2 Fuzzy Logic Controller (FLC) Technique for PV MPPT

Recently, fuzzy logic control (FLC) has been presented in many researches as in (Eltamaly 2010; Eltamaly et al. 2010) to make PV work closer to MPP (Rezk and Eltamaly 2015). In one hand, FLC offers the advantage of being robust and relatively simple to develop and it does not require the exact knowledge of the regulate. In the other hand, the FLC has the advantages of working with imprecise inputs, not needing an accurate mathematical model, and handling nonlinearity. A FLC generally consists of three stages: fuzzification, aggregation, and defuzzification Fig. 3.22 (Seyedmahmoudian et al. 2016).

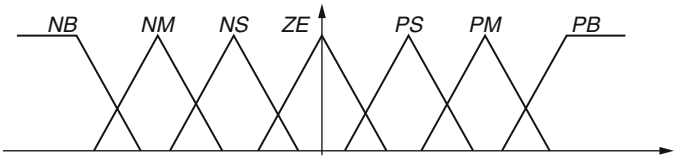

Fig. 3.23 Membership function of FLC

Fuzzification

During fuzzification, numerical input variables are converted into a membership function. The input values of this module are I_{pv} and V_{pv}. These values are used to calculate the power from PV array. Then the error signal $E(k)$ can be calculated depending on (3.36). The value of $\Delta E(k)$ is calculated as shown in (3.37).

$$E(k) = \frac{P_{pv}(k) - P_{pv}(k-1)}{V_{pv}(k) - V_{pv}(k-1)} \tag{3.36}$$

$$\Delta E(k) = E(k) - E(k-1) \tag{3.37}$$

Thus, these variables are expressed of linguistic variables such as PB (Positive Big), PM (Positive Medium), PS (Positive Small), ZE (Zero), NS (Negative Small), NM (Negative Medium), NB (Negative Big) using basic fuzzy subset. Each of these acronyms is defined by mathematical membership functions, MF as shown in Fig. 3.23 (Rezk and Eltamaly 2015).

Rule Inference

This stage is designed to control the output variables according to a calculation and conversion to the linguistic variables based on MF between E and ΔE. The change of duty cycle, ΔD of the power converter, which is the FLC output, can be searched in a rule base given in Table 3.2 (Rezk and Eltamaly 2015). The strategy of these rules is based on the "if-then" concept and necessitates information about the systems. In this algorithm, the Mamdani Inference method uses the approach of the max-min operation (Seyedmahmoudian et al. 2016).

Defuzzification

We must carry out the inverse operation of the fuzzification, here; we have to calculate a numerical value comprehensible by the external environment from a Fuzzy definition.

Table 3.2 Rules for a fuzzy system

	e						
Δe	**NB**	**NS**	**NM**	**EZ**	**PS**	**PM**	**PB**
NB	NB	NB	NB	NB	NM	NS	EZ
NM	NB	NB	NB	NM	NS	EZ	PS
NS	NB	NB	NM	NS	EZ	PS	PM
EZ	NB	NM	NS	EZ	PS	PM	PB
PS	NM	NS	EZ	PS	PM	PB	PB
PM	NS	EZ	PS	PM	PB	PB	PB
PB	EZ	PS	PM	PB	PB	PB	PB

3.5 Simulation of PV Modeling and DC/DC Converter

3.5.1 Simulation of PV Modeling

The photovoltaic system consists of four blocks as shown in Fig. 3.24. The first block represents the energy source (photovoltaic panel), the second block is a static DC-DC converter, the third block represents the load and the fourth block represents the control system (MPPT). Radiation (R) is incident on the photovoltaic panel. It generates a voltage (V) and current (I). The temperature of the PV solar is measured at T (Seyedmahmoudian et al. 2016). The main role of the static converter is to ensure impedance matching so that the photovoltaic panel PV delivers maximum energy. For commanding the DC/DC converter, we have been carried out using MPPT based on two techniques; INC and FLC (Abbes et al. 2014).

3.5.1.1 PV Solar Module

The PV solar module used in this study consists of 66 polycrystalline silicon solar cells electrically configured as five series strings. Its main electrical specifications are shown in Table 3.3.

Mathematical Models of the PV Panel

Mathematical models of the PV panel are defined below. Figure 3.25 shows the equivalent circuit of a solar panel. A solar panel is composed of several photovoltaic cells employing series or parallel or series-parallel external connections.

The following equation (3.38) describes the $I - V$ characteristic of a solar panel (Villalva et al. 2009).

$$I = I_{pv} - I_0 \left[\exp\left(\frac{V + R_s I}{a V_t} \right) - 1 \right] - \frac{V + R_s I}{R_p} \tag{3.38}$$

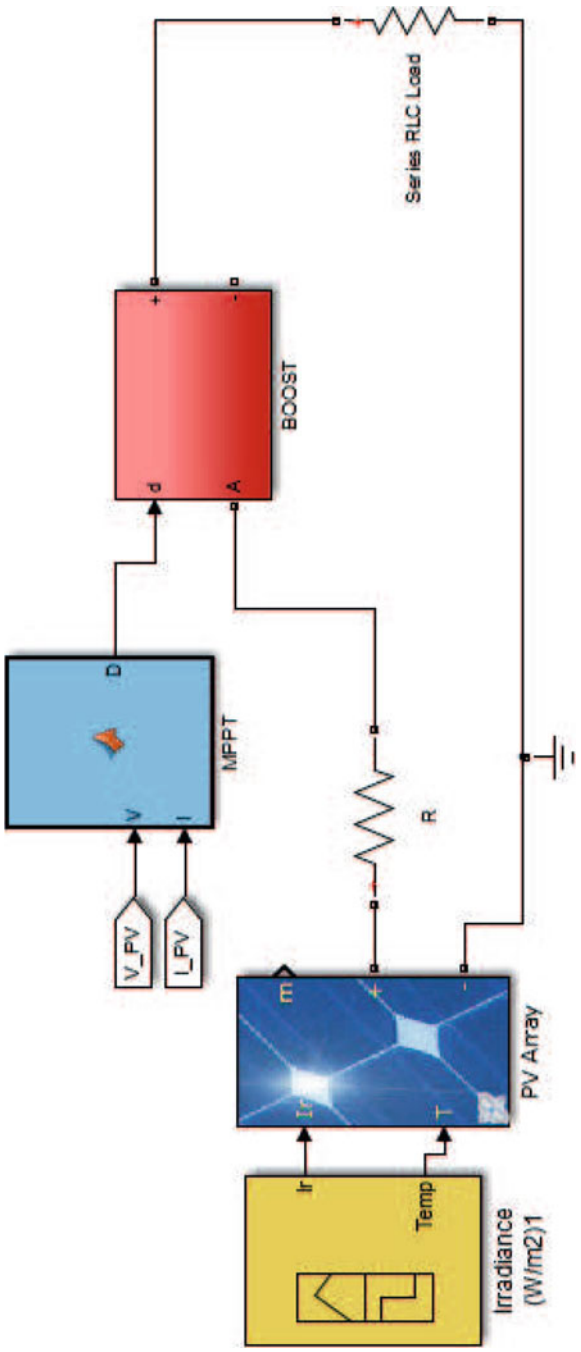

Fig. 3.24 Block diagram of a general photovoltaic system

Table 3.3 Technical data of the model manufacturer SUNPOWER SPR-305E ($T = 25\,°$, $G = 1000\,\text{W/m}^2$)

Maximum power (W)	305
Open circuit voltage Voc (V)	64.2
Short-circuit current Isc (A)	5.96
Current at maximum power point Imp(A)	5.58
Voltage at maximum power point Vmp (V)	54.7

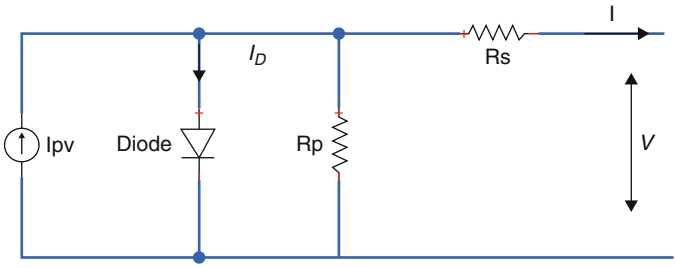

Fig. 3.25 Equivalent circuit of solar module

where:

I_{pv} is the PV current.
I_0 is the saturated reverse current.
a is a constant known as the diode ideality factor.
R_s and R_p are the series and parallel equivalent resistances of the solar panel respectively;
$V_t = \dfrac{N_s K T}{q}$ is the thermal voltage associated with the cells.
N_s is the number of cells connected in series.
q is the charge of the electron.
K is the Boltzmann constant.
T is the absolute temperature of the $p - n$ junction.

I_{pv} has a linear relationship with light intensity and varies with temperature variations. I_0 is dependent on temperature variations. Values of I_{pv} and I_0 are calculated from the following equations:

$$I_{pv} = (I_{pvn} + K_i \Delta T)\frac{G}{G_n} \tag{3.39}$$

$$I_0 = \frac{I_{scn} + K_i \Delta T}{\exp\left(\dfrac{V_{0cn} + K_v \Delta T}{a V_t}\right) - 1} \tag{3.40}$$

where: I_{pvn}, V_{0cn} and I_{scn} are the PV current, open circuit voltage and short circuit current respectively under standard conditions ($T_n = 25\,°\text{C}$ and $G_n = 1000\,\text{W/m}^2$).
K_v is the ratio of the open circuit voltage to temperature;

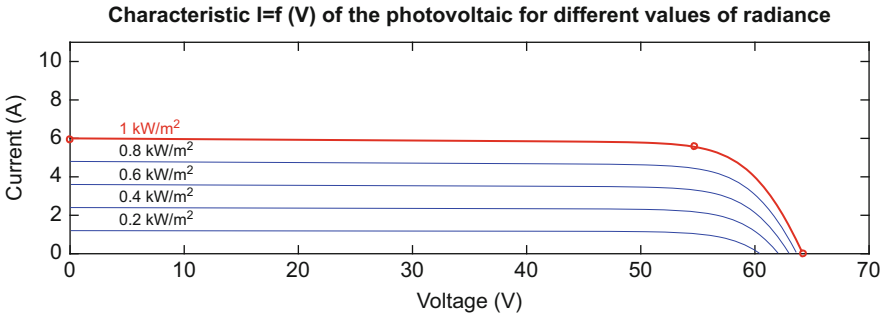

Fig. 3.26 Characteristic $I = f(V)$ of the photovoltaic system for different values of radiation

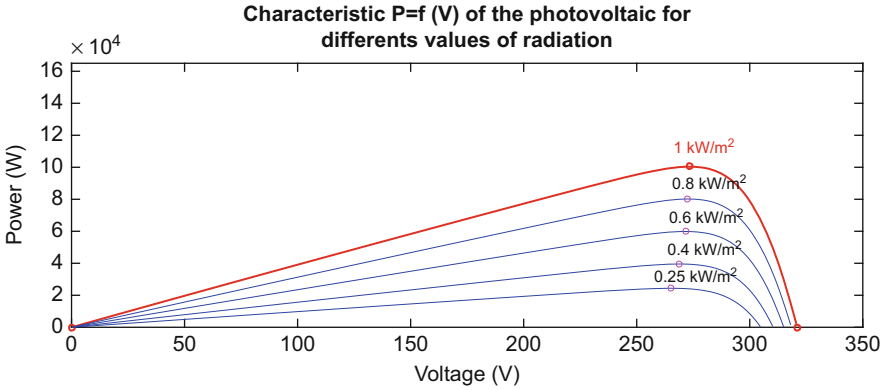

Fig. 3.27 Characteristic $P = f(V)$ of the photovoltaic system for different values of radiation

K_i is the coefficient of short-circuit current variation with temperature;
$\Delta T = T - T_n$ is the deviation from standard temperature, G the light intensity (Reza Reisi et al. 2013).

Influence of Irradiation on PV

($T = 25\,°C$, G = 200, 400, 600, 800, 1000 W/m^2) Figures 3.26 and 3.27 show the characteristics of the PV solar module for different values of radiation. When the radiation rate increases, I_{sc} increases and V_{co} decreases slightly, therefore, the maximum power undergoes a significant increase.

Influence of Temperature

Figures 3.28 and 3.29 illustrate the variations of the characteristic curves when there is a change in temperature.

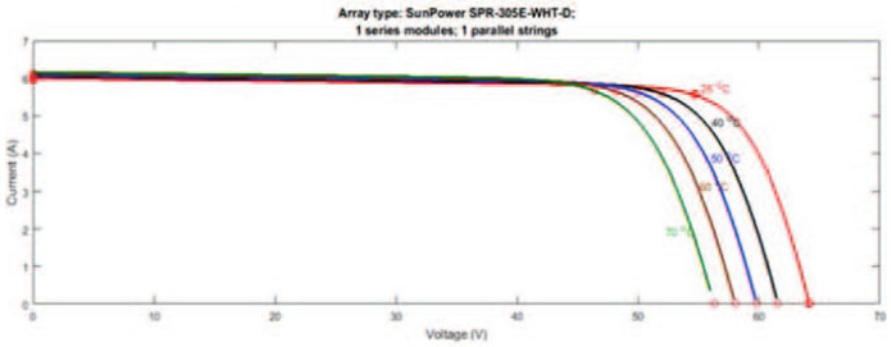

Fig. 3.28 Characteristic $I(V)$ of a module for different temperatures (at 1000 W/m^2)

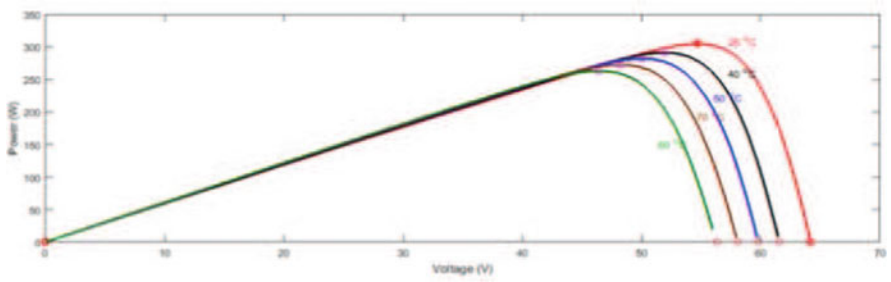

Fig. 3.29 Characteristic $P(V)$ of a module for different temperatures (at 1000 W/m^2)

The above figures show the influence of temperature on the PV cell. We note that when the ambient temperature increases, increases slightly and decreases according to the temperature coefficient of the cell, consequently there is an increase of the MPP in a negligible way.

3.5.2 Simulation of the BOOST Converter DC/DC

In the simulation, we examine the adaptation of a resistive load, which is fed by a field of the panels, through a boost converter. The structure of the boosting circuit in Matlab-Simulink environment is given in Fig. 3.30.

3.5.2.1 Simulation Result of Boost Converter

Figure 3.31 shows the simulation of the boosting circuit:

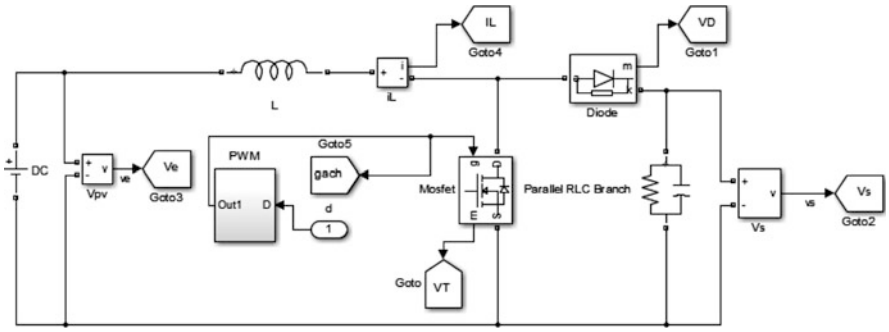

Fig. 3.30 Simulation diagram of the boost converter

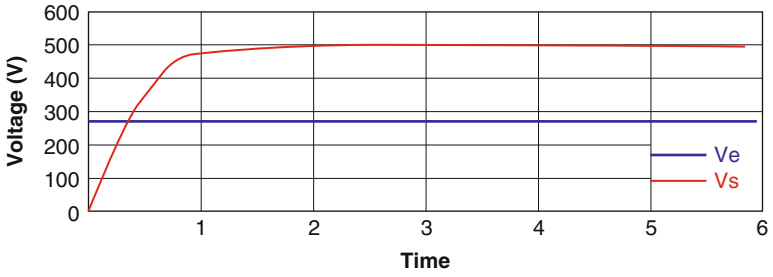

Fig. 3.31 Simulation result of Boost converter

The Input voltage is $V_e = 273\,\text{V}$ and the output voltage is $V_s = 500\,\text{V}$. After simulation, this circuit shows us that the output voltage is higher than the input voltage. So, this type give us the result that we looking for it.

3.6 Analysis and Discussion of the Simulation Results

3.6.1 The Simulation Results

3.6.1.1 Results with Temperature = 25 °C and Irradiation = 1000 W/m^2

Simulation results to compare two algorithms (INC and FLC) previously studied are given in Figs. 3.32, 3.33 and 3.34. These figures show the output values of the power, the voltage and the current for a pair of the temperature and the irradiation equal to (25 °C and 1000 W/m^2).

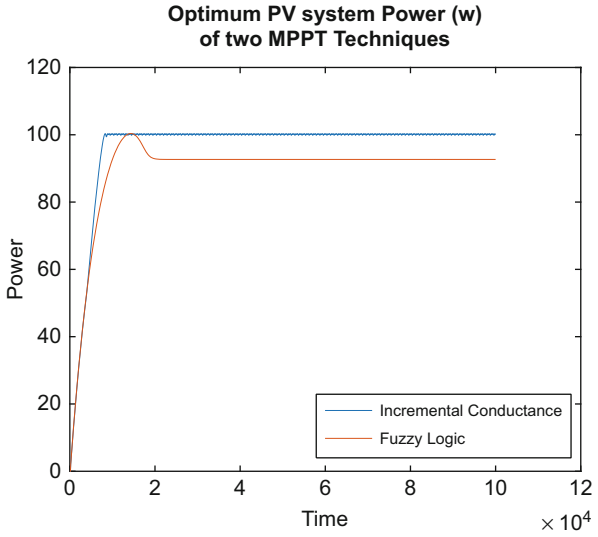

Fig. 3.32 Optimum PV system power (W) of two MPPT techniques

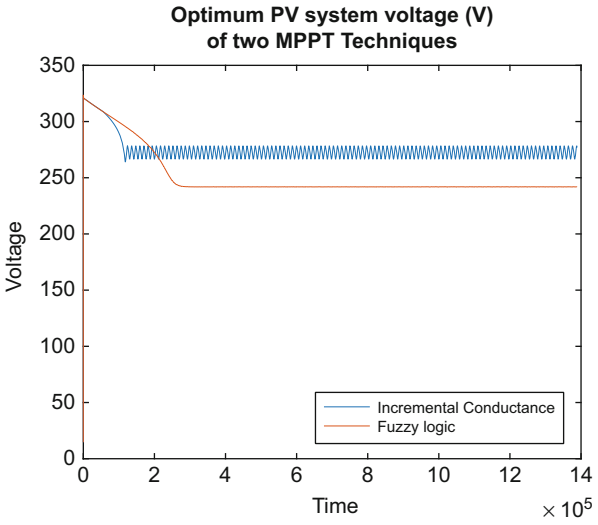

Fig. 3.33 Optimum PV system voltage (V) of two MPPT techniques

Figures 3.32, 3.33 and 3.34 that are successively the responses of the power, the voltage and the current of two algorithms for the photovoltaic system show a convergence towards the optimal values with oscillations for the INC algorithm while the FLC algorithm converges rapidly and without oscillation.

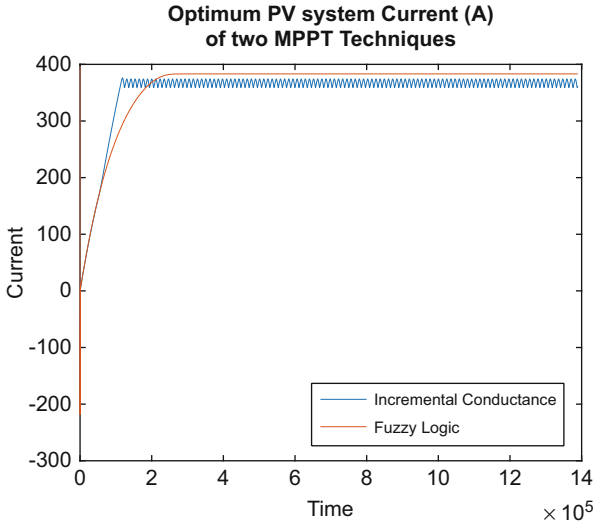

Fig. 3.34 Optimum PV system Current (A) of two MPPT techniques

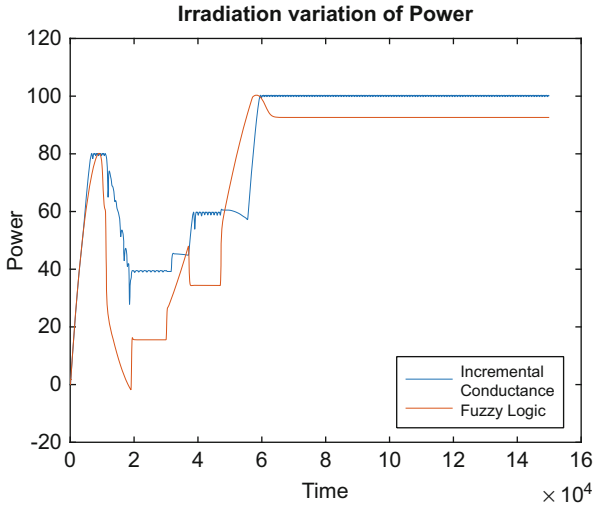

Fig. 3.35 Irradiation variation of the PV system optimal power of two MPPT techniques

3.6.1.2 Results with Temperature = 25 °C and Different Values of Irradiation

The simulation results of the algorithms previously studied are given in Figs. 3.35, 3.36 and 3.37. These figures show the output values of the power, the voltage and the current for a pair of the temperature equal to 25 °C and different values of irradiations.

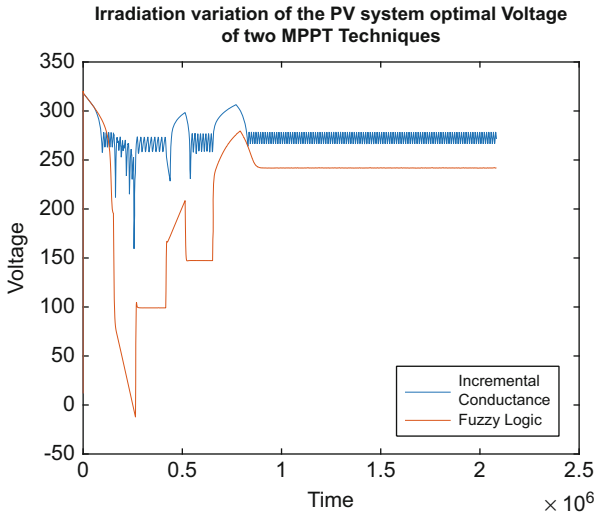

Fig. 3.36 Irradiation variation of the PV system optimal voltage of two MPPT techniques

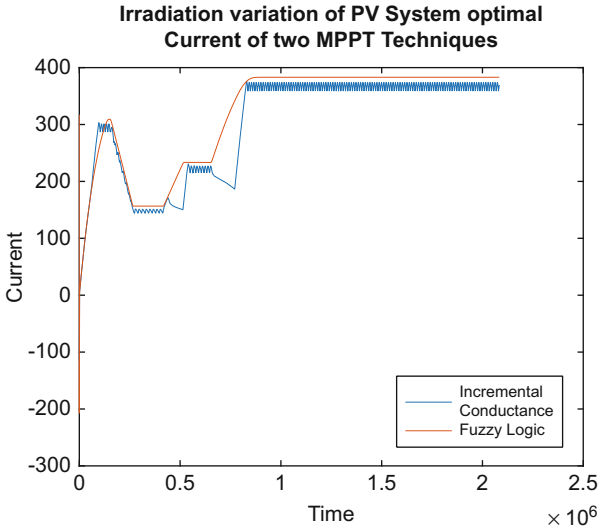

Fig. 3.37 Irradiation variation of the PV system optimal current of two MPPT techniques

After the variation of radiations, the two algorithms undergo a great modification that show in their responses of PV system, however, the algorithm INC remains still a great oscillation at the maximum point while FLC no oscillations.

3.6.2 Analysis and Discussion

T = 25 °C and Ir = 1000 W/m^2

The algorithm based on Incremental conductance (INC), gives fast response in transient state but it works at the optimal point with large oscillations in steady state.

The algorithm based on fuzzy logic is a robust and efficient algorithm. Indeed, this algorithm works at the optimal point without oscillations. In addition, it is characterized by good behavior in a transient state. However, the implementation of this type of algorithm is more complex than the classical algorithms. Moreover, the efficiency of this algorithm depends very much on the inference table.

T = 25 °C and different values of irradiation

The same things when our Pv system has a variation irradiation, even if, each algorithm in the beginning, shows a large movement due to different values of irradiation, but always the FLC has more stable and better then the INC technique. Since this gives more oscillation, that make our PV system far than the MPP, therefore no energy has extract.

3.7 Conclusion

The work presented in this chapter focuses on the tracking of the maximum power point MPP of a photovoltaic system. In this chapter, we have shown the importance of photovoltaic systems, their properties, their operating, their modeling, their PV characteristics and the variations of these characteristics due to the variation of temperature and radiation, especially at point of maximum power.

In this work, we have studied the modeling of a photovoltaic chain, which consists of a photovoltaic generator (with a single diode), an adaptation stage (DC/DC converter Boost), a resistive load and a MPPT control stage to drive the boost converter.

Different simulations, under the Matlab/Simulink environment, are carried out to show the influence of the variations of the climatic conditions (illumination and temperature) on the MPP where the operating power of the system is maximum.

The conventional or intelligent MPPT technique allows the best connection between the photovoltaic generator (GPV) and the load and forces it to always operate at the maximum power point, however, the comparative study of the simulation results has found that Intelligent MPPT command FLC has better performance (reduced response time and steady state error).

Therefore, the results of the simulations show in the both test that, FLC technique has a good behavior in transient state and it presents a lack oscillation in steady state. However, the INC presents a large oscillation in steady state. The algorithm, "INC" is widely used, but fuzzy logic control FLC shows the best behavior and it is capable to harvest the maximum energy from the PV system due to his membership's functions in comparison with INC technique.

References

Abbes, H., Abid, H., Loukil, K., Toumi, A., & Abid, M. (2014). Etude comparative de cinq algorithmes de commande MPPT pour un système Photovoltaique. *Revue des Energies Renouvelables, 17*(3), 435–445.

Abdelhak, B., & Boubaker, A. (2014). *Contribution à l'optimisation d'une chaine de conversion d'énergie Photovoltaique*. Ph.D. thesis, Universite de Constantine.

Amarouayache, M. (2014). *Contribution à l'optimisation d'une chaine de conversion d'énergie Photovoltaique*. Ph.D. thesis, Constantine 1 University.

Azab, M. (2008). A new maximum power point tracking for photovoltaic systems. World Academy of Science, Engineering and Technology. *International Journal of Electrical, Computer, Energetic, Electronic and Communication Engineering, 2*(8).

Carrero, C., Amador, J., & Arnaltes, S. (2007). A single procedure for helping PV designers to select silicon PV module and evaluate the loss resistances. *Renewable Energy, 32*(15), 2579–2589.

Eltamaly, A. M. (2010). Modeling of fuzzy logic controller for photovoltaic maximum power point tracker. In *Solar Future 2010 Conference Proceedings*, Istanbul (pp. 4–9).

Eltamaly, A. M., Alolah, A. I., & Abdulghany, M. Y. (2010). Digital implementation of general purpose fuzzy logic controller for photovoltaic maximum power point tracker. In *Power Electronics Electrical Drives Automation and Motion (SPEEDAM), International Symposium on Digital Object Identifier* (pp. 622–627).

Gow, J. A., & Manning, C. D. (1999). Development of a photovoltaic array model for use in power-electronics simulation studies. *IEE Proceedings Electric Power Applications, 146*(2), 193–200.

Hyvarinen, J., & Karila, J. (2003). New analysis method for crystalline silicon cells. In *Proceedings of 3rd World Conference on Photovoltaic Energy Conversion* (Vol. 2, pp. 1521–1524).

Kanji, B., (2012). Intelligent techniques for the tracking of the maximum power point of a supervised photovoltaic system. MA thesis, Lebanese University.

Koutroulis, E., Kalaitzakis, K., & Tzitzilonis, V. (2008). Development of a FPGA-based system for real-time simulation of photovoltaic modules. *Microelectronics Journal, 40*(7), 1094–1102.

Moller, H. J. (1993). *Semiconductors for solar cells*. Norwood: Artech House.

Naffouti, S. E. (2012). Dimensionnement et commande d'un hacheur parallèle alimenté par une source Photovoltaique. M.S. thesis, University of Burgundy, France.

Nishioka, K., Sakitani, N., Uraoka, Y., & Fuyuki, T. (2007). Analysis of multicrystalline silicon solar cells by modified 3-diode equivalent circuit model taking leakage current through periphery into consideration. *Solar Energy Materials and Solar Cells, 91*(13), 1222–1227.

Rauschenbach, H. S. (1980). *Solar cell array design handbook*. New York: Van Nostrand Reinhold.

Rezaee Jordehi, A. (2016). Maximum power point tracking in photovoltaic (PV) systems: A review of different approaches. *Renewable and Sustainable Energy Reviews, 65*, 1127–1138.

Rezk, H., & Eltamaly, A. M. (2015). A comprehensive comparison of different MPPT techniques for photovoltaic systems. *Solar Energy, 112*, 1–11.

Reza Reisi, A., Moradi, M.H., & Jamasb, S. (2013). Classification and comparison of maximum power point tracking techniques for photovoltaic system: A review. *Renewable and Sustainable Energy Reviews 19*, 433–443.

Salas, V., Olias, E., Barrado, A., & Lazaro, A. (2006). Review of the maximum power point tracking algorithms for stand-alone photovoltaic systems. *Solar Energy Materials and Solar Cells, 90*(11), 1555–1578.

Sedra, A. S., & Smith, K. C. (2006). *Microelectronic circuits*. London: Oxford University Press.

Seyedmahmoudian, M., Horan, B., Kok Soon, T., Rahmani, R., Thango, A. M., Mekhilef S., & Stojcevskiet, A. (2016). State of the art artificial intelligence-based MPPT techniques for mitigating partial shading effects on PV systems-a review. *Renewable and Sustainable Energy Reviews, 64*, 435–455.

Verma, D., Nema, S., Shandilya, A. M., & Dash, S. K. (2016). Maximum power point tracking (MPPT) techniques: Recapitulation in solar photovoltaic systems. *Renewable and Sustainable Energy Reviews, 54*, 1018–1034.

Villalva, M. G., Gazoli, J. R., & Ruppert Filho, E. (2009). Comprehensive approach to modeling and simulation of photovoltaic arrays. *IEEE Transactions on Power Electronics, 24*(5), 1198–1208.

Xiao, W., Dunford, W. G., & Capel, A. (2004). A novel modeling method for photovoltaic cells. In *Proceedings of IEEE 35th Annual Power Electronics Specialists Conference (PESC)* (Vol. 3, pp. 1950–1956).

Yi-Bo, W., Chun-Sheng, W., Hua, L., & Hong-Hua, X. (2008). Steady-state model and power flow analysis of grid-connected photovoltaic power system. In *IEEE International Conference on Industrial Technology, ICIT 2008* (pp. 1–6).

Zainudin, H. N., & Mekhilef, S. (Dec 2010). Comparison study of maximum power point tracker techniques for PV systems. In *14th Middle East Power Systems Conference, Mepcon'10*, Cairo University.

Zagroubaa, M., Bouaïchaa, M., Sellamia, A., Ksouric, M., et al. (2010). Optimisation par les Algorithmes Genetiques et modélisation par la méthode LPV d'un systéme photovoltaique. Vème Congrès Int. sur les Energies Renouvelables et l'Environnement, 4–6 Novembre, Sousse.

Chapter 4
Modeling and Comparison of Boost Converter With Cascaded Boost Converters

Nesrine Boujelben, Ferdaous Masmoudi, Mohamed Djemel, and Nabil Derbel

Abstract Photovoltaic (PV) energy is a very important renewable energy source. The output voltage in renewable energy sources a is improved using DC-DC converters, which are the key part in a photovoltaic chain. Among the classic DC-DC topologies, the boost converter is the most used because of its simplicity and high efficiency. The aim with this converter that the switching frequency is limited so the output voltage is reduced. A possible solution to this problem is to use other topologies; the quadratic boost converter results from the generalized cascaded boost topologies with a single switch and the double cascade boost results from the association of two identic elementary boost converters connected in tandem. In this chapter a comparison of the efficiency of the classic boost converter with the two cascaded boost converters is discussed.

Keywords Boost converter · Quadratic boost converter · Double cascade boost converter · Efficiency

4.1 Introduction

For many years, fossil fuel cells have been the primary source of energy. The wide use of these sources has leaded to the emission of green houses gases. Climate change, caused by these greenhouse gases, has seriously damaged the environment. Due to the limited supply of these sources on the earth and their environmental effects, the world trend nowadays is to find a non-depletable and clean source of energy.

N. Boujelben (✉) · F. Masmoudi · M. Djemel · N. Derbel
Control and Energy Management Laboratory (CEMLab), Sfax Enginering School, University of Sfax, Sfax, Tunisia
e-mail: boujelben_nesrine@hotmail.fr; ferdaous.masmoudi@gmail.com; Mohamed.djemel@enis.rnu.tn; n.derbel@enis.rnu.tn

N. Derbel, Q. Zhu (eds.), *Modeling, Identification and Control Methods in Renewable Energy Systems*, Green Energy and Technology,
https://doi.org/10.1007/978-981-13-1945-7_4

Therefore, renewable energy sources such as Fuel cells, photovoltaic (PV) and Wind etc, are experiencing a fast development. Unlike conventional energy sources, such systems are environmentally friendly and produce clean electricity. Solar energy is considered one of the most promising energy sources due to its infinite power (Shen zt al. 2012; Suntio et al. 2010).

PV systems should be designed to operate at their maximum output power levels for any temperature and solar irradiation level at all times.

The demand of PV generation systems pretends to be increased for both standalone and grid-connected modes of PV systems.

The difference between the PV peak power voltage and the peak amplitude of the grid voltage waveform requires high voltage gain. Both transformer-based and transformer-less topologies can be proposed. The increase of the size and the cost of the transformer make the transformer-less solutions a more attractive choice (Lopez-Santos and Martinez-Salamero 2015; Lopez-Santos et al. 2013a).

Statics converters have the capability to step-up a low voltage to a high-voltage level. Hence, different topologies of boost are used for the boost up action (Priya et al. 2016; Veera Raghava and Ranga Rao 2014).

The development of new technologies is requiring wider conversion ratios. The possibility to overcome this problem has been introduced over 40 years ago by Matsuo el al., with their work on the cascaded connection of the conventional converter topologies (Maksimovic and Cuk 1991).

The presented work deals with the comparison of the conventional boost converter with two topologies of cascaded boost converters. The first one is the quadratic boost converter with a single switch. The second topology named the double cascade boost converter.

The remainder of this chapter is organized as follows. In Sect. 4.2, design and modeling of the converters are given. Simulation results are developed in Sect. 4.3. A discussion about the three converters is presented in Sect. 4.4. This chapter concludes with some final remarks given in Sect. 4.5.

4.2 Converter Modeling

4.2.1 Boost Converter

A boost converter is used to convert a DC voltage from lower level to higher level. The input to this converter can be from any DC source like solar panel, batteries etc (Erickson and Maksimovic 1999; Park and Choi 2010; Selva Kumar et al. 2016).

The circuit diagram for the boost converter is shown in Fig. 4.1 where V_{in} is the input voltage, S an active switch, D a passive switch, L and C are the corresponding eliminate of inductance and capacitance of the converter.

As it is shown in Fig. 4.2, the boost converter has two possible structures in continuous mode. In on-state, switch S is turned on. The inductor gets charged via the supply voltage from the capacitor and stores the energy. During this state, the inductor current increases gradually. In off-state, switch S is turned off. The energy stored in the inductor changes its polarity to charge the capacitor through the diode.

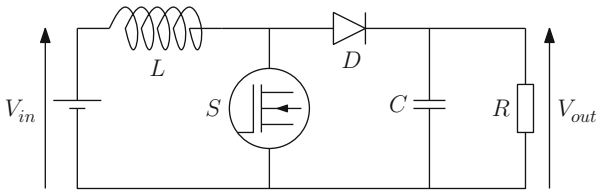

Fig. 4.1 Circuit diagram for the boost converter

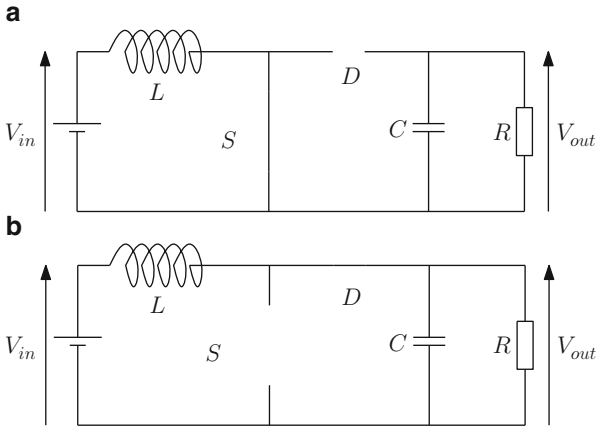

Fig. 4.2 Circuit configurations of the boost converter. (**a**) On-state; (**b**) Off-state

4.2.1.1 Dimensioning of the Circuit

The duty cycle is given by:

$$D = 1 - \frac{V_{in}}{V_{out}} \tag{4.1}$$

where V_{in} is the input voltage and V_{out} is the output voltage

The load R is calculated as follows:

$$R = \frac{V_{out}^2}{P_{pv}} \tag{4.2}$$

where P_{pv} is the input power

The output and the input currents are given by:

$$I_{out} = \frac{V_{out}}{R} \tag{4.3}$$

$$I_{in} = \frac{I_{out}}{1 - D} \tag{4.4}$$

The inductor value is designed using:

$$L = \frac{DV_{in}}{f\Delta i_L} \tag{4.5}$$

where f is the switching frequency and Δi_L is the ripple current

The capacitor value is designed using:

$$C = \frac{DV_{out}}{fR\Delta v_c} \tag{4.6}$$

Where Δv_c is the ripple voltage

The input power is equal to 50 w. The input voltage given to the circuit is 18 v and it works on 40 kHz.

4.2.2 Quadratic Boost Converter

A quadratic boost converter results by assembling the components of two boost converters by using single switch. This converter allows covering gain ranges which are not available with the single boost converter (Lopez Santos et al. 2013b; Silveira et al. 2014).

This converter is a fourth-order structure having two inductors and two capacitors. The circuit diagram of a quadratic boost converter is shown in Fig. 4.3. This converter comprises of an input voltage V_{in}, an active switch S, three passive switches D_1, D_2 and D_3, two capacitors C_1 and C_2 and two inductors L_1 and L_2. Thus, diodes D_1 and D_2 are replaced by voltage sources, and diode D_3 and the transistor switch by the corresponding current source (Lopez-Santos 2015; Selva Kumar et al. 2016).

As it is shown in Fig. 4.4, the quadratic boost converter has two possible structures in continuous mode. In on-state, switch S and diode D_3 are turned on, and diodes D_2 and D_1 are turned off. In off-state, switch S and diode D_3 are turned off, and diodes D_2 and D_1 are turned on.

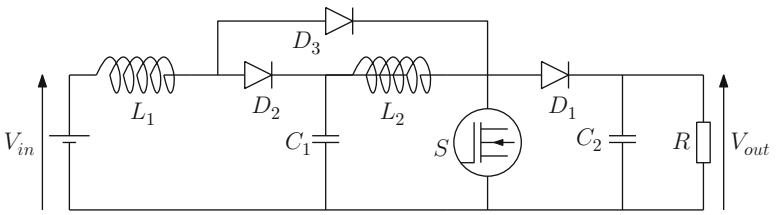

Fig. 4.3 Circuit diagram for the quadratic boost converter

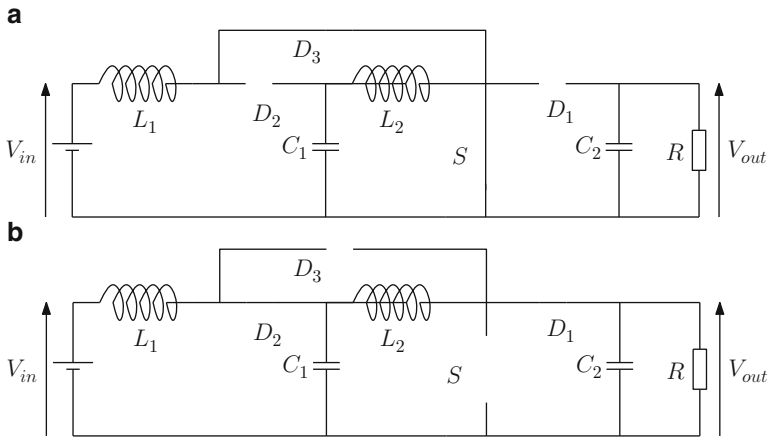

Fig. 4.4 Circuit configurations of the quadratic boost converter. (**a**) On-state; (**b**) Off-state

4.2.2.1 Dimensioning of the Circuit

The duty cycle is given by (Hauke 2014):

$$D = 1 - \frac{\sqrt{V_{in}}}{\sqrt{V_{out}}} \tag{4.7}$$

The output and the inductor currents are calculated as follows:

$$I_{out} = \frac{V_{out}}{R} \tag{4.8}$$

$$I_{L1} = \frac{I_{out}}{(1-D)^2} \tag{4.9}$$

$$I_{L2} = \frac{I_{out}}{(1-D)} \tag{4.10}$$

The inductors values are given by:

$$L_1 = \frac{DV_{in}}{f\Delta i_{L1}} \tag{4.11}$$

$$L_2 = \frac{DV_{in}}{f\Delta i_{L2}} \tag{4.12}$$

The capacitors values are designed using:

$$C_{1,2} = \frac{DV_{in}}{(1-D)\Delta v_c Rf} \tag{4.13}$$

4.2.3 *Double Cascade Boost Converter*

The double cascade boost converter shown in Fig. 4.5 results from the association of two identic elementary boosts connected in tandem. It consists of an input voltage source V_{in}, two independently controlled switches S_1 and S_2, two freewheeling diodes D_1 and D_2, two capacitors C_1 and C_2 and two inductors L_1 and L_2 (Chen et al. 2014; Sira-Ramirez and Silva-Origoza 2006).

- Step 1: This step begins when the switch S_1 is turned on. During this step, S_2 will remain off. The inductor L_1 gets loaded through the supply voltage and stores the energy. This step finishes when S_1 is turned off.
- Step 2: During this period of operation, S_1 is turned off and S_2 is turned on. The output of the first stage is now the input of the second stage. The inductor L_2 gets loaded through the supply voltage and stores the energy. This step finish when S_2 Is turned off.

Figure 4.6 shows different structures of the double cascade boost converter in continuous mode.

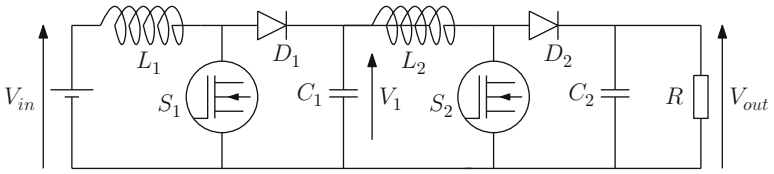

Fig. 4.5 Circuit diagram for the double cascade boost converter

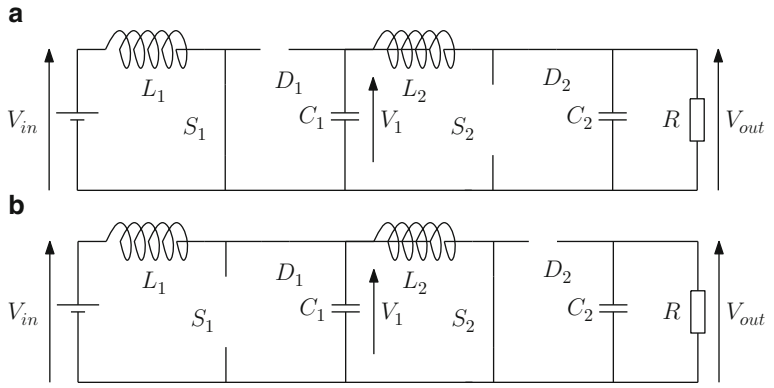

Fig. 4.6 Circuit configurations of the double cascade boost converter. (**a**) Step 1; (**b**) Step 2

4.2.3.1 Dimensioning of the Circuit

The voltage ratio is calculated as follows (Aamir and Shinwari 2010; Meddah et al. 2012):

$$\frac{V_{in}}{V_{out}} = \frac{1}{(1-D_1)}\frac{1}{(1-D_2)} \tag{4.14}$$

where D_1 is the duty cycle for the first boost and D_2 is the duty cycle for the second boost.

The output and the inductor currents are given by:

$$I_{out} = \frac{V_{out}}{R} \tag{4.15}$$

$$I_{L2} = \frac{I_{out}}{(1-D_2)} \tag{4.16}$$

$$I_{L1} = \frac{I_{L2}}{(1-D_1)} \tag{4.17}$$

where I_{L2} is the output current of the first boost.

The inductors values are calculated as follows:

$$L_1 = \frac{D_1 V_{in}}{f \Delta i_{L1}} \tag{4.18}$$

$$L_2 = \frac{D_2 V_{in}}{f \Delta i_{L2}} \tag{4.19}$$

The capacitors values are designed using:

$$C_1 = \frac{D_1 V_1}{\Delta V_{c1} f R} \tag{4.20}$$

$$C_2 = \frac{D_2 V_{out}}{\Delta V_{c2} f R} \tag{4.21}$$

where V_1 is the output voltage for the first boost.

4.3 Simiulation Results

The three topologies are simulated using the SABER simulator.

4.3.1 Boost Converter

The simulation circuit diagram for the boost converter is shown in Fig. 4.7.

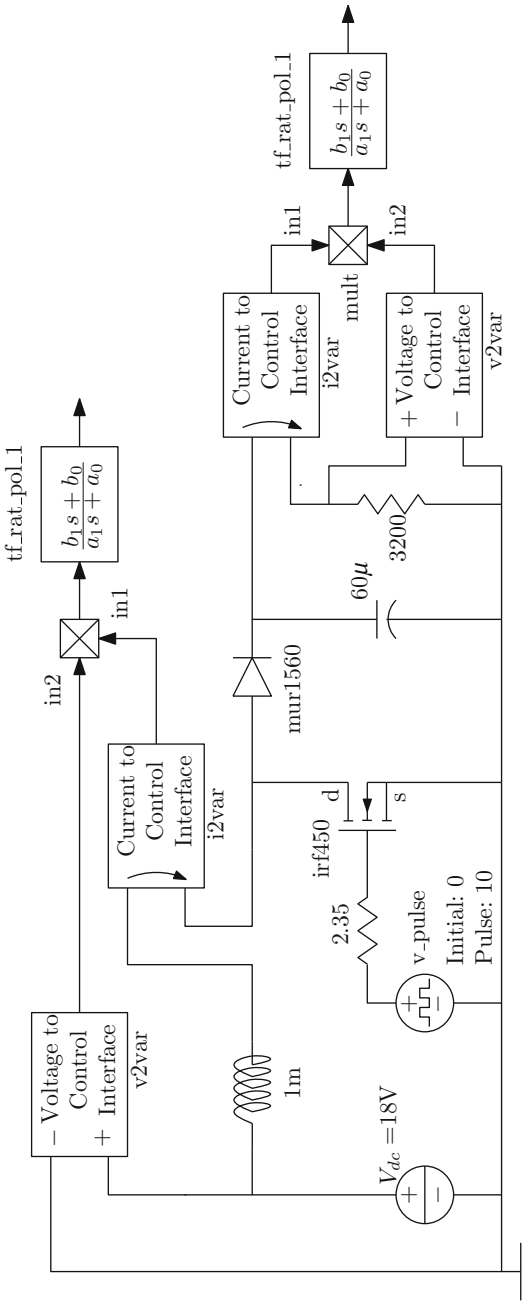

Fig. 4.7 Simulation circuit diagram for boost converter

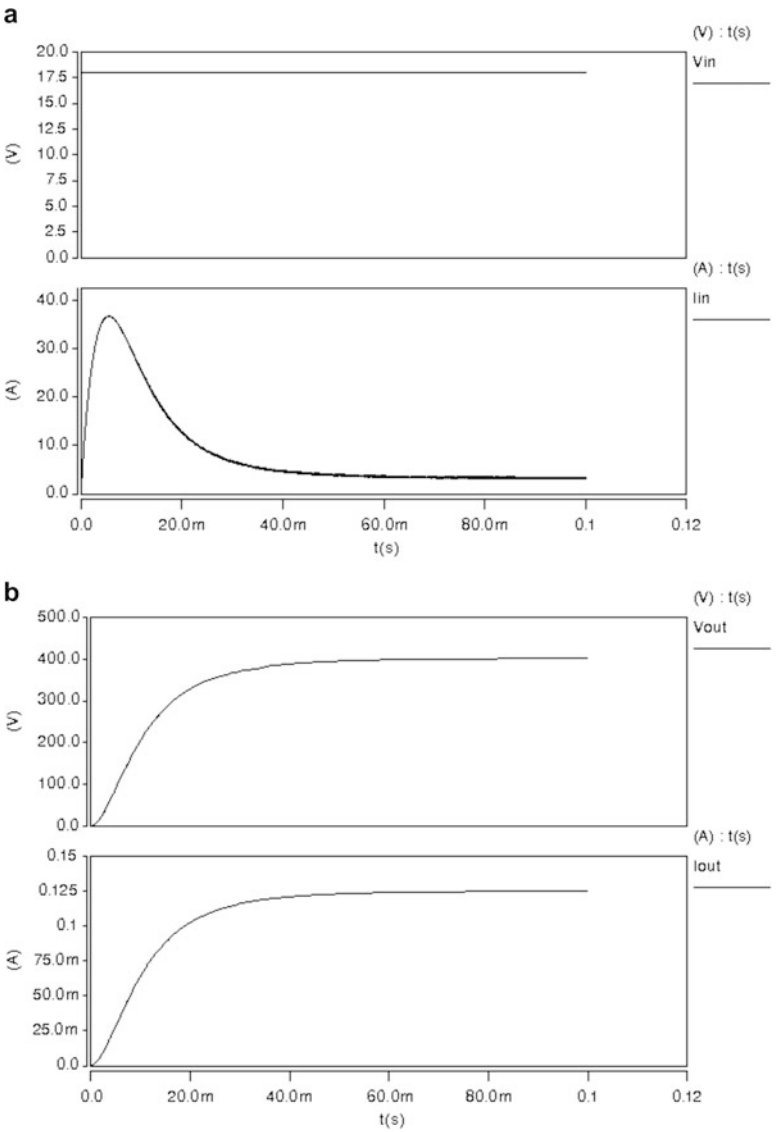

Fig. 4.8 Waveforms of electrical signals. (**a**) The input; (**b**) The output of the boost converter

Simulation results are shown in Fig. 4.8.

As it shown in Fig. 4.8a, the input voltage is constant at the value of 18 V and the inductor current is maintained constant at the value of 3 A after the transitional regime. Figure 4.8b illustrates the waveform of the output voltage which achieve to 400 V and the waveform of the output current which is stabilized at 0.1 A.

4.3.2 Quadratic Boost Converter

The simulation circuit diagram for the quadratic boost converter is shown in Fig. 4.9.

Simulation results are shown in Figs. 4.10 and 4.11.

The input voltage is kept constant at the value of 18 V as well as the input current at the value of 3 A as it shown in Fig. 4.10a. Ripple in the input current is very less. Figure 4.10.b illustrates the output voltage waveform as a constant at 400 V and the output current at 0.1 A The waveform of the current I_{L2} is shown in Fig. 4.11. Ripple in the inductor current is also very less.

4.3.3 Double Cascade Boost Converter

The simulation circuit diagram for the double cascade boost converter is shown in Fig. 4.12.

Simulation results are shown in Fig. 4.13.

Figure 4.13a illustrates the waveform of the input voltage and the output voltage where the values are 18 V and 3 A respectively. Figure 4.13b represents the waveforms of electrical signals at the output of the converter, the voltage reaches 400 V and the current is kept constant at the value of 0.1 A. Figure 4.13c shows the waveforms of the electrical signals at the output of the first stage.when the steady state is achieved, the voltage is maintained constant at 100 V and the current I_{L2} attain 0.5 A. Ripple in the input current and in the inductor current I_{L2} are very less.

The value of the output voltage of the first boost is determined by evaluating the efficiency of the converter with different value of the voltage V_1.

The result is shown in Fig. 4.14.

At the value 100 V, the converter gives the high efficiency 0.945.

4.4 Discussion

For the boost converter, Table 4.1 represents different values of duty ratio for different values of input voltage. To satisfy the operating conditions, the duty ratio must be very high for low values of input voltage. For example, with an input voltage of 9 V, the structure is unable to assure 400 V at the output.

In the Table 4.2, different values of duty ratio are presented for different values of input voltage for the quadratic boost converter. For low values of input voltage, the structure is unable to satisfy the condition of operation.

For the double cascade boost converter, different values of duty ratio are presented in Table 4.3 and this for different values of input Voltage. For low values of input voltage, the structure is able to satisfy the operating conditions. For

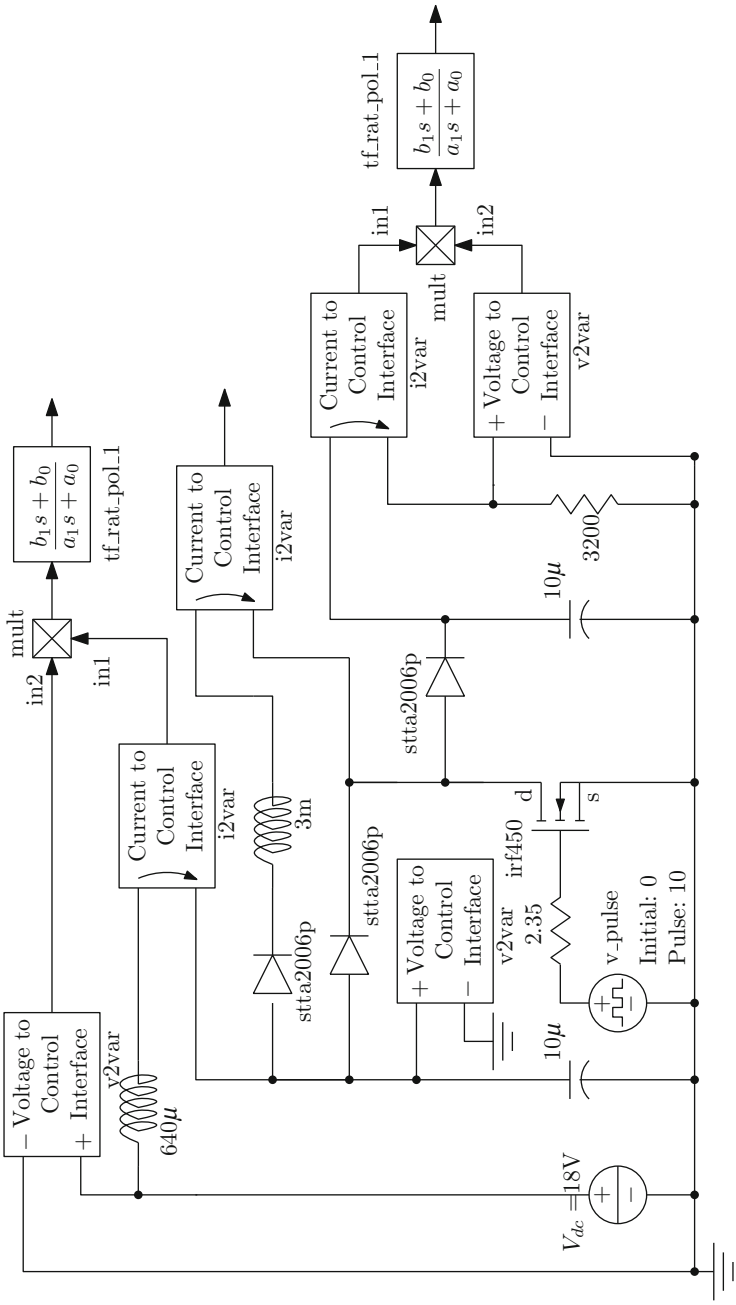

Fig. 4.9 Simulation circuit diagram for the quadratic boost converter

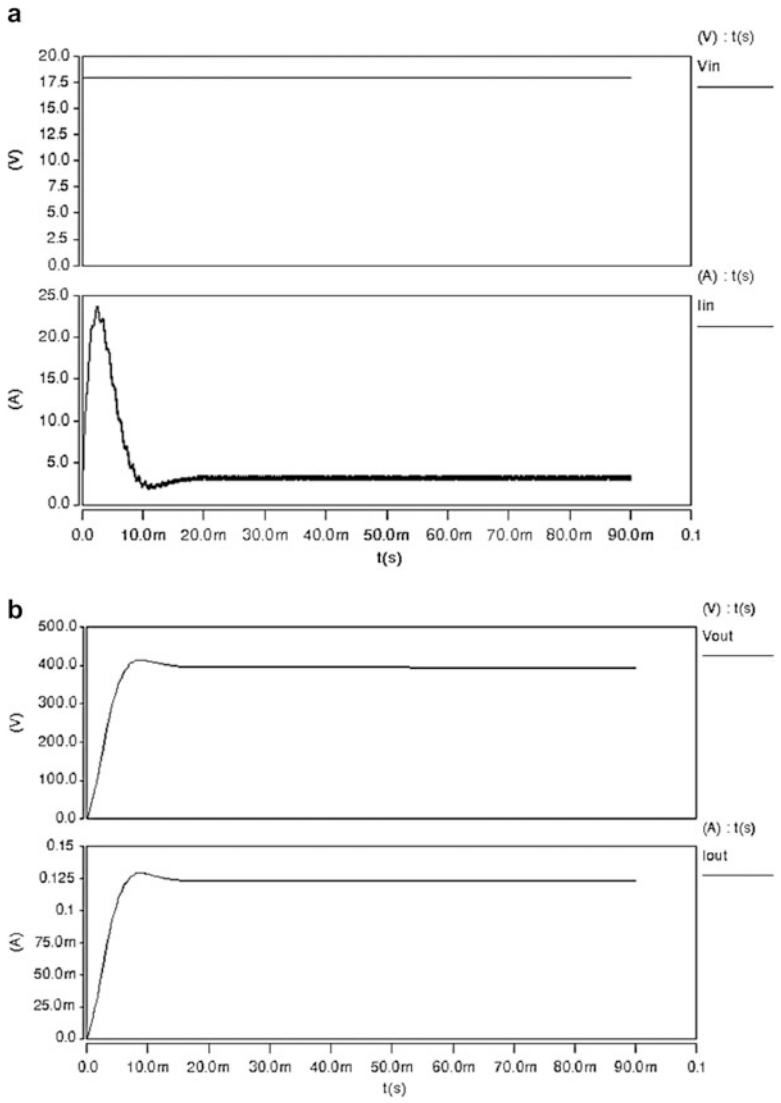

Fig. 4.10 Waveforms of electrical signals. (**a**) The input; (**b**) The output of the quadratic boost converter

example, with a 9 V of input voltage, we get 400 V at the output with an efficiency of the order of 0.86.

The performance study of each converter has been evaluated in two steps:

- Step 1: Evaluation of the efficiency by varying the input voltage with a fixed output voltage

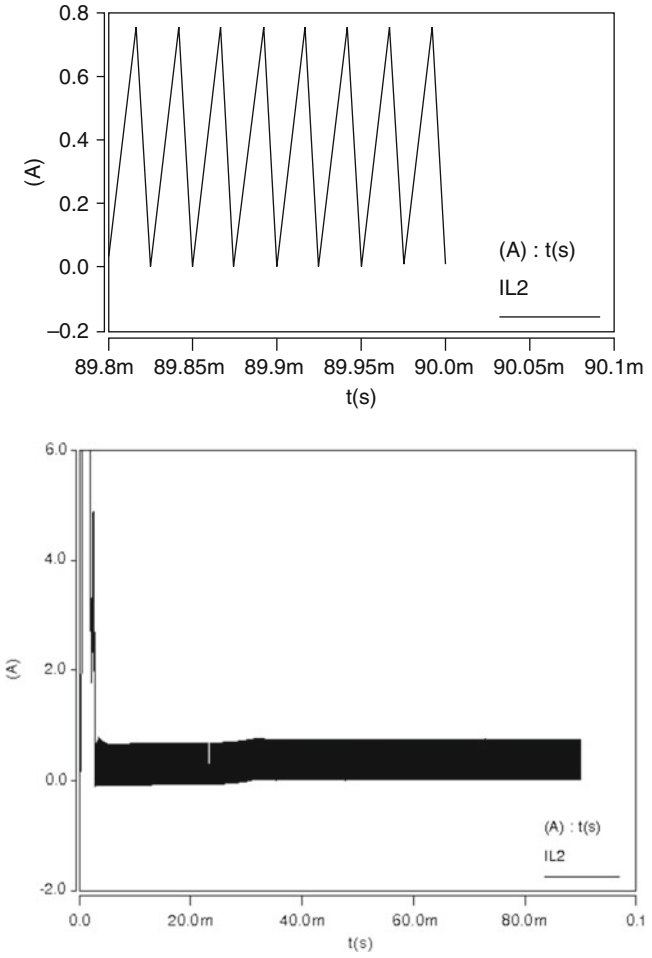

Fig. 4.11 Waveform of current at the inductor L2

- Step 2: Evaluation of the efficiency by varying the output voltage with a fixed input voltage

  The efficiency is calculated as follows:

$$eff = \frac{P_{out}}{P_{pv}} \tag{4.22}$$

where P_{out} is the output power and P_{pv} is the input power

Results are shown in Fig. 4.15.

Table 4.4 shows values of the efficiency of each converter at the nominal point (18 V, 400 V).

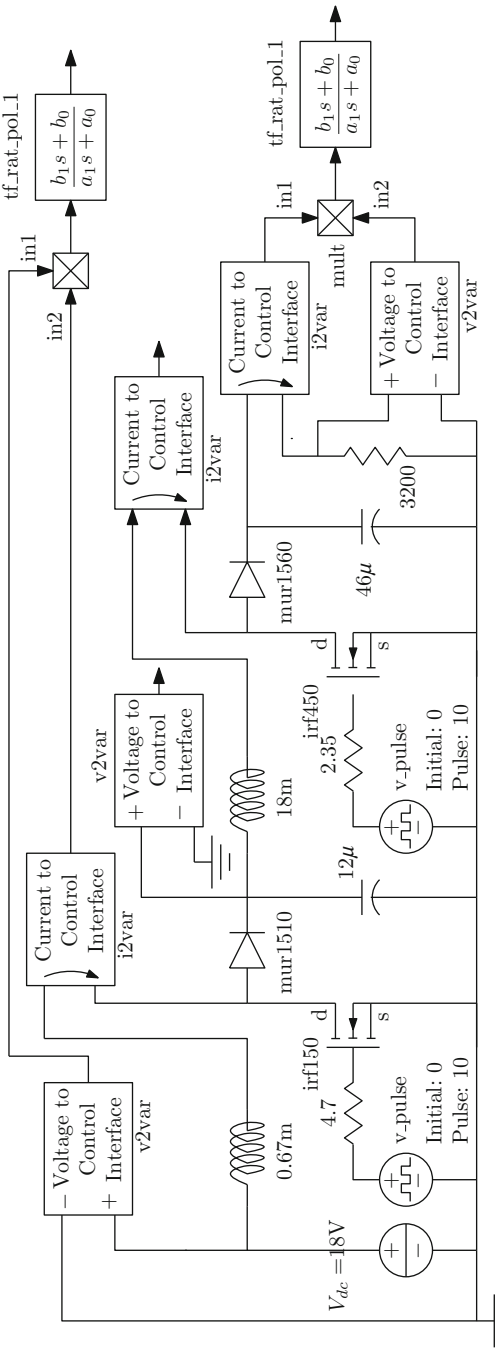

Fig. 4.12 Simulation circuit diagram for the double cascade boost converter

From Table 4.4 and Fig. 4.15, we remark that the double cascade boost converter has the best yield matched to the conventional boost converter and the quadratic boost converter. To have an idea about the losses of each converter, a study of the losses is evaluated by varying the input power. Figure 4.16 represents the result of this study.

It's clear from Fig. 4.16 that for different values of the input power, the double cascade boost converter has the minimum losses compared to the other converters.

4.5 Conclusion

Renewable energy sources are experiencing a fast development. Solar energy seems to be most attractive in present days. PV-systems offer a wide range of possibilities and configurations for the use of power electronic converters. The need to have converters with wider conversion rates has brought us to work with DC-DC cascade converters. Various converter topologies have been proposed in the literature, to improve performance and adapt to requirements.

In this chapter a comparison of three topologies of DC/DC converters has been presented. A complete modeling and a dimensioning of each topology have been evaluated. Simulation results for these converters have been discussed. An idea about the waveforms of electrical signals for the three topologies has been delivered. The dynamic behavior analysis shows that the double cascade boost has the best

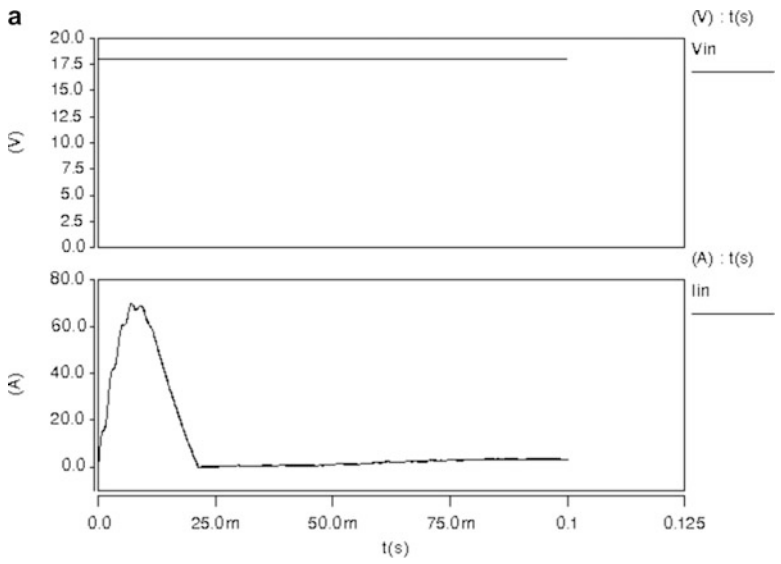

Fig. 4.13 Waveforms of electrical signals. (**a**) The input; (**b**) The output of the double cascade boost; (**c**) The output of the first boost

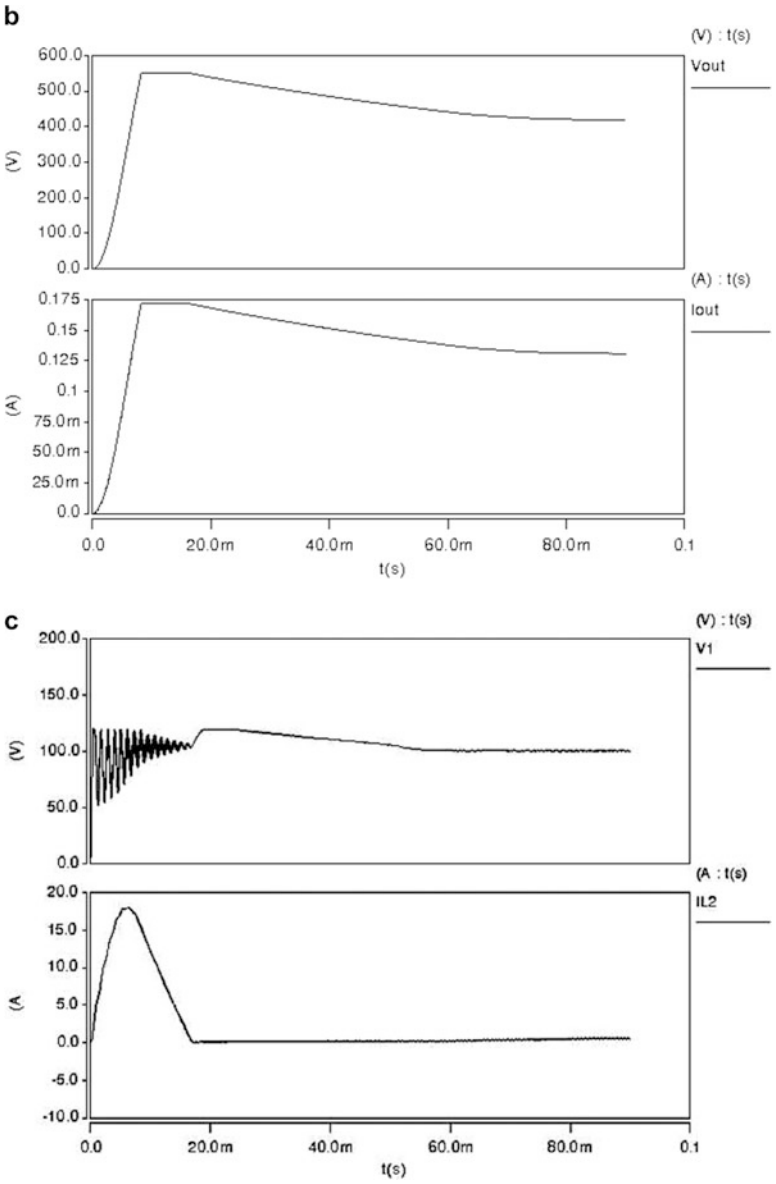

Fig. 4.13 (continued)

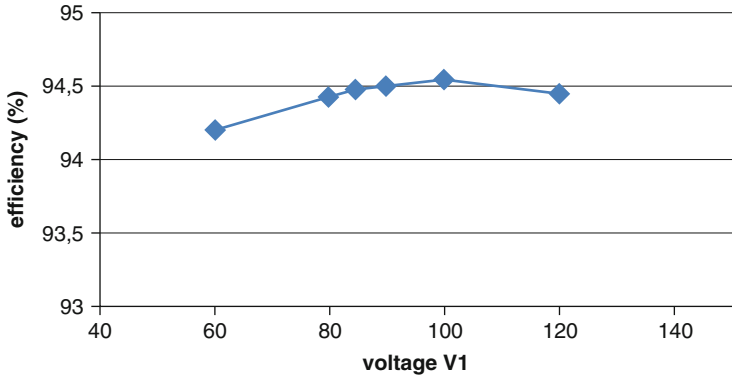

Fig. 4.14 Efficiency of the double cascade boost converter according to the voltage V1

Table 4.1 Duty ratio according to input voltage for the boost converter

Input voltage (V)	Output voltage (V)	Duty ratio	Efficiency %
9	X	X	X
18	400	0.955	85.32
48	420	0.88	96.98

Table 4.2 Duty ratio according to input voltage for the quadratic boost converter

Input voltage (V)	Output voltage (V)	Duty ratio	Efficiency %
9	X	X	X
18	400	0.787	85.37
48	406	0.653	93.2

Table 4.3 Duty ratio according to input voltage for the double cascade boost converter

Input voltage (V)	Intermediary voltage V_1(V)	Output voltage (V)	Duty Ratio D_1	Duty Ratio D_2	Efficiency %
9	100	400	0.91	0.75	85.7
18	100	400	0.82	0.75	94.54
48	100	420	0.52	0.75	96.92

response as the result of its ability to boost up the voltage even with a low input values. The efficiency analysis reveals that the best topology is the double cascade boost converter. The obtained results of the losses study show that the double cascade boost converter has the minimum losses. However, the operation with a single active switch such as the quadratic boost converter is a very attractive although its efficiency can be slightly lower.

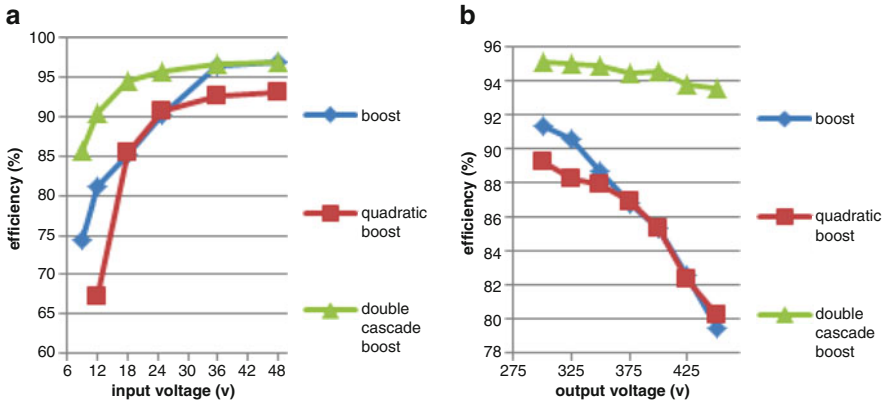

Fig. 4.15 Efficiency for the three converters according to. (**a**) The input voltage; (**b**) The output voltage

Table 4.4 Efficiency of different converters at the nominal point

Type of converter	Boost	Quadratic boost	Double cascade boost
Efficiency %	85.32	85.37	94.54

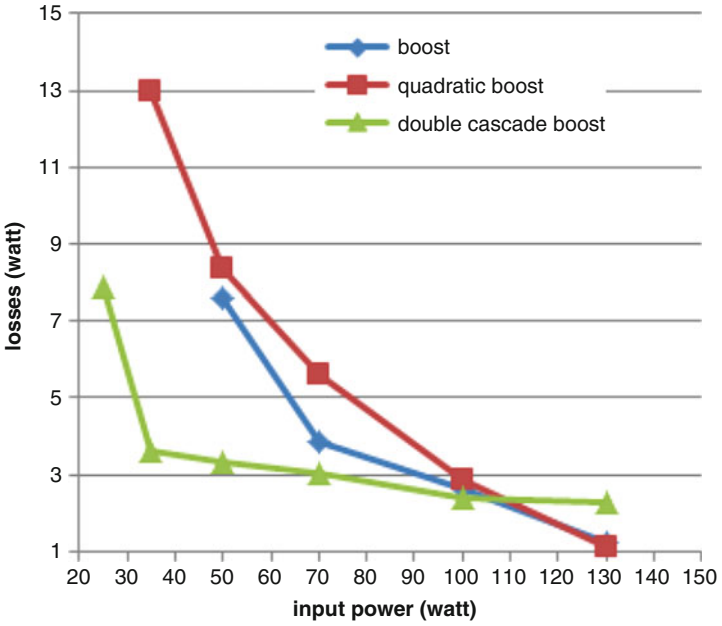

Fig. 4.16 losses of the three converters according to the input power

References

Aamir, M., & Shinwari, M. Y. (2010). Design, implementation and experimental analysis of two-stage boost converter for grid connected photovoltaic system. In *3rd IEEE International Conference on Computer Science & Information Technology, 5*, 194–199.

Chen, Z., Yong, W., & Gao, W. (2014). PI and Sliding Mode Control of a Multi-Input-Multi-Output Boost-Boost Converter. *WSEAS Transactions on Power Systems, 9*, 87–102.

Erickson, R. W., & Maksimovic, D. (1999). *Fundamentals of power electronics.* Boston: Kluwer Academic.

Hauke, B. (2014). *Basic calculation of a boost converter's power stage*. Application Report SLVA372C, Texas Instruments.

Lopez-Santos, O. (2015). *Contribution to the DC-AC conversion in photovoltaic systems: Module oriented converters* (pp. 99). Ph.D. thesis. LAAS-Toulouse, France.

Lopez-Santos, O., & Martinez-Salamero, L. (2015). Robust sliding-mode control design for a voltage regulated quadratic boost converter. *IEEE Transaction on Power Electronics, 30*(4), 2313–2327.

Lopez-Santos, O., Martinez-Salamero, L., Garcia, G., Valderrama-Blavi, H., & Sierra-Polanco, T. (2013a). Comparison of quadratic boost topologies operating under sliding-mode control. In *2013 Brazilian Power Electronics Conference*, Gramado, Brazil.

Lopez Santos, O., Martinez-Salamero, L., Garcia, G., Valderrama-Blavi, H., & Mercuri, D. O. (2013b). Efficiency analysis of a sliding-mode controlled quadratic boost converter. *IET Power Electronics, 6*, 364–373.

Maksimovic, D., & Cuk, S. (1991). Switching converters with wide DC conversion range. *IEEE Transaction on Power Electronics, 6*(1), 151–157.

Meddah, M., Bourahla, M., & Bouchetata, N. (2011). Synthèse des convertisseurs statiques DC/AC pour les systèmes photovoltaïques. *Revue des Energies Renouvelables ICESD'11 Adrar* (pp. 101–112).

Park, S., & Choi, S. (2010). Soft-switched CCM boost converters with high voltage gain for high-power applications. *IEEE Transaction on Power Electronics, 25*(5), 1211–1217.

Priya, P., Shabbeer Basha, G., Sujith Niranjan, S. V., & Seyezha, R. Dr. (2016). Investigation of sic mosfet based quadratic boost converter for photovoltaic applications. *International Journal of Precious Engineering Research & Applications, 1*(3), 26–29.

Selva Kumar, R., Gayathri Deivanayaki, V. P., Vignesh, C. J., & Naveena, P. (2016). Design and comparison of quadratic boost converter with boost converter. *International Journal of Engineering Research & Technology, 5*(1), 878–881.

Shen, J.-M., Jou, H.-L., & Wu, J.-C. (2012). Novel transformerless grid-connected power converter with negative grounding for photovoltaic generation system. *IEEE Transaction on Power Electronics, 27*(4), 1818–1829.

Silveira, G. C., Lessa Tofoli, F., Santos Bezerra, L. D., & Torrico-Bascope, R. P. (2014). A nonisolated DC-DC boost converter with high voltage gain and balanced output voltage. *IEEE Transaction on Industrial Electronics, 61*(12), 6739–6746.

Sira-Ramirez H., & Silva-Origoza, R. (2006). *Control design techniques in power electronics devices*. New Mexico City: Springer.

Suntio, T., Leppaaho, J., Huusari, J., & Nousiainen, L. (2010). Issues on solar-generator interfacing with current-fed MPP-tracking converters. *IEEE Transaction on Power Electronics, 25*(9), 2409–2419.

Veera Raghava, J. H. V., & Ranga Rao, C. (2014). A new converter topology for grid connected PV application. *International Journal of Engineering & Science Research, 4*(6), 256–269.

Chapter 5
Control of Power of a DFIG Generator with MPPT Technique for Wind Turbines Variable Speed

Yasmine Ihedrane, Chakib El Bekkali, Badre Bossoufi, and Manale Bouderbala

Abstract This chapter presents the study and the modeling of a variable speed wind system based on Doubly Fed Induction Generator controlled by a linear control type PI, in order to independently control the active and reactive stator powers generated by the wind turbine system.

The proposed control is applied to a Doubly Fed Induction Generator whose stator is directly connected to the grid in contrast to the rotor which is connected via "Back-to-Back" converters.

The objective of the modeling is to apply the direct and indirect control of the active and reactive power generated by the wind turbine based on the Doubly Fed Induction Generator via the Maximum Power Point Tracking (MPPT) strategy, to extract the maximum power from the wind.

Simulation results are tested and compared in order to evaluate the performance of the proposed system.

Keywords Doubly fed induction generator (DFIG) · Wind turbine · Direct field oriented control (DFOC) · Indirect field oriented control (IFOC) · Maximum power point tracking (MPPT)

5.1 Introduction

Today, energy demands has increased enormously. Fossil fuel sources are declining and the preoccupations concern the levels of pollution in the environment are the main drivers for electricity generation from renewable energy sources.

Y. Ihedrane (✉) · C. E. Bekkali
Laboratory of STIC, Faculty of Sciences Dhar El Mahraz, Sidi Mohamed Ben Abdellah University, Fez, Morocco

B. Bossoufi · M. Bouderbala
Laboratory of Electrical Engineering and Maintenance, Higher School of Technology, EST-Oujda, University of Mohammed I, Oujda, Morocco

N. Derbel, Q. Zhu (eds.), *Modeling, Identification and Control Methods in Renewable Energy Systems*, Green Energy and Technology,
https://doi.org/10.1007/978-981-13-1945-7_5

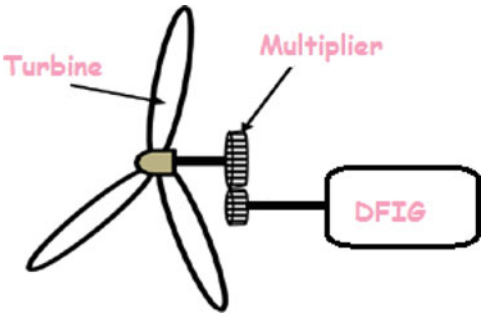

Fig. 5.1 Wind conversion chain

Renewable energies, such as solar energy and wind energy, are clean, inexhaustible energies, because of all these factors there has been a great deal of interest in wind power generation in recent years (Kazemi and Kojabadi 2010).

The induction machine in variable speed drives poses some difficulties which make its control more complex compared to a DC machine. Indeed, this type of machine is characterized by a multivariable, nonlinear mathematical model, with a strong coupling between the two control variables, which are the magnetic Field and the electromagnetic torque (de Wit 2000). In other words, it is not possible to control independently the input variables (voltage or current). Moreover, some state variables are not accessible to measurements, and its parameters are subject to variations over time. For this reason, several methods of controlling the DFIG have emerged, among them, the field oriented control technique.

The principle of this technique was developed by BLASCHKE in the early 1970s; it consists in orienting the field along one of the axes of the referential d, q in order to make this machine's behavior similar to that of a Separately Excited DC Machine. This control is based on PI controllers.

In this chapter, we begin with the modeling of the turbine. Next, a tracking technique operating point at maximum power point tracking (MPPT) will be presented (Bekakra and Attous 2011; Ghoudelbourk et al. 2016). Then, we will present a model of the DFIG in the referential (d, q). After that, we will tackle the principle of field oriented control. Finally with the use of MATLAB/SIMULINK, we will present and analyze the simulation results to validate our theoretical study.

5.2 Modeling of the Wind Conversion Chain

The turbine studied in this chapter comprises three blades of length R. They are fixed on a drive shaft rotating at a turbine speed Ω_t connected to a gain multiplier G which drives an electric generator as shown in Fig. 5.1 (Ihedrane et al. 2017a).

5.2.1 Model of the Turbine

5.2.1.1 Turbine Power

The kinetic power of the wind is defined by the following equation (Ihedrane et al. 2017a,b)

$$P_v = \frac{\rho \times S \times V^3}{2} \tag{5.1}$$

where:

ρ: Density of the air

S: Surface swept by the turbine

v: Wind Speed

The turbine can convert only a percentage of the wind power presented by the coefficient C_p, hence the expression of the aerodynamic power can be described as follows:

$$P_{aero} = C_p(\lambda, \beta) \times \frac{\rho \times S \times V^3}{2} \tag{5.2}$$

5.2.1.2 Power Coefficient

The power coefficient $C_p(\lambda, \beta)$ represents the aerodynamic efficiency of the wind turbine. The latter depends on the specific speed λ and the angle of the orientation of the blades β. It is approximated by the following function (Bossoufi et al. 2014; Ihedrane et al. 2017a):

$$C_p(\lambda, \beta) = C_1 \times \left(\frac{C_2}{A} - C_3 \times \beta - C_4\right) \times \exp\left(-\frac{C_5}{A}\right) + C_6 \times \lambda \tag{5.3}$$

where: $\frac{1}{A} = \frac{1}{(\lambda + 0.08 \times \beta)} - \frac{0.035}{\beta^3 + 1}$

5.2.1.3 Specific Speed

Specific speed λ is defined as the ratio of the linear turbine speed and the wind speed (Ihedrane et al. 2017a; Youcef 2014), it is given by (5.4):

$$\lambda = R \times \frac{\Omega_t}{V} \tag{5.4}$$

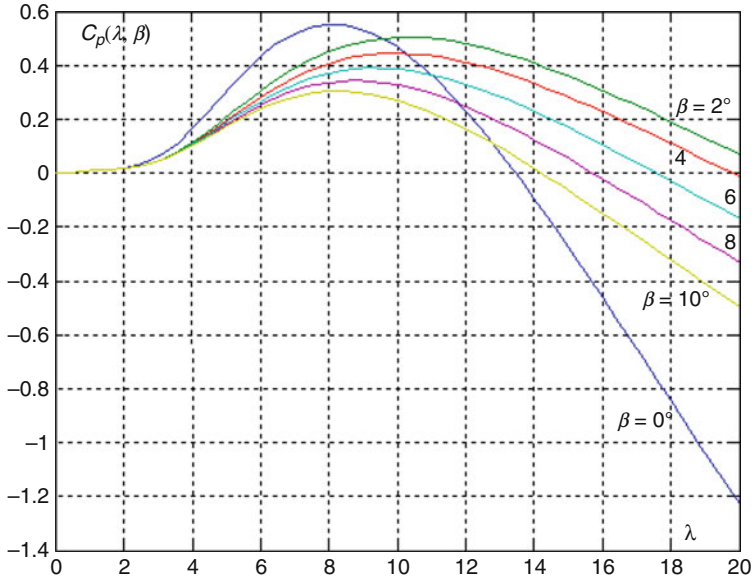

Fig. 5.2 Power coefficient C_P in function of speed ratio λfor different values of β

Figure 5.2 shows the variation of power coefficient C_P in function of speed ratio λ for different values of β (Bossoufi et al. 2014; Ihedrane et al. 2017a). From this figure we can note that the power coefficient C_p reaches its maximum 0.5506 for a speed ratio $\lambda_{opt} = 8$ and $\beta = 0°$.

5.2.1.4 Mechanical Torque

From the expression of the power produced by the turbine and knowing the speed turbine, the mechanical torque can be expressed by 5.5 (Ihedrane et al. 2017a):

$$C_{aero} = \frac{P_{aero}}{\Omega_t} = C_p(\lambda, \beta) \times \frac{\rho \times S \times V^3}{2 \times \Omega_t} \tag{5.5}$$

5.2.2 Model of the Multiplier

The multiplier transforms the turbine speed into the generator speed and the aerodynamic torque into the generator torque according to the following system (Ihedrane et al. 2017a; Youcef 2014):

$$\begin{cases} \Omega_t = \dfrac{\Omega_{mec}}{G} \\ C_g = \dfrac{C_{aero}}{G} \end{cases} \tag{5.6}$$

where:

Ω_{mec}: rotation speed of the generator.

C_g: The generator torque.

5.2.3 Dynamic Equation of the Transmission Shaft

From the mechanical torque exerted on the rotor shaft of the wind turbine and the electromagnetic torque C_{em}, the fundamental equation of the dynamics makes it possible to determine the evolution of the mechanical speed (Guda 2005):

$$C_{mec} = J\frac{d\Omega_t}{dt} = C_g - C_{em} - C_f \tag{5.7}$$

with:

J: the total inertia, it is constituted by the turbine inertia J_t, and the generator inertia J_g (Aimani 2004):

$$J = \frac{J_t}{G} + J_g \tag{5.8}$$

The block diagram corresponding to the model of the turbine is given in Fig. 5.3.

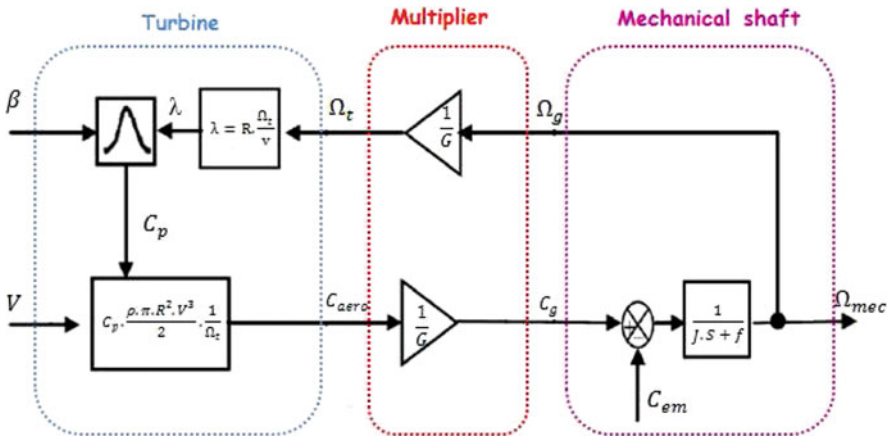

Fig. 5.3 Block diagram of the wind converter model

5.2.4 Control Strategy for Wind Turbine

5.2.4.1 Maximum Power Point Search Method

The characteristic of the optimal power of a wind turbine is strongly non-linear and "bell-shaped" (Johansen et al. 2001).

The wind system must find the maximum power, for each wind speed, which is equivalent to finding the optimum rotational speed.

Figure 5.4 illustrates the characteristic curves of the wind turbine in the plane (power,rotational turbine speed). Each curve corresponds to a wind speed V_v. The vertices of these characteristics present the optimal points sought which define a curve called the optimal power curve given by:

$$P_{opt} = C_p opt(\lambda_{opt}) \times \frac{\rho \times \pi \times R^2 \times V^3}{2} \tag{5.9}$$

The wind system requires a perfect tracking of the optimum power curve in order to have an ideal operation, to do that, a specific command called Maximum Power Point Tracking (MPPT) must be used. The strategy of this control consists in controlling the electromagnetic torque in order to adjust the mechanical speed in a way to maximize the electrical power generated.

There are two approaches:

- The first approach considers that the characteristic $C_p = f(\lambda)$ is not known (Johansen et al. 2001).
- The second one considers that the characteristic $C_p = f(\lambda)$ is known. Simply follow the optimum power curve for the wind turbine to be in optimum conditions.

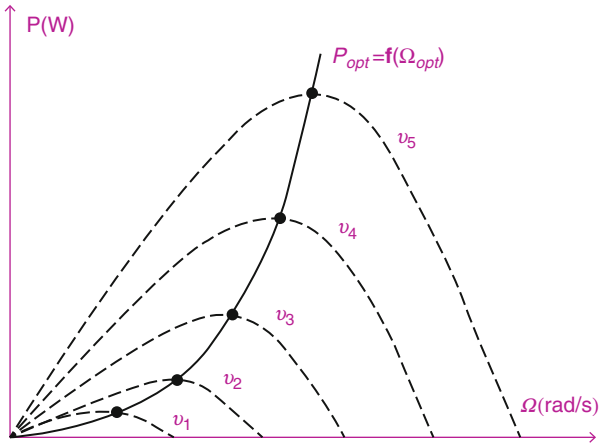

Fig. 5.4 Characteristics of the wind turbine in the plane (power,rotational turbine speed)

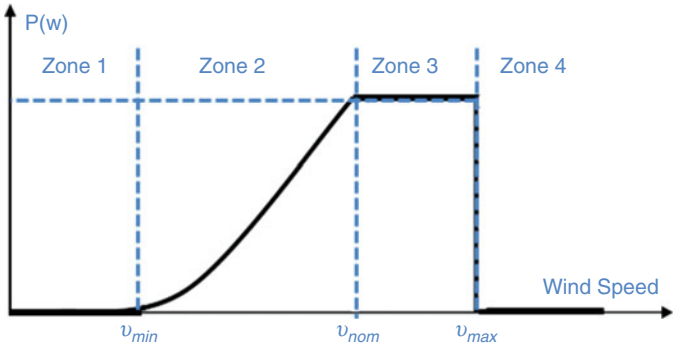

Fig. 5.5 Characteristics (Power, wind speed)

This approach Simplifies the algorithm of the maximum power and allows to use more basic and less expensive converters.

5.2.4.2 Operation of a Variable Speed Wind Turbine

Figure 5.5 illustrates the different operating phases of a variable speed wind turbine (Mourad 2016).

- Wind speeds are very low and insufficient to drive the wind turbine and produce power.
- the wedge angle is kept constant, and the control of the electromagnetic torque will be implemented in order to capture the maximum power for each wind speed (MPPT principle). In this zone, the generator power curve keeps a rapid progression (Mourad 2016).
- Zone 3: The generator speed is kept constant at its maximum as opposed to a suitable torque. The increase in the wind speed leads to a decrease in the coefficient C_p and a slower increase in the recovered power. When the maximum of the power generator is reached, the angle of the blades (pitch) is modified (Passage from β_1 to β_2) in order to degrade the coefficient C_p.
- Zone 4: In this zone, when the wind speed becomes too high V_M, an emergency device is used to stop the wind turbine (No electricity production) and to prevent damage.

5.2.4.3 Maximum Power Extraction Technique

In order to extract the maximum power from the wind turbine, we need an algorithm acting on the set point variables, to have a good efficiency of the device.

In the literature we have found two types of control structures for the maximization of power extracted:

- The MPPT control without mechanical speed control.
- The MPPT control with mechanical speed control

In this chapter we are interested in the MPPT control without mechanical speed control.

In practice, an exact measurement of wind speed is difficult to achieve. Due to the following reasons (Aimani 2004; Mourad 2016).

- The anemometer is located behind the rotor of the turbine, which gives an erroneous reading of the wind speed.
- Since the diameter of the surface swept by the blades is large (typically 70 m for a 1.5 m wind turbine), a significant variation in wind appears depending on the height of the anemometer. So, the use of a single anemometer leads to use only one local measurement of the wind speed which is therefore not sufficiently representative of its average value appearing on all the blades.

An incorrect measurement of the speed therefore necessarily leads to a degradation of the power captured according to the power extraction technique. This is why most wind turbines are controlled without speed control. This control structure is based on the assumption that the wind speed varies very steadily (Gaillard 2010):

$$J\frac{d\Omega_{mec}}{dt} = C_g - Cem - f \times \Omega_{mec} = 0 \tag{5.10}$$

According to this equation, and by neglecting the mechanical torque Cmec and the effect of the couple of viscous friction $f \times \Omega_{mec}$, we obtain the following equation:

$$C_{em} = C_g \tag{5.11}$$

The reference electromagnetic torque is determined from an estimation of the aerodynamic torque:

$$C_{emref} = \frac{C_{aeroref}}{G} \tag{5.12}$$

We know that:

$$\begin{cases} C_{aero} = C_p(\lambda, \beta)\dfrac{\rho \times \pi \times R^2 \times V^3}{2 \times \Omega_t} \\ \Omega_t = \dfrac{\Omega_{mec}}{G} \\ V_{est} = R\dfrac{\Omega_{test}}{2 \times \lambda_{test}} \end{cases} \tag{5.13}$$

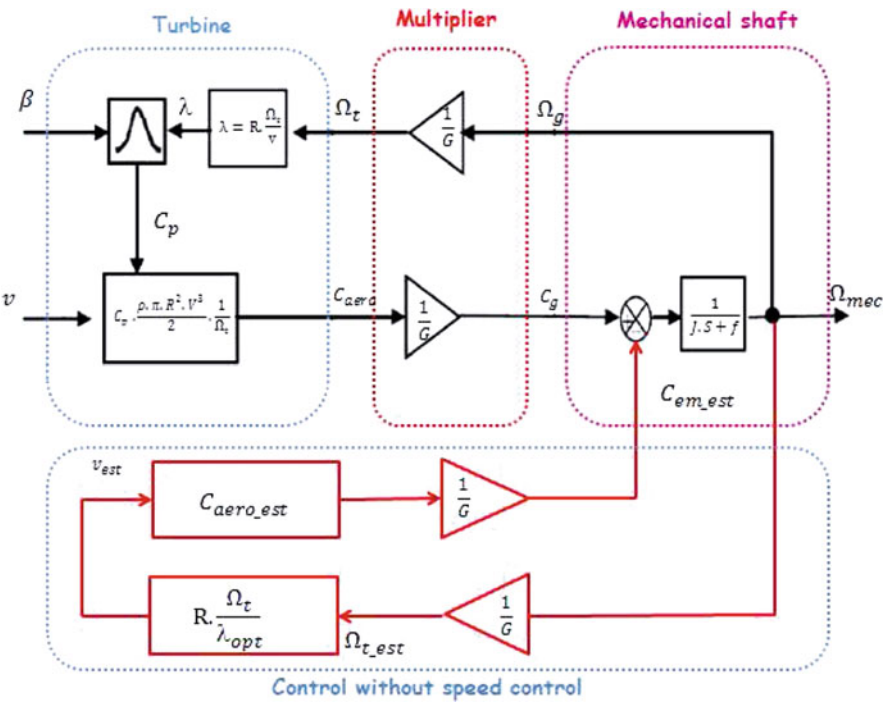

Fig. 5.6 Block diagram of the MPPT strategy without speed control

After calculation and a series of combinations, we get the following equation:

$$C_{emref} = \frac{C_p(\lambda, \beta)}{\lambda_{opt}^3} \times \frac{\rho \times \pi \times R^3}{2} \times \frac{\Omega_{mec}^3}{G^3} \tag{5.14}$$

The block diagram of the MPPT strategy without mechanical speed measurement is shown in Fig. 5.6.

5.3 Modeling of the Doubly Fed Induction Generator DFIG

5.3.1 Structure of the Electrical Machine

The wind turbine conversion system studied in this chapter is shown in Fig. 5.7. It is divided into two main parts which will be modeled separately: the Doubly Fed Induction Generator whose stator is directly connected to the grid, in contrast to the rotor which is connected to the grid via powers converters "Back to Back",

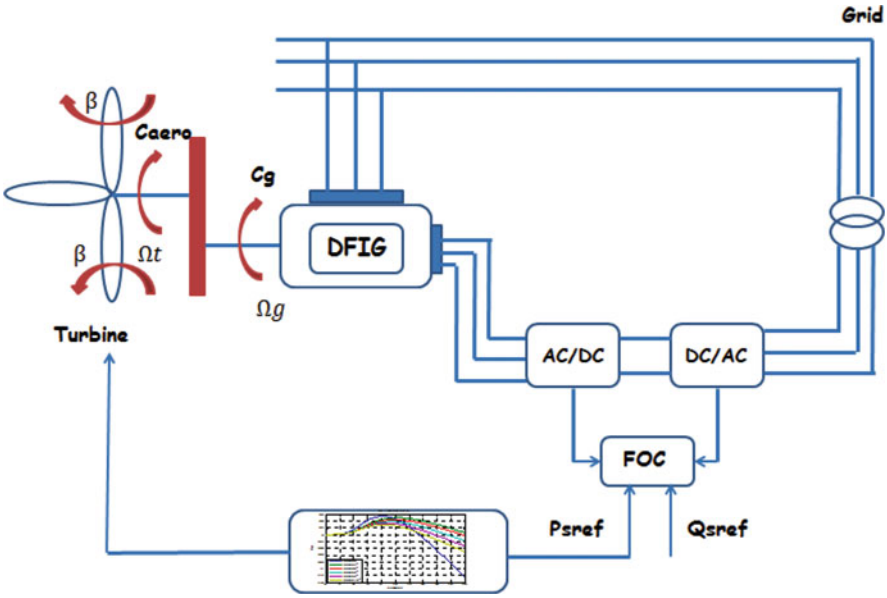

Fig. 5.7 General structure of a wind turbine conversion chain

these converters being able to operate as a rectifier or an inverter according to the direction of the energy transit.

This structure has been retained in this work, in order to establish a control strategies with the objective of controlling the power exchange between the generator and the electrical grid.

The stator magnitudes have the same frequency as that of the grid, that is why it is useless to use power converters to transfer the stator power. On the other hand, the rotor magnitudes don't have the same frequency as the alternating magnitudes of the grid, which depend on the speed of the rotor and consequently the wind speed, which justifies the use of a voltage converter feeding the rotor.

In the context of the production of electrical energy from wind power, this device can operate at fixed or variable speed, operate in hypo-synchronous or hyper-synchronous mode.

The powers converter side generator allows the control of the active and reactive power produced by the DFIG, and the powers converter side grid allows the control of the DC bus voltage and the power factor at the connection of the wind turbine with the power grid (Datta 2002).

The use of a doubly Fed Induction Generator presents an excellent compromise between the range of speed variation and the dimensioning of the converters compared to the nominal power of the machine.

5.3.2 *Operation of the Doubly Fed Induction Machine in Generator Mode*

The Doubly Fed Induction Machine, unlike other electrical machines, is reversible and can operate in generator mode and motor mode.

Figure 5.8 shows the form of the mechanical torque/speed characteristic of the induction machine (Mourad 2016).

From Fig. 5.8 it can be seen that the induction machine operates in motor mode for $g > 0$ and in generator mode in the opposite case.

For operation with Doubly fed Induction Machine, the stator is powered by a first balanced three-phase voltage source of frequency f, the rotor is connected to a second alternating frequency source f_r.

The currents flowing in the stator windings create rotating field at the speed $\Omega_s = \frac{\Omega_s}{P}$, similarly, the rotor currents produce a rotor field rotating at a speed $\Omega_r = \frac{\Omega_r}{P}$.

When the rotating field of the ror rotates in the same direction of rotation of the stator field, the slip 'g' is positive and the rotor rotates slower than the stator field $\Omega < \Omega_s$, so, the machine operates in Hypo-Synchronous mode.

In the opposite case, the rotating field created by the windings of the rotor rotates in the opposite direction than that of the stator, the slip 'g' becomes negative and the rotor rotates faster than the rotating field created by the stator $\Omega > \Omega_s$, so, the machine operates in hyper-synchronous mode.

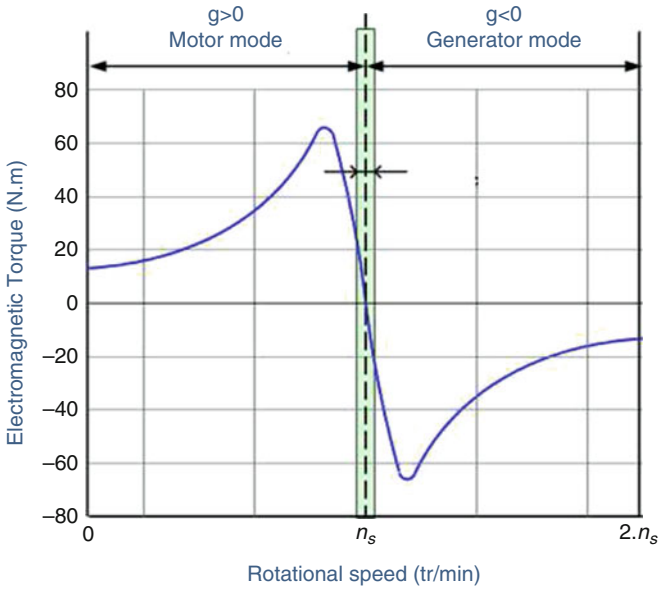

Fig. 5.8 Torque/speed characteristic of the induction machine

For the conventional induction machine, a positive sign of slip 'g' corresponds to a motor operation of the machine, whereas a negative sign translates to a generator operation, which may lead to confusion in the understanding of the DFIM operating principle, in which the sign of the slip reflects hypo or hyper-synchronous operation and not the operating mode of the machine (motor or generator) (Bennani 2011).

The possibility of operating in hyper-synchronism or in hypo-synchronism, both in motor mode and in generator mode, is obtained by controlling the amplitude and phase of the rotor voltages, these making it possible to control the magnetic field at inside the machine.

5.3.3 Modeling of the Doubly Fed Induction Generator

5.3.3.1 Simplifying Assumptions

The basic structure of the three-phase induction machine is given by Fig. 5.9.

Despite its simplicity of construction, the mathematical model of the Doubly Fed Induction Gnerator DFIG is complex. In the three-phase referential fixed and linked to the stator, the model of the induction machine present the disadvantage of arriving at differential equations with variable coefficients as a function of the position of the rotor, and therefore of time.

To remediate to this problem, several approaches have been used, among them the approach based on the theory of the two axes RH Park (Park 2012) which

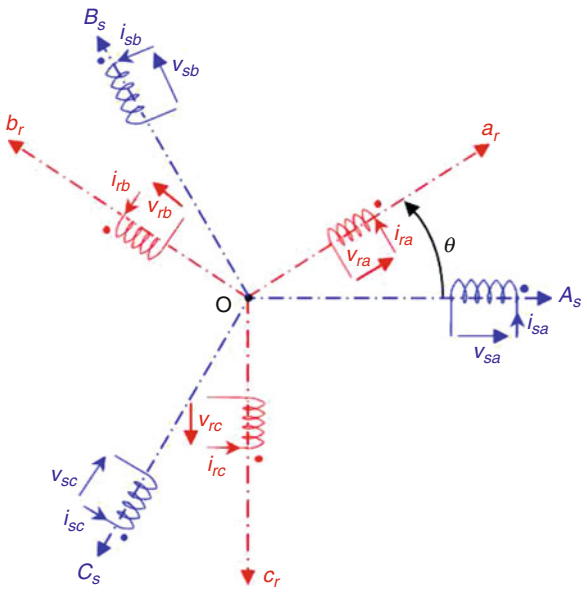

Fig. 5.9 Structure of the three-phase induction machine

consists in transforming the three-phase system into an equivalent two-phase system, moving from the fixed frame of reference (A, B, C) to a second mobile reference frame (d, q): 'd' presents the direct axis and 'q' the quadrature axis, perpendicular and mutually coupled, the angle between the two referential is called 'the Park angle'.

5.3.3.2 Application of Park Transformation to DFIG

Figure 5.10 presents the DFIM model in the PARK referential.

From Fig. 5.10 we obtain:

$$\theta_s = \theta_r + \theta \tag{5.15}$$

So its derivative can be writing as follows:

$$\frac{d\theta_s}{dt} = \frac{d\theta_r}{dt} + \frac{d\theta}{dt} \tag{5.16}$$

The modeling of the DFIG is identical to that of the induction machine cage. The only difference lies in the fact that the rotor voltages are not null because these windings are not 'short-circuited'.

The general equations obtained after the application of the Park transformation are given by the following equations.

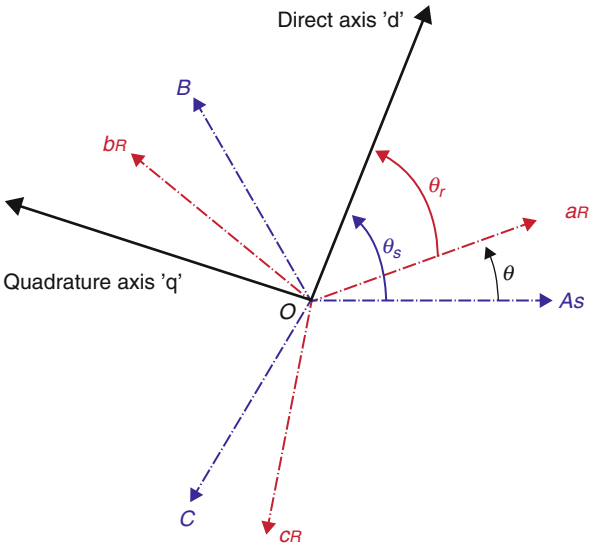

Fig. 5.10 Graphical representation of DFIG in the park referential

- Stator Voltages:

$$\begin{cases} V_{sd} = R_s \times I_{sd} + \dfrac{d\Phi_{sd}}{dt} - \omega_s \times \Phi_{sq} \\ V_{sq} = R_s \times I_{sq} + \dfrac{d\Phi_{sq}}{dt} + \omega_s \times \Phi_{sd} \end{cases} \tag{5.17}$$

- Rotor Voltages:

$$\begin{cases} V_{rd} = R_r \times I_{rd} + \dfrac{d\Phi_{rd}}{dt} - \omega_r \, \Phi_{rq} \\ V_{rq} = R_r \times I_{rq} + \dfrac{d\Phi_{rq}}{dt} + \omega_r \times \Phi_{rd} \end{cases} \tag{5.18}$$

- Stator Field:

$$\begin{cases} \Phi_{sd} = L_s \times I_{sd} + M \times I_{rd} \\ \Phi_{sq} = L_s \times I_{sq} + M \times I_{rq} \end{cases} \tag{5.19}$$

- Rotor Field:

$$\begin{cases} \Phi_{rd} = L_r \times I_{rd} + M \times I_{sd} \\ \Phi_{rq} = L_r \times I_{rq} + M \times I_{sq} \end{cases} \tag{5.20}$$

- Electromagnetic Torque:

$$C_{em} = p \times (\Phi_{sd} \times I_{sq} - \Phi_{sq} \times I_{sd}) \tag{5.21}$$

- The active and reactive powers of the stator:

$$\begin{cases} P_s = V_{sd} \times I_{sd} + V_{sq} \times I_{sq} \\ Q_s = V_{sq} \times I_{sd} - V_{sd} \times I_{sq} \end{cases} \tag{5.22}$$

- The active and reactive powers of the rotor:

$$\begin{cases} P_r = V_{rd} \times I_{rd} + V_{rq} \times I_{rq} \\ Q_r = V_{rq} \times I_{rd} - V_{rd} \times I_{rq} \end{cases} \tag{5.23}$$

5.4 Modeling of Power Converters

The converter powered by a source of perfect voltage imposes an AC voltage at its output, which is formed by a succession of two levels rectangular square waves, this

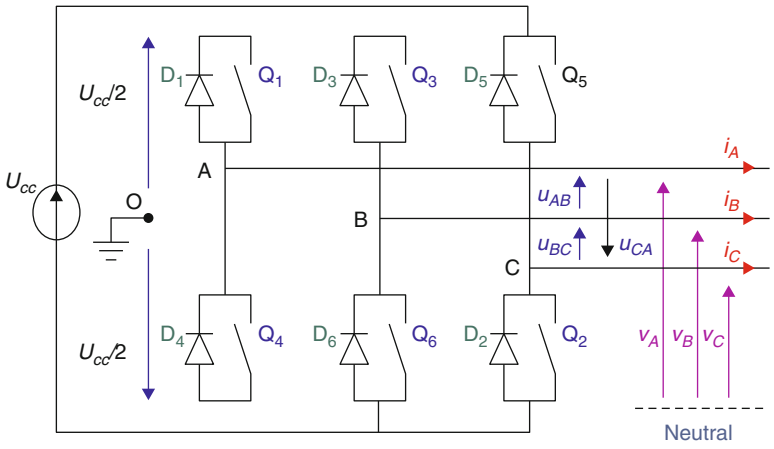

Fig. 5.11 Diagram of a three-phase voltage converter

being due to the opening and closing of the switches. The operating frequency is set by the control of the switches.

The three-phase system obtained at the output of the converter is a balanced voltage system containing odd harmonics that are different from rank three and their multiples (Mourad 2016).

The structural diagram of a three-phase voltage converter is given by Fig. 5.11.

The compound voltages are given by the following relations:

$$\begin{cases} U_{AB} = v_{AO} - v_{BO} \\ U_{BC} = v_{BO} - v_{CO} \\ U_{CA} = v_{CO} - v_{AO} \end{cases} \tag{5.24}$$

At the level of the charge, the simple voltages are giving as follows:

$$\begin{cases} U_{AB} = v_A - v_B \\ U_{BC} = v_B - v_C \\ U_{CA} = v_C - v_A \end{cases} \tag{5.25}$$

We have:

$$\begin{cases} U_{AB} - U_{CA} = 2v_A - (v_B + v_C) \\ U_{BC} - U_{AB} = 2v_B - (v_C + v_A) \\ U_{CA} - U_{BC} = 2v_C - (v_A + v_B) \end{cases} \tag{5.26}$$

The voltages (v_A, v_B, v_C) form a balanced three-phase system, so we can write:

$$\begin{cases} U_{AB} - U_{CA} = 3v_A \\ U_{BC} - U_{AB} = 3v_B \\ U_{CA} - U_{BC} = 3v_C \end{cases} \tag{5.27}$$

The expression of the simple voltages is presented by the following system (5.28)

$$\begin{cases} v_A = \frac{1}{3}(U_{AB} - U_{CA}) \\ v_B = \frac{1}{3}(U_{BC} - U_{AB}) \\ v_C = \frac{1}{3}(U_{CA} - U_{BC}) \end{cases} \tag{5.28}$$

Hence, the matrix form of simple voltages is giving as follows:

$$\begin{bmatrix} v_A \\ v_B \\ v_C \end{bmatrix} = \frac{1}{3} \begin{bmatrix} 2 & -1 & -1 \\ -1 & 2 & -1 \\ -1 & -1 & 2 \end{bmatrix} \begin{bmatrix} v_{AO} \\ v_{BO} \\ v_{CO} \end{bmatrix} \tag{5.29}$$

Each arm of the converter consists of two switches which are supposed perfect and operate in a complementary manner, it is therefore possible to associate a binary control (S_i) value with each arm with (i = A; B; C) and such that:

$$\begin{bmatrix} v_{AO} \\ v_{BO} \\ v_{CO} \end{bmatrix} = \frac{U_{CC}}{3} \begin{bmatrix} S_A \\ S_B \\ S_C \end{bmatrix} \tag{5.30}$$

By replacing the voltages with their values, we obtain:

$$\begin{bmatrix} v_A \\ v_B \\ v_C \end{bmatrix} = \frac{1}{3} \begin{bmatrix} 2 & -1 & -1 \\ -1 & 2 & -1 \\ -1 & -1 & 2 \end{bmatrix} \frac{U_{CC}}{3} \begin{bmatrix} S_A \\ S_B \\ S_C \end{bmatrix} \tag{5.31}$$

The simple voltages delivered by the converter will be obtained directly from the states of the control quantities S_A, S_B and S_C which represent the control signals of the switches.

The states of these quantities will also be determined by the envisaged control strategy.

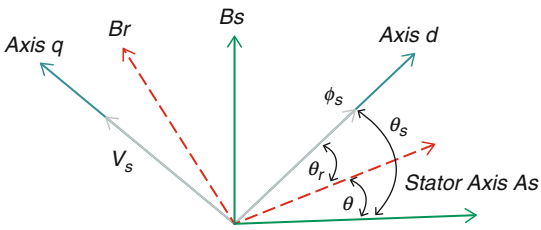

Fig. 5.12 Stator Field-orientation along the d axis

5.5 Field Oriented Control Strategy Applied to DFIG

5.5.1 Principle of Control by Field Orientation Control Strategy

The principle of control by field oriented control consists in orienting field along one of the axes in order to make the behavior of the induction machine similar to that of machine DC separately excited (Aimani 2004; Ihedrane et al. 2017a).

We have chosen to orient the stator field along the axis 'd' as shown in Fig. 5.12

According to this orientation we obtain:

$$\begin{cases} \Phi_{sd} = \Phi_s \\ \Phi_{sq} = 0 \end{cases} \tag{5.32}$$

In the referential (ABC), the voltage at the terminals of a phase 'i' of the stator is expressed as follows:

$$v_{si} = R_s \times I_{si} + \frac{d\Phi_{si}}{dt} \tag{5.33}$$

with: $i = 1, 2, 3$

Assuming the resistance of the stator winding 'R_s' is negligible for the medium and high power machines generally employed in the wind energy conversion (Ihedrane et al. 2017a; Mourad 2016), we obtain:

$$v_{si} = \frac{d\Phi_{si}}{dt} \tag{5.34}$$

We supposed that the voltages of the electrical grid are stable; the stator flux will also be constant. So, we can write:

$$\begin{cases} v_{sd} = 0 \\ v_{sq} = v_s = \omega_s \times \Phi_s \end{cases} \tag{5.35}$$

We have chosen to orient the stator flux along the axis 'd', we obtain:

$$\begin{cases} I_{sd} = \dfrac{1}{L_s} \times (\Phi_s - M \times I_{rd}) \\ \\ I_{sq} = -\dfrac{M}{L_s} \times I_{rq} \end{cases} \tag{5.36}$$

So, the previous relations become as follows:

- Relation between the electromagnetic torque and the rotor currents:
  The expression of the torque is written as follows:

$$C_{em} = p \times I_{sq}.\Phi_s = -p \times \frac{M}{L_s} \times \Phi_s \times I_{rq} \tag{5.37}$$

- Relation between stator powers and rotor currents:
  We replaced I_{sq} and I_{sd} by their expressions in the expression of the stator power (P_s and Q_s) and knowing that $v_{sd} = 0$,the expression of the active and reactive stator powers become as follows:

$$\begin{cases} P_s = V_{sq} \times I_{sq} = -V_s \times \dfrac{M}{L_s} \times I_{rq} \\ \\ Q_s = V_s \times I_{sd} = \dfrac{V_s^2}{\omega_s \times L_s} - V_s \times \dfrac{M}{L_s} \times I_{rd} \end{cases} \tag{5.38}$$

- Relation between rotor voltage and rotor current:
  By replacing I_{sq} and I_{sd} with their expressions in Φ_{rd} and Φ_{rq} we get:

$$\begin{cases} \Phi_{rd} = (L_r - \dfrac{M^2}{L_s}) \times I_{rd} + \dfrac{M \times v_s}{L_s \times \omega_s} \\ \\ \Phi_{rq} = (L_r - \dfrac{M^2}{L_s}) \times I_{rq} \end{cases} \tag{5.39}$$

By injecting these equations into the expressions of the rotor voltages, we obtain the following expression:

$$\begin{cases} V_{rd} = \left[R_r + S \left(L_r - \dfrac{M^2}{L_s} \right) \right] I_{rd} - \omega_s \, g \, \left(L_r - \dfrac{M^2}{L_s} \right) \, I_{rq} \\ \\ V_{rq} = \left[R_r + S \left(L_r - \dfrac{M^2}{L_s} \right) \right] I_{rq} - \omega_s \, g \, \left(L_r - \dfrac{M^2}{L_s} \right) I_{rd} + \dfrac{g \, M \, V_s}{L_s} \end{cases} \tag{5.40}$$

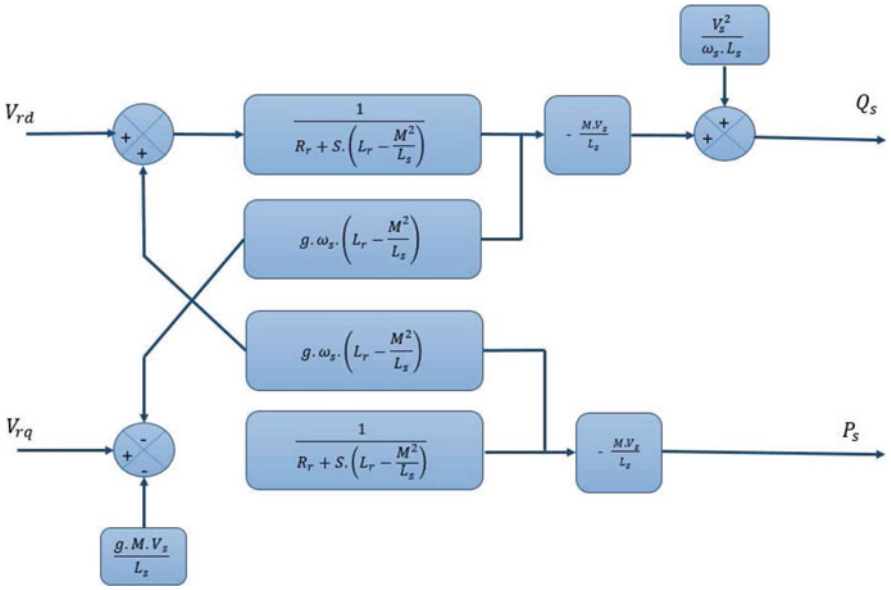

Fig. 5.13 Simplified model of the DFIG

with:

g: the slip of the induction machine.

$\omega_r = g \times \omega_s$: the rotor pulsation

ω_s: The stator pulsation

These equations make it possible to establish a block diagram of the electrical system that can be regulated (Fig. 5.13):

According to this block diagram, we can note that the rotor voltages and the stator powers are linked by transfer functions with the first order. This allows to set up a vector control with the influence of the couplings, each axis can be controlled independently with its own controller.

For these controllers, the reference values will be the active power for the rotor axis 'q' and the reactive power for the rotor axis 'd' (Allam et al. 2014; Poitiers 2003).

The reactive power reference will be kept zero in order to ensure a unit power factor on the stator side so as to optimize the quality of the energy sent to the grid. The active power reference should allow keeping the wind power factor optimal.

To carry out the power control of this machine, there are two structures:

- Structure of the direct control.
- Structure of the indirect control.

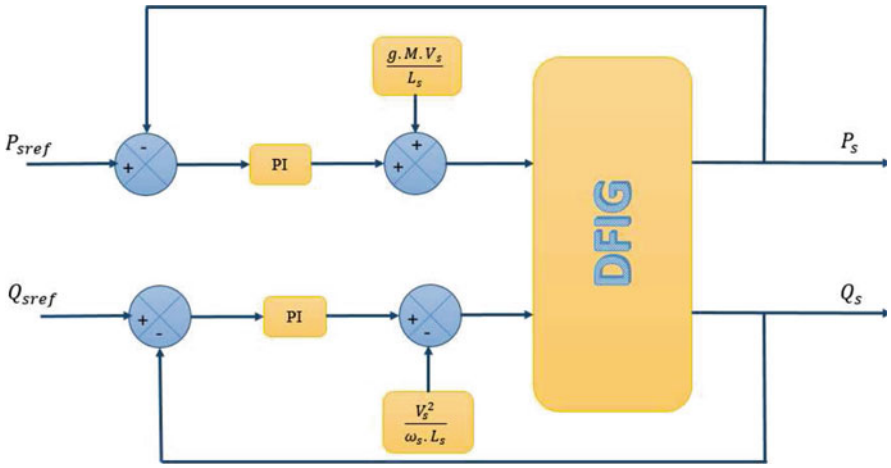

Fig. 5.14 Direct control of the doubly fed induction generator

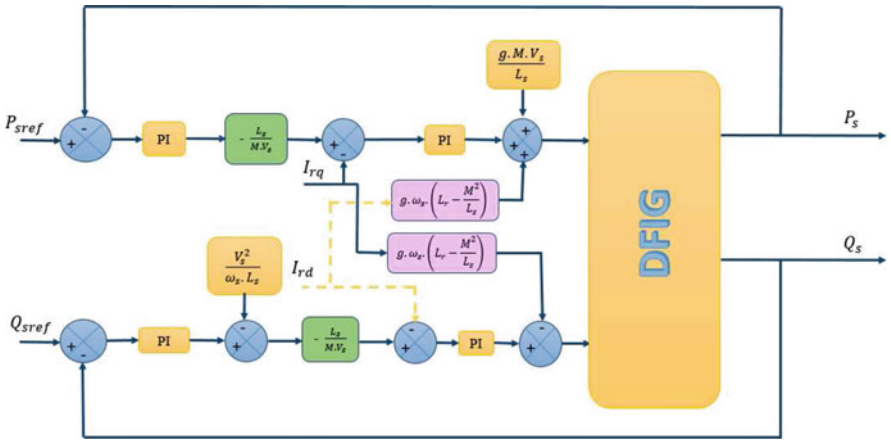

Fig. 5.15 Indirect control of the doubly fed induction generator

5.5.1.1 Structure of Direct Control

The block diagram of the direct control of the Doubly Fed Induction Generator is shown in Fig. 5.14.

This method consists in neglecting the coupling terms and setting up a regulator on each axis in order to control independently the active and reactive powers (Sejir 2006; Tarfaya et al. 2015).

5.5.1.2 Structure of Indirect Control

The indirect control of the Doubly Fed Induction Generator is given by Fig. 5.15.

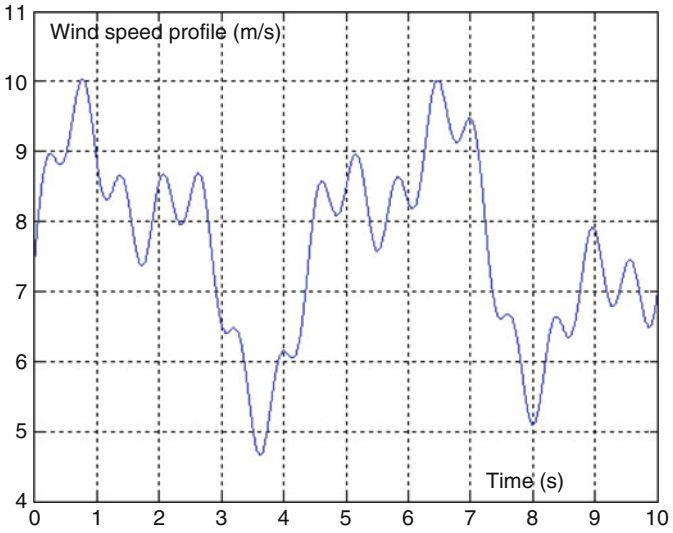

Fig. 5.16 Wind profile

The second method consists in considering the coupling terms and compensates them by performing a system with two loops in order to control the powers and the rotor currents. This technique wich called indirect method, allows to controlling the rotor currents in order to ensure protection of the generator DFIG by limiting the currents and giving more flexibility to the machine (Allam et al. 2014; Ihedrane et al. 2017a).

5.6 Simulation and Interpretations

In order to examine the robustness of the Field Oriented Control Technique with the turbine control by the MPPT strategy, we applied a random wind profile given by Fig. 5.16.

The rotational speed of the DFIG (Fig. 5.17) has less oscillation and high reliability with respect to wind speed profile (Fig. 5.16).

5.6.1 Simulation Result of the Direct Field Oriented Control DFOC

Figure 5.18 shows the simulation results of Direct Field Oriented Control DFOC:

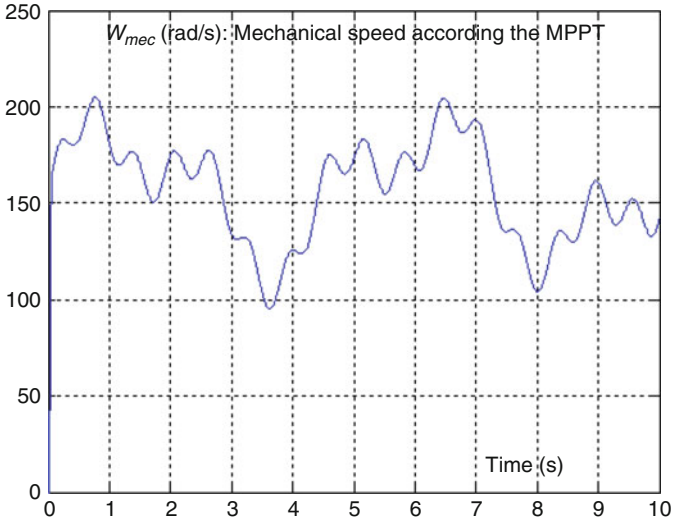

Fig. 5.17 Rotational speed of the DFIG ω_{mec}

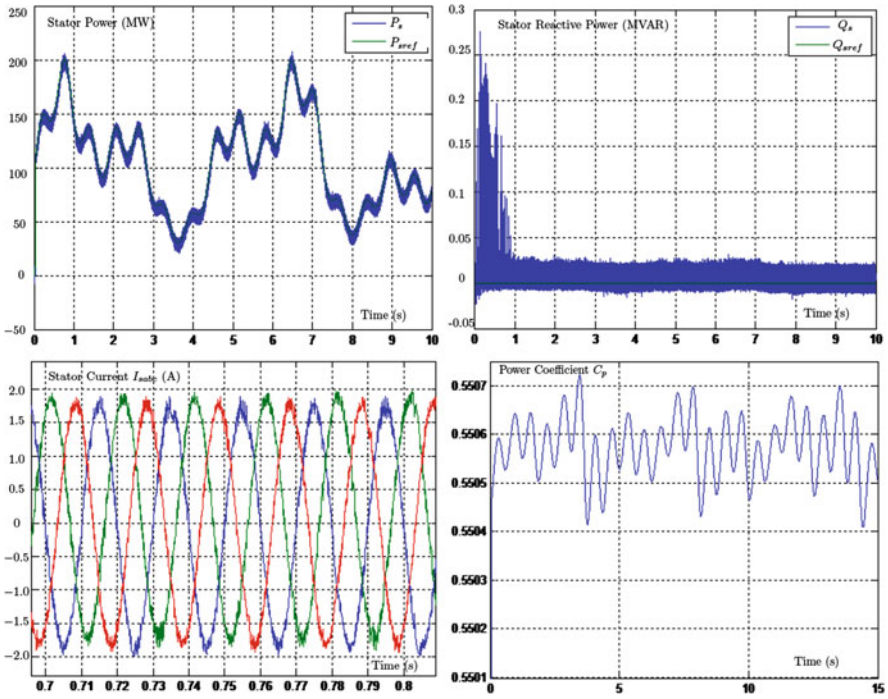

Fig. 5.18 Simulation results of direct field oriented control

- The active power (a) follows its reference values (which is the mechanical power obtained according to the MPPT control strategy) for all the variations of the wind, which shows the robustness of the field oriented control of the DFIG during the variation of the wind speed.
- The stator reactive power (b) is maintained at zero in order to ensure a unit power factor on the stator side.
- The output currents I_{sabc} (c) in the wind system is almost sinusoidal with a fixed frequency equivalent to that of the grid ($50H_z$), which implies a good injection into the grid.
- The power coefficient C_p(d) reach its maximum values $C_p = 0.5505$, which implies that the system provide an optimal power from the wind.

5.6.2 *Simulation Result of the Indirect Field Oriented Control IFOC*

Figure 5.19 presents the different performances of the Indirect Field Oriented Control, which shows the robustness of the wind system and the good tracking.

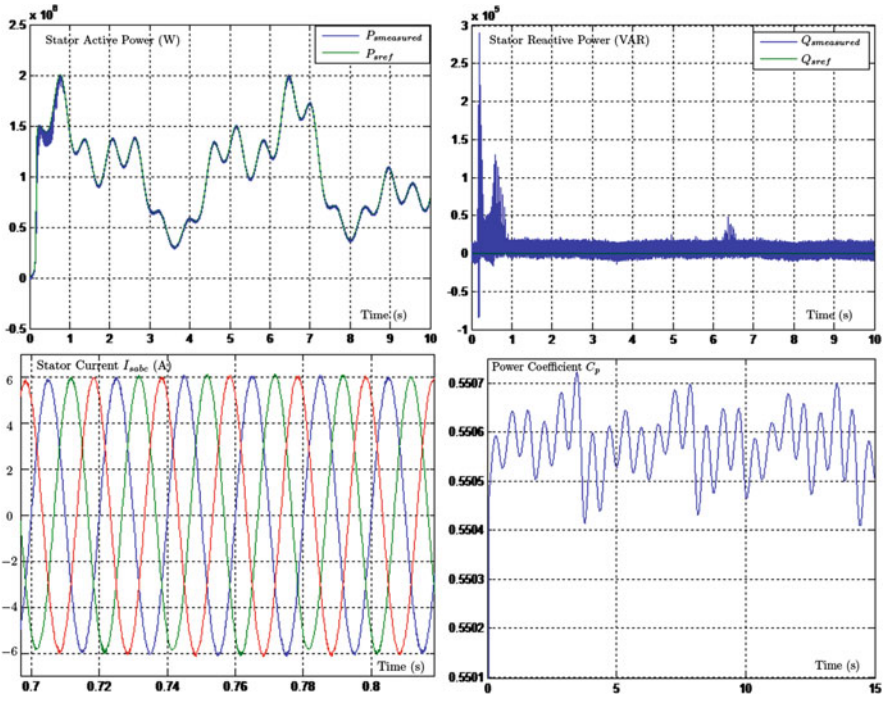

Fig. 5.19 Simulation results of indirect field oriented control IFOC

- The stator active and reactive power (a, b) show a perfect decoupling and a good tracking of their references values with a reduction of the undulations, compared to the direct control. Consequently, the harmonics are minimized.
- The stator currents (c) are also sinusoidal in shape, with an improvement in quality compared to those obtained by the direct control, which implies a clean power without harmonics echanged between the DFIG and the grid.
- From (d) we can note that the power coefficient kept around its optimum $C_{pmax} = 0.5505$.

So, the results obtained from the IFOC show the reliability and robustness of the proposed control and provide better control for injecting power into the grid.

5.7 Conclusion

This work has been devoted to the modeling and control of the wind turbine conversion system based on the doubly-fed induction generator DFIG in order to regulate the active and reactive stator power, with the MPPT strategy to extract the maximum of the power generated by DFIG.

Thus, we presented two methods of control of the DFIG which were implemented under MATLAB/SIMULINK in order to visualize the results of simulation.

Direct methods in which the active and reactive powers are measured and compared with their references. The indirect method has the role to improve the tracking of the instructions and therefore, ameliorate the performance of the wind system.

We have seen that the direct control has good results with low implementation complexity, On the other hand, the indirect method allows to obtain an efficient and robust system. It is true that it is more complex but it makes possible to achieve an optimal operation of the electrical generation system by minimizing the worries linked to the parametric variations of the DFIG.

As perspective, this work can be continued and completed by the implementation of this command in an FPGA.

References

Aimani, S. E. (2004). *Modélisation de Différentes Technologies d'Eoliennes Intégrées dans un Réseau de Moyenne Tension*. Ph.D. thesis, Université des Sciences et Technologies de Lille.

Allam, M., Dehiba, B., Abid, M., Djeriri, Y., & Adjoudj, R. (2014). Etude comparative entre la commande vectorielle directe et indirecte de la machine asynchrone à double alimentation(mada) dédiée à une application éolienne. *Journal of Advanced Research in Science and Technology, 1*(2), 88–100.

Bossoufi, B., Karim, M., Lagrioui, A., Taoussi, M., & Hafyani, M. (2014). Backstepping control of DFIG generators for wide-range variable-speed wind turbines. *IJAAC International Journal of Automation and Control, 8*(2), 122–140.

Bekakra, Y., & Attous, D. B. (2011). Sliding mode controls of active and reactive power of a DFIG with MPPT for variable speed wind energy conversion. *Australian Journal of Basic and Applied Sciences, 5*, 2274–2286.

Bennani, H. (2011). *Machine asynchrone à double alimentation: Les lois de commande en régime permanent*. Ph.D. thesis, Université de Laval, Québec.

Datta, R., & Ranganathan, V. R. (2002). Variable-speed wind power generation using doubly fed wound rotor induction machine a comparison with alternative schemes. *IEEE Transaction on Energy Conversion, 17*, 414–421.

de Wit, C. C. (2000). Commande des moteurs asynchrone modélisation contrôle vectoriel et DTC. *Lavoisier, 1*, 10–22.

Gaillard, A. (2010). *Systéme éolien basé sur une MADA: Contribution l'étude de la qualité de l'énergie électrique et de la continuité de service*. Ph.D. thesis, Université Henri Poincaré, Nancy-I.

Ghoudelbourk, S., Dib, D., Omeiri, A., & Azar, A. T. (2016). MPPT control in wind energy conversion systems and the application of fractional control (PI^{α}) in pitch windturbine. *International Journal of Modelling, Identification and Control, 26*, 140–151.

Guda, S. R. (2005). *Modeling and power management of a hybrid wind-microturbine power generation*. Master's thesis, Université de Bozeman, Monata.

Ihedrane, Y., Chakib, E., & Bossoufi, B. (2017a). Power control of DFIG-generators for wind turbines variable-speed. *International Journal of Power Electronics and Drive Systems (IJPEDS), 8*(1), 444–453.

Ihedrane, Y., Chakib, E., & Bossoufi, B. (2017b). Direct and indirect field oriented control of DFIG-generators for wind turbines variable-speed. In *IEEE 14th International Multi-Conference on Systems, Signals & Devices*, Marrakech, Morocco (pp. 27–32).

Johansen, P. R., Patterson, D., O'Keefe, C., & Swenson, J. (2001, January–March). The use of an axial flux permanent magnet in wheel direct drive in an electric bicycle. *Renewable Energy, 22*(1–3), 151–157.

Kazemi, M. V., Yazdankhah, A. S., & Kojabadi, H. M. (2010). Direct power control of DFIG based on discrete space vector modulation. *Renewable Energy, 35*, 1033–1042.

Mourad, L. (2016). *Synthèse de lois de commande non-linéaires pour le contrôle d'une machine asynchrone à double alimentation dédiée à un système aérogénérateur*. Ph.D. thesis, Université Aboubakr Belkaid – Tlemcen – Faculté de Technologie.

Park, R. H. (2012). Two-reaction theory of synchronous machines: Generalized method of analysis – Part I. In *Transaction of the AIEE, 48*, 716–730.

Poitiers, F. (2003). *Etude et commande de génératrice asynchrones pour l'utilisation de l'énergie éolienne*. Ph.D. thesis, Ecole polytechnique de l'Université de Nantes.

Sejir, K. (2006). *Commande Vectorielle d'une Machine Asynchrone Doublement Alimentée (MADA)*. Ph.D. thesis, Institut National Polytechnique de Toulouse, France.

Tarfaya, A., Dib, D., & Ouada M. (2015). Variable-speed wind power generation using doubly fed wound rotor induction machine a comparison with alternative schemes. *International Conference on Mechanical And Industrial Engineering ICMAIE'2015*, Kuala Lumpur, Malaysia.

Youcef, B. (2014). *Contribution à l'étude et à la Commande Robuste d'un Aérogénérateur Asynchrone à Double Alimentation*. Ph.D. thesis, Université Mohamed Khider – Biskra.

Chapter 6
The Ripple Correlation Optimal Point Determination in a Medium Power Wind Conversion System and Performance Evaluation with Respect to Conventional Algorithms

Hassan Abouobaida and Said EL Beid

Abstract This paper deals with the application of the method called ripple correlation speed (RCS) in a power wind conversion system (PWCS) based a permanent magnet synchronous generator (PMSG). This method is widely used in photovoltaic systems for optimal maximum power point determination. The contribution of this work is the use of two electrical sensors instead of mechanical sensors in order to find the maximum power point (MPP). This method is justified by a ratio of proportionality between the mechanical speed of the (PMSG) generator and the output voltage of the three-phase rectifier. The reading of the power curve as a function of the output voltage of the three-phase rectifier showed that the optimum point has a maximum according to the wind speed. The desired point is characterized by a determined voltage. This observation allows to apply the ripple correlation between power and voltage at the output of the three-phase rectifier. The (PMSG) generator associated with the three-phase diode rectifier is considered as a continuous source whose voltage is dependent on the wind speed and hence the mechanical speed of the generator. This paper uses a power conversion structure based on a synchronous generator, a three-phase rectifier and a boost converter. The choice of this structure is justified by the reliability, simplicity of implementation and control. The boost converter ensures maximum power point tracking. The control duty cycle of the boost converter is determined by the ripple correlation of the input voltage and power of the Boost converter. This paper discusses the performance evaluation of a MPPT method called RCS (ripple correlation speed) in comparison with the conventional methods. To achieve this objective, four criteria are chosen: speed convergence, need of mechanical sensors, accuracy and dependence of the previous position. The main features presented in this paper are as follows: (a) modeling the

H. Abouobaida (✉) · S. EL Beid
Laboratory of Engineering Sciences for Energy, National School of Applied Sciences, Chouaib-Doukkali University, El Jadida, Morocco
e-mail: abouobaida.h@ucd.ac.ma

N. Derbel, Q. Zhu (eds.), *Modeling, Identification and Control Methods in Renewable Energy Systems*, Green Energy and Technology,
https://doi.org/10.1007/978-981-13-1945-7_6

power wind conversion system, (b) presenting and detailing the conventional MPPT method (c) detailing the proposed (MPPT), (d) presenting simulation results, (e) conducting a discussion and evaluation performance of the proposed method and comparison with conventional methods.

Keywords MPPT · TSR · RCC · PMSG · HCF · PSF · PWCS

6.1 Introduction

The production of electric energy from the wind power source is today one of the most promising electrical energy sources and one of the most widely discussed themes in the scientific research. For small wind generation (typically less than 100 kW) and for the reasons of simplicity of control, reliability and low cost, the power conversion structure based a (PMSG) generator, an uncontrolled three-phase rectifier with diodes and boost converter is chosen (Urtasun et al. 2013).

The intermittent nature of the weather conditions and to obtain a better efficiency of the power wind conversion structure, the wind system must be equipped with an MPPT algorithm that allows to permanently search for a point corresponding to maximum power operation. The desired point is characterized by a optimal speed of the (PMSG) generator as a function of the available wind speed (Laraa et al. 2015).

Several research papers in the literature have addressed the methods called (MPPT: maximum power point tracking) in power wind conversion systems (Blaabjerg et al. 2011). Among the most popular methods are TSR (Tip Speed Ratio) control, power signal feedback (PSF) and hill-climb search (HCS). The TSR method is based on controlling the speed of the wind turbine in order to maintain the TSR at its optimum value, which allows to operation at a maximum power. The PSF method is based on the knowledge of the power curve of the wind generator. A practical reading of the power curve as a function of the generator speed implies prior knowledge of the optimum speed. The (HCS) is similar (MPPT) method to the Perturb and Observ (P&O method Zhang et al. 2012). The optimum point determination is based on the continuous calculation of the power variation and the speed variation. The (TSR) and (PSF) MPPT method are based on the use of mechanical sensors (speed and wind sensors). These sensors lack precision, which implies an inaccuracy in the search for optimal point tracking. This problem is explained in Dalala et al. (2013) and in Kot et al. (2013). The accuracy of these methods is degraded following a change in ambient temperature, which presents a second problem (Pena et al. 2011).

The disadvantage of the (HCS) MPPT method is the large ripple around optimal point. A small variation in wind speed causes an optimal point shift which involves adjusting the control to find the new point (MPP) and oscillating again around this point. For sudden changes in wind speed, the (MPPT) method lose the direction of the new optimal point displacement and therefore finds a difficulty in the optimal point detection.

Several works in the literature have addressed the study of different (MPPT) and an evaluation of their performances. The paper (Kot et al. 2013) details the comparison of the (TSR), (PSF) and (INC-COND) methods according to criteria based on the efficiency, the flexibility, the speed, the cost and the complexity of the implementation.

The paper (Pena et al. 2011) limits the study of the comparison of the (P&O) and (ODC) method according to the efficiency of the power wind conversion system. The evaluation according to the efficiency and the dynamics of searching maximum power point is approached in Shirazi et al. (2009). The objective of this work is the evaluation performance of three (MPPT) method. The first (MPPT) is called IHC (intelligent Hill-Climb), the second is the optimum control (OC) and the third is based on successive measurements of power.

In this paper, a new high-precision method named RCS (ripple correlation speed) is proposed. The discussed method uses two electrical sensors instead of the mechanical sensors used in the other method. The determination of maximum power point is based a correlation between the power and voltage at the input of the DC/DC converter. Limitation of accuracy of the mechanical sensors is avoided by the better accuracy and the low cost of the electrical sensors. The rest of the paper is organized as follows. While Sect. 6.2 deals mainly with the modeling of the power wind conversion system (PWCS), a presentation of each (MPPT) method is explained and detailed in Sect. 6.3. Presentation and simulation results of the proposed method in Sect. 6.4. Section 6.5 presents a conclusions drawn from this work.

6.2 Wind Conversion System Modeling

The power wind conversion system (PWCS) is composed of blades that capture wind speed and electrical generator that converts the wind power into electrical energy. The electrical generator based (PMSG) machine is coupled directly to the blades. The (PMSG) generator is cascaded to AC/DC rectifier and a DC/DC Boost converter. The function of the adaptation circuit is to operate the (PWCS) at maximum power (Lahfaoui et al. 2014; Lahfaoui et al. 2015a,b). Figure 6.1 illustrates the power wind conversion structure.

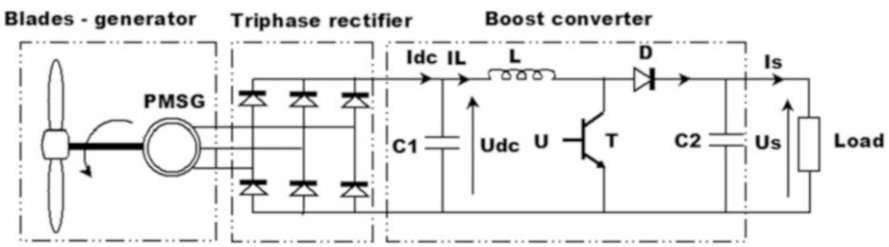

Fig. 6.1 Power wind conversion system (PWCS)

6.2.1 The Turbine Model

The aerodynamic power Pt captured by the wind turbine is expressed by the following relation:

$$P = \frac{1}{2}\ \pi\ \rho\ R^2\ C_p(\lambda)\ v^3 \tag{6.1}$$

where the tip speed ratio λ is given by:

$$\lambda = \frac{R\Omega_m}{v} \tag{6.2}$$

and where v is the wind speed, ρ is the air density, R is the rotor radius and C_p is the power coefficient.

In a wind turbine, the power coefficient C_p is expressed as function of tip speed ratio λ in place of pitch angle β as:

$$C_p = 0.576\ \left(\frac{116}{\lambda_i} - 0.4\beta - 5\right)\ \exp\left(\frac{21}{\lambda_i}\right) + 0.0068\lambda \tag{6.3}$$

with:

$$\frac{1}{\lambda_i} = \frac{1}{\lambda + 0.08\beta} - \frac{0.035}{1 + \beta^3} \tag{6.4}$$

The aerodynamic power is also defined by:

$$P = T_m \omega_m \tag{6.5}$$

where T_m is the aerodynamic torque and ω_m is the rotor speed. The power coefficient in term of rotor speed and the aerodynamic power in term of tip speed ratio are respectively illustrated in Figs. 6.2 and 6.3.

In this paper, the control of the power wind conversion system is carried out keeping the pitch angle equal to zero ($\beta = 0$). The following mechanical model gives the dynamic of the turbine:

$$J\frac{d\omega_m}{dt} = T_m - T_{em} - f\omega_m \tag{6.6}$$

where T_{em} is the electromagnetic torque of the synchronous generator, J is the turbine total inertia and f is the turbine total external damping.

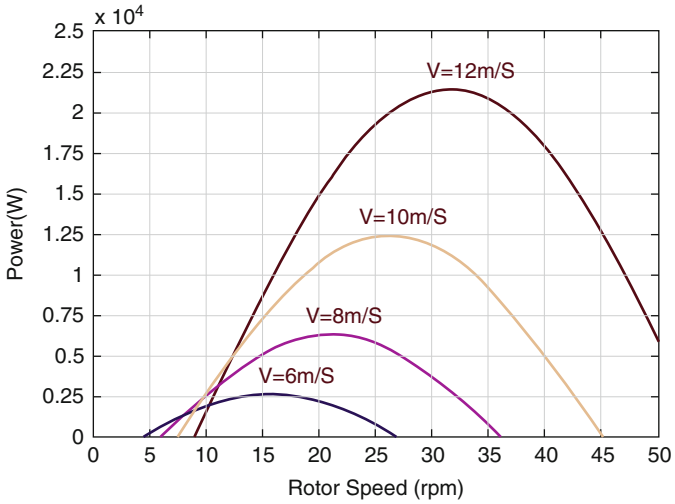

Fig. 6.2 Power curve a function of the rotor speed

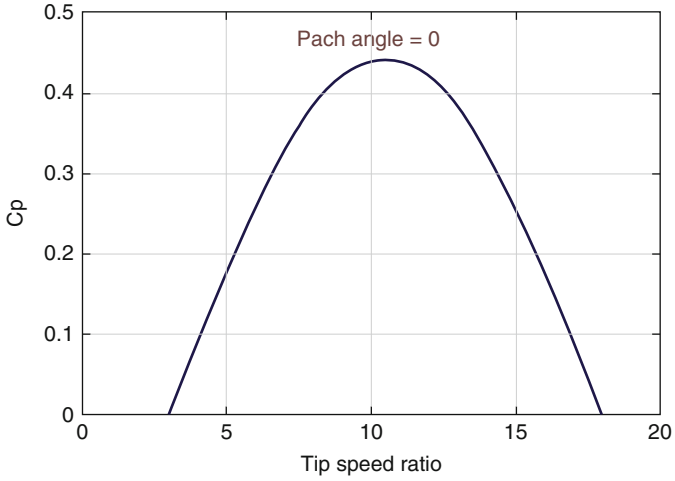

Fig. 6.3 Power coefficient as function of tip speed ratio

6.2.2 The PMSG Model

The dynamic equations of a three-phase permanent magnetic synchronous generator (PMSG) can be written in a synchronously rotating dq reference frame as Ben Ali et al. (2017):

$$V_{sd} = -R_s\, i_{sd} - L_d \frac{di_{sd}}{dt} + L_q \omega_r i_{sq} \tag{6.7}$$

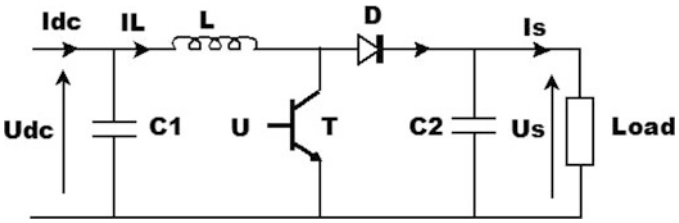

Fig. 6.4 DC/DC boost converter

$$V_{sq} = -R_s\, i_{sq} - L_q \frac{di_{sq}}{dt} - L_d \omega_r i_{sd} + \phi_{st} \omega_r \tag{6.8}$$

where V_{sq} and V_{sd} are the q-axis and d-axis stator voltages. i_{sd} and i_{sq} are the q-axis and d-axis stator currents, R_s is the stator winding resistance, $\omega_r = p\omega_m$ is the electrical angular velocity of the rotor and p is the number of pole pairs and ϕ_{st} is the rotor flux linkage (Djagarov et al. 2016).

The output electrical power is expressed as the following equation:

$$P = \frac{3}{2}(V_{sd} i_{sd} + V_{sq} i_{sq}) \tag{6.9}$$

6.2.3 The Boost Converter Model

The boost converter is illustrated in Fig. 6.4. The dynamic model of the boost converter is expressed as follows:

$$C_2 \dot{U}_s = (1-u) I_L - I_s \tag{6.10}$$

$$L \dot{I}_L = U_{dc} - (1-u) U_s \tag{6.11}$$

where L and I_L represents the storage inductance and the current across it, U_s is the output voltage and u is the switched control signal that can only take the discrete values 0 (switch open) and 1 (switch closed).

6.3 Maximum Power Point Tracking Methods (MPPT)

A wind system is characterized by the presence of a maximum power point in the power curve (see Fig. 6.2) as a function of the generator speed (Almozayen et al. 2016; Sahin et al. 2016). Depending on the wind speed, the maximum power point can move up or down, which implies a change in the rotor speed at which the synchronous generator must rotate (Asri et al. 2017; Biweta and Mamo 2017).

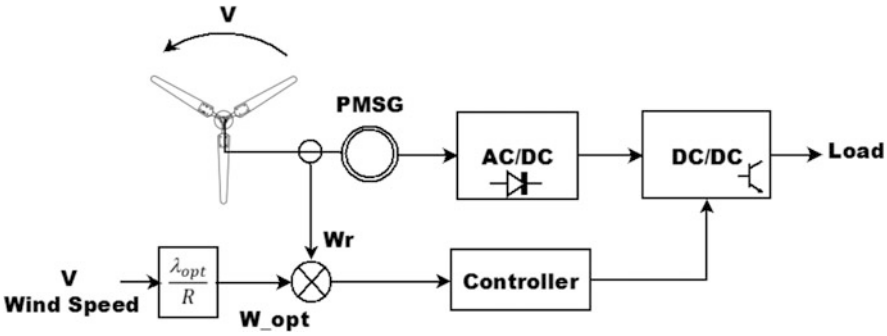

Fig. 6.5 MPPT method based TSR control

Several methods of maximum power point tracking are discussed in the literature, among the most popular methods are TSR, HCS, PSF. When the maximum power point tracking (MPPT) method finds the optimum speed, a control loop is required to adjust the rotational speed to its reference (Fantino et al. 2015; Koch et al. 2015).

In the literature, the (MPPT) methods are classified into three categories: Tip Speed Ratio Control (TSR), Hill Climbing Searching Control (HCS) and Power Signal Feedback Control (PSF). In the next paragraph, the operating principle of the (MPPT) methods, the simulation results are presented, discussed and commented.

6.3.1 Tip Speed Ratio Control

The principle of the TSR method is based on a continuous measurement of the wind speed. A prior knowledge of the tip speed ratio (TSR) allows to determine the optimum speed which corresponds to maximum power operation. Figure 6.5 illustrates the principle of the (TSR) method.

The TSR method is based on the continuous measurement of wind speed. An inaccuracy in the measurement by an anemometer cause an operating of the power wind conversion system a far from its maximum power. The knowledge of the tip speed ratio is necessary to determine the optimal speed.

The model of the power wind conversion system based (PMSG) generator, AC/DC rectifier and the boost converter is built using Matlab/Simulink software. The synchronous generator provides a power of 22 kW. The switching frequency is set to 20 kHz. The simulations of the (TSR), (PSF), (HCS) and the proposed method are carried out using the same parameters and the same power conversion structure.The simulation parameters are given in Tables 6.1 and 6.2

The validation of the (TSR) method and the simulations results of the (TSR) MPPT are given in Fig. 6.6. Figure 6.6a shows the wind profile applied to the wind turbine blades. The profile used is characterized by two rising steps (8 to 10 m/s and 10 to 12 m/s).

Table 6.1 Parameters of the boost converter and RCS MPPT

	Parameters	Values	Units
Boost Converter	L	3	mH
	C_2	470	μF
	U_s	800	V
	f	20	kHz
RCS MPPT	k	10^{-4}	–

Table 6.2 Parameters of the power wind conversion system

	Parameters	Values	Units
Turbine	V_{tn}	12	m/s
	R	4	m
PMSG	U	500	V
	P_n	22	kW
	f	50	Hz
	R_s	50	mΩ
	$L_d = L_q$	0.6	mH
	J_m	0.011	kgm^2
	P	10	–

Figure 6.6.b shows the power extracted as a function of time according to the wind speed changes. According to the power curve given in Fig. 6.3, the mechanical power is well regulated to its maximum value. In Fig. 6.6.b, the wind system reaches the optimal point very quickly in transient mode and in the event of a sudden change in wind speed. In addition, the oscillations around the optimal point are very weak. This is justified by the ease of optimal point determination based on the formula $\omega_{opt} = \frac{\lambda_{opt}}{R} v$.

Figure 6.6c illustrates the mechanical speed of the synchronous generator. According to Fig. 6.3, the rotor speed is well regulated to its optimal value.

Figure 6.6d illustrate the voltage at the input of the boost converter. According to this figure, the voltage at the input of the boost converter is well adjusted to its reference. Figure 6.6e shows the power coefficient as a function of time. According to Fig. 6.3, the power coefficient is well maintained at its optimum value of 0.43 in the presence of the sudden changes of wind speed.

6.3.2 Hill Climbing Searching Control

The (HCS) MPPT method determines the optimal point from the variation of the mechanical power and the variation of the generator speed. The calculation of the power variation and the rotor speed variation is carried out continuously in order to detect any change in the wind speed. The detection of the speed change implies

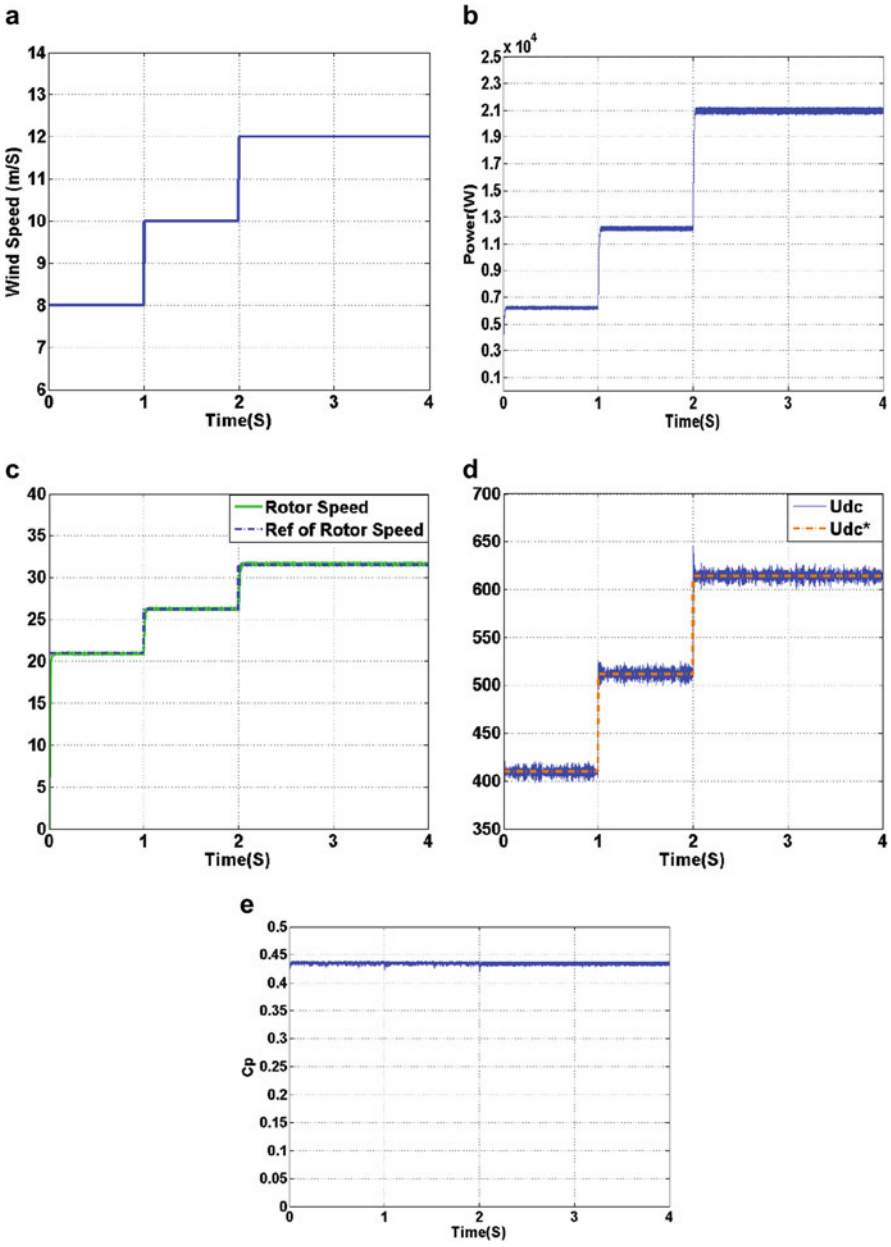

Fig. 6.6 TSR MPPT Results. (**a**) Wind speed (m/s). (**b**) Generator power (W). (**c**) Rotor Speed ω_m (rad/s). (**d**) U_{dc} Voltage (V). (**e**) Power coefficient

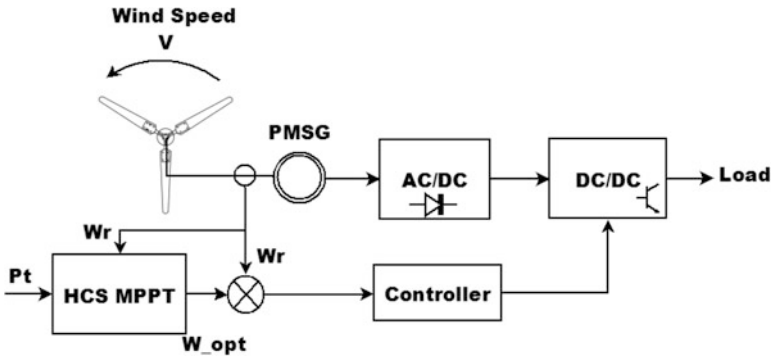

Fig. 6.7 Principle operation of the (HCS) Method

a positioning of the wind system in a new optimal point. The principle of (HCS) method is summarized by the following two points:

- If the variation of the power and the variation of the speed have the same sign, the optimal point is to the right of the actual point.
- If the variation of power and the variation of the voltage have a different sign, the optimal point is to the left of the actual point. Figure 6.7 shows the operation principle of the (HCS) method.

A very rapid change in the wind speed cause a possible loss of optimal point because the new optimal point is determined from the previous point, which constitutes a disadvantage of the (HCS) method.

The validation of the (HCS) method and the simulations results of this MPPT are given in Fig. 6.8. Figure 6.8a shows the wind profile applied to the wind turbine blades. Figure 6.8b illustrates the power as function of time. According to this figure, the system finds the optimal point in transient mode after 200 milliseconds. During abrupt changes in wind speed, the (HCS) method finds the new optimum point after 100 milliseconds. Figure 6.8c illustrates the mechanical speed of the synchronous generator. According to Fig. 6.3, the generator speed is well regulated to the optimal value. Figure 6.8d illustrate the voltage at the input of the boost converter. The input voltage is well regulated to its optimal value. Figure 6.8e shows the power coefficient as a function of time. According to Fig. 6.3, the power coefficient is well maintained at its optimum value of 0.43 in the presence of the sudden changes of the wind speed. According to Fig. 6.8e, the power coefficient deviates at $t = 1S$ and at time $t = 2S$ from its optimal value of 0.43 due to sudden changes in wind speed. The (HCS) MPPT was able to restore the power coefficient to its optimal value. The simulations results show that the oscillations of the power coefficients and the oscillation of the voltage around the optimal point using the (HCS) MPPT method are greater than the oscillations observed using the (TSR) method.

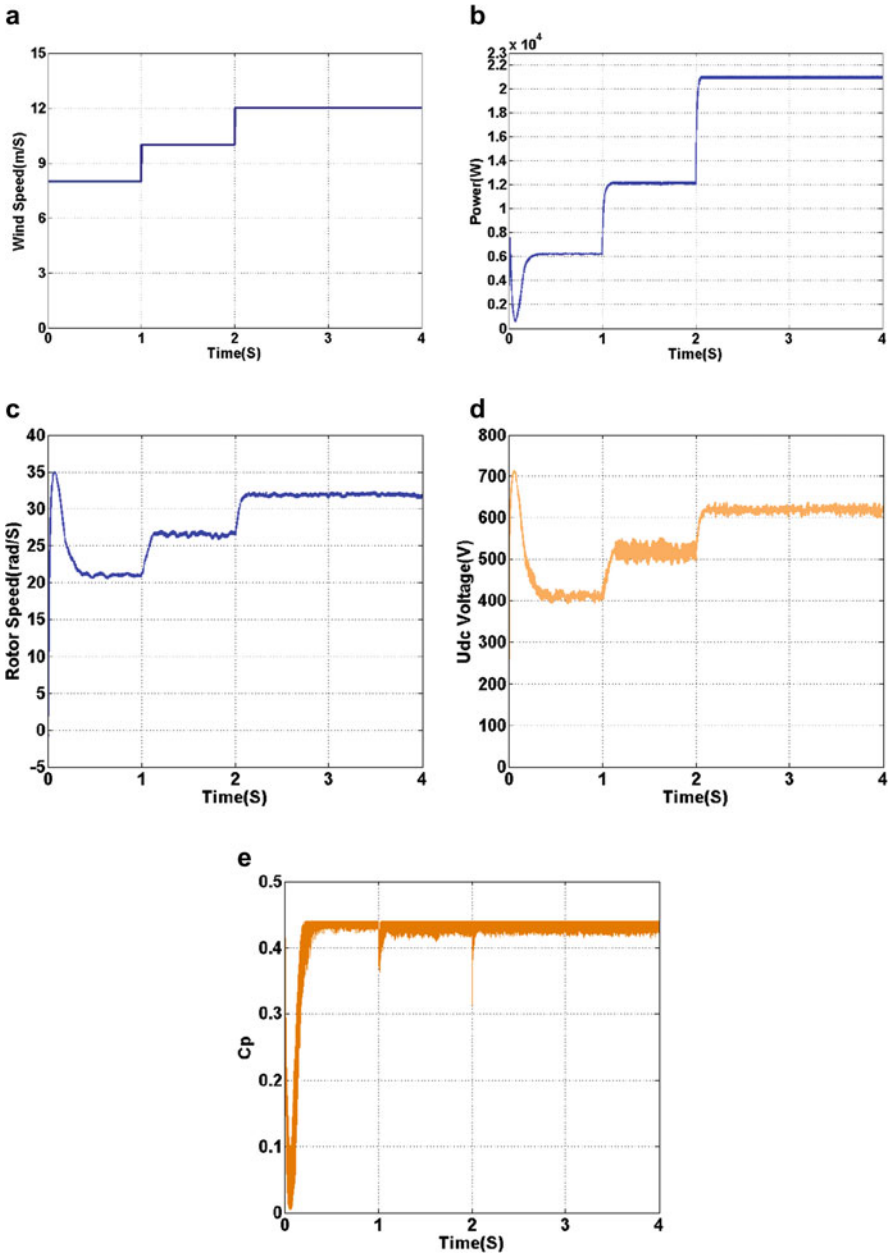

Fig. 6.8 HCS MPPT Results. (**a**) Wind speed (m/s). (**b**) Generator power (W). (**c**) Rotor Speed ω_m (rad/s). (**d**) U_{dc} Voltage (V). (**e**) Power coefficient

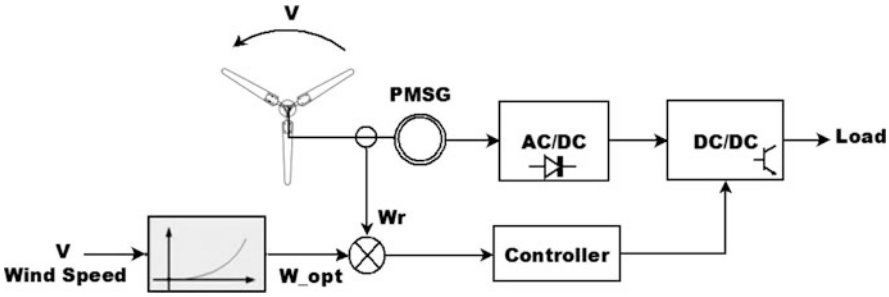

Fig. 6.9 Principle operation of the (PSF) method

6.3.3 Power Signal Feedback Control

The (PSF) method is based on a prior knowledge of the power characteristic as a function of the generator speed. The first step consists in learning of the power characteristic as a function of the speed of the generator. Depending on the wind speed, the (PSF) MPPT method provides the optimum speed which corresponds to a maximum power operation of the wind system. Figure 6.9 shows the principle operation of the (PSF) method.

The disadvantage of this method lies in the change of the power curve due to a degradation of the performance of the wind system which affects the optimal point determination. A second disadvantage is the stopping of production of the wind system at the time of learning of the power characteristic. The validation of the (PSF) method and the simulations results of this MPPT are given in Fig. 6.10. Figure 6.10a shows the wind profile applied to the wind turbine blades. The wind profile applied to the (PSF) method is identical to the wind profile applied to the (HCS) and (TSR) method. Figure 6.10b illustrates the power extracted as a function of time. According to Fig. 6.10b, the power wind conversion system reaches the optimal value after a few milliseconds ($t < 10$ mS). Figure 6.10c illustrates the mechanical speed of the synchronous generator. The generator speed is well regulated to the optimal value. Figure 6.10d illustrate the voltage at the input of the boost converter. The voltage at the input of the boost converter is adjusted to its reference. According to Fig. 6.10d, the input voltage is adjusted to its reference. Figure 6.10e shows the power coefficient as a function of time. The power coefficient is well maintained at its optimum value of 0.43.

6.4 Proposed MPPT Method

The proposed method is named (RCS: ripple correlation speed), uses the correlation between the power and the generator speed (Abouobaida et al. 2014). The (RCS) method is based on the following hypothesis: the output voltage of the boost converter is assumed to be constant. If the wind system is cascaded with a

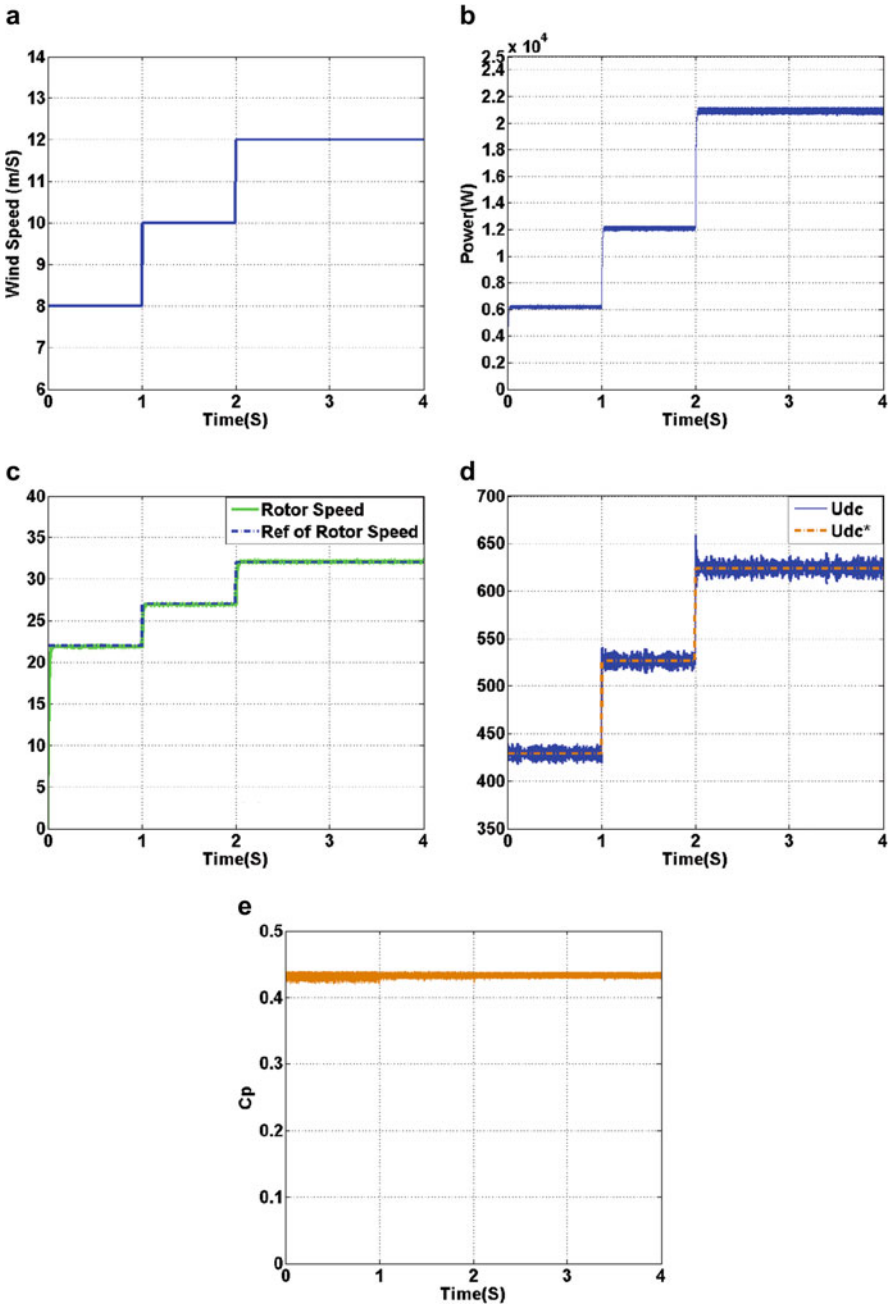

Fig. 6.10 PSF MPPT Results. (**a**) Wind speed (m/s). (**b**) Generator power (W). (**c**) Rotor Speed ω_m (rad/s). (**d**) U_{dc} Voltage (V). (**e**) Power coefficient.

three-phase inverter, the output voltage of the boost converter is regulated using another control loop (part not studied in this chapter).

The proposed (MPPT) method is inspired by the following remarks:

- If the variation of the generator speed and the change of power have the same signs (positive or negative), the optimal point is to the right of the operating point,
- If the variation of the generator speed and change of the power have opposite signs, the optimal point is to the right.

By combining these observations, it can be concluded that the product of the change of the speed and the change of the power $\dot{P}\dot{\omega}$ is positive to the left of optimal point and negative to the right of this point.

The choice of sensors is justified by the simplicity of implementation and the limitation of the cost and precision. The justifications are explained as follows:

- Instead of measuring the generator speed with a tachometer speed sensor, a higher accuracy voltage sensor is used at the input of the DC/DC converter since this voltage is proportional to the generator speed.
- A second current sensor is used at the input of the DC/DC converter, which allows to determine the power extracted by multiplying the voltage and the current at the input of the DC/DC converter.
- A reading of the power curve as a function of the voltage at the input of the DC/DC converter allows to identify the new curve of the wind system at the input of the DC/DC converter. The advantage of this method is that it is easy to determine the optimal point by two electrical sensors. The new observed power curves are characterized by maximum power points according to the wind speed.

To show the linear relation between the generator speed and the input voltage of the DC/DC converter, a reading is made for four wind speeds. According to Fig. 6.11, the factor of proportionality between the speed and the voltage is constant and independent of the wind speed.

The proportionality relation between the generator speed and the rectified voltage Udc is justified by the following relation:

$$U_{dc} = \frac{3\sqrt{6}}{\pi} \phi_{eff} \; P \; \omega_m \tag{6.12}$$

where U_{dc} is the rectified voltage, ϕ_{eff} is the effective value of the internal flux of the (PMSG) generator, P is the number of poles and ω_m the rotation speed of the asynchronous generator (Marmouh et al. 2016; Saihi and Boutera 2016; Sarkar and Khule 2016).

Figure 6.12 illustrate the principle of the proposed (MPPT) method.

The electrical power at the input of the boost converter is expressed by the following relation:

$$P_{dc} = U_{dc} \; I_{dc} \tag{6.13}$$

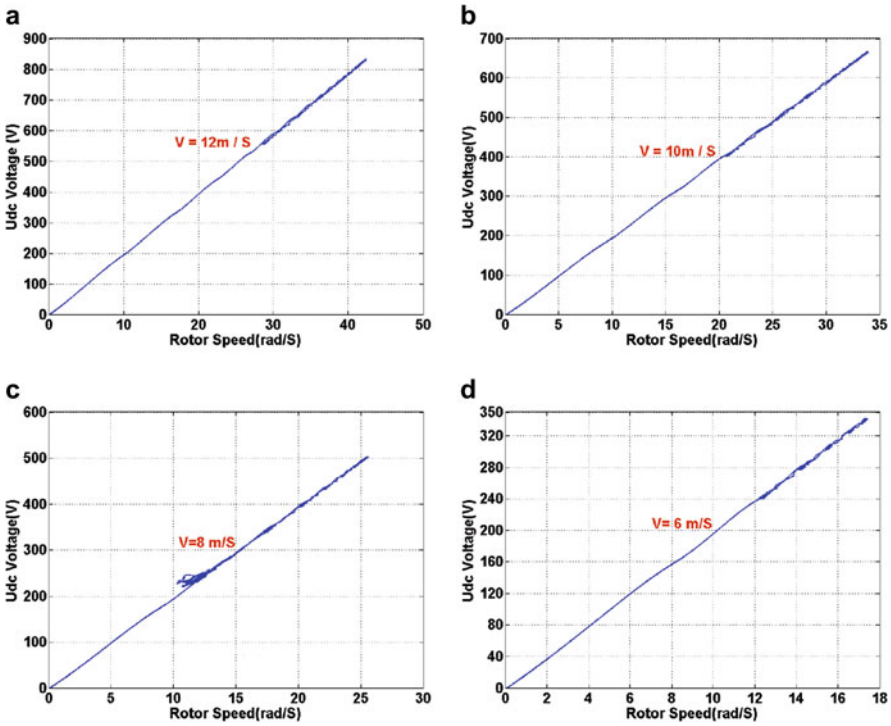

Fig. 6.11 U_{dc} voltage as a function of generator speed. (**a**) $v = 12\,\mathrm{m/s}$, (**b**) $v = 10\,\mathrm{m/s}$, (**c**) $v = 8\,\mathrm{m/s}$, (**d**) $v = 6\,\mathrm{m/s}$.

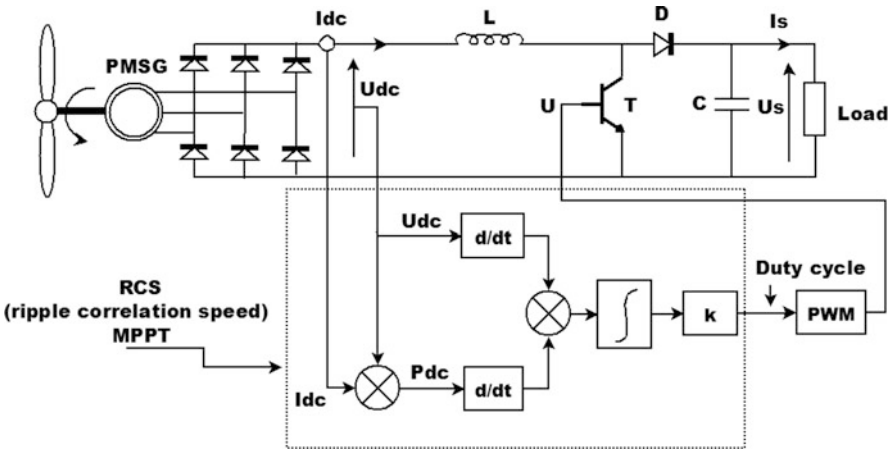

Fig. 6.12 Principle of the proposed (MPPT) method

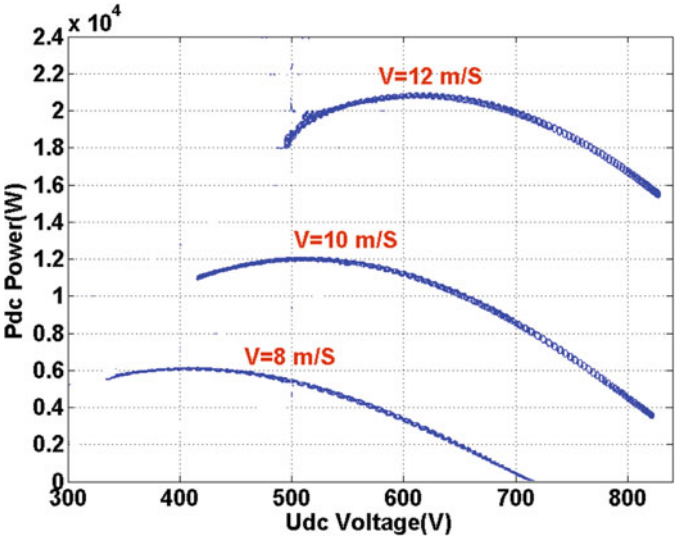

Fig. 6.13 Power as function DC voltage $P_{dc} = f(U_{dc})$ at the input of the boost converter

where U_{dc} and I_{dc} are respectively the voltage and the current at the input of the boost converter (Ayadi et al. 2017; Zou and He 2016).

According to Fig. 6.12, the duty cycle of controlling of the boost converter is expressed by the following relation:

$$\alpha = k = \int \dot{P}_{dc}\, \dot{U}_{dc} dt \tag{6.14}$$

where k is a positive parameter, $\dot{P}_{dc}$ and $\dot{U}_{dc}$ are the time derivative of the power and the time derivative of the voltage, respectively.

Figure 6.13 illustrates the power curve as a function of the voltage at the input of the boost converter.

The validation of the (RCS) method and the simulations results are given in Fig. 6.14. Figure 6.14a shows the wind profile applied to the wind turbine blades. The profile used is characterized by a descending step (10 to 8 m/s) and two rising steps (8 to 10 m/s and 10 to 12 m/s). The applied steps are abrupt which is the extreme case of a wind scale and also allows to show the capacity of the proposed (MPPT) of a tracking as quickly as possible to the new optimal point. Figure 6.14b shows the extracted power at the input of the boost converter as a function of time. According to the power curve given in Fig. 6.3, it is noted that the extracted power is well regulated to maximum power. The difference between the extracted power and the power given in Fig. 6.3 represents the power losses in the wind system which is logical since the curve in Fig. 6.3 represents the mechanical power not the available power at the input of the boost converter. A comparison between the

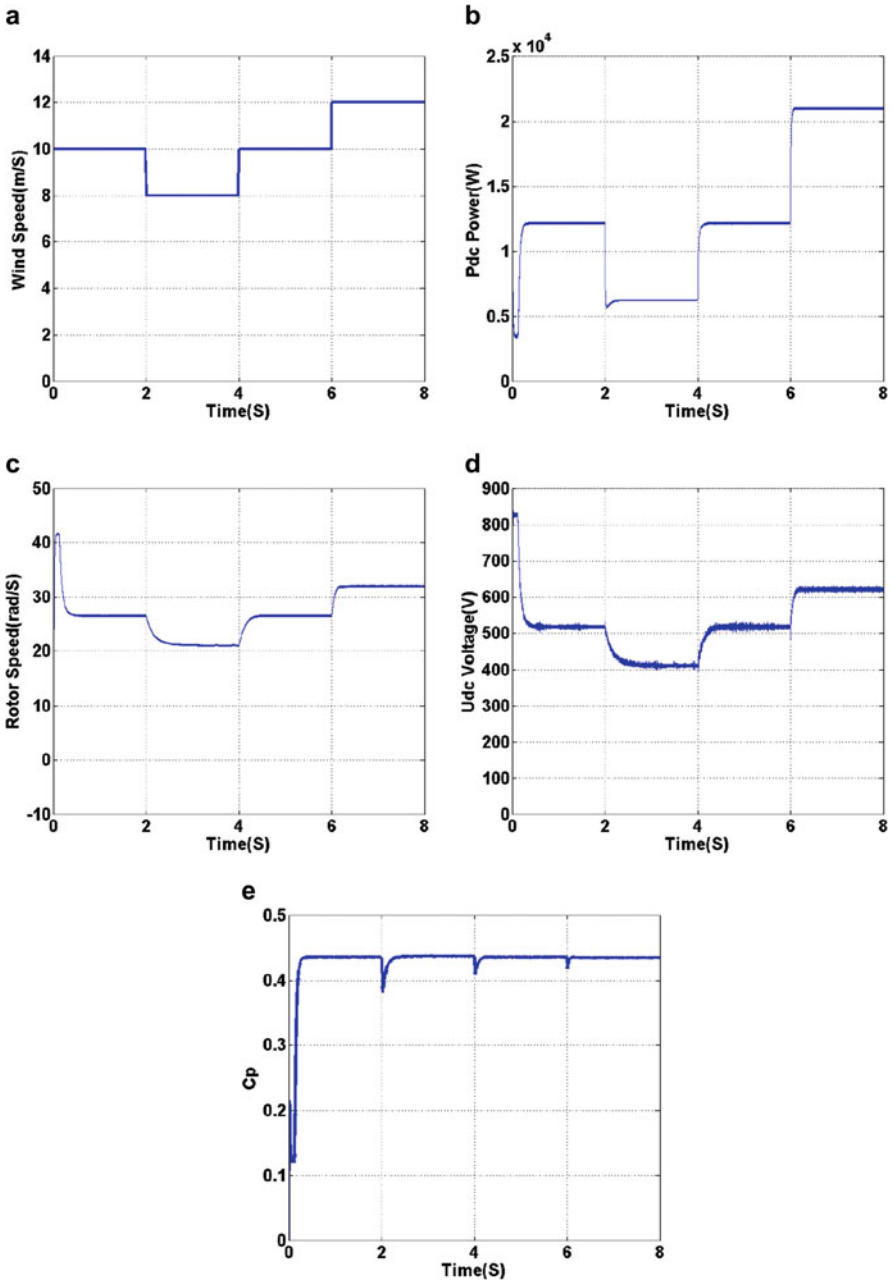

Fig. 6.14 RCS MPPT Results. (**a**) Wind speed (m/s). (**b**) Generator power (W). (**c**) Rotor Speed ω_m (rad/s). (**d**) U_{dc} Voltage (V). (**e**) Power coefficient

power extracted and the power curve given in Fig. 6.9 shows a similarity between these two values. Figure 6.14c illustrates the mechanical speed of the synchronous generator. According to Fig. 6.3, the generator speed is well regulated to the optimal value that correspond to a maximum power operation of the wind system.

Figure 6.14d illustrates the voltage at the input of the boost converter. Figure 6.14d shows that Udc voltage is well regulated to the optimal value. According to Fig. 6.9, U_{dc} voltage must be regulated at 400 V when the wind speed is 8 m/s and adjusted to 520 V when the wind speed is equal to 10 m/s and regulated to 620 V when the wind speed is equal to 12 m/S. Figure 6.14d shows that U_{dc} voltage follows the desired value.

Figure 6.14e illustrates the power coefficient. According to Fig. 6.2, the optimal value of power coefficient is equal to 0.43. According to Fig. 6.14, the power coefficient is well regulated at its optimal value in the presence of sudden changes in wind speed.

In summary, Fig. 6.14 justify the validity of the proposed approach to extract the maximum of the available wind energy and thus a good exploitation of the power wind conversion system in a situation characterized by sudden, fast and successive changes in wind speed.

Table 6.3 summarizes a general evaluation and comparison of the proposed method and the conventional methods. The criteria of comparisons are: speed of convergence, need for mechanical sensors, precision and dependence of the previous position.

According to Table 6.3, the proposed (MPPT) method has many advantages:

- a response time and therefore quick searching and optimal point tracking,
- the use of two electrical sensors with better accuracy, low cost and simplicity of implementation instead of two mechanical sensors,
- a better accuracy than the other method that reflects a very small distance from the optimum point and an operation at the maximum power point.

Table 6.3 Comparison between MPPT algorithms

MPPT	TSR	HCS	PSF	RCS (Proposed)
Speed convergence	FAST	Medium(1) (depends on step size)	Fast	Good(2) (depends on parameter k)
Mechanical sensor	Yes	Yes	Yes	No(3) (2 electrical sensor)
Dependence of previous position	No	Yes	No	Yes
Accuracy	Good	Medium	Good	Very Good

6.5 Conclusion

This paper has addressed a new method of tracking maximum power point in a power wind conversion system (PWCS). The proposed method called (RCS: ripple correlation speed) is based on a correlation calculation between the power and the voltage at the input of the DC/DC converter.

A summary table at the end of the chapter illustrate the comparison of the suggested method and the conventional methods. The evaluation performance is based on four criteria: convergence speed, sensors need, dependence on the previous position and accuracy. According to the simulation results, the proposed method showed a better performance in terms of optimal point detection speed, need of the electrical sensors and better accuracy. Another advantage, the proposed method seems simpler, efficient and promising due to the elimination of the wind speed sensor and the generator speed sensor which implies a low cost and a flexibility. The major advantage of this approach is that the control method does not need to the parameters of the turbines which constitutes an inconvenience of the other approaches because of the uncertainties in the measurement of the turbine parameters. In conclusion, the simulation results proved the validity of the proposed approach.

References

Abouobaida, H., EL Khayat, M., & Cherkaoui, M. (2014). Combination of RCC MPPT and Backstepping controler to design a standard continuous source (12V–24V) supplied by a PV panels. *Journal of Electrical Engineering, 14*(3), 364–371.

Almozayen, M. A., El-Nemr, M. K., Rashad, E. M., & Shobair., A. I. (2016). Finite-element-based design of axial field PMSG for wind energy conversion with MPPT control. In *18th International Middle East Power Systems Conference (MEPCON)* (pp. 610–616).

Asri, A., Mihoub, Y., Hassaine, S., & Allaoui, T. (2017). Intelligent maximum power tracking control of PMSG wind energy conversion system. In *5th International Conference on Electrical Engineering – Boumerdes (ICEE-B)*, Algeria (pp. 1–6).

Ayadi, M., Naifar, O., & Derbel, N. (2017). Sensorless control with an adaptive sliding mode observer for wind PMSG systems. In *14th International Multi-conference on Systems, Signals & Devices (SSD)*, Morocco (pp. 33–37).

Ben Ali, R., Schulte, H., & Mami, A. (2017). Modeling and simulation of a small wind turbine system based on PMSG generator. In *Evolving and Adaptive Intelligent Systems (EAIS)*, Ljubljana, Slovenia (pp. 1–6).

Biweta, M., & Mamo, M. (2017). Closed loop control strategy of back to back PWM converter fed by PMSG using PLECS toolbox on Matlab/Simulink for wind energy application. In *IEEE AFRICON*, Cape Town, South Africa (pp. 1313–1318).

Blaabjerg, F., Liserre, M., & Ma, K. (2011). Power electronics converters for wind turbine systems. *Energy Conversion Congress Exposit (ECCE)*, Arizona, USA (pp. 281–90).

Dalala, Z. M., Zahid, Z. U., Yu, W., Cho, Y., & Lai, J. S. (2013). Design and analysis of an MPPT technique for small-scale wind energy conversion systems. *IEEE Transaction on Energy Conversion, 28*, 756–767.

Djagarov, N., Djagarova, J., Grozdev, Z., Bonev, M., Pazderin, A., & Kokin, S. (2016). PI vector control study for wind PMSG. In *IEEE 16th International Conference on Environment and Electrical Engineering (EEEIC)*, Italy (pp. 1–6).

Fantino, R., Solsona, J., & Busada, C. (2015). Mechanical sensorless controller for a small size PMSG-based wind energy conversion system. In *XVI Workshop on Information Processing and Control (RPIC)*, Cordoba, Argentina (pp. 1–6).

Koch, G., Gabbi, T., Henz, G., Vieira, R. P., & Pinheiro, H. (2015). Sensorless technique applied to PMSG of WECS using sliding mode observer. In *IEEE 13th Brazilian Power Electronics Conference and 1st Southern Power Electronics Conference (COBEP/SPEC)* (pp. 1–6).

Kot, R., Rolak, M., & Malinowski, M. (2013). Comparison of maximum peak power tracking algorithms for a small wind turbine. *Mathematics and Computers in Simulation, 91*, 29–40.

Lahfaoui, B., Zouggar, S., Elhafyani, M. L., Seddik, M., Kadda, F. Z. (2014). Experimental modeling and control of a small wind PMSG turbine. In *International Renewable and Sustainable Energy Conference (IRSEC)*, Ouarzazate (pp. 802–807).

Lahfaoui, B., Zouggar, S., Elhafyani, M. L., & Seddik, M. (2015a). Experimental study of P&O MPPT control for wind PMSG turbine. *3rd International Renewable and Sustainable Energy Conference (IRSEC)*, Marrakech-Ouarzazate, Morocco (pp. 1–6).

Lahfaoui, B., Zouggar, S., Elhafyani, M. L., Seddik, M., & Benslimane, A. (2015b). Modeling validation and MPPT technique of small wind PMSG turbines using DSPACE hardware. In *3rd International Renewable and Sustainable Energy Conference (IRSEC)*, Marrakech-Ouarzazate, Morocco (pp. 1–6).

Laraa, D., Merinoa, G., & Salazarb, L. (2015). Power converter with maximum power point tracking, MPPT for small wind-electric pumping systems. In *Energy Convers Manage* (pp. 53–62).

Marmouh, S., & Boutoubat, M., Mokrani, L. (2016). MPPT fuzzy logic controller of a wind energy conversion system based on a PMSG. In *8th International Conference on Modelling, Identification and Control (ICMIC)*, Algeria (pp. 296–302).

Pena, J. C. U., de Brito, M. A. G., e Melo, G. de A., & Canesin, C. A. (2011). A comparative study of MPPT strategies and a novel single phase integrated buck-boost inverter for small wind energy conversion systems. In *XI Brazilian Power Electronics Conference* (pp. 458–465).

Sahin, P., Resmi, R., & Vanitha, V. (2016). PMSG based standalone wind electric conversion system with MPPT. In *International Conference on Emerging Technological Trends (ICETT)*, Kollam, India (pp. 1–5).

Saihi, L., & Boutera, A. (2016). Robust control of a variable-speed wind turbine with fixed pitch angle and strategy MPPT control associated on a PMSG. In *8th International Conference on Modelling, Identification and Control (ICMIC)*, Algeria (pp. 326–331).

Sarkar, J., & Khule, S. S. (2016). A study of MPPT schemes in PMSG based wind turbine system. In *International Conference on Electrical, Electronics, and Optimization Techniques (ICEEOT)*, Chennai, Tamilnadu, India (pp. 100–105).

Shirazi, M., Hooshmand Viki, A., & Babayi, O. (2009). A comparative study of maximum Power extraction strategies in PMSG wind turbine system. In *IEEE Electrical Power & Energy Conference (EPEC)*, Montreal, Canada (pp. 1–6).

Urtasun, A., Sanchis, P., & Marroyo, L. (2013). Small wind turbines sensorless MPPT: Robustness analysis and lossless approach. In *IEEE Energy Conversion Congress and Exposition*, Denver, Colorado, USA (pp. 2420–2427).

Zhang, X., Li, Q., Yin, M., Ye, X., & Zou Y. (2012). An improved hill-climbing searching method based on halt mechanism. In *Zhongguo Dianji Gongcheng Xuebao/Proceed Chinese Society of Electrical Engineering*, China (pp. 128–134).

Zou, Y., & He, J. (2016). Maximum power point tracking (MPPT) of sensorless PMSG wind power system. In *IEEE Energy Conversion Congress and Exposition (ECCE)*, Milwaukee (pp. 1–6).

Chapter 7
Control of Wind Turbine Based on PMSG Using Pitch Angle Control

Aroua Slimen, Hatem Tlijani, Mehdi Dhaoui, and Rached B. Younes

Abstract this chapter focuses on wind power. At present, wind turbines are installed with variable wind speed. Using intelligent systems, we can harness this energy that stores the wind and transforms it into electrical energy relying on such machines. In order to produce the maximum amount of electricity, the obstacles due to synergistic effects must be taken into consideration. The chapter also presents a solution enabling to convert the final energy demanded. A design of an intelligent wind turbine (3.8 kW) pitch angle control with a permanent magnet synchronous generator (PMSG) (3.5 kW), with the DC bus voltage controller, output from the converter for a 150 V pumping load, where a mechanism of fuzzy inference is used to estimate the upper limit of uncertainties. In addition, the fuzzy inference makes it possible to adjust the output voltage, obtain greater efficiency in the use of wind energy and protect the blades of the turbine. In the first part, we presented the modeling system with a pitch angle control. In the second part, a presentation of the results of the simulation system is analyzed and validated by the simulations in the MatLab/simulink environment.

Keywords Turbine · PMSG · Wind · Pitch control · Fuzzy logic

A. Slimen (✉)
Unity of Physical Research, Computer Science and Mathematics, University of Gafsa, Gafsa, Tunisia

National Engineering School of Gabes, University of Gabes, Gabes, Tunisia

H. Tlijani · R. B. Younes
Unity of Physical Research, Computer Science and Mathematics, University of Gafsa, Gafsa, Tunisia

Faculty of Science of Gafsa, University of Gafsa, Gafsa, Tunisia
e-mail: Rached.benyounes@fsgf.rnu.tn

M. Dhaoui
Unity of Photovoltaic Research, Wind and Geothermal Energy, University of Gabes, Gabes, Tunisia

National Engineering School of Gabes, University of Gabes, Gabes, Tunisia

N. Derbel, Q. Zhu (eds.), *Modeling, Identification and Control Methods in Renewable Energy Systems*, Green Energy and Technology,
https://doi.org/10.1007/978-981-13-1945-7_7

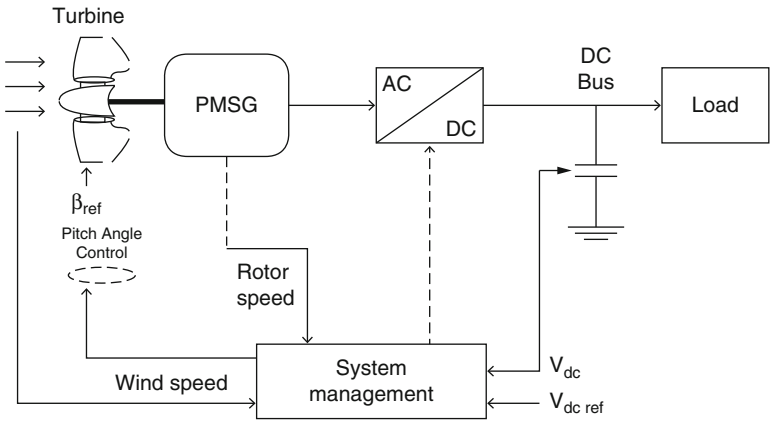

Fig. 7.1 General diagram of the control system

7.1 Introduction

Generally, a wind turbine system is constructed with a pitch angle controller, pitch control mechanisms, backup power and a feedback module monitoring the output power of the generator. In addition, the pitch control system makes it possible to adjust the output voltage and provide protection for the turbine blades. This chapter focuses on dynamic modeling of the wind pump system, modeling of the pitch control turbine based on a synchronous machine with permanent magnets controlled by a hysteresis rectifier for pumping 150 V load. Pitch variable-speed wind turbines is become the dominant type over the past years. For variable speed wind turbines, there are generally two control strategies.

In low wind speed lower than a nominal value, the cruise control can always adjust the rotor speed to maintain the speed at a level that gives the maximum power coefficient, and otherwise, when the wind speed is higher in the event of saturation, the controller stops the rotation of the blades to protect them, and then the efficiency of the turbine is increased, the control system is illustrated in Fig. 7.1 and detailed in the following (Akhmatov 2001, 2002; Akhmatov et al. 2003).

7.2 Mechanical Model of the Turbine

The mechanical power obtained by the conversion of kinetic energy (wind energy) into mechanical energy available at the output of the wind turbine:

$$P_m = \frac{1}{2}\,\rho\, C_p(\lambda, \beta)\, S\, v^3 \tag{7.1}$$

where, $C_p(\lambda, \beta)$ is the power coefficient, λ is the speed ratio, β is the pitch angle, ρ is the air density, V is the wind speed and $S = \pi R^2$ is the blades swept of the turbine. The mechanical torque of wind is obtained as:

$$T_m = \frac{1}{2} \pi \rho C_p(\lambda, \beta) S \frac{R^3 v^2}{\lambda} \tag{7.2}$$

The power coefficient $C_p(\lambda, \beta)$ depending on the speed ratio λ and the pitch angle β given by:

$$C_p(\lambda, \beta) = (0.44 - 0.167\beta) \sin \frac{\pi(\lambda - 3)}{15 - 0.3\beta} - 0.00184(\lambda - 3)\beta \tag{7.3}$$

The speed ratio λ is obtained depended by the wind speed and the mechanical speed:

$$\lambda = \frac{R Omega_m}{V} \tag{7.4}$$

where: $Omega_m$ is the angular velocity and R is the radius of the turbine blades. The developed turbine torque is:

$$\lambda = \frac{P_m}{Omega_m} \tag{7.5}$$

The maximum power is given when the power coefficient is at maximum of the turbine and the speed ratio is at optimum, we can express by the following relation:

$$P_{max} = \frac{1}{2} \pi \rho C_{pmax} S \frac{R^5 \Omega_m^3}{\lambda_o pt^3} \tag{7.6}$$

The power coefficient describes the production of the turbine, Fig. 7.2 shows the shape of the power coefficient C_p according to the different values of the speed ratio

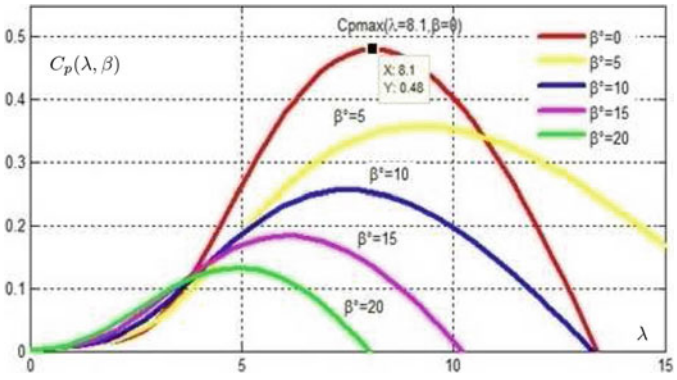

Fig. 7.2 Allure of $C_p(\lambda, \beta)$

and the pitch angle, the production is maximum at value $C_{pmax} = 0.48$ for a value of speed ratio $\lambda_{opt} = 7.1$ and height angle $\beta_{opt} = 0°$.

7.3 Pitch Angle Control

The wind goes through wind turbines at variable speed, to control the wind system, and to optimize the extracted power, the only parameter that controls the extracted power is the parameter C_p (Fig. 7.2). This parameter depends on the type of turbine and the type of design of the manufacturer. It is also a function of the pitch angle control, used mainly for optimizing the output power of wind turbines and thus the DC bus voltage according to our needs, for strong winds (wind speed above Nominal value) the mechanical power does not exceed the nominal power and protection against overloading the structure of the turbine and the risks of damage to its physical structure (Macêdo and Mota 2012). This procedure makes it possible to control the power supply of the wind farm and to avoid a possible higher generation in situations of strong winds and low consumption. This can be achieved by using the blade angle control to stabilize the wind farm when contingencies occur in the network (to reduce imbalance between generation and loads). This principle of control must therefore be taken into account in the transient stability studies and represented in the dynamic models of wind turbines. The purpose of the pitch control system proposed in this chapter is to maintain the speed of the wind turbine rotor at nominal value in strong winds. When the rotor speed is higher than the nominal speed, each blade will be rotated about its axis to reduce the angle (Hafsi et al. 2016).

The position of the angle β is controlled by the value Y, which can be characterized in various ways such as:

1. An electric value: for example, electric power P_e as described in Akhmatov (2001);
2. A single mechanical value: for example, the mechanical power P_m, or the generator speed ω_g, as described in Hansen et al. (2004), Lopes and Almeida (2004), Slootweg (2003), Akhmatov (2002), Akhmatov et al. (2003), Mota (2006);
3. A combination of mechanical and electrical power values, according to Miller et al. (2003), Akhmatov et al. (2003).

Ideally, the control parameters should be chosen depending on wind speed, but this is not an appropriate procedure, because it is not possible to precisely measure this variable. The wind speed can be changed by the turbine nacelle. Assuming that the turbine system is well controlled, the generated power can be used as a control parameter (Macêdo and Mota 2012).

In this chapter, power supply error criteria are used. The error between the reference and the measured power at the output of the PMSG is sent to a controller to generate the reference value β_{ref} of the pitch angle (Anjun et al. 2011), two

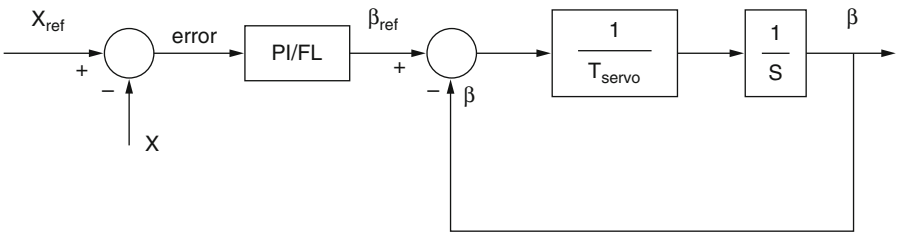

Fig. 7.3 Strategy of the pitch angle controller

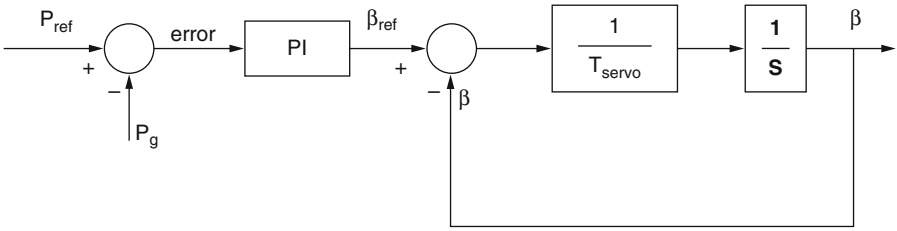

Fig. 7.4 Power regulation pitch angle controller by PI

controllers are applied, a control system by the conventional PI regulator and a regulator by fuzzy logic is illustrated is in following.

7.3.1 PI Control for the Pitch Angle

The generic blade angle control model (Anjun et al. 2011), using the PI control block is shown in Fig. 7.3.

Figure 7.4 shows the comparison between the generated power Pg with its value of reference obtained a error, by applying the PI controller to get the β_{ref}, $T_{servo} = 0.01$ is a time constant, it is the servomechanism used to correct the rate of change of the adjustment angle.

7.3.2 Fuzzy Logic Control for the Pitch Angle

Fuzzy logic control considered one of the most control Fuzzy logic, proposed by Lotfi Zadeh (1965), essentially generates output values without the need for precise inputs.

Provides a method for translating vague, imprecise and qualitative verbal expressions common to human communication into numerical values (Simães and Shaw 2007). Its main advantage is not to require an analytical description of the

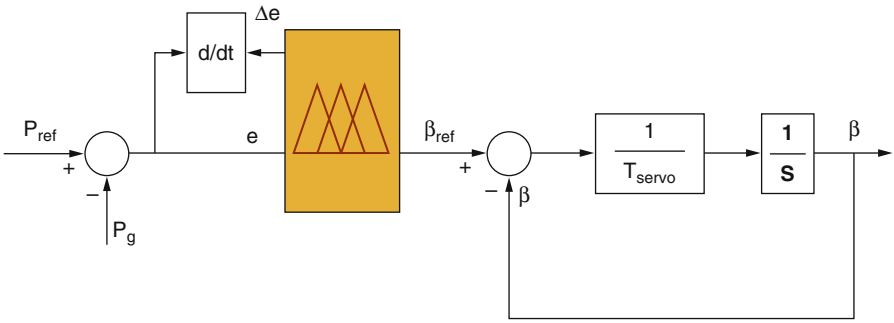

Fig. 7.5 Power regulation pitch angle controller by fuzzy logic

Table 7.1 Inference rules for the pitch angle

	e				
Δe	NB	NS	EZ	PS	PB
NB	NB	NB	NS	NS	EZ
NS	NB	NS	NS	EZ	PS
EZ	NB	NS	EZ	PS	PS
PS	NS	EZ	PS	PS	PB
PB	EZ	PS	PS	PB	PB

controlled system (Macêdo and Mota 2012). The fuzzy logic control is considered one of the most effective control methods. The fuzzy logic algorithm is suitable for controlling wind turbines with nonlinear models. The fuzzy controller uses observation to obtain the optimum pitch angle without knowing the characteristic of the wind turbine (Akhmatov et al. 2003).

The structure of the fuzzy logic controller basic on three stages: Fuzzification, decision making Unit and defuzzification unit. The inputs of the fuzzification are selected as error and rate of change of error and the output is the pitch angle reference. The input variables are calculated (Nguen and Naidu 2011).

$$e(k) = P_{ref}(k) - P_g(k)\,, \quad \Delta e(k) = \frac{e(k) - e(k-1)}{T} \tag{7.7}$$

where, $P_{ref}(k)$ and $P_g(k)$ are respectively the reference and generated power at step k (Akhmatov et al. 2003). In Fuzzification stage the crisp variables $e(k)$ and $\Delta e(k)$ are converted into fuzzy variables which can be identified by membership function (Fig. 7.5). In Fuzzification stage the crisp variables $e(k)$ and $\Delta e(k)$ are converted into fuzzy variables which can be identified by membership function. The proposed controller uses following linguistic labels: NB (Negative Big), NS (Negative Small), EZ (Equal Zero), PS (Positive Small), PB (Positive Big) (Table 7.1).

Triangular membership functions are used to define both inputs (error e, variation error Δe) and output (pitch angle β_{ref}) as shown as on the different figure: Figs. 7.6, 7.7, 7.8.

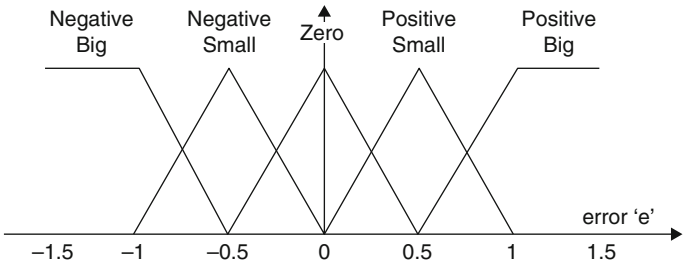

Fig. 7.6 Fuzzy inference for the input error e

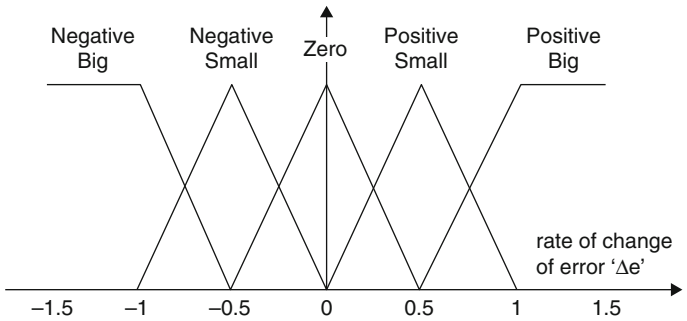

Fig. 7.7 Fuzzy inference for the input rate of change of error Δe

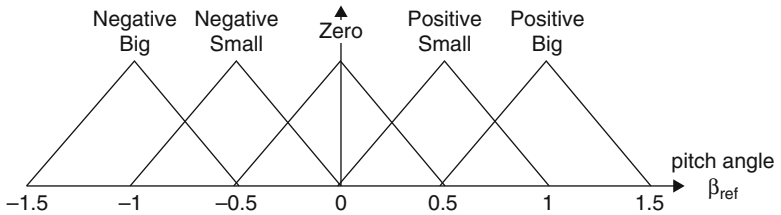

Fig. 7.8 Fuzzy inference for the output pitch angle β_{ref}

7.3.3 Simulation Results

For evaluating the robustness of the fuzzy logic controller compared with the conventional PI controller at variable wind speed, the simulations have been carried out using MATLAB/Simulink software.

Figure 7.9 shows the variation of the wind model, the wind varies around its nominal value 10 m/s and reaches a maximum value 25 m/s to evaluate the robustness of the control of the pitch angle control.

Figure 7.10 shows the results of the control strategy of the pitch angle by the conventional regulator PI.

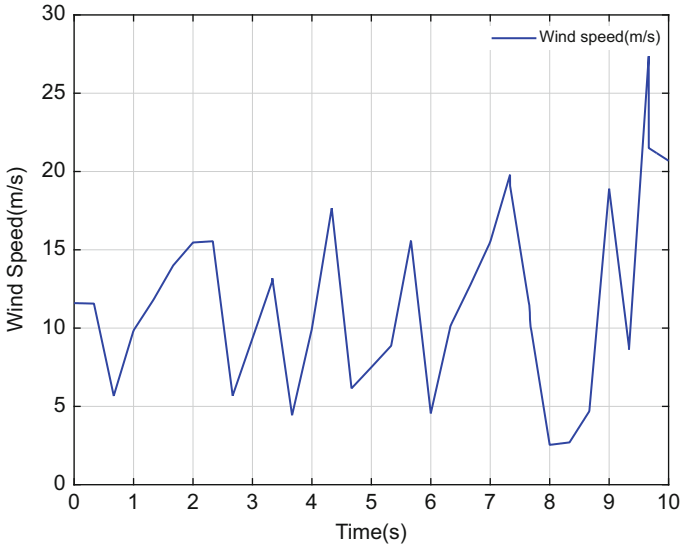

Fig. 7.9 Wind speed (m/s)

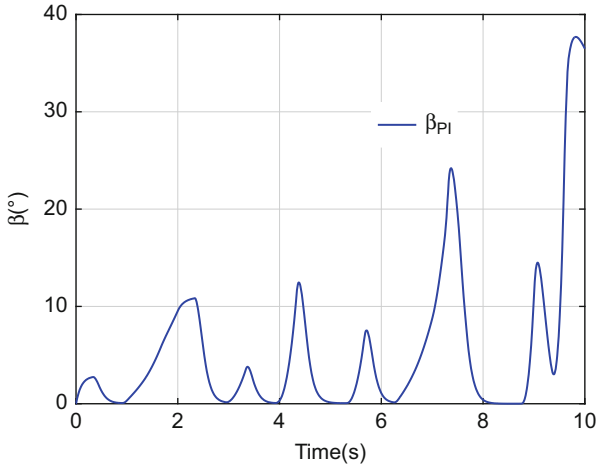

Fig. 7.10 Pitch angle control with PI

Figure 7.11 shows the results of the control strategy of the pitch angle by the regulator fuzzy logic.

Figure 7.12 shows the results of the power mechanical with the different regulator fuzzy logic and PI. The Comparisons of different control strategies of the pitch angle β with the conventional PI regulator and the fuzzy controller show that the control strategies of the fuzzy logic the control of the pitch angle.

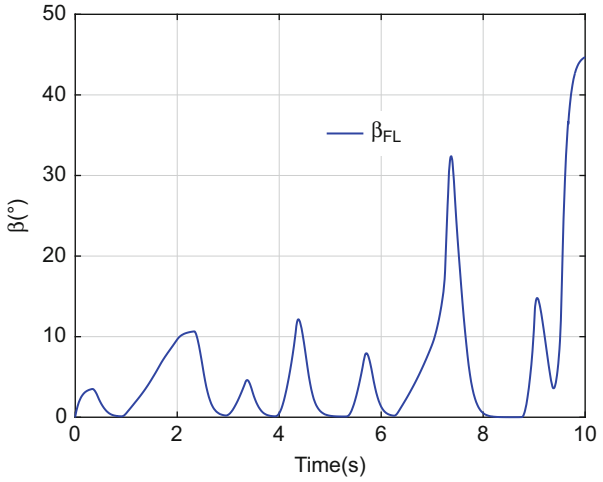

Fig. 7.11 Pitch angle with fuzzy logic

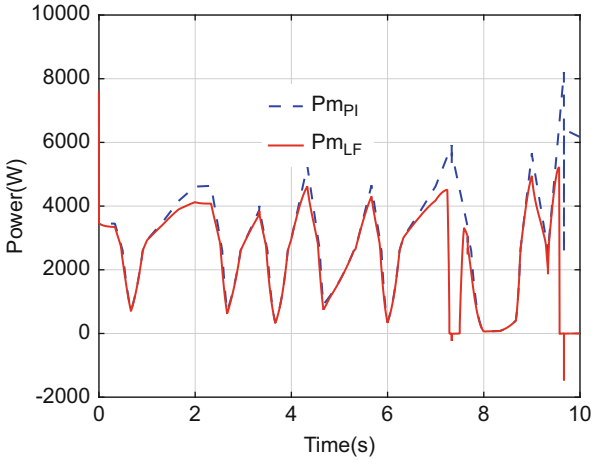

Fig. 7.12 Comparisons power with pitch angle control strategies

7.4 Model of the PMSG

The wind turbine drives a permanent magnet synchronous generator PMSG. By considering only the fundamental harmonic of the flux distribution in the air-gap of the machine and by neglecting the homopolar component, the theory of the space vector gives the dynamic equations of the stator currents as follows:

$$\begin{cases} V_{sd} = -R_s i_{sd} - L_s \dfrac{i_{sd}}{dt} - p\Omega L_s i_{sq} \\ V_{sq} = -R_s i_{sq} - L_s \dfrac{i_{sq}}{dt} + p\Omega L_s i_{sd} + p\omega\phi \\ T_{em} = p\phi i_{sq} \end{cases} \tag{7.8}$$

where R_s is the phase resistance of the stator winding, L_s is the stator cyclic inductance, ϕ is the flux of the permanent magnetic, V_{sd} and V_{sq} are the d-q components of the stator voltages respectively, i_{sd} and i_{sq} are the d-q components of the stator currents respectively, p is the number of pairs of pole, Ω is the mechanical speed rotor and T_{em} is the electromagnetic torque.

7.5 DC Bus Control

The generator-side inverter is controlled to catch maximum power from available wind power. According to (7.8), in order to control the electromagnetic torque T_{em}, this study just controls the q-axis current i_{sq} with the assumption that the d-axis current i_{sd} is equal to zero. Furthermore, Veermani and Mohan (2011), Rolan et al. (2009) show that, in order to catch maximum power, the optimum value of the rotation speed is adjusted. The tip speed ratio λ is taken into account due to the equation being addressed as follows:

$$\Omega_{ref} = \frac{\lambda_{opt} V}{R} \tag{7.9}$$

where Ω_{ref} is the blade angular velocity reference, λ_{opt} is the tip speed ratio optimum and V is the wind speed. We apply two regulator, a conventional regulator PI and à fuzzy logic regulator, between the reference voltages (V_{dcref}) and the voltage (V_{dc}) to get the error and sent it to the controllers to adjust the voltage to a desired quantity which is detailed in the following.

7.6 Fuzzy Logic Controller for DC Bus

The fuzzy logic controller for the DC bus has three parameters. The first input is the error of DC voltage, the second is the rate of change of error and the output is the power controlling current component. The inputs variables are calculated at every sampling time k (Yin et al. 2007).

$$e(k) = V_{dcref}(k) - V_{dc}(k)\,, \quad \Delta e(k) = \frac{e(k) - e(k-1)}{T} \tag{7.10}$$

Table 7.2 Rules table for DC bus

	e						
Δe	NB	NS	NM	EZ	PS	PM	PB
NB	NB	NB	NB	NB	NM	NS	EZ
NM	NB	NB	NB	NM	NS	EZ	PS
NS	NB	NB	NM	NS	EZ	PS	PM
EZ	NB	NM	NS	EZ	PS	PM	PB
PS	NM	NS	EZ	PS	PM	PB	PB
PM	NS	EZ	PS	PM	PB	PB	PB
PB	EZ	PS	PM	PB	PB	PB	PB

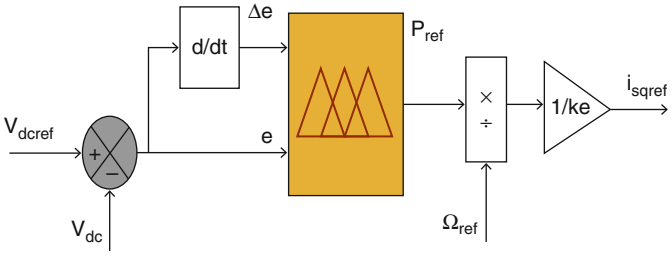

Fig. 7.13 Strategy fuzzy DC bus controller

where $V_{dcref}(k)$ and $V_{dc}(k)$ are the reference and measured voltage at time k, respectively. In Fuzzification stage the crisp variables $e(k)$ and $\Delta e(k)$ are converted into fuzzy variables which can be identified by membership function. The fuzzification maps the error and change in error to linguistic labels of fuzzy sets.

The proposed controller uses following linguistic labels: NB (Negative Big), NM (Negative Medium), NS (Negative Small), EZ (Zero), PS (Positive Small), PM(Positive Medium), PB(Positive Big) (Table 7.2).

The activation function of both the output layer are linear and unbiased while that of the hidden layer is sigmoid and biased (Hafsi et al. 2016).

7.6.1 PI Controller DC Bus

For the regulation of the DC bus controller, we apply the regulator PI between the reference voltage Vdcref and the voltage measured V_{dc} as shown in Fig. 7.14 (Slimen et al. 2016).

For the control of the DC bus, it is assumed that the transfer function on the rectifier side is equal to zero G(s) = 1 detailed on Fig. 7.15 (Slimen et al. 2016).

$$\frac{V_{dc}}{V_{dcref}} = \frac{\frac{k_{pv}}{C}s + \frac{k_{iv}}{C}}{s^2 + \frac{k_{pv}}{C}s + \frac{k_{iv}}{C}} \tag{7.11}$$

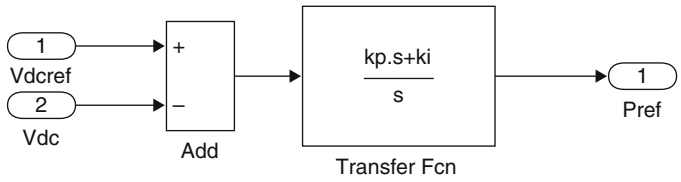

Fig. 7.14 DC bus PI controller

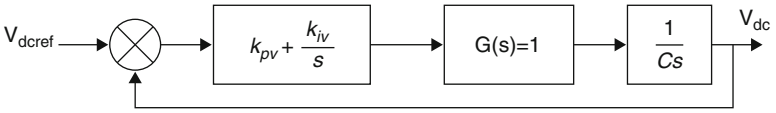

Fig. 7.15 Transfer function DC bus

The characteristic equation function is a second-order dynamics is of the form:

$$s^2 + \frac{k_{pv}}{C}s + \frac{k_{iv}}{C} = 0 \tag{7.12}$$

The parameters of the PI regulator can be expressed by the canonical form by identifying the denominator with:

$$k_{pv} = 2Cx\omega_p\ , \quad k_{iv}C\omega_p^2 \tag{7.13}$$

using the value of the capacitor C = 380 μF and the clean pulse $\omega_p = 60$ rad/s (Slimen et al. 2016).

7.6.2 Simulation Results and Discussion

The simulation show that the combination of PI and Fuzzy Logic DC bus controller. In order to evaluate the performance of the control system for the variable DC bus reference concept with PMSG, we set reference to 100 V in the first, next 130 V and finally 150 V.

Figure 7.16 shows the behavior of the control response of the DC bus voltage by the fuzzy logic regulator with the desired reference voltage.

Figure 7.17 shows the behavior of the control response of the DC bus voltage by the PI regulator with the desired reference voltage.

Figures 7.16, 7.17 and 7.18 show the responses of the system when using respectively IP and fuzzy logic controllers. From Fig. 7.18, showing the comparison of the two responses; we note that the use of fuzzy provides a response with a smaller overshoot and faster compared to the conventional PI controller.

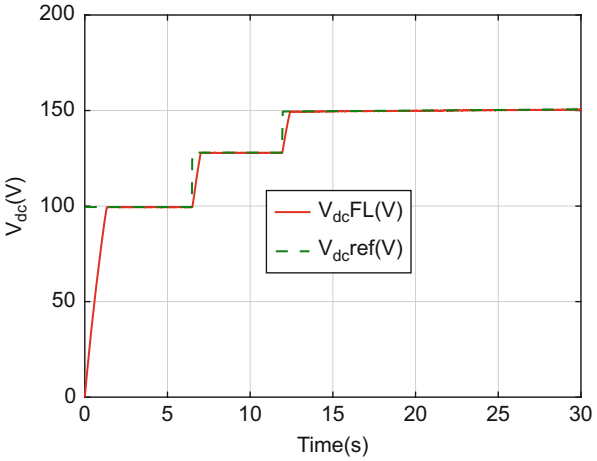

Fig. 7.16 DC bus control with fuzzy Logic regulator

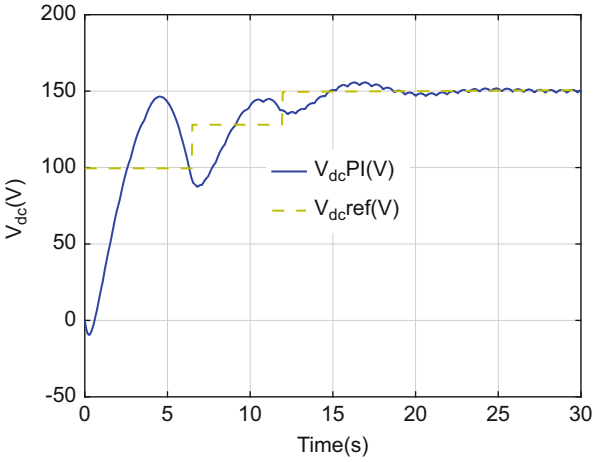

Fig. 7.17 DC bus control with the regulator PI

The fuzzy control is efficient in terms of reducing the oscillations of monitored variables compared to the conventional PI control.

7.7 Conclusion

This chapter presents the dynamic model of PSMG wind generation system in Matlab/Simulink. The model of generator side can capture the maximum power from variable wind. In the first, we begin with a control design scheme proposed

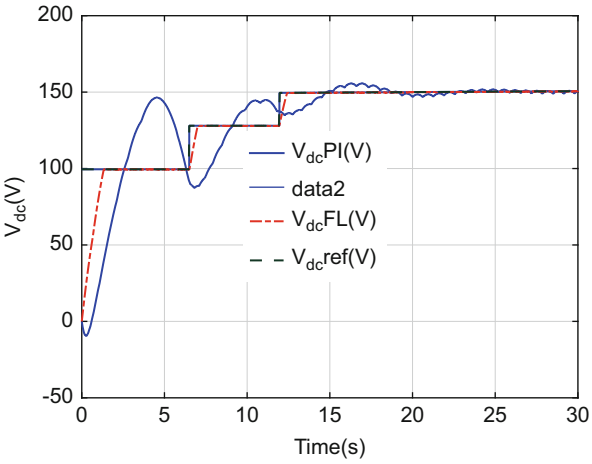

Fig. 7.18 Comparisons DC bus control with the regulators PI and fuzzy logic

for the control of the blade pitch angle in variable speed wind turbine using two regulator PI and fuzzy logic (Akhmatov 2002). Simulation results demonstrated good performance for both proposed schemes. In the second part, we control the DC bus side generator (Yang and Zhang 2013).

By combining the two controllers, pitch angle control and the DC bus control, using the two tested regulators, PI regulator and fuzzy logic regulator, good performance to track the power maximum to can feed our pump load.

References

Akhmatov, V. (2001). Note concerning the mutual effects of grid and wind turbine voltage stability control. *Wind Engineering, 25*, 367–371.

Akhmatov, V. (2002). Speed wind turbines with doubly-fed induction generators – Part I: Modelling in dynamic simulation tools. *Wind Engineering, 26*, 85–108.

Akhmatov, V., Knudsen, H., Nielsen, A. H., & Poulsen, J. (2003). Modelling and transient stability of large wind farms. *International Journal Electrical Power and Energy Systems, 25*(2), 123–144

Anjun, X., Hao, X., Shuju, H., & Honghua, X. (2011). Pitch control of large scale wind turbine based on expert PID control. In *International Conference on Electronics, Communications and Control (ICECC)*, Ningbo, China, September 9–11, 2011 (pp. 3836–3839).

Hafsi, S., Dhaoui, M., & Sbita, L. (2016). Advanced control of a PMSG wind turbine. *International Journal of Modern Nonlinear Theory and Application, 5*, 1–10.

Hansen, A. D., Sorensen, P., Loy, F., & Blaabjer, F. (2004). Speed wind turbines with doubly-fed induction. *Engineering, 28*, 247–263.

Lopes, J. A. P., & Almeida, R. G. (2004). Descrição de Modelos Matemáticos de Máquinas de Indução Convencional e Duplamente Alimentada e Estratégias de Controlo para Estudo Dinâmico e de Estabilidade Transitória, Trabalho de Consultoria parao ONS Brasil, INESC PORTO.

Macêdo, A. V. A., & Mota, W. S. (2012). Wind turbine pitch angle control using fuzzy logic. In *IEEE/PES Transmission and Distribution: Latin America Conference and Exposition (T&D-LA)*, Montevideo, Uruguay, September 3–5, 2012 (pp. 1–6).

Miller, N. W., Price, W., & Sanchez-Gasca, J. J. (2003). Dynamic modelling of GE 1.5 and 3.6 wind turbine generators (p. 31). Technical Report, Power Systems Energy Consulting, General Electric Int., Shenectady.

Mota, W. S. (2006). Simulação de Transitórios Eletromec â Potência (p. 368). Campina Grande, Epgraf.

Nguen, H. M., & Naidu, S. (2011). Advanced control strategies for wind energy systems. In *IEEE PES, Power Systems Conference & Exposition (PSCE)*, Phoenix, AZ, USA, March 20–23, 2011.

Rolan, A., Luna, A., Vazquez, G., Aguilar, D., & Azevedo, G. (2009). Modeling of a variable speed wind turbine with a permanent magnet synchronous generator. In *IEEE International Symposium on Industrial Electronics (ISlE 2009)*, Seoul, South Korea, July 5–8, 2009 (pp. 734–739).

Simães, M. G., & Shaw, I. S. (2007). *Controle modelagem fuzzy* (2nd ed., p. 186). SãoPaulo: Blucher.

Slimen, A., Tlijani, H., Dhaoui, M., & Ben Younes, R. (2016). Study of wind turbine system based on PMSG with fuzzy-PI controller. In *International Journal of Control Theory and Applications* (pp. 111–123).

Slootweg, J. G. (2003). Modelling and Impact on Power System Dynamics. Ph.D. Thesis, University of Technology, Delft.

Veermani, C., & Mohan, G. (2011). A fuzzy based pitch angle control for variable speed wind turbines. In *IEEE, Student Conference on Research and Development (SCOReD)* (pp. 36–39).

Yang, S., & Zhang, L. (2013). Modeling and control of the PMSG wind generation system with a novel controller. In *3rd International Conference on Intelligent System Design and Engineering Applications*, Hong Kong, China, January 16–18, 2013 (pp. 946–949).

Yin, M., Li, G., & Zhou, M. (2007). Modeling of the wind turbine with a permanent magnet synchronous generator for integration. In *IEEE, Power Engineering Society General Meeting* (pp. 1–6).

Zadeh, L. A. (1965). Fuzzy sets. *Information and Control, 8*, 338–353.

Chapter 8
Nonlinear Control of a Variable Speed Wind Energy Conversion System Based PMSG

Marwa Ayadi and Nabil Derbel

Abstract In this chapter, we present a control system for a variable speed wind turbine based direct-drive permanent magnet synchronous generator. In order to capture the optimal power from the wind and to ensure a maximum efficiency for this system, nonlinear control laws namely backstepping controller and sliding mode controller have been synthesized. Moreover, a blade pitch angle controller has been introduced above rated wind speed to keep the generated power at the designed limit. Finally, to avoid the power fluctuation, the transition between the two control regions has been investigated.

Keywords Wind turbine · PMSG · Blade pitch control · Robust control · Stability

8.1 Introduction

Nowadays, Renewable energy systems receive a great interest in the research community thanks to economic, social and environmental benefits.

In fact, because of the earth greenhouse effects, the oil price increases, the nuclear world security and the rapid growth of the global economy, the renewable energy, which includes geothermal energy, wind energy and photovoltaic energy, etc., has been widely investigated and rapidly developed (Bull 2001).

Wind energy is considered to be the most competitive and the fastest growing renewable energy as it is a clean energy source with an exhaustible supply (Burton et al. 2011).

Several types of wind turbine exist nowadays with variation in the number of blades, the generator type and the control surface. The most prevalent turbine

M. Ayadi (✉) · N. Derbel
National School of Engineering of Sfax (ENIS), University of Sfax, Sfax, Tunisia
e-mail: marwaayadii@yahoo.fr; n.derbel@enis.rnu.tn

N. Derbel, Q. Zhu (eds.), *Modeling, Identification and Control Methods in Renewable Energy Systems*, Green Energy and Technology,
https://doi.org/10.1007/978-981-13-1945-7_8

existing in the control literature is the 3-blade, horizontal axis wind turbine (HAWT).

For several decades, the wind turbine has been operated at a fixed speed. Despite it has a simple structure and a lower construction and maintenance cost, this type presents some problems as the poor power quality and the low efficiency. Thus, it has been replaced by a variable speed wind turbine (VSWT) to enhance efficiency, reduce audible noise and mechanical stresses (Abulanwar et al. 2016; Burton et al. 2011; Yang et al. 2014b).

For VSWT, the direct− driven permanent magnet synchronous generators (PMSG) are widely used in small and medium-size wind turbine systems. There are several advantages of using PMGs for electrical power generations.

First, they can provide high-reliability and high-efficiency, since there are no copper losses in the rotor circuit and no need for external excitation (Cai et al. 2000).

Second, PMGs with high−power−density are small in size, which reduces the weight and the cost of the wind turbine system (Michalke et al. 2007).

In addition, the wind turbine with a direct-drive PMSG offers the ability to remove the gearbox. According to the statistical data reported in Ribrant and Bertling (2007), failures of gearboxes cause about 19.4% downtime of WTGs. Without gearboxes, the system needs less maintenance and have a higher reliability and a reduced downtime.

The overall configuration of a direct-drive PMSG wind turbine shown in Fig. 8.1. This structure includes a generator control for maintaining the desired rotor speed, a pitch angle control for limiting the output power, a constant DC link control and a grid side inverter control for active and reactive power control.

The main challenge in wind energy conversion system (WECS) control is to extract the optimal accessible power and cope with the nonlinearity of the system. Therefore, in this chapter, we will focus only on analyzing modern nonlinear control techniques for the generator-side to achieve maximum performances.

For the generator side, there are typically two control strategies according to the wind speed velocity.

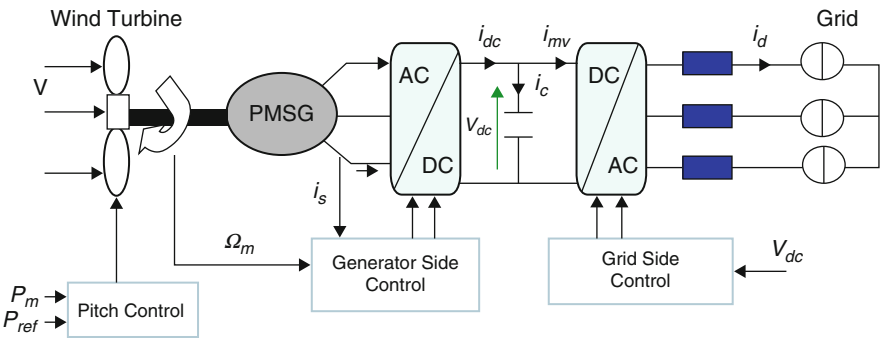

Fig. 8.1 Process structure

In partial load region, the speed controller can continually adjust the speed of the rotor to ensure as much as possible energy yield. Thus, the efficiency of the system will be increased.

For full load zone, the pitch angle regulation is required to keep the generated power constant.

In wind turbine system, control strategies hold a crucial role to enhance the efficiency. Without a good control system, a considerable portion of the produced power is wasted.

Several works of the literature are addressing the issue of controlling the wind turbine system. The simplest techniques are based on PI controllers and the Perturb and Observe algorithm (Kesraoui et al. 2011; Mansour et al. 2011). However, these classical methods show limited performances. Even though neural networks may guarantee a fast response, the performance of control fails along the system variation.

Moreover, fuzzy logic approaches have been widely applied and have presented better effectiveness (Bahraminejad et al. 2014; Jerbi et al. 2009; Simoes et al. 1997), but, the major problems are the strict theoretical analysis and the lack of stability.

A backstepping approach has been studied and developed to the control of the PMSG (Karabacak and Eskikurt 2012; Wang et al. 2013; Yang et al. 2014a). This technique provides a good performance result. Sliding mode control emerges also as a suitable option to deal with such complex system and it has been applied in several works. Lee et al. (2010) propose the sliding mode control scheme to maximize the generated power below the rated wind speed, Results demonstrated by research (Vu et al. 2013; Zhang et al. 2013) involving the use of SMC with PMSG continue to prove the strength of SMC as a viable strategy for effective control of synchronous machines

Although the positive attributes of SMC, the phenomenon known as chattering gives an understandable level of criticism. Because of the nonidealities in switching devices, the response of the system oscillates with high frequencies about the desired reference, known as the sliding surface which leads to low control accuracy and even damages of mechanical parts.

In order to face this undesirable phenomenon, the literature proposes different improvement techniques Such as the approach presented in Kachroo and Tomizuka (1996) which places a boundary layer around the switching surface such that the relay control is replaced by a saturation function. Another class of techniques is based on introducing high order sliding mode algorithms for speed control (Feng et al. 2012; Valenciaga and Puleston 2008). In Evangelista et al. (2013), the speed tracking was achieved using a super-twisting sliding mode control based on Lyapunov techniques.

From this point of view, The main objective of this paper is to study the control algorithms for a variable speed wind turbine based permanent magnet synchronous generator.

In order to achieve a maximum power capture efficiency for the system in safety conditions, a nonlinear control strategy based on backstepping controller and sliding

mode controller has been proposed. Furthermore, a blade pitch angle controller is proposed to enhance system performances in high wind speed region.

The rest of the paper is organized as follow. Section 8.2 presents the system modeling. The control technique applied to the wind system is introduced in Sect. 8.3. The Control below rated wind speed: MPPT zone is presented in Sect. 8.4. Section 8.5 describes the control above rated wind speed (the pitch control). The transition between the two control regions is detailed in Sect. 8.6. Finally, some conclusion remarks are drawn in the last Section.

8.2 Modeling of the Wind Turbine System

8.2.1 Wind Turbine Modeling

Consider a horizontal axis wind turbine (HAWT). The potentially available power by the wind is defined as:

$$P_w = \frac{1}{2}\pi\rho R^2 V^3 \tag{8.1}$$

where:

- R denotes the blade radius of the WT(m)
- ρ is the air density (1.25 kg/m in normal atmosphere)
- V is the wind speed (m/s)

However, this expression can only stand if the wind passes through the swept area of the wind turbine.

In 1919, A German physicist Albert Betz state that no more than 59% of the kinetic energy, contained in a steam tube that shares the same cross-section as the disc, can be converted to useful works.

Figure 8.2 presents a schematic of fluid flow which helps to contextualize the statement.

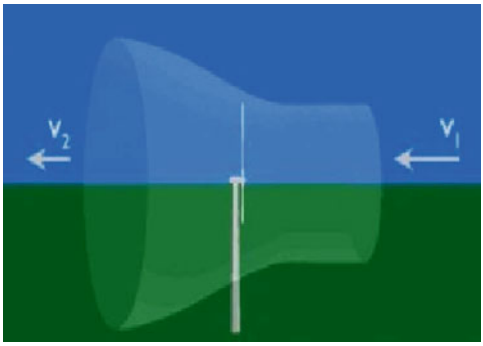

Fig. 8.2 Schematic of fluid flow through a wind turbine

Thus, a power coefficient term is introduced and can be understood as:

$$C_p = \frac{\text{mechanical power captured by the wind turbine}}{\text{maximum power available in the wind}} \tag{8.2}$$

C_p represents the performance of the wind turbine. It depends on the tip-speed ratio (TSR) λ and the pitch angle β which is the angle between the orientation of the blade and the wind velocity vector:

$$\begin{aligned} C_p(\lambda, \beta) &= 0.22\left(\frac{116}{\lambda_i} - 0.4\beta - 5\right)e^{\frac{-12.5}{\lambda_i}} \\ \frac{1}{\lambda_i} &= \frac{1}{\lambda + 0.08\beta} - \frac{0.035}{\beta^3 + 1} \end{aligned} \tag{8.3}$$

with

$$\lambda = \frac{\Omega_t R}{V} \tag{8.4}$$

where Ω_t is the turbine speed

The nonlinear relation between C_p, λ and β is presented in Fig. 8.3.

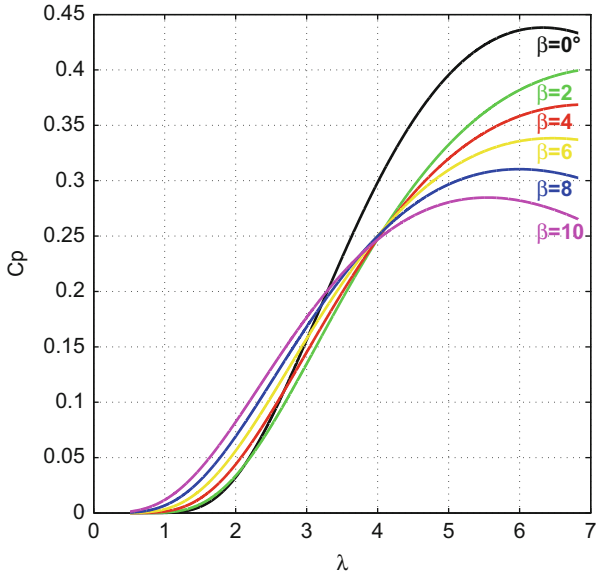

Fig. 8.3 Aerodynamic power coefficient variation C_p against the speed ratio λ and the pitch angle β

It is obvious that C_p is maximised when β =0 and it decreases with the increase of β. For a constant pitch angle, there is a unique peak of the curve corresponding to C_{pmax}.

The aerodynamic torque is given by:

$$T_m = \frac{P_m}{\Omega_t} = \frac{1}{2}\,\pi\,\rho\,C_p(\lambda,\beta)\,\frac{R^2\,V^3}{\Omega_t} \tag{8.5}$$

8.2.2 PMSG Modeling

The mathematical model of the PMSG in the d-q reference is Kim et al. (2010):

$$\begin{cases} U_d = R_s I_d + L_d \dfrac{di_d}{dt} - \Omega_e \Phi_q \\ U_q = R_s I_q + L_q \dfrac{di_q}{dt} + \Omega_e \Phi_d \end{cases} \tag{8.6}$$

where R_s is the stator resistance. Φ_d and Φ_q are the d and q axis flux linkage, respectively:

$$\begin{aligned} \Phi_d &= L_d I_d + \Phi_m \\ \Phi_q &= L_q I_q \end{aligned} \tag{8.7}$$

Furthermore, consider $L_q = L_d = L_s$ denotes the inductance of the stator (a PMSG with a nonsalient pole is considered in this study).

8.3 Control Technique

Wind Turbine systems present intense nonlinearities, and are subjected to disturbances and parameter uncertainties. Such factors transform their control to a hard task.

Therefore, a high level control is often required in order to ensure a certain convergence of the system to the requested state condition and to operate at maximum power coefficient over a wide range of wind speeds.

In fact, wind turbines should be driven differently according to the speed of the wind.

Therefore, the WT generator needs to be controlled to operate in three different modes as shown in Fig. 8.4.

- Parking Mode (I): The wind speed is lower than the cut-in speed which is (2 m/s) in this system, the wind turbine stays in a parking status and does not rotate.

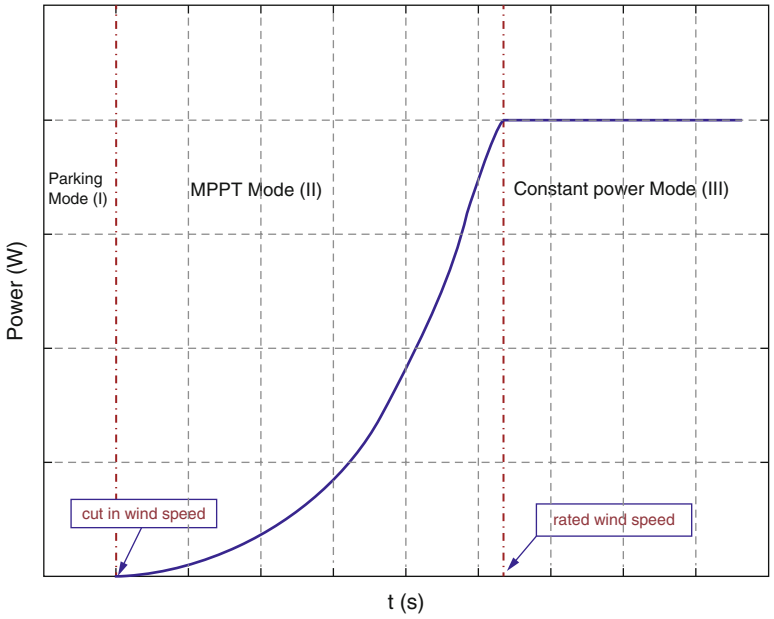

Fig. 8.4 Power versus wind speed characteristic

- MPPT (Maximum Power Point Tracking) mode (II): The system starts to work and generates electrical power. The MPPT is applied until arrived to the rated wind speed, (12.7 m/s), for this case-study system. The blade angle is usually controlled at zero degree to maximize the wind energy capture.
- Constant power Mode (III): It is necessary to control the extracted power above rated wind value by adjusting properly the blade pitch angle of the wind turbine to keep the power at constant power region, as its name implies.

8.4 Control Below Rated Wind Speed: MPPT Zone

In this region, the wind speed is below the rated value. The objective of the controller is to maximize the wind energy capture and to achieve the Maximum Point Power Tracking (MPPT). For that, The tip speed ratio λ is set to its optimal value λ_{opt} which contributes to the power coefficient peak C_{pmax}. Therefore, the optimum rotor speed of the Wind turbine can be written as follows:

$$\Omega_{opt} = \frac{\lambda_{opt} v}{R} \tag{8.8}$$

Thus, the maximum power output of the wind turbine can be expressed as:

$$P_{max} = k_{opt}\Omega_{opt}^3 \tag{8.9}$$

$$k_{opt} = \frac{1}{2}C_{pmax}\rho\pi R^2\left(\frac{R}{\lambda_{opt}}\right)^3$$

In addition, to achieve the MPPT operation mode, the pitch angle is kept at zero degree to ensure a high efficiency of energy capture.

The optimum rotor speed given in Eq. (8.8) is considered as the speed reference of the PMSG. Consequently, by using a robust control technique the generator speed will reach its reference value in the static state, and then the MPPT control is achieved.

In this work, the control system proposed to command the wind turbine generator is the Field Oriented Control (FOC), which controls the torque indirectly by adjusting the stator currents. In this method, the torque angle is maintained at 90°. The d-axis current is set to zero and then the stator current has only the q-axis component. Thus, the torque depends only on the q-axis stator current. This technique removes current cross coupling between the d and q axes components.

Based on the FOC technique, different controller design have been investigated in this work to the PMSG to optimize the wind turbine power output.

- Proportional Integral (PI) control
- backstepping control
- Sliding mode control

Remark 1 For the control design, the following assumptions are required:

Assumption 1 Variables i_q, i_d and Ω are available.

Assumption 2 The reference speed Ω_{ref} is determined referring to the MPPT algorithm.

Assumption 3 The d-axis reference current should be equal to zero $i_d = 0$.

8.4.1 Vector Control Based PI Controlller

8.4.1.1 Controller Design

This technique is the most commonly applied algorithm for the PMSG control (Ayadi and Derbel 2017). It involves two control loops:

- two inner current loops are used to adjust the generator currents i_d and i_q allowing the control of the flux and the torque, respectively.
- an external mechanical loop in order to ensure the speed regulation.

Then, to improve the dynamic response, compensation voltage, Δ_{Uq} and Δ_{Ud} are added into the control law.

$$\begin{aligned} \Delta_{Ud} &= \Omega_e i_q L_s \\ \Delta_{Uq} &= \Omega_e i_q L_s + \Omega_e \Phi_m \end{aligned} \tag{8.10}$$

- d-axis current controller design

The control of this component aims to keep the stator flux constant. Its reference value is set to zero.

$$\frac{i_d}{U_d} = \frac{\frac{1}{R_s}}{1 + s\frac{L_d}{R_s}} \tag{8.11}$$

The PI transfer's function is:

$$G(s) = k_d \left(\frac{1 + \tau_d s}{\tau_d s} \right) \tag{8.12}$$

Based on the compensation pole method, the synthesis of this PI can be determined $\tau_d = \frac{L_d}{R_s}$, $K_d = \frac{R_s^2}{L_d}$, and the closed loop transfer function between the actual and the desired direct current is:

$$F_d(s) = \frac{1}{1 + s\frac{L_s}{R_s}} \tag{8.13}$$

- q-axis current controller design

The control of the quadrature current i_q affects directly the electromagnetic torque. The reference value of i_q is determined from the speed control loop. The control law is implemented in the same way as the d-axis current controller yielding: $\tau_q = \frac{L_s}{R_s}$ and $K_q = \frac{R_s^2}{L_s}$.

- Speed control loop

The reference value of this loop is the optimal speed Ω_{opt} determined based on the MPPT strategy Eq. (8.8). The transfer function between Ω_r and i_q is given by:

$$\frac{i_q}{\Omega_r} = \frac{\frac{3}{2} p \Phi_m}{f + sJ} \tag{8.14}$$

Table 8.1 Turbine and PMSG parameters

Wind turbine parameters	PMSG parameters
3 blades	$P_{nom} = 25$ KW
Variable speed	$R_s = 0.82$ m
$R = 4.5$ m	$L_{sd} = L_{sq} = 15.1$ mH
$Cp_{max} = 0.42$	$\phi = 0.5$ Wb
$J_{tot} = 99$ e-4	$f = 1$e-3
$\rho = 1.225$ kg/m	p = 4

The PI transfer's function is:

$$G_{\Omega}(s) = k_{\Omega}\left(\frac{1+\tau_{\Omega}s}{\tau_{\Omega}s}\right) \tag{8.15}$$

Thus, the closed-loop transfer function is:

$$F_{\Omega}(s) = \frac{1+\tau_{\Omega}s}{1+(\tau_{\Omega}+\frac{f}{\frac{3}{2}p\phi_m K_{\Omega}})s+\frac{J}{\frac{3}{2}p\phi_m K_{\Omega}}s^2} \tag{8.16}$$

The output of the PI represents the quadrature reference current $\bar{i}_q$.

8.4.1.2 Simulation Results

Results have been presented, using numerical simulations carried under the Matlab-SIMULINK tool to test the control strategy and to evaluate the performance of the system.

Characteristics of the turbine and the Permeant Magnetic Synchronous Machine are presented in Table. 8.1.

System simulation has been performed considering an aleatory wind profile to evaluate the behavior of the system similar to real conditions.

As shown in Fig. 8.4, for different regions of the wind speed, there is a specific control strategy. Therefore in this part, The wind speed will be limited to (11.5 m/s) as we are interested in the control below rated wind speed region(II).

- Figure 8.5a presents the wind speed profile.
- Figure 8.5b shows that the power coefficient C_p is maintained close to its maximum value $C_{pmax} = 0.41$. Thus, the Maximum Power Point Tracking MPPT has been achieved.
- The system response under PI is shown in Fig. 8.6.

  Figure 8.6a shows the rotational speed response. It converges to its reference track which is supplied from the Maximum Power Point Tracking (MPPT) controller. Figure 8.6b presents the rotational speed error which exceeds the 0.2(rad/s). The direct and the quadrature currents are shown in Fig. 8.6c, e respectively. It is obvious from Fig. 8.6d, f that current errors present a considerable distorted values due to the nonlinear characteristics of the system

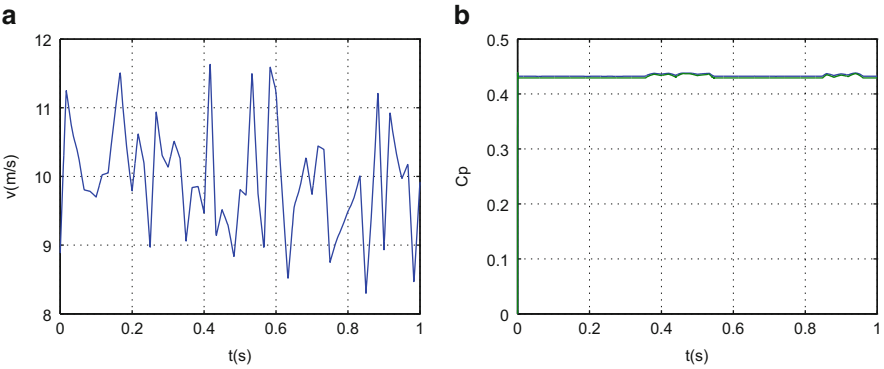

Fig. 8.5 wind speed profile

This control laws gives good dynamic response of the speed tracking and remarkable rejection of disturbances.

However, it should be noted that it is better to minimize as possible the tracking error, hence we propose two non-linear regulators namely the backstepping control and the sliding mode control in the sequel.

8.4.2 Backstepping Controller

8.4.2.1 Controller Design

This control approach is designed in such a way it keeps the same general structure of the vector control while ensuring at the same time the regulation and the limitation of the currents. The objective of the nonlinear backstepping controller is to track the speed of PMSG with the choice of appropriate regulated variables (Ayadi and Derbel 2017). Based on the PMSG model given in Eq. (8.6), The control design can be determined by following three steps as shown in Fig. 8.7.

- *Step 1: Control design based on rotational speed dynamics:*

The speed error is:

$$e_{\Omega} = \bar{\Omega}_r - \Omega_r \tag{8.17}$$

The error dynamics derived can be obtained as:

$$\dot{e}_{\Omega} = \dot{\bar{\Omega}}_r - \frac{T_m}{J} + \frac{3p}{2J}\Phi_m i q + \frac{B}{J}\Omega_r \tag{8.18}$$

Consider the following Lyapunov function candidate:

$$V_{\Omega} = \frac{1}{2}e_{\Omega}^2 \tag{8.19}$$

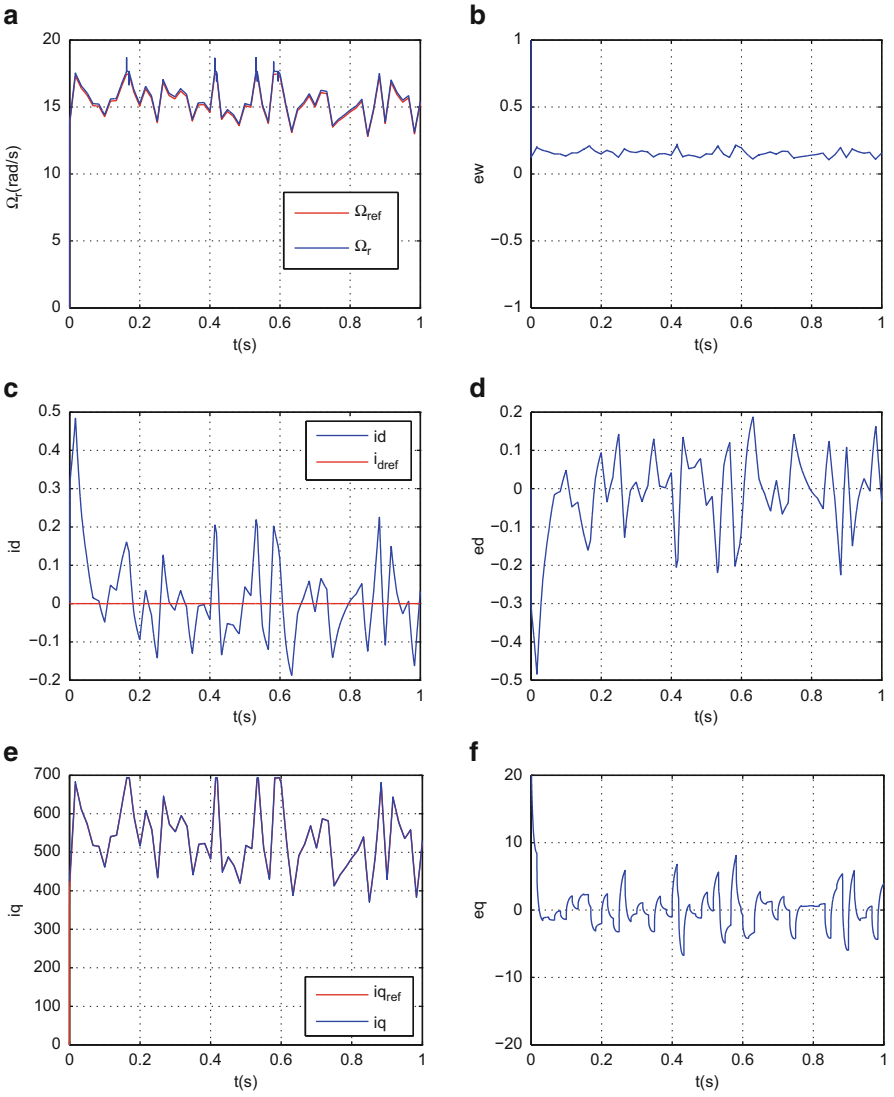

Fig. 8.6 Simulation results of the FOC based PI controller. (**a**): rotational speed, (**b**): Speed error, (**c**):direct current, (**d**): direct current error, (**e**):quadrature current, (**f**):quadrature current error

Its derivative is:

$$\dot{V_{\Omega}} = e_{\Omega}\dot{e}_{\Omega} = e_{\Omega}\left(\dot{\bar{\Omega}}_r - \frac{T_m}{J} + \frac{3p}{2J}\Phi_m iq + \frac{B}{J}\Omega_r\right) \tag{8.20}$$

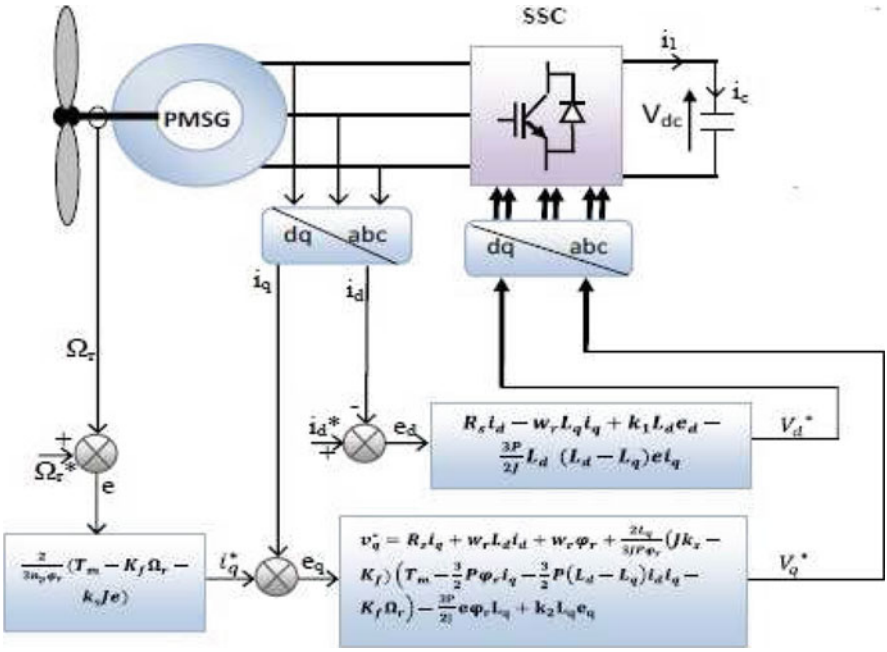

Fig. 8.7 Internal structure of the backstepping controller block

The direct and quadrature current i_d and i_q are chosen as virtual control elements:

$$\begin{cases} \bar{i}_d = 0 \\ \bar{i}_q = \dfrac{2J}{3p\Phi_m}\left(-\dot{\bar{\Omega}}_r + \frac{T_m}{J} - \frac{B}{J}\Omega_r - K_\Omega e_\Omega\right) \end{cases} \tag{8.21}$$

where $K_\Omega > 0$

Thus:

$$\dot{V_\Omega} = -K_\Omega e_\Omega^2 \tag{8.22}$$

- *Step 2:Current components control design*

The current error can be determined as:

$$\begin{aligned} e_d &= \bar{i}_d - i_d \\ e_q &= \bar{i}_q - i_q \end{aligned} \tag{8.23}$$

The error dynamics derived from Eqs. (8.18), (8.21) and (8.23) are:

$$\dot{e}_d = \frac{R_s}{L_s} i_d - p i_q \Omega_r - \frac{1}{L_s} U_d$$
$$\dot{e}_q = \frac{2J}{3p\Phi_m}\left(-\ddot{\Omega}_r - \frac{B}{J}\dot{\Omega}_r - K_\Omega e_\Omega\right) + \frac{R_s}{L_s} i_q + p\left(i_d + \frac{\Phi_m}{L_s}\right)\Omega_r - \frac{1}{L_s} U_q$$
$$\dot{e}_\Omega = -\frac{3p\Phi_m}{2J} e_q - K_\Omega e_\Omega$$

- *Step 3: Control laws design*

The Lyapunov function is determined as:

$$V_2 = \frac{1}{2}(e_\Omega^2 + e_d^2 + e_q^2) \tag{8.24}$$

Its time derivative is:

$$\dot{V}_2 = (e_\Omega \dot{e}_\Omega + e_d \dot{e}_d + e_q \dot{e}_q) - K_{\Omega_r} e_{\Omega_r}^2 - K_d e_d^2 - K_q^2 e_q - e_\Omega \frac{3p\Phi_m}{2J} e_q$$
$$+ e_q \left[\frac{2J}{3p\Phi_m}\left(-\ddot{\Omega}_r - \frac{B}{J}\dot{\Omega}_r - K_\Omega e_\Omega\right) + \frac{R_s}{L_s} i_q + p(i_d + \frac{\Phi_m}{L_s})\Omega_r\right.$$
$$\left. - \frac{1}{L_s} U_q + K_q e_q\right] + e_d \left[\frac{R_s}{L_s} i_d - p i_q \Omega_r - \frac{1}{L_s} U_d + K_d e_d\right] \tag{8.25}$$

The control inputs which stabilize The current tracking errors dynamics are:

$$\bar{v}_d = R_s i_d - L_s p i_q \Omega_r + L_s K_d e_d \tag{8.26}$$
$$\bar{v}_q = \frac{2J L_s}{3p\Phi_m}\left(-\ddot{\Omega}_r - \frac{B}{J}\dot{\Omega}_r - K_\Omega e_\Omega\right) + R_s i_q + p(i_d L_s + \Phi_m)\Omega_r + K_d L_s e_d$$

This choice yields:

$$\dot{V}_2 = -K_\Omega e_{\Omega_r}^2 - K_d e_d^2 - K_q e_q^2 \leq 0 \tag{8.27}$$

where K_d and K_q are positive gains.

8.4.2.2 Simulation Results

The same wind speed profile is applied in this part with varying degrees of wind speed between (8 m/s) and (11.5 m/s).

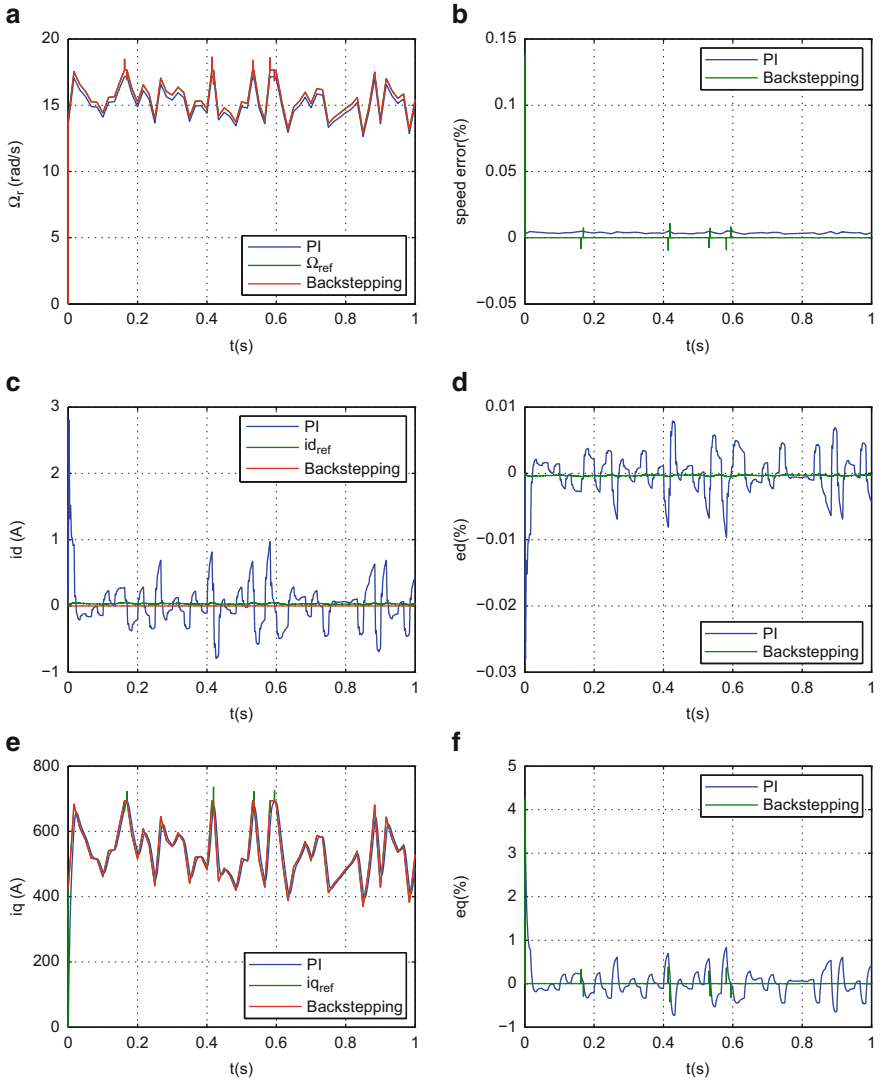

Fig. 8.8 Simulation results

- The system response under PI controller and nonlinear backstepping control has been presented in Fig. 8.8.

  Figure 8.8a presents the rotational speed response which converges perfectly to its reference track. Figure 8.8b shows the speed error. Its is neglected for the backstepping control compared to PI controller. Figures 8.8c, e illustrate the direct and the quadrature currents, respectively. The evolution of the currents errors (Fig. 8.8d, f) shows that the backstepping control has a good dynamic response.

8.4.3 Sliding Mode Control

8.4.3.1 Controller Design

The sliding mode control has proved to be an efficient technique able to cope with aforementioned complex characteristics. In this context, this technique is applied in this section to design a robust controller for nonlinear multi-input multi-output permanent magnet synchronous generator based WECS. The controller design is ensured by the following steps.

1. ***Sliding surfaces:***
   Based on the system model, the sliding surfaces are to be defined as:

$$S_d(t) = e_d(t) + \lambda_1 \int e_d(t)dt \tag{8.28}$$

$$S_q(t) = e_q(t) + \lambda_2 \int e_q(t)dt \tag{8.29}$$

$$S_{\Omega_r}(t) = e_{\Omega_r}(t) + \lambda_3 \int e_{\Omega_r}(t)dt \tag{8.30}$$

   where $e_d(t) = i_d(t) - i_{dref}(t)$, $e_q(t) = i_q(t) - i_{qref}(t)$ and $e_{\Omega_r}(t) = \Omega_r(t) - \Omega_{rref}(t)$.
   The integral action has been included to overcome the state error and to improve the sliding surface where λ_1, λ_2, λ_3 are the integral gains.
2. ***Reachability:***
   The reachability condition for Eqs. (8.28), (8.29) and (8.30) are defined respectively as:

$$S_d(t)\dot{S}_d(t) < 0 \tag{8.31}$$

$$S_q(t)\dot{S}_q(t) < 0 \tag{8.32}$$

$$S_{\Omega_r}(t)\dot{S}_{\Omega_r}(t) < 0 \tag{8.33}$$

3. ***d-axis current control design***
   The control of i_d component current aims to keep the stator flux constant. Its reference value is set to zero.
   From Eq. (8.21), the inequality Eq. (8.31) can be rewritten as:

$$S_d(t)\left[\left(\lambda_1 - \frac{R_s}{L_s}\right) i_d + p i_q \Omega_r + \frac{1}{L_s} U_d\right] < 0 \tag{8.34}$$

   The d-axis control law is given by:

$$U_d(t) = U_{deq}(t) + \Delta U_d \tag{8.35}$$

with the equivalent controlU_{deq} is:

$$U_{deq}(t) = (R_s - \lambda_1 L_s) i_d - p i_q \Omega_r L_s \tag{8.36}$$

The switching control ΔU_d is defined as:

$$\Delta U_d = K_d \text{sign}[S_d(t)] \tag{8.37}$$

where K_d is a positive constant

4. ***q-axis current control design***

Based on the system model and following the similar method, Eq. (8.32) becomes:

$$S_q(t) \left[\left(\lambda_2 + \frac{R_s}{L_s} \right) i_q - p \left(i_d + \frac{\Phi_m}{L_s} \right) \Omega_r + \frac{1}{L_s} U_q + \lambda_2 i q_{ref} \right] < 0$$

Denoting the control law as:

$$U_q(t) = U_{qeq}(t) + \Delta U_q \tag{8.38}$$

The equivalent control can be given as:

$$U_{qeq} = (R_s + L_s \lambda_2) i_q + p(L_s i_d + \phi_m) \Omega_r - \lambda_2 L_s i q_{ref} - L_s \frac{d i q_{ref}}{dt} \tag{8.39}$$

where i_{qref} is a dynamic value that will be determined as a resulting output of the rotational speed control.

The switching portion of the $U_q(t)$ can be expressed by:

$$\Delta U q = K_q \text{sign}[S_q(t)] \tag{8.40}$$

where K_q is a positive constant

5. ***Rotational speed dynamics control***

This controller should ensure that the rotational speed. It is driven to its reference determined by the MPPT algorithm. Considering the rotational speed motion equation, the inequality Eq. (8.33) becomes:

$$S_{\Omega_r}(t) \left[\frac{T_m}{J} - \frac{3}{2J} p \Phi_m i_q + \left(\lambda_3 - \frac{B}{J} \right) \Omega_r - \lambda_3 \Omega_{ref} \right] < 0 \tag{8.41}$$

The control variable for the rotational speed controller is the quadrature axis reference current which is designed as:

$$i_{qref}(t) = i_{qeq,ref}(t) + \Delta i_{qref} \tag{8.42}$$

The equivalent control law is given as:

$$i_{qref} = \frac{2}{3p\phi_m}\left[T_m + (\lambda_3 J - B)\Omega_r - \lambda_3 \Omega_{ref}\right] \tag{8.43}$$

It then follows that:

$$\Delta i_{qref} = K_{iq}\text{sign}[S_{\Omega_r}(t)] \tag{8.44}$$

where K_{iq} is a positive constant

In order to reduce the chattering effect, a smooth control discontinuity is introduced around the switching surface. The sign $[S(t)]$ is replaced by sat$[S(t),\Delta]$ which can be expressed as:

$$\text{sat}[S(t)] = \begin{cases} \frac{S(t)}{\Delta} & \text{if } |S(t)| \leq \Delta \\ \text{sign}(S(t)) & \text{otherwise} \end{cases} \tag{8.45}$$

where Δ is the boundary layer thickness.

8.4.3.2 Simulation Results

The system response under the Sliding Mode concept has been presented in Fig. 8.9.

The rotational speed $\Omega_r(t)$ is shown in Fig. 8.9a. The second result shown is that of $i_d(t)$. As it can be seen by Fig. 8.9c, the d-axis current accurately tracks the reference value $i_{dref} = 0$. Figure 8.9e. shows the actual value of $i_q(t)$, accurately tracking the defined reference.

8.5 Control Above Rated Wind Speed: Pitch Control

8.5.1 Introduction

The key part of a variable-speed wind turbine is the pitch system. Its main purpose is to keep the generated power constant above the rated wind speed.

In fact, when the wind speed becomes larger than the rated value and the MPPT algorithm is still applied, the power generated by the system will exceed the optimal power if the blade angle β stays fixed at zero degrees.

This will make the power devices and the generator work in a higher zone than optimum output, which is harmful to the mechanical system if sustained for a period of time.

Based on this concern, a control system for the regulation of the pitch angle according to different wind conditions is required for the wind turbine.

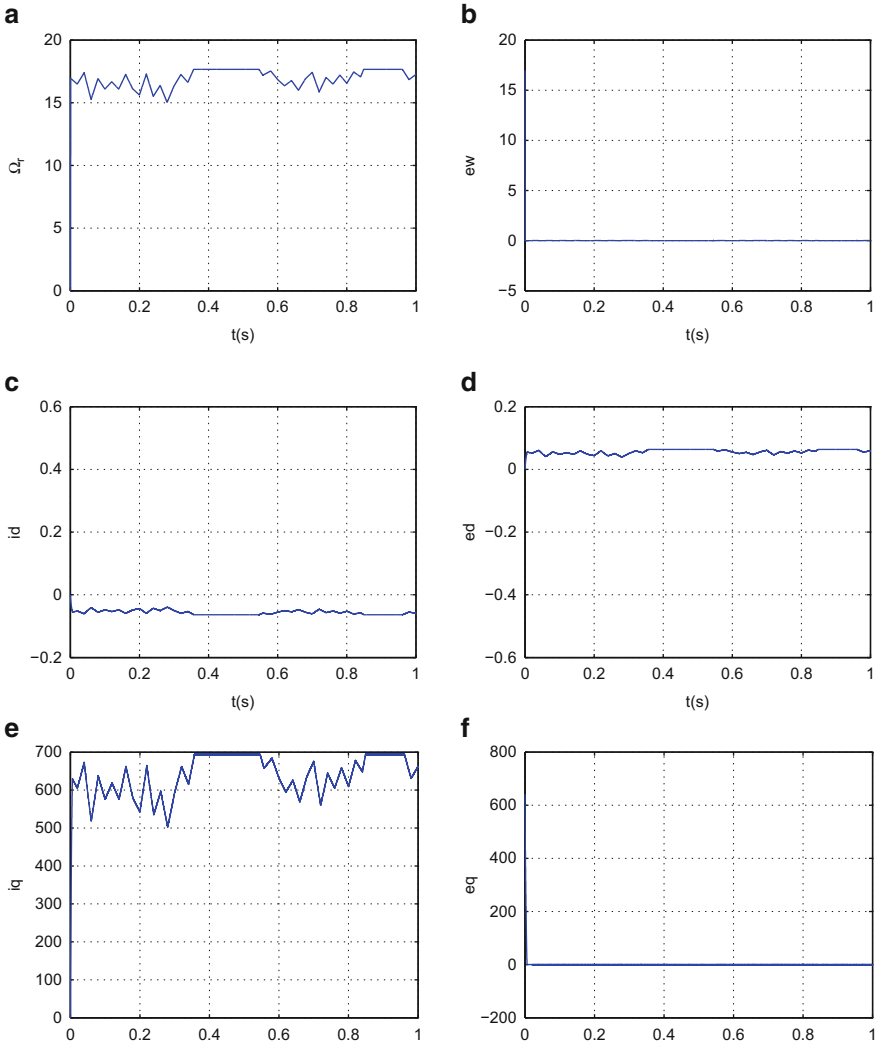

Fig. 8.9 Simulation results of the Sliding mode strategy

Small changes in the blade angle can have dramatic effects on the output power. The advantages of the pitch control system might be summarized as follows:

1. Optimize the output power of the wind turbine. Indeed, to give the maximum power in partial load region, the pitch setting should be at its optimum value
2. Prevent input mechanical power to exceed the design limits. This controller provides a good regulation of the aerodynamic power and the loads produced by the rotor.

3. Minimize the fatigue loads of the turbine mechanical components. The design of the controller must take into account the load.

Thus, the blade pitch angle control should have a good dynamic quality and a strong robustness.

Several works on pitch control have been done to improve the quality of the generated power. For example, a gain scheduling controller, proposed in Lescher et al. (2005), changes the controller gain with the variation of the wind speed. However, the practical implementation of the gain scheduling is very difficult because the wind speed is usually measured on the tower and does not represent the wind speed at the turbine plant. Disturbance accommodating control (DAC) has been developed in Stol et al. (2000, 2003), but it presents a large estimation error when the system operates far away from the rated wind speed. H_∞ controllers for blade pitch control and electromagnetic torque control have been used in Rocha et al. (2003). However, this controller has not been experienced on a nonlinear turbine model.

Based on the analysis of the above studies, we propose two types of controllers to solve the variable pitch control problem of a direct-drive PMSG wind turbine (Ayadi et al. 2017):

- Pitch Control based on a Proportional Integrator controller
- Pitch Control based on a Sliding Mode controller

8.5.2 System Description

The blade pitch control system is the key part of a variable speed wind turbine. It acts directly on the system responses for different wind speed zones (Fig. 8.10).

To regulate the blade angle, the power deviation from its reference value is used.

An electromechanical system called actuator is then used to put the blade angle into the desired position. It can be modeled as a first-order system as Hwas and Katebi (2012):

Fig. 8.10 Schematic illustration of the Kinematics of the WT

$$G(s) = \frac{k_0}{1 + \tau s} \tag{8.46}$$

k_0 is the proportional gain and τ is the time constant.

According to industrial recommendations, it is necessary to include a pitch rate adjusted to $10°/s$

8.6 Transition Between the Two Control Regions

8.6.1 Switched Wind Turbine System

Variable speed wind turbines operate within a large range of wind speeds. During the power generation and depending on the prevailing wind speed, the wind turbine switches between two operation modes as shown in Fig. 8.4: the low wind speed region (also called Region II) where the control objective is to capture the maximum power from the wind and the high wind speed region (also called Region III) where the control aim is to limit the output power to the required power.

The control of a variable speed wind turbine is usually achieved based on two distinct control laws for Regions (II) and (III), respectively. The switching or called also transition between these two regions cause undesirable effects such as vibrations in drive train, tower and blades (Pao and Johnson 2009) which cause system fatigue and premature failure.

Therefore, it is necessary to develop a control algorithm to smooth out the undesirable effects of the switching actions and also to stabilize the switching operation.

The synthesis of the blade angle controller is divided typically into two zones according to the wind speed value:

- Partial load zone: $v < v_{ref} \longrightarrow \beta = \beta_{ref} = 0$
- Full load zone: $v \geq v_{ref} \longrightarrow \beta$ changes with the wind variation to keep $P = P_{opt}$

There are usually two controllers for the variable-speed wind turbines which are cross-coupled each other, shown as in Fig. 8.11.

In order to smooth the wind power fluctuations in the intermediate zone, a fuzzy logic controller has been investigated.

8.6.2 Simulation Results

To validate the stability of the system when it switches between Region (II) and Region (III) modes, simulations have been performed on a system with the following conditions:

1. Maximum Power Coefficient $(C_{pmax}) = 0.4109$

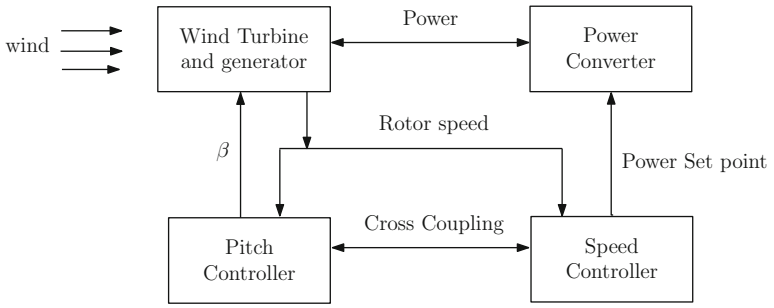

Fig. 8.11 Structure of a model of variable-speed wind turbine

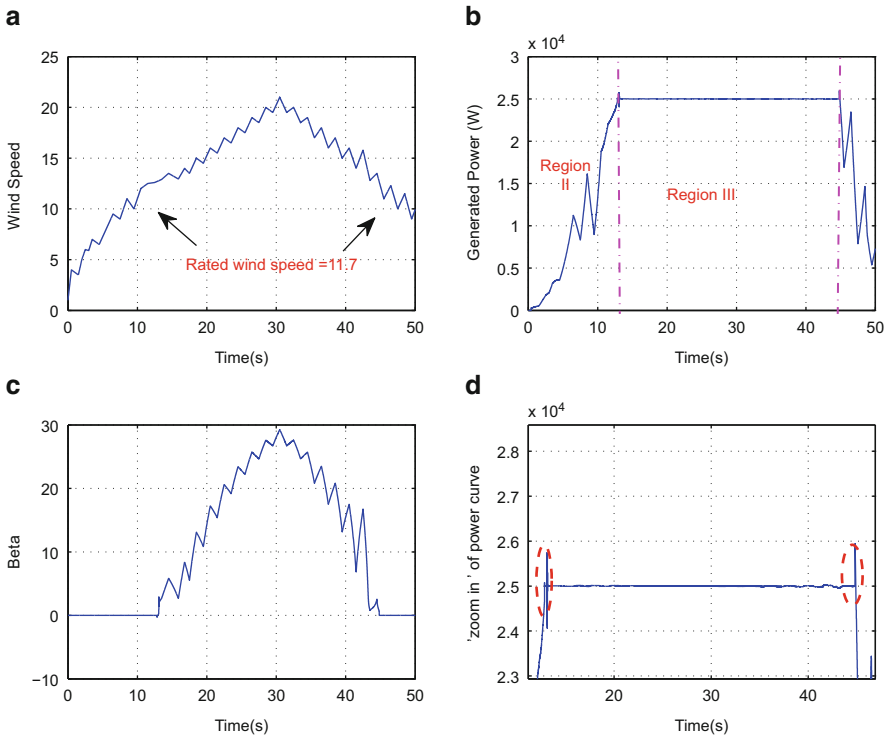

Fig. 8.12 Simulation results in full range of operation

2. Rated wind speed $V_m = 11.7$
3. Nominal Demand Power $(P_{max}) = 2.5\,\text{kW}$

Figure 8.12a presents the wind speed profile which involves the two operational areas, i.e., the low wind speed area ($V < 11.7$ m/s) and the high wind speed area ($V \geq 11.7$ m/s).

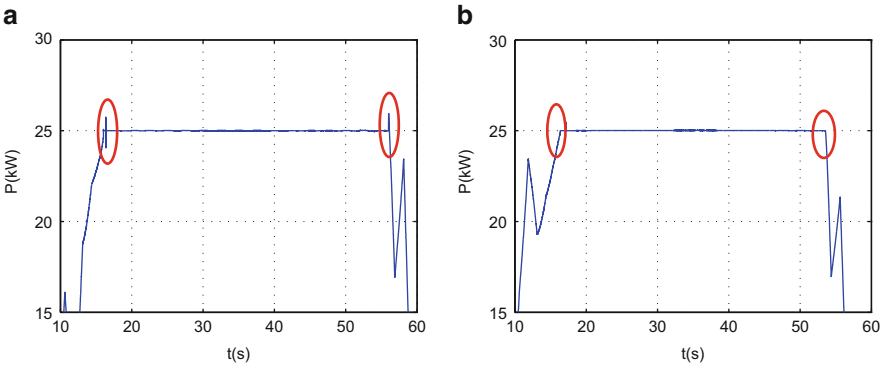

Fig. 8.13 Simulation in the transition region

The power characteristic is shown in Fig. 8.13b. The turbine starts operating when the wind speed exceeds cut-in wind speed 3 m/s. In this region (II), The MPPT algorithm and the torque control come into action with a constant pitch angle.

When the wind speed exceeds its nominal value (region III), the control objective shifts from maximizing the power capture to regulate the power to the turbine rated output.

Figure 8.12c shows the pitch angle variation. Below the rated wind speed the blade pitch angle is set at 0. It is the optimal value that allows the turbine to extract the maximum energy from the incident wind. Otherwise, the pitch control is active: the angle changes with the variations of the wind to avoid over rated power.

Figure 8.12d presents a zoomed in section of Fig. 8.13b. It is obvious that Between the high and the low wind speed region, the curve of the output power presents a noticeable fluctuation caused by the transition between the two regions which causes system fatigue and premature failure.

As a solution, a fuzzy logic controller has been applied with the aim of smoothing the wind power fluctuations in the intermediate zone. Figure 8.13a presents the wind speed profile with varying degrees. Figure 8.13b presents the power coefficient C_p. It can be observed that the C_p curve is maintained close to its maximum value $C_{pmax} = 0.41$ which proves that the MPPT has been achieved. In region (III) as the power coefficient depends on the blade pitch angle, it varies with the blade variations.

Figure 8.13c presents the generated power for the 2 control zones: It is remarkable that the fluctuation between the intermediate zone has been eliminated. The wind speed moves from zone to another fluently. The variation of the pitch angle is illustrated in Fig. 8.13d. The pitch angle controller shows a perfect capability of giving to the actuator the right angle demand in different wind speed zones. The rotational speed is presented in Fig. 8.13e, (in region II) the speed is varying to optimal power extraction, overrated wind speed, the speed control input is considered as its maximum value.

8.7 Conclusion

This chapter discusses the control systems used for a variable speed wind turbine equipped with PMSG. In the first part, a control algorithm has been synthesized to extract the maximum of the power based on two nonlinear control techniques namely the backstepping controller and the sliding mode controller. Comparative studies between these algorithms have been presented. Then, above rated wind speed, a pitch angle regulation has been investigated to keep the generated power at the designed limit.

Finally, the transition between the two control regions has been discussed to avoid the power fluctuation.

References

Abulanwar, S., Hu, W., Chen, Z., & Iov, F. (2016). Adaptive voltage control strategy for variable-speed wind turbine connected to a weak network. *IET Renewable Power Generation, 10*(2), 238–249.

Ayadi, M., & Derbel, N. (2017). Nonlinear adaptive backstepping control for variable-speed wind energy conversion system-based permanent magnet synchronous generator. *The International Journal of Advanced Manufacturing Technology, 92*(1–4), 39–46.

Ayadi, M., Ben Salem, F., & Derbel, N. (2017). Power control of a variable speed wind turbine based on direct torque control of a permanent magnet synchronous generator. *International Journal of Digital Signals and Smart Systems, 1*(3), 204–223.

Bahraminejad, B., Iranpour, M. R., & Esfandiari, E. (2014). Pitch control of wind turbines using IT2FL controller versus T1FL controller. *International Journal of Renewable Energy Research (IJRER), 4*(4), 1065–1077.

Bull, S. R. (2001). Renewable energy today and tomorrow. *Proceedings of the IEEE, 89*(8), 1216–1226.

Burton, T., Jenkins, N., Sharpe, D., & Bossanyi, E. (2011). *Wind energy handbook* (2nd ed.). John Wiley & Sons.

Cai, W., Fulton, D., & Reichert, K. (2000). Design of permanent magnet motors with low torque ripples: A review. *International Conference on Electrical Machines* (pp. 1384–1388).

Evangelista, C., Puleston, P., Valenciaga, F., & Fridman, L. M. (2013). Lyapunov-designed super-twisting sliding mode control for wind energy conversion optimization. *IEEE Transactions on Industrial Electronics, 60*(2), 538–545.

Feng, Y., Chen, B., Yu, X., & Yang, Y. (2012). Terminal sliding mode control of induction generator for wind energy conversion systems. In *IECON 2012: 38th Annual Conference on IEEE Industrial Electronics Society* (pp. 4741–4746). IEEE.

Hwas, A., & Katebi, R. (2012). Wind turbine control using PI pitch angle controller. *IFAC Proceedings Volumes, 45*(3), 241–246.

Jerbi, L., Krichen, L., & Ouali, A. (2009). A fuzzy logic supervisor for active and reactive power control of a variable speed wind energy conversion system associated to a flywheel storage system. *Electric Power Systems Research, 79*(6), 919–925.

Kachroo, P., & Tomizuka, M. (1996). Chattering reduction and error convergence in the sliding-mode control of a class of nonlinear systems. *IEEE Transactions on Automatic Control, 41*(7), 1063–1068.

Karabacak, M., & Eskikurt, H. I. (2012). Design, modelling and simulation of a new nonlinear and full adaptive backstepping speed tracking controller for uncertain PMSM. *Applied Mathematical Modelling, 36*(11), 5199–5213.

Kesraoui, M., Korichi, N., & Belkadi, A. (2011). Maximum power point tracker of wind energy conversion system. *Renewable Energy, 36*(10), 2655–2662.

Kim, H.-W., Kim, S.-S., & Ko, H.-S. (2010). Modeling and control of PMSG-based variable-speed wind turbine. *Electric Power Systems Research, 80*(1), 46–52.

Lee, S.-H., Joo, Y.-J., Back, J., & Seo, J. H. (2010). Sliding mode controller for torque and pitch control of wind power system based on pmsg. In *IEEE International Conference on Control Automation and Systems* (ICCAS) (pp. 1079–1084).

Lescher, F., Zhao, J. Y., & Borne, P. (2005). Robust gain scheduling controller for pitch regulated variable speed wind turbine. *Studies in Informatics and Control, 14*(4), 299.

Mansour, M., Mansouri, M., & Mmimouni, M. (2011). Study and control of a variable-speed wind-energy system connected to the grid. *International Journal of Renewable Energy Research, 1*(2), 96–104.

Michalke, G., Hansen, A. D., & Hartkopf, T. (2007). Control strategy of a variable speed wind turbine with multipole permanent magnet synchronous generator. In *European Wind Energy Conference and Exhibition*.

Pao, L. Y. & Johnson, K. E. (2009). A tutorial on the dynamics and control of wind turbines and wind farms. In *IEEE American Control Conference, ACC'09* (pp. 2076–2089).

Ribrant, J., & Bertling, L. (2007). Survey of failures in wind power systems with focus on swedish wind power plants during 1997–2005. In *Power Engineering Society General Meeting. IEEE*, (pp. 1–8). IEEE.

Rocha, R., Filho, L. S. M. (2003). A multivariable H_∞ control for wind energy conversion system. In *IEEE Conference on Control Applications, CCA* (pp. 206–211).

Simoes, M. G., Bose, B. K., Spiegel, R. J. (1997). Fuzzy logic based intelligent control of a variable speed cage machine wind generation system. *IEEE Transactions on Power Electronics, 12*(1), 87–95.

Stol, K., Rigney, B., & Balas, M. (2000). Disturbance accommodating control of a variable-speed turbine using a symbolic dynamics structural model. In *2000 ASME Wind Energy Symposium* (p. 29).

Stol, K. A., Balas, M. J., et al. (2003). Periodic disturbance accommodating control for blade load mitigation in wind turbines. *Transactions-American Society of Mechanical Engineers Journal of Solar Energy Engineering, 125*(4), 379–385.

Valenciaga, F., & Puleston, P. (2008). High-order sliding control for a wind energy conversion system based on a permanent magnet synchronous generator. *IEEE Transactions on Energy Conversion, 23*(3), 860–867.

Vu, N. T.-T., Yu, D.-Y., Choi, H. H., & Jung, J.-W. (2013). T–S fuzzy-model-based sliding-mode control for surface-mounted permanent-magnet synchronous motors considering uncertainties. *IEEE Transactions on Industrial Electronics, 60*(10), 4281–4291.

Wang, G.-D., Wai, R.-J., & Liao, Y. (2013). Design of backstepping power control for grid-side converter of voltage source converter-based high-voltage DC wind power generation system. *IET Renewable Power Generation, 7*(2), 118–133.

Yang, F., Li, S.-S., Wang, L., Zuo, S., & Song, Q.-W. (2014a). Adaptive backstepping control based on floating offshore high temperature superconductor generator for wind turbines. In *Abstract and applied analysis*. Hindawi Publishing Corporation.

Yang, W., Tavner, P. J., Crabtree, C. J., Feng, Y., & Qiu, Y. (2014b). Wind turbine condition monitoring: Technical and commercial challenges. *Wind Energy, 17*(5), 673–693.

Zhang, X., Sun, L., Zhao, K., & Sun, L. (2013). Nonlinear speed control for PMSM system using sliding-mode control and disturbance compensation techniques. *IEEE Transactions on Power Electronics, 28*(3), 1358–1365.

Chapter 9
Direct Power Control of DFIG Using Sliding Mode Control Approach

Aicha Daoud and Nabil Derbel

Abstract This paper investigates direct active and reactive power control for a variable-speed wind energy conversion system with doubly fed induction generator (DFIG). The stator windings of DFIG are directly connected to the grid whereas rotor windings are connected to an inverter. A nonlinear sliding mode control (SMC) strategy is employed to control the instantaneous active and reactive powers of DFIG. Simulation results show the effectiveness of the proposed control law.

Keywords Wind energy conversion system · Doubly fed induction generator · Direct power control(DPC) · Sliding mode control (SMC)

9.1 Introduction

Over the last decade, wind energy conversion systems have rapidly evolved, wherefore, efficient and reliable exploitation tools are necessary to make these installations more profitable (Cheng 2014). Several types of wind energy conversion system subsist. The most popular is based on the control of the doubly fed induction generator (DFIG). The benefits of DFIG consist in low converter cost, reduced power losses, limited operating speed range (−30 to +20%).

The development of power electronics related to the onset of rapid switches and the progress of digital technologies have permitted the control of powerful of high efficient controllers. New control strategies have been suggested such as direct power control (DPC) (Giglia et al. 2007).

Several DPC strategies with a constant switching frequency have also been proposed for the DFIG (Hu et al. 2010). The switching states were initially selected based on conventional LUT in Zhang et al. (2012), despite the fact that their

A. Daoud (✉) · N. Derbel
Control and Energy Management Laboratory (CEMLab), Sfax Engineering School, University of Sfax, Sfax, Tunisia
e-mail: aicha.daoud@hotmail.fr; n.Derbel@enis.rnu.tn

N. Derbel, Q. Zhu (eds.), *Modeling, Identification and Control Methods in Renewable Energy Systems*, Green Energy and Technology,
https://doi.org/10.1007/978-981-13-1945-7_9

durations were calculated based on the objectives of reduced active and reactive power oscillations (Zhang et al. 2011).

In this work a new strategy is proposed to control the power of doubly fed induction generator connected to grid, using sliding mode control (SMC) (Bouaziz and Bacha 2013). This method is a nonlinear robust control that alters the dynamics of a nonlinear system by designing the discontinuous control signal, which slides the system states towards the normal behavior (Lajimi and Shahabi 2011).

Moreover, the paper is organized as follows. Section 9.2 presents the mathematical model of a wind turbine conversion system. A nonlinear Sliding Mode Control (SMC) strategy is designed in Sect. 9.3. Section 9.4 presents simulation results to demonstrate performances of the proposed DPC strategy. Finally, some conclusion remarks are made in the last section.

9.2 Wind Turbine Conversion System

9.2.1 Wind Turbine Model

The mechanical power available on the rotor is given by:

$$P_m = \frac{1}{2}\,\pi\,\rho\,R^2\,V^3\,C_p\,(\lambda,\beta) \tag{9.1}$$

where ρ designates the air density, R is the blade radius, V is the wind speed and C_p represents the power coefficient. It depends on the tip speed ratio λ and the blade pitch angle β:

$$C_p\,(\lambda,\beta) = 0.22\left(\frac{116}{\lambda_i} - 0.4\,\beta - 5\right) e^{\left(-\frac{12.5}{\lambda_i}\right)} \tag{9.2}$$

where λ_i is given by:

$$\frac{1}{\lambda_i} = \frac{1}{\lambda + 0.08\,\beta} - \frac{0.035}{\beta^3 + 1} \tag{9.3}$$

with

$$\lambda = \frac{\Omega_t\,R}{V} \tag{9.4}$$

Referring to Equation (9.1), there is a unique optimal power which shows a cubic function of the generator speed for each wind speed (Cardenas et al. 2005) (Fig. 9.1). Their relationship can be given by:

$$P_{m-opt} = \frac{1}{2}\,C_{pmax}\left(\lambda_{opt}\right)\,\rho\,S\,V^3 \tag{9.5}$$

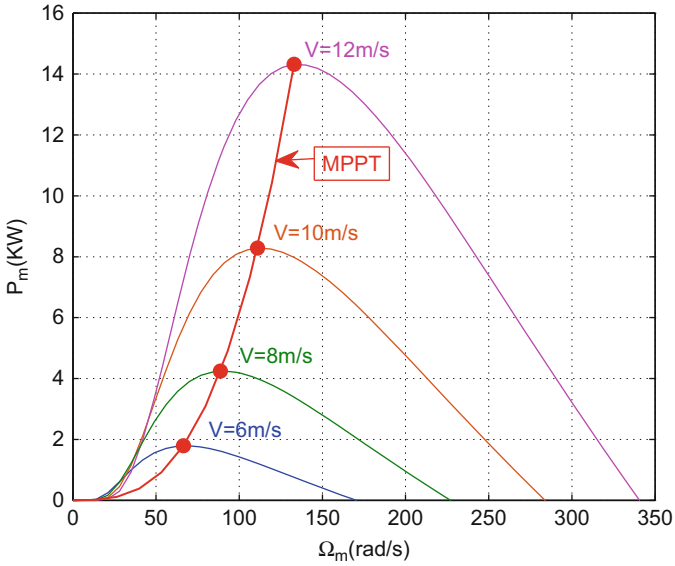

Fig. 9.1 Characteristic of the generated power based on the mechanical speed and wind speed

Then, the value of the reference power can be expressed by:

$$P_{sref} = K_{opt}\ \Omega_m^3 \tag{9.6}$$

where $K_{opt} = \frac{1}{2}\pi R^2\ C_{pmax}\rho \left(\frac{R}{\lambda_{opt}}\right)^3$

9.2.2 *Doubly Fed Induction Generator Model*

A DFIG can be modelled in the (d-q) reference frame adopting active sign convention for stator and passive sign convention by the following equations (Belmokhtar et al. 2014; Shukla and Tripathi 2014).

The stator and rotor voltages can be written as:

$$\begin{cases} v_{sd} = -R_s i_{sd} - \dfrac{d}{dt}\phi_{sd} - \omega_s \phi_{sq} \\ v_{sq} = -R_s i_{sq} - \dfrac{d}{dt}\phi_{sq} + \omega_s \phi_{sd} \end{cases} \tag{9.7}$$

$$\begin{cases} v_{rd} = R_r i_{rd} + \dfrac{d}{dt}\phi_{rd} - \omega_r \phi_{rq} \\ v_{rq} = R_r i_{rq} + \dfrac{d}{dt}\phi_{rq} + \omega_r \phi_{rd} \end{cases} \tag{9.8}$$

and the stator and rotor fluxes are expressed as:

$$\begin{cases} \phi_{sd} = L_s i_{sd} + M i_{rd} \\ \phi_{sq} = L_s i_{sq} + M i_{qr} \end{cases} \tag{9.9}$$

$$\begin{cases} \phi_{rd} = L_r i_{rd} + M i_{sd} \\ \phi_{rq} = L_r i_{rq} + M i_{sq} \end{cases} \tag{9.10}$$

The electromagnetic torque is given as:

$$T_{em} = -\frac{3}{2} N_p (\phi_{sd}\, i_{sq} - \phi_{sq}\, i_{sd}) \tag{9.11}$$

The mechanical equation of the doubly fed generator is:

$$T_m - T_{em} = J \frac{d\Omega_m}{dt} \tag{9.12}$$

The instantaneous stator active and reactive power can be expressed in terms of the stator voltages and currents as follows:

$$\begin{cases} P_s = \frac{3}{2}(V_{sd} i_{sd} + V_{sq} i_{sq}) \\ Q_s = \frac{3}{2}(V_{sq} i_{sd} - V_{sd} i_{sq}) \end{cases} \tag{9.13}$$

According to (9.9) and (9.10), the rotor flux vector can be expressed as:

$$\phi_{rdq} = \frac{L_r}{M}\, \phi_{sdq} + M\, \sigma\, i_{sdq} \tag{9.14}$$

where ω_s is the electric angular speed for stator windings, ω_r is the electric angular speed for rotor windings and ω_m the electric angular speed for rotor windings. Let's the following notations: $\sigma = 1 - \dfrac{Lr\ Ls}{M^2}$ and $\alpha = L_r R_s + L_s R_r$.

The time differentiation of the stator current can be expressed as follows:

$$\frac{di_{sd}}{dt} = \frac{1}{\sigma M^2}[\alpha i_{sd} - (\omega_s - \omega_r) L_r \phi_{sq} - R_r \phi_{sd} + L_r V_{sd}] + \frac{\alpha}{\sigma M} V_{rd} + \omega_r i_{sq} \tag{9.15}$$

$$\frac{di_{sq}}{dt} = \frac{1}{\sigma M^2}[\alpha i_{sq} + (\omega_s - \omega_r) L_r \phi_{sd} - R_r \phi_{sq} + L_r V_{sq}] + \frac{\alpha}{\sigma M} V_{rq} - \omega_r i_{sd} \tag{9.16}$$

By (9.13), time derivative of the stator active and reactive power can be determined as:

$$\begin{bmatrix} \frac{dP_s}{dt} \\ \frac{dQ_s}{dt} \end{bmatrix} = \begin{bmatrix} \frac{\alpha}{\sigma M^2} & -\omega_r \\ \omega_r & \frac{\alpha}{\sigma M^2} \end{bmatrix} \begin{bmatrix} P_s \\ Q_s \end{bmatrix} + \frac{3(\omega_s - \omega_r)L_r}{2\sigma M^2} \begin{bmatrix} V_{sq} & -V_{sd} \\ -V_{sd} & -V_{sq} \end{bmatrix} \begin{bmatrix} \phi_{sd} \\ \phi_{sq} \end{bmatrix}$$
$$- \frac{3R_r}{2\sigma M^2} \begin{bmatrix} V_{sd} & V_{sq} \\ V_{sq} & -V_{sd} \end{bmatrix} \begin{bmatrix} \phi_{sd} \\ \phi_{sq} \end{bmatrix} + \frac{3}{2\sigma M} \begin{bmatrix} V_{sd} & V_{sq} \\ V_{sq} & -V_{sd} \end{bmatrix} \begin{bmatrix} V_{rd} \\ V_{rq} \end{bmatrix}$$
$$+ \frac{3L_r}{2\sigma M^2} \begin{bmatrix} V_{sd}^2 + V_{sq}^2 \\ 0 \end{bmatrix} \tag{9.17}$$

9.3 Conception of Sliding Mode Controller

A non linear sliding mode strategy is based on the conception of the discontinuous control signal that drives the system states toward special manifolds in the state space (Rajendran and Jena 2014; Utkin 1993). These manifolds are chosen in such a way that the control system will have the desired behavior as the states converge to them (Barambones et al. 2014; Kairous and Belmadani 2015). The strategy of the DPC uses a nonlinear sliding-mode control scheme to directly generate the rotor voltage reference components from the stator active and reactive power errors. The conception of SMC can be defined by the following steps:

1. Sliding Surface:

$$S = \begin{bmatrix} S_P & S_Q \end{bmatrix}^T \tag{9.18}$$

Two integral switching functions has been included to overcome the state errors and to improve the sliding surfaces. The sliding surfaces of the active and reactive powers are chosen as:

$$S_P = e_P + K_P \int_0^t e_P \, dt \tag{9.19}$$

$$S_Q = e_Q + K_Q \int_0^t e_Q \, dt \tag{9.20}$$

where $e_P = P_s - P_s^*$, $e_Q = Q_s - Q_s^*$ are errors between the actual values and the references of instantaneous stator active and reactive powers, respectively. K_P and K_Q are the integral gains.

2. Define the condition of the convergence by the Lyapunov theory as follows:

$$S_{PQ}\dot{S}_{PQ} < 0 \tag{9.21}$$

3. Law of SMC: The control signal V_{rdq} is determined as follows:

$$V_{rdq} = V_{req} + \triangle V_r \tag{9.22}$$

with V_{req} is the equivalent control and $\triangle V_r$ is the switching control. The equivalent command is obtained on the basis of the system behaviour by:

$$\begin{aligned} \dot{S_P} &= \dot{P}_s - \dot{P}_s^* + K_P(P_s - P_s^*) = 0 \\ \dot{S_Q} &= \dot{Q}_s - \dot{Q}_s^* + K_Q(Q_s - Q_s^*) = 0 \end{aligned} \tag{9.23}$$

Substituting (9.25) into (9.23) leads to

$$\dot{S} = F(x) + G(x)V_{rdq} \tag{9.24}$$

with $F = (F_P \quad F_Q)^T$ and $V_{rdq} = (V_{rd} \quad V_{rq})^T$

$$\begin{aligned} \begin{bmatrix} F_P \\ F_Q \end{bmatrix} = &\begin{bmatrix} \dfrac{\alpha}{\sigma M^2} & -\omega_r \\ \omega_r & \dfrac{\alpha}{\sigma M^2} \end{bmatrix} \begin{bmatrix} P_s \\ Q_s \end{bmatrix} + \frac{3(\omega_s - \omega_r)L_r}{2\sigma M^2} \begin{bmatrix} V_{sq} & -V_{sd} \\ -V_{sd} & -V_{sq} \end{bmatrix} \begin{bmatrix} \phi_{sd} \\ \phi_{sq} \end{bmatrix} \\ &- \frac{3R_r}{2\sigma M^2} \begin{bmatrix} V_{sd} & V_{sq} \\ V_{sq} & -V_{sd} \end{bmatrix} \begin{bmatrix} \phi_{sd} \\ \phi_{sq} \end{bmatrix} + \frac{3L_r}{2\sigma M^2} \begin{bmatrix} V_{sd}^2 + V_{sq}^2 \\ 0 \end{bmatrix} \\ &+ \begin{bmatrix} K_P(P_s - P_s^*) \\ K_Q(Q_s - Q_s^*) \end{bmatrix} \end{aligned} \tag{9.25}$$

and:

$$G = \frac{3}{2}\frac{1}{\sigma M}\begin{pmatrix} V_{sd} & V_{sq} \\ V_{sq} & -V_{sd} \end{pmatrix}$$

Let us consider the following Lyapunov function:

$$V = \frac{1}{2}S^T S \tag{9.26}$$

The time derivative of the quadratic Lyapunov function is:

$$\dot{V} = S^T \dot{S} = S^T[-H \text{ sign}(S) - \delta S] \tag{9.27}$$

H and δ are diagonal matrices as described below.

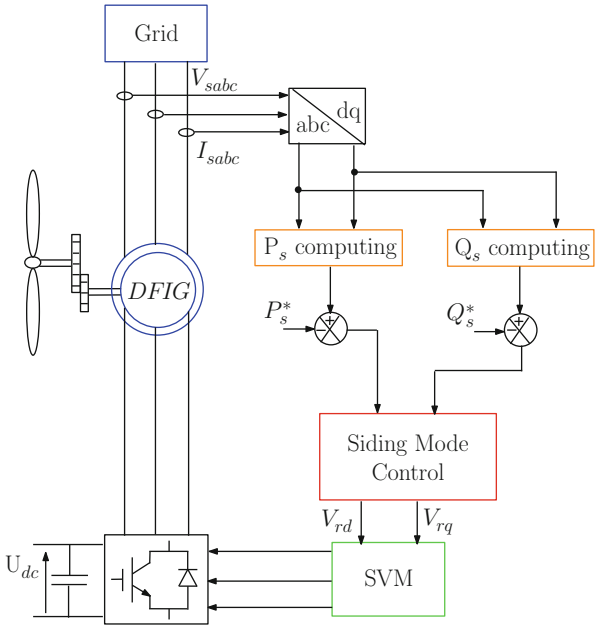

Fig. 9.2 Basic DPC bloc diagram using SMC approach

In view of the following expression of the switching control:

$$\triangle V_r = -(G(x))^{-1} \begin{pmatrix} H_P \text{ sign}(S_P) + \delta_P \, S_P \\ H_Q \text{ sign}(S_Q) + \delta_Q \, S_Q \end{pmatrix} \tag{9.28}$$

where H_P, H_Q, δ_P and δ_Q are positive control gains, sign(S_P) and sign(S_Q) are switch functions for active and reactive powers.

4. Synthesis of SMC:
   Figure 9.2 shows the bloc diagram of the basic DPC strategy, using the SMC approach. Actual values of stator active and reactive powers are compared to their corresponding references. Errors are achieved to stator active and reactive powers SMC controller. Considering SMC approach, rotor voltage reference values are determined.
   Then, the Space Vector Modulation (SVM) technique is used to transform the switching patterns of the RSC with a constant switching frequency.

9.4 Simulation Results

Simulation works have been carried out considering a sampling period $T_0 = 10\,\mu s$ and a bus voltage $V_{dc} = 620\,V$. The control design exposed in Fig. 9.2 is simulated in the MATLAB/Simulink environment with parameters given in Tables. 9.1 and 9.2.

Table 9.1 Parameters of the turbine

Denotation	Numerical value of the parameter
Radius of the wind	3.24 m
G	2.5
Air density (ρ)	1.22 kg/m^3

Table 9.2 DFIG parameters

Denotation	Numerical value of the parameter
Power output	20 kW
Voltage	220 V
Speed (ω_s, f_s)	1500 tr/mn; 50 Hz
Number of pole pairs (N_p)	4
Stator inductance (L_s)	0.05 H
Rotor inductance (L_r)	0.05 H
Mutual inductance (M)	0.0473 H
Stator resistance (R_s)	0.29 Ω
Rotor resistance (R_r)	0.38 Ω
Moment of inertia (J)	1 kg.m^2

The simulation is effected supposing which the chain of wind energy conversion expands, according to the MPPT, the stator active power reference ($P_{s\,ref} = K_{opt}\,\Omega_m^3$), and imposing a stator reactive power $Q_{s\,ref} = 0$.

Figure 9.3 demonstrates that the mechanical speed pursues the wind but with a delay that is due to slow dynamics of the generator against the very rapid variation of the wind. Moreover, stator currents have honest evolutions regarding to their amplitudes and their frequency.

Foremost, investigate the expression of the i_{as} current, around a steady state operating point (Bekakra and Attous 2011), as follows:

$$i_{as}(t) = \sum_{n=1}^{\infty} I_n \cos\left(n\omega_s t + \varphi_n\right) \tag{9.29}$$

$|I_1|$ is the amplitude of the fundamental, and $|I_n|$ is the amplitude of the harmonic n.

The index criterion is the average total harmonic distortion (THD) of the stator current which is determined as follows:

$$\mathrm{THD} = \frac{\sqrt{\sum_{n=2}^{\infty} |I_n|^2}}{|I_1|} \tag{9.30}$$

In Figs. 9.4, 9.5 and 9.6, the frequency spectrum of stator current i_{as} has been visualized by different wind values. They consist to observe amplitudes of all

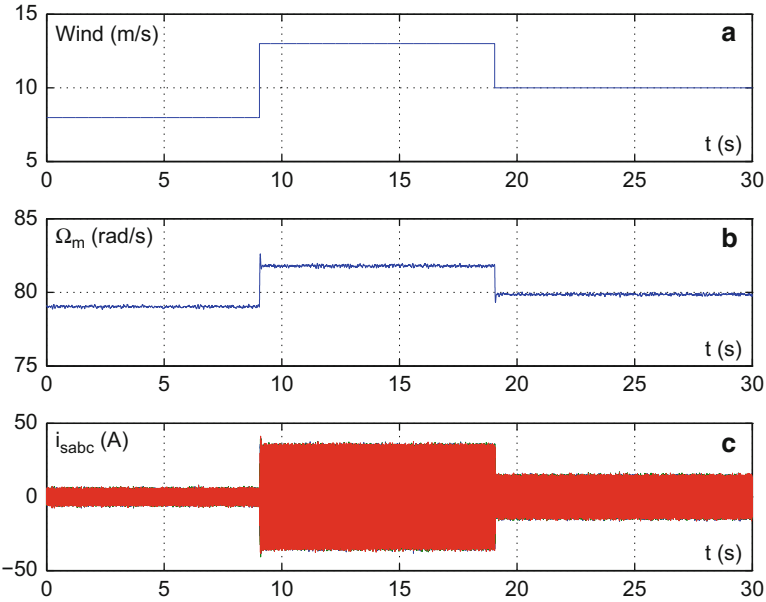

Fig. 9.3 Simulation results. (**a**): The trial wind profile, (**b**): Mechanical speed of DFIG Ω_m, (**c**): currents of stator i_{sabc}

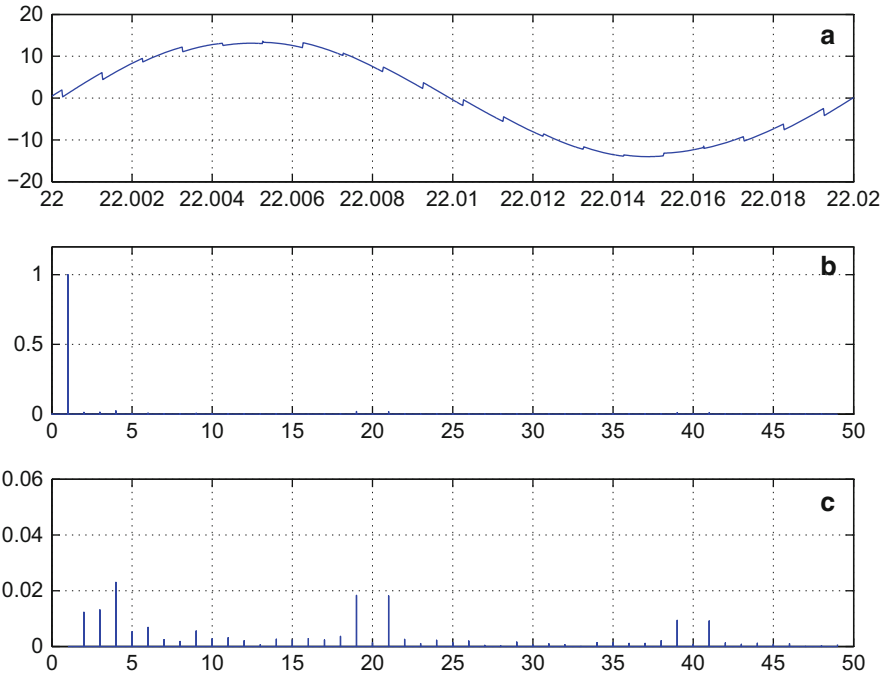

Fig. 9.4 Simulated basic signal waveforms and stator current harmonic spectrum under purely sinusoidal stator voltage for $V = 10$ m/s. (**a**) one period of i_{as} current, (**b**) reduced spectrum of i_{as} with respect to its fundamental, and (**c**) harmonics of i_{as} (fundamental = 1)

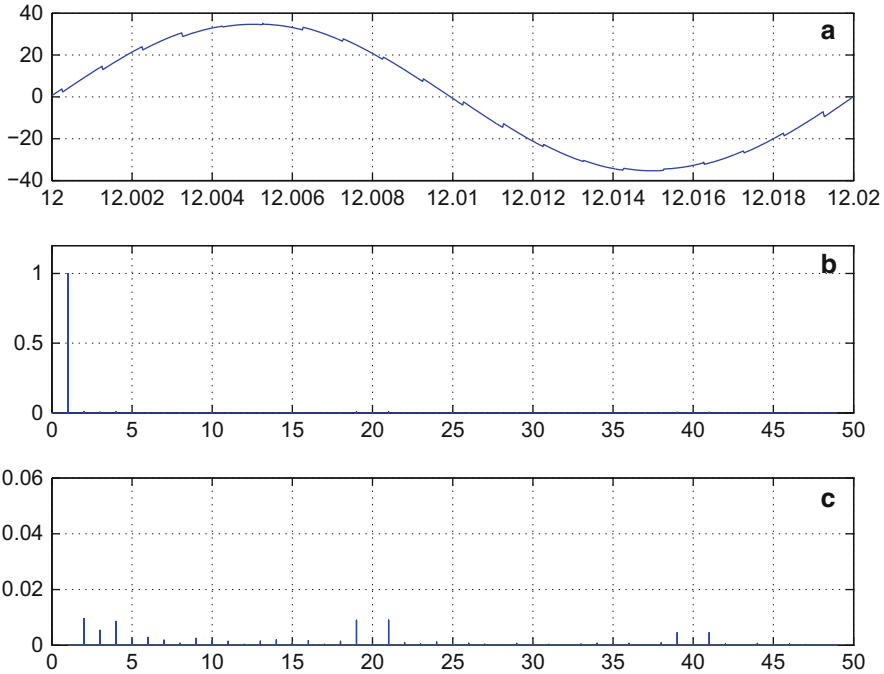

Fig. 9.5 Simulated basic signal waveforms and stator current harmonic spectrum under purely sinusoidal stator voltage for $V = 13$ m/s. (**a**) one period of i_{as} current, (**b**) reduced spectrum of i_{as} with respect to its fundamental and (**c**) harmonics of i_{as} (fundamental = 1)

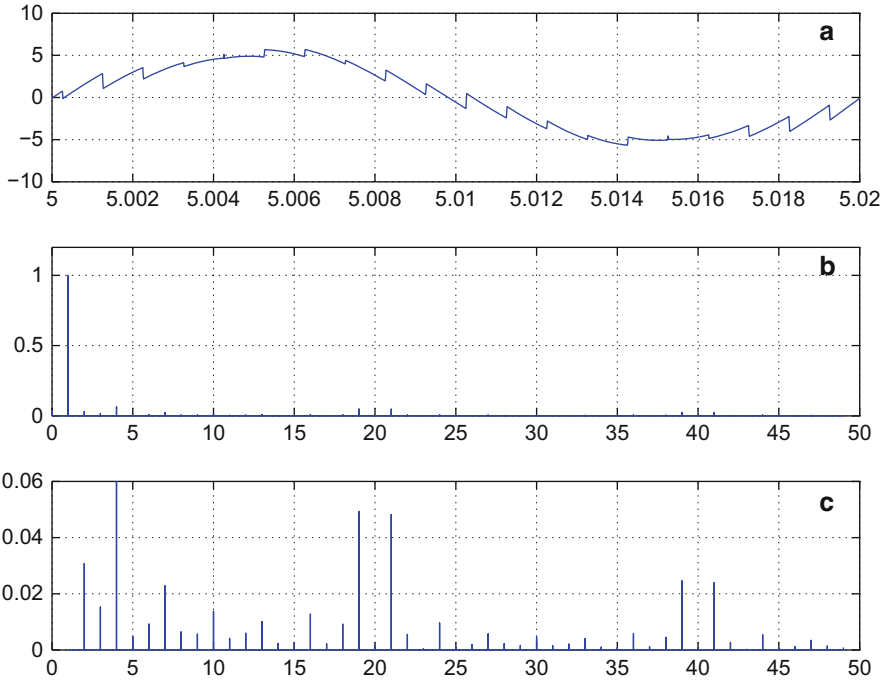

Fig. 9.6 Simulated basic signal waveforms and stator current harmonic spectrum under purely sinusoidal stator voltage for $V = 8$ m/s. (**a**) one period of i_{as} current, (**b**) reduced spectrum of i_{as} with respect to its fundamental, and (**c**) harmonics of i_{as} (fundamental = 1)

Table 9.3 Evaluation of THD

Wind values (m/s)	8	10	13
THD (%)	3.303	1.22	0.96

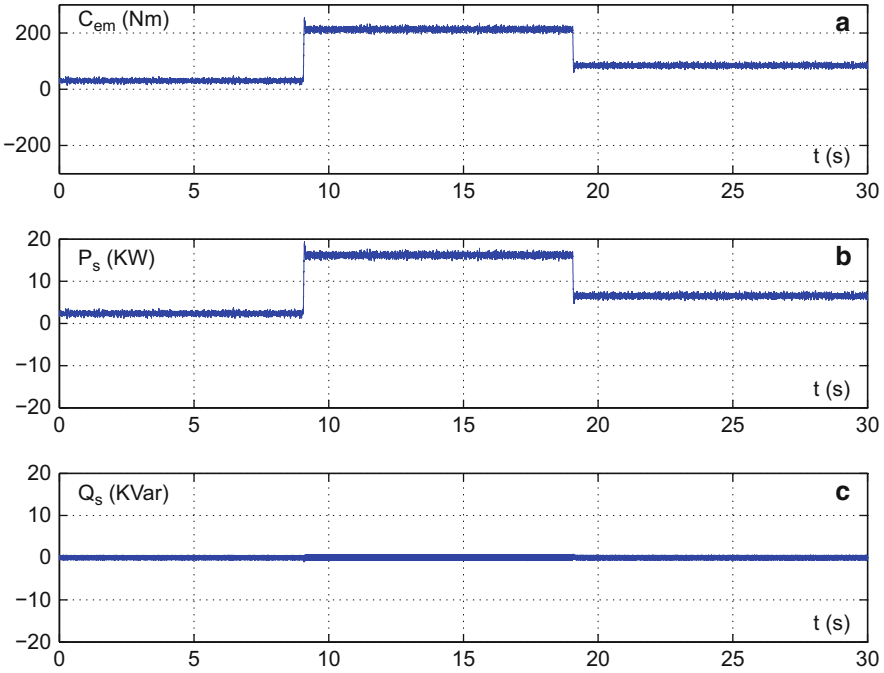

Fig. 9.7 Simulation results. (**a**): Electromagnetic torque of the DFIG, (**b**): Stator active power transmitted to the grid, (**c**): Reactive power of the stator

harmonics in terms of harmonic frequencies. Subscribing the fast Fourier transform (FFT), the performance index THD is evaluated.

Table 9.3 shows the evaluation of performance index THD using a sliding mode control. By increasing wind values, it is clear that results donated from the SMC controllers have lower values of the performance index.

Figure 9.7 presents the electromagnetic torque and stator active and reactive powers. It is found that, the responses of the SMC regulator follow the wind profile with a very fast time response.

9.5 Conclusion

In this work, a nonlinear sliding mode control approach of a DFIG based on wind turbine has been investigated to improve the efficiency of the wind energy conversion system. Using the Lyapunov stability theorem, the synthesis of this

controller is developed. As demonstrated by the obtained results, it is observed that this tuning is useful to improve the damping of the oscillatory modes and also to enhance the fault ride-through capability of the DFIG system.

References

Barambones, O., Cortajarena, J. A., Alkorta, P., & de Durana, J. M. G. (2014). A real-time sliding mode control for awind energy system based on a doubly fed induction generator. *Energies, 7*, 6412–6433.

Bekakra, Y., & Attous, D. B. (2011). Sliding mode controls of active and reactive power of a DFIG with mppt for variable speed wind energy conversion. *Australian Journal of Basic and Applied Sciences, 5*, 2274–2286.

Belmokhtar, K., Doumbia, M., & Agbossou, K. (2014). Novel fuzzy logic based sensorless maximum power point tracking strategy for wind turbine systems driven DFIG (doubly-fed induction generator). *Energy, 76*, 679–693.

Bouaziz, B., & Bacha, F. (2013). Direct power control of grid-connected converters using sliding mode controller. *Electrical Engineering and Software Applications, 5*, 801–806.

Cardenas, R., Pena, R., Perez, M., Clare, J., Asher, G., & Wheeler, P. (2005). Control of a switched reluctance generator for variable-speed wind energy applications. *IEEE Transactions on Energy Conversion, 20*, 781–791.

Cheng, M. Y. Z. (2014). The state of the art of wind energy conversion systems and technologies: A review. *Energy Conversion and Management, 88*, 332–347.

Giglia, G. M., Pucci, C. S., & Vitale, G. (2007). Comparison of control techniques for three-phase distributed generation based on VOC and DPC, I.S.S.I.A.-C.N.R. (Institute on intelligent systems for the automation). *IEEE Transactions on Energy Conversion, 1*, 1–12.

Hu, J., Nian, H., Hu, B., He, Y., & Zhu, Z. Q. (2010). Direct active and reactive power regulation of DFIG using sliding-mode control approach. *IEEE Transactions on Energy Conversion, 25*, 1028–1039.

Kairous, D., & Belmadani, B. (2015). Robust fuzzy-second order sliding mode based direct power control for voltage source converter. *International Journal of Advanced Computer Science and Applications, 6*, 167–175.

Lajimi, A. B., & Shahabi, M. (2011). Modeling and control of a DFIG-based wind turbine during a grid voltage drop. *ETASR Engineering Technology and Applied Science Research, 1*, 121–125.

Rajendran, S., & Jena, D. (2014). Control of variable speed variable pitch wind turbine at above and below rated wind speed. *Electrical Engineering and Software Applications, 1*, 1–14.

Shukla, R. D., & Tripathi, R. K. (2014). A novel voltage and frequency controller for standalone DFIG based wind energy conversion system. *Renewable and Sustainable Energy Reviews, 37*, 69–89.

Utkin, V. (1993). Sliding mode control design principles and applications to electric drives. *IEEE Transactions on Industrial Electronics, 40*, 23–36.

Zhang, Y., Zhu, J., & Guo, Y. (2011). A simple method to reduce torque ripple in direct torque-controlled permanentmagnet synchronous motor by using vectors with variable amplitude and angle. *IEEE Transactions on Energy Conversion, 58*, 2848–2859.

Zhang, Y., Li, Z., & Xu, W. (2012). A novel three-vectors-based predictive direct power control of doubly fed induction generator for wind energy applications. In *Energy Conversion Congress and Exposition (ECCE)* (pp. 793–800).

Chapter 10
A Comparative Study Between PI and Sliding Mode Control for the DFIG of a Wind Turbine

Basma Boujoudi, Elm'kaddem Kheddioui, Nadia Machkour, and Mohammed Bezza

Abstract This chapter presents a comparative study between the indirect field-oriented control (IFOC) with Proportional-Integral controller (PI) and the sliding mode control of a doubly fed induction machine (DFIG), dedicated to the production of the electrical energy in a wind system. Both types of control are presented in this paper to compare their performances in terms of follow-up of deposits and robustness towards parametric variations of the DFIG.

Keywords DFIG · Indirect field-oriented control · IFOC · PI · Sliding mode · Wind turbine

10.1 Introduction

Nowadays, due to multiple benefits of wind turbines, their integration into the field of alternative and renewable energy sources has been growing increasingly. Several research studies are currently focusing on the management and control of wind conversion systems, and more particularly the control of the electrical machine which forms the core of the process of energy conversion. The aim of my research work is to study the connection of the wind turbine system to an electrical network affected by voltage dip, in earlier work (Boujoudi et al. 2016) a classification of existing voltage dips and their impacts are presented.

In this paper we compare the performances of the two control modes to choose the appropriate command for the wind turbine system, but in future work we are

B. Boujoudi (✉) · E. Kheddioui · N. Machkour
Laboratory of Physics of the atmosphere, materials and modeling, Faculty of Sciences and Techniques of Mohammedia, Hassan II University of Casablanca, Mohammedia, Morocco

M. Bezza
Laboratory of Electronics, Energy, Automation and Information Processing, Faculty of Sciences and Techniques of Mohammedia, Hassan II University of Casablanca, Mohammedia, Morocco

N. Derbel, Q. Zhu (eds.), *Modeling, Identification and Control Methods in Renewable Energy Systems*, Green Energy and Technology,
https://doi.org/10.1007/978-981-13-1945-7_10

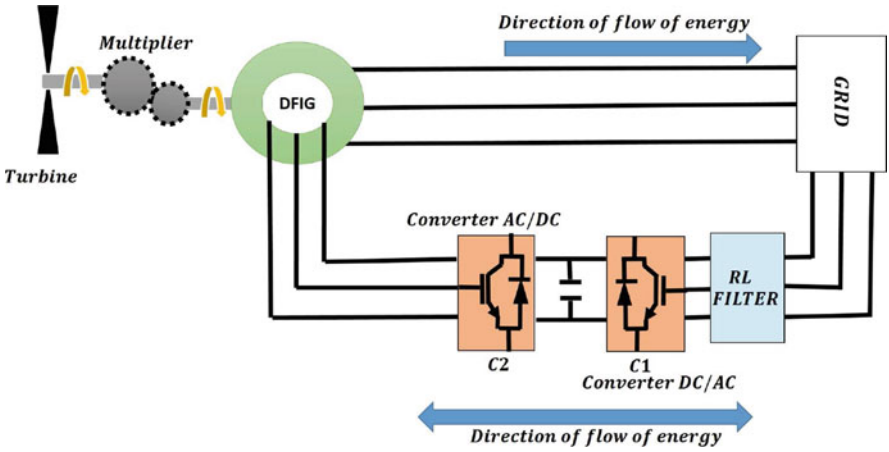

Fig. 10.1 Doubly-fed induction generator in wind power generation

going to study the command performances of the system connected to an electrical network affected by voltage dip.

The used machine in this work is the doubly fed asynchronous machine (DFIG). Its stator is connected directly to the electrical network, while its rotor is connected to the network by means of two converters (Fig. 10.1). The converter C_1 maintains the unit power factor while the C_2 acts on the regulation of the active and reactive powers injected into the network. In this chapter we present two control strategies of the converter C_2: one concerns the control by a PI regulator and the other is articulated around the nonlinear control based on the sliding mode. A modeling of the wind turbine and DFIG assembly was carried out, in order to synthesize the indirect field-oriented control with the PI and the sliding mode.

Simulation results of both commands are presented in Matlab-Simulink environment. The overall system is illustrated in Fig. 10.1.

Firstly, the modeling of the "wind turbine – DFIG" is exposed, then, we present the strategy of controlling the wind turbine with the MPPT. At last, we synthesize the indirect vector control by the two methods. A comparative study of both methods is established to present the performances of these two control techniques.

10.2 System Modeling (Turbine & DFIG)

10.2.1 Wind Turbine Modeling

A wind V_v is applied to the blades of radius R of the wind turbine to create its rotation (Delenclos 2016). This rotation generates a mechanical power which is transmitted to the mechanical shaft of the turbine. It is expressed as follows (Allam

et al. 2014; Bedoud et al. 2013; Sabzevari et al. 2017; Tamaarat et al. 2013):

$$P_m = \frac{1}{2}\,\rho\, C_p(\lambda, \beta)\, S\, V_v^3 \tag{10.1}$$

The mechanical torque can be represented by:

$$T_t = \frac{P_t}{\Omega_t} = \frac{1}{2\lambda}\,\pi\,\rho\, C_p(\lambda, \beta)\, R^3\, V_v^2 \tag{10.2}$$

where $C_p(\lambda, \beta)$ is the power coefficient of the wind turbine which represents the aerodynamic efficiency of the wind turbine and also depends on the characteristic of the turbine. Several forms of this coefficient can be found in the literature. In this chapter we opt for the following expression (Bedoud et al. 2013):

$$C_p(\lambda, \beta) = 0.46\left(\frac{151}{\lambda_i} - 0.58\beta - 0.002\beta^{214} - 1.32\right)\exp\left(-\frac{184}{\lambda_i}\right) \tag{10.3}$$

$$\frac{1}{\lambda_i} = \frac{1}{\lambda + 0.2\beta} - \frac{0.003}{1 + \beta^3} \tag{10.4}$$

where λ represents the tip-speed ratio which is the ratio of the blade-tip linear speed to the wind speed, defined as:

$$\lambda = \frac{R\Omega_t}{V_v} \tag{10.5}$$

The mechanical part of the turbine comprises three steerable blades of length R. They are fixed on a drive shaft rotating at a speed of rotation Ω_t, connected to a gain multiplier G_m which drives the electric generator. The multiplier, considered as perfect, guarantee the adaptation between the speed of rotation of the turbine and that of the generator according to the following relation:

$$G_m = \frac{T_t}{T_m} = \frac{\Omega_{mec}}{\Omega_t} \tag{10.6}$$

The wind turbine system mechanical equation can be represented by:

$$T_m - T_{em} = \left(J_m + \frac{J_t}{dt}\right)\frac{d\Omega_m}{dt} + f_v\Omega_m \tag{10.7}$$

where T_{em} is the torque produced by the electrical generator.

The block diagram of the wind turbine is illustrated in Fig. 10.2.

In order to extract the maximum power from the incident wind energy, it is necessary to permanently regulate the speed of rotation of the turbine so that it adapts to the wind speed. This permanent search technique is called “Maximum Power Point Trackin”.

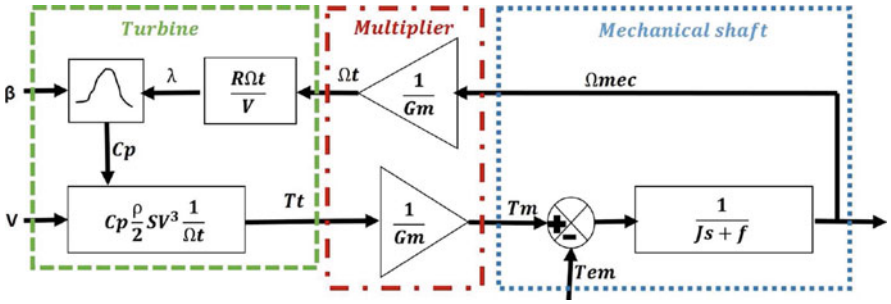

Fig. 10.2 Modeling of the mechanical part of the wind turbine

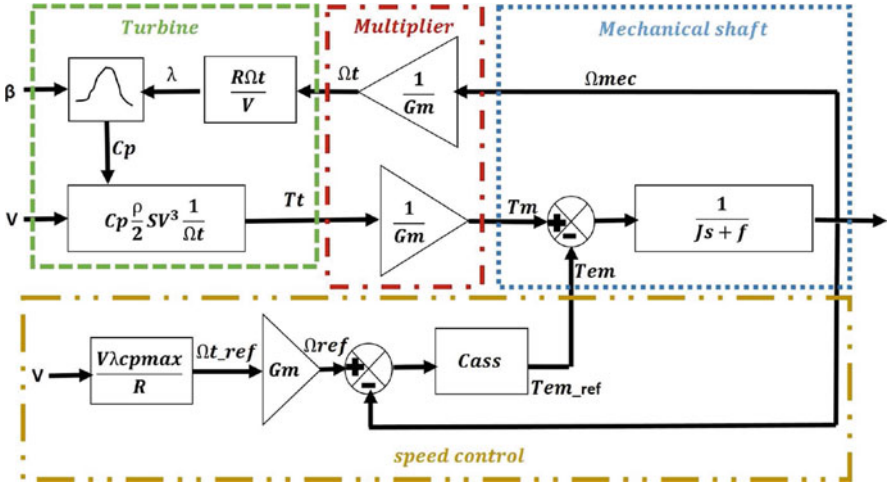

Fig. 10.3 MPPT control with rotational speed control

The search for the maximum is made constantly and the wind turbine adapts to each variation of the wind to be in a configuration of maximum power extraction (El Aimani 2004; Mirecki 2005).

There are several techniques to pursue MPPT. These techniques differ according to the type of information they need to deliver the speed reference, the technique used in this paper is that of power maximization with speed control (Fig. 10.3).

10.2.2 DFIG Modeling

In general, a squirrel cage induction machine can operate in two modes: motor or generator. Indeed, the machine operates as a motor when it rotates below its synchronous speed and it functions as a generator when it exceeds this speed (El Aimani 2004).

In the case of a DFIG, it is no longer the speed of rotation which imposes the mode of operation. It is the control of the rotor voltages which control the magnetic field inside the machine, thus offering the possibility of operating in hyper-synchronism or in hypo-synchronism in both the motor and generator modes. The following equation system describes the global modeling of DFIG in Park's repository (Bedoud et al. 2013; El Aimani 2004; Uma and Manikandan 2013).

- Electrical equations
  - Stator voltage

$$\begin{cases} V_{sd} = R_s i_{sd} + \dfrac{\varphi_{sd}}{dt} - \dot{\theta}_s \varphi_{sq} \\ V_{sq} = R_s i_{sq} + \dfrac{\varphi_{sq}}{dt} + \dot{\theta}_s \varphi_{sd} \end{cases} \tag{10.8}$$

  - Rotor voltage

$$\begin{cases} V_{rd} = R_r i_{rd} + \dfrac{\varphi_{rd}}{dt} - \dot{\theta}_r \varphi_{rq} \\ V_{rq} = R_r i_{rq} + \dfrac{\varphi_{rq}}{dt} + \dot{\theta}_r \varphi_{rd} \end{cases} \tag{10.9}$$

- Magnetic equations

$$T_{em} = -\frac{M}{L_s}(i_{rd}\varphi_{sq} - i_{rq}\varphi_{sd}) \tag{10.10}$$

Thus, the equations of the machine are established, we notice that the mechanical equation requires a decoupling to be able to control independently the active and reactive powers.

In order to facilitate this control, one chooses the synchronously rotating reference frame so the stator flux vector φ_s is placed on the axis d (Bühler 1986) and this results in (Fig. 10.4):

$$\begin{cases} \varphi_{sd} = \varphi_s \\ \varphi_{sq} = 0 \end{cases} \tag{10.11}$$

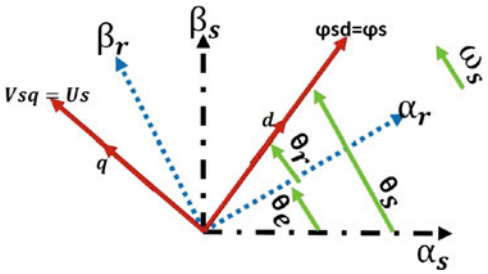

Fig. 10.4 Reference frame related to the stator rotating field

Assuming that the stator flux is constant and neglecting the stator resistance R_s, the stator voltages in the plane dq are presented below (Betin 2003).

$$\begin{cases} V_{sd} = 0 \\ V_{sq} = \sqrt{3}V_s = U_s = \omega_s \varphi sd \end{cases} \tag{10.12}$$

Thus, equations of the stator flux become:

$$\begin{cases} \varphi_{sd} = \varphi_s = L_s i_{sd} + M i_{rd} \\ \varphi_{sq} = 0 = L_s i_{sq} + M i_{rq} \end{cases} \tag{10.13}$$

From the above equations and taking into account the simplifying hypotheses we obtain the following equations:

- Stator Current

$$\begin{cases} i_{sd} = \dfrac{1}{L_s}\varphi_s - \dfrac{M}{L_s} i_{rd} \\ i_{sq} = -\dfrac{M}{L_s} i_{rq} \end{cases} \tag{10.14}$$

- Active power

$$P_s = -V_{sq}\frac{M}{L_s} i_{sq} \tag{10.15}$$

- Electromagnetic torque

$$T_{em} = p\frac{M}{L_s}\varphi_{sd} i_{rq} \tag{10.16}$$

- Reactive power

$$Q_s = \frac{V_{sq}\varphi_{sd}}{L_s} - \frac{V_{sq} M}{L_s} i_{rd} \tag{10.17}$$

- Rotor voltage

$$\begin{cases} V_{rd} = R_r i_{rd} - \sigma L_r \dfrac{di_{rd}}{dt} - \sigma L_r \omega_r i_{rq} \\ V_{rq} = R_r i_{rq} + \sigma L_r \dfrac{di_{rq}}{dt} + \sigma L_r \omega_r i_{rd} + \dfrac{M}{L_s}\omega_r \varphi_{sd} \end{cases} \tag{10.18}$$

Where σ is the dispersion coefficient of the DFIG, and ω_r is the rotor pulsation. From these equations, Fig. 10.5 presents the block diagram of the system to be regulated (El Aimani 2004; Uma and Manikandan 2013).

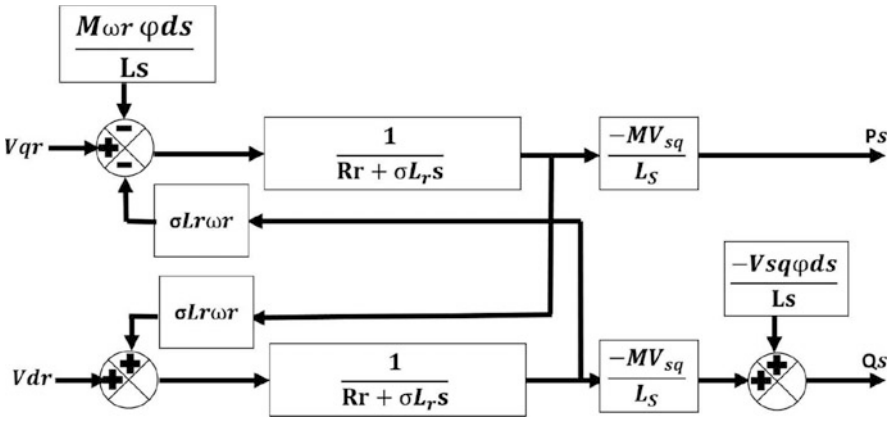

Fig. 10.5 Block diagram of the DFIG

The expressions of the active and reactive powers show that, assuming that the stator flux along the axis dq is kept constant, the choice of the reference dq makes the electromagnetic torque and consequently the stator active power proportional to the rotor current of axis q, as regards the reactive power is not proportional to the rotor current i_{rq} due to a constant imposed by the network. This allows the control of the stator powers independently of one another, by regulating the rotor currents in the axis dq.

10.3 Indirect Field-Oriented Control of the DFIG

The wind power generation system has two converters, the first on the grid side and the second on the rotor side of the DFIG. In this chapter, we are interested only in the converter rotor side, responsible for the regulation of active and reactive power. The rotor-side converter is controlled by the PI control at first, then by the sliding mode control, a setpoint and robustness test is performed to compare the performance of these two control strategies. The reference current i_{rq} is derived from the MPPT control via the reference electromagnetic torque or via the reference stator power, the expression of the current is presented by:

$$i_{rq-ref} = -\frac{L_s}{pM\varphi_{sd-est}} T_{em-ref} \tag{10.19}$$

which we can written as:

$$i_{rq-ref} = -\frac{L_s}{MV_{sq}} P_{s-ref} \tag{10.20}$$

The reference current i_{rd} is derived from the control of the stator reactive power.

$$i_{rd-ref} = \frac{\varphi_{sd-est}}{M} - \frac{L_s}{MU_s} Q_{s-ref} \tag{10.21}$$

10.3.1 Indirect PI Field-Oriented Control of the DFIG

Expressions above show that the stator flux is necessary for the generation of the reference rotor currents (Allam et al. 2014; Bedoud et al. 2013; El Aimani 2004; Uma and Manikandan 2013). The stator flux of axis d can be estimated in open loop from the measurements of the stator and rotor currents with axis d (El Aimani 2004):

$$\varphi_{sd-est} = L_s i_{sd} + M i_{rd} \tag{10.22}$$

The control diagram of the converter C_2 is illustrated in Fig. 10.6.

PI regulators have been used. Their parameters depend on the system parameters. The open loop transfer function of the rotor current regulators can be written as follows:

$$OLTF = K_{ir} \left(\frac{1 + \frac{K_{pr}}{K_{ir}} s}{s} \right) \left(\frac{\frac{1}{R_s}}{1 + \frac{\sigma L_r}{R_r} s} \right) \tag{10.23}$$

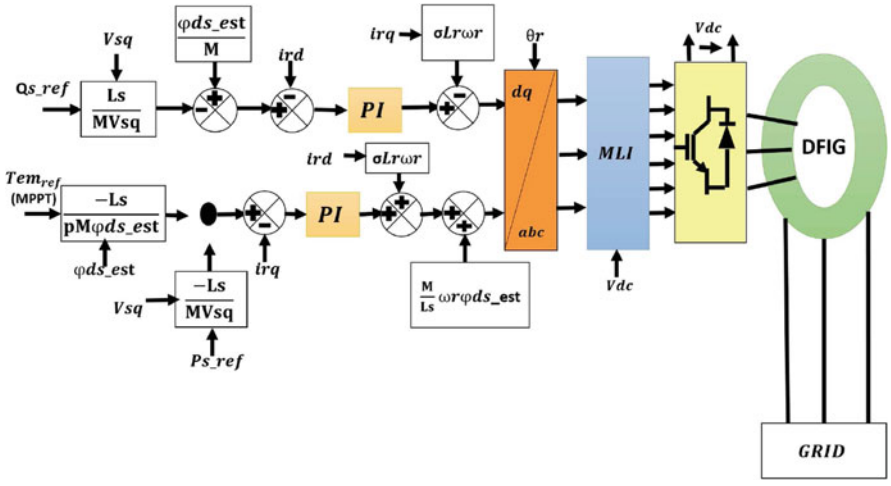

Fig. 10.6 Machine-side converter control with PI

Using the pole compensation method for determining the parameters of the regulator, we obtain:

$$K_{ir} = \frac{3R_r}{t_{r5\%}} \tag{10.24}$$

$$K_{pr} = \frac{3\sigma L_r}{t_{r5\%}} \tag{10.25}$$

10.3.2 Indirect Field-Oriented Control of the DFIG with the Slidding Mode

The principle of this command is to choose a surface or a region of slip, and to attract the states of the system in this region, then to elaborate a law of control which allows the maintenance of the system in this region.

The choice of the non-linear sliding surface is based on the system state variables. The variables to be regulated are expressed by the model previously established (Betin 2003).

The design of the sliding mode algorithm takes into account the problems of stability and good performance in a systematic way in its approach, which is carried out mainly in three complementary steps (Bühler 1986; Bekakra and Ben Attous 2009; Bekakra and Ben Attous 2010; Bekakra and Ben Attous 2011; Ben attous et al. 1998)

- Choice of sliding surfaces;
- Definition of the conditions of existence and convergence of the rolling regime;
- Determination of the control law.

Based on the model established for control with the PI controller, the slip surfaces chosen in this chapter are the direct and quadrature rotor current, since the rotor currents are the image of the stator powers.

10.3.2.1 Active Power Control (P_s)

In the following, an indirect control of the active power of the DFIG is performed by acting on the current irq. The error of the quadrature rotor current irq is defined by Ben attous et al. (1998), Namuduri and Sen (1986), and Young (1989)

$$e = i_{rq-ref} - i_{rq} \tag{10.26}$$

For $n = 1$, the surface of the quadrature rotor current can be defined from the following equation:

$$S_q(i_{rq}) = e_q = i_{rq-ref} - i_{rq} \tag{10.27}$$

By taking the time derivative of (10.27) and by replacing the expression $\frac{di_{rq}}{dt}$ with its expression according to the term of the command, one obtains:

$$\dot{S}_q = \dot{e}_q = \frac{d}{dt} i_{rq-ref} - \left[-\frac{1}{\sigma} \left(\frac{1}{T_r} + \frac{M^2}{L_r L_s T_s} \right) i_{rq} - g\omega_s i_{rd} + \frac{1}{\sigma L_r} V_{rq} \right] \tag{10.28}$$

The expression of V_{rq} is:

$$V_{rq} = V_{rq-eq} + V_{rq-n} \tag{10.29}$$

During the sliding mode:

$$S_q = \dot{S}_q = 0 \tag{10.30}$$

This gives the so called equivalent control:

$$V_{rq-eq} = \sigma L_r \left(\frac{d}{dt} i_{rq-ref} + \frac{1}{\sigma} \left(\frac{1}{T_r} + \frac{M^2}{L_r L_s T_s} \right) i_{rq} + g\omega_s i_{rd} \right) \tag{10.31}$$

Consequently:

$$V_{rq-n} = K_q \text{ sat } (S_q) \tag{10.32}$$

where K_q is a positive constant.

In this chapter we use the function "sat" instead of "sign" in order to eliminate the chattering of the control.

10.3.2.2 Reactive Power Control

The reactive power generated by the DFIG is controlled by controlling the direct rotor current i_{rd}. The error of the direct rotor current is defined by Ben attous et al. (1998), Hashimoto et al. (1986), Namuduri and Sen (1986), and Young (1989):

$$e_d = i_{rd-ref} - i_{rd} \tag{10.33}$$

For $n = 1$, the surface of the direct rotor current can be defined from the following equation:

$$S_d(i_{rd}) = e_d = i_{rd-ref} - i_{rd} \tag{10.34}$$

Its derivative:

$$\dot{S}_d = \dot{e}_d = \frac{d}{dt} i_{rd-ref} - \left[\frac{1}{\sigma T_r} i_{rd} + g\omega_s i_{rq} + \frac{1}{\sigma L_r} V_{rd} \right] \tag{10.35}$$

The expression of V_{rd} is then:

$$V_{rd} = V_{rd-eq} + V_{rd-n} \tag{10.36}$$

During the sliding mode:

$$S_d = \dot{S}_d = 0 \tag{10.37}$$

This gives the so called equivalent control:

$$V_{rd-eq} = \sigma L_r \left(\frac{d}{dt} i_{rd-ref} - \frac{1}{\sigma T_r} i_{rd} - g\omega_s i_{rq} \right) \tag{10.38}$$

Consequently:

$$V_{rq-n} = K_d \text{ sat } (S_q) \tag{10.39}$$

where K_d is a positive constant.

Figures 10.7 and 10.8 summarize the principle of the sliding mode.

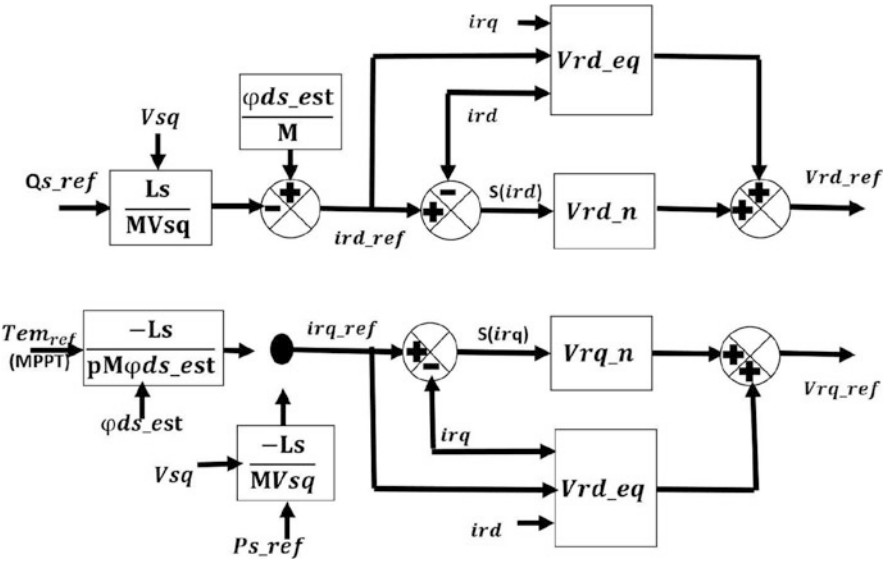

Fig. 10.7 Principle of control with sliding mode with addition of equivalent control

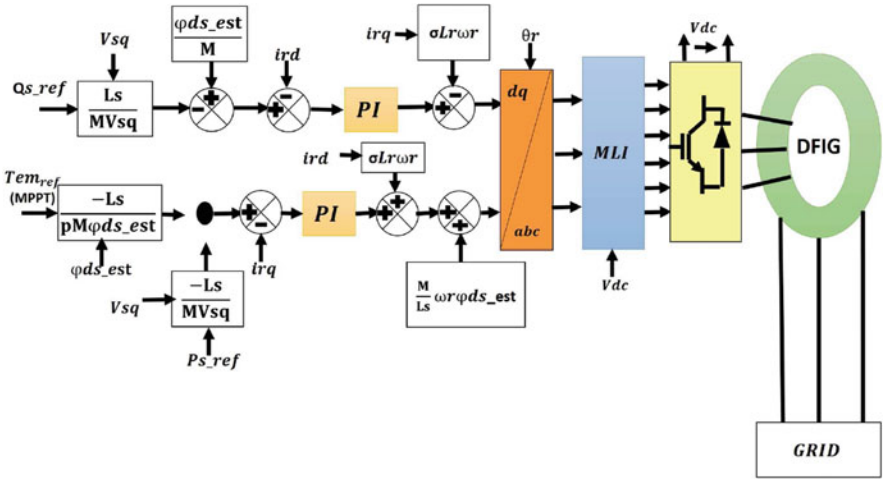

Fig. 10.8 Control of the machine side converter with sliding mode

Table 10.1 Parameters of the DFIG and the wind turbine

Parameter	P_n	R_s	R_r	L_s	L_r	M	F	J	R	G_m
Value	20	0.455	0.19	70	21.3	34	0.0024	0.53	3	5.4
Unit	W	Ω	Ω	mH	mH	mH	Nm/s	kg m^2	m	–

10.4 Simulation Result, Performance Analysis

This part deals more specifically with the comparison and analysis of the performances of the regulators synthesized and detailed in the previous section. To do this, a series of tests were carried out with different conditions in order to establish a model closest to the experimental device. Parameter of the DFIG and the wind turbine are given in Table 10.1.

10.4.1 Follow-Up of the Reference

Test conditions are chosen as:

- The wind speed is assumed to be constant 7 m/s, which means that the generator will run at a speed of 900 rpm.
- At $t = 1$ s active power step (P_{ref} switches from 0 to -10 kW).
- At $t = 2$ s step of reactive power (Q_{ref} varies from 0 to 6 kVAR).

Figures 10.9, 10.10, 10.11, 10.12, 10.13, and 10.14 show the simulation results obtained with MATLAB / SIMULINK in the case of the indirect control of the DFIG with the sliding mode and the PI controller.

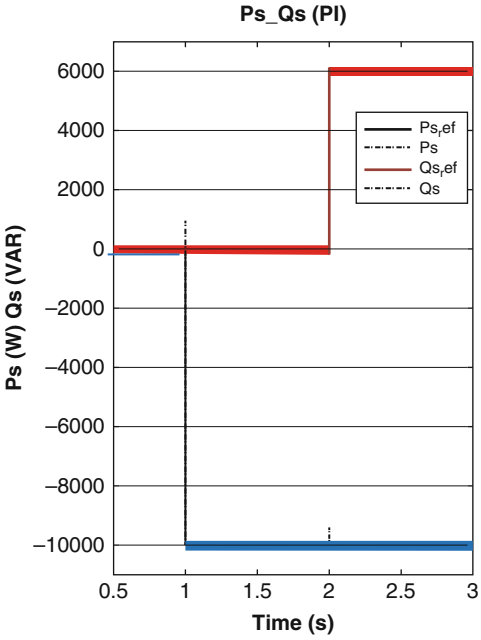

Fig. 10.9 Active and reactive stator power with PI controller

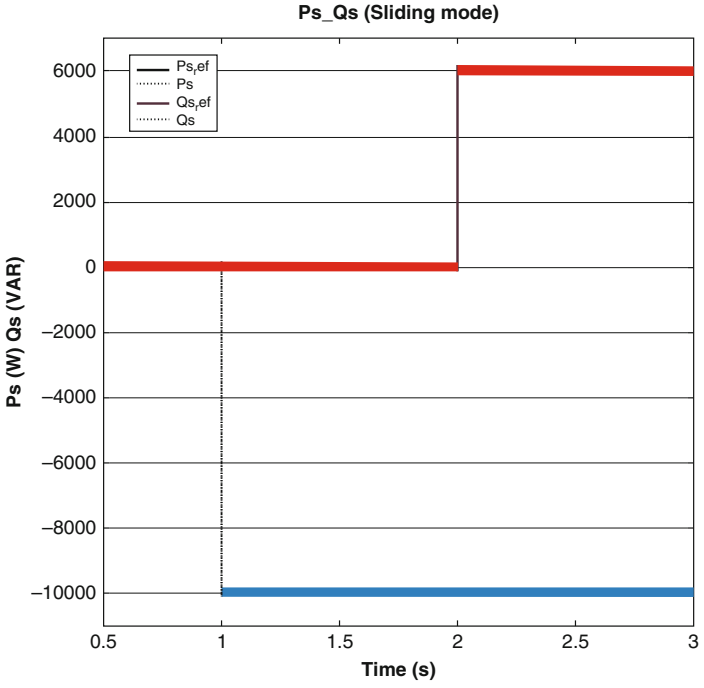

Fig. 10.10 Active and reactive stator power with sliding mode controller

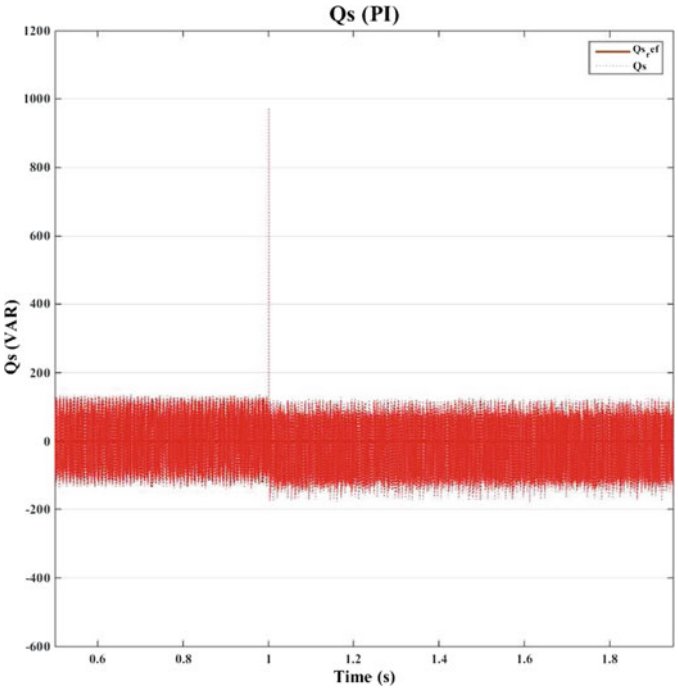

Fig. 10.11 Reactive power at t = s with the PI

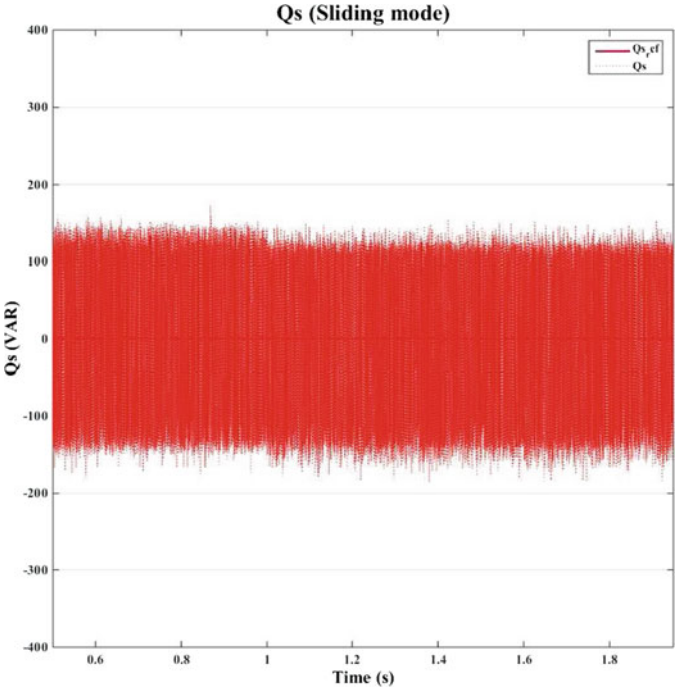

Fig. 10.12 Reactive stator power at t = 1 s with the sliding mode controller

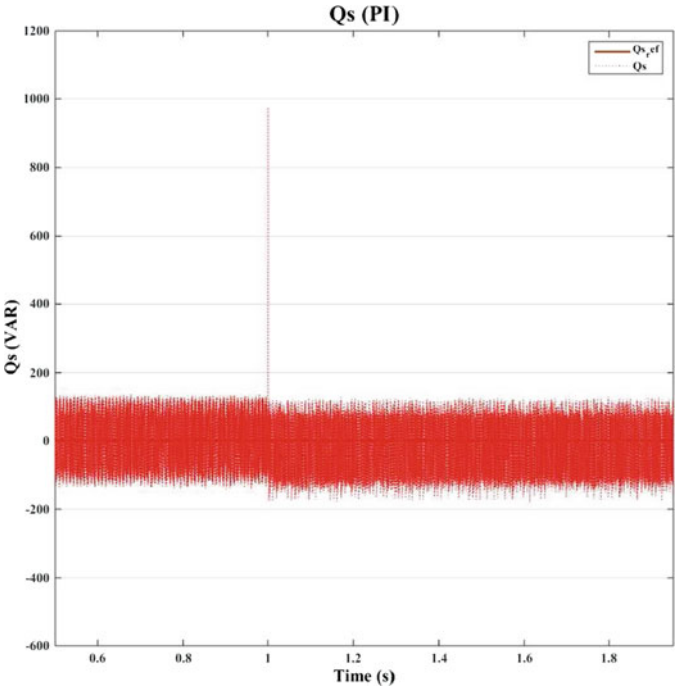

Fig. 10.13 Active stator power at $t = 2$ s with PI controller

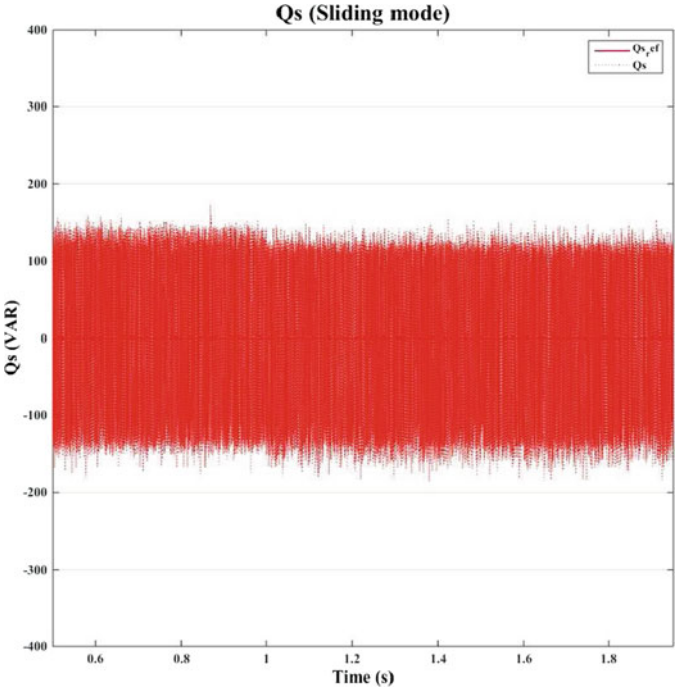

Fig. 10.14 Active stator power at $t = 2$ s with sliding controller

The previous figures show that the active and reactive powers generated by the DFIG follow their references perfectly. Obviously the results assert that the active stator power depends on the quadrature rotor current and that the reactive stator power depends on the direct rotor current, hence the effect of decoupling between the d-axis and q. The almost zero static error is approximately the same for both control modes. The system has a satisfactory fast dynamic and no overshoot. The coupling between the two powers is virtually absent in the case of the control by the sliding mode, contrary to the indirect vector control with the PI, it is observed that the stator powers undergo a transition peak. To conclude, the control of active and reactive stator power by the sliding mode brings a remarkable improvement compared to the PI regulator.

10.4.2 Robustness Testing

The calculation of the regulators is based on transfer functions whose parameters are assumed to be fixed. However, in reality, these parameters may vary because of the various physical phenomena, in particular the heating of the resistors. In order to get closer to the actual behavior of the system, we will perform a robustness tests which consist in varying the parameters of the machine.

- A 50% increase in resistances R_s and R_r.
- A 20% decrease in mutual inductance M.
- The wind speed is set at 7 m/s, which causes the machine to run at 900 rpm.
- At $t = 1$ s the active power goes from 0 to -10 kW.
- At $t = 1.5$ s the wind speed increases from 7 to 10 m/s, so the machine speed increases from 900 to 1290 rpm.
- At $t = 2$ s the reactive power increases from 0 to 6 kVAR.

Figures 10.15, 10.16, 10.17, 10.18, 10.19, 10.20, 10.21, 10.22, and 10.23, show the result obtained for the two types of control in the case of a parametric variation. It can be seen that the PI regulator loses its robustness, contrary to the sliding mode control. From the figures, it can be seen that the reactive stator power controlled by the PI is slightly short of its reference value, thus causing a static error of 5%, contrary to that regulated by the sliding mode. In the end, a very satisfactory performance is obtained by using the sliding mode in terms of follow-up of the reference when a variation of the parameters of the machine.

10.5 Conclusion

This chapter presents a comparative study between the indirect field-oriented control with the PI controller and the sliding mode control of the active and reactive stator powers generated by the DFIG in a wind turbine. In a first step we have established

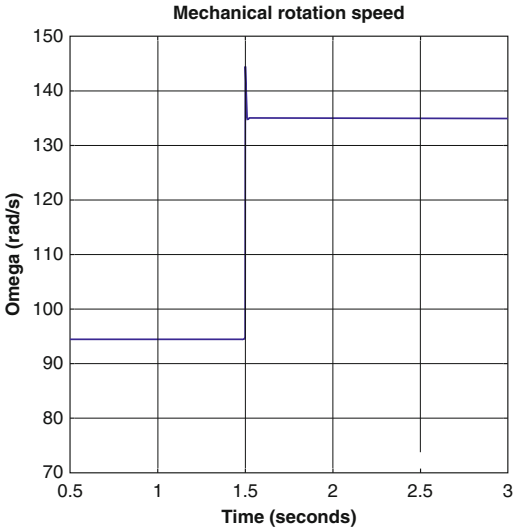

Fig. 10.15 Mechanical rotation speed

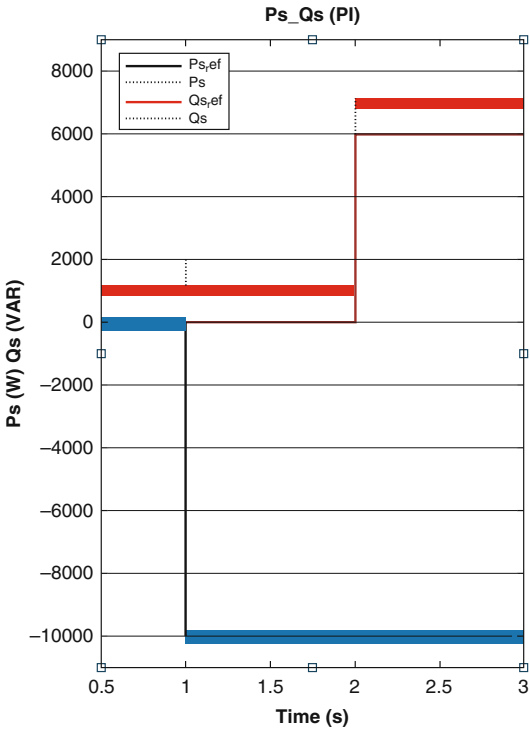

Fig. 10.16 Active and reactive stator power with PI controllers

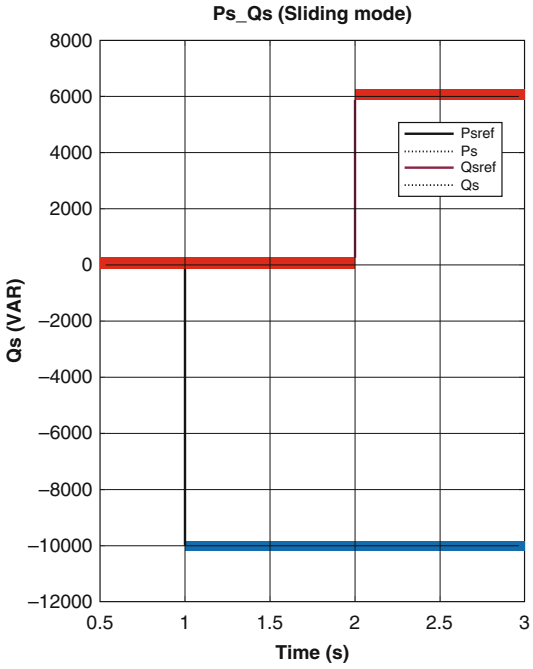

Fig. 10.17 Active and reactive stator power with sliding mode controller

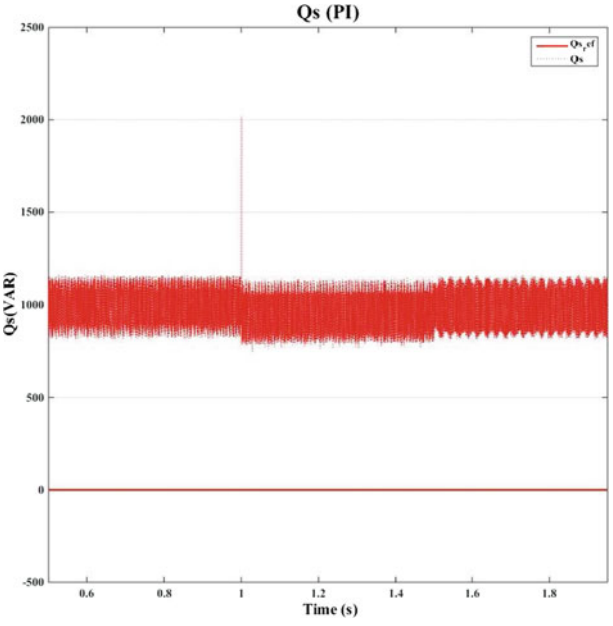

Fig. 10.18 Reactive stator power at $t = 1$ s with PI controller

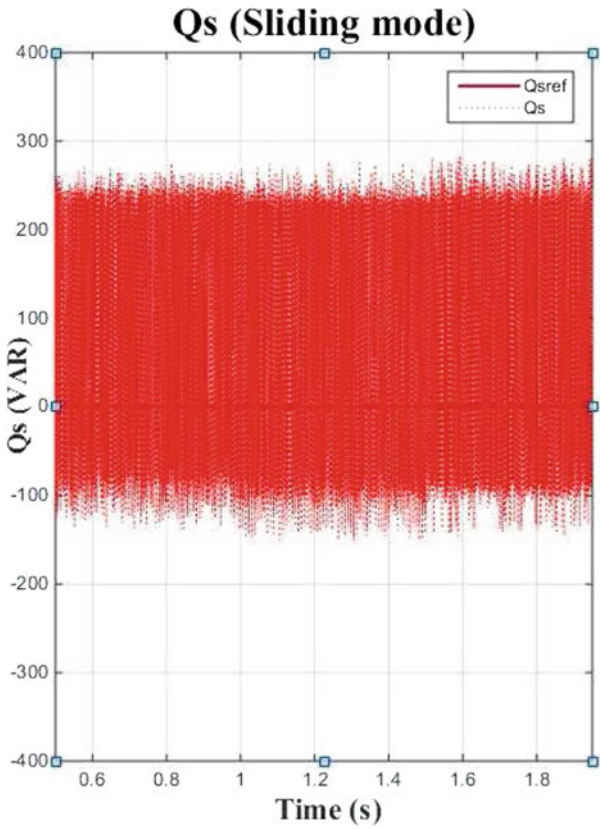

Fig. 10.19 Reactive stator power at $t = 1$ s with sliding mode controller

a model of the set consisting of the wind turbine and the DFIG. Secondly, the synthesis of the two types of regulators was carried out. Then we effectuated two tests in order to compare the performance of each control technique from the point of view of the follow up of the reference and the robustness. The results obtained show that the control by the sliding mode presents better performances than that with the PI controller, whether for the reference tracking or the robustness thus showing a good insensitivity to the disturbances and the parametric uncertainties. Given the satisfactory results of the sliding mode, the next step is to inject the different types of voltage dips into the grid in order to study the behavior of the system controlled by the sliding mode when it's affected by voltage dips.

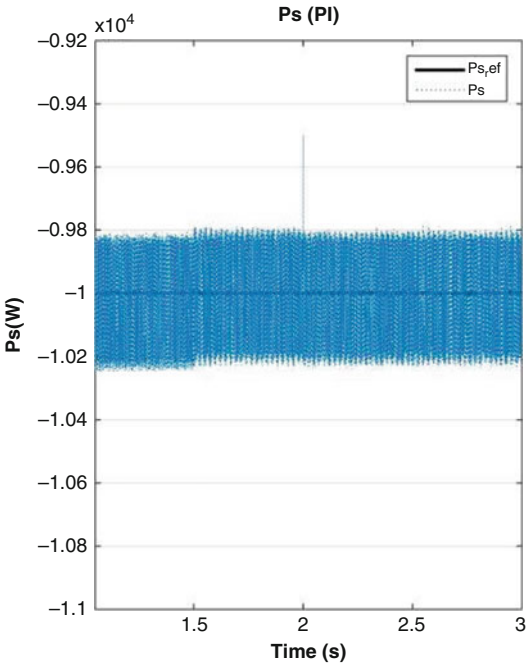

Fig. 10.20 Active stator power at $t = 2$ s with the PI controller

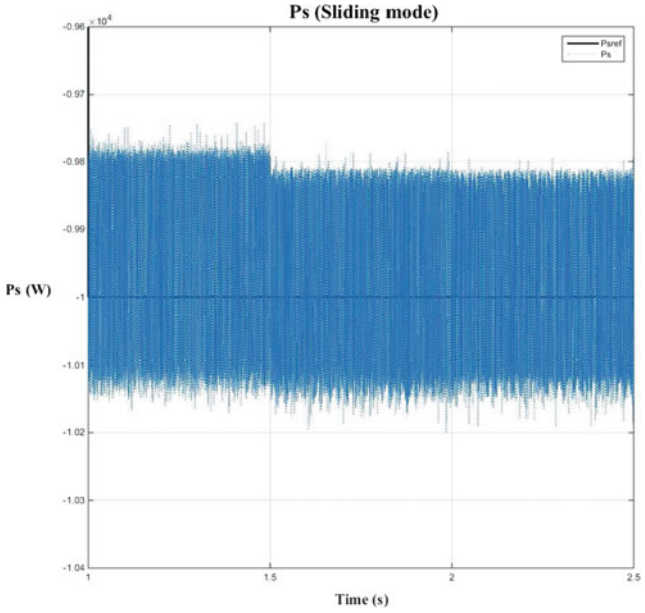

Fig. 10.21 Active stator power at $t = 2$ s with sliding controller

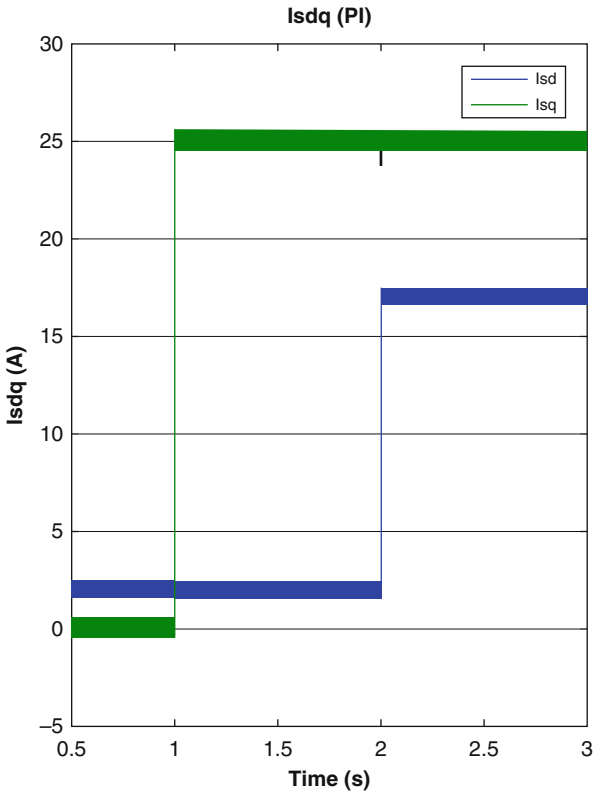

Fig. 10.22 Stator currents (axis dq) with PI controller

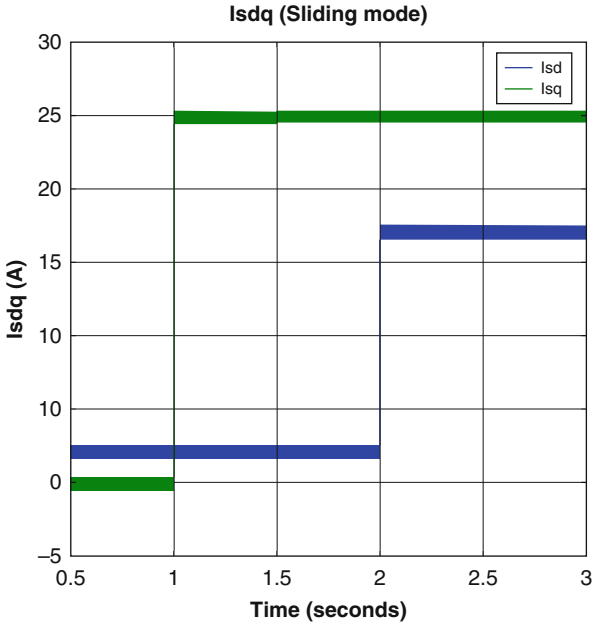

Fig. 10.23 Stator currents (axis dq) with sliding mode controller

References

Allam, M., Allam, M., & Djeriri, Y. (2014). Etude comparative entre la commande vectorielle directe et indirecte de la Machine Asynchrone à Double Alimentation (MADA) dédiée à une application éolienne. *Journal of Advanced Research in Science and Technology, 1*(2), 88–100.

Bedoud, K., Lakel, R., Ali-Rachedi, M., Lekhchine, S., & Bahi, T. (2013). Modelisation d'une chaine de conversion d'energie eolienne basee sur une machine asynchrone a double alimentation. 21 Congres Francais de Mecanique, Bordeaux.

Bekakra, Y., & Ben Attous, D. (2009). A sliding mode speed and flux control of a doubly fed induction machine. In *Electrical and Electronics Engineering, IEEE Conference*, (I) (pp. 174–178).

Bekakra, Y., & Ben Attous, D. (2010). Speed and flux control for DFOC of doubly fed induction machine using sliding mode controller. *Acta Electrotechnica and Informatica, 10*(4), 75–81.

Bekakra, Y., & Ben Attous, D. (2011). Sliding mode controls of active and reactive power of a DFIG with MPPT for variable speed wind energy conversion. *Australian Journal of Basic and Applied Sciences, 5*(12), 2274–2286.

Ben attous, D., Golea, A., & Abdessemed, R. (1998). Commande à structure variable par mode glissant pour la commande vectorielle d'un moteur asynchrone. In *ICEL98*, USTOran.

Betin, F. (2003). Commande d'actionneurs électriques soumis à une charge mécanique à fortes variations paramétriques. Habilitation à diriger des recherches, Centre de Robotique d'Electrotechnique et d'Automatique, Université de Picardie Jules Verne, 02880 Cuffies.

Boujoudi, B., Machkour, N., & Kheddioui, Elm. (2016). New method for detection and characterization of voltage dips. *Molecular Crystals and Liquid Crystals, 641*(1), 86–94.

Bühler, H. (1986). Réglage par Mode de Glissement. Presses Polytechniques Romandes, EPFL, Ecublens, Lausanne.

Delenclos, S. (2016). L'énergie éolienne. http://gte.univ-littoral.fr

El Aimani, S. (2004). Modélisation de différentes technologies d'éoliennes intégrées dans un réseau de moyenne tension. Thesis, Ecole Centrale de Lille, France.

Hashimoto, H., Yamamoto, H., Yanagisawa, D., & Harachima, F. (1986). Brushless servomotor control using VSS approach. In *IEEE TAS Annuel Meeting* (pp. 72–79).

Mirecki, A. (2005). Etude comparative de chaînes de conversion d'énergie dédiées à une éolienne de petite puissance. Thesis, Institut National Polytechnique, Toulouse.

Namuduri, C., & Sen, P. C. (1986). A servo control system using a self-controlled synchronous motor (SCSM) with sliding mode controller. In *IEEE IAS Annuel Meeting* (pp. 56–65).

Sabzevari, S., Karimpor, A., & Monfared, M. (2017). MPPT control of wind turbines with wind speed estimation using direct adaptive fuzzy-pi controller. *Journal of Renewable and Sustainable Energy, 9*, 013302. https://doi.org/10.1063/1.4973447

Tamaarat, A., Benakcha, A., & Menacer, A., (2013). Commande des puissances active et réactive dans d'une Chaine de Conversion basée sur une Machine Asynchrone à Double Alimentation. http://hdl.handle.net/123456789/2513

Uma, S. P., & Manikandan, S. (2013). Control technique for variable speed wind turbine using PI controller. In *IEEE International Conference on Emerging Trends in Computing, Communication and Nanotechnology* (pp. 640–643).

Young, M. (1989). *The technical writer's handbook*. Mill Valley: University Science.

Chapter 11
Emulation of Wind Turbine for Standalone Wind Energy Conversion Systems

L. Benaaouinate, M. Khafallah, A. Mesbahi, A. Martinez, T. Bouragba, and D. Breuil

Abstract In this chapter, a Wind Turbine Emulator (WTE) based on permanent magnet DC motor controlled by Pulse-Width Modulated (PWM) is proposed to satisfy the further study of the wind energy conversion system (WECS) in the laboratory. The main objective of the emulation system is to reproduce the dynamic behavior of the wind turbine torque on the generator shaft. The electrical, mechanical, aerodynamic models of horizontal axis wind turbines (HAWTs) are analyzed in detail. The control of a permanent magnet DC motor and the mathematical models of the wind turbine are elaborated using Matlab/Simulink environment. Simulation and experiment results are also presented to demonstrate the functionality and effectiveness of the system and to confirm that a WTE can provide all necessary parameters of the wind turbine system such as wind speed, output torque, power coefficient and tip speed ratio.

Keywords Wind turbine emulator · DC motor drive · Real time control · Modeling · Electrical generator · Wind turbine

11.1 Introduction

Recently, with the growing energy demands and environmental crisis such as global warming, there had led to the development of renewable sources for the

L. Benaaouinate (✉) · M. Khafallah · M. Mesbahi
High National School of Electricity and Mechanics, Hassan II University, Casablanca, Morocco
e-mail: l.benaaouinate@ieee.org

A. Martinez · T. Bouragba · D. Breuil
Industrial systems engineering school, La Rochelle University, La Rochelle, France
e-mail: andre.martinez@eigsi.fr; tarik.bouragba@eigsica.ma; dominique.breuil@eigsi.fr

N. Derbel, Q. Zhu (eds.), *Modeling, Identification and Control Methods in Renewable Energy Systems*, Green Energy and Technology,
https://doi.org/10.1007/978-981-13-1945-7_11

production of electricity. One of the leading prospects in this search for clean and safe renewable power sources is wind generation system, as it is environmentally friendly, socially beneficial and economically competitive.

The wind energy has been exploited for thousands of years. The oldest applications of wind power were providing mechanical power to pump water from wells and making flour out of grain. During the last decade of the twentieth century, worldwide wind capacity doubled approximately every three years. By the end of 2016, an increase of 12.5% compared to the previous year of the worldwide total cumulative installed electricity generation capacity from wind power amounted to 486.790 MW. Currently, five countries have achieved relatively high levels of wind power penetration, such as 39% of stationary electricity production in Denmark, 18% in Portugal, 16% in Spain, 14% in Ireland and 9% in Germany (Council 2011).

In order to increase the profits of wind power and to improve the performance and reliability of next generation wind technologies, a great deal of research has been focused on the better way to exploit and generate this kind of energy while lowering the cost of wind energy. The research has helped to increase the power plant productivity from 22% for wind turbines installed before 1998 to an average of 33% today (Council 2011).

A wind power conversion system involves wind turbine, induction or synchronous generator, power electronics, and control. The analysis of the functionality and efficiency of wind turbines is an important step to improve the design of wind energy conversion systems and to develop efficient effective generator control strategies. Wind speed is not predictable or reliable all time, therefore it is difficult to use a real wind turbine in the laboratory environment. So there is the need to build a WTE to emulate different aerodynamic phenomena present in the rotor of a wind turbine and to provide an easier testing environment for generator control strategies. WTE can drive an electrical generator in similar ways as a real wind turbine for given wind velocities in a controlled and safe environment. Moreover, it is an excellent tool for academic purposes such as control, operation, and characterization of a wind turbine.

The goal of this project was to develop such a test platform using as much real-world data as possible. The WTE is composed of a 0.8 KW DC motor coupled to the shaft of a permanent magnet synchronous generator (PMSG). The DC motor has an electrical drive system controlled in real time by a software developed in Matlab/Simulink environment. The interface between software and drive system is performed by a Data Acquisition Card NI6009 (DAC).

11.2 Literature Survey

Many studies describe wind turbine emulators either based on DC motor (Arifujjaman et al. 2008; Kouadria et al. 2013; Li et al. 2007), induction motor (Kenneth et al. 2016; Martinello et al. 2016; Soltoski et al. 2016; Voltolini et al. 2012) or permanent magnet synchronous machine (PMSM) (Yan et al. 2016). The most

common type of motor used in the construction of WTE is DC motor because it is easy to implement and because the direct relationship between armature current and the torque produced by the machine.

There are several approaches for emulators used in different situations depending on the desired requirements such as the power range and the type of wind turbine. The input to the emulator is wind speed profile, which is instantiated in a mathematical wind turbine model to determine the reference torque output which in turn is used to control the torque of the motor shaft. This mathematical model is one of the key issues for the efficiency of WTE. The fundamental aspect of turbine modeling is the aerodynamics effects, that is, a model which interprets the effects of the wind on the turbine system. The fundamentals of this idealized model are widely available in the literature (Han and Chen 2009; Lu et al. 2012; Pao and Johnson 2009) where the aerodynamic power output of the wind turbine is a function of parameters such as wind speed, turbine rotor speed, air density and turbine rotor area.

Another key issue in the aerodynamic model of the wind turbine is the blade pitch control. The wind turbine operates mainly in four regions delimited by the critical operating points. The first critical point encountered by the wind turbine is the cut-in speed. Below this speed the wind turbine does not operate at all; once this speed reached, the turbine begins to produce power. As the wind speed increases the next critical point that is reached is the rated speed. At this point, the blades have been pitched to capture as much energy from the wind as it can and the generator produces as much power as possible. Once the wind speed exceeds the rated wind speed, the turbine blades begin to adjust their pitch to minimize the capturing of energy by shedding some of the energy in the wind. The turbine continues to produce its maximum power even though the wind speed is larger than the turbines rated value. As the wind speed increases, the turbine continues to adjust the pitch of its blades until they reach their mechanical limit. At this point, the turbine must shut-down to prevent damages. This point is well known the cut-out speed (Clark et al. 2010; Hardy and Jewell 2011).

These regions of operation are shown in Fig. 11.1 where θ represents the blade pitch angle. The best way to exploit the maximum capacity of the wind in wind energy conversion systems is through the variable speed wind turbines with pitch angle control. However previous studies into the emulation of wind turbine system do not pay attention to the control of pitch angle system (Van et al. 2015).

In order to make the WTE system more efficient and able to provide a complete substitution of the real wind turbine, we presented the pitch control using a Fuzzy Logic Controller for their usefulness when the system is nonlinear, such as the wind.

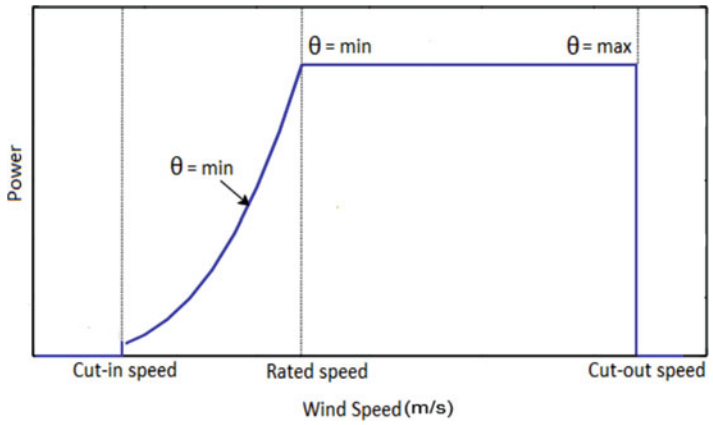

Fig. 11.1 Regions of wind turbine operation

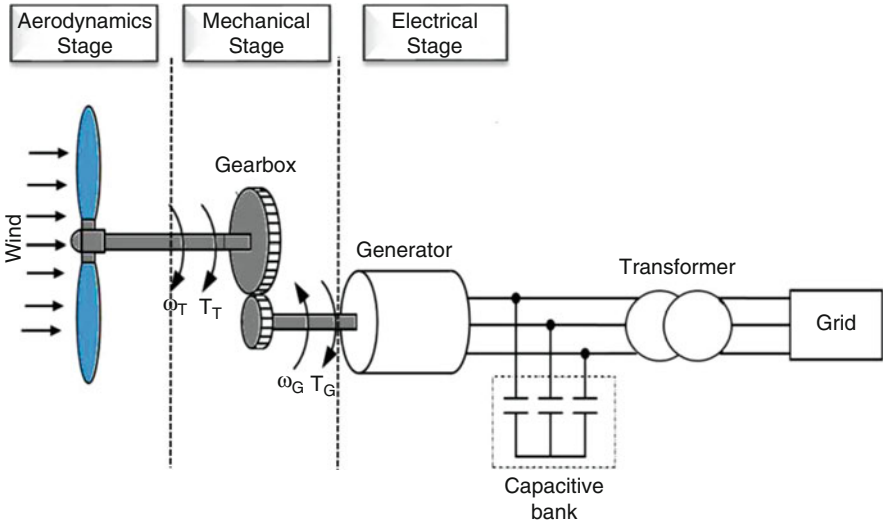

Fig. 11.2 Wind power system

11.3 Dynamic Models for Wind Power System

A wind power system can be described using three mathematical models: aerodynamic, mechanical, and electrical model. Figure 11.2 shows the basic structure of the wind power system.

11.3.1 Aerodynamic Model

11.3.1.1 Aerodynamic Power

The mechanical power extracted by the wind turbine is expressed as:

$$P_T = \frac{1}{2}\pi\rho R^2 V^3 Cp(\lambda, \beta) \tag{11.1}$$

where, ρ is the air density (kg/m3), R is the turbine radius (m), V is the wind speed (m/s) and Cp is the power coefficient which is a function of both blade pitch angle β and tip speed ratio (TSR) λ. The tip speed ratio λ is expressed as:

$$\lambda = \frac{\omega R}{V} \tag{11.2}$$

where, ω is the angular speed of the turbine rotor (rad/s), and R is the radius of turbine blades and V is the wind speed (m/s). The curve power that relates Cp to the different value of pitch angle β and TSR λ is different for each wind turbine and it is obtained from direct measurements of the turbine in operation. The generic equation used to model the Cp is obtained from the curve power for different points of operation of the turbine. A numerical approximation that is commonly used for the determination of Cp is:

$$C_p(\lambda, \beta) = c_1\left(\frac{c_2}{\lambda_i} - c_3\beta - c_4\right)\exp\frac{-c_5}{\lambda_i} + c_6\lambda \tag{11.3}$$

$$\frac{1}{\lambda_i} = \frac{1}{\lambda + c_7\beta} - \frac{c_8}{\beta^3 + 1} \tag{11.4}$$

Table 11.1 shows the parameters of the performance coefficient.

The torque developed in the shaft of a wind turbine is expressed as:

$$T_a = \frac{\frac{1}{2}\pi\rho R^3 V^2 Cp(\lambda, \beta)}{\lambda} \tag{11.5}$$

According to Eq. (11.5), the mechanical torque of the wind turbine is relative to the wind speed. Therefore it is expected to produce a torque with a stochastic profile.

Table 11.1 Parameters of the performance coefficient

c_1	c_2	c_3	c_4	c_5	c_6	c_7	c_8
0.5109	116	0.4	5	21	0.0068	0.08	0.0035

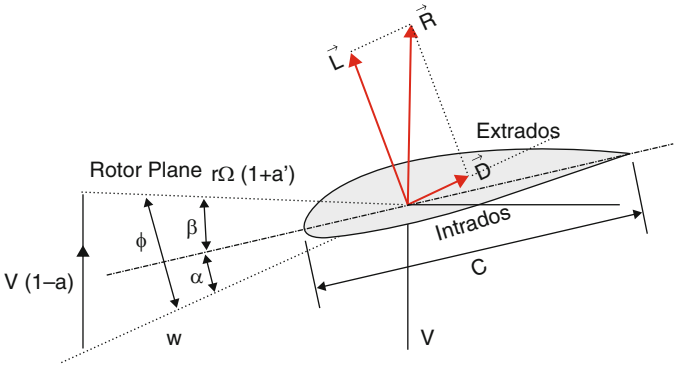

Fig. 11.3 Profile of a turbine blade

11.3.1.2 Blade Aerodynamics

Blade Element Momentum (BEM) method can be used to examine how a wind turbine works and to predict the blade forces produced due to the interaction of the blade and the wind. When the wind passes through the rotor plane and interacts with the moving rotor, a resultant relative velocity at the blade is introduced, depicted as W in Fig. 11.3, which is the difference between the undisturbed wind velocity and the blade tip velocity.

$$W = \sqrt{V^2(1-a^2) + \Omega^2 r^2 (1+a')^2} \tag{11.6}$$

Where V is the wind velocity perpendicular to the rotor plane, r is the distance of blade element from the rotor axis, a and a' are the flow factors and Ω is the angular velocity of blades.

The aerodynamics forces on the blade are the lift force and the drag. The lift force is:

$$\mathbf{L} = \frac{1}{2}\rho c W^2 C_L \tag{11.7}$$

The drag force is:

$$\mathbf{D} = \frac{1}{2}\rho c W^2 C_D \tag{11.8}$$

where C_L and C_D are respectively the lift and drag coefficient, c is the chord length of the blade and ρ is the air density.

The resultant relative velocity at the blade W creates an angle with the blade chord C, depicted as α in Fig. 11.3, the angle of attack. It is controlled by rotating the blade about its axis. The pitch angle β is the angle formed by the blade chord C and the rotor plane. The power of the wind turbines depends on the wind velocity,

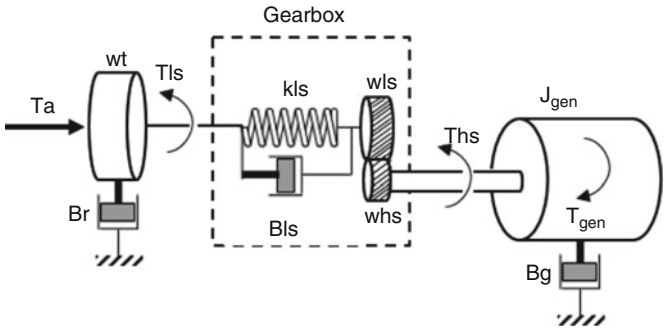

Fig. 11.4 Mechanical model of wind turbine

it increases as the wind increases. Therefore the wind turbine must be protected against the risk of damages from the strong wind. This can be achieved by rotating the blade about its axis in a position where a part of incoming wind will pass by the wind turbine. The angle of attack α decreases when the pitch angle β increases. The lift force **L** decreases as well and this reduces the wind turbine's mechanical power.

11.3.2 Coupling System and Transmission

The mechanical model of a wind turbine is currently modeled by two rotating masses. Such model includes the rotor of the wind turbine and the generator shaft. A gearbox or direct coupling connects them. Figure 11.4 shows the structure of the mechanical model of the wind turbine.

The parameters presented in Fig. 11.4 are described below:

T_a: Torque of the turbine applied on the rotor;
T_{ls}: Torque applied on low-speed shaft;
T_{hs}: Torque applied on high-speed shaft;
T_{gen}: electromagnetic torque of generator;
ω_t: rotor angular speed;
ω_{ls}: angular speed of the low-speed shaft;
ω_{hs}: angular speed of the high-speed shaft;
B_r: rotor damping effect;
B_{ls}: low speed damping effect;
B_g: high speed damping effect;
k_{ls}: Stiffness of low speed shaft;
J_g: moment of inertia of the generator;
n_g: speed multiplication ratio.

Thus, the equations for the mechanical model of the wind turbine are:

$$T_a - T_l s = J_r \dot{w}_t + B_r w_t \tag{11.9}$$

$$T_l s = B_l s(w_t - w_l s) + k_l s(\theta_t - \theta_l s) \tag{11.10}$$

$$T_h s - T_g en = J_g \dot{w_h} s + B_g w_h s \tag{11.11}$$

$$n_g = \frac{T_l s}{T_h s} \tag{11.12}$$

11.3.3 Electrical Model

The electrical dynamic equations of permanent magnet synchronous generator PMSG are expressed as:

$$V_d = R_s i_d - \omega_e L_q i_q + L_d \frac{di_d}{d_t} \tag{11.13}$$

$$V_q = R_s i_q + \omega_e (L_d i_d + \Psi_f) + L_q \frac{di_q}{d_t} \tag{11.14}$$

$$\frac{di_d}{dt} = \frac{1}{L_d s + L_l s}(-R_s i_d + \omega_e (L_q s + L_l s) i_q + V_d) \tag{11.15}$$

$$\frac{di_q}{dt} = \frac{1}{L_q s + L_l s}(-R_s i_d - \omega_e [(L_d s + L_l s) i_d + \Psi_f] + V_q) \tag{11.16}$$

Where ω_e is the angular speed of the reference frame ($\omega_e = p\omega_g$), p is the number of pole pairs, L_d and L_q are the inductance of the stator winding in the synchronous reference frame, Ł$_l s$ is the leakage inductance, Rs is the stator resistance, and ψ_f is the flux constant of the generator rotor.

Figure 11.5 shows the equivalent circuit of the PMSG in d-q synchronous rotating reference frame.

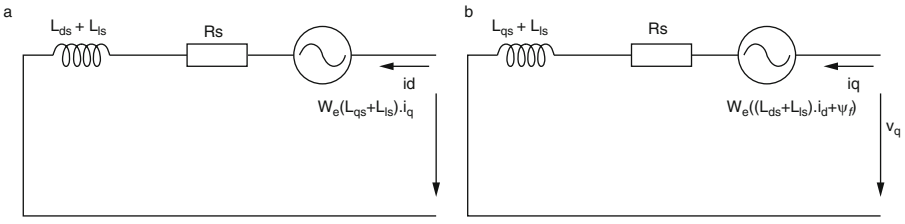

Fig. 11.5 Equivalent circuit of the PMSG: (**a**) d-axis equivalent circuit, (**b**) q-axis equivalent circuit

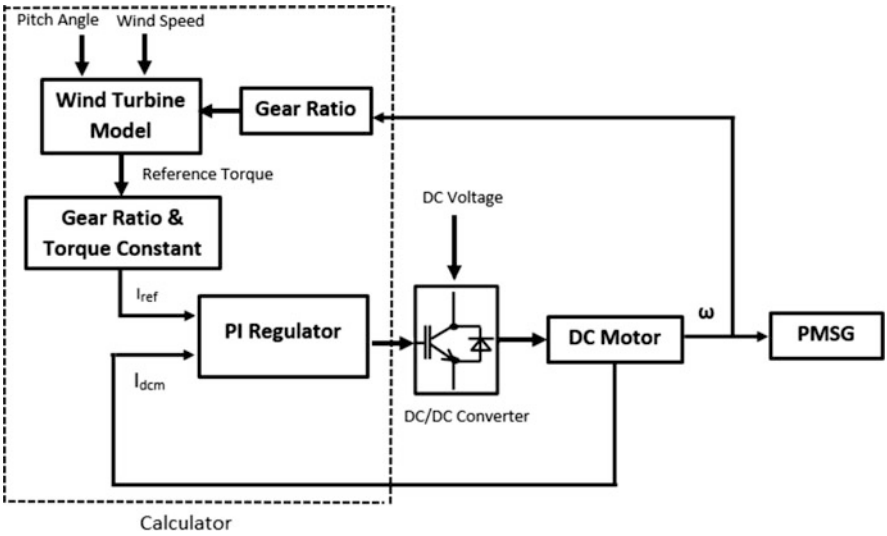

Fig. 11.6 Structure of wind turbine emulator

The electrical torque T_g of the generator is expressed as:

$$T_g = \frac{3}{2}(\psi_p m i_q + (L_d - L_q) i_d i_q) \tag{11.17}$$

11.4 Wind Turbine Emulator Design

The structure of the WTE using a permanent magnet DC motor is represented in Fig. 11.6.

In order to emulate the real behavior of the wind turbine with a DC machine and its control, it is necessary to determine the electromagnetic reference torque. The inputs to the wind turbine's mathematical model are angular speed, pitch angle, and wind speed. The reference torque derived from the model of the turbine is multiplied by Gear Ratio and motor constant to obtain the reference current, which is compared with the actual DC motor armature current. The difference between the two currents is the input of a proportional-integral (PI) controller. It is then used to generate PWM gate pulses to drive the transistor of the DC-DC buck converter that regulates the DC motor armature voltage. Then the variation in armature voltage generates a variation in the speed of DC motor, which allows obtaining a mechanical torque which depends on the wind velocity and varies over the time in a similar way as the torque of the wind turbine.

11.5 Pitch Angle Control

11.5.1 Dynamic Actuator

The main objectives for blade angle control are:

- Optimization of the wind turbine output power, by producing as much power as possible with the available wind.
- Prevention for mechanical power does not exceed the rated power in high winds.
- Protection against overloading of the turbine structure and risks of damage to their physical structure at the strong wind.

The pitch angle actuator consists of a mechanical and hydraulic system, it is used to turn the blades along their longitudinal axis. The blade angle control can be done in two stages (Macedo and Mota 2012)

1. Pitch control: the mechanical power is reduced when the pitch angle grows. This principle is applied, in most cases, in variable wind speed turbine. Fixed speed turbines can also use this control;
2. Active stall control: the mechanical power is reduced when the pitch angle decreases. This type of control is commonly applied in fixed wind speed turbines.

11.5.2 Pitch Angle Control Using Fuzzy Control

As the aerodynamic power depends on the wind speed, it is nonlinear. Therefore the control of variable speed wind turbine could not perform correctly with conventional methods (Sahoo et al. 2016). The use of fuzzy logic controller FLC can overcome these problems. It does not require a well-known system, ease of its modeling and its implementation. It is presented as an alternative for Proportional-Integral (PI) controllers currently used in wind turbine Pitch Angle Control (Yin et al. 2015). The FLC uses the rules determined with linguistic expressions derived from a human expert who has some experience and knowledge about the system. Figure 11.7 shows the diagram of general FLC. It consists of three stages: an input stage, a processing stage, and output stage. The Fuzzification stage translates the input data to the fuzzy representation incorporating the vagueness and imprecision in a natural language. The processing stage or the inference consists in evaluating the rules and generates results. The De-Fuzzification stage converts the results into a specific control output value.

Figure 11.8 shows the pitch angle control block diagram using fuzzy control.

The present work developed the fuzzy control using the Fuzzy Logic ToolboxTM of Matlab/Simulink. Figure 11.9 represents Membership function plots of input and output of the FLC using Mamdani's fuzzy inference method to define how each point in the universe of discourse is mapped to a degree of membership between 0 and 1.

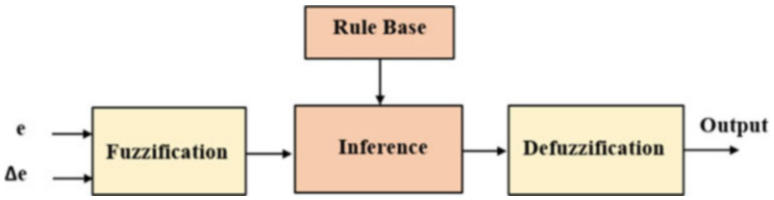

Fig. 11.7 Diagram of general FLC

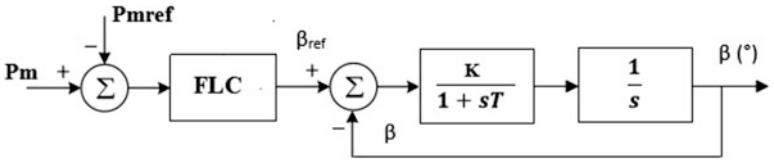

Fig. 11.8 Pitch angle block diagram using Fuzzy Logic controller

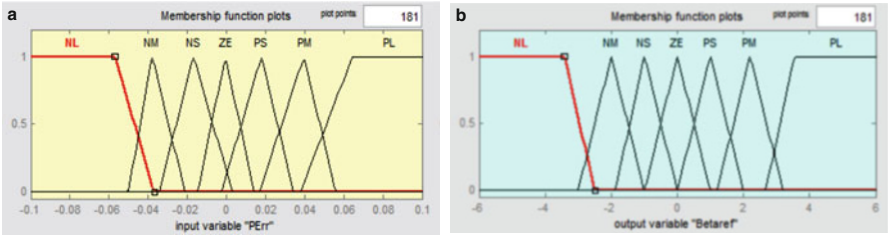

Fig. 11.9 The Membership function plots of the FLC: (**a**) Membership function input, (**b**) Membership function output

Table 11.2 Rules base for FLC

ΔP	NL	NM	NS	ZE	PS	PM	PL
β_r	NL	NM	NS	ZE	PS	PM	PL

Table 11.2 gives the rule base modeled in this work for the FLC.
The abbreviations used in the presented tables are defined as follows:

- NM is negative medium;
- NS is negative small;
- ZE is Zero;
- PL is positive large;
- PM is positive medium;
- PL is positive large.

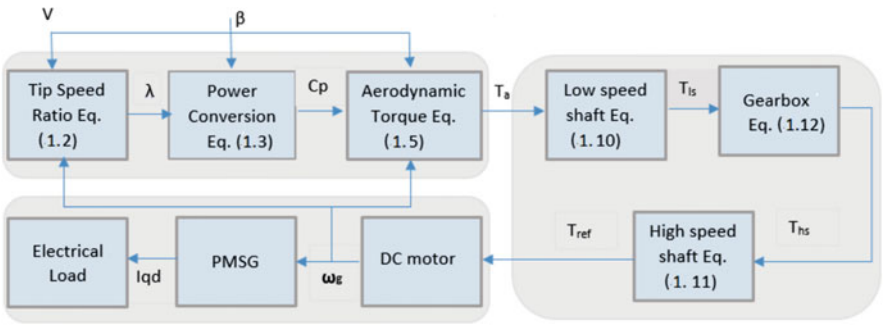

Fig. 11.10 Block diagram of the WTE

11.6 Simulation Results

Based on the different mathematical models of wind power system presented previously, a software application was developed in Matlab/Simulink® to compare them with the waveforms of the experimental results. Figure 11.10 presents the block diagram of the implemented and simulated WTE system. The wind profile exploited in this simulation is presented in Fig. 11.14 and it is modeled in the deterministic form of a sum of several harmonics:

$$V(t) = 9 + 0.2\sin 0.0021t + 2\sin 0.0053t + \sin 0.0259t + 0.2\sin r0.0733t \tag{11.18}$$

As it can be analyzed from Fig. 11.11, there is a high level of correspondence between wind speed profiles applied to wind turbine model and the characteristics of different responses of WTE such as the torque, the speed and the armature current of DC motor. This demonstrates that the PI controller has a good performance tracking.

Figure 11.11 shows the different values of the pitch angle β for different wind velocities. Adjusting the pitch angle of the blades provides an effective way to regulate or limit the turbine performance in strong wind speeds. The pitch angle β, increases and the angle of attack, decreases when the wind speed increases. The lift force decreases as well and the mechanical power of WTE is then reduced.

The simulation waveforms obtained in this section will be used to verify the emulator dynamics in the next section.

11.7 Experimental Results

In order to duplicate the similar waveform of the aerodynamic torque of the wind turbine on a small scale, an adaptation of the torque's magnitude is required. This adaptation is simply achieved through a gain which is the ratio between the rated power of the machine and that of the turbine (Fig. 11.12):

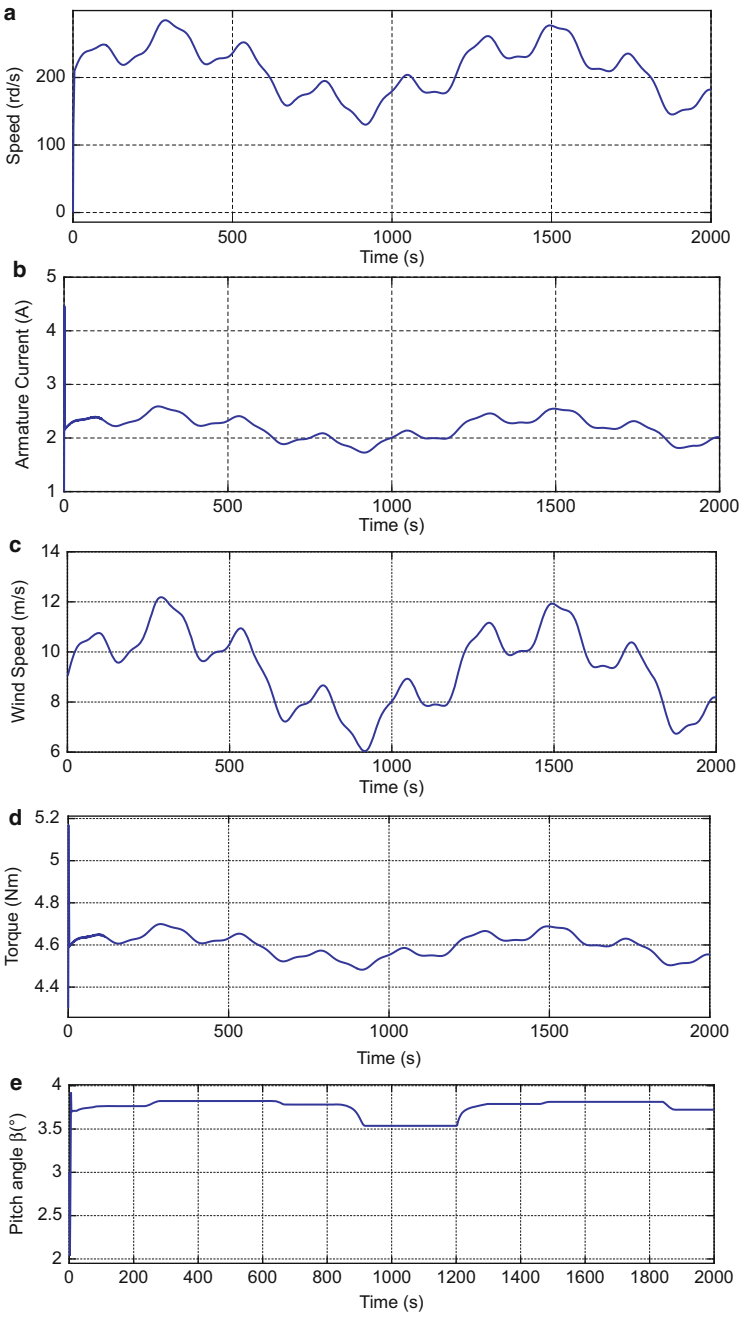

Fig. 11.11 Simulation results of WTE: (**a**) Variation of rotational speed of DC motor, (**b**) Variation of armature current of DC motor, (**c**) Wind speed profile, (**d**) Variation of torque of DC motor, (**e**) Variation of pitch angle β

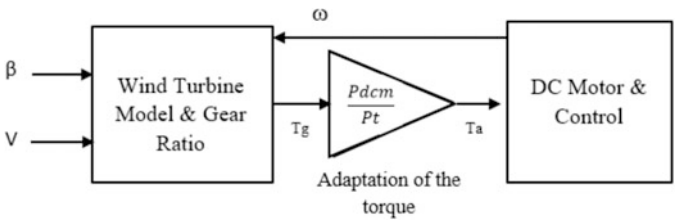

Fig. 11.12 Adaptation of the aerodynamic torque

Table 11.3 Parameters of the DC motor and PMSG

Equipment	Parameters
DC motor	Type MSS-8
	Permanent magnet
	Rated power: 0.8 kW
	Rated armature voltage: 90 V
	Rated armature current: 10.7 A
	Rated speed: 3000 rpm
PMSG	Type MA-6
	Stall torque: 3.6 N
	Rated armature voltage: 127 V
	Stall current: 4.2 A
	Max mechanical speed: 6000 rpm

$$G = \frac{P_d cm}{P_T} \tag{11.19}$$

The test setup consists of the following:

- DC motor with rated values shown in Table 11.3;
- Permanent Magnet Synchronous Generator (PMSG) with rated values shown in Table 11.3;
- DC-DC Buck Converter;
- Electronic card with voltage sensors and current sensors;
- Calculator;
- Data acquisition card NI6009.

Table 11.3 shows the parameters of DC motor and PMSG.

Figure 11.13 shows the hardware structure of the wind energy system and the photograph of the experimental setup.

A real time calculator monitors the control parameters whilst in operation. The Data Acquisition Card NI6009 (DAC) allows communication between the setup and the user. Various turbine parameters like the wind velocity and pitch angle can be set by the user. To calculate the current reference the program reads wind velocity and pitch angle value from the input data file and measured armature current from current sensor and speed from the tachometer. The calculated reference current is

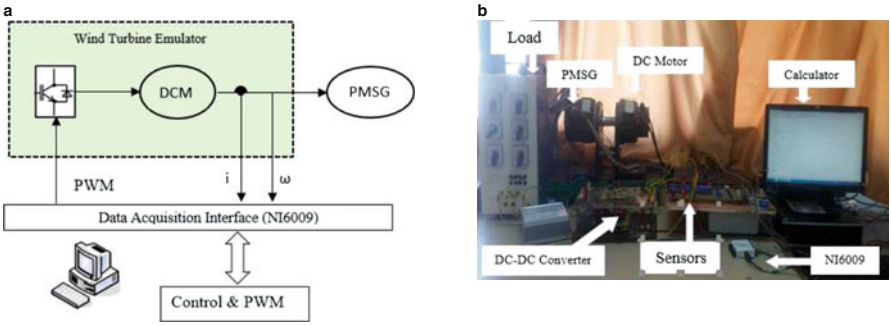

Fig. 11.13 Experiment setup: (**a**) Hardware structures of wind energy systems, (**b**) Photograph of experiment setup

given to the PI controller. The output of PI controller is passed to hardware interface (PWM Control Circuits) through analog output channel of DAC and finally, DC-DC buck converter drives the DC motor where the firing pulses are generated by changing the armature voltage. The output voltage profile of the generator (PMSG) directly depends on the shaft speed.

Most of the effort during the experimentation was focused on adjusting the weighting for the PI controller for DC motor.

Figure 11.14 shows the results of rotational speed, armature current and torque characteristics of WTE for different wind velocities. As it can be concluded from the figures, there is a high level of correspondence between the wind speed profiles applied to wind turbine model and characteristics of different responses of WTE such as the torque, the speed, and the power coefficient. It means that the PI controller has a good performance tracking.

As it can be depicted from obtained figures, there is a good deal of match between simulated and experimental results.

The results verified that the WTE can efficiently reproduce the steady-state and dynamic behavior of a wind turbine for a given wind velocity.

11.8 Conclusion

This chapter described the main components of a WTE based a on permanent magnet DC motor controlled by PWM implemented in the laboratory.

In order to check the emulator's dynamics, an experimental evaluation was presented and compared with simulated ones. Considering simulation and experimental waveforms for different wind conditions and their effects on several aerodynamic and mechanical variables, The WTE can supply all required parameters of the wind turbine system such power coefficient, tip speed ratio, output torque and output power.

The control of pitch angle is one of the main steps in the emulation of the wind turbine for providing more realistic conditions for the emulator and a complete substitution of the real wind turbine. However, most of the previous studies into the WTE systems do not take into account the control of pitch angle despite the best way to extract the maximum power of the wind is through the variable speed wind turbines with pitch angle control.

Fuzzy Logic Controller FLC is used in the pitch angle control system for their high accuracy, fast dynamic response, stability, solving nonlinear systems such as the wind which has the nonlinearity as its main characteristic.

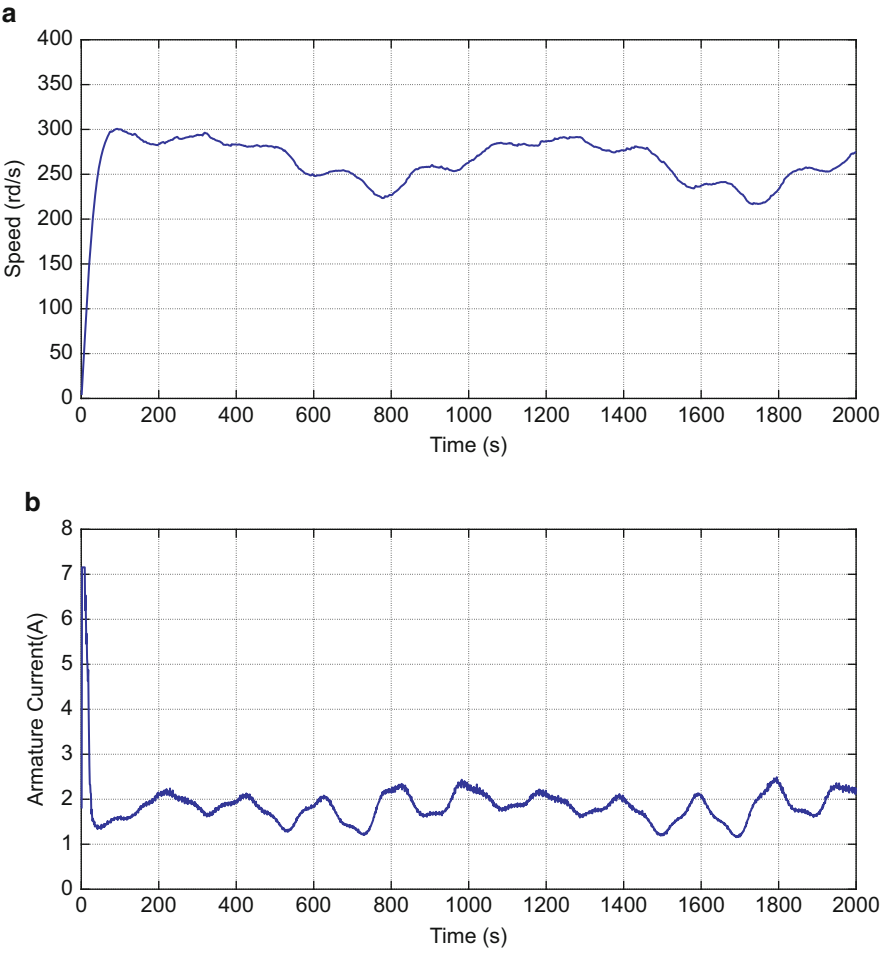

Fig. 11.14 Experimental results of WTE: (**a**) Variation of rotational speed of DC motor, (**b**) Variation of armature current of DC motor, (**c**) Wind speed profile, (**d**) Variation of torque of DC motor

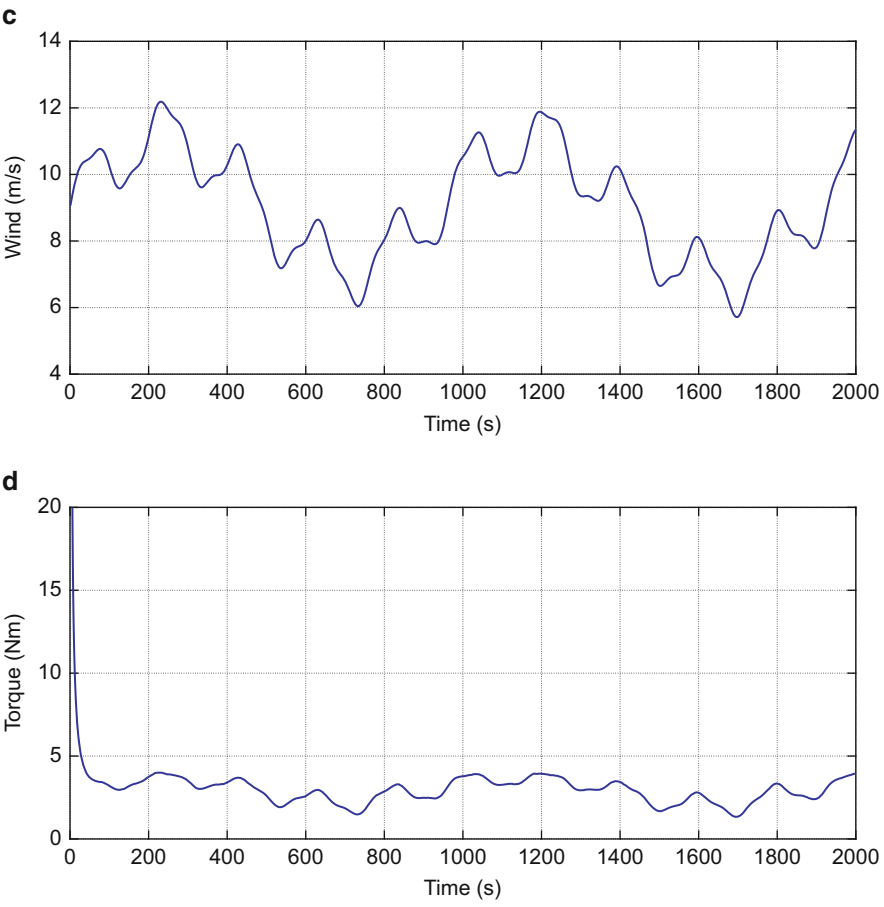

Fig. 11.14 (continued)

A key limitation of this research is the high cost of the DC motor in the structure of WTE systems compared to other electrical machines in the same power range and also it demands higher maintenance requirements due to its commutators and brushes. The next stage of our research will be an emulation system of a wind turbine based on an induction motor (IM) to overcome this limitation.

References

Arifujjaman, M., Iqbal, M., & Quaicoe, J. E. (2008). Emulation of a small wind turbine system with a separately-excited DC machine. *IU-Journal of Electrical & Electronics Engineering, 8*(1), 569–579.

Clark, K., Miller, N. W., & Sanchez-Gasca, J. J. (2010). Modeling of GE wind turbine-generators for grid studies. *GE Energy, 4*, 4.13–4.17.

Council, G. W. E. (2011). Annual market update 2011. Global Wind Report, Online: http://www.gwec.net

Han, K., & Chen, G.-Z. (2009). A novel control strategy of wind turbine MPPT implementation for direct-drive PMSG wind generation imitation platform. In *Power Electronics and Motion Control Conference, 2009. IPEMC'09. IEEE 6th International*, Wuhan, China (pp. 2255–2259). IEEE.

Hardy, T., & Jewell, W. (2011). Emulation of a 1.5 MW wind turbine with a DC motor. In *Power and Energy Society General Meeting, 2011 IEEE*, Detroit, MI, USA (pp. 1–8). IEEE.

Kenneth, A., et al. (2016). Emulator for fixed pitch wind turbine studies. *Renewable energy*. London: Taylor & Francis Ltd.

Kouadria, S., Belfedhal, S., Meslem, Y., & Berkouk, E. M. (2013). Development of real time wind turbine emulator based on DC motor controlled by hysteresis regulator. In *2013 International Renewable and Sustainable Energy Conference (IRSEC)*, Ouarzazate, Morocco (pp. 246–250). IEEE.

Li, W., Xu, D., Zhang, W., & Ma, H. (2007). Research on wind turbine emulation based on DC motor. In *2nd IEEE Conference on Industrial Electronics and Applications, ICIEA 2007*, Harbin, China (pp. 2589–2593). IEEE.

Lu, L., Xie, Z., Zhang, X., Yang, S., & Cao, R. (2012). A dynamic wind turbine simulator of the wind turbine generator system. In *2012 Second International Conference on Intelligent System Design and Engineering Application (ISDEA)*, Sanya, Hainan, China (pp. 967–970). IEEE.

Macedo, A., & Mota, W. (2012). Wind turbine pitch angle control using fuzzy logic. In *Transmission and Distribution: Latin America Conference and Exposition (T&D-LA), 2012 Sixth IEEE/PES* Montevideo, Uruguay (pp. 1–6). IEEE.

Martinello, D., Carati, E. G., da Costa, J. P., Cardoso, R., & Stein, C. M. (2016). Emulation of wind turbines. In A. G. Aissaoui & A. Tahour (Eds.), *Wind turbines-design, control and applications*. Rijeka: InTech.

Pao, L. Y., & Johnson, K. E. (2009). A tutorial on the dynamics and control of wind turbines and wind farms. In *American Control Conference*, *ACC'09*, St. Louis, MO, USA (pp. 2076–2089). IEEE.

Sahoo, S., Subudhi, B., & Panda, G. (2016). Pitch angle control for variable speed wind turbine using fuzzy logic. In *2016 International Conference on Information Technology (ICIT)*, Bhubaneswar, India (pp. 28–32). IEEE.

Soltoski, J. C. F., dos Santos, P. T. P., & Font, C. H. I. (2016). Development of a small scale wind turbine emulator work bench. In *12th IEEE International Conference on Industry Applications (INDUSCON)*, 2016, Curitiba, Brazil (pp. 1–8). IEEE.

Van, T. L., Nguyen, T. H., & Lee, D.-C. (2015). Advanced pitch angle control based on fuzzy logic for variable-speed wind turbine systems. *IEEE Transactions on Energy Conversion, 30*(2), 578–587.

Voltolini, H., Granza, M. H., Ivanqui, J., & Carlson, R. (2012). Modeling and simulation of the wind turbine emulator using induction motor driven by torque control inverter. In *10th IEEE/IAS International Conference on Industry Applications (INDUSCON), 2012*, Fortaleza, Brazil (pp. 1–6). IEEE.

Yan, J., Feng, Y., & Dong, J. (2016). Study on dynamic characteristic of wind turbine emulator based on PMSM. *Renewable Energy, 97*, 731–736.

Yin, X.-x., Lin, Y.-g., Li, W., Gu, Y.-j., Wang, X.-j., & Lei, P.-f. (2015). Design, modeling and implementation of a novel pitch angle control system for wind turbine. *Renewable Energy, 81*, 599–608.

Chapter 12
SSDI-Max Control and Its Applications in Renewable Energies

Aida Chérif, Djamila Zehar, Nabil Derbel, and Claude Richard

Abstract The vibration control using piezoelectric elements is an area interesting several industrial sectors. Modal synchronized switch damping on inductor control is a vibration damping technique that combines advantages of passive and active control techniques based on a modal strategy. Within this framework, we propose an improved control technique, which is called modal SSDI-Max. The particularity of this new approach is to maximize the self-generated voltage amplitude by a proper definition of the switch instants (voltage inversion) according to the chosen targeted mode. Following the basic modal synchronized switch damping on inductor technique, the switch is synchronized with the chosen modal coordinate extremum. In the investigated approach, the voltage is increased by waiting for the next voltage extremum following immediately any targeted modal coordinate extremum in a given time window. This chapter presents simulations performed on a model representative of a clamped plate. Damping results are given in the case of multimodal, pulse or noise excitations. The chapter analyses the control time window influence on the damping performance of the system.

Keywords Piezoelectric · Smart structures · Modal control · Semi active control · SSDI-Max · Time window

A. Chérif (✉)
LAS Laboratory, University of Bordj Bou Arréridj, El Anasser, Algeria
e-mail: aida.cherif@univ-bba.dz

D. Zehar
LSI Laboratory, University of Bordj Bou Arréridj, El Anasser, Algeria
e-mail: djamila.zehar@univ-bba.dz

N. Derbel
CEMLab Laboratory, University of Sfax, Sfax, Tunisia
e-mail: n.derbel@enis.rnu.tn

C. Richard
LGEF Laboratory, INSA, University of Lyon, Lyon, France
e-mail: claude.richard@insa-lyon.fr

N. Derbel, Q. Zhu (eds.), *Modeling, Identification and Control Methods in Renewable Energy Systems*, Green Energy and Technology,
https://doi.org/10.1007/978-981-13-1945-7_12

12.1 Introduction

All mechanical systems are subjected to various conditions that may result in vibration motion. These vibrations often lead to material fatigue, structural damage and failure, deterioration of system performances and increase of noise levels. These effects are usually prominent around natural frequencies of the system. Such vibrations cannot be tolerated and, therefore, developing a strategy for reducing these vibrations has been a major focus of research. This subject has considerable industrial consequences. Vibrations and acoustic control are used in many domains such as automobiles, aeronautics, aerospace, machine tools, etc.

In vibration control the aim is the amplitude limitation of the vibrating structure in order to improve the reliability of their functions. Vibration control of a structure also allows increasing its resistance to fatigue then increasing the duration of its live. One of recent strategies of vibration and acoustic control is the control by intelligent materials. In general, three types of vibration control using piezoelectric inserts are pointed out in the literature:

- Passive techniques (Eielsen and Fleming 2010; Forward 1979; Hagood and Von Flotow 1991) consist of connecting a passive electrical network (usually an inductive network) to the piezoelectric insert(s), these techniques can be difficult to implement: attainable trade-off between performances and bandwidth or feasibility of the required inductor are the usual drawbacks (Wu and Bicos 1997).
- Active techniques (Fuller and Jones 1987; Meyer and Collet 2011; Preumont et al. 2002; Snyder and Hansen 1991) consist of a control system with actuators supplied by a controlled electric field usually generated by an amplifier driven by a feedback loop using sensors and according to a given control theory approach. It is a very powerful and global technique allowing a diversity of strategies. In these techniques, there is an external source supplying both the control energy for the control loop circuitry and the operative energy delivered by the power amplifier.
- Semi active techniques (Clark 2000; Cunefare and Holdhusen 2004; Niederberger et al. 2004; Petit et al. 2004; Richard et al. 2000) are techniques using no external operative energy. They rely on switches allowing management of the piezoelement electrostatic energy and/or electric boundary conditions.

Among these vibration damping techniques are synchronized switch damping (SSD) techniques originally developed by (Guyomar and Badel 2006). The overall principle is to introduce, using a proper switching sequence, strong nonlinearities in the voltage generated by the piezoelectric inserts, which have the effect of modifying significantly the voltage amplitude and phase, resulting in increased dissipation and mode damping. Among these methods, synchronized switch damping on inductor (SSDI) consists in inverting the piezo voltage each time it reaches an extremum.

Another way to address the multimodal problem is the so-called modal SSDI control developed by Harari et al. (2009). The principle is to combine advantages

of both active control techniques and the semi active SSD damping. Relying on a modal model of the structure, this method allows controlling a given targeted mode. The principle is to shape the piezoelement voltage nearly out of phase with the targeted modal speed. To do so, the technique relies on a modal filter allowing the computation of the modal coordinates of the vibrating structure and on an SSDI switch device synchronized with the extremum of the targeted modal coordinate. An improvement of the modal SSDI control was proposed by Richardet et al. (2009); the purpose of this latter technique called "SSDI-Max" is to use part of the energy of the non targeted mode to improve the piezoelement voltage. The inversion is scheduled at the maxima of the target modal coordinate, unless the voltage varies with the corresponding slope at that moment.

This chapter presents an analysis of the performance of the SSDI-Max damping technique with a plate-structure. It relies on simulations, made with the Matlab-Simulink environment, using a realistic model of a plate structure previously identified. For this structure the piezoelement coupling coefficient are not optimal and very representative of a real target application structure. Moreover, compared to the beam case, frequency modes are rather close to each other. The proposed method aims at maximizing the amplitude of the piezoelectric actuator by the definition of an optimal switching time according to the chosen targeted mode. The smart structure modeling along with the plate structure investigated is described. The SSDI-Max strategy is then exposed. The performances of the SSDI Max method for the control of single modes of the structure are described in the case of sinusoidal, pulse and white noise excitation. Finally, the influence of the delay time window used is described again for various type of excitation.

12.2 Vibration Controls by Piezoelectric Elements

In many industrial and defense applications, vibrations present a major scientific and technological issue. The objectives sought by vibration damping have different aspects, such as improving comfort in acoustics and mechanics, the stability of increasingly light structures or increasing the life of materials... In the field of embedded systems, the aim is to reduce vibrations as efficiently as possible while limiting the mass and the volume of the control system. In order to achieve this goal, it is necessary to use efficient methods while reducing or even eliminating the energy required to control these vibrations.

In this part we present the state of the art on the vibration control, the different types of control that excite and finally we briefly give a summary on nonlinear methods developed in the laboratory of electrical and ferroelectric engineering LGEF for the control.

12.2.1 Passive Control

Passive control has the advantage of requiring neither energy nor information to function. It consists of connecting the piezoelectric element to a circuit consisting of passive components, for example a resistor. The purpose of this circuit is to dissipate the electrical energy provided by the piezoelectric element Joule effect. The advantages of passive techniques are:

- Easy adjustment of the electrical system,
- A weight and a size of elements to be added to the structure insignificant,
- An unconditionally stable system.

While passive damping can greatly improve the damping of the system, beyond their simplicity, passive techniques possess certain number of limitations. First, for low structural frequencies, the value of inductance to the resonant shunt circuit can be quite large. A passive inductor of this size could easily preclude its use for lightweight applications (air/space, tennis rackets, etc.). Secondly, the resonant shunt technique can only be compatible to one structural mode (Carriere 2010; Franklin et al. 1990; Wu and Bicos 1997).

12.2.2 Active Control

This type of control is usually more performing than passive technique. But the fundamental difference is on the need of the external source of energy for driving control actuators. Nevertheless, they are complex for practical implementation and in general rely on a complete chain comprising sensors, calculation unit, power amplifiers and actuators. The raw principle of the active control uses an external source to generate forces that interfere with the wave or the system vibration in order to minimise it. This method needs a network of sensors along with a good model of the structure to get a situation of the vibration or acoustic and actuators to act on the vibration or the acoustic field. These diverse elements are controlled by an advanced system of management (microcontroller, DSP. . .) that calculate the optimal control permitting the minimisation of waves or vibrations of the system (Davis and Lesieutre 2000).

12.2.3 Semi-active Control

In order to improve damping performances without using external operative energy for the actuator drive, several semi-active vibration control techniques have been proposed and developed. The advantages of semi-active vibration control present a much lower energy requirement, a rather overall low cost, and a lower complexity

compared to active control systems. Better damping performances can be obtained compared to passive control systems. The Synchronized Switch Damping (SSD) techniques have been developed by Richard et al. (2000). SSD techniques reach a good trade-off between the simplicity, external energy requirements and vibration control performances. This nonlinear technique consists of connecting intermittently the piezoelectric element to a passive shunt (small resistance or inductor) each time the voltage (or strain) reaches an extremum. It is implemented with a simple switch driven during short periods synchronously with the structure motion. No external operative energy is needed. It is extracted from the structure itself as a result of the switch process.

12.2.3.1 SSDI Control

The SSDI technique consists of a switching device in parallel with the piezoelectric elements shown on Fig. 12.1a. The capacitance of piezoelectric element C_0, inductance L and resistance R could constitute an LCR oscillator when the switch is turned on. The switch is triggered-on each time the piezoelectric voltage reaches an extremum. When the switch closes, an oscillating discharge is initiated. The on-time t_i is set to one half of the electric period of oscillator network as defined in Eq. (12.1). The switch is therefore kept closed until the piezoelectric voltage has been reversed. The voltage inversion results from the oscillating discharge of the piezoelectric element blocked capacitance in the inductance during the switching time. Because of a small inductor L value, this switching time t_i is much smaller than a mechanical oscillation period.

If the structure is excited by a sinusoidal force, when this switching sequence is repeated, the displacement of the structure and the piezoelectric voltage result in the waveforms shown on Fig. 12.1b. It is seen that the switch is nearly always open excepted for each voltage extremum. Due to the resistance R, the absolute value of piezoelectric voltage after the inversion is smaller than the initial value. This loss is modeled by the electrical quality factor Q_i of the oscillation network, which is expressed in Eq. (12.2). It is also quantified by the inversion factor γ defined by Eq. (12.3):

$$t_i \simeq \pi\sqrt{LC_0} \tag{12.1}$$

$$Q_i = \frac{1}{R}\sqrt{\frac{L}{C_0}} \tag{12.2}$$

$$\gamma = \frac{V_{after}}{V_{before}} = \exp\left(-\frac{\pi}{2Q_i}\right) \tag{12.3}$$

where, V_{before} and V_{after} are the absolute value of the piezoelectric element voltage before and after the switching, respectively.

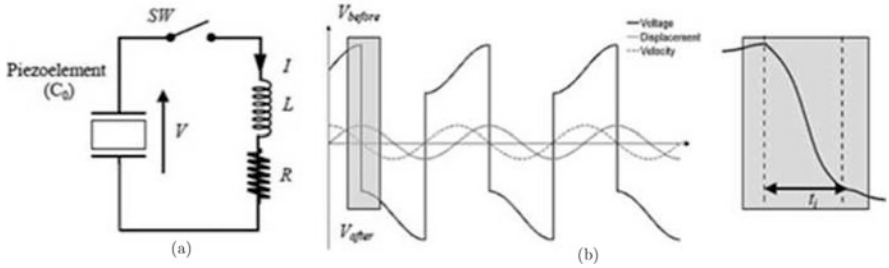

Fig. 12.1 Classic SSDI method. (**a**) SSDI circuit. (**b**) SSDI waveforms

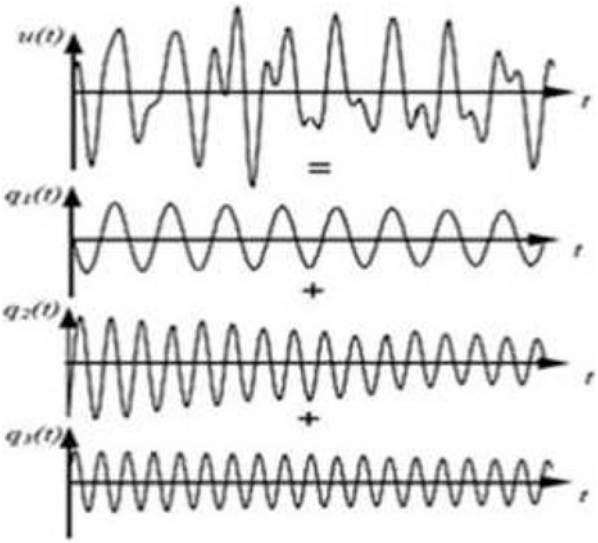

Fig. 12.2 Sum of the displacement of three modes

12.2.3.2 Modal-SSDI Control

The classical low-powered SSD techniques perform well in mono-modal excitation. However, it hardly deals with cases of the multimodal and complex vibrations. The principal difficulty is the definition of the proper switching sequence. It is illustrated on Fig. 12.2 with a composite displacement $u(t)$ built as the superposition of these modal components. Many extremum are visible making the choice of the optimal switching time.

To overcome this limitation and work on a multimodal problem with a wide bandwidth excitation, a modal approach has been implemented. It is assumed that the motion of the vibrating structure can be decomposed on a given modal basis. This decomposition is a good approximation in the case of structures with low viscous losses for which the resonance modes are clearly distinct and uncoupled. Based on the principle of the modal approach, Modal-SSDI method was developed by Harari et al. (2009).

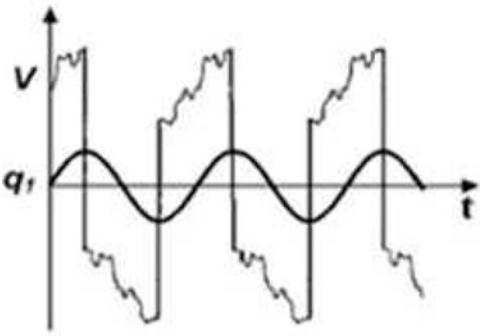

Fig. 12.3 Piezoelectric voltage V waveform when inversion is focused on the modal displacement of the first mode

The modal SSDI control is developed and based on basic SSDI method. It consists of synchronizing the switch sequence on a given modal coordinate instead of the voltage. The voltage across the actuator is therefore inversed when the displacement of the targeted mode is extremum as shown on Fig. 12.3. The principle and strategy of semi-active Modal-SSD for multimodal control is illustrated in Fig. 12.4.

The targeted modal displacement q_i can not be directly monitored by any kind of direct sensor. Several methods can be used to derive this displacement by a set of appropriate sensors. The technique implemented by Chérif et al. (2012), is based on the use of an observer which is designed using a modal model of the structure. Figure 12.4 is a schematic of the global control loop for modal SSDI control. On the upper side, the real system comprises the structure itself, which can be represented by a state-space equation. It is excited by an external force and controlled via the actuator voltage V_a. The motion of the structure can be represented by the state space vector $(q, \dot{q})$ consisting of modal displacements and modal speed coordinates. Moreover, many actuation or sensing piezoelectric patches are installed on the structure. The open-circuit voltages of the sensors V_s can be used for state monitoring of the structure. The voltage V_a developed on the piezoelectric element used as control actuator is processed according to the usual SSDI technique. On the lower side, there is the control observation loop. The purpose of this loop is to derive from the measurement voltages V_s, the proper modal coordinate q_i used to trigger the switch device. This observation loop is based on an observer, which estimates both the space-state vector $(\hat{q}, \hat{\dot{q}})$ and the sensor voltages measurement $\hat{V}_s$. This observer consists of a feedback loop gain L and of the space-state model of the structure. Modal state x is estimated and corrected due to the convergence, more or less rapidly as a function of gain L, between the measured and estimated outputs V_s and $\hat{V}_s$. The gain matrix L must be chosen so that the error on the state is globally stable and vanishes exponentially with a dynamic much quicker than the structure itself. To calculate this gain of the observer, two methods can be used such as pole placement or LQG techniques (Chérif et al. 2012).

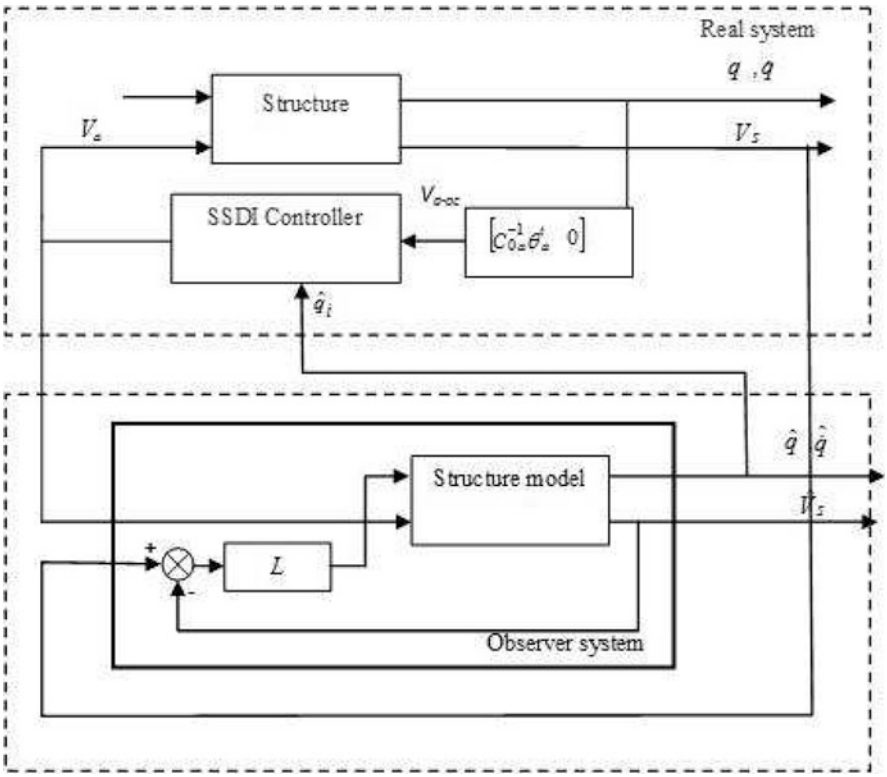

Fig. 12.4 Modal SSDI control architecture (Chérif et al. 2012)

12.3 Smart Structure Definition

12.3.1 Smart-Structure Definition

The structure coupled with one piezoelectric element is in the simplest approach described by the single of degree of freedom electromechanical model as shown in Fig. 12.5. The structure mass M is driven by an external force F. u is the displacement of the vibration structure and V is the voltage of the piezoelectric element. Based on usual hypothesis, the mechanical and electric equations governing the motion of the single degree of freedom structure are: The electromechanical behavior equations of a smart structure using usual assumption are (Harari et al. 2009):

$$m\ddot{\delta} + c\dot{\delta} + k_E\delta = -\alpha V + \beta F \tag{12.4}$$

$$I = \alpha\dot{\delta} - C_0\dot{V} \tag{12.5}$$

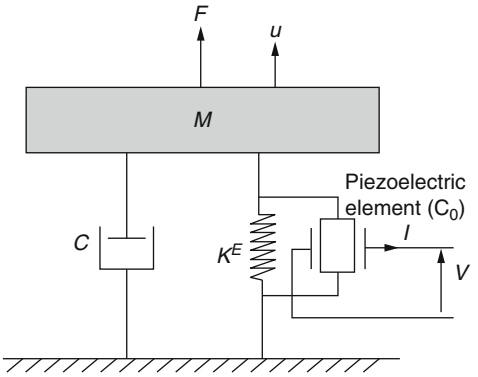

Fig. 12.5 Structure of the electromechanical model for a single degree of freedom structure corresponding to mono-modal with one piezoelectric element

with δ the nodal displacement vector, m, c and k_E are the mass, the damping and the stiffness matrices, respectively, when piezoelectric patches are in short circuit, α is the electromechanical coupling matrix, V is the voltage vector of the i piezoelectric patches, I is the electric current vector, and C_0 is the diagonal capacitance matrix. F is the force applied to the system.

By using the following variable change where ϕ is the mode shape matrix limited to n modes and q the modal displacement vector:

$$\delta = \phi\, q \tag{12.6}$$

Equations (12.4) and (12.5) can be well represented by the projection in the modal basis by:

$$M\ddot{q} + C\dot{q} + K_E q = -\theta V + \beta F \tag{12.7}$$

$$I = \theta^T \dot{q} - C_0 \dot{V} \tag{12.8}$$

θ is the modal electromechanical coupling matrix with a $[n, i]$ matrix size. θ is defined as follows:

$$\theta = \phi^T \alpha \tag{12.9}$$

M, C, K_E are respectively the mass, damping and stiffness modal matrices. The structure is assumed to be lightly damped, with proportional damping and with decoupled modes. Equation (12.7) is normalized in order to have the modal mass matrix equal to identity. Modal matrices can therefore be written as a function of ξ the modal damping vector, ω_E the short circuit frequency vector and ω_D the open circuit frequency vector as follows:

$$M = I_d\ ,\quad C = 2(\xi)\mathrm{diag}(\omega_D)\ ,\quad K_E = (\omega_E) \tag{12.10}$$

By separating the actuators and sensors voltages, named V_a and V_s, respectively, Eq. (12.7) becomes:

$$M\ddot{q} + C\dot{q} + K_E q = -\theta_a V_a - \theta_s V_s + \beta F \tag{12.11}$$

In an open circuit or when the sensor voltage is monitored with a voltage amplifier, sensor intensity is null, therefore:

$$\theta_s^T q - C_{0s} V_s = 0 \tag{12.12}$$

By reintroducing Eq. (12.12) in Eq. (12.11):

$$M\ddot{q} + C\dot{q} + \left(K_E \theta_s C_{0s}^{-1} \theta_s^T\right) q = -\theta_a V_a + \beta F \tag{12.13}$$

Linear systems (12.13) and (12.12) can be written in modal state under form:

$$\begin{cases} \dot{x} = Ax + Bu \\ y = \quad Cx \end{cases}, \quad x = \begin{bmatrix} q \\ \dot{q} \end{bmatrix}, \quad u = \begin{bmatrix} F \\ V_a \end{bmatrix}, \quad y = \begin{bmatrix} q \\ \dot{q} \\ V_s \end{bmatrix} \tag{12.14}$$

with x being the state vector, u is the control vector, y is the output vector, A, B, C are the state matrices:

$$A = \begin{bmatrix} 0 & I_d \\ A_0 & -M^{-1}C \end{bmatrix}, \quad B = \begin{bmatrix} 0 \\ M^{-1}(\beta - \theta_a) \end{bmatrix}, \quad C = \begin{bmatrix} I_d & 0 \\ 0 & I_d \\ C_{0s}^{-1}\theta_s^T & 0 \end{bmatrix} \tag{12.15}$$

with: $A_0 = -M^{-1}\left(K_E \theta_s C_{0s}^{-1} \theta_s^T\right)$ and:

$$V_a = C_{0s}^{-1} \theta_a^T q \tag{12.16}$$

and C_{0a} is the capacity of actuator and the matrix C_{0s} is capacity sensors.

12.3.2 Smart-Structure Definition

The structure that will be used in the following simulations and analyses is a steel clamped plate equipped with four P_{188} piezoelectric inserts. Its dimensions and physical properties are given in Tables 12.1 and 12.2. This plate is clamped on all four sides. Figure 12.6 illustrates this plate which is representative of a protective panel. This structure has been identified according to the previously described model. The measurement process and parameter identification is described in Richard (2007).

Table 12.1 Characteristics of the plate (Richard 2007)

Length	Width	Thickness	Young modulus	Poisson ratio	Density
0.6 m	0.4 m	1 mm	210 GPa	0.345	7500

Table 12.2 Characteristics of $PZT\ P_{189}$ piezoelectric inserts (Richard 2007)

Properties	Symbol	Value
Density	ρ	7650 kg m^3
Compliances Short-circuit	s_{E11}	10.66×10^{-12} Pa^{-1}
	s_{E12}	-3.34×10^{-12} Pa^{-1}
	s_{E13}	-4.52×10^{-12} Pa^{-1}
	s_{E33}	13.25×10^{-12} Pa^{-1}
Permittivity	ε_{33}^{T}	10.17 nF m^{-1}
Piezoelectric coefficient	d_{13}	-108 pC N^{-1}

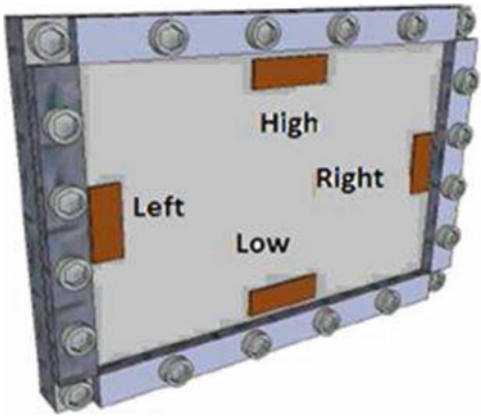

Fig. 12.6 Protective panel structure used in simulations. The plate is clamped on the four sides. Each four piezoelectric elements are 12×4 cm and 600 μm thick

Table 12.3 Frequencies of the four simulated modes of the plate embedded (Richard 2007)

Modes	Mode 1	Mode 2	Mode 3	Mode 4
Frequency	96 Hz	175 Hz	204 Hz	228 Hz

Table 12.3 summarizes the frequencies of the four modes considered in the model. Due to the position of various piezoelectric patches, and according to symmetry conditions, only symmetric modes are efficiently electromechanically coupled. As a result, on the lowest part of the frequency spectrum, only a few modes are significantly coupled, which means that they can be targeted effectively by the proposed control if the patches are used as actuators, it also means that only these modes can produce a significant response if the patches are used as sensors. These modes are taken into account by the model used in simulations.

The resonance frequencies of the lower modes are given in Table 12.3.

12.4 SSDI Max Modal Control

The main disadvantage of Modal-SSDI control technique is the need for numerical computation. The technique can not be self-powered. However, once implemented, the numerical control loops offer different opportunities such as hybridization with active techniques or alternative switching sequences improved in terms of voltage inversion.

The technical implementation SSDI-Max is an alternate modal-SSDI control which increases the growth of the piezoelectric actuator voltage V_a. The damping performance is strongly dependent on this voltage amplitude. The SSDI allows a natural growth of this voltage using a cumulative effect (Richardet et al. 2009). However, if this cumulative effect is affected by local maximum, the voltage magnification is not optimal. It is the objective of the modal-SSDI-Max technique to correct this point.

Modal-SSDI-Max strategy in comparison with Modal-SSDI consists in delaying the switch instant to the next voltage extremum immediately following the targeted modal coordinate extremum. The switch still allows the brief V_a voltage inversion.

According to this strategy, the inversion is triggered from a higher voltage, resulting in an amplification of the cumulative effect. However, it could imply an important added phase shift resulting with a voltage only approximately synchronized with the targeted modal displacement. This could result in a significant damping depreciation. In order to limit this desynchronization, the delay is limited to a given time window. This process is illustrated on Fig. 12.7 which schematically illustrates the gain attainable in the voltage amplitude when modifying the switch instant. The dashed line represents the targeted modal coordinate. Usual modal-SSDI technique would trigger the switch at each extremum. The thick line represents the open-circuited actuator voltage V_{a-oc}. It is clear that due to the modal content of the vibration, maximum of the voltage and maximum of the targeted modal coordinate do not necessarily match. Note that in Fig. 12.7, V_{a-oc} is represented for sake of simplicity, but it is clear that it is the switched voltage V_a that have normally to be taken into account The grey area starting after each modal coordinate extremum represents the imposed time window limitation. Finally, arrows figure the effective switching time defined following the proposed strategy. The (A) switching example illustrates the fact that immediate switching would result in an actuator voltage with the wrong phase because the voltage is negative when the modal coordinate is maximum positive. Waiting for the next positive maximum is therefore necessary to ensure both the correct phase and the optimal amplitude. The (B) switching example illustrates that even if the voltage sign is correct, waiting for the next extremum allows to increase the voltage amplitude. If the voltage extremum occurs immediately before the modal coordinate extremum as illustrated by (C), it is appropriate to switch immediately. Example (D) illustrates the fact that if no voltage extremum with the correct sign is located in the maximum time allowed, the switch must occur at the end of the time window to limit the resulting voltage phase shift. Finally, this procedure can be seen as a way to use the modal energy of the other modes to increase the voltage devoted to the control of the targeted mode.

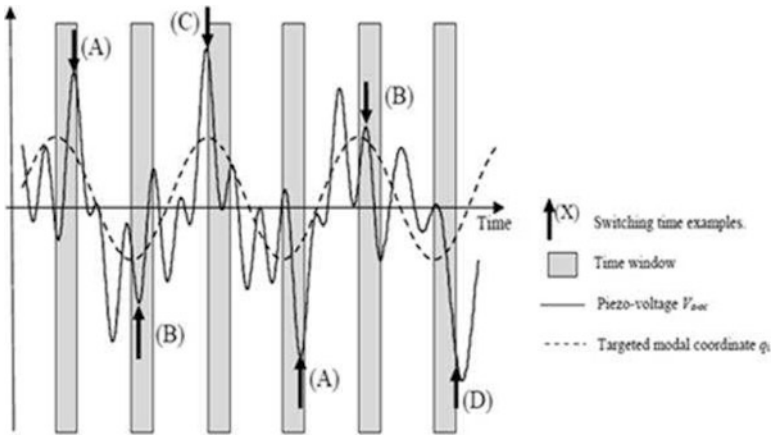

Fig. 12.7 Illustration of the SSDI-Max strategy: definition of the switch instant according to the targeted modal coordinate, the piezoelectric actuator open-circuit voltage and the maximum delay authorized

This methodology can be summarized by the following algorithm. When a maximum of the modal displacement $\hat{q}_i$ occurs the limitation time window starts. Then the signs of the voltage V_a and its derivative are considered during the window:

1. If the voltage is positive and the derivative is negative, the switch trigger is immediate.
2. If the voltage is positive and the derivative is positive, the system waits for the next maximum voltage. This delay is nevertheless limited by the time window.
3. If the voltage is negative, the system waits for one of the above conditions.
4. If no switching occurred and the end of the time window is reached, the switching is triggered.

This algorithm is anti-symmetric if a minimum modal displacement is reached.

12.5 Simulations

Simulations are performed using the Matlab/Simulink^{TM} software environment. The inversion coefficient γ is set to 0.7 which is a realistic value (Richard et al. 2000). The first step in SSDI-Max validation is the control of a single mode of the structure. This single mode control is considered with different type of multimodal excitation: multi-sinusoidal excitation or broadband excitation with a pulse or white noise. The second stage of validation protocol consists in the control of the four modes simultaneously excited with a pulse or with a white noise. The effect of the time window on SSDI-Max performance is established in the later section.

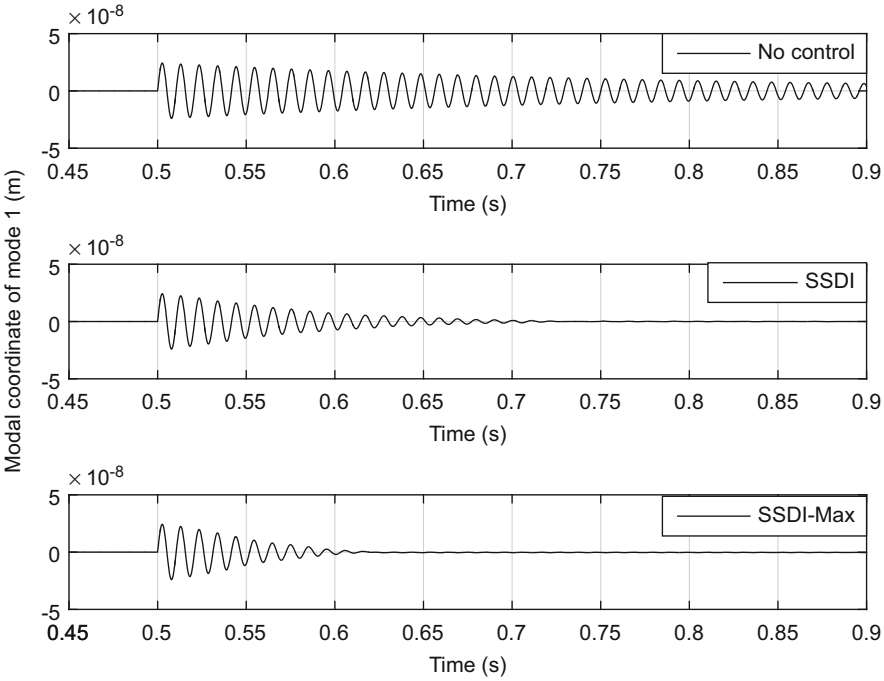

Fig. 12.8 Simulation of the mode 1 modal coordinate with a pulse excitation in the case of mode 1 control

12.5.1 Pulse Excitation

The excitation is a wide frequency square force pulse 50 μs long, and with a normalized amplitude. This signal is applied on the structure space-state block Force input shown Fig. 12.4. Figure 12.8 illustrates simulation results in the time domain in the case of mode 1 targeting. A clear strong improvement of damping using SSDI max is clearly visible. The voltage build-up improvement is illustrated in Fig. 12.9 showing that small shifts in the switch instants result in amplification of the self-generated control voltage. This result is remarkable since the reference which corresponds to the structure controlled using modal SSDI is already well damped.

12.5.2 White Noise Excitation

In this case the plate model is excited with a white noise of normalized amplitude applied on the structure space-state block Force input shown in Fig. 12.3. Like a pulse this type of broadband excitation results in vibration energy shared on all the four considered modes of the model.

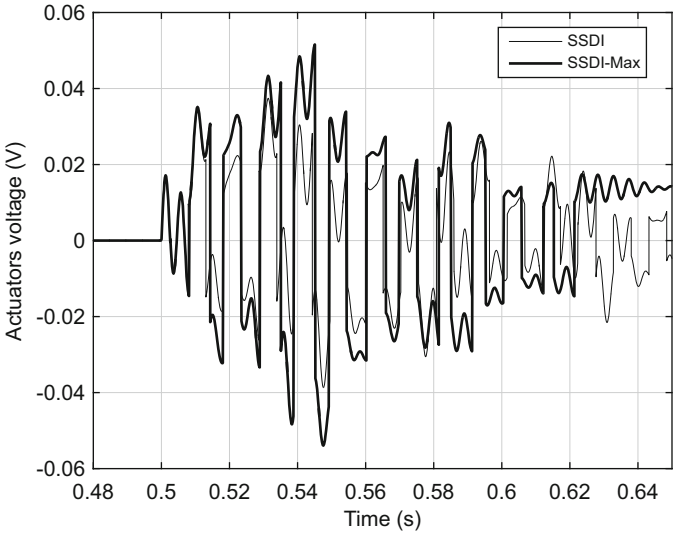

Fig. 12.9 Simulation of the actuator voltage with a pulse excitation in the case of mode 1 control

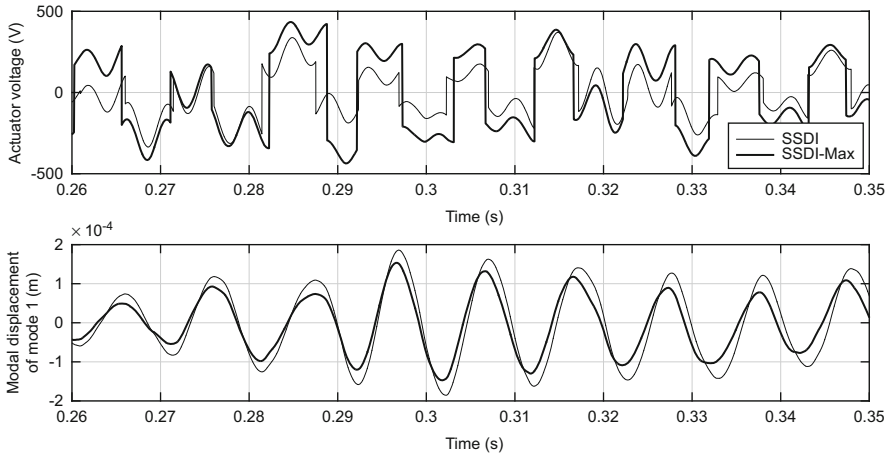

Fig. 12.10 Modal displacement and the voltage across the actuator when the mode 1 is targeted by the control

Figure 12.10 shows a comparison of the modal SSDI and modal SSDI-Max damping performances. It shows a partial time window representative of the 3 s long simulation time. The lower plot presents the first modal coordinate which is targeted by the control. The upper illustrates the control voltage actuator. Again it is clearly visible that a slight shift in the switching time definition leads to a much improved actuator voltage amplitude, thus resulting in more efficient damping.

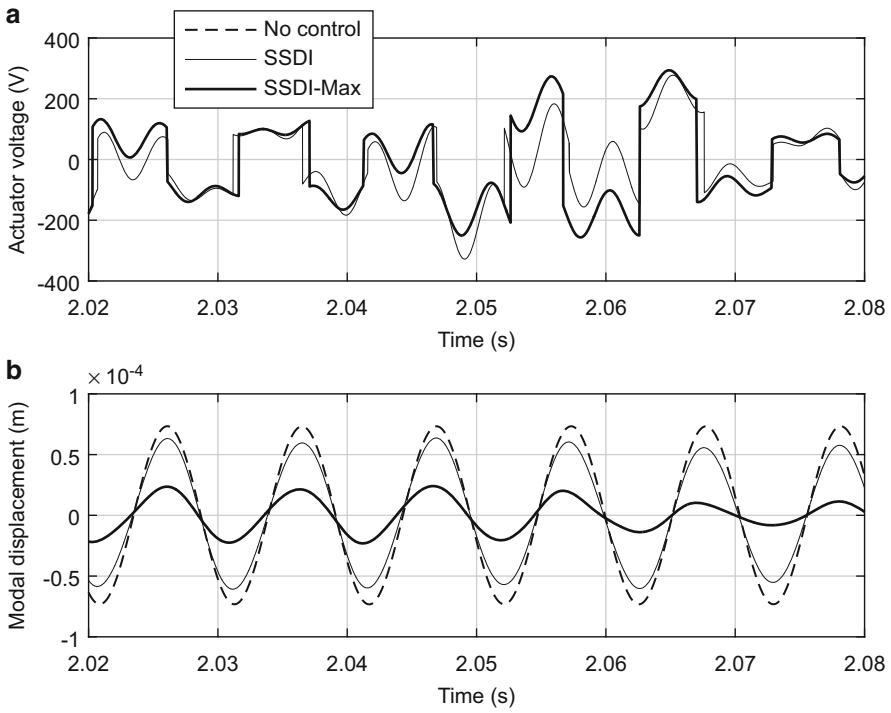

Fig. 12.11 Modal displacement (**b**) and the piezoelectric actuator voltage (**a**) for single mode control (mode 1) and in the case of multi-sine excitation. The ratio of the controlled mode energy to the structure vibrational energy is $E1/E2 = -3.8\,\mathrm{dB}$

12.5.3 Sinusoidal Excitation

In this case the excitation is composed of the sum of four sine signals whose frequencies are those of the four modes of the structure. The interest of this type of excitation relies in the fact that it is possible to adjust the energy associated with the various modal contents of the vibration.

Figure 12.11a illustrates the increase in self-generated control power: A slight variation of the moment of inversion (time window is 1/10 of the first mode period) can lead to a significant change in the control voltage responsible for mitigation. It should be noted that this change led to a much greater reduction of the targeted mode (Fig. 12.11b).

12.5.4 Influence of the Time Window on the Performance of SSDI Max

According to the SSDI-Max strategy the time window, which is used to limit the possible time shift prior to switching, is a very important and critic parameter. If it is too small, the voltage will not have the possibility to increase and no significant enhancement will be observed. If it is too long, there is a risk of desynchronization of the actuator voltage with the targeted modal speed, thus resulting altered damping. In order to define an optimal time window, simulations were made while varying the value of this window from zero (pure modal SSDI) to 2/5th of the targeted mode period. This analyze was conducted for single mode control (mode 1). Figure 12.12 illustrates the variation of the targeted mode damping as a function of the time window for pulse excitation.

As shown on Fig. 12.12, a time window lying between 1/10th and 1/5th of the period is nearly optimal for SSDI-Max control, ensuring an increase of the actuator voltage while not inducing a too important phase shift between the voltage and the targeted modal speed, thus resulting in additional damping.

12.6 Conclusions

It has been shown that performances of the modal SSDI control can be significantly improved using an algorithm that exploits the complexity of the shape of the piezoelectric voltage in the case of multimodal vibration. Instead of inversing the voltage on the extremum of the modal displacement, the proposed technique, named modal SSDI-Max, consists of waiting for the next voltage extremum immediately after an extremum of the targeted modal coordinate to inverse the voltage across the piezoelectric element used as an actuator. Thus, the inversion is done from a higher voltage, resulting in improved voltage build-up. The resulting quasi square control voltage is still approximately synchronized with the targeted modal displacement mode and nearly in phase with the targeted modal speed which implies a significant damping improvement.

Validation of this concept has been done using numeric simulation in the case study of a clamped steel plate. The entire control scheme has been simulated and evaluated. Modal SSDI-Max Damping simulation results showed nearly improved damping performances compared to modal SSDI for the control of a single mode of the structure, in the case of sinusoidal excitation on the four modes of the plate, pulse or white noise excitation. Remarkable gains in attenuation lying between 6 and 11 db were obtained with actuators presenting a rather low coupling coefficient (lower than 9%). Finally, the influence of the maximum time delay between the targeted modal coordinate extremum and the switch instant has been evaluated. Simulations show that a maximum delay lying between 1/10th and 1/5th of the targeted mode period is nearly optimal for considered cases.

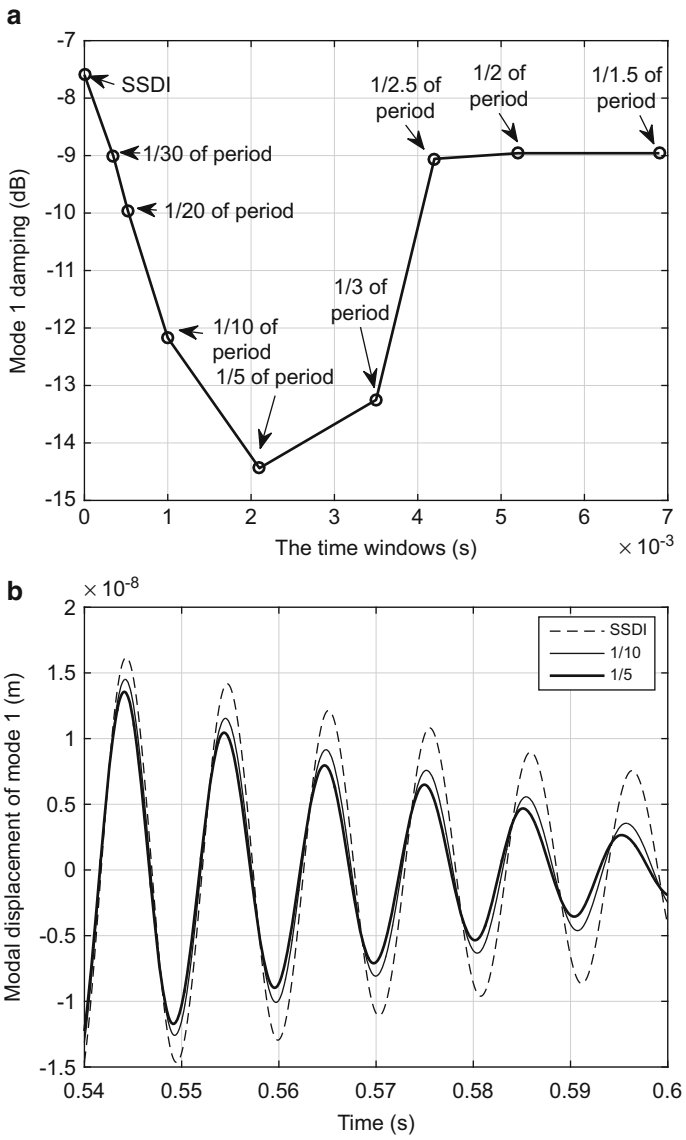

Fig. 12.12 Influence of the time window for pulse excitation. (**a**) Influence of the time window on mode 1 damping. (**b**) Corresponding time domain results

References

Carriere, M. S. (2010). *Crossed synthesis of controllers and observers for robust control of synchronous machine*. Ph.D. Thesis, University of Toulouse, France.

Chérif, A., Richard, C., Guyomar, D., Belkhiat, S., & Meddad, M. (2012). Simulation of multimodal vibration damping of a plate structure using a modal SSDI-Max technique. *Journal of Intelligent Material Systems and Structures, 23*(6), 675–689.

Clark, W. W. (2000). Vibration control with state-switching piezoelectric materials. *Journal of Intelligent Material and Structures, 11*, 263–271.

Cunefare, K. A., & Holdhusen, M. (2004). Optimization of a state-switched absorber applied to a continuous vibrating system. In *SPIE SSM Conference Passive Damping and Isolation*, San Diego.

Davis, C. L., & Lesieutre, G. A. (2000). Actively tuned solid-state vibration absorber using capacitive shunting of piezoelectric stiffness. *Journal of Sound and Vibration, 232*, 601–617.

Eielsen, A. A., & Fleming, A. J. (2010). Passive shunt damping of a piezoelectric stack nanopositioner. In *American Control Conference*, Baltimore (pp. 4963–4968).

Forward, R. L. (1979). Electronic damping of vibrations in optical structures. *Applied Optics, 18*(5), 690–697.

Franklin, G. F., Powell, J. D., & Workman, M. L. (1990). *Digital control of dynamic systems* (2nd ed.). Reading: Addison-Wesley.

Fuller, C. R., & Jones, J. D. (1987). Experiments on reduction of propeller induced interior noise by active control of cylinder vibration. *Journal of Sound and Vibration, 112*(2), 398–395.

Guyomar, D., & Badel, A. (2006). Nonlinear semi-passive multimodal vibration damping: An efficient probabilistic approach. *Journal of Sound and Vibration 294*(1–2), 249–268.

Hagood, N. W., & Von Flotow, A. (1991). Damping of structural vibrations with piezoelectric materials and passive electrical networks. *Journal of Sound and Vibration, 146*(2), 243–268.

Harari, S., Richard, C., & Gaudiller, L. (2009). New semi-active multi-modal vibration control using piezoceramic components. *Journal of Intelligent Material Systems and Structures, 20*, 1603–1613.

Meyer, Y., & Collet, M. (2011). Active vibration isolation of electronic components by piezocomposite clamped-clamped beam. *Mechanical Systems and Signal Processing, 25*, 1687–1701.

Niederberger, D., Morari, M., & Pietrzko, S. (2004). A new control approach for switching shunt damping. In *SPIE SSM Conference Passive Damping and Isolation*, San Diego.

Petit, L., Lefeuvre, E., Richard, C., & Guyomar, D. (2004). A broadband semi-passive piezoelectric technique for structural damping. In *SPIE SSM Conference, Damping and Isolation*, San Diego.

Preumont, A., François, A., Bossens, A., & Abu-Hanieh, A. (2002). Force feedback versus acceleration feedback in active vibration isolation. *Journal of Sound and Vibration, 257*(4), 605–613.

Richard, T. (2007). Diminution du coefficient de transmission acoustique d'une paroi à l'aide d'amortisseurs piézoélectriques semi-passifs. Thèse de doctorat, Institut National des Sciences Appliquées de Lyon, no 2007ISAL0112.

Richard, C., Guyomar, D., Audigier, D., & Bassaler, H. (2000). Enhanced semi passive damping using continuous switching of a piezoelectric device on an inductor. In *SPIE Smart Structures and Materials Conference, Passive Damping and Isolation*, Newport Beach (Vol. 3689, pp. 288–299).

Richard, C., Harari, S., & Gaudiller, L. (2009). Enhanced piezoelectric voltage build-up for semi-active control of smart structures. In *SPIE Smart Structures and Materials*, San Diego.

Snyder, S. D., & Hansen, C. H. (1991). Mechanisms of active noise control by vibration sources. *Journal of Sound and Vibration, 147*(3), 519–525.

Wu, S., & Bicos, A. S. (1997). Structural vibration damping experiments using improved piezoelectric shunts. *Proceedings of the SPIE, 3045*, 40–50.

Chapter 13
Feedback T-S Fuzzy Controller in Finite Frequency for Wind Turbine

Youssef Berrada, Abderrahim El-Amrani, and Ismail Boumhidi

Abstract This chapter investigates a feedback finite frequency Takagi-Sugeno (T-S) fuzzy controller synthesis for a variable speed wind turbine. The proposed control design is based on both the T-S fuzzy modeling and the finite frequency approach. The T-S fuzzy model is used to deal with a nonlinear behavior of wind turbine system, and the finite frequency approach allows the command in a specific domain of frequency. The control constraints are given in terms of a set of LMIs which can be efficiently solved using existing numerical tools. In order to illustrate the performance of the proposed control algorithm, numerical simulations are performed using Matlab software.

Keywords Finite frequency · Takagi-Sugeno fuzzy · Variable wind speed · Wind turbine

Notations

- The superscript ^{T} stands for matrix transposition.
- I denotes an identity matrix with appropriate dimension.
- "diag" stands for block diagonal matrix.
- "tr(A)" denotes the trace of matrix A.
- $A > 0$ (resp. $A < 0$) mean that matrix A is positive definite (resp. negative definite).

Y. Berrada (✉) · A. El-Amrani · I. Boumhidi
LESSI Laboratory, Sciences Faculty, Department of Physics, University of Sidi Mohammed Ben Abdellah, Fez, Morocco
e-mail: youssef.berrada@usmba.ac.ma; abderrahim.elamrani@usmba.ac.ma; ismail.boumhidi@usmba.ac.ma

N. Derbel, Q. Zhu (eds.), *Modeling, Identification and Control Methods in Renewable Energy Systems*, Green Energy and Technology,
https://doi.org/10.1007/978-981-13-1945-7_13

13.1 Introduction

Global warming effect and fossil fuel pollution has caused great damage in the earth's environment, and has become a serious problem for people. As renewable energies sources are environment-friendly and sustainable, wind and solar energy have attracted increased attention during the last years. In light of this, improving the efficiency of wind turbine becomes an important research topic. Furthermore, control techniques have a major effect on wind energy conversion systems, and remain a key factor in maximizing the extracted energy from the wind and reducing the stresses caused by aerodynamic loads. To achieve satisfactory wind turbine performances, Takagi-Sugeno (T-S) fuzzy has received increasing attention during the past decades from many researchers. There are a lot of research results on the T-S fuzzy in the literature, such that, in Lasheen et al. (2016) the authors proposed a new algorithm of fuzzy predictive for collective pitch control of large wind turbines. A Neuro-fuzzy inertia controller has been addressed in Hafiz et al. (2016) to control parameter selection which ensures the optimal use of available Kinetic Energy reserve. Neural network is also coupled in Medjber et al. (2016) with fuzzy logic controller to monitor maximum power for wind energy conversion system. A new kind of T-S fuzzy control technique used for capturing maximum wind energy under multi-operating condition has been discussed in An et al. (2015). A data driven design methodology able to generate a Takagi-Sugeno fuzzy model for maximum energy extraction from variable speed wind turbines has been examined in Galdi et al. (2008). A sensorless wind energy conversion system maximum wind power point tracking using Takagi-Sugeno fuzzy cerebellar model articulation control to achieve maximum power transfer under various wind speeds without actual measurement of the wind velocity has been proofed in Liu et al. (2015). Note that all those control techniques and other given in this area can improve the wind turbine robustness against the random wind speed and maximize the extracted wind power. However, when the external disturbance belong to a certain frequency range which is known beforehand, it is not favorable to control the system in the full frequency domain, because this may introduce some conservatism and poor system performance. Recently, the control synthesis in a finite frequency domain has been addressed, and there have appeared many results in this domain (Berrada et al. 2017; Chen et al. 2010; El-Amrani et al. 2016; Li et al. 2015; Zhang et al. 2014).

In light of the above, we propose feedback Finite Frequency Takagi-Sugeno Fuzzy (FFTSF) to control wind turbine under various wind conditions. We first represent the wind turbine, which is a two mass model, as a highly nonlinear dynamical model. To carry out the FFTSF design, we then rewrite the wind turbine model as a T-S fuzzy representation. Next the proposed feedback control is established by the finite frequency approach to command the wind turbine system in a specific band of frequency. Based on the generalized Kalman-Yakubovich-Popov (GKYP) lemma (Iwasaki et al. 2005), the controller constraints are given in terms of linear matrix inequalities (LMIs) which can be efficiently solved numerically. The control technique acts on generator in order to apply the electromagnetic

torque reference and on the pitch actuator in order to control the pitch angle of the blades according to wind speed value, calculated from the measurements of the rotational speed of the shaft at the generator side, and of the speed of the wind by an accelerometer located at the top of the tower.

The paper is organized as follows. In Sect. 13.2, we will describe the model of the wind turbine system. In the next section, we will rewrite the obtained model as a T-S Fuzzy representation, and the controller will be designed by the Finite frequency technique. In Sect. 13.4, the performances of the proposed control strategy will be shown carried out by simulation results. Finally, some conclusions are given in Sect. 13.5.

13.2 Wind Turbine Model

The wind turbine is established by combining a model of a mechanical structure represent the drive trains and nonlinear model representing the blades aerodynamic properties. The mathematics model of the wind turbine is clearly described in Bououden et al. (2012), which is represented by the following state representation:

$$\dot{x}_0 = \begin{bmatrix} 0 & 1 & -1 \\ -\frac{K_s}{J_r} & -\frac{B_s}{J_r} & \frac{B_s}{J_r} \\ -\frac{K_s}{J_g} & -\frac{B_s}{J_g} & \frac{B_s}{J_g} \end{bmatrix} x_0 + \begin{bmatrix} 0 & 0 \\ \frac{1}{J_r} & 0 \\ 0 & \frac{1}{J_g} \end{bmatrix} \begin{bmatrix} T_a \\ T_g \end{bmatrix} \tag{13.1}$$

where $x_0 = [\theta_s,\ \omega_r,\ \omega_g]^T$, θ_s, ω_r, ω_g, B_s and K_s are the torsion angle, the rotor speed, the generator speed, the damping of the transmission and the stiffness of the transmission, respectively. J_r and J_g are the inertia of the rotor and the generator, respectively. T_g is the generator torque which is a nonlinear function depends to the generator speed and the zero-torque speed ω_z.

$$T_g = B_s(\omega_g - \omega_z) \tag{13.2}$$

T_a is the aerodynamic torque which is expressed as:

$$T_a = \frac{1}{2}\pi\ \rho\ R^3\ C_q(\lambda, \beta)\ v^2 \tag{13.3}$$

with $C_q(\lambda, \beta) = \frac{1}{\lambda} C_p(\lambda, \beta)$ is the torque coefficient. $C_p(\lambda, \beta)$ is the power coefficient that is a nonlinear function of the pitch angle β and the reduced speed λ. So, T_a is a nonlinear function depends to wind speed, rotor speed and pitch angle, can be linearized by the following expression:

$$T_a = T_{av} v + T_{a\beta}\beta + T_{a\lambda}\lambda \tag{13.4}$$

where T_{av}, $T_{a\beta}$ and $T_{a\lambda}$ are individual partial derivatives of the aerodynamic torque T_{av} for rotor speed, wind speed and pitch angle at the operating point, respectively.

The actuator describes the dynamic behavior between the desired pitch β_d and the actuation of this desired pitch β is modeled as:

$$\dot{\beta} = \frac{1}{\tau}(\beta_d - \beta) \tag{13.5}$$

where τ is a time constant.

Finally, according to the Eqs. (13.1), (13.2), (13.3), (13.4), and (13.5), and replacing T_a and T_g with their approximated expressions, the dynamic model of the wind turbine can be represented as:

$$\begin{aligned} \dot{x} &= Ax + Bu + Ev \\ y &= Cx \end{aligned} \tag{13.6}$$

where $x = [\theta_s,\ \omega_r,\ \omega_g,\ \beta]^T$, $u = [\beta_d,\ \omega_z]^T$, $y = \omega_g$ and matrices A, B and E are given by:

$$A = \begin{bmatrix} 0 & 1 & -1 & 0 \\ -\frac{K_s}{J_r} & -\frac{B_s}{J_r} & \frac{B_s}{J_r} & \frac{T_{a\beta}}{J_r} \\ -\frac{K_s}{J_g} & -\frac{B_s + B_g}{J_g} & \frac{B_s}{J_g} & 0 \\ 0 & 0 & 0 & -\frac{1}{\tau} \end{bmatrix},\ B = \begin{bmatrix} 0 & 0 \\ 0 & 0 \\ 0 & \frac{B_g}{J_g} \\ \frac{1}{\tau} & 0 \end{bmatrix},\ E = \begin{bmatrix} 0 \\ \frac{T_{av}}{J_r} \\ 0 \\ 0 \end{bmatrix} \tag{13.7}$$

Let $\xi = x - x_{ref}$ so $x = x_{ref} + \xi$ and then $\dot{x} = \dot{x}_{ref} + \dot{\xi}$.

The system dynamic model (13.6) becomes:

$$\begin{aligned} \dot{\xi} &= A\xi + Bu + Dw \\ \chi &= C\xi \end{aligned} \tag{13.8}$$

where $w = [x_{ref},\ \dot{x}_{ref},\ v]^T$ and $D = [A,\ -I,\ E]$ with x_{ref} is the reference signal.

13.3 Finite Frequency T-S Fuzzy Control

13.3.1 T-S Fuzzy Representation

The best possible performance from the highly nonlinear system (13.6) can be obtained using T-S fuzzy model. The wind turbine variables are assumed varying in the operating range $v_1 \leq v \leq v_2, \beta_1 \leq \beta \leq \beta_2$. Consequently, The T-S fuzzy model

of system (13.6) is established by the following rules IF-THEN for $i = 1, \ldots, 4$ and $l, k = 1, 2$:

$$\text{If}(\beta \text{is} M_l)\text{And}(v \text{is} N_k)\text{Then} \begin{cases} \dot{\xi} = A_i\xi + B_i u + D_i w \\ \chi = C_i\xi \end{cases} \tag{13.9}$$

Membership functions are given by:

$$h_1 = M_1(\beta)N_1(v),\ h_2 = M_1(\beta)N_2(v),\ h_3 = M_2(\beta)N_1(v),\ h_4 = M_2(\beta)N_2(v)$$

with:

$$M_1(\beta) = \frac{\beta - \beta_1}{\beta_2 - \beta_1},\ M_2(\beta) = \frac{\beta_2 - \beta}{\beta_2 - \beta_1},\ N_1(v) = \frac{v - v_1}{v_2 - v_1},\ N_2(v) = \frac{v_2 - v}{v_2 - v_1}$$

The fuzzy basis functions satisfies: $h_i \geq 0$ and $\sum_{i=1}^{4} h_i = 1$.

The fuzzy system can be written as following form:

$$\begin{aligned} \dot{\xi} &= A(h)\xi + B(h)u + D(h)w \\ \chi &= C(h)\xi \end{aligned} \tag{13.10}$$

where:

$$A(h) = \sum_{i=1}^{4} h_i A_i,\ B(h) = \sum_{i=1}^{4} h_i B_i,\ D(h) = \sum_{i=1}^{4} h_i D_i,\ C(h) = \sum_{i=1}^{4} h_i C_i$$

The fuzzy state feedback controller can be designed as:

$$u = \sum_{i=1}^{4} h_i K_i \xi = K(h)\xi \tag{13.11}$$

Combining (13.10) and (13.11) together, we can get the following closed-loop fuzzy system:

$$\begin{aligned} \dot{\xi} &= A_c(h)\xi + D(h)v \\ \chi &= C(h)\xi \end{aligned} \tag{13.12}$$

where: $A_c(h) = A(h) + B(h)K(h)$.

The transfer function from the input ξ to the output χ is given by:

$$G(j\omega) = c(h)[j\omega I - A(h)]^{-1}D(h) \tag{13.13}$$

13.3.1.1 Problem Description

The objective is to design a state feedback controller in (13.11) for system (13.12) such that two conditions are satisfied:

1. Closed-loop system (13.12) is asymptotically stable.
2. The following finite frequency index holds:

$$\int_{\omega_1 \le \omega \le \omega_2} \chi(\omega)^T \chi(\omega) d\omega \;\le\; \int_{\omega_1 \le \omega \le \omega_2} w(\omega)^T w(\omega) d\omega \tag{13.14}$$

where ω_1 and ω_2 are known scalars.

13.3.2 Finite Frequency

We start this section by introducing some basic lemmas, which we will be used in the proof of our results.

Lemma 1 *Let be a given scalar. For the system* (13.12) *is asymptotically stable, and the FF* H_∞ (13.14) *is satisfied if there exists Hermitian matrices, such* $P = P^T$ *that:*

$$\begin{bmatrix} A_c(h) & D(h) \\ I & 0 \end{bmatrix}^T \begin{bmatrix} -Q(h) & P(h) + j\omega_c Q(h) \\ I & 0 \end{bmatrix} \begin{bmatrix} P(h) - j\omega_c Q(h) & -\omega_1\omega_2 Q(h) \\ I & 0 \end{bmatrix}$$
$$+ \begin{bmatrix} C(h)^T C(h) & 0 \\ 0 & -\gamma^2 I \end{bmatrix} \;<\; 0 \tag{13.15}$$

where $\omega_c = \frac{1}{2}(\omega_1 + \omega_2)$.

Proof First, suppose (13.15) holds. Post multiplying by $[\xi^T \;\; w^T]$ from the left and by its conjugate transpose from the right, we have:

$$2\dot{\xi}^T P\xi - \dot{\xi}^T P\dot{\xi} + j\omega_c \dot{\xi} Q\xi - j\omega_c \xi^T Q\dot{\xi} - \omega_1\omega_2 \xi^T Q\xi + \chi^T\chi - \gamma^2 w^T w \;\le\; 0 \tag{13.16}$$

Note that for any vectors ϕ and φ, the equality $\phi^T Q\varphi = \mathrm{tr}(\varphi\phi^T Q)$ holds. Then (13.16) can be rewritten as

$$\frac{d}{dt}(\xi^T P\xi) + \chi^T\chi - \gamma^2 w^T w \le \mathrm{tr}\left[H_e\left(\omega_1\xi + j\dot{\xi}\right)\left(\omega_2\xi + j\dot{\xi}\right)^T Q\right] \tag{13.17}$$

Taking the integrating from $t = 0$ to ∞ using the stability property, we have

$$\xi(\infty)^T P\xi(\infty) + \int_0^\infty \chi^T\chi dt - \gamma^2 \int_0^\infty w^T w dt \le \mathrm{tr}[H_e(S)Q] \tag{13.18}$$

where:

$$S = \int_0^\infty \left(\omega_1 \xi + j\dot{\xi}\right)\left(\omega_2 \xi + j\dot{\xi}\right)^T dt \tag{13.19}$$

Note that $\xi(\infty)^T P \xi(\infty) \geq 0$ for $P > 0$, then we have:

$$\int_0^\infty \chi^T \chi dt \leq \gamma^2 \int_0^\infty w^T w dt + \text{tr}[H_e(S)Q] \tag{13.20}$$

By the Parseval's theorem (Goodwin et al. 2001; Skenton et al. 1998), we have:

$$S = \frac{1}{2\pi} \int_{-\infty}^{\infty} (\omega_1 - \omega)(\omega_2 - \omega) X(\omega) X(\omega)^T dt \tag{13.21}$$

$$\int_0^\infty \chi^T \chi dt = \frac{1}{2\pi} \int_{-\infty}^{\infty} Y(\omega)^T Y(\omega) dw \tag{13.22}$$

$$\int_0^\infty w^T w dt = \frac{1}{2\pi} \int_{-\infty}^{\infty} W(\omega)^T W(\omega) dw \tag{13.23}$$

And hence S is Hermitian and the bound on the right-hand side of (13.20) becomes, and hence (13.20) is equivalent to:

$$\int_0^\infty \chi^T \chi d\omega - \gamma^2 \int_0^\infty w^T w d\omega \leq 2\pi \text{ tr}(SQ) \tag{13.24}$$

Note that $X^T Q X \geq 0$ for $Q > 0$, and $(\omega_1 - \omega)(\omega_2 - \omega) \leq 0$ for $\omega_1 \leq \omega \leq \omega_2$. Then we have

$$\begin{aligned} 2\pi \text{ tr}(SQ) &= \int_{\omega_1 \leq \omega \leq \omega_2} (\omega_1 - \omega)(\omega_2 - \omega) \text{ tr}(X X^T Q) d\omega \\ &= \int_{\omega_1 \leq \omega \leq \omega_2} (\omega_1 - \omega)(\omega_2 - \omega) X^T Q X d\omega \quad \leq 0 \end{aligned} \tag{13.25}$$

From (13.24) and (13.25), we have statement (13.14), and hence the finite frequency performance is satisfied.

Remark 1 If all the matrices in Lemma 1 are independent on h, then the fuzzy system becomes a linear system, and Lemma 1 is reduced to the generalized KYP lemma (Iwasaki et al. 2005), which proved to be an effective tool to deal with the Finite Frequency problem of linear time-invariant systems.

Lemma 2 (Projection Lemma Apkarian et al. 2001) *Given a symmetric matrix Φ and two matrices Γ, Π of column dimension m, there exists a symmetric matrix F such that the following LMI holds*

$$\Phi + \Gamma F \Pi + \Pi^T F^T \Gamma^T \quad < 0 \tag{13.26}$$

If and only if the following projection inequalities with respect to F are satisfied:

$$\Gamma^{\perp}\Phi\Gamma^{\perp T} < 0 \tag{13.27}$$

$$\Pi^{\perp}\Phi\Pi^{\perp T} < 0 \tag{13.28}$$

Now, an important theorem which can guarantee the asymptotical stability and the FF H_∞ performance of the system in (13.12) is going to be proposed.

Theorem 1 *For a given constant $\gamma > 0$, consider the closed-loop system (13.12), if there exist symmetric matrices $\overline{Q}(h) > 0$, $X > 0$, $Z(h)$ and general matrix $Y(h)$ such that the following linear matrices inequality holds*

$$\Psi = \begin{bmatrix} -\overline{Q}(h) & -X + Z(h) + j\omega_c\overline{Q}(h) & 0 & 0 \\ \star & \Upsilon & D(h) & XC(h)^T \\ \star & \star & -\gamma^2 I & 0 \\ \star & \star & \star & -I \end{bmatrix} < 0 \tag{13.29}$$

$$S = A(h)X + XA(h)^T + B(h)Y(h) + Y(h)^T B(h)^T < 0 \tag{13.30}$$

with: $\Upsilon = A(h)X + XA(h)^T - B(h)Y(h) - Y(h)^T B(h)^T - \omega_1\omega_2\overline{Q}(h)$.

The controller gains K_i are given by:

$$K(h) = Y(h)X^{-1} \tag{13.31}$$

Proof Using the Lemma 1, and according to the close loop system (13.12). The inequality (13.15) can be rewritten as:

$$\begin{bmatrix} A(h) & D(h) \\ I & 0 \\ 0 & I \end{bmatrix}^T \Phi \begin{bmatrix} A(h) & D(h) \\ I & 0 \\ 0 & I \end{bmatrix} < 0 \tag{13.32}$$

where:

$$\Phi = \begin{bmatrix} -Q(h) & P(h) + j\omega_c Q(h) & 0 \\ P(h) - j\omega_c Q(h) & \omega_1\omega_2 Q(h) + C(h)^T C(h) & 0 \\ 0 & & -\gamma^2 I \end{bmatrix} \tag{13.33}$$

On the other hand, we can obtain

$$\begin{bmatrix} I & 0 \\ 0 & 0 \\ 0 & I \end{bmatrix}^T \Phi \begin{bmatrix} I & 0 \\ 0 & 0 \\ 0 & I \end{bmatrix} = \begin{bmatrix} -Q(h) & 0 \\ 0 & -\gamma^2 I \end{bmatrix} < 0 \tag{13.34}$$

According to the projection Lemma 2, with:

$$\Gamma^{\perp} = \begin{bmatrix} A(h)^T & I & 0 \\ D(h)^T & 0 & I \end{bmatrix} \tag{13.35}$$

$$\Pi^{\perp} = \begin{bmatrix} I & 0 & 0 \\ 0 & 0 & I \end{bmatrix} < 0 \tag{13.36}$$

The following inequality is a sufficient condition for (13.15).

$$\Phi + \begin{bmatrix} -I \\ A(h)^T \\ D(h)^T \end{bmatrix} F \begin{bmatrix} 0 & I & 0 \end{bmatrix} + \begin{bmatrix} 0 & I & 0 \end{bmatrix}^T F \begin{bmatrix} -I \\ A(h)^T \\ D(h)^T \end{bmatrix}^T < 0 \tag{13.37}$$

By substituting $A_c(h) = A(h) + B(h)X$, we obtain:

$$\begin{bmatrix} -Q(h) & -F + P(h) + j\omega_c Q(h) & 0 \\ \star & \Lambda & FD(h) \\ \star & \star & -\gamma^2 I \end{bmatrix} < 0 \tag{13.38}$$

with: $\Lambda = A(h)^T F + FA(h) + FB(h)K(h) + K(h)^T B(h)^T F - \omega_1\omega_2 Q(h) + C(h)^T C(h)$.

Multiplying both sides of (13.36) by the full rank matrix diag(F^{-1} F^{-1} I) and its transpose from the left and right, and defining new variables $\overline{Q}(h) = F^{-1}Q(h)F^{-1}$, $Z(h) = F^{-1}P(h)F^{-1}$, $Y(h) = K(h)F^{-1}$ then (13.36) is rewritten as follows:

$$\begin{bmatrix} -\overline{Q}(h) & -X + Z(h) + j\omega_c \overline{Q}(h) & 0 \\ \star & \overline{\Lambda} & D(h) \\ \star & \star & -\gamma^2 I \end{bmatrix} < 0 \tag{13.39}$$

with: $\overline{\Lambda} = A(h)X + CA(h)^T + B(h)Y(h) + Y(h)^T B(h)^T F - \omega_1\omega_2 \overline{Q}(h) + XC(h)^T + C(h)X$.

Applying the Schur complement to inequality (13.39), we obtain exactly the inequality (13.29).

For the second sufficient condition of Theorem 1, let us construct a Lyapunov function inequality, $A(h)$ is stable if and only if there exists $F = F^T$ such that:

$$A_c(h)^T F + FA_c(h) < 0 \tag{13.40}$$

By substituting, $A_c(h) = A(h) + B(h)K(h)$, we get

$$A(h)^T F + FA(h) + FB(h)K(h) + K(h)^T B(h)^T F < 0 \tag{13.41}$$

Multiplying both sides of (13.41) by the matrix F^{-1} and its transpose from the left and right, then we can get

$$F^{-1}A(h)^T + A(h)F^{-1} + B(h)K(h)F^{-1} + F^{-1}K(h)^T B(h)^T < 0 \tag{13.42}$$

Let $X = F^{-1}$ and $Y(h) = K(h)F^{-1}$, then (13.40) became exactly the inequality (13.28).

Theorem 2 *Given a positive scalar $\gamma > 0$, there exists a T-S fuzzy control law (13.11) which makes the H_∞ norm of the T-S fuzzy system (13.12) less than γ in the frequency domain, if there exist matrices $\overline{Q}_i > 0$, $X > 0$, Z_i and general matrix Y_i, such that the following LMIs hold for all $i < j = 1, \ldots, 4$.*

$$\Psi_{ii} < 0 \tag{13.43}$$

$$\Psi_{ij} + \Psi_{ji} < 0 \tag{13.44}$$

$$S_{ii} < 0 \tag{13.45}$$

$$S_{ij} + S_{ji} < 0 \tag{13.46}$$

where:

$$\Psi_{ij} = \begin{bmatrix} -\overline{Q}_i & -X + Z_i + j\omega_c \overline{Q}_i & 0 & 0 \\ \star & A_i X + X A_i^T - B_i Y_j - Y_j^T B_i^T - \omega_1\omega_2 \overline{Q}_i & D_i & XC_i^T \\ \star & \star & -\gamma^2 I & 0 \\ \star & \star & \star & -I \end{bmatrix} \tag{13.47}$$

Proof Taking the following summations:

$$\sum_{i=1}^{4}\sum_{j=1}^{4} h_i h_j \Psi_{ij};\ \sum_{i=1}^{4}\sum_{j=1}^{4} h_i h_j S_{ij} \tag{13.48}$$

Using Theorem 1, the proof is completed.

13.4 Simulation Results

The wind turbine model (13.6) with the numerical values listed in Table 13.1 is considered under the variable wind speed $12 \leq v \leq 35\,\text{m/s}$. The Rotor speed is maintained around the nominal speed value in the high speed region, and the operated range of pitch angle is $-2 \leq \beta \leq 24°$. Matrices of the T-S fuzzy model are:

Table 13.1 Wind turbine parameters

Parameter	K_s	B_s	B_g	J_g	J_r	ρ	R	τ
Value	1.566×10^6	3029.5	15.993	5.9	83×10^4	1.225	30	500
Unit	N/m	Nms/rad	Nms/rad	kg m^2	kg m^2	kg/m^3	m	μs

$$A_1 = A_2 = \begin{bmatrix} 0 & 1 & -1 & 0 \\ -\frac{K_s}{J_r} & -\frac{B_s}{J_r} & \frac{B_s}{J_r} & \frac{T_{a\beta 1}}{J_r} \\ -\frac{K_s}{J_g} & -\frac{B_s + B_g}{J_g} & \frac{B_s}{J_g} & 0 \\ 0 & 0 & 0 & -\frac{1}{\tau} \end{bmatrix} \tag{13.49}$$

$$A_3 = A_4 = \begin{bmatrix} 0 & 1 & -1 & 0 \\ -\frac{K_s}{J_r} & -\frac{B_s}{J_r} & \frac{B_s}{J_r} & \frac{T_{a\beta 3}}{J_r} \\ -\frac{K_s}{J_g} & -\frac{B_s + B_g}{J_g} & \frac{B_s}{J_g} & 0 \\ 0 & 0 & 0 & -\frac{1}{\tau} \end{bmatrix} \tag{13.50}$$

$$B_1 = B_2 = B_3 = B_4 = \begin{bmatrix} 0 & 0 \\ 0 & 0 \\ 0 & \frac{B_g}{J_g} \\ \frac{1}{\tau} & 0 \end{bmatrix} \tag{13.51}$$

$$D_1 = \begin{bmatrix} 0 \\ \frac{T_{av1}}{J_r} \\ 0 \\ 0 \end{bmatrix}, \quad D_1 = \begin{bmatrix} 0 \\ \frac{T_{av2}}{J_r} \\ 0 \\ 0 \end{bmatrix} \tag{13.52}$$

where $T_{a\beta 1} = T_{a\beta}(\beta = \beta_1)$, $T_{a\beta 2} = T_{a\beta}(\beta = \beta_2)$, $T_{av1} = T_{av}(v = v_1)$ and $T_{av1} = T_{av}(v = v_2)$.

The simulation is carried out under the following operating conditions:

- Wind speed profile $17 \leq v \leq 31$ m/s (see Fig. 13.1)
- The operating frequency domain represents the rotation frequency maximum and minimum of the aerodynamics rotor (3–42 rpm) which is equivalent to

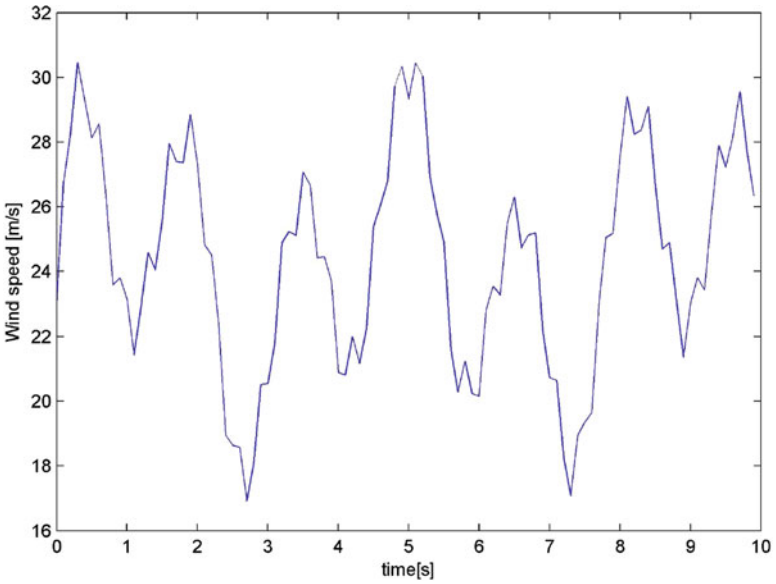

Fig. 13.1 Wind speed input profile

[0.05, 0.7] Hz, and for the generator (1500–1550 rpm) which is equivalent to [25, 25.83] Hz.

By solving the linear matrix inequalities (13.43), (13.44), (13.45), and (13.46) for $i < j = 1, \ldots, 4$ with the optimized variable $\gamma > 0$ and the ranges of frequency:

- $[\omega_1 = 0.05\,\text{Hz}, \omega_2 = 0.7\,\text{Hz}]$,
- $[\omega_1 = 25\,\text{Hz}, \omega_2 = 25.83\,\text{Hz}]$,

for the regulators of pitch angle and zero-torque speed, respectively, we can obtain the control gains:

$$K_1 = 10^3[1.049\ 3.484\ -0.953\ -0.052\ -97.814\ 0.160\ -4.743\ -0.005]$$

$$K_2 = 10^3[1.064\ 3.531\ -1.042\ -0.053\ -97.874\ -0.040\ -2.363\ -0.002]$$

$$K_3 = 10^3[0.585\ 2.029\ -0.731\ -0.030\ -97.877\ -0.050\ -2.089\ -0.002]$$

$$K_4 = 10^3[0.621\ 2.139\ -0.595\ -0.032\ -98.022\ -0.527\ -2.721\ 0.005]$$

The performance of the proposed Feedback T-S fuzzy controller in finite frequency (FFTSF) is illustrated using a comparison with the predictive controller (MPC) strategy [16] carried out by Bououden et al. (2012).

From the simulation results, Fig. 13.2 represents the time response of the generator speed equipped with controller FFTSF and controller MPC in dashed and

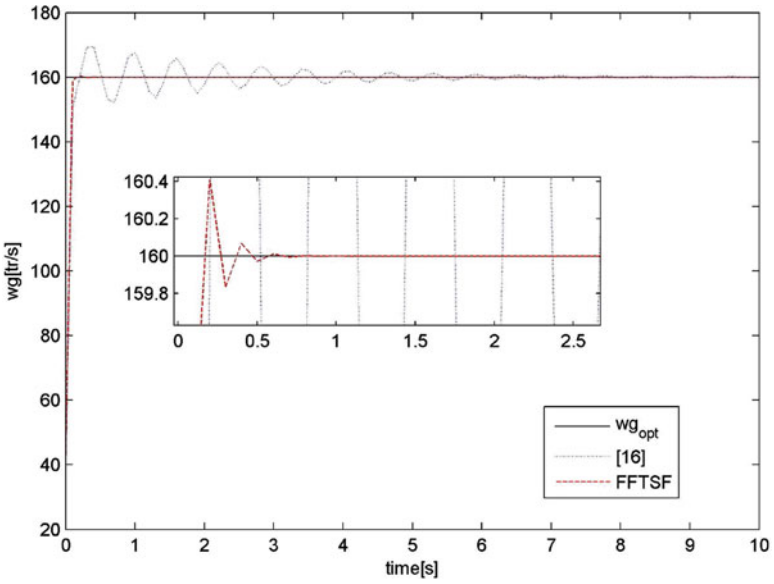

Fig. 13.2 Response time of the generator speed

dotted lines respectively, the solid line represents the optimal signal of the generator speed. The time response of controller laws: Pitch angle β_d and Zero-torque speed Ω are shown in Figs. 13.3 and 13.4, respectively. Figure 13.5 represents the variation of the membership functions.

According to these results, the generator speed with the proposed control strategy converges faster without any oscillatory behavior to its optimal value (Fig. 13.2) compared to this of the MPC controller which has some oscillators at the beginning of convergence. We can also observe that the proposed control laws, the pitch angle β_d (Fig. 13.3) and the Zero-torque Ω (Fig. 13.4), yields the best performance in terms of stability and convergence. Moreover, the applied effort at the regime transient is too small despite the presence of strong variations in wind speed.

13.5 Conclusions

This chapter proposes a Feedback T-S fuzzy controller in finite frequency synthesis for a variable speed wind turbine, which is designed using GKYP lemma extended to T-S fuzzy model. The T-S fuzzy is used to deal with the highly nonlinear term of aerodynamics torque, and the finite frequency in order to design the feedback control. The main objective of the developed control strategy is to improve the robustness of the system in a certain finite frequency range where the system operates or the external disturbance has existed. The effectiveness of the control

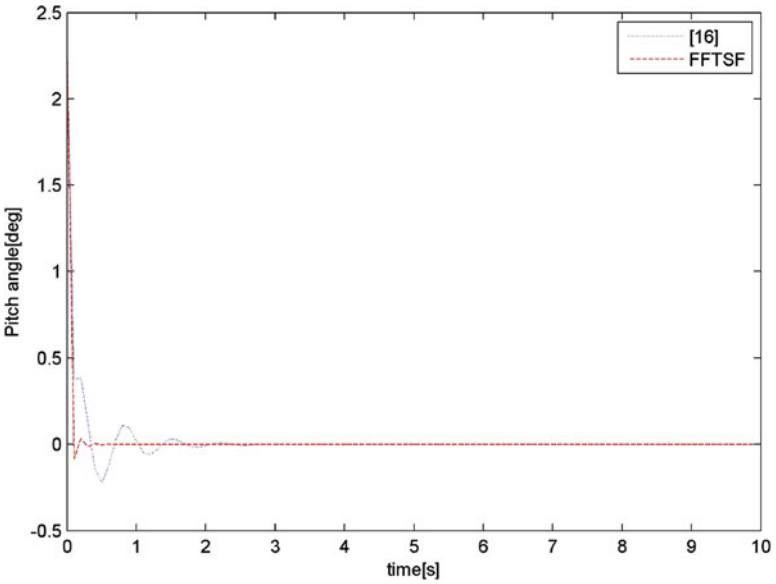

Fig. 13.3 Desired pitch angle control

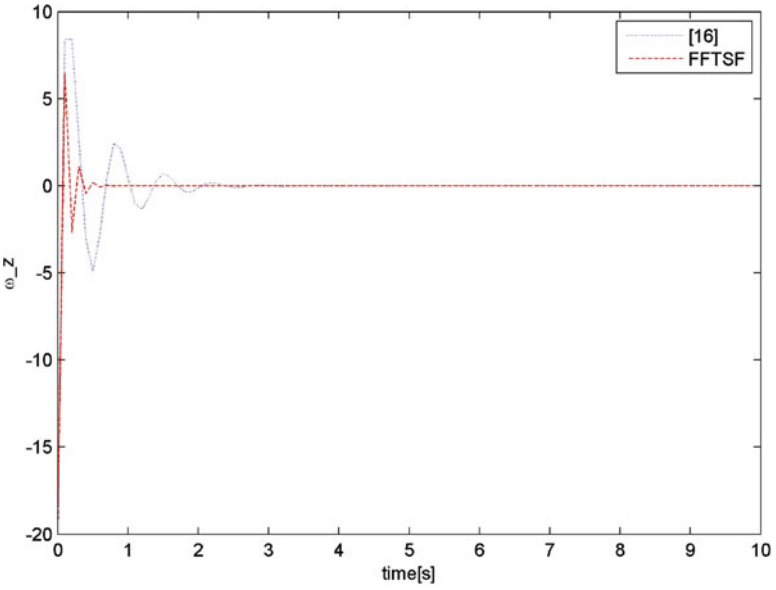

Fig. 13.4 Zero-torque speed control

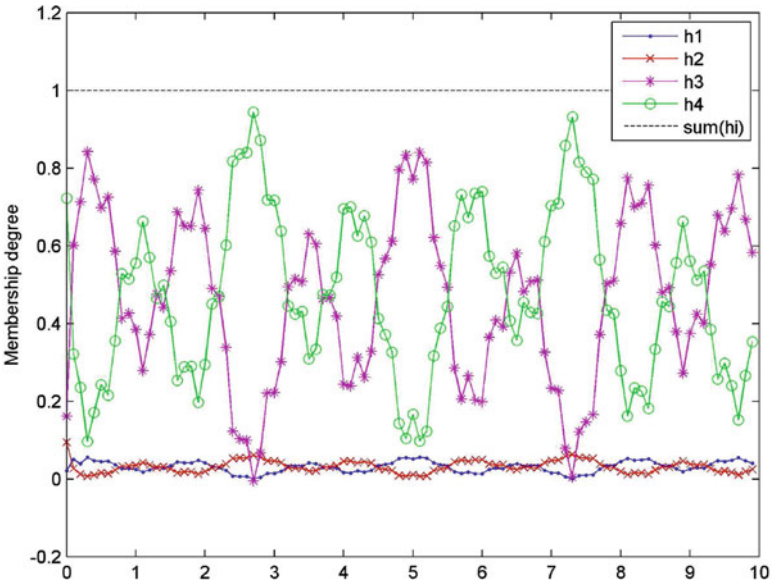

Fig. 13.5 Membership functions

strategy compared with a predictive controller has been realized, and simulation results have shown an interesting performance of the proposed control strategy in terms of stability and convergence speed, allowing a better regulation of the power generated by the wind turbine.

References

An, A., Yang, G., Zhang, H., & Du, P. (2015). PMSG maximum wind power tracking control based on TS fuzzy method. In *IEEE 27th Chinese Control and Decision Conference (CCDC)*, Qingdao (pp. 2844–2849).

Apkarian, P., Tuan, H. D., & Bernussou, J. (2001). Continuous-time analysis, eigenstructure assignment, and H/sub 2/synthesis with enhanced linear matrix inequalities (LMI) characterizations. *IEEE Transaction on Automatic Control, 46*(12), 1941–1946.

Berrada, Y., El Amrani, A., & Boumhidi, I. (2017). Finite frequency T-S fuzzy control for a variable speed wind turbine. In *14th IEEE International Multi-conference on Systems, Signals & Devices (SSD)*, Marrakech (pp. 505–510).

Bououden, S., Chadli, M., Filali, S., & El Hajjaji, A. (2012). Fuzzy model based multivariable predictive control of a variable speed wind turbine: LMI approach. *Renewable Energy, 37*(1), 434–439.

Chen, Y., Zhang, W., & Gao, H. (2010). Finite frequency H∞ control for building under earthquake excitation. *Mechatronics, 20*(1), 128–142.

El-Amrani, A., Hmamed, A., Boukili, B., & El Hajjaji, A. (2016). H_∞ filtering of TS fuzzy systems in finite frequency domain. In *5th IEEE International Conference on Systems and Control (ICSC)*, Marrakech (pp. 306–312).

Galdi, V., Piccolo, A., & Siano, P. (2008). Designing an adaptive fuzzy controller for maximum wind energy extraction. *IEEE Transaction on Energy Conversion, 23*(2), 559–569.

Goodwin, G. C., Graebe, S. F., & Salgado, M. E. (2001). *Control system design*. Upper Saddle River: Prentice Hall.

Hafiz, F., & Abdennour, A. (2016). An adaptive neuro-fuzzy inertia controller for variable-speed wind turbines. *Renewable Energy, 92*, 136–146.

Iwasaki, T., & Hara, S. (2005). Generalized KYP lemma: Unified frequency domain inequalities with design applications. *IEEE Transaction on Automatic Control, 50*(1), 41–59.

Lasheen, A., & Elshafe, I. A. L. (2016). Wind-turbine collective-pitch control via a fuzzy predictive algorithm. *Renewable Energy, 87*, 298–306.

Li, X. J., & Yang, G. H. (2015). Adaptive H_∞ control in finite frequency domain for uncertain linear systems. *Information Sciences, 314*, 14–27.

Liu, P., Yang, W. T., Yang, C. E., & Hsu, C. L. (2015). Sensorless wind energy conversion system maximum power point tracking using Takagi-Sugeno fuzzy cerebellar model articulation control. *Applied Soft Computing, 29*, 450–460.

Medjber, A., Guessoum, A., Belmili, H., & Mellit, A. (2016). New neural network and fuzzy logic controllers to monitor maximum power for wind energy conversion system. *Energy, 106*, 137–146.

Skelton, R. E., & Iwasaki, T. (1998). *A unified algebraic approach to linear control design*. London/Bristol: Taylor and Francis.

Zhang, H., Wang, R., Wang, J., & Shi, Y. (2014). Robust finite frequency H_∞ static-output-feedback control with application to vibration active control of structural systems. *Mechatronics, 24*(4), 354–366.

Chapter 14
Intelligent Load Frequency Control in Presence of Wind Power Generation

Nour EL Yakine Kouba and Mohamed Boudour

Abstract With the advent of large-scale interconnected power systems, many new problems have emerged, which include frequency fluctuations problem. In many parts of the world, installed capacity and energy production levels for electric generation from non-conventional renewable resources such as wind power generation are growing rapidly. However, the fluctuations of these generators affect the system frequency. The purpose of this work is to design an intelligent load frequency control (LFC) strategy based on Fuzzy Logic-PID controller to suppress all the fluctuations of the total power output of the wind generation and maintain the constancy of the system frequency. To show the effectiveness of the proposed control strategy, a two-area multi-sources power system was investigated for the simulation. The observed simulation results of the proposed Fuzzy Logic-PID controller are compared with the results obtained by the classical Ziegler-Nichols method and the meta-heuristic Particle Swarm Optimization (PSO) technique. The transient responses showing the integration impact of the wind farm are depicted and the results are tabulated as a comparative performance in view of peak overshoot and settling time. The results are compared and the ability of the proposed approach to evaluate load frequency control over large wind farm integration is confirmed.

Keywords Load frequency control (LFC) · PID controller · Fuzzy logic control (FLC) · Wind power generation · Wind farm

N. EL. Y. Kouba (✉) · M. Boudour
Laboratory of Electrical and Industrial Systems, Faculty of Electrical Engineering and Computing, University of Sciences and Technology Houari Boumediene, Bab Ezzouar, Algiers, Algeria
e-mail: nkouba@ieee.org; mboudour@ieee.org

N. Derbel, Q. Zhu (eds.), *Modeling, Identification and Control Methods in Renewable Energy Systems*, Green Energy and Technology,
https://doi.org/10.1007/978-981-13-1945-7_14

14.1 Introduction

The endeavor for a more sustainable power generation has led to a fast increase in green power generation from renewable energy sources (RES), such as wind, biomass, hydro and solar power. These sources are of a fluctuating nature; consequently, many new challenges must be introduced in power system stability and control. Amongst them, a wind farm type of power generation is considered the most viable alternative (Kouba et al. 2016c,d). The generation of wind energy is clean, exhaustless and more economic. However, this energy is not stable and cannot ensure the constant power generation because it depends on the wind as a natural source (Bevrani and Daneshmand 2012). In addition, a large wind farm can include hundreds of wind turbines and the output of each one of them depends on wind direction and velocity, which result into frequency oscillations (Eduardo et al. 2011; Kouba et al. 2016a). The control of system frequency is a vital aspect for a secure and stable electrical network with good power quality. Frequency control can be called upon for a variety of conditions ranging from a gradual change in load levels over time to a sudden loss of generation or step increase/decrease in load. A continuous balance between active power generated and active power consumed by the load and losses is required to maintain frequency constant at nominal system frequency value within an acceptable tolerance (Patnaik and Dash 2015; Sahu et al. 2013). The frequency and load have an inverse relationship; therefore any imbalance in active power will result in a frequency deviation. Maintaining the frequency at its nominal value requires that both active power produced and consumed be controlled to keep the load and supply in equilibrium. The increasing size of the interconnected power systems has been accompanied with the appearance of the frequency fluctuations problems, which may results in disconnection actions, loss of several lines, zone isolation and black-out. Therefore, the frequency control on an interconnected electrical network is particularly challenging function and can be considered to be one of the most crucial aspects of ancillary services (Bihui et al. 2011; Kouba et al. 2016b). In large-scale interconnected power system, balancing power production and consumption is usually guaranteed by Automatic Generation control (AGC) scheme adjusting production of some power plants to meet the current demand (Ramakrishna and Bhatti 2008). If there is a power mismatch, system frequency will change as the rotating mass in generators will be either accelerated, thus increasing frequency, if too much electric power is produced, or decelerated, thus decreasing frequency, if the demand is bigger than the production (Kiaee et al. 2013; Prakash and Sinha 2014). In the case of any contingencies such as the change in load, failure of a plant or the outage of a line, if no action is taken and the power mismatch remains, system frequency will diverge until a critical point is reached resulting in a black-out, which is an undesirable case. Generally, in the Transmission System Operators (TSOs) the AGC scheme is mapped to three control levels which are: primary, secondary and tertiary control. The primary control is implemented through the governor control system and is used to stabilize the system frequency. The secondary control named also load

frequency control (LFC), reacts slower than primary control and is used to relieve the primary control and restore the system frequency to its pre-disturbance nominal value. Finally, Tertiary control refers to the economic dispatching control (EDC) of each unit and is used to relieve the secondary control loop (LFC) (Kouba et al. 2014b; Tofighi et al. 2015). As major functions of automatic generation control (AGC), power system frequency regulation named load frequency control (LFC) become one of the most important research topics in power system operation. The main goals of LFC are to suppress the fluctuations of the system frequency and maintain the frequency and the power interchanges with neighboring control areas at the scheduled values. To satisfy these objectives, a control error signal called the Area Control Error (ACE) is measured, which represents the real power imbalance between generation and load, where this signal combines both frequency and net interchange flow deviations (Kiaee et al. 2013; Ramakrishna and Bhatti 2008). A PID controller is used to support the frequency regulation LFC loop in each control area, while the measured ACE signal is the input of the PID controller in each control area (Kouba et al. 2014b). In fact, small variations in system frequency will not result in a reduction of system reliability and security. In contrast, large frequency fluctuations in particularly with the increasing integration of renewable energy sources such as wind power generation can have a serious impact on power system equipments and power quality (Chung et al. 2011; Hooshmand et al. 2012). The large increase integration of wind farm in the grid causes extensive changes in power systems, and the generation does not equal scheduled generation at all times, while this mismatch adds to the usual imbalances between supply and demand. However, if a large amount of wind power generation is installed in the grid; it becomes difficult to remove frequency fluctuations. Therefore, it's necessary to study the effects on the frequency control and assess the impact of wind integration. In the aim to balance the deviation between power production and power demand in presence of a large penetration of wind power generation, a robust LFC controller scheme is needed to satisfy these objectives. Various studies consider new control methods dealing with the design of the secondary frequency controller (LFC) have been proposed and discussed in last decades. In 1942, Ziegler and Nichols proposed two heuristic approaches based on their experience and some simulations to quickly adjust the controller parameters: P, PI, and PID (Kouba et al. 2014b). Many others techniques were used for tuning the PID controller parameters such as the stochastic particle swarm optimization (PSO) (RamaSudha et al. 2010), bacterial foraging optimization algorithm (BFOA) (Nanda et al. 2009), hybrid algorithm between bacterial foraging and particle swarm optimization (BF-PSO) (Kouba et al. 2014a), genetic algorithm (GA) (Demirören et al. 2002; Panda and Yegireddy 2013), differential evolution algorithm (DEA) (Pandey et al. 2013), firefly algorithm (FA) (Saikia and Sahu 2013), and many others strategies have been proposed for the LFC study such as the artificial neural network (ANN) (Kouba et al. 2014c; Mahabuba and Khan 2009; Saikia et al. 2011) and H-infinity techniques (Singh et al. 2013). In this work, a dynamic study of the load frequency control (LFC) with a large penetration of wind power generation is presented. The LFC problem has been analyzed using a new algorithm based on the implicit integration

Trapezoidal rule with variable time step and iterative Newton-Raphson method. The wind farm is modeled using a high-number of wind turbines and its impact on the system frequency and the tie-line power flow is examined. A dynamic model of the IEE Japan East 107-bus 30-generator power system is investigated for the purpose of studying long-term frequency stability and control on an interconnected two-area power system concerning high penetration of wind farm. The obtained results are compared to the classical LFC based Ziegler-Nichols method and, thereby to the optimal LFC based particle swarm optimization (PSO) technique. This work is organized as follows. In Sect. 14.2, the interconnected power system model is presented. In Sect. 14.3, the Load Frequency Control (LFC) model is described, and the algorithm used for the frequency stability analysis in this work is explained in detail. Section 14.4 illustrates the proposed Fuzzy Logic-PID controller technique. Section 14.5 is devoted to the modeling of the wind farm. Results of the wind farm integration analysis are given and discussed in Sect. 14.6. Finally, Sect. 14.7 includes the conclusion of this work.

14.2 Interconnected Power System Model

To investigate the performance of the proposed control strategy, the multi-machines power generation (hydro, thermal, and nuclear) IEE Japan East is considered as the test system. This electrical system is widely used in the literature as a standard system for testing of new power system analysis and control strategies. Figure 14.1 shows a single-line diagram of the test system (Arita et al. 2006). This electrical network consists of 107 buses, 30 generators, 31 loads, 191 branches, 136 transmission lines and 55 transformers. The power system is divided to two interconnected control areas. All power generating units in the power system are equipped with generator, turbine and speed governor. The interconnection between the control areas is made using a tie-line power flow. It is noted that, outputs of hydro, thermal and nuclear power plants are controlled automatically with the LFC signal.

In this work, all proposed thermal and nuclear units are modeled with an equivalent thermal unit and all proposed hydro power plans are modeled with an equivalent hydro unit. For the load frequency control study, a classical model of synchronous machine is needed, which includes the mechanicals equations of the generator (swing equation) and the speed regulation system (governor-turbine) model. In our problem, the differential equations representing dynamics of rotating machines are linearized by a numerical integration method, such as the implicit integration Trapezoidal rule, and solved using the iterative Newton-Raphson method for each time step Δt. The control loop model of a synchronous machine which is used in this work is shown in Fig. 14.2.

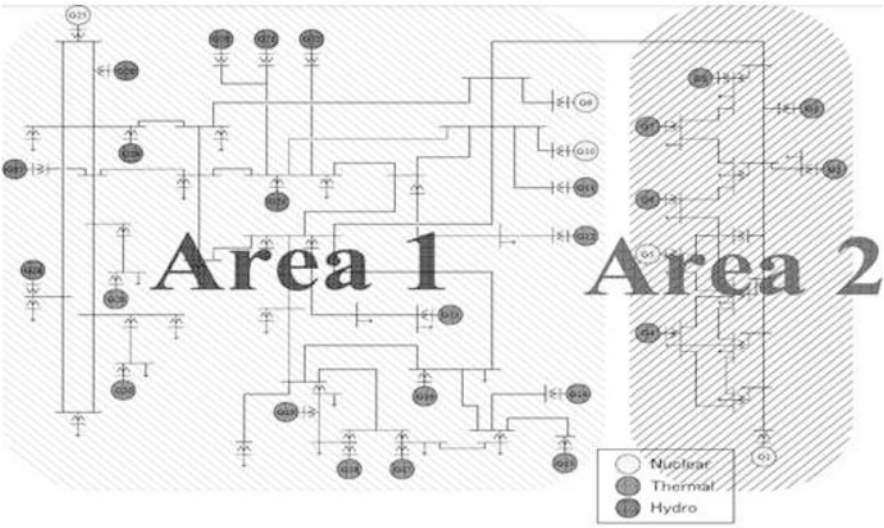

Fig. 14.1 IEE Japan East 107-bus 30-machine power system model

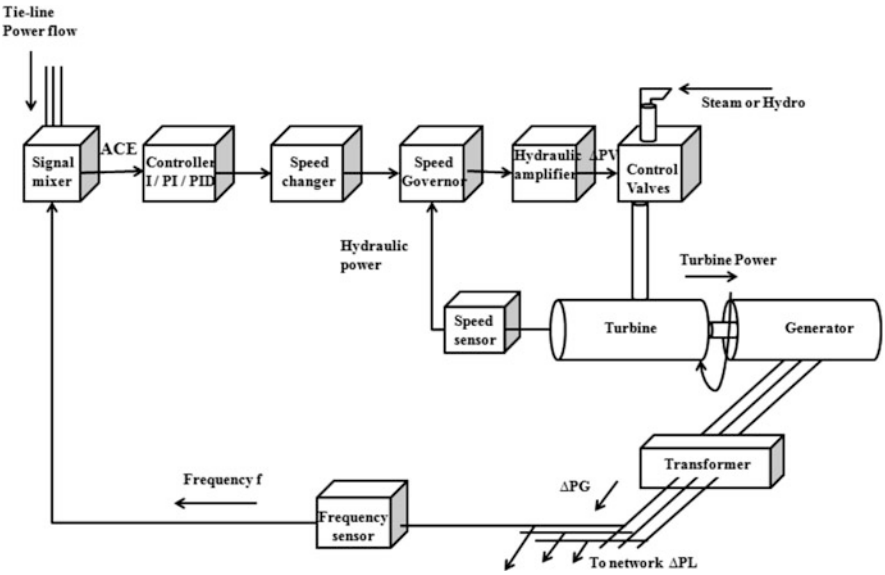

Fig. 14.2 Load frequency control loop of a synchronous machine

14.2.1 Generator Model

The relationship between the mechanical power ΔP_m and the electrical power ΔP_e is given by Arita et al. (2006):

$$M\frac{d\Delta\omega}{dt} = \Delta P_m - \Delta P_e \tag{14.1}$$

The load in a power system is the sum of various power demands and varies randomly over time. Some loads depend on the change of frequency and others don't. In general, the expression of the electrical power which depends on the frequency change can be expressed by Kouba et al. (2014b):

$$\Delta P_e = \Delta P_L + D\Delta\omega \tag{14.2}$$

In multi-machines system, if all generators are assumed to turn with the same speed of synchronism, the equations of the equivalent generator can be expressed with:

- The equivalent inertia constant:

$$M_{eq} = \frac{\sum_{i=1}^{i=n} M_i}{n} \tag{14.3}$$

- The equivalent load-damping constant:

$$D_{eq} = \frac{\sum_{i=1}^{i=n} D_i}{n} \tag{14.4}$$

The block diagram representation of equivalent generator used in this work is shown in Fig. 14.3.

The equivalent generator can be expressed by the following equation:

$$\frac{d\Delta\omega}{dt} = \frac{1}{M_{eq}}\left[\Delta P_{mth} + \Delta P_{mh} - (\alpha\Delta P_{tie}) - \Delta P_L - (D_{eq}\Delta\omega)\right] \tag{14.5}$$

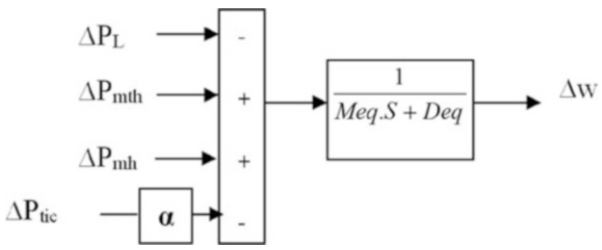

Fig. 14.3 Block diagram representation of equivalent generator

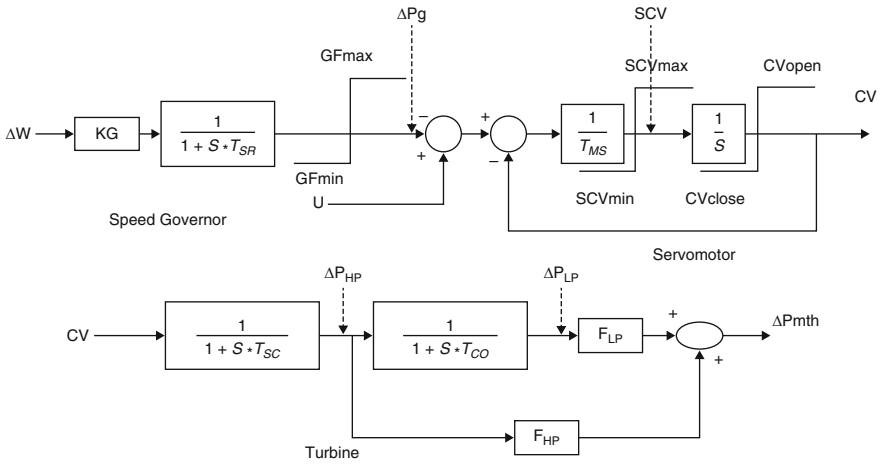

Fig. 14.4 Block diagram of governor-turbine model for thermal/nuclear unit

14.2.2 Governor-Turbine System Model

The main role of a speed governor control system is to adjust the turbine valve to stabilize the system frequency. The schematics of such governors control systems used in this work are shown in Fig. 14.4 for the thermal and nuclear unit and in Fig. 14.5 for the hydro unit (Kouba et al. 2014b).

The equations representing the thermal/nuclear power plant are given by:

$$\begin{cases} \dfrac{d\Delta P_g}{dt} = \dfrac{1}{T_{SR}}(K_G \Delta\omega - \Delta P_g) \\ With: \quad GF_{min} < \Delta P_g < GF_{max} \end{cases} \tag{14.6}$$

$$\begin{cases} SCV = \dfrac{1}{T_{SM}}(U - \Delta P_g - CV) \\ With: \quad SCV_{min} < SCV < SCV_{max} \end{cases} \tag{14.7}$$

$$\begin{cases} \dfrac{dCV}{dt} = \dfrac{1}{T_{SM}}(U - \Delta P_g - CV) \\ With: \quad CV_{close} < CV < CV_{open} \end{cases} \tag{14.8}$$

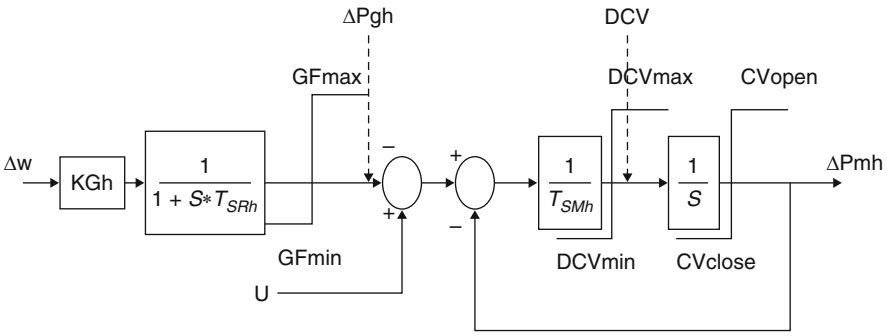

Fig. 14.5 Block diagram of governor-turbine model for hydro unit

$$\begin{cases} \dfrac{d\Delta P_{HP}}{dt} = \dfrac{1}{T_{SC}}(CV - \Delta P_{HP}) \\ \dfrac{d\Delta P_{LP}}{dt} = (\dfrac{1}{T_{CO}})(\Delta P_{HP} - \Delta P_{LP}) \end{cases} \tag{14.9}$$

The mechanical power for the thermal unit is calculated by this expression:

$$\Delta P_{mth} = (F_{HP}\Delta P_{HP}) + (F_{LP}\Delta P_{LP}) \tag{14.10}$$

The equations representing the hydro power plant are given by:

$$\begin{cases} \dfrac{d\Delta P_{gh}}{dt} = (\dfrac{1}{T_{SRH}})((\Delta\omega K_{Gh}) - \Delta P_{gh}) \\ With: \quad GF_{min} < \Delta P_{gh} < GF_{max} \end{cases} \tag{14.11}$$

$$\begin{cases} DCV = (\dfrac{1}{T_{SMh}})(U - \Delta P_{gh} - \Delta P_{mh}) \\ With: \quad DCV_{min} < DCV < DCV_{max} \end{cases} \tag{14.12}$$

$$\begin{cases} \dfrac{d\Delta P_{mh}}{dt} = (\dfrac{1}{T_{SMh}})(U - \Delta P_{gh} - \Delta P_{mh}) \\ With: \quad CV_{close} < CV < CV_{open} \end{cases} \tag{14.13}$$

14.2.3 Tie-Line Model

Using DC load flow method and assuming that the tie-line is from area-1 to area-2, the deviation ΔP_{12} from the nominal flow can be expressed (Kouba et al. 2014a) by:

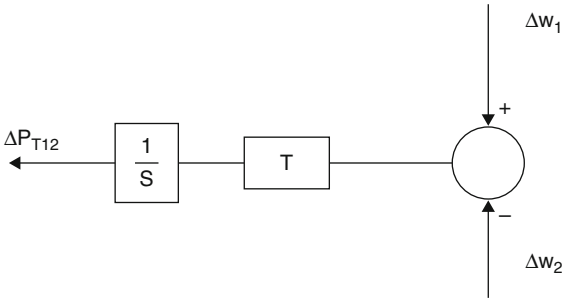

Fig. 14.6 Block diagram of the tie-line power flow model

$$\frac{d\Delta P_{tie}}{dt} = T_{12}(\Delta\omega_1 - \Delta\omega_2) \tag{14.14}$$

The block diagram representation for the tie-line is shown in Fig. 14.6.

14.3 Load Frequency Control (LFC) Model

The frequency has an inverse relationship with the load that is changing continually. Hence, the change in real power affects the system frequency. To maintain the system frequency constant, the power supply must follow the momentary power load change. Corresponding to the demand fluctuation, three control strategies as mentioned in the introduction are used in the electrical network to solve frequency fluctuation problem. The primary control: is a local control through the speed governor control system, is used to stabilize the frequency and is effective for the load change within ten seconds of the disturbance. The secondary control: named the load frequency control (LFC) is used for the disturbance with the period of several minutes to about 30 min. The objective of the LFC loop is to adjust operating point reference of governor in the control area and maintain the system frequency at the nominal value. The tertiary control: refers to the economic dispatching control (EDC) of units, and presents a part of the regular market clearing mechanism. Tertiary control acts on minute-to-hours time scale (30 min–h) (Kassem et al. 2013; Liu et al. 2015; Pan and Das 2015; Pandey et al. 2013; Rahmani and Sadati 2013). In large and interconnected power systems, the load frequency control is considered as the most important control strategy to remove the fluctuations with a long-period. In the centralized LFC model, to evaluate the area requirement (AR), the actual frequency and net interchange power flow are measured by the independent system operator (ISO). The LFC output power signal is sent to each generator when the frequency deviation is detected. Then, each speed governor output of the selected power plant is adjusted by the LFC signal to change the power plant output. To better understanding the function of LFC, Fig. 14.7 depicts the general LFC algorithm. To keep the system frequency and power balance at the scheduled values, each generator is equiped with PID controller. The PID parameters are tuned using the

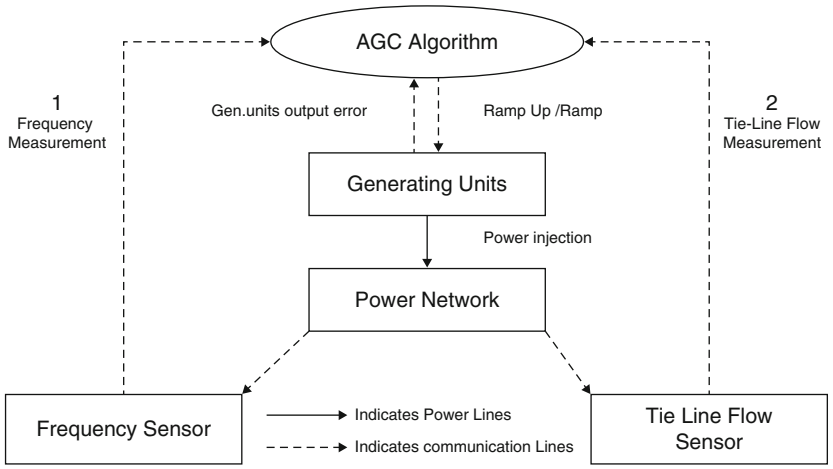

Fig. 14.7 AGC/LFC algorithm

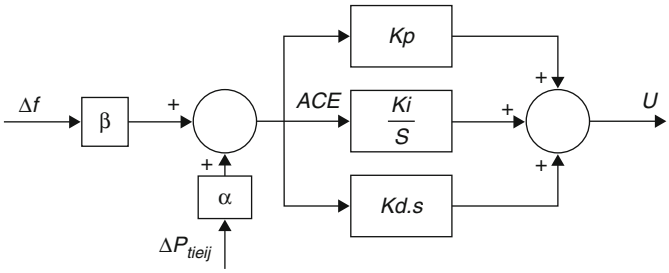

Fig. 14.8 Block diagram of LFC model

traditional Ziegler-Nichols method, the meta-heuristic particle swarm optimization (PSO) algorithm, and the Fuzzy Logic (FL) strategy. The diagram of the LFC model used in this work is shown in Fig. 14.8 (Kouba et al. 2014a). The input signal of each PID controller is the area control error (ACE), which is given by:

$$ACE_i = \alpha \Delta P_{tie} + \beta_{fi} \Delta \omega_i \tag{14.15}$$

The control equation U in each control area is given by:

$$U = ACE(K_p + \frac{K_i}{S} + K_d S) \tag{14.16}$$

In order to analyze the LFC problem in the two-area interconnected power system, the differential equations system in Eq. (14.17) is algebraized using the implicit Trapezoidal integration rule. After that, the resulting algebraic equations are solved using the iterative Newton-Raphson method at each time step based on

the work developed in Kouba et al. (2014b). By application of implicit integration Trapezoidal rule with a variable integration time step ($h = \Delta t$), the following equations can be obtained:

$$F = \left[X_{n+1} - \frac{\Delta t}{2} f(X_{n+1}, t_{n+1})\right] - \left[X_n + \frac{\Delta t}{2} f(X_n, t_n)\right] \tag{14.17}$$

The differential equations system for the LFC analysis is given by:

$$\begin{cases} \dfrac{d\Delta P_g}{dt} = \dfrac{1}{T_{SR}}(K_G \Delta\omega - \Delta P_g) \\ \dfrac{dCV}{dt} = \dfrac{1}{T_{SM}}(U - \Delta P_g - CV) \\ \dfrac{d\Delta P_{HP}}{dt} = \dfrac{1}{T_{SC}}(CV - \Delta P_{HP}) \\ \dfrac{d\Delta P_{LP}}{dt} = \dfrac{1}{T_{CO}}(\Delta P_{HP} - \Delta P_{LP}) \\ \dfrac{d\Delta P_{gh}}{dt} = \dfrac{1}{T_{SRH}}(K_{Gh}\Delta\omega - \Delta P_{gh}) \\ \dfrac{d\Delta P_{mh}}{dt} = \dfrac{1}{T_{SMh}}(U - \Delta P_{gh} - \Delta P_{mh}) \\ \dfrac{d\Delta\omega}{dt} = \dfrac{1}{M_{eq}}(\Delta P_{mth} + \Delta P_{mh} - \alpha\Delta P_{tie} - \Delta P_L - D_{eq}\Delta\omega) \\ \dfrac{dU_I}{dt} = K_I(\alpha\Delta P_{tie} - \beta_f\Delta\omega) \\ \dfrac{d\Delta P_{tie}}{dt} = T_{12}(\Delta\omega_1 - \Delta\omega_2) \end{cases} \tag{14.18}$$

By applying Eq. (14.17) to the deferential equations system (14.18), the obtained algebraic equations system is given in (14.20), where:

$$F_{1(j,i)} = \begin{bmatrix} F_{11(j,i)} \\ F_{12(j,i)} \\ F_{13(j,i)} \\ F_{14(j,i)} \end{bmatrix};\ F_{2(j,i)} = \begin{bmatrix} F_{21(j,i)} \\ F_{22(j,i)} \end{bmatrix};\ F_{3(i)} = \begin{bmatrix} F_{31(i)} \\ F_{32(i)} \end{bmatrix};\ F_{4(i)} = \begin{bmatrix} F_{4(i)} \end{bmatrix}$$

$$F = [F_1, F_2, F_3, F_4]^t \tag{14.19}$$

At each time step h, the equation $[F] = 0$ is solved by Eq. (14.21).

$$
\begin{cases}
F_{11}(x_n+1,x_n) = \left[\Delta P_{g_{n+1}} - \dfrac{\Delta t}{2T_{SR}}(K_G\Delta\omega_{n+1} - \Delta P_{g_{n+1}})\right] \\
\qquad - \left[\Delta P_{g_n} + \dfrac{\Delta t}{2T_{SR}}[((\Delta\omega_n K_G) - \Delta P_{g_n})]\right] \\
F_{12}(x_n+1,x_n) = \left[CV_{n+1} - \dfrac{\Delta t}{2T_{SM}}(U_{n+1} - \Delta P_{g_{n+1}} - CV_{n+1})\right] \\
\qquad - \left[CV_n + \dfrac{\Delta t}{2T_{SM}}(U_n - \Delta P_{g_n} - CV_n)\right] \\
F_{13}(x_n+1,x_n) = \left[\Delta P_{HP_{n+1}} - \dfrac{\Delta t}{2T_{SC}}(CV_{n+1} - \Delta P_{HP_{n+1}})\right] \\
\qquad - \left[\Delta P_{HP_n} + \dfrac{\Delta t}{2T_{SC}}(CV_n - \Delta P_{HP_n})\right] \\
F_{14}(x_n+1,x_n) = \left[\Delta P_{LP_{n+1}} - \dfrac{\Delta t}{2T_{CO}}(\Delta P_{HP_{n+1}} - \Delta P_{LP_{n+1}})\right] \\
\qquad - \left[\Delta P_{LP_n} + \dfrac{\Delta t}{2T_{CO}}(\Delta P_{HP_n} - \Delta P_{LP_n})\right] \\
F_{21}(x_n+1,x_n) = \left[\Delta P_{gh_{n+1}} - \dfrac{\Delta t}{2T_{SRH}}(K_{Gh}\Delta\omega_{n+1} - \Delta P_{gh_{n+1}})\right] \\
\qquad - \left[\Delta P_{gh_n} + \dfrac{\Delta t}{2T_{SRH}}(K_{Gh}\Delta\omega_n - \Delta P_{gh_n})\right] \\
F_{22}(x_n+1,x_n) = \left[\Delta P_{mh_{n+1}} - \dfrac{\Delta t}{2T_{SMh}}(U - \Delta P_{gh_{n+1}} - \Delta P_{mh_{n+1}})\right] \\
\qquad - \left[\Delta P_{mh_n} + \dfrac{\Delta t}{2T_{SMh}}(U - \Delta P_{gh_n} - \Delta P_{mh_n})\right] \\
F_{31}(x_n+1,x_n) = (\Delta\omega_{n+1} - \Delta\omega_n) - \dfrac{\Delta t}{2M_{eq}}\times \\
\qquad \left[(\Delta P_{mth_{n+1}} + \Delta P_{mh_{n+1}} - \alpha\Delta P_{tie_{n+1}} - \Delta P_L - D_{eq}\Delta\omega_{n+1})\right. \\
\qquad \left.-(\Delta P_{mth_n} + \Delta P_{mh_n} - \alpha\Delta P_{tie_n} - \Delta P_L - D_{eq}\Delta\omega_n)\right] \\
F_{32}(x_n+1,x_n) = (U_{I_{n+1}} - U_{In}) - \dfrac{\Delta t}{2}\times \\
\qquad \left[K_I\alpha(\Delta P_{tie_{n+1}} - \Delta P_{tie_n}) - \beta_f(\Delta\omega_{n+1} - \Delta\omega_n)\right] \\
F_4(x_n+1,x_n) = (\Delta P_{tie_{n+1}} - \Delta P_{tie_n}) - \dfrac{\Delta t}{2}\times \\
\qquad \left[T_{12}(\Delta\omega_{1_{n+1}} - \Delta\omega_{1_n}) - (\Delta\omega_{2_{n+1}} - \Delta\omega_{2_n})\right]
\end{cases}
\tag{14.20}
$$

In our problem of LFC, the Newton-Raphson iterates are:

$$(J)^k[\Delta x_{n+1}]^k = -[F]^k \tag{14.21}$$

$$\begin{pmatrix} J_1 & J_2 & J_3 & J_4 & J_5 & J_6 \\ J_7 & J_8 & J_9 & J_{10} & J_{11} & J_{12} \\ J_{13} & J_{14} & J_{15} & J_{16} & J_{17} & J_{18} \\ J_{19} & J_{20} & J_{21} & J_{22} & J_{23} & J_{24} \\ J_{25} & J_{26} & J_{27} & J_{28} & J_{29} & J_{30} \\ J_{31} & J_{32} & J_{33} & J_{34} & J_{35} & J_{36} \end{pmatrix}^k \begin{pmatrix} \Delta X_1(1) \\ \Delta X_2(1) \\ \Delta X_3(1) \\ \Delta X_4 \\ \Delta X_1(2) \\ \Delta X_3(2) \end{pmatrix}^k = \begin{pmatrix} F_1(1) \\ F_2(1) \\ F_3(1) \\ F_4 \\ F_1(2) \\ F_3(2) \end{pmatrix}^k \tag{14.22}$$

The state vector is given by:

$$[X] = [\Delta P_{g_1} \quad CV_1 \quad \Delta P_{HP_1} \quad \Delta P_{LP_1} \quad \Delta P_{gh_1} \quad \Delta P_{mh_1} \quad \Delta\omega_1 \quad U_{I_1} \quad \Delta P_{tie}$$
$$\Delta P_{g_2} \quad CV_2 \quad \Delta P_{HP_2} \quad \Delta P_{LP_2} \quad \Delta\omega_2 \quad U_{I_2}]^t \tag{14.23}$$

The Jacobian matrix J is given by:

$$J = \begin{bmatrix} \frac{dF_1(1)}{dX_1(1)} & \frac{dF_1(1)}{dX_2(1)} & \frac{dF_1(1)}{dX_3(1)} & \frac{dF_1(1)}{dX_4} & \frac{dF_1(1)}{dX_1(2)} & \frac{dF_1(1)}{dX_3(2)} \\ \frac{dF_2(1)}{dX_1(1)} & \frac{dF_2(1)}{dX_2(1)} & \frac{dF_2(1)}{dX_3(1)} & \frac{dF_2(1)}{dX_4} & \frac{dF_2(1)}{dX_1(2)} & \frac{dF_2(1)}{dX_3(2)} \\ \frac{dF_3(1)}{dX_1(1)} & \frac{dF_3(1)}{dX_2(1)} & \frac{dF_3(1)}{dX_3(1)} & \frac{dF_3(1)}{dX_4} & \frac{dF_3(1)}{dX_1(2)} & \frac{dF_3(1)}{dX_3(2)} \\ \frac{dF_4}{dX_1(1)} & \frac{dF_4}{dX_2(1)} & \frac{dF_4}{dX_3(1)} & \frac{dF_4}{dX_4} & \frac{dF_4}{dX_1(2)} & \frac{dF_4}{dX_3(2)} \\ \frac{dF_1(2)}{dX_1(1)} & \frac{dF_1(2)}{dX_2(1)} & \frac{dF_1(2)}{dX_3(1)} & \frac{dF_1(2)}{dX_4} & \frac{dF_1(2)}{dX_1(2)} & \frac{dF_1(2)}{dX_3(2)} \\ \frac{dF_2(2)}{dX_1(1)} & \frac{dF_2(2)}{dX_2(1)} & \frac{dF_2(2)}{dX_3(1)} & \frac{dF_2(2)}{dX_4} & \frac{dF_2(2)}{dX_1(2)} & \frac{dF_2(2)}{dX_3(2)} \end{bmatrix} \tag{14.24}$$

The new solution at the iteration $k+1$ is calculated using the flowing equation:

$$x^{k+1} = \Delta x^k + x^k \tag{14.25}$$

1. The initial condition values x^0 are fixed.
2. The convergence of iterative Newton-Raphson is based on the max absolute error $\max |F(x^{k+1})|$ and the specified tolerance $\epsilon = 10^{-6}$.
3. If $\max|F(x^{k+1})| < \epsilon$, iterative Newton-Raphson have converged.

With: $i = 1 : ng$ number of area, and $j = 1 : m$ number of machines; (In our case $ng = 2$ and $m = 30$).

14.4 Fuzzy Logic Control

Nowadays, one of promising control methods in industrial automation and process control is the Fuzzy Logic Control (FLC). Because of simplicity, robustness, and reliability fuzzy logic is used in almost all research areas, including solving a wide range of control problems in power system control and operation. Fuzzy logic is an intelligent technique developed by Professor Lotfi Zadeh. He first introduced the theory of fuzzy sets and fuzzy logic in 1965 when he wrote his first paper entitled Fuzzy Sets (Pothiya and Ngamroo 2008; Shayeghi et al. 2008). This logic is the mathematical representation of the formation of human concepts and of reasoning concerning human concepts. Several published papers have shown and proven that fuzzy systems are strong and efficacy solution schemes. Moreover, the FLC is used in many commercial, domestic, automotive control applications, and has been successfully applied to many control problems (e.g. washing machines, televisions and photocopiers) because no mathematical modeling is involved. This work addresses the problem of tuning the optimal PID controller parameters using fuzzy logic strategy. Our aim in this work is to design a robust load frequency controller based Fuzzy Logic-PID controller to regulate the system frequency concerning large wind power penetration. A general scheme for Fuzzy Logic-PID controller based LFC system is designed as depicted in Fig. 14.9. As shown, the parallel combination between Fuzzy Logic and PID controller is adopted in this system. The Fuzzy Logic controller is implemented in three phases given as follow:

1. Fuzzification module (Fuzzifer).
2. Rule base and Inference engine.
3. Defuzzification module (Defuzzifier).

For the purpose of load frequency control analysis, the inputs of the fuzzy logic controller are the variables error (ACE) and change of error ($dACE$), and the outputs of the fuzzy logic are the PID parameters. The K_P, K_I, K_D values are calculated out according to offline rules in fuzzy controller.

A label set corresponding to linguistic variables of the input control signals, $ACE(Z)$ and $dACE(Z)$, with a sampling time of 0.01 s is as follows:

$$Li(ACE, dACE) = (NB, NS, ZE, PS, PB) \tag{14.26}$$

A label set corresponding to linguistic variables of the output control signals is as follows:

$$Lo(K_P, K_I, K_D) = (ZE, PS, PM, PB) \tag{14.27}$$

The membership function for the control input variables are shown in Fig. 14.10, and the membership function for the control output variables are given as shown in Fig. 14.11.

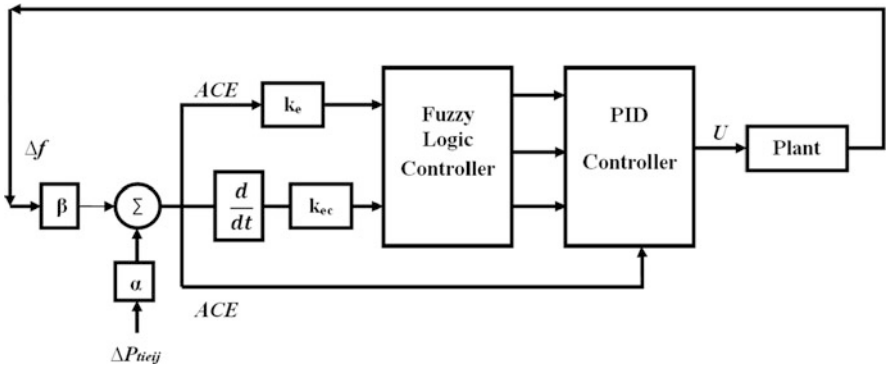

Fig. 14.9 Structure of fuzzy logic-PID controller

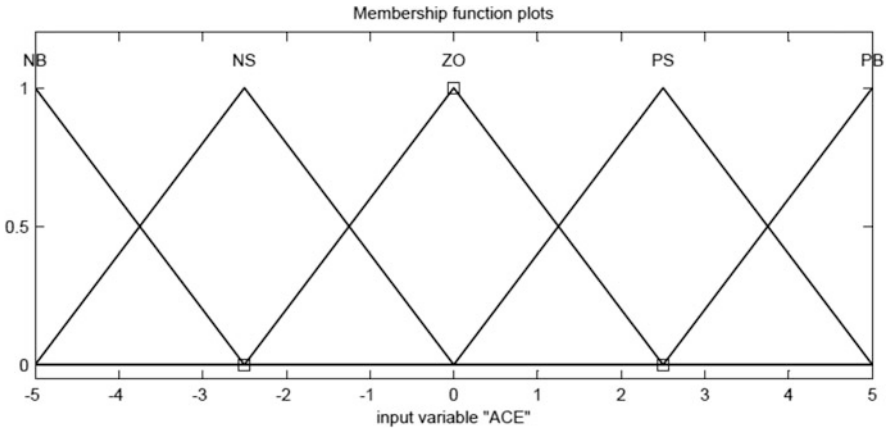

Fig. 14.10 Membership function for the control input variables

The control rules are built from the statement: if input a and input b then output Z, while Table 14.1 resumes the control rules used in this work. In this work the Triangular membership functions is used. The two input signals $(ACE, dACE)$ are converted to fuzzy numbers first in fuzzifier using five membership functions (NB, NS, ZE, PS, PB). Then they are used in the rule table shown in Table 14.1 to determine the fuzzy number of the compensated output signals. The proposed FLC model is shown in Fig. 14.12. The Fuzzy Logic Controller(FLC) is used to reach the optimal PID controller parameters. The proposed approach is compared to the heuristic Particle Swarm Optimization (PSO) technique, and to the classical Ziegler-Nichols method.

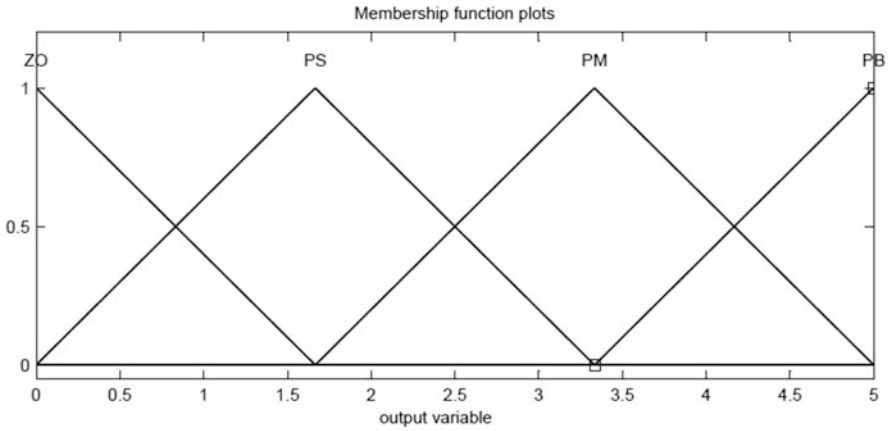

Fig. 14.11 Membership function for the control output variables

Table 14.1 Control rules

	ACE				
$dACE$	NB	NS	ZE	PS	PB
NB	PB	PB	PB	PB	PS
NS	PB	PM	PM	PB	PB
ZE	PB	PM	ZE	PB	PB
PS	PB	PM	PM	PM	PB
PB	PS	PB	PM	PM	PB

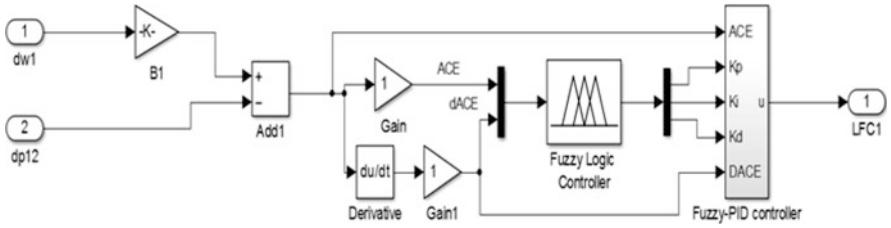

Fig. 14.12 Proposed fuzzy logic-PID controller structure

14.5 Wind Power Generation System

The increasing share of fluctuating renewable energy sources (RES) in the electrical networks poses new challenges for power systems operation and control. On the one hand, renewable energy sources can cover part of the increasing demand and provide electricity production with low marginal costs and reduce CO_2 emissions. In the other hand, large RES integration could influence the power quality and disturb the system stability. Presently, the grid integration of variable distributed generations (DG), such as wind power plants presents one of the most important issues in power system stability and control. Among all renewable energy sources,

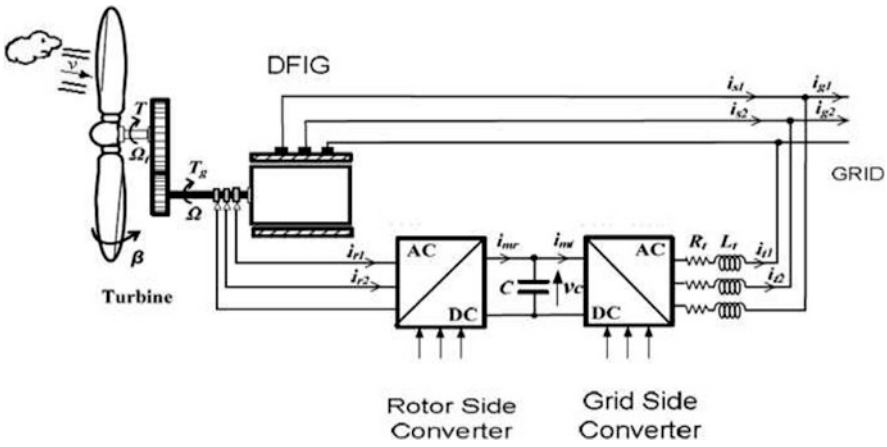

Fig. 14.13 Doubly fed induction generator model

the wind power is the most used in power system. Wind energy is a renewable electricity production from converting kinetic energy of moving air masses into electricity. The wind power is the most renewable energy source utilized in power systems, while this energy depends on the fluctuating nature of the wind direction and its velocity. In the last decades, wind turbines are effectively displacing classical generators and their rotating machinery (e.g. thermal, gas, or nuclear). Nowadays wind power plays an important role in the generation of electrical power as a single wind power plant with operational capabilities similar to a conventional power plant (Jafarian and Ranjbar 2013; Mandal et al. 2014; Wang and McCalley 2013). Therefore, the large deployment of wind turbine led to significant generation shares of wind farms in electrical power networks. Currently, wind power technology is becoming very important, while in the wind farms construction, the variable-speed wind turbine type is the most used technology. Today the doubly fed induction generator (DFIG) shown in Fig. 14.13 is the most used wind turbine, because of his high power control capability since a partial-scale power converter and variable speed operation. The impact analysis of wind farms on power system stability and control requires the development of suitable models. Many dynamic models of wind farms have been developed by researchers and network operators with different detail levels depending on the scope of the study (Ge et al. 2013; Michigami and Oishi 2001). However, high wind turbines penetration causes many implications in frequency dynamics and making frequency stability and control more challenging. When a large penetration of wind power generation is integrated in a small control area, it influences the area frequency control and the tie-line power flow. For that, it is necessary to study the impact of large-scale integration of wind power into interconnected power systems. Hence, maintaining the frequency stability in the electrical network depending to the active power balance is a necessary requirement for a good power quality. This makes the importance of impact study of wind power

integration into the grid a major issue especially during a contingency, which in the scope of this work. The purpose of this work is to analyze the impact of large wind farm integration in interconnected power system using the wind turbine model. Two hundred wind turbines (of 1.5 MW each) are used to represent a 300 MW wind farm, while the mathematical model of such wind turbine is given below.

14.5.1 Wind Turbine Model

Wind turbines produce electricity by using the power of the wind to drive an electrical generator. The power in the airflow is given by Hang et al. (2016), Schlechtingen et al. (2013), Zhang et al. (2013), Sarrias-Mena et al. (2015), and Attya and Hartkopf (2012):

$$P_{air} = \frac{1}{2}(\rho.S.V^3) \tag{14.28}$$

The extracted power from the wind can be expressed as follows:

$$P_{mech} = \frac{1}{2}(\rho.\pi.R^2.V^3.Cp(\lambda, \beta)) \tag{14.29}$$

The tip-speed ratio λ is defined by:

$$\lambda = \frac{\omega_{tr}.R}{V} \tag{14.30}$$

The power coefficient Cp is given by:

$$Cp(\lambda, \beta) = (\frac{1}{2} - 0,167).\beta.\sin(\frac{\pi.(\lambda + 1)}{18,5 - 0,3.\beta}) - 0,00184.(\lambda - 3).\beta \tag{14.31}$$

Figure 14.14 depicts the 1.5 MW wind turbine simulation model in MATLAB.

14.5.2 Wind Farm Model

Increased penetration of wind farm in the interconnected network poses new challenges to conventional power system operation and control. The impacts of increasing a large wind power penetration on system frequency regulation and active power control are of significant interest in the industry. As a result, there is a rising interest in the supplementary services such as the frequency regulator (i.e. load frequency control) in presence of wind farm. In a traditional interconnected power system (without RES), the purpose of the secondary control LFC is to take

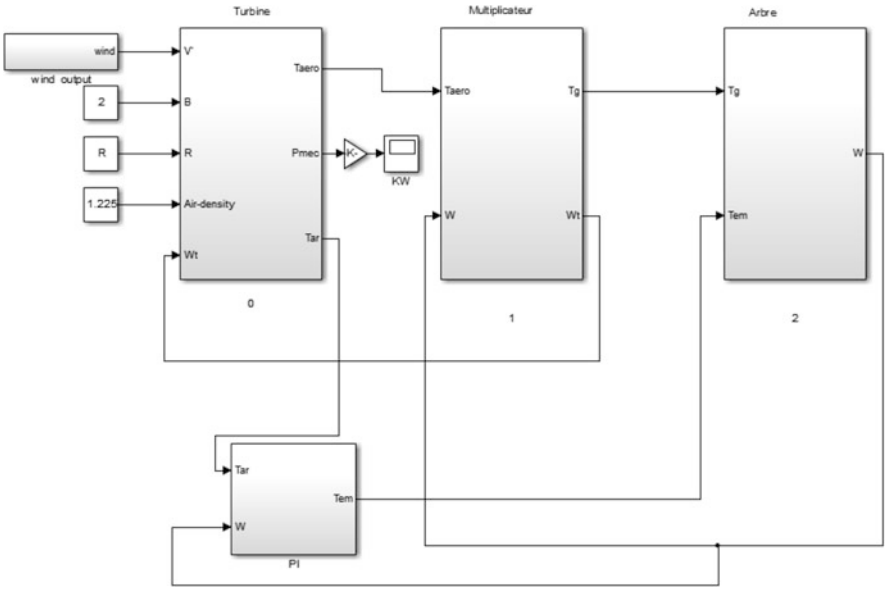

Fig. 14.14 1.5 MW wind turbine simulation model in MATLAB

back the system frequency to nominal value and maintain the balancing between the interconnected control areas. In contrast, due to the fluctuating nature of wind power, equilibrium between production and demand in presence of wind turbines is not an easy operation (Attya and Hartkopf 2012; Vrakopoulou 2013). Wind turbines are non-dispatchable and non-controllable such as the conventional power plants. Therefore, employing the stochastic nature of wind power may result in an adverse effect on the network. Furthermore, the increasing integration of wind farms to satisfy consumption it may has an opposite influence on both frequency control and power quality. It should thus be apparent that it is necessary to design a robust load frequency controller for optimal solution in presence of wind power generation. In a normal state of power system, automatic load frequency control takes place to keep the system within the safety margins, following generation and demand fluctuations. This LFC loop is also depending on the ability of the interconnected network to withstand disturbances. In presence of wind farm, the supply-demand active power mismatch occurs and the frequency will deviate from its nominal value. However, to analyze the additional fluctuation caused by wind farm, optimal LFC controller needs to be employed. The objective is to bring frequency fluctuation back to zero and maintain the power flow on the tie-lines that connect it with the other control areas at its scheduled value. Therefore, each power plant could be controlled using the supplementary frequency control LFC loop (Vrakopoulou 2013). In the case of a high number of wind turbines are installed into a balancing control area, fluctuations in wind power may reduce the balancing areas ability and makes the frequency control more difficult as shown in Fig. 14.15. Towards a stable

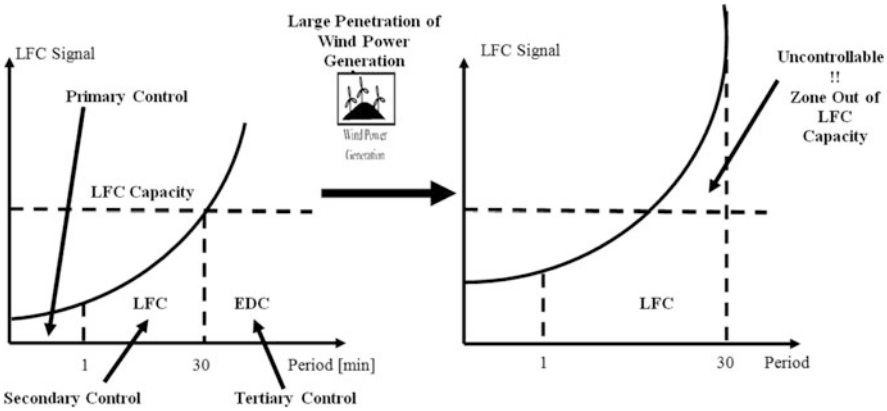

Fig. 14.15 Impact of integration wind farm on LFC

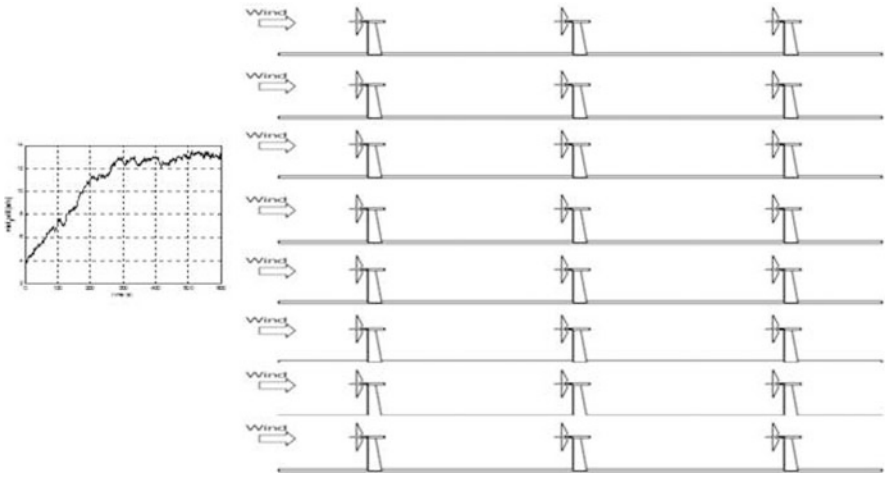

Fig. 14.16 Layout of a typical wind farm

power system operation, the study of possibility of integration a large wind farm in interconnected electrical networks and analysis its impact, an issue which serves as motivation for this work. In this work, a typical wind farm composed of 200 wind turbines of 1.5 MW each is used for the simulation as shown in Fig. 14.16. It is assumed that a large control area is interconnected to a small control area with a large penetration of wind turbines. The wind farm is mapped into eight groups, where each group produces a power of 37.5 MW. This wind farm is based on the wind turbine model, and the wind profile is presented using the dynamic load model proposed by Michigami and Oishi (2001) as shown in Fig. 14.17.

An equivalent wind speed calculated in Eq. (14.32) is applied to the wind farm. We propose that the same wind profile shown in Fig. 14.18 is applied to all wind

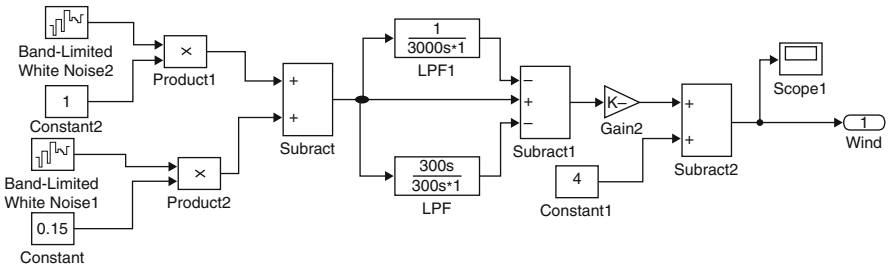

Fig. 14.17 Wind speed model

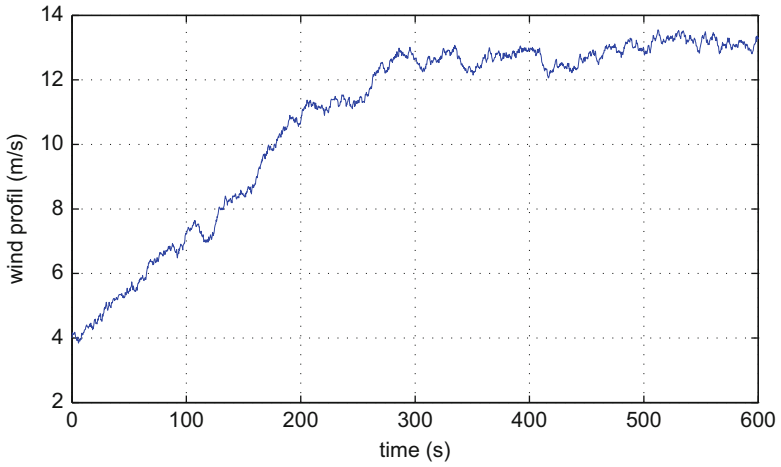

Fig. 14.18 Wind speed output

turbines of the same group: (n_r is number of groups):

$$V_{eq} = \frac{\sum_{i=1}^{i=n} V_i}{n_r} \tag{14.32}$$

The dynamic load model proposed by T. Michigami and T. Ishii is used to represent the wind speed (Michigami and Oishi 2001). The wind speed profile is generated by a block diagram shown in Fig. 14.17. A load consists of base and fringe components obtained from the white noise generators, since the component with period shorter than 5 min or longer than 30 min are out of LFC control, the component is eliminated by applying filters HPF and LPF. The energy penetration of wind farm is defined as:

$$p\ (\%) = \frac{E_w}{E} \times 100\ (\%) \tag{14.33}$$

On the whole and in a simplified manner, the wind farm model is present by:

$$S_{eq} = \sum_{1}^{n} S_i;\ Pm_{eq} = \sum_{1}^{n} Pm_i;\ Q_{eq} = \sum_{1}^{n} Q_i;\ Cp_{eq} = \sum_{1}^{n} Cp_i \tag{14.34}$$

where: the subscript i represents the single turbine.

14.6 Simulation Results and Discussion

To satisfy the load frequency control objectives concerning the integration of wind farm, a dynamic time domain simulation has been carried out using the interconnected IEE Japan East 107-bus, 30-machine. It consists of two areas interconnected by a tie-line power flow. As mentioned, the main goal is to design an effective load frequency controller model with a desirable performance in the presence of large-scale integration of wind turbines. An additional 300 MW wind farm generation is assumed to be installed in area-2. As presented in Sect. 14.5.2, Fig. 14.16 shows the wind farm structure considered in this work. It presents 200×1.5 MW DFIG groups, while the wind farm model operates with the same variable wind profile. All wind turbines are assumed connected to the same PCC. The algorithm developed to analyze the load frequency control LFC is shown in Figs. 14.19 and 14.20. In order to verify the effectiveness of the proposed algorithm, the new LFC model proposed in this work is verified by comparing their responses with those of the conventional LFC based Ziegler-Nichols and the optimal LFC based PSO. The numerical parameters used in the simulation are included in the "Appendix" (Arita et al. 2006) (Tables 14.5, 14.6, 14.7, 14.8, and 14.9).

Using the proposed wind farm model, the impact of wind power fluctuations on the system frequency and tie-line power flow in the two-area interconnected network is examined. Figures 14.21 and 14.22; depict the output power of the first wind turbine and the power coefficient $C_p(\lambda, \beta)$ characteristics respectively. The total wind farm power generation is shown in Fig. 14.23 generation is analyzed. For comparison purpose, four cases are carried out as presented in Table 14.2, whilst the PID controller parameters are given in Table 14.3. The deviations in system frequency and tie-line power flow are shown in Figs. 14.24, 14.25, and 14.26, respectively. It can be seen that the fluctuations of system frequency and tie-line power flow are very important when the penetration of wind power generation is large. However, the system frequency and the tie-line power flow are suppressed most effectively if both areas adopt LFC based optimal PID controller. The effect of the PID controller on the system fluctuations caused by the wind farm is clear that in the difference between the blue corves (without control) and the other corves (using LFC with PID controller). It is clear that in the case of using the conventional LFC design shows more oscillations. In contrast, using the PSO method, global and local solutions could be found simultaneously for a better agreement of the PID controller parameters. Also, these figures show the superior

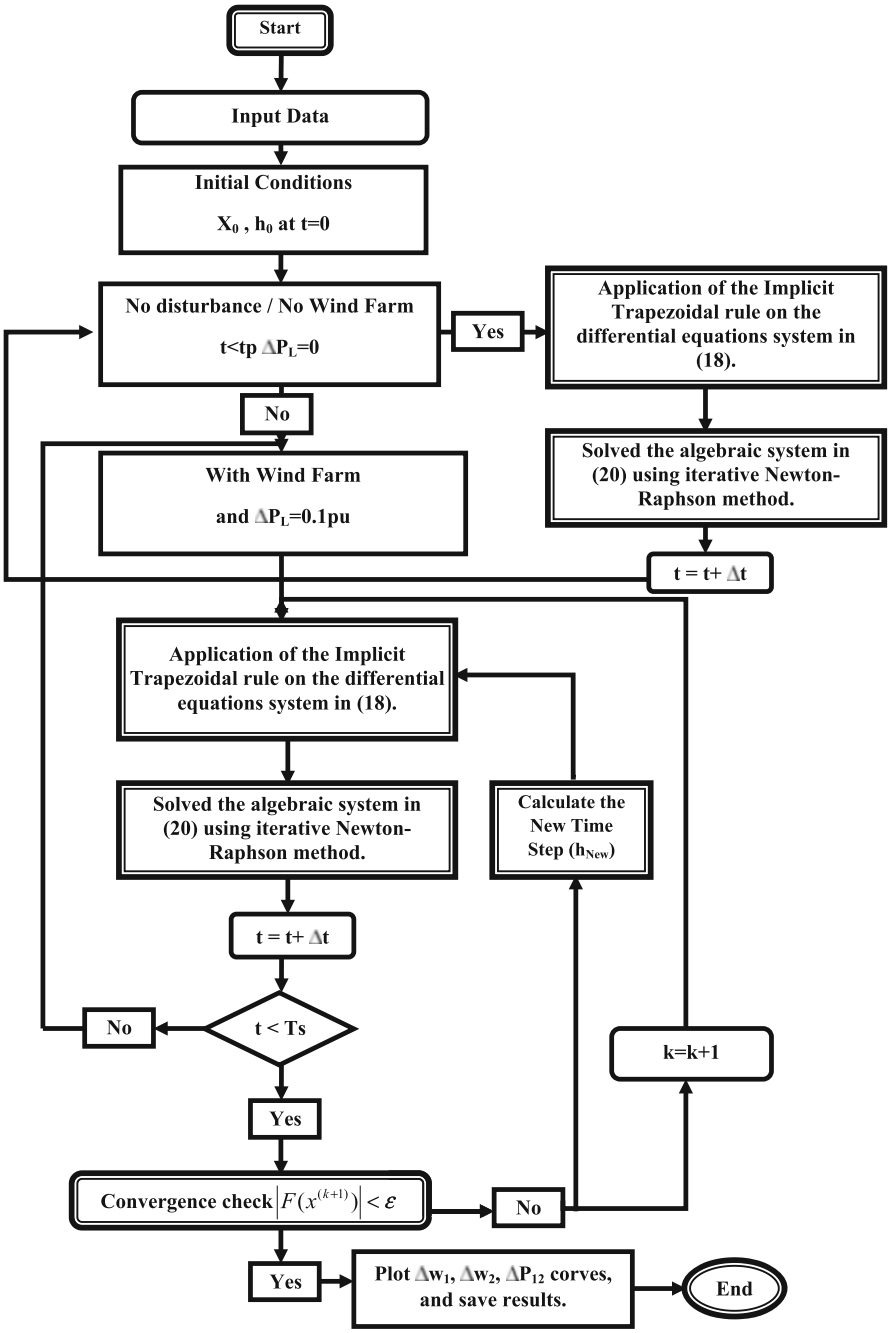

Fig. 14.19 Proposed flowchart for LFC analysis

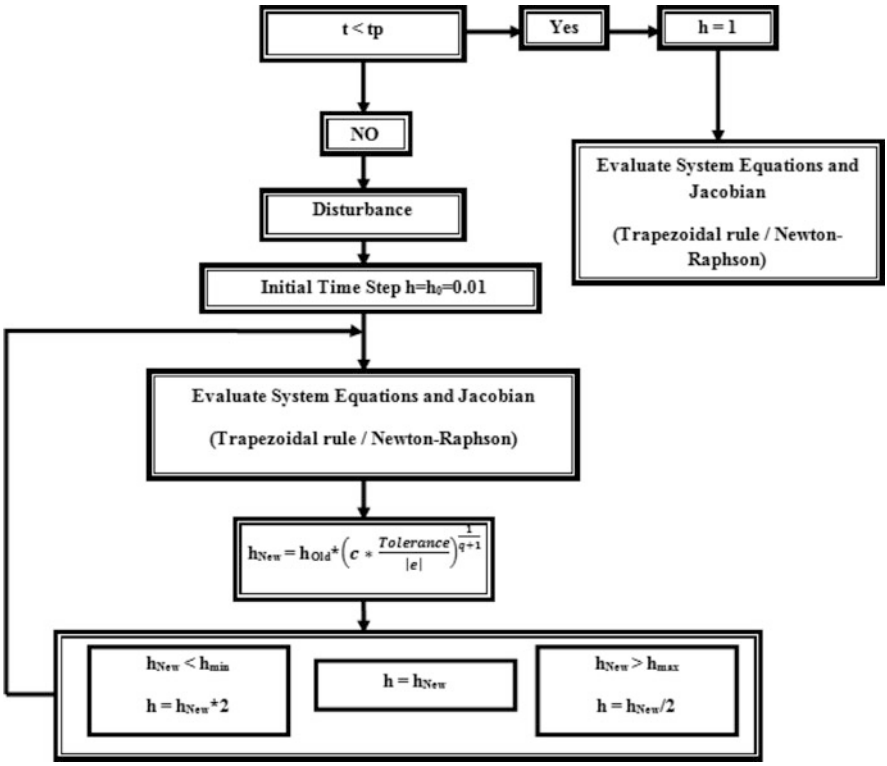

Fig. 14.20 Proposed flowchart for variable time step

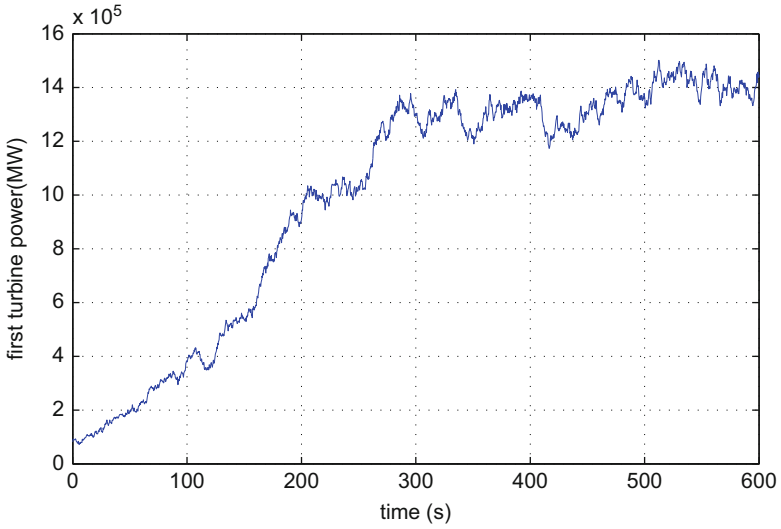

Fig. 14.21 Output power of first wind turbine

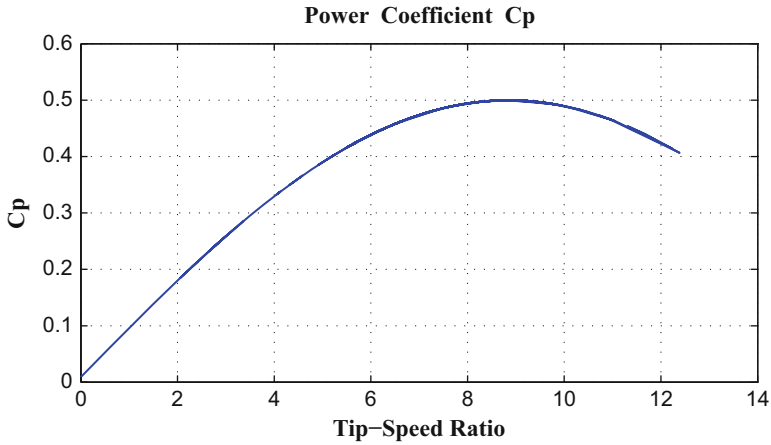

Fig. 14.22 Power coefficient $CP(\lambda, \beta)$ characteristic

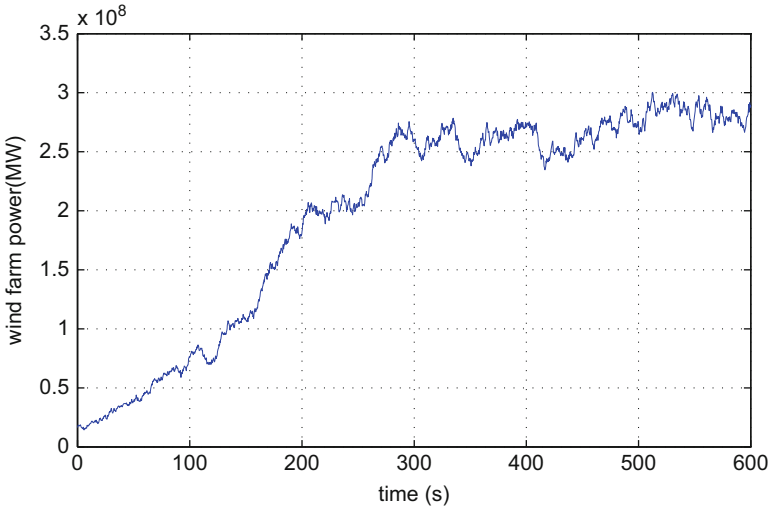

Fig. 14.23 Output power of the wind farm

Table 14.2 Simulation case study

Case 1	Case 2	Case 3	Case 4
Without LFC	Ziegler-Nichols	PSO	Fuzzy-PID

Table 14.3 PID controller parameters

	Parameters		
Methods	K_P	K_I	K_D
Ziegler-Nichols	0.06168	0.0173	0.055
PSO	13.9506	0.2524	1.8796
Fuzzy logic	3.33	1.65	3.33

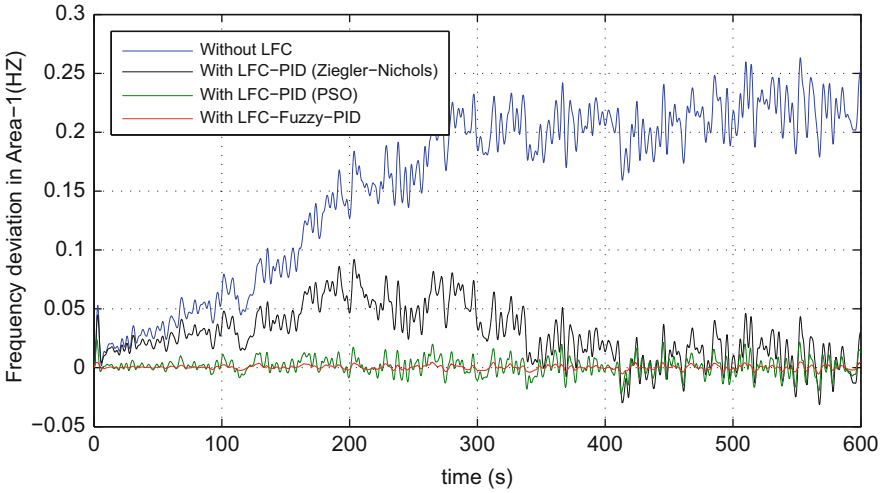

Fig. 14.24 Frequency fluctuation in area-1

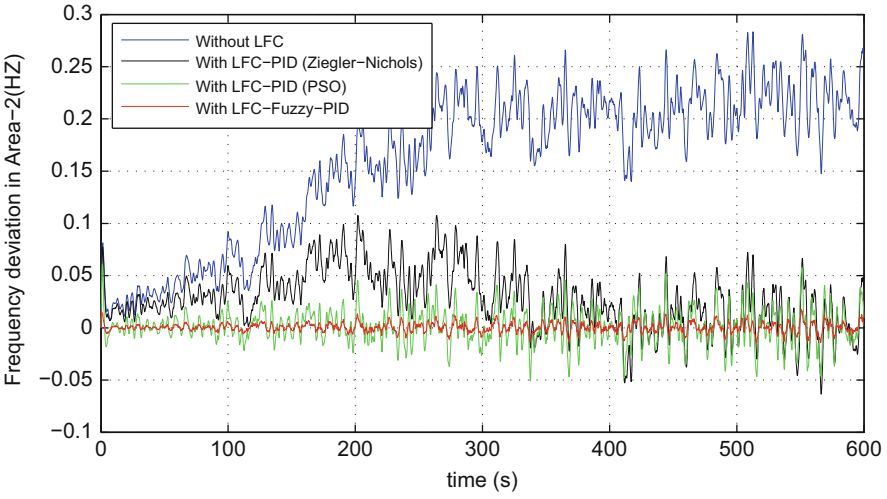

Fig. 14.25 Frequency fluctuation in area-2

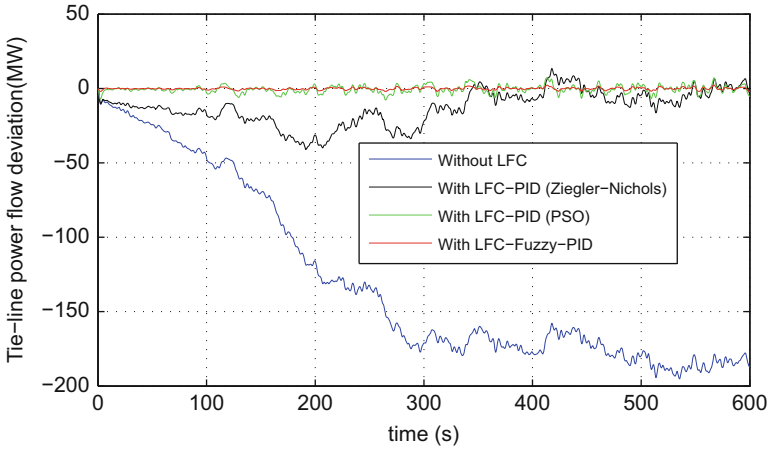

Fig. 14.26 Tie-line power flow fluctuation

Table 14.4 Results and comparison

Tuning PID controller techniques	Without control	Ziegler-Nichols	PSO	Fuzzy logic
Max frequency deviation in Area-1 [Hz]	0.2633	0.09184	0.02176	0.00474
Max frequency deviation in Area-2 [Hz]	0.2827	0.1074	0.05776	0.0148
Max tie-line power flow deviation [MW]	194.1	16.06	3.735	1.044

Table 14.5 Data of the two-area power system

	Area	
Parameters	Area-1	Area-2
Reference frequency [Hz]	50	50
Inertia constant [s]	8.85	9.02
Load-damping constant [pu]	2	2

performance of the proposed Fuzzy Logic-PID controller based LFC scheme to the other conventional and optimal LFC models. Using the proposed Fuzzy Logic-PID controller, the fluctuations of the system frequency and the tie-line power flow are better suppressed compared to the results given by the classical Ziegler-Nichols method and the PSO technique. In other hand, the proposed algorithm based on the implicit integration Trapezoidal rule with variable time step and the iterative Newton-Raphson method is proven to be very efficient for the frequency stability study. The results are compared in view of peak overshoot and settling time; where, the proposed Fuzzy logic-PID controller based LFC scheme is proven to be better as shown in Table 14.4.

Table 14.6 Thermal and nuclear unit parameters

K_G	T_{SR}	T_{SM}	T_{SC}	T_{CO}	F_{HP}	F_{LP}	CV_{close}	CV_{open}	SCV_{min}	SCV_{max}
20	0.2	0.2	0.25	0.9	0.3	0.7	0	1.05	−1000	0.2

Table 14.7 Hydro unit parameters

K_{Gh}	T_{SRh}	T_{SMh}	CV_{close}	CV_{open}	DCV_{min}	DCV_{max}
20	10	0.3	0	1.02	−1000	0.1

Table 14.8 Generation data

Area	Rated capacity [MW]	Initial output [MW]	Inertia constant [Sec]	Total load [MW]
Area-1	53509	30247	8.85	33090
Area-2	11560	10600	9.02	7090

Table 14.9 Wind turbine parameters

Blades number	Rotor diameter	Gearbox ratio	Moment inertia	Coefficient of friction
3	36.5	1 : 104	50	0.0071

14.7 Conclusion

This work investigates the impact of integration a large wind farm on frequency stability and control, which is an important issue in power system control and operation. For this purpose, a Fuzzy Logic structure was proposed to design a new robust load frequency control (LFC) scheme in two-area interconnected power system with diverse sources of power generation concerning high penetration of wind turbines. As the wind power fluctuations influence power system frequency, this study investigated the impact of large wind farm integration on the system frequency and the tie-line power flow in large-scale interconnected electrical network. A typical wind farm equipped with 200 DFIG wind turbines of 1.5 MW each was used for dynamic study, from the frequency stability point of view and control of the electrical power system. The fuzzy logic strategy was used to achieve the optimal values of the PID controller parameters. A new methodology to solve the load frequency control based on the implicit integration Trapezoidal rule with variable time step and iterative Newton-Raphson method was used in this work. The main objective of the proposed algorithm and the suggested LFC scheme is to analyze the frequency stability in an interconnected electrical network in presence of wind farm and solve the frequency fluctuations problem by keeping system frequency and tie-line power interchange between interconnected areas within an acceptable range close to the scheduled values. The proposed strategy was examined on the IEE Japan East 107-bus, 30-machine power system including wind farm, while this system is divided into two control areas: a big control area is interconnected into a small control area. The wind farm is installed in the small control area, where the deviations of the system frequency and the tie-line power

flow in this network are examined to improve the LFC capacity of the conventional power units. The results obtained using the proposed Fuzzy Logic-PID controller based LFC scheme was compared with those of the conventional LFC based Ziegler-Nichols method and the optimal LFC based PSO technique. The results show that the main advantage of using Fuzzy Logic structure is to reduce the fluctuations, while achieving a good performance of the whole response of system in presence of wind farm. Further, the robustness of the proposed control strategy is confirmed and the LFC scheme provides desirable performance against wind power fluctuations.

Appendix

List of Abbreviations and Symbols

Abbreviations

ACE:	Area Control Error.
AGC:	Automatic Generation Control.
ANN:	Artificial Neural Network.
AR:	Area Requirement.
$BFOA$:	Bacterial Foraging Optimization.
$BF-PSO$:	Hybrid Bacterial Foraging and Particle Swarm Optimization.
DEA:	Differential Evolution Algorithm.
$DFIG$:	Doubly Fed Induction Generator.
DG:	Distributed Generations.
EDC:	Economic Dispatching Control.
FA:	Firefly Algorithm.
FLC:	Fuzzy Logic Control.
GA:	Genetic Algorithm.
HPF:	High-Pass Filter.
ISO:	Independent System Operator.
LFC:	Load Frequency Control.
LPF:	Low-Pass Filter.
PCC:	Point of Common Coupling.
PID:	Proportional-Integral-Derivation Controller.
PSO:	Particle Swarm Optimization.
RES:	Renewable Energy Sources.
$TSOs$:	Transmission System Operators.

Symbols

M:	Inertia Constant.
M_{eq}:	Equivalent Inertia Constant.
D:	Load-Damping.
D_{eq}:	Equivalent Load-Damping.
$\Delta\omega$:	Frequency Deviation.
ΔP_m:	Mechanical Power Variation.
ΔP_e:	Electrical Power Variation.
ΔP_L:	Non-Frequency-Sensitive Load Change.
ΔP_{tie}:	Tie-Lien Power Flow Deviation.
ΔP_{mh}:	Hydro Unit Mechanical Power Variation.
ΔP_{mth}:	Thermal Unit Mechanical Power Variation.
ΔP_g:	Thermal Unit Governor Power Variation.
ΔP_{gh}:	Hydro Unit Governor Power Variation.
CV:	Control Valve.
SCV:	Speed Control.
DCV:	Distributor Valve and Gate Servomotor.
CV_{open}, CV_{close}:	Valve or Gate Position Limits.
$SCV_{min}, DCV_{min}, SCV_{max}, DCV_{max}$:	Valve/ Gate Servomotor Rate Limits.
GF_{min}, GF_{max}:	Speed Governor Limits.
T_{CO}:	Time Constants for the Cross Over.
T_{SC}:	Time Constants for the Steam Chest.
F_{HP}:	High-Pressure Turbine Power Fraction.
F_{LP}:	Low-Pressure Turbine Power Fraction.
K_G:	Thermal Unit Speed Governor Regulation Gain.
K_{Gh}:	Hydro Unit Speed Governor Regulation Gain.
T_{SR}:	Thermal Unit Time Constant of the Speed Relay.
T_{SM}:	Thermal Unit Time Constant of the Servomotor.
T_{SRh}:	Hydro Unit Time Constant of the Speed Relay.
T_{SMh}:	Hydro Unit Time Constant of the Servomotor.
U:	Control Signal.
U_I:	Integral Control Signal.
β_f:	Frequency Bias.
a:	Constant ($a = [1, -1]$).
T_{12}:	Tie-Line Rigidity Factor.
X_{T12}:	Tie-Line Reactance.

T_s:	Simulation Time.
t_p:	Perturbation time.
P_{mech}:	Power from Wind.
ρ:	Air Density.
R:	Blade Radius.
S:	The Swept Area of the Rotor.
V:	Wind Speed.
V_{eq}:	Equivalent Wind Speed.
Cp:	Power Coefficient.
λ:	Tip-Speed Ratio.
β:	Blade Pitch Angle.
w_{tr}:	Turbine Rotation Speed.
E_w:	The Energy Supplied by Wind Farm.
E:	The Energy Supplied by all Generation.
S_{eq}:	Apparent Power of the Whole Wind Farm.
Pm_{eq}:	Equivalent Active Power of the Whole Wind Farm.
Q_{eq}:	Equivalent Reactive Power of Whole Wind Farm.
Cp_{eq}:	Equivalent Power Coefficient of Whole Wind Farm.
$\Delta torh$:	Integration Time Step.
h_{Old}, h_{New}:	Old and New Integration Time Step.
ϵ:	Tolerance.
c:	Constant between the interval [0.6, 0.9].
q:	Order of the Method, for the Trapezoidal Method $q = 2$.
$\|e\|$:	Is a Weighted Root Square Mean Norm.
k:	Iteration Number.

References

Arita, M., Yokoyama, A., & Tada, Y. (2006). Evaluation of battery system for frequency control in interconnected power system with a large penetration of wind power generation. In *IEEE International Conference on Power System Technology*, Chongqing (pp. 1–7).

Attya, A., & Hartkopf, T. (2012). Penetration impact of wind farms equipped with frequency variations ride through algorithm on power system frequency response. *Electrical Power and Energy Systems, 40*, 94–103.

Bevrani, H., & Daneshmand, P. (2012). Fuzzy logic-based load-frequency control concerning high penetration of wind turbines. *IEEE Systems Journal, 6*, 173–180.

Bihui, L., Hong, S., Yong, T., Hongyun, Z., Feng, S., & DongFu, L. (2011). Study on the frequency control method and AGC model of wind power integration based on the full dynamic process simulation program. In *International Conference on Advanced Power System Automation and Protection*, Beijing (pp. 246–251).

Chung, I.-Y., Liu, W., Cartes, D., & Moon, S.-I. (2011). Control parameter optimization for multiple distributed generators in a microgrid using particle swarm optimization. *European Transactions on Electrical Power, 21*, 1200–1216.

Demirören, A., Kent, S., & Günel, T. (2002). A genetic approach to the optimization of automatic generation control parameters for power systems. *European Transactions on Electrical Power, 12*, 275–281.

Eduardo, V.-N., Andreas, S., Oriol, G.-B., Adriã, J.-F., & Marcela, M.-R. (2011). Pitch control system design to improve frequency response capability of fixed-speed wind turbine systems. *European Transactions on Electrical Power, 21*, 1984–2006.

Ge, B., Wang, W., Bi, D., Rogers, C. B., Peng, F. Z., de Almeida, A. T., & Abu-Rub, H. (2013). Energy storage system-based power control for grid-connected wind power farm. *Electrical Power and Energy Systems, 44*, 115–122.

Hang, J., Zhang, J., & Cheng, M. (2016). Application of multi-class fuzzy support vector machine classifier for fault diagnosis of wind turbine. *Fuzzy Sets and Systems, 297*, 128–140.

Hooshmand, R., Ataei, M., & Zargari, A. (2012). A new fuzzy sliding mode controller for load frequency control of large hydropower plant using particle swarm optimization algorithm and kalman estimator. *European Transaction on Electrical Power, 22*, 812–830.

Jafarian, M., & Ranjbar, A. (2013). The impact of wind farms with doubly fed induction generators on power system electromechanical oscillations. *Renewable Energy, 50*, 780–785.

Kassem, A. M., Hasaneen, K. M., & Yousef, A. M. (2013). Dynamic modeling and robust power control of DFIG driven by wind turbine at infinite grid. *Electrical Power and Energy Systems, 44*, 375–382.

Kiaee, M., Cruden, A., Infield, D., & Chladek, P. (2013). Improvement of power system frequency stability using alkaline electrolysis plants. *Proceedings of the Institution of Mechanical Engineers, Part A: Journal of Power and Energy, 227*, 115–123.

Kouba, N. E. Y., Menaa, M., Hasni, M., Boussahoua, B., & Boudour, M. (2014a). Optimal load frequency control based on hybrid bacterial foraging and particle swarm optimization. In *IEEE, 11th International Multi-conference on Systems, Signals and Devices (SSD-PES)*, Barcelona (pp. 1–6).

Kouba, N. E. Y., Menaa, M., Hasni, M., Boussahoua, B., & Boudour, M. (2014b). Optimal load frequency control in interconnected power system using PID controller based on particle swarm optimization. In *IEEE, International Conference on Electrical Sciences and Technology in Maghreb (CISTEM)*, Tunis (pp. 1–8).

Kouba, N. E. Y., Menaa, M., Hasni, M., & Boudour, M. (2014c). Application of artificial neural networks to load frequency control in multi-area power system. In *Proceedings of the 3rd International Conference on Information Processing and Electrical Engineering (ICIPEE)*, Tebessa (pp. 357–362).

Kouba, N. E. Y., Menaa, M., Hasni, M., & Boudour, M. (2016a). Design of intelligent load frequency control strategy using optimal fuzzy-PID controller. *International Journal of Process Systems Engineering, 4*, 41–64.

Kouba, N. E. Y., Menaa, M., Hasni, M., & Boudour, M. (2016b). Frequency stability enhancement in two-area deregulated power system based competitive electricity markets with redox flow batteries and power flow controllers. In *IEEE 8th International Conference on Modelling, Identification and Control (ICMIC)*, Algiers (pp. 1029–1036).

Kouba, N. E. Y., Menaa, M., Hasni, M., & Boudour, M. (2016c). LFC enhancement concerning large wind power integration using new optimised PID controller and RFBS. *IET Generation, Transmission and Distribution, 10*, 4065–4077.

Kouba, N. E. Y., Menaa, M., Hasni, M., & Boudour, M. (2016d). A novel optimal frequency control strategy for an isolated wind-diesel hybrid system with energy storage devices. *SAGE, Wind Engineering, 40*, 497–517.

Liu, P., Yang, W.-T., Yang, C.-E., & Hsu, C.-L. (2015). Sensorless wind energy conversion system maximum power point tracking using Takagi-Sugeno fuzzy cerebellar model articulation control. *Applied Soft Computing, 29*, 450–460.

Mahabuba, A., & Khan, M. (2009). Small signal stability enhancement of a multi-machine power system using robust and adaptive fuzzy neural network-based power system stabilizer. *European Transactions on Electrical Power, 19*, 978–1001.

Mandal, P., Zareipour, H., & Rosehart, W. D. (2014). Forecasting aggregated wind power production of multiple wind farms using hybrid wavelet-PSO-NNS. *International Journal of Energy Research, 28*, 1654–1666.

Michigami, T., & Oishi, T. (2001). Construction of dynamic fluctuation load model and simulation with AFC control of BTB interconnection. *Electrical Engineering in Japan, 136*, 15–25.

Nanda, J., Mishra, S., & Saikia, L. (2009). Maiden application of bacterial foraging-based optimization technique in multiarea automatic generation control. *IEEE Transactions on Power Systems, 24*, 602–609.

Pan, I., & Das, S. (2015). Fractional-order load-frequency control of interconnected power systems using chaotic multi-objective optimization. *Applied Soft Computing, 29*, 328–344.

Panda, S., & Yegireddy, N. (2013). Automatic generation control of multi-area power system using multi-objective non-dominated sorting genetic algorithm-II. *Electrical Power and Energy Systems, 53*, 54–63.

Pandey, S., Mohanty, S., & Kishor, N. (2013). A literature survey on load frequency control for conventional and distribution generation power systems. *Renewable and Sustainable Energy Reviews, 25*, 318–334.

Patnaik, R., & Dash, P. (2015). Impact of wind farms on disturbance detection and classification in distributed generation using modified adaline network and an adaptive Neuro-fuzzy information system. *Applied Soft Computing, 30*, 549–566.

Pothiya, S., & Ngamroo, I. (2008). Optimal fuzzy logic-based PID controller for load-frequency control including superconducting magnetic energy storage units. *Energy Conversion and Management, 49*, 2833–2838.

Prakash, S., & Sinha, S. (2014). Simulation based Neuro-fuzzy hybrid intelligent PI control approach in four-area load frequency control of interconnected power system. *Applied Soft Computing, 23*, 152–164.

Rahmani, M., & Sadati, N. (2013). Two-level optimal load-frequency control for multi-area power systems. *Electrical Power and Energy Systems, 53*, 540–547.

Ramakrishna, K. S. S., & Bhatti, T. S. (2008). Automatic generation control of single area power system with multi-source power generation. *Proceedings of the Institution of Mechanical Engineers, Part A: Journal of Power and Energy, 222*, 1–11.

RamaSudha, K., Vakula, V., & Shanthi, R. V. (2010). PSO based design of robust controller for two area load frequency control with nonlinearities. *International Journal of Engineering Science and Technology, 2*, 1311–1324.

Sahu, R. K., Panda, S., & Padhan, S. (2013). A novel hybrid gravitational search and pattern search algorithm for load frequency control of nonlinear power system. *Applied Soft Computing, 13*, 4718–4730.

Saikia, L., & Sahu, S. (2013). Automatic generation control of a combined cycle gas turbine plant with classical controllers using firefly algorithm. *Electrical Power and Energy Systems, 53*, 27–33.

Saikia, L., Mishra, S., Sinha, N., & Nanda, J. (2011). Automatic generation control of a multi area hydrothermal system using reinforced learning neural network controller. *Electrical Power and Energy Systems, 33*, 1101–1108.

Sarrias-Mena, W., Fernãndez-Ramírez, L., García-Vázquez, C., & Jurado, F. (2015). Dynamic evaluation of two configurations for a hybrid DFIG-based wind turbine integrating battery energy storage system. *Wind Energy, 18*, 1561–1577.

Schlechtingen, M., Santos, I. F., & Achiche, S. (2013). Wind turbine condition monitoring based on scada data using normal behavior models. Part 1: System description. *Applied Soft Computing, 13*, 259–270.

Shayeghi, H., Jalili, A., & Shayanfar, H. (2008). Multi-stage fuzzy load frequency control using PSO. *Energy Conversion and Management, 49*, 2570–2580.

Singh, V., Mohanty, S., Kishor, N., & Ray, P. (2013). Robust H-infinity load frequency control in hybrid distributed generation system. *Electrical Power and Energy Systems, 46*, 294–305.

Tofighi, M., Alizadeh, M., Ganjefar, S., & Alizadeh, M. (2015). Direct adaptive power system stabilizer design using fuzzy wavelet neural network with self-recurrent consequent part. *Applied Soft Computing, 28*, 514–526.

Vrakopoulou, M. (2013). *Optimal decision making for secure and economic operation of power systems under uncertainty*. Ph.D. thesis, Eidgenössische Technische Hochschule ETH, Zürich.

Wang, C., & McCalley, J. (2013). Impact of wind power on control performance standards. *Electrical Power and Energy Systems, 47*, 225–234.

Zhang, W., Wang, J., Wang, J., Zhao, Z., & Tian, M. (2013). Short-term wind speed forecasting based on a hybrid model. *Applied Soft Computing, 13*, 3225–3233.

Chapter 15
Fault Tolerant Control of Switch Power Converter in WECS Based on a DFIG

Amina Tamer, Azeddine Bendiabdellah, Bilal Djamal Eddine Cherif, and Djillali Toumi

Abstract In the field of Wind Energy Conversion Systems(WECS), the prediction and early detection of wind power converter failures is one of the most promising ways to control and optimize the operational costs. This chapter presents the detection of converter open switch faults and the fault tolerant of power converters fed Doubly Fed Induction Generator (DFIG) in Wind Energy Conversion Systems (WECS). The proposed control approach is based on using the grid side converter to regulate the DC link voltage constant. The mean of the rotor side converter is to track the maximum power point for the wind turbine and to maintain unity power factor at stator terminals. The description of the proposed system is presented with the detailed dynamic modeling equations. The mean value of the rotor current diagnosis technique is adopted for fault detection. The fault tolerant topology used for service continuity is that with a redundant leg. The simulations are performed using the Matlab/Simulink environment and Sim power. The fault operation is analyzed and the detection method and fault tolerant topology used are tested with encouraging results.

Keywords DFIG · WECS · Open switch · Detection · Fault tolerant · Redundancy

15.1 Introduction

The large industrialization during the last decade has led to considerable needs in the electrical energy. To meet this high demand, countries are increasingly turning

A. Tamer (✉) · A. Bendiabdellah · B. D. E. Cherif
Laboratory of Electrical Drives Development (LDEE), University of Science and Technology of Oran, Oran, Algeria

D. Toumi
Laboratory of Electrical and Computer Engineering (L2GEGI), Ibn Khaldun University, Tiaret, Algeria

N. Derbel, Q. Zhu (eds.), *Modeling, Identification and Control Methods in Renewable Energy Systems*, Green Energy and Technology,
https://doi.org/10.1007/978-981-13-1945-7_15

to the use of clean and renewable energy sources. Indeed, in the medium term, these countries have committed themselves to increase the share of renewable energy in their electricity production.

Among the various renewable energy sources, wind energy is considered as the one with the greatest potential. The power from wind turbines and wind farms installed in the world is increasing every year. The (WECS) although designed initially as an active power generator linked to the grid system, it is now required to provide system services such as reactive power compensation and electric power quality improvement.

Nowadays, most of the wind turbines installed are equipped with the Doubly Fed Induction Generator (DFIG), which has become very popular. The DFIG benefits from certain advantages over all other types with variable speed. It allows operating over a wide range of wind speed, and drawing the maximum possible power for each of its speeds. The use of the (DFIG) associated with the (WECS) as a wind turbine has grown dramatically in recent years. Indeed, the energy converter used as rectifier-inverter for the alternating currents of the rotor has a nominal power fractional to that of the generator, which reduces its cost compared to the competing topologies (Boukhriss et al. 2014; Touati et al. 2014).

The presence of power convertors as key elements in the wind turbine structure impacts negatively the reliability and may jeopardize the whole system. The power semiconductor switches are the most fragile components in power converters. If the (WECS) stops because of a fault in a convertor switch, it may take longer before it can be repaired. As a consequence, the concepts of reliability and availability have become increasingly an issue of paramount importance for the (WECS). In order to guarantee the needed reliability and availability many researchers have focused their investigation to designing (WECS) to include fault detection and fault tolerant systems. The fault tolerance has the ability to tolerate faults by detecting failures and isolating the faulty converter switches so that the rest of the system can operate correctly and the continuity of service is achieved (Bensouda and Haddi 2014; Polinder et al. 2009; Sarati and Kyeong-Hwa 2014).

Several overview papers have covered the topics on power convertor switch fault diagnosis methods (Cherif et al. 2016; Lu and Sharma 2009; Mohamed et al. 2013). In reference (Cherif et al. 2015) the mean value stator currents and measurement of semiconductor switch currents techniques were introduced and applied to a three phase voltage inverter fed induction motor, in which the faults are detected (ElKachani et al. 2014).

In this present chapter, the open-circuit fault in the power converter switches of the rotor side is investigated. The diagnosis method adopted for the detection and localization of this fault is based on the mean value of the rotor currents technique. The fault tolerant power converter topology used for continuity of service is that with a redundant leg reconfiguration (Guediri and Attous 2015; Riouch and Bachtiri 2014).

The rest of the chapter is organized as follows. Section 15.2 describes the wind Energy Conversion System (WECS) with (DFIG). Section 15.3 presents a detailed mathematical modelling of the various parts of the wind system with a

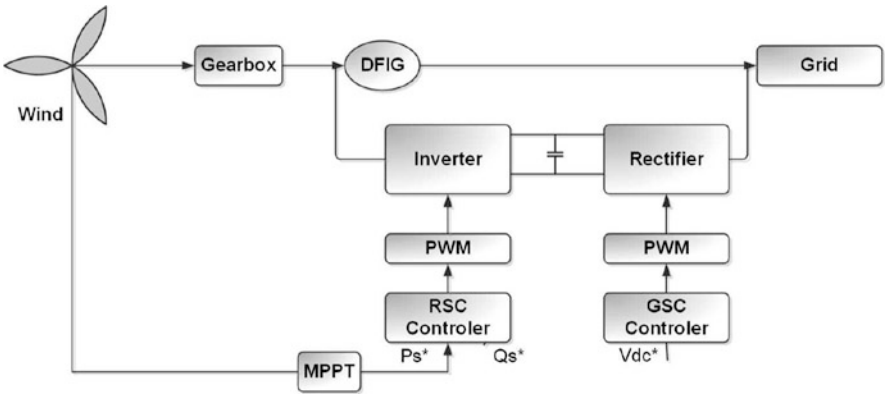

Fig. 15.1 Structure diagram of the WECS-DFIG

DFIG. Section 15.4 explains the detection and localization techniques of power convertor open switch faults. Section 15.6 presents the topology of the fault-tolerant redundancy reconfiguration. Finally, some conclusion remarks are drawn in the last Section.

15.2 WECS-DFIG Description and Modelling

The structure of a wind turbine-DFIG set used in this paper is shown in Fig. 15.1.

The structure of the (WECS) is constituted of two main parts; the mechanical part of the turbine; which is mechanically coupled to the DFIG; is composed of steerable blades, a gearbox (speed reducer), a coupling shaft system. The electrical part is composed by a doubly fed induction generator (which is fed from stator and rotor sides), an electronic power converters chain with its continuous bus. The stator is directly connected to the grid, whereas the rotor is also connected to the grid, but through a back-to-back converter via a Pulse Width Modulation (PWM) control (Tamer et al. 2014). The converter on the rotor side will be referred as the rotor side converter (RSC), while the converter on the grid side as the grid side converter (GSC) (Cordeiro et al. 2014). The rotor side converter (RSC) usually provides active and reactive power control of the machine while the grid-side converter (GSC) keeps the voltage of the DC-link constant. In this way, the active and reactive stator power is controlled indirectly by means of the inner rotor current control loop. The maximum power point tracking (MPPT) control is integrated to ensure the optimum active power output. The control technique is based on the field oriented vector, whereas the rotor current is controlled in the stator flux-oriented referential (Elazzaoui 2015).

15.2.1 Wind Turbine Modelling

A wind turbine converts the wind power to mechanical power. The mechanical power P_m is given by the following equation:

$$P_m = \frac{1}{2}\pi\,\rho\,\frac{C_p\,(\lambda,\beta)}{\lambda}\,R^3\,V_1^2 \tag{15.1}$$

where ρ the air density (kg/m3), R the wind turbine rotor radius (m), V_1 the equivalent wind speed (m/s), β the pitch angle of rotor (deg), C_p the power coefficient with its maximum value at 0.48 (Betz limit) and λ is the tip speed ratio. The ratio λ can be expressed by the following equation:

$$\lambda = \frac{R\,\Omega_{tur}}{V_1} \tag{15.2}$$

The power coefficient is intrinsic to the formation of wind turbine and depends on the profiles of the blades. The power coefficient can be modeled with a single equation that depends on the speed ratio λ and the orientation angle β of the blades as follows equation:

$$C_p\,(\lambda,\beta) = C_1\left(C_2\,\frac{1}{\lambda_i} - C_3\,\beta - C_4\right)\exp\left(\frac{-C_5}{\lambda_i}\right) + C_6\,\lambda \tag{15.3}$$

In this formula, the parameter also depends on λi and β.

$$\frac{1}{\lambda_i} = \frac{1}{\lambda + 0.08\,\beta} - \frac{0.035}{1+\beta^3} \tag{15.4}$$

Figure 15.2 shows curves of the power coefficient as a function of λ for various β values. This gives a maximum power coefficient of 0.48 for a speed ratio λ which is 8.1 maintaining β at 0°. By setting β and λ respectively to their optimal values, the wind system will provide optimum electrical power.

This particular value of λ is defined as the optimal value λ_{opt} where the maximum power is captured from wind by the wind turbine. So it is necessary to keep the rotor speed at an optimum value of the tip speed ratio λ_{opt}. If the wind speed varies, the rotor speed should be adjusted to follow the change. The aerodynamic torque on the slow axis(speed reducer) is expressed by:

$$T_{aero} = \frac{P_{aero}}{\Omega_{tur}} = C_p\,\frac{\rho\,S\,V_1^3}{2}\,\frac{1}{\Omega_{tur}} \tag{15.5}$$

Mechanical speed is related to the speed of rotation of the turbine by the coefficient of the gearbox. The torque on the slow axis is connected to the torque on the fast axis (generator side) by the coefficient of the gearbox (Fig. 15.3).

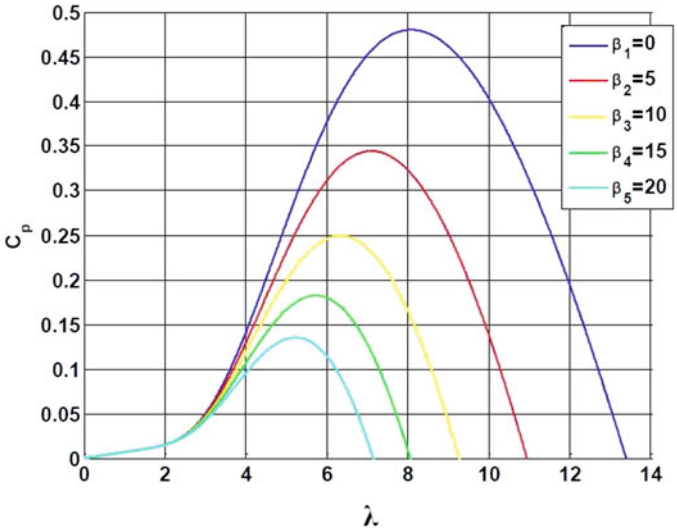

Fig. 15.2 Power coefficient as a function of λ for various β values

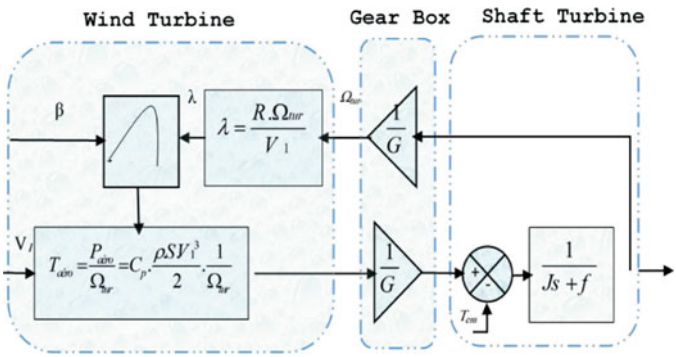

Fig. 15.3 Wind turbine modeling

The total inertia J is made up of the inertia of the turbine plotted on the generator rotor and inertia of the generator:

$$J = \frac{J_t}{G^2} + J_g \tag{15.6}$$

J_t: inertia of the turbine.
J_g: inertia of the generator.

The evolution of the mechanical speed from the total mechanical torque T_m is determined by the fundamental equation of dynamics.

$$J\,\frac{d\Omega_{mec}}{dt} = T_{mec} = T_{fa} - T_{em} - f\,\Omega_{mec} \tag{15.7}$$

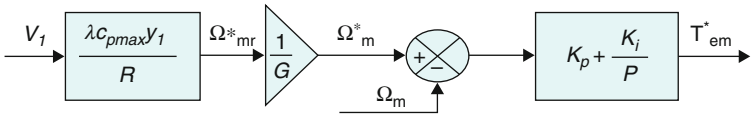

Fig. 15.4 MPPT control

Ω_m: mechanical speed of DFIG.
T_{fa}: aerodynamic torque on the fast axis of the turbine.
T_{em}: Electromagnetic torque.
f: coefficient of friction.

15.2.2 Extraction of Maximum Power MPPT

In order to capture the maximum power of the incident wind, the rotational speed of the turbine must permanently be adjusted to that of the wind. The optimum mechanical speed of the turbine corresponds 0°. The speed of DFIG is used as a reference value for a proportional-integral controller type. The latter determines the set of the command that is the electromagnetic torque that we will apply to the machine to run the generator at its optimum speed. The torque thus determined by the regulator is used as reference variable torque model of the turbine (Fig. 15.4).

15.2.3 DFIG Modelling

The doubly fed induction generator is typically modeled in the Park plane, leading to the following equations (Singh et al. 2010; Tapia et al. 2003):

$$\begin{cases} v_{sd} = R_s i_{sd} + \dfrac{d\phi_{sd}}{dt} - \omega_s \phi_{sq} \\ v_{sq} = R_s i_{sq} + \dfrac{d\phi_{sq}}{dt} + \omega_s \phi_{sd} \\ v_{rd} = R_r i_{rd} + \dfrac{d\phi_{rd}}{dt} - \omega_r \phi_{rq} \\ v_{rq} = R_r i_{rq} + \dfrac{d\phi_{rq}}{dt} + \omega_r \phi_{rd} \end{cases} \tag{15.8}$$

With:

$$\begin{cases} \phi_{sd} = L_s i_{sd} + M_{sr} i_{rd} \\ \phi_{sq} = L_s i_{sq} + M_{sr} i_{rq} \\ \phi_{rd} = L_r i_{rd} + M_{sr} i_{sd} \\ \phi_{rq} = L_r i_{rq} + M_{sr} i_{sq} \end{cases} \tag{15.9}$$

The expression of the electromagnetic torque of the DFIG based on the flux and stator currents is written as follows:

$$T_{em} = p\left(\phi_{sd} i_{sq} - \phi_{sq} i_{sd}\right) \tag{15.10}$$

The active and reactive power of the stator are written as follows

$$\begin{cases} P_s = V_{ds} I_{ds} + V_{qs} I_{qs} \\ Q_s = V_{qs} I_{ds} - V_{ds} I_{qs} \end{cases} \tag{15.11}$$

15.3 WECS-DFIG Control Strategy

The control strategy is based on:

- Control of RSC by controlling active and reactive stator power of DFIG.
- Control of GSC by controlling the voltage of the DC bus

15.3.1 RSC Control

The control principle of the rotor side converter (RSC) allows the control of active and reactive power as well as the extraction of maximum wind power. We will adopt conventional controllers (PI) necessary to achieve control of reactive and active power of the DFIG. The control of rotor currents is done by Proportional Integral (PI) controllers, as shown in Fig. 15.5.

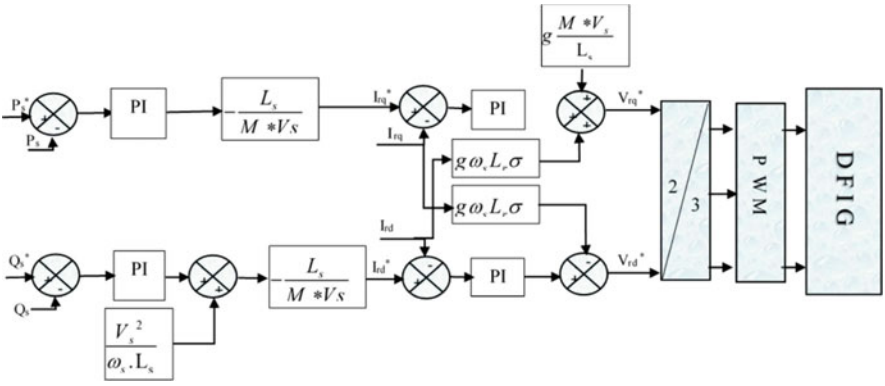

Fig. 15.5 Block diagram of RSC control

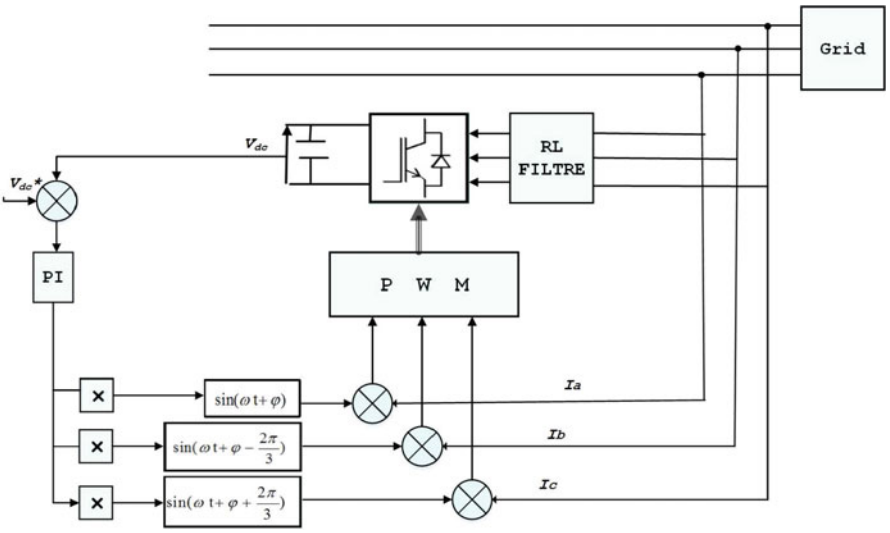

Fig. 15.6 Block diagram of GSC control

15.3.2 GSC Control

In the grid side control, mainly voltage of the DC bus is compared with a reference DC bus voltage and an error is fed to a PI controller to maintain constant DC bus voltage Fig. 15.6.

15.4 Fault Detection Technique

15.4.1 Open Switch Faults

The converter is the most sensitive subsystem of the (WECS-DFIG) from a reliability point of view and hence it is the element that the fault detection is the most required and profitable. Within the converters used in the (WECS-DFIG) structure, the most common and most critical faults are related in most cases to the control of the power semiconductor switch. A failure of the power switch may also be due to the degradation caused by excessive electrical, thermal or mechanical stress. Its origin can be internal and related to the function itself, or externally and linked to the environment or to an out of specification use (Ahmed and Zobaa 2016). A 2011 survey (Yang et al. 2011) indicates that the power switches are often the weakest link in converters, presenting 30% of total failures.

The two main types of switch failures in converters are short-circuit faults and open circuit switch faults. While short-circuit faults are usually very destructive and

require immediate actions to shut down the system, open switch faults do not cause a stop of the system and can stay undetected for some time. Unfortunately, such faults may generate secondary problems in the system that can cause failure in other parts of the system and can eventually lead to high repair costs (Yanhui et al. 2013). For this reason, open switch faults should be detected as soon as the fault occurs and properly localized.

In this chapter, only the open switch fault of the converter is considered. Several papers have been published for the detection and localization of faults. Most techniques are based on the analysis of output voltages or currents within the system. In Cherif et al. (2016), the authors suggested the park vector method to detect and localize the open switch fault. This technique is based on the mean value of the vector currents of the Park in the α-β plane and the determination of the phase angle and it is fully described in the following subsection.

15.4.2 Mean Value of the Rotor Current Detection Technique

This technique uses the mean phase current value for fault detection. It is to note that, a fault in a converter semiconductor switch can produce offsets in the currents of the electrical machine phases. The principle of this detection technique is to determine the mean value of the tree mean value phase rotor currents from which the fault can be detected and localized. A current threshold is usually defined in order to distinguish between the converter open switch faults. After the introduction of a fault in the converter power switch, a change can be clearly noticed in the rotor current waveforms shape and their corresponding means values. This technique enables us therefore to easily calculate the mean value of the rotor current phases and hence detect and localize the open switch faults in a converter. Table 15.1 summarizes the open switch faults characteristics of a power converter rotor side (Tamer et al. 2017).

Table 15.1 Open switch fault characteristics of a power converter rotor side

State	Leg A	Leg B	Leg C
Healthy	0	0	0
K_1open	$-I_{thresh} < Ia_{mean} < 0$	$Ib_{mean} > 0$	$Ic_{mean} > 0$
K_2open	$Ia_{mean} > 0$	$-I_{thresh} < Ib_{mean} < 0$	$Ic_{mean} > 0$
K_3open	$Ia_{mean} > 0$	$Ib_{mean} > 0$	$-I_{thresh} < Ic_{mean} < 0$
K'_1open	$0 < Ia_{mean} < I_{thresh}$	$Ib_{mean} < 0$	$Ic_{mean} < 0$
K'_2open	$Ia_{mean} < 0$	$0 < Ib_{mean} < I_{thresh}$	$Ic_{mean} < 0$
K'_3open	$Ia_{mean} < 0$	$Ib_{mean} < 0$	$0 < Ic_{mean} < I_{thresh}$

15.5 Fault Tolerant Reconfiguration in Case of Open Switch Fault

Several researchers have been engaged in investigating the behaviour of the static converters during the occurrence of a power semiconductor switch fault as well as the associated fault tolerance topologies and therefore suggesting various propositions in order to overcome failures and thus to reduce such problems. The fault tolerant topology Fig. 15.7 includes a redundant leg connected using bidirectional voltage and current switches (triacs) to the converter. This redundant leg is constituted of two power switches K and K' and replaces one of the other converter legs when a fault occurs on a switch of that leg (Gaillard et al. 2007, 2013; Yanhui et al. 2013).

To ensure the continuity of service of the wind systems in the case of open switch fault, the following steps should be applied:

- Calculate the mean value of the rotor currents
- Compare it with the threshold current
- Isolate the faulty leg

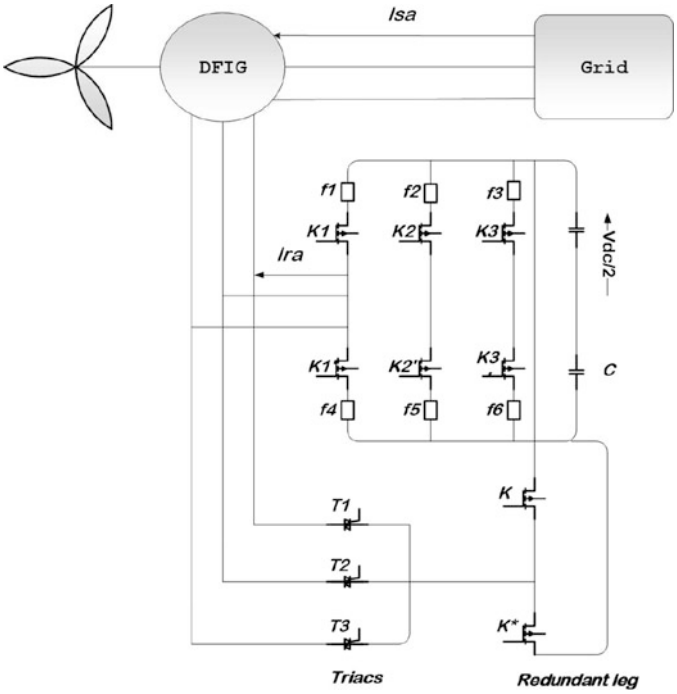

Fig. 15.7 Fault tolerant converter topology for WECS-DFIG

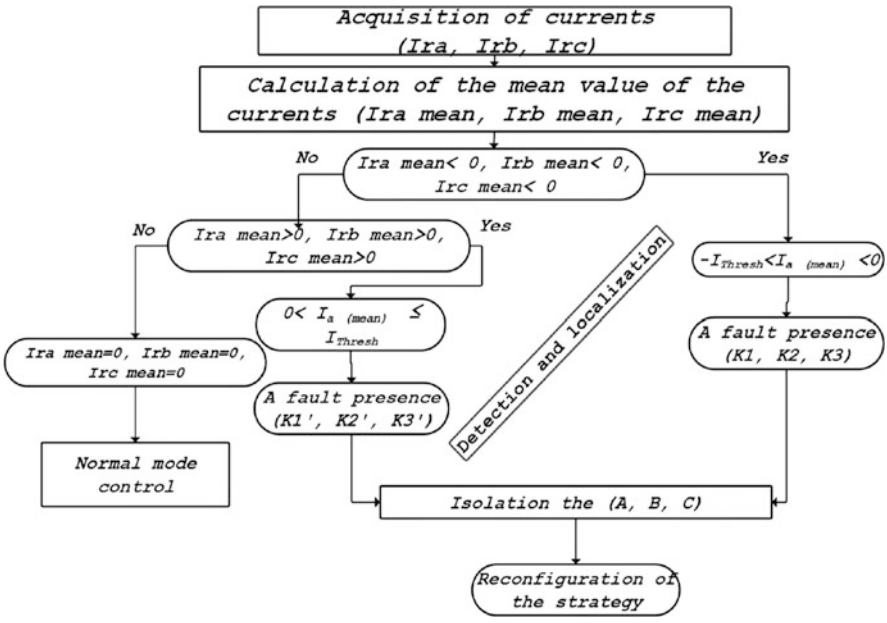

Fig. 15.8 Detection and reconfiguration algorithm of open switch fault

- Reconfigure by closing one of the bidirectional switches (triac) corresponding to the faulty phase
- At the same time, apply of the order command switches of the redundant leg
- Stop function "Fault detection".

Figure 15.8 below depicts in a synoptic diagram manner the required steps for converter open switch fault detection and localization.

15.6 Results Presentation and Discussion

This section presents simulation results of the (WECS-DFIG) control in the MATLAB-Simulink environment. Firstly, the simulation results of the vector controlled (DFIG) efficiency for normal operation condition, are presented in Fig. 15.9, it can be seen that the dynamics of the speed (Fig. 15.9b) is fast and it follows its reference under MPPT control. The active and reactive powers (Fig. 15.9c, d) control shows a good correlation compared to their references. Similar results for direct and quadrature rotor currents (Fig. 15.9e, f) are obtained. The DC link voltage (Fig. 15.9g) is well regulated.

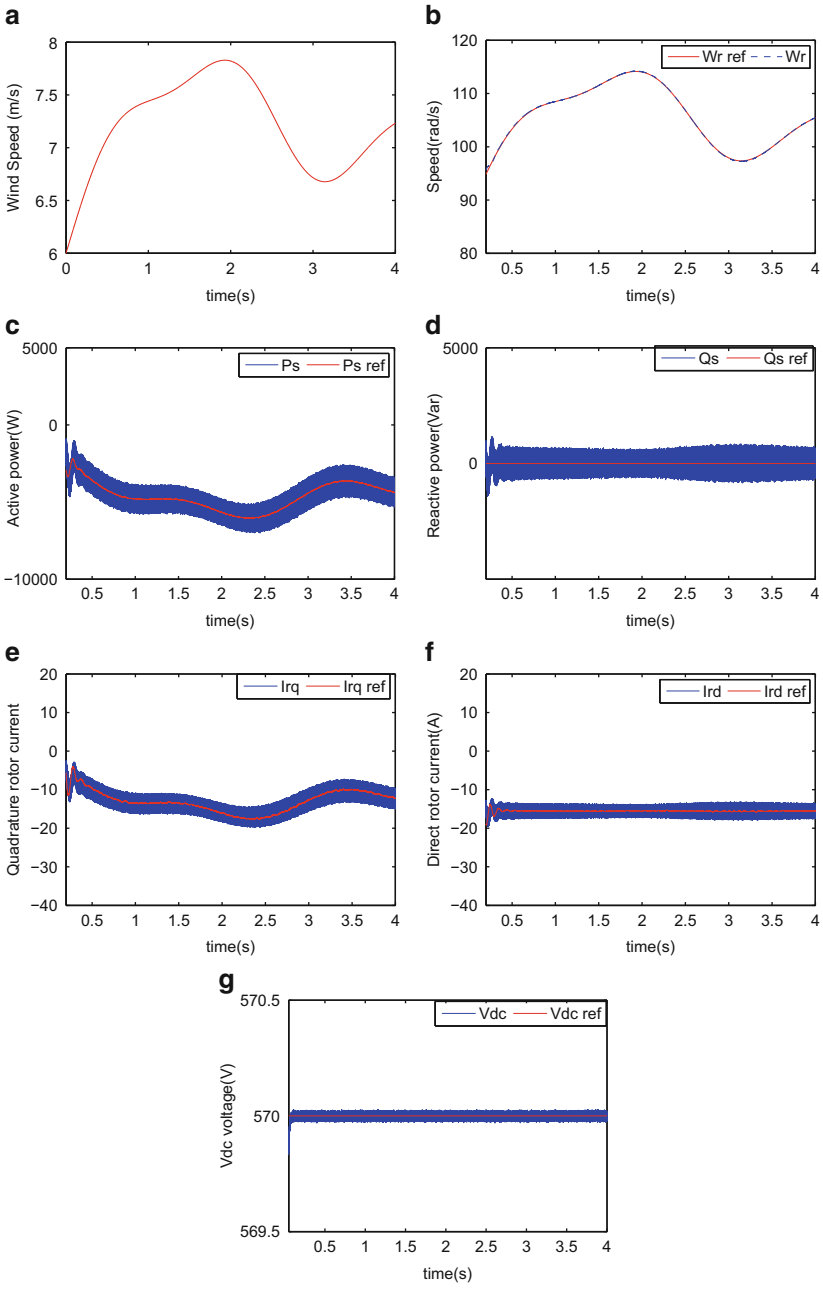

Fig. 15.9 DFIG speed, active and reactive powers, direct and quadrature rotor currents, and V_{DC} voltage

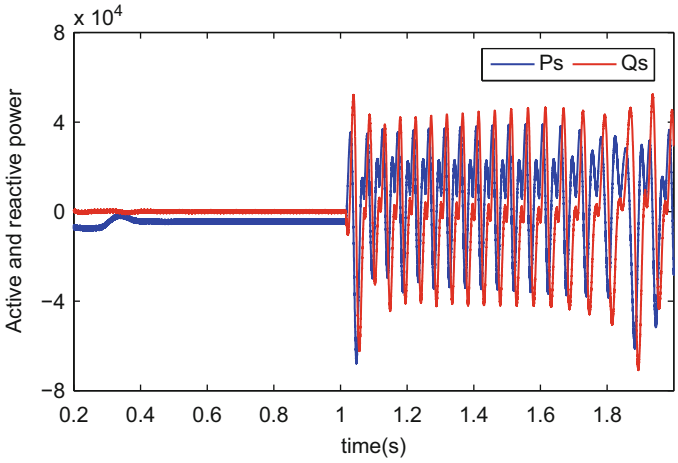

Fig. 15.10 Active and reactive powers with open switch fault K_3

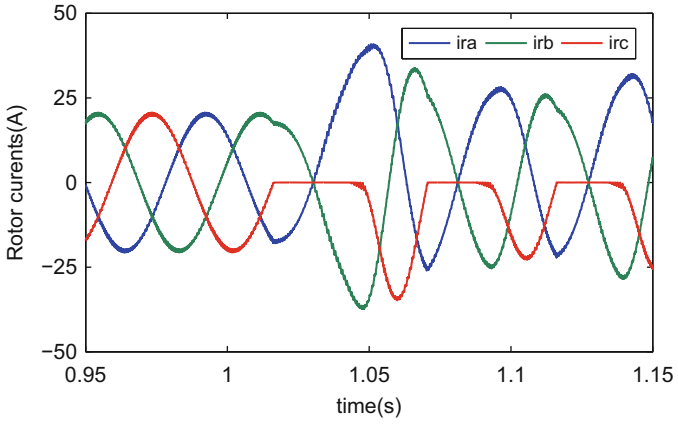

Fig. 15.11 Rotor phase current with open switch fault K_3

The obtained results without fault detection and with compensation are shown in the case of an open-circuit fault on switch (K_3). The active and reactive power in Fig. 15.10, presents oscillations and fluctuations at the moment of application the fault (at time = 1 s). It is to note that the current in the phase concerned is zero during half of the modulation period as seen in Fig. 15.11.

The mean value of the faulty phase rotor current is negative and the other values are positive as depicted in Fig. 15.12. The command signal sent to the converter switch K_3 is as shown in Fig. 15.13. In the case of an open-circuit fault in the switch

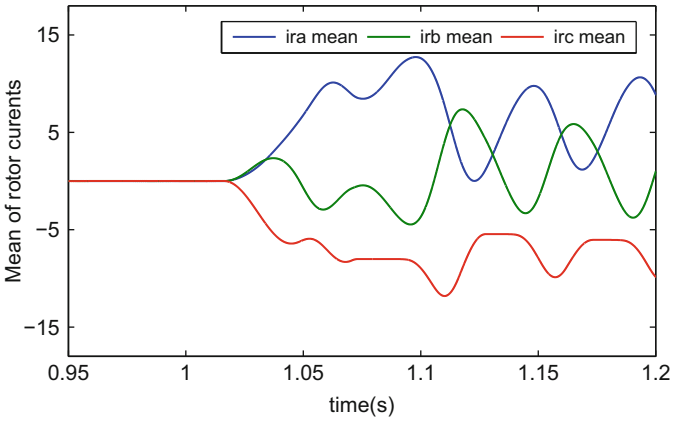

Fig. 15.12 Mean value of rotor current with open switch fault K_3

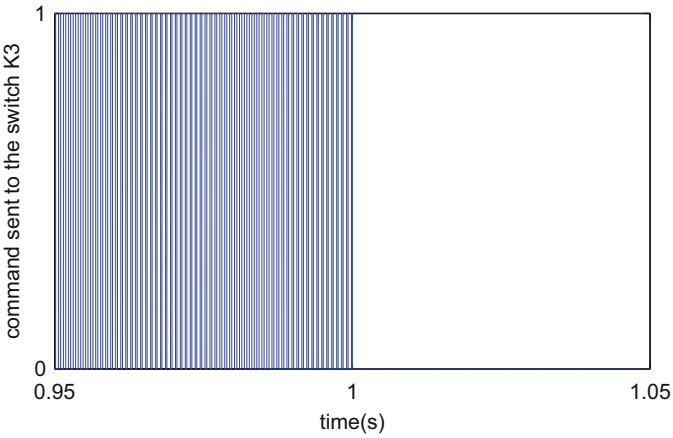

Fig. 15.13 Order command signal to switch K_3

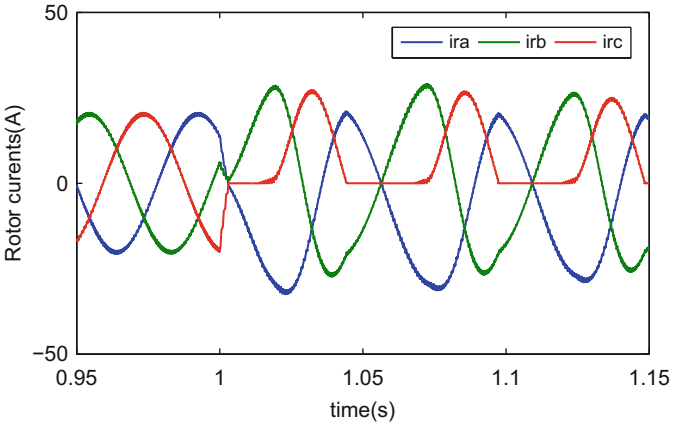

Fig. 15.14 Rotor phase current with open switch fault K_3'

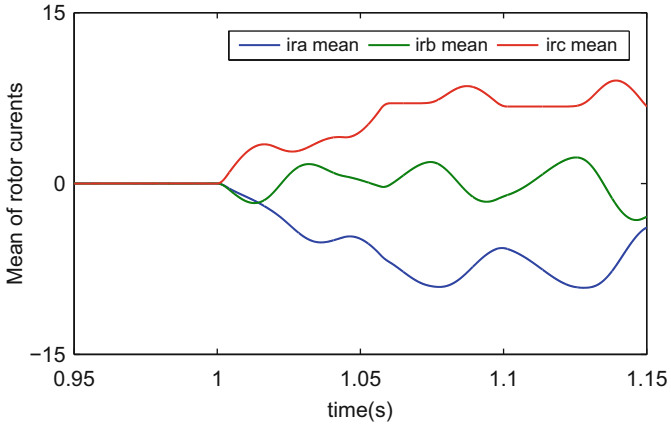

Fig. 15.15 Mean value of rotor current with pen switch fault K_3'

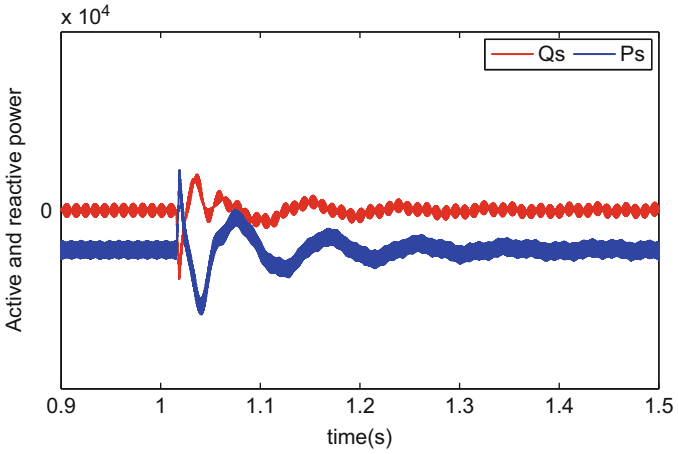

Fig. 15.16 Open switch fault compensation in active and reactive powers

of the lower half-leg K_3' (that is in the complementary converter switch) as shown in both Figs. 15.14 and 15.15, it is to notice that at the instant of the occurrence of the fault and in case of a fault in the switch of the upper half arm see Fig. 15.14, the mean value of the current of the faulty phase is then positive and the other values are negative as seen in Fig. 15.15. It can be also noted that with a short detection time, the converter with redundant leg reconfiguration cancels the existing fault and ensure the continuity of service of the wind systems as depicted in Figs. 15.16 and 15.17.

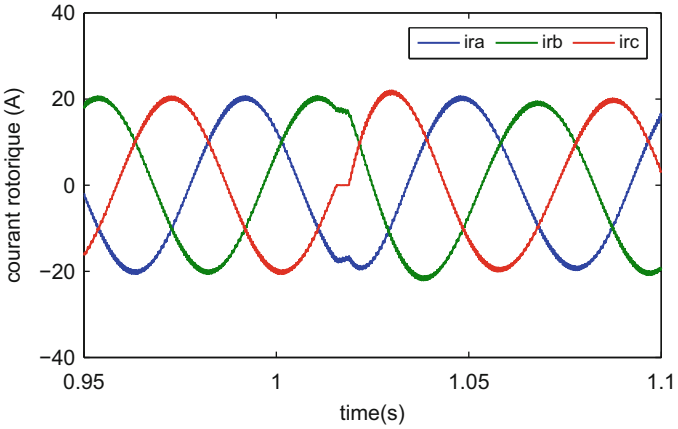

Fig. 15.17 Open switch fault compensation in rotor phase current

15.7 Conclusion

This chapter is addressing the issue of fault detection and fault tolerance reconfiguration for an open switch fault in power converter rotor side of a (WECS- DFIG). First a detection of the open switch fault is performed using the method of the mean value of the rotor currents technique. The use of this technique can detect the faulty leg as well as the accurate location of the faulty switch in the converter leg. For the continuity of service of the (WECS- DFIG), the fault tolerant power converter reconfiguration is then carried out based on a leg redundancy approach. With the use of the redundant leg fault tolerant topology, it is shown that the system can continue to operate without any problems after detection and isolation of the fault with the same performance as that before the fault occurrence. The performed simulation results illustrate well the feasibility of the proposed chapter contributions. Due the importance of the reliability in systems such as the (WECS- DFIG) which is always associated to power convertors, rapid and efficient detection methods are to be investigated to accurately localize the faulty converter switch. To ensure the continuity of (WECS- DFIG) service, more research work for robust fault tolerant control topologies needs to be investigated.

References

Ahmed, I., & Zobaa, A. (2016). Comparative power quality study of variable speed wind turbines. *International Journal on Energy Conversion, 4*(4), 97–104.

Bensouda, F., & Haddi, A. (2014). Introduction on advances in diagnosis for power electronics devices in wind energy, based on a doubly-fed asynchronous generator. In *International Conference on Green Energy and Environmental Engineering (GEEE)*, Tunisia.

Boukhriss, A., Nasser, T., Essadki, A., & Boualouch, A. (2014). Improved control for DFIG used in wind energy conversion systems. *International Review of Automatic Control (IREACO), 7*(4), 403–411.

Cherif, B., Bendjebbar, M., & Bendiabdellah, A. (2015). Diagnostic of open-circuit fault in three phase voltage inverter fed induction motor. In *IEEE Conference on Electrical Engineering, (ICEE 2015)*, Boumerdes, Algeria.

Cherif, B., Bendiabdellah, A., & Khelif, M. (2016). Detection of open-circuit fault in a three-phase voltage inverter fed induction motor. *International Review of Automatic Control, 9*(6), 374–382.

Cordeiro, A., Palma, J., Maia, J., & Resende, M. (2014). Detection and diagnosis solutions for fault-tolerant VSI. *Journal of Power Electronics, 14*(6), 1272–1280.

Elazzaoui, M. (2015). Modeling and control of a wind system based doubly fed induction generator: Optimization of the power produced. *Electrical & Electronic Systems Journal, 4*(141), 1–8.

ElKachani, A., Chakir, E., Laachir, A., Jarou, A., Niaaniaa, T., & Sedra, J. A. (2014). AC grid connected DFIG-based wind turbine with shunt active power filter. *International Review on Modelling and Simulations, 8*, 354–361.

Gaillard, A., Karimi, S., Saadate, S., Poure, P., & Gholipour, E. (2007). A fault tolerant converter topology for wind energy conversion system with doubly fed induction generator. In *European Conference on Power Electronics and Applications*, Aalborg, Denmark (pp. 1–6).

Gaillard, A., Poure, P., & Saadate, S. (2013). FPGA-based reconfigurable control for switch fault tolerant operation of WECS with DFIG without redundancy. *Renewable Energy Journal, 55*, 35–48.

Guediri, A., & Attous, D. B. (2015). Modeling and fuzzy control of a wind energy system based on double-fed asynchronous machine for supply of power to the electrical network. *International Journal of System Assurance Engineering and Management, 8*(1), 363–360.

Lu, B., & Sharma, S. K. (2009). A literature review of IGBT fault diagnostic and protection methods for power inverters. *IEEE Transactions on Industry Applications, 45*, 1770–1777.

Mohamed, S., Haitham, Z., & Ashraf, S. (2013). Open-circuit fault diagnosis of three-phase induction motor drive systems. *Journal of Electrical Engineering, 13*, 60–68.

Polinder, H., Lendenmann, H., Chin, R., & Arshad, W. (2009). Fault tolerant generator systems for wind turbines. In *International IEEE Conference on Electric Machines and Drives* (pp. 675–681).

Riouch, T., & Bachtiri, R. (2014). Advanced control strategy of doubly fed induction generator based wind-turbine during symmetrical grid fault. *International Review of Electrical Engineering, 9*(4), 829–834.

Sarati, D. P., & Kyeong-Hwa, H. (2014). Voltage-based on-line fault detection and faulty switch identification under multiple open-switches in grid-connected wind power converter. *International Journal of Control and Automation, 7*(11), 419–434.

Singh, B., Aggarwal, S., & Chandra, T. (2010). Performance of wind energy conversion system using a doubly fed induc-tion generator for maximum power point tracking. *IEEE Transactions, 978*, 4244–6395.

Tamer, A., Toumi, D., Bendiabdellah, A., & Boucherit, M. (2014). Inter-turn stator and rotor fault in doubly-fed induction generator based wind power system. In *Second International Conference on Electrical Engineering and Control Applications ICEECA Constantine*, Algeria.

Tamer, A., Toumi, D., Bendiabdellah, A., & Cherif, B. (2017). Open switch fault detection and fault tolerant of power converter fed DFIG in WECS. *International Review of Automatic Control, 10*(3), 274.

Tapia, A., Tapia, G., & Ostolaza, J. (2003). Modeling and control of a wind turbine driven doubly fed induction generator. *IEEE, 18*(2), 194–204.

Touati, A., Abouloifa, A., Elmounim, E. A., Aboulfatah, M., Majdoul, R., & Moutabir, A. (2014). Modeling and control of a three phase DC-AC converter connected to the network for a wind power system equipped with a DFIG. *International Review on Modelling and Simulations (IREMOS), 7*(2), 231–237.

Yang, S., Bryant, A., Mawby, P., Xiang, D., Ran, L., & Tavner, P. (2011). An industry-based survey of reliability in power electronic converters. *IEEE Transactions on Industry Applications, 47*, 1441–1451.

Yanhui, F., Junwei, Z., Yingning, Q., & Kai, F. (2013). Fault tolerance for wind turbine power converter. In *Renewable Power Generation Conference (RPGC)*, Beijing, China (pp. 1–4).

Chapter 16
ZedBoard-FPGA Control of the DFIG Based Wind Power System

Hassane Mahmoudi, Marouane El Azzaoui, and Chafik Ed-Dahmani

Abstract This work deals with the field oriented control of the doubly fed induction generator (DFIG) based wind energy conversion system using ZedBoard-FPGA. Most of previous works use very expensive embedded processor to control the doubly fed like Dspace. Using ZedBoard-FPGA reduces the cost of the complete system. This is a quick way to create hardware/software for different algorithm using Simulink. Simulation results show the performance of the field oriented control of DFIG, and experiment results present an overview of this control using ZedBoard-FPGA compared to simulation.

Keywords DFIG · ZedBoard · FPGA · FOC · Turbine emulator · HDL

16.1 Introduction

The developed research in this chapter focuses on modeling and the numerical implementation of control algorithms applied to the doubly fed induction generator (DFIG).

DFIG is a type of wind turbine that has been the subject of numerous studies in recent years. It operates at variable wind speed. Its main feature is that it consists of an asynchronous wound rotor machine and can thus provide active power to the grid by the stator and rotor. It allows to obtain a good performance over a wide range of wind speed (Meng et al. 2016). The DFIG is sized so that the power converters on the rotor are only traversed by 30% of the nominal power. Therefore it use less expensive converters (Yaramasu and Wu 2017).

H. Mahmoudi (✉) · M. El Azzaoui · C. Ed-Dahmani
Power Electronics and Control Team, Department of Electrical Engineering Mohammadia School of Engineers, Mohammed V University, Rabat, Morocco
e-mail: mahmoudi@emi.ac.ma; marouane.elazzaoui@research.emi.ac.ma; chafik.eddahmani@research.emi.ac.ma

N. Derbel, Q. Zhu (eds.), *Modeling, Identification and Control Methods in Renewable Energy Systems*, Green Energy and Technology,
https://doi.org/10.1007/978-981-13-1945-7_16

Despite these advantages, it remains a problem: its connection to the network. The power grid is not always stable. It regularly undergoes voltage deterioration (overvoltage voltage type). These damages can lead to fault currents in the machine and thus damage or even destroy the power converters (Amin and Uddin 2017).

The first implementations of control algorithms for electrical machines were realized with analog solutions. These solutions ensure the execution of controls having a high bandwidth and a high resolution. However, they lacked reliability due to their sensitivity to perturbations and variations in control parameters related to the thermal stresses of analog circuits. To remedy these drawbacks, digital solutions naturally imposed themselves. The first numerical implementations of control algorithms for electrical machines were performed using microcontrollers, microprocessors and DSPs (Digital Signal Processor), which also solve problems related to the use of analog controls. On the other hand, in spite of the advantages offered by digital solutions, some advantages offered by analogue installations are lost. This is mainly due to the fact that the discretization and the quantification of the control algorithms to be implemented, as well as the calculation time delays, deteriorate the control performance in terms of correction speed and control resolution.

With technological advances in the field of microelectronics, new hardware design solutions, such as Field Programmable Gate Array (FPGA) or Application Specific Integrated Circuit (ASIC) such as ZedBoard, are available and can be used as digital targets for the implementation of control algorithms (Azzaoui et al. 2016c).

ZedBoard is a low-cost development board for the Xilinx Zynq-7000 all programmable SoC (AP SoC). This board contains everything necessary to create several application. Additionally, several expansion connectors expose the processing system and programmable logic I/Os for easy user access. Take advantage of the Zynq-7000 AP SoCs tightly coupled ARM processing system and 7-series programmable logic to create unique and powerful designs with the ZedBoard. Target applications include motor control.

In the following lines a field oriented control strategy of the doubly fed induction generator is studied and implemented using ZedBoard FPGA.

16.2 Mathematical Model of Wind Energy Conversion System (WECS)

Wind energy system is composed from different mechanical and electrical components such as blades, gearbox, generator, power converter and more… In the following, all these parts are described with their mathematical model, and in the end of this section, a different controls strategies of the system are depicted.

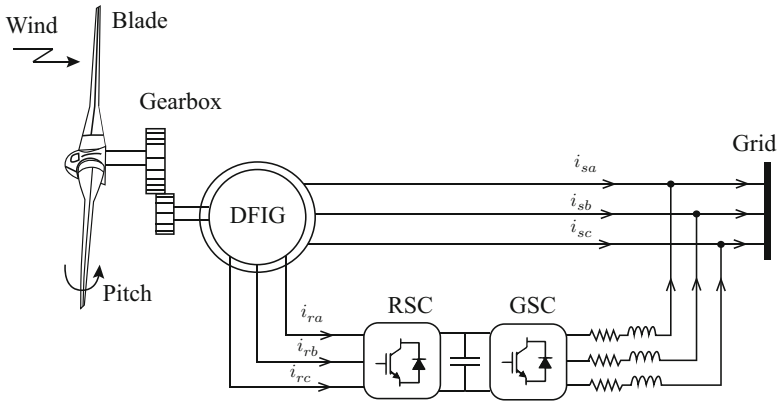

Fig. 16.1 DFIG based wind energy conversion system

Figure 16.1 illustrates a classical structure of the DFIG on variable wind turbine. The DFIG's stator is connected directly to the grid, and its rotor is connected to the grid via a power electronics system. The DFIG is powered by the grid voltage and the voltage in the out of the power electronics system which is having a variable frequency linked to the rotor of the generator. The power electronic system must be bidirectional to feed the generator or to generate the power to the grid according to the mode of operation (hypo or hyper synchrone). This is achieved by using a back-to-back converter which is composed from : rotor side converter (RSC), grid side converter (GSC), and DC bus voltage. GSC is connected to the grid through RL filter to decrease the harmonics generated using the converters.

The Mechanical part is composed from orientable blades (variable pitch), gearbox to increase the velocity, and the shaft allowing the transmission of the power to the generator. In the next, we will develop the mathematical model of the important parts.

16.2.1 Blade Model

Each turbine is characterized by its energy efficiency. This efficiency is the ratio between the power extracted and the power contained in the wind. This ratio is called power coefficient and it's limited to 0.5926 according to Betz. Further, the power extracted is expressed as following (Azzaoui et al. 2016b):

$$P_t = \frac{1}{2} C_p(\lambda, \beta) \rho R \pi^2 v^3 \tag{16.1}$$

There is another expression of this power that can be writing as function of mechanical velocity and turbine torque:

$$P_t = \Omega_t T_t \tag{16.2}$$

From this two last equation the expression of the torque is deduced:

$$T_t = \frac{1}{2\Omega_t} C_p(\lambda, \beta)\rho R\pi^2 v^3 \tag{16.3}$$

λ ratio is defined as the fraction between the linear speed of the turbine Ω_t and the speed of the wind v, its expression is given by Abulanwar et al. (2013):

$$\lambda = \frac{\Omega_t R}{v} \tag{16.4}$$

with:
Ω_t: Mechanical velocity of the turbine (rad/s).
ρ: Air density $\rho = 1.225\,\text{kg/m}^3$.
R: Raduis of the turbine (m).
v: Wind speed (m/s).
β: Pitch angle (degree).
In this study, we consider a power coefficient expressed by this equation:

$$C_p(\lambda, \beta) = (0.4 - 0.0167\beta)\sin\left[\frac{\pi(\lambda + 0.1)}{14.34 - 0.2\beta}\right] - 0.00184\beta(\lambda - 3) \tag{16.5}$$

Figure 16.2 shows the curves of power coefficient as function of λ and β. We get a maximal $C_p = 0.4$ at $\lambda = 7$.

16.2.2 Gearbox Model

The Gearbox that is located between the turbine and the generator has the purpose to adopt the slow speed of the turbine to the fast of the generator. It's described by the following two equations:

$$\Omega_t = \frac{1}{G}\Omega_m \tag{16.6}$$

$$T_m = \frac{1}{G}T_t \tag{16.7}$$

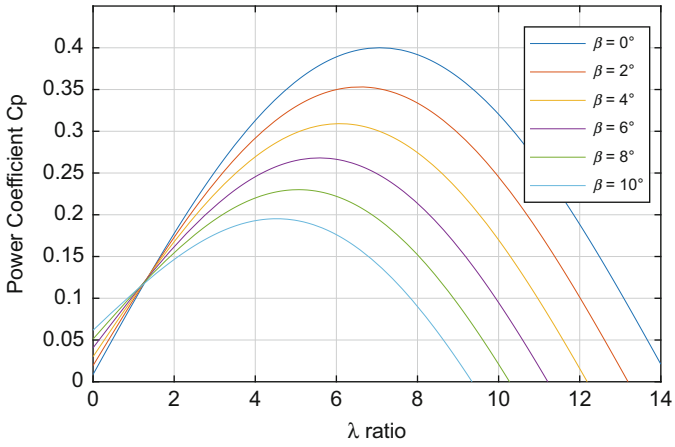

Fig. 16.2 Curves of power coefficient

where:
Ω_m: Mechanical velocity of the generator.
T_m: Torque applied to the generator.
G: Gain of gearbox.

16.2.3 Shaft Model

By applying the fundamental equation of dynamics, the dynamic of mechanical velocity of the generator is given by (Fig. 16.3):

$$J\frac{d\Omega_m}{dt} = T_m - T_{em} - f\Omega_m \tag{16.8}$$

With:
T_{em}: Electromagnetic torque of the DFIG.
J: Moment of inertia total.
f: Coefficient of viscosity total.
By grouping the blade, gearbox, and shaft models, we can construct the block diagram of the turbine is presented in Fig. 16.3.

16.2.4 DFIG Model

Modeling of the DFIG in stationary frame reference using park transformation is presented by Shehata (2015):

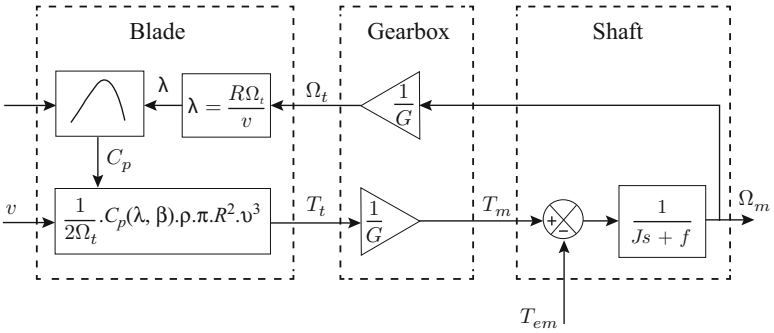

Fig. 16.3 Block diagram of turbine

- Voltage equations:

$$V_{sd} = R_s I_{sd} + \frac{d\varphi_{sd}}{dt} - \omega_s \varphi_{sq} \tag{16.9}$$

$$V_{sq} = R_s I_{sq} + \frac{d\varphi_{sq}}{dt} + \omega_s \varphi_{sd} \tag{16.10}$$

$$V_{rd} = R_r I_{rd} + \frac{d\varphi_{rd}}{dt} - \omega_r \varphi_{rq} \tag{16.11}$$

$$V_{rq} = R_r I_{rq} + \frac{d\varphi_{rq}}{dt} + \omega_r \varphi_{rd} \tag{16.12}$$

- Flux equations:

$$\varphi_{sd} = L_s I_{sd} + L_m I_{rd} \tag{16.13}$$

$$\varphi_{sq} = L_s I_{sq} + L_m I_{rq} \tag{16.14}$$

$$\varphi_{rd} = L_r I_{rd} + L_m I_{sd} \tag{16.15}$$

$$\varphi_{rq} = L_r I_{rq} + L_m I_{sq} \tag{16.16}$$

- Frequencies equations:

$$\omega_r = \omega_s - p\Omega \tag{16.17}$$

- Powers equations:

$$P_s = V_{sd} I_{sd} + V_{sq} I_{sq} \tag{16.18}$$

$$Q_s = V_{sq} I_{sd} - V_{sd} I_{sq} \tag{16.19}$$

$$P_r = V_{rd} I_{rd} + V_{rq} I_{rq} \tag{16.20}$$

$$Q_r = V_{rq} I_{rd} - V_{rd} I_{rq} \tag{16.21}$$

16.3 WECS Control Strategies

16.3.1 MPPT Control

This control structure is based on the assumption that the wind speed varies very little in steady state. In this case, from the dynamic equation of the turbine, we obtain the static equation describing the standing turbine speed (El Azzaoui 2015):

$$J \frac{d\Omega_m}{dt} = 0 = T_{mec} = T_{fa} - T_{em} - f\Omega_m \tag{16.22}$$

The electromagnetic torque becomes:

$$T_{em}^* = \frac{1}{2G\Omega_t} C_{pmax} \rho S v^3 - f\Omega_m \tag{16.23}$$

Assuming that the orientation angle β of the blades is constant, the wind speed can be written as follows:

$$v = \frac{R\Omega_t}{\lambda_{opt}} \tag{16.24}$$

The electromagnetic torque reference will be expressed as:

$$T_{em}^* = \frac{1}{2G^3 \lambda_{opt}^3} C_{pmax} \rho \pi R^5 \Omega_m^2 - f\Omega_m \tag{16.25}$$

Figure 16.4 present the block diagram of MPPT without control of speed.

16.3.2 Pitch Control

Pitch control regulates the power generated by the turbine by the nominal electrical output of the DFIG. This control allows the automatic changing of the blades angle over the maximal generator speed, therefore protects it before overloading at high wind speeds. The optimal angle for the wind speed below the nominal value is

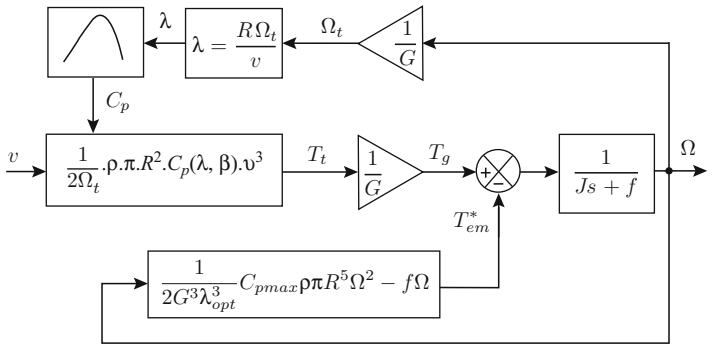

Fig. 16.4 MPPT block diagram without control of the speed

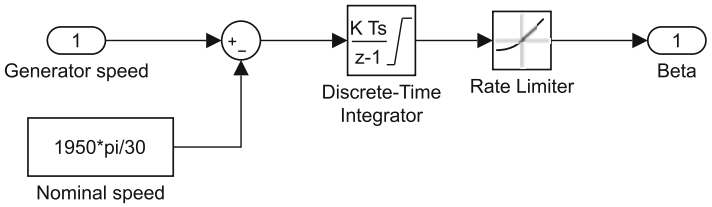

Fig. 16.5 Model of pitch control in Simulink

approximately zero and then it increases with the wind speed growing. It have considerable impact on the performance coefficient and on the value of the turbine torque. During the modelling of this controller, it is very important to take into account that changes of the blades angle must be fluent with a finite rate, maximal 10° per second, depending on the size of the wind turbine. The structure of the aerodynamic controller in the Simulink, which is shown in Fig. 16.5, is relatively simple.

The basic parameters set is formed by the nominal generator speed, the rate of pitch angle and by the maximal and minimal value of this angle. The input value is the speed of the generator, which is during the simulation compared with its nominal value and the output is the value of the pitch angle of the blades

16.3.3 DFIG Control

To control active and reactive power independently, field oriented is applied by aligning the stator flux with d-axis, this make quadratic flux equal to zero. In this stage, assuming that the grid is stable, and neglecting stator resistance, we get the simplified expression of stator voltages (Amrane et al. 2017).

$$\varphi_{sd} = \varphi_s \quad ; \quad \varphi_{sq} = 0 \tag{16.26}$$

$$V_{sd} = 0 \quad ; \quad V_{sq} = V_s = \omega_s \varphi_s \tag{16.27}$$

Consider the above assumption, rotor voltages are written as:

$$V_{rd} = R_r I_{rd} + \sigma L_r \frac{dI_{rd}}{dt} - g\sigma L_r \omega_s I_{rq} \tag{16.28}$$

$$V_{rq} = R_r I_{rq} + \sigma L_r \frac{dI_{rq}}{dt} + g\sigma L_r \omega_s I_{rd} + g\frac{V_s L_m}{L_s} \tag{16.29}$$

Expressions of stator powers become:

$$P_s = -\frac{V_s L_m}{L_s} I_{rq} \tag{16.30}$$

$$T_{em} = \frac{pL_m}{L_s}(\varphi_{sq} I_{rd} - \varphi_{sd} I_{rq}) \tag{16.31}$$

$$Q_s = -\frac{V_s L_m}{L_s} I_{rd} + \frac{V_s^2}{\omega_s L_s} \tag{16.32}$$

16.3.3.1 Rotor Side Converter Control

The control of the rotor side converter (RSC) enables us to control the stator active and reactive powers independently. From Eqs. (16.30) and (16.32), it's clear that the active and reactive powers are based on the q and d axis rotor currents respectively. Therefore, the powers are checked by controlling the rotor currents. These currents are controlled by a PI controllers. Then, we must add terms of compensation and decoupling. The voltages obtained are transformed to abc frame using dq to abc transformation which the angle is the difference between the stator angle obtained using a PLL and the rotor angle (Azzaoui et al. 2016d). Finally, the abc results voltages are converted to PWM signals by comparing these voltages with a carrier signal in order to control the gates of IGBTs used in the rotor side converter (RSC) as set forth in Fig. 16.6.

16.3.3.2 Grid Side Converter Control

The aim of controlling the grid side converter (GSC) is to produce a unitary power factor in the connection node of the grid, and to regulate the DC bus voltage of the back-to-back converter to a constant value. As presented in Fig. 16.7, a PI controller is used to control the d-axis current which its reference is kept null to have a unitary

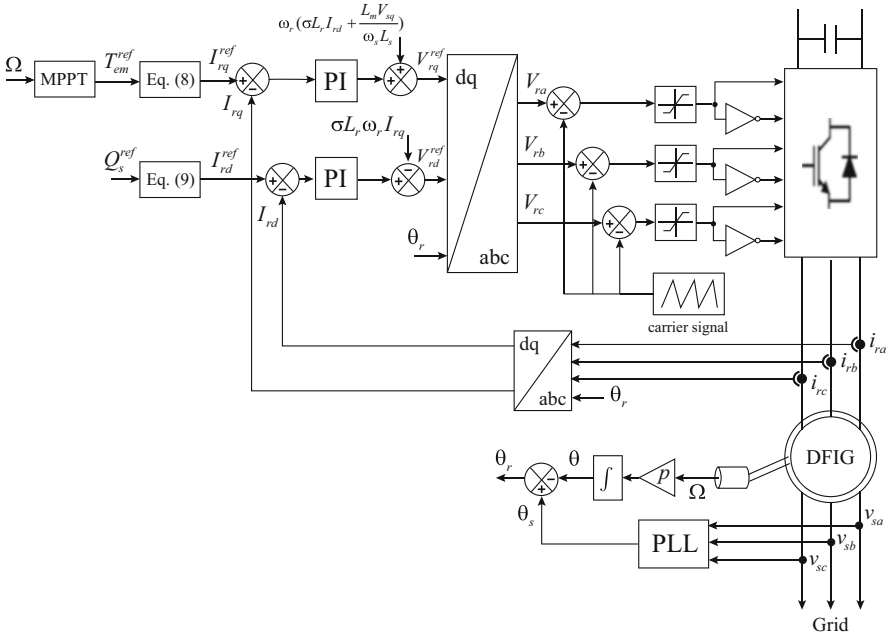

Fig. 16.6 Rotor side converter control using PI

power factor. DC bus voltage is regulated using two control loops, an inner loop that control the q-axis current using a PI controller, and an outer loop that regulate the DC bus voltage using a second PI controller. Reference results voltages are transformed in abc frame using the dq to abc transformation using stator angle. Finally, the abc results voltages are converted to PWM signals by comparing these voltages with a carrier signal in order to control the gates of IGBTs used in the grid side converter (GSC).

16.3.4 Simulation Results

The entire wind energy conversion system is simulated in Matlab/Simulink environment as shown in Fig. 16.8 where the parameters of DFIG in DC motor are given in "Appendix". The reference DC bus voltage is set at 600 V. By cons, we will vary the stator reactive power by adjusting its reference value in the RSC control. 8 kHz pulses width modulation (PWM) signals are generated with Space vector modulation (SVM).

Figure 16.9a shows the wind speed used in simulation, while Fig. 16.9b presents the mechanical speed derived from the turbine. Figure 16.10a, b illustrate that both electromagnetic torque and stator reactive power follow their references.

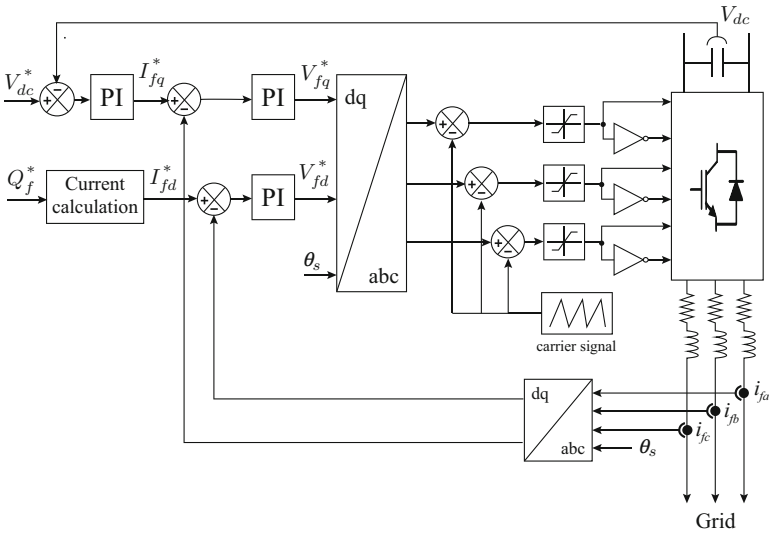

Fig. 16.7 Grid side converter control using PI

Figure 16.11a, b show the power generated by the turbine and the stator power produced by the DFIG. Figure 16.12a shows that the power coefficient is equal to it optimal values, thus guaranteeing the operating in MPPT mode, and Fig. 16.12b presents that the DC bus voltage is regulated perfectly to 600 V. Finally, Fig. 16.13a, b show the curves of pith angle and speed ratio respectively. While the power exceeds its nominal value (3 kW), the pitch increase to adjust this power to its nominal value.

16.4 Laboratory Experiment

This section covers the final laboratory setup, based upon the components covered in the previous section.

16.4.1 Laboratory Setup

Figure 16.14 shows the block diagram of laboratory setup. The DFIG is driven by a DC motor that emulates the mechanical part of the system (turbine). DC motor excitation is supplied by a DC voltage source while the armature is power via a dc chopper (in our case the seven arm in SomiKron Inverter) from the rectifier. Stator of DFIG is linked directly to the grid and its rotor is linked to the grid through the inverter and the rectifier cause in our study the DFIG is driven

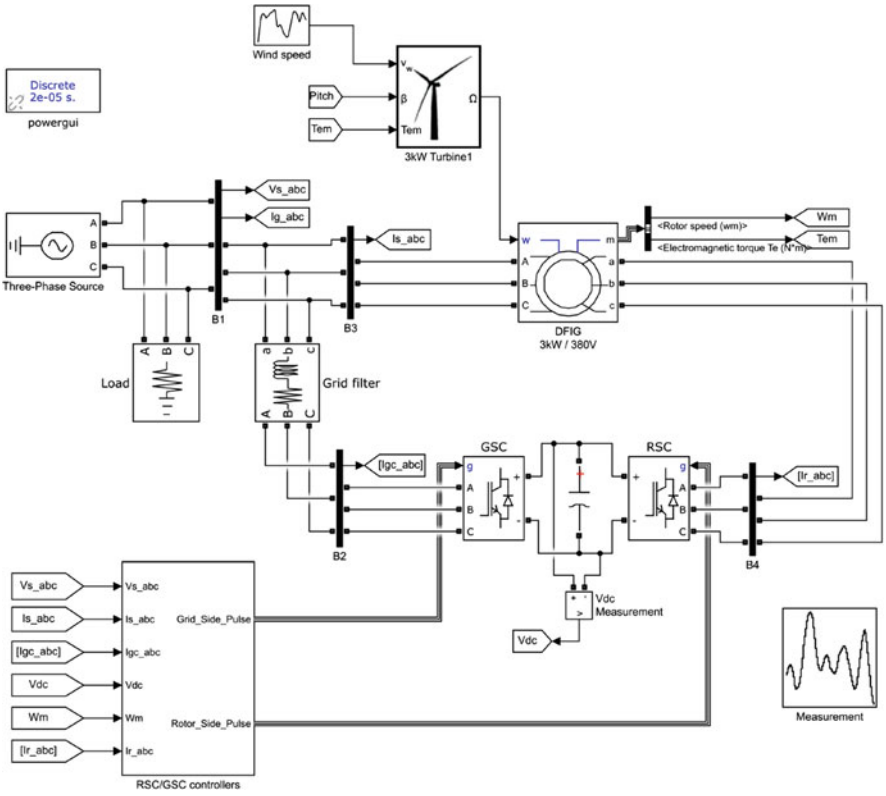

Fig. 16.8 WECS based DFIG in Simulink

in hypo-synchronous mode. Therefore in this case there will be no need for an independent voltage source to power the armature of DC motor. thus the inverter is replaced by the rectifier to simplify the control of the entire system. ZedBoard FPGA control the system via two board; the first one is the acquisition which acquire currents and voltages sensors and converts this information into digital format using 8 channels MCP3208 from microchip. The second one allows adapting PWM signal outgoing from 3.3 to 15 V needs to control the inverter and chopper. In Final step, the ZedBoard communicate to Host computer through Ethernet protocol to monitor data using external mode of simulink. Figure 16.15 presents Matalb hardware/software workflow for ZedBoard. In this workflow, we create model in Simulink that represent a complete dynamic system, and rapidly design hardware-software implementations for ZedBoard directly from the this model. This approach is structured as follow:

- developers used simulation in Simulink to create models for entire to evaluate design concepts, make high-level tradeoffs, and partition algorithms into software and hardware elements.

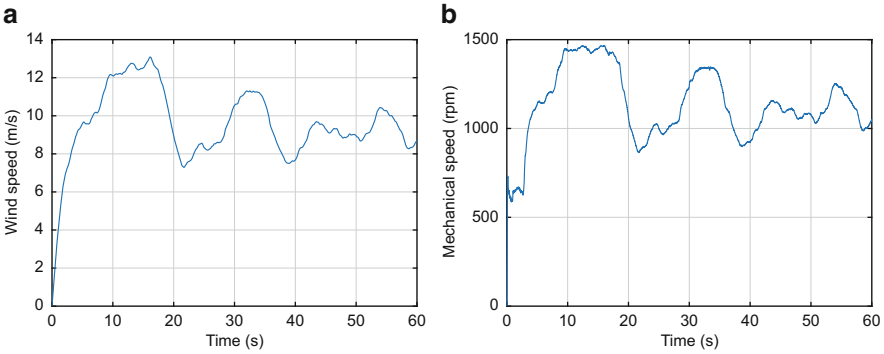

Fig. 16.9 Evolution of (**a**) wind speed, (**b**) mechanical velocity

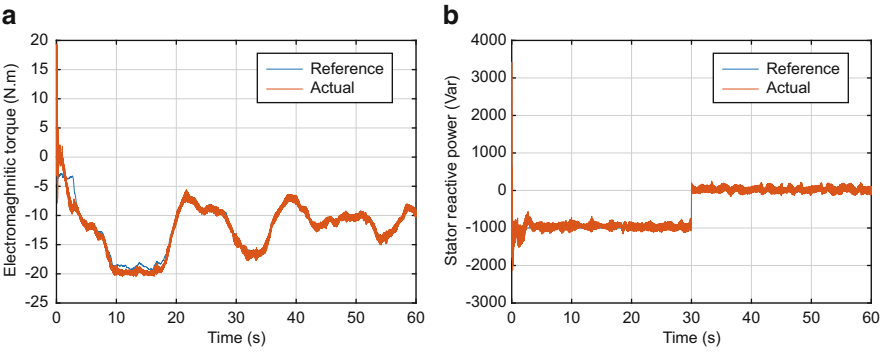

Fig. 16.10 Evolution of (**a**) electromagnitic torque, (**b**) stator reactive power

- HDL code generation from Simulink enabled the creation of IP cores and high-speed I/O processing on the fabric of the ZedBoard.
- C/C++ code generation from Simulink enabled the programming of the ARM Cortex-A9 cores in ZedBord, supporting rapid embedded software iteration.
- Automatic generation of the AXI4 interfaces linking the ARM processing system and programmable logic with support for Zynq in ZedBoard.
- Integration with downstream tasks, such as C/C++ compilation and building the executable for the ARM, bitstream generation using Xilinx implementation tools and downloading to ZedBoard development boards allows for a rapid prototyping workflow.

This IP core is designed to be connected to an embedded processor with an AXI4 interface. The processor acts as master, and the IP core acts as slave. By accessing the generated registers via the AXI4 interface, the processor can control the IP core, and read and write data from and to the IP core (Fig. 16.16).

Figure 16.17 provides an overview of the laboratory setup.

Laboratory setup is composed from the following parts:

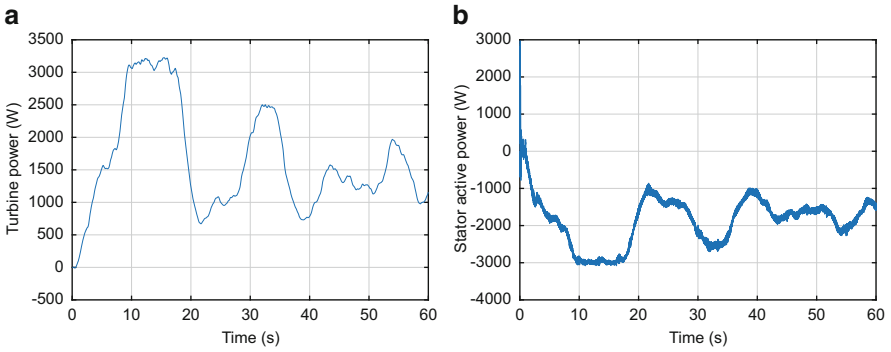

Fig. 16.11 Evolution of (**a**) turbine power, (**b**) stator active power

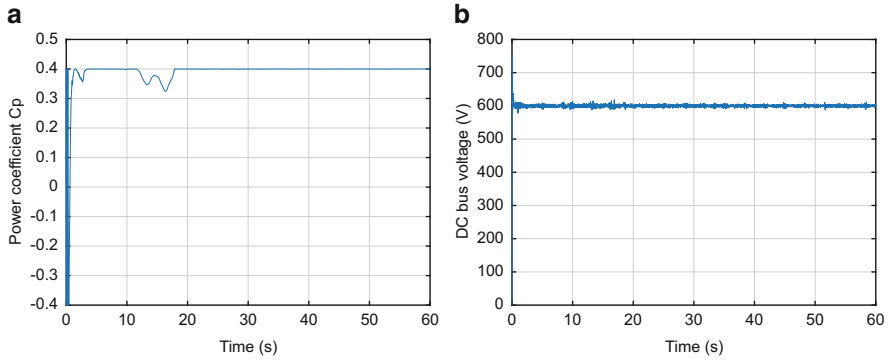

Fig. 16.12 Evolution of (**a**) power coefficient, (**b**) DC bus voltage

1. 3 kW Doubly fed induction generator (DFIIG) DELORENZO brand.
2. 3 kW DC motor DELORENZO brand.
3. Host computer.
4. 4 kW SomiKron inverter/rectifier which contains seven arms IGBT, the first six are used as inverter, and the last one is used as chopper in our study, and six diodes which are used as non-controlled rectifier
5. ZedBoard FPGA which is a complete development kit for designers interested in exploring designs using the Xilinx Zynq-7000 All Programmable SoC. The board contains all the necessary interfaces and supporting functions to enable a wide range of applications. The expandability features of the board make it ideal for rapid prototyping and proof-of-concept development.
6. Power board that generates three levels of voltages +15, 0, and −15 V, which are used in adaptation and acquisition board.
7. Adaptation board convert the level of voltage from 3.3 V in the out of ZedBoard FPGA to 15 V used by the inverter.

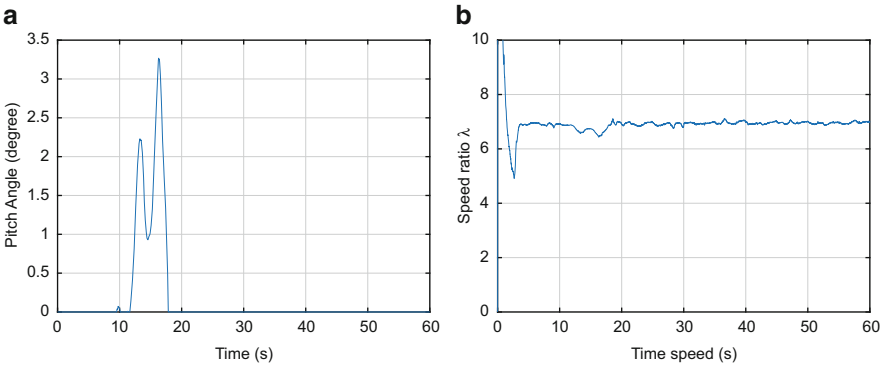

Fig. 16.13 Evolution of (**a**) power coefficient, (**b**) DC bus voltage

8. Acquisition Board that contains currents and voltages sensors, and ADC to convert analog data to digital, in our case, we use 8 channels MCP3208 from Microchip.
9. Incremental encoder Omron E2b2 CWZ1x brand provides 2000 pulses per revolution (PPR).

16.4.2 Turbine Emulator

In our laboratory there is no turbine, so, we decide to emulate it with a DC motor, cause it's simple to control it using a PI controller. Once the DC machine control sets, must be added the turbine previously studied, this collection emulates the mechanical part of the wind turbine, the synopsis of the control is shown in Fig. 16.18.

The turbine has in output the mechanical speed which is considered as rotational speed reference whose DC machine is to be driven. The purpose of DC motor control is the regulation of its speed to follow the speed of the turbine. A simple PI controller is used to control the DC motor as presented in Fig. 16.19. There are many methods to synthesize the parameters of PI as poles placement presented in this work (Azzaoui et al. 2016a).

Figure 16.20 presents the emulator program designed in Simulink and implemented in Zedboard-FPGA. The main part of the program is the PI controller that regulates mechanical speed of DC motor to mechanical speed in the out of the turbine to emulates this last. MPPT block allow to follow the maximal operating point and therefore to extract the maximal of power from kinetic energy of wind. Pitch control is used here to for orienting angle β of the blades, so as, not to exceed the maximum wind speed limit. There is also a encoder demodulation block that allow to acquire the rotational speed. Finally, the out of PI block is modulated with 8kHz triangular wave to generate the pulse width modulation that used to control the input chopper of the SomiKron inverter.

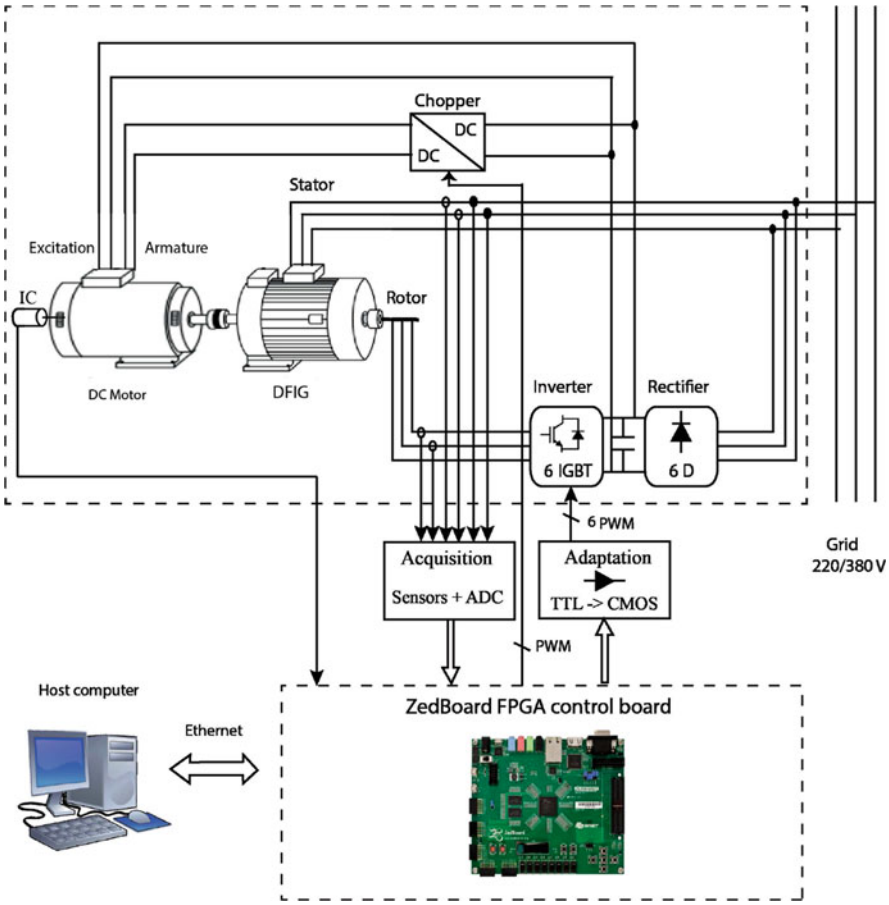

Fig. 16.14 Block diagram of test bench

The previous program is flashed into the ZedBoard, and all connection with the DC motor and chopper are made. Figure 16.21 shows that the mechanical speed of the DC motor follows exactly the mechanical speed imposed by the turbine. Hence, this test of control presents a good performance in term of tracking.

16.4.3 Experiment Results

After setup and implementing the laboratory setup. We did the parameters identifications of DFIG and DC motor. And we add the field oriented control studied to previous turbine emulator. The model that generate the IP cores is presented in Fig. 16.22. We did our test in hypo-synchronous mode as noted previously, and we

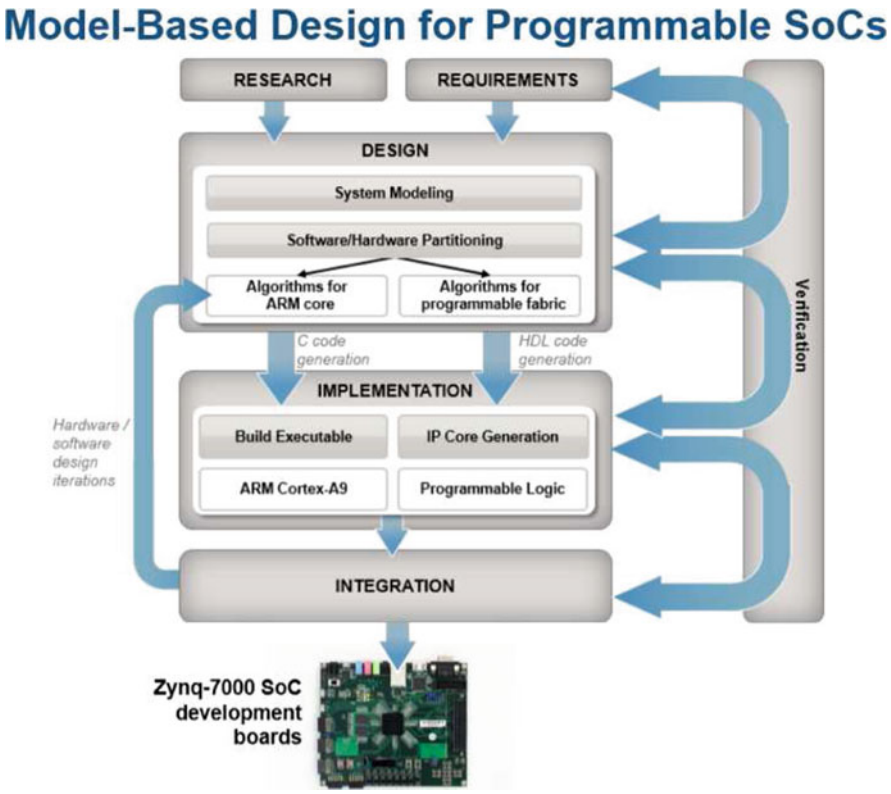

Fig. 16.15 Workflow Matlab and ZedBoard

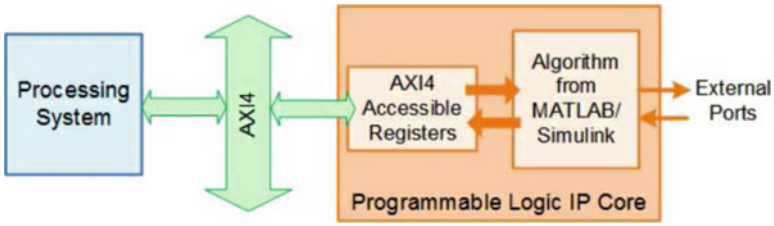

Fig. 16.16 Generation of IP core

notice that a start-up approach is necessary before controlling the DFIG in normal mode. The start-up process consists of two steps that are: calibration of the encoder and grid voltage synchronization as described in these works (Abad et al. 2011; Abo-Khalil 2012; Tapia et al. 2009). ZedBoard generate 8 kHz PWM to control both inverted and chopper. Using external mode interface in simulink the parameters of PI are tuning.

The next plots shows the experiment evolution of different measures.

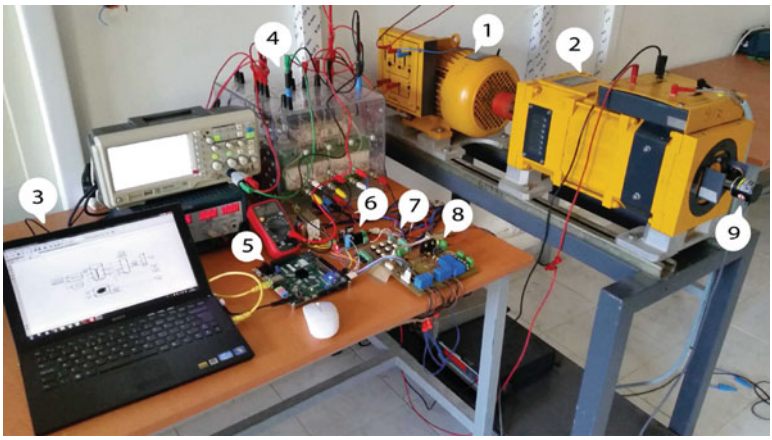

Fig. 16.17 Overview of test bench

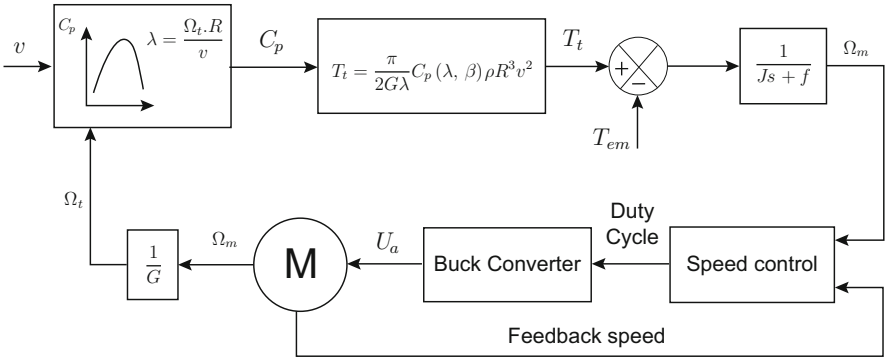

Fig. 16.18 Synopsis of the control of DC motor

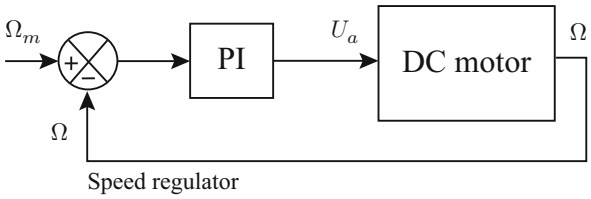

Fig. 16.19 Block diagram of DC machine control

Figure 16.23a, b present the profile of wind speed and the mechanical speed of the DFIG. the waveform of the mechanical speed brings together that of wind speed. Electromagnetic torque and stator reactive power follows their references as shown in Fig. 16.24a, b. We observe that the power produced has the same wave with tubine power as depicted in Fig. 16.25a, b. Figure 16.26a shows that the system operates in MPPT mode. Finally, Fig. 16.26b shows that the pitch is triggered so as not to exceed the nominal value of the power. Generally, the experimental results are

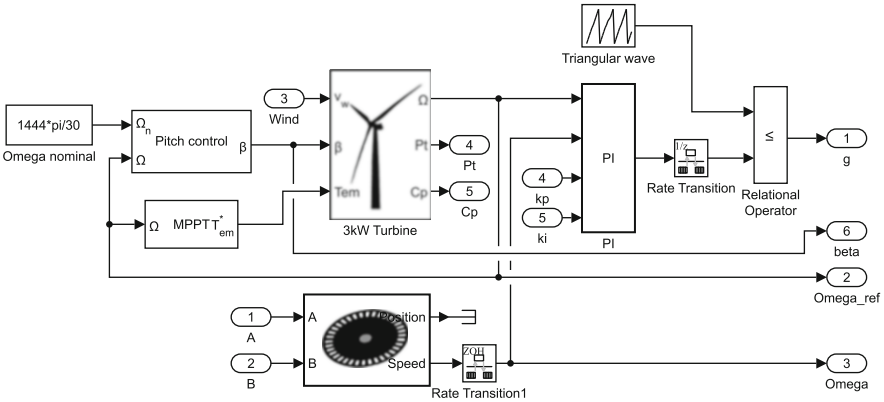

Fig. 16.20 Simulink model of turbine emulator

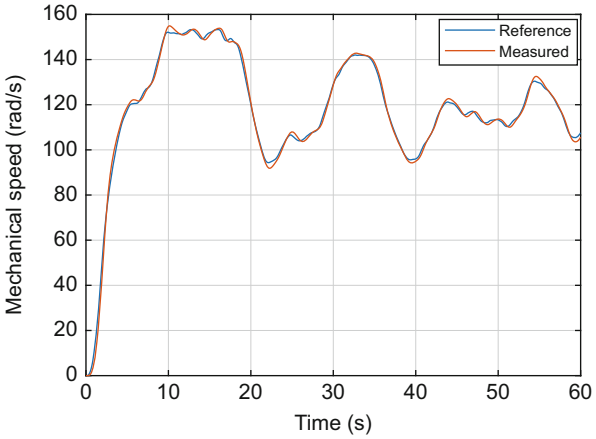

Fig. 16.21 Block diagram for the control of DC machine

somewhat identical to the results of the simulation except some noise due to errors of measurements.

16.5 Conclusion

The aim of this work was to improve the performance of the doubly fed induction generator and to analyze and highlight the contribution of ZedBoard-FPGAs in the control of electrical machines. To this end, the work presented in this report was mainly concerned with the modeling and implementation on the ZedBoard-FPGA target of control algorithms of doubly fed induction generator. In order to reduce

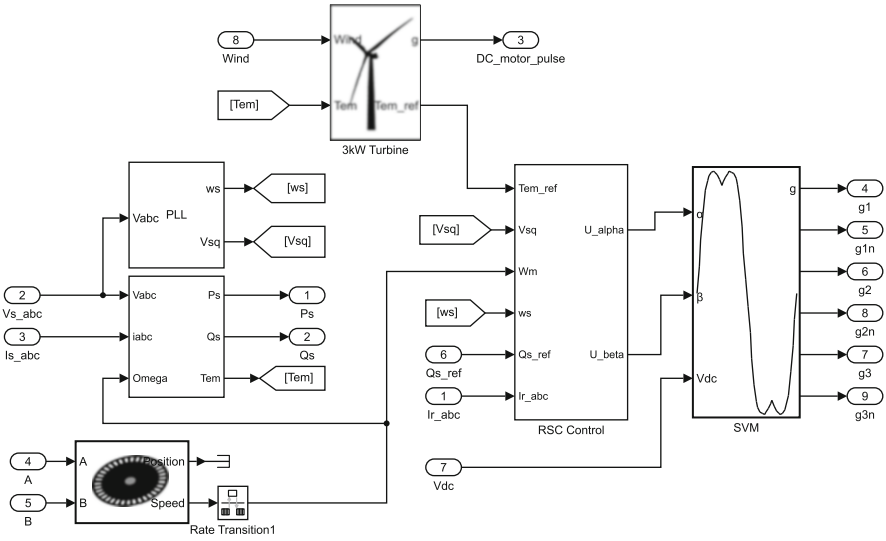

Fig. 16.22 Block diagram for the control of DC machine

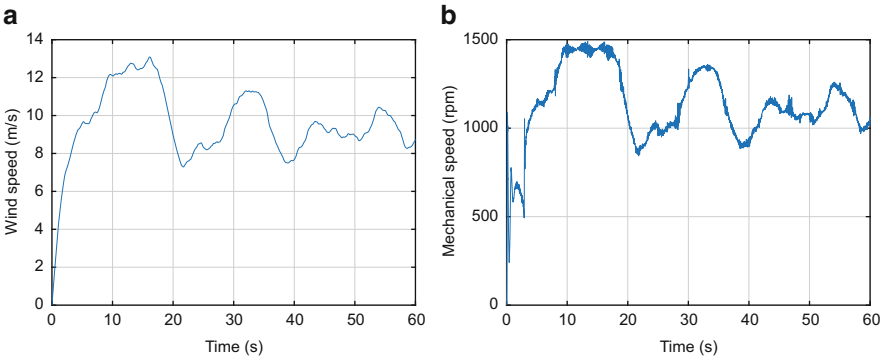

Fig. 16.23 Evolution of (**a**) wind speed, (**b**) mechanical velocity

the complexity of using FPGA solutions, a methodical and less intuitive approach was used. This approach is based on the appropriate development methodology that allows to answer the different constraints of the architecture of the control algorithms. In addition, this approach enabled the implementation of a specific library of reusable hardware architectures dedicated to the control of electrical machines.

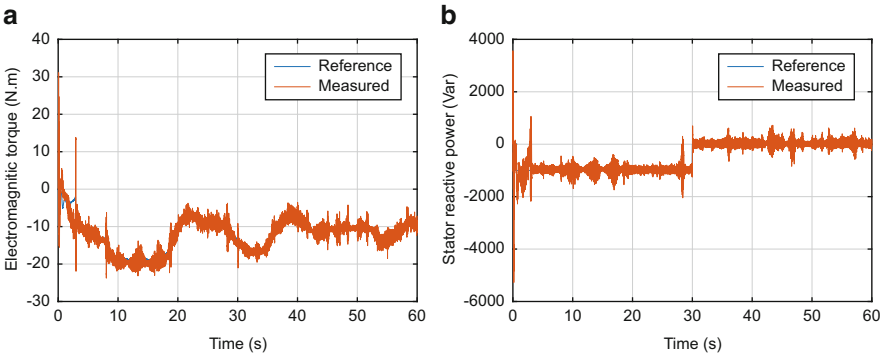

Fig. 16.24 Evolution of (**a**) electromagnitic torque, (**b**) stator reactive power

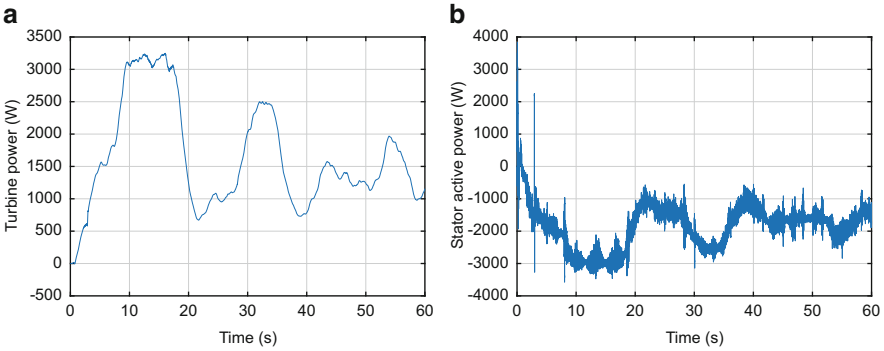

Fig. 16.25 Evolution of (**a**) turbine power, (**b**) stator active power

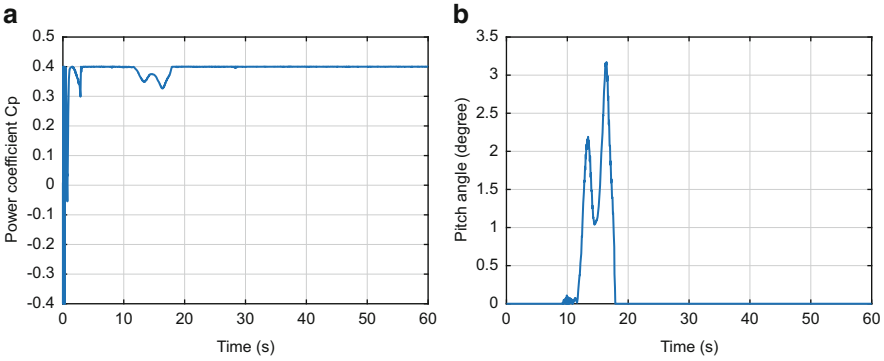

Fig. 16.26 Evolution of (**a**) power coefficient, (**b**) DC bus voltage

Acknowledgements The authors would like to thank all researchers and professors of the electrical department of Mohammadia School of Engineers.

Appendix

Table 16.1 DFIG nominal parameters

Designation	Value
Rated power	3 kW
Rated stator voltage	220/380 V
Nominal frequency	50 Hz
Number of pole pairs	$p = 2$
Rotor resistance	$R_r = 0.44\ \Omega$
Stator resistance	$R_s = 1.77\ \Omega$
Rotor inductance	$L_r = 0.138$ H
Stator inductance	$L_s = 0.309$ H
Mutual inductance	$L_m = 0.103$ H
Moment of inertia	$J = 0{,}017$ kg.m^2
Damping coefficient	$f = 0.0073$ N.m.s.rd^{-1}

Table 16.2 DC motor nominal parameters

Designation	Value
Rated power	3 kW
Armature resistance	$R_a = 1.5\ \Omega$
Armature inductance	$L_a = 0.9$ H
Coefficient k_e	$k_e = 0.3$
Moment of inertia	$J_{dc} = 0.021$ kg.m^2
Moment of inertia	$f_{dc} = 0.004$ N.m.s.rd^{-1}

References

Abad, G., Lopez, J., Rodriguez, M. A., Marroyo, L., & Iwanski, G. (2011). *Doubly fed induction machine modeling and control for wind energy generation*. Canada: Wiley.

Abo-Khalil, A. G. (2012). Synchronization of DFIG output voltage to utility grid in wind power system. *Renewable Energy, 44*, 193–198.

Abulanwar, S., Chen, Z., & Bak-Jensen, B. (2013). Study of DFIG wind turbine fault ride-through according to the Danish grid code. In *2013 IEEE Power Energy Society General Meeting*, Vancouver, BC, Canada (pp. 1–5).

Amin, I. K., & Uddin, M. N. (2017). MPPT based efficiently controlled DFIG for wind energy conversion system. In *2017 IEEE International Electric Machines and Drives Conference (IEMDC)*, Miami, FL, USA (pp. 1–6).

Amrane, F., Chaiba, A., Francois, B., & Babes, B. (2017). Experimental design of stand-alone field oriented control for WECS in variable speed DFIG-based on hysteresis current controller. In *2017 15th International Conference on Electrical Machines, Drives and Power Systems (ELMA)*, Sofia, Bulgaria (pp. 304–308).

Azzaoui, M. E., Mahmoudi, H., Bossoufi, B., & Ghamrasni, M. E. (2016a). Emulation of wind conversion chain equipped with a doubly fed induction generator. In *2016 International Symposium on Fundamentals of Electrical Engineering (ISFEE)*, Bucharest, Romania (pp. 1–6).

Azzaoui, M. E., Mahmoudi, H., & Ed-dahmani, C. (2016b). Backstepping control of a doubly fed induction generator integrated to wind power system. In *2016 International Conference on Electrical and Information Technologies (ICEIT)*, Tangier, Morocco (pp. 306–311).

Azzaoui, M. E., Mahmoudi, H., & Ed-Dahmani, C. (2016c). Backstepping control of the doubly fed induction generator using Xilinx system generator for implementation on FPGA. In *2016 5th International Conference on Multimedia Computing and Systems (ICMCS)*, Marrakech, Morocco (pp. 599–604).

Azzaoui, M. E., Mahmoudi, H., Ed-Dahmani, C., & Boudaraia, K. (2016d). Comparing performance of PI and sliding mode in control of grid connected doubly fed induction generator. In *2016 International Renewable and Sustainable Energy Conference (IRSEC)*, Marrakech, Morocco (pp. 769–774).

El Azzaoui, M., & Mahmoudi, H. (2015). Modeling and control of a doubly fed induction generator base wind turbine system optimizition of the power. *Journal of Theoretical and Applied Information Technology, 80*(2), 304–314.

Meng, W., Yang, Q., & Sun, Y. (2016). Guaranteed performance control of DFIG variable-speed wind turbines. *IEEE Transactions on Control Systems Technology, 24*(6), 2215–2223.

Shehata, E. (2015). Sliding mode direct power control of RSC for DFIGS driven by variable speed wind turbines. *Alexandria Engineering Journal 54*, 1067–1075. Elsevier.

Tapia, G., Santamaría, G., Telleria, M., & Susperregui, A. (2009). Methodology for smooth connection of doubly fed induction generators to the grid. *IEEE Transactions on Energy Conversion, 24*(4), 959–971.

Yaramasu, V., & Wu, B. (2017). *Control of DFIG WECS with voltage source converters* (pp. 512–). Hoboken: Wiley/IEEE Press.

Chapter 17
An FPGA-Based Control of the PMSG on Variable Wind Speed Turbine

Hassane Mahmoudi, Chafik Ed-Dahmani, and Marouane El Azzaoui

Abstract This chapter presents a study of variable wind speed turbine based on Permanent Magnet Synchronous Generator (PMSG) and turbine emulation system by a DC motor with experimental validation. The proposed controls of maximum power point tracking and pitch angle controls enables to extract the maximum power from wind. A field oriented control (FOC) technique was implemented for generator side converter. A new concept of controlling based on Matlab-Simulink for developing compatible controllers with HDL coder in order to generate a VHDL code, will be implemented on System on Chip (SoC) FPGA, the Xilinx Zynq-7000. Simulation and experimental results concerning proposed controls of the Wind Energy Conversion System (WECS) are presented and compared.

Keywords FPGA · PMSG · Wind energy conversion system · Vector control · VHDL · Turbine emulation · Matlab-Simulink · DC motor · HDL coder

17.1 Introduction

In recent years, the new interest related to wind energy results from two concerns, firstly, the environmental view that is a clean energy. Secondly, the development of wind turbines and power electronic technologies makes the conversion of the wind kinetic energy more efficient and therefore its use becomes economically competitive with other conventional sources. The wind turbines can be classified into fixed-speed and variable turbine (Blaabjerg and Chen 2006; Blaabjerg and Ma 2013).

H. Mahmoudi · C. Ed-Dahmani (✉) · M. El Azzaoui
Power Electronics and Control Team, Department of Electrical Engineering Mohammadia School of Engineers, Mohammed V University, Rabat, Morocco
e-mail: mahmoudi@emi.ac.ma; chafik.eddahmani@research.emi.ac.ma; marouane.elazzaoui@research.emi.ac.ma

N. Derbel, Q. Zhu (eds.), *Modeling, Identification and Control Methods in Renewable Energy Systems*, Green Energy and Technology,
https://doi.org/10.1007/978-981-13-1945-7_17

Comparing to fixed speed, the variable-speed turbine presents a several advantages including increased wind energy output, improved quality, and reduced mechanical stress (Ackermann and Söder 2005). But, it presents also drawbacks such as a high cost of manufacturing and prower losses due to use of power converters, and a complexity of the system. However, the drawbacks can be compensated by the additional energy production.

The converter system enables the control of the generator speed that is mechanically coupled with the wind turbine shaft through the gearbox system if needed (Wu et al. 2011a).

Different generators have been used in wind energy systems over the past years (Boldea 2005; Polinder et al. 2006). The Permanent Magnet Synchronous Generator PMSG and Doubly Fed Induction Generator DFIG are widely used for the new wind turbines. PMSG is normally controlled by a full-capacity power converter which presents drawbacks comparing the DFIG (around 30% of total power), but it is well suited for direct drive wind turbines, and is used for the high power rating up to 7.5 MW. PMSG is known for their high efficiency and power density. Also, the gearbox system can be eliminated for multi-poles PMSG architecture, which can minimize the installation and maintenance costs, and mechanical disturbances. Therefore, the PMSG is considered as a promising candidate for new designs in Wind Energy Conversion Systems WECS (Pena et al. 2013).

The presented topology is a subject to a number of control structures such as the Maximum Power point Tracking control for maintaining the desired tip speed ratio λ, the pitch angle control for the safety of WECS in strong wind and to limit the power at the rated value, and the generator control to maintain the desired rotor velocity (Busca et al. 2010). The Generator Side Converter GSC, a rectifier, will be controlled by the Field Orientation Control strategy (FOC) using space vector modulation (SVM) technique, this method allows a precise speed and torque control with minimal losses while reducing the torque ripple (Rogers et al. 2016).

The control algorithm GSC, needs to be implemented, the motor control technology was dominated by the Digital Signal Processor (DSPs), but several research has been using the Field Programmable Gate Arrays FPGA for driver controls (Azzaoui et al. 2016; Kocur et al. 2014; Kung et al. 2016; Mohammadi et al. 2016; Monmasson et al. 2011). Hardware solutions such as FPGA have advantages in price, execution speed, large processing capability and flexibility but are restricted for their poor calculation ability. The FPGA used in this chapter,was a System on Chip (SoC) device, that include a powerful general purpose processors and FPGA in the same chip, which is suitable for Real-Time (RT) simulation of Electromechanical system (Tormo et al. 2016). The zynq-7000 allows to build in one single device a complete system mixing soft and hardware functionalities which increases integration in the test bench.

This chapter is organized as follows, in Sect. 17.2 a mathematical model of WECS will be developed with determining the optimal conditions of work. Section 17.3 the MPPT, pitch angle, and PMSG control strategies will be presented with a diagram control schemes. In Sect. 17.4, a test bench and Turbine emulation system will be given, with a comparison of simulation and experimental results.

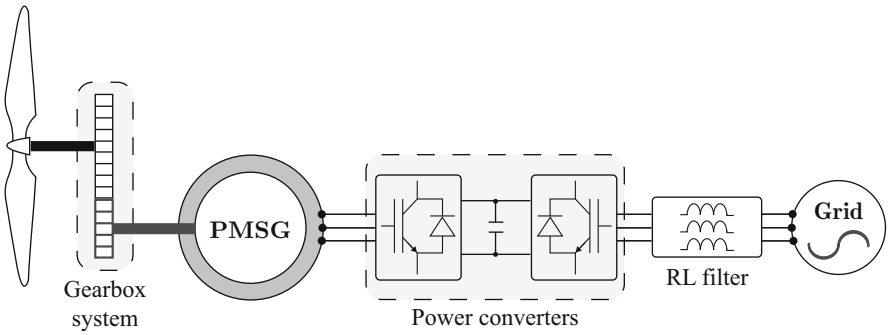

Fig. 17.1 Wind energy conversion system based on permanent magnet synchronous generator connected to the grid

17.2 Mathematical Model of Wind Energy Conversion System (WECS)

The wind energy conversion system is composed of several components such as wind turbine, PM synchronous generator, power converters, etc. In this section, the different components are presented with their mathematical models.

17.2.1 Wind Turbine Model

The Turbine converts the kinetics energy of wind into mechanical energy (Bakouri et al. 2015), the mechanical power extracted by the turbine is given by (17.1).

$$P_t = \frac{1}{2}\rho\pi C_p R^2 v^3 \tag{17.1}$$

Where, P_t is the mechanical power extracted by turbine, ρ the air density, C_p the power coefficient, R the turbine blade radius, and v is the wind speed.

Due to various losses in the wind energy conversion system, the power extracted by the turbine is less than the aerodynamic power of wind. Therefore, the power coefficient comes as a ratio between the aerodynamic and turbine power. This coefficient depends mainly on the blades inclination angle (pitch angle: β) and the ratio of wind speed v and turbine speed w_t (tip speed ratio: λ) as shown in (17.2) and (17.3).

$$C_p = 0.5\left(\frac{116}{\lambda_i} - 0.4\beta - 5\right) exp\left(\frac{-21}{\lambda_i}\right) + 0.0068\lambda \tag{17.2}$$

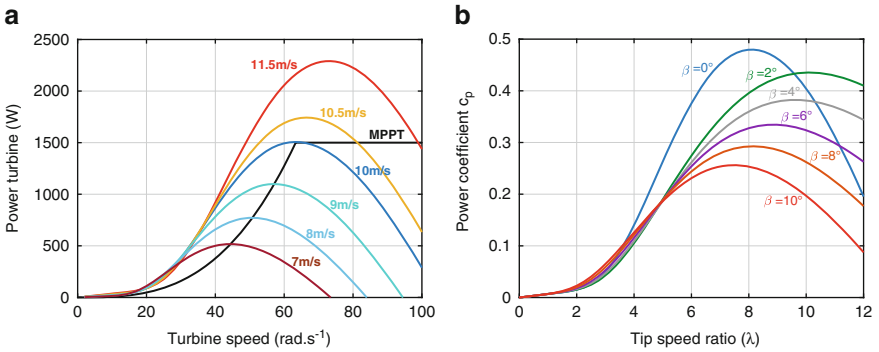

Fig. 17.2 Power turbine P_t and coefficient C_p curves under different values of wind speed and pitch angle. (**a**): Power turbine curves. (**b**): Power coefficient curves

$$\frac{1}{\lambda_i} = \frac{1}{\lambda + 0.08\beta} - \frac{0.035}{1 + \beta^3} \tag{17.3}$$

$$\lambda = \frac{R.w_t}{v} \tag{17.4}$$

By implementing previous equations, the nominal turbine power is given for $w_t = 63.43\,\text{rad.s}^{-1}$ with the maximal power coefficient $C_{p-max} = 0.48$ which is achieved for a specific value of tip speed ratio called optimal $\lambda_{opt} = 8.1$. Accordingly, for a given value of wind speed, the power coefficient will depend on rotor turbine velocity w_t. In order to provide the power extraction from the wind, the turbine must be operated with the optimal values of tip speed ratio and power coefficient regardless of wind velocity, in that case, the power curve is optimal as shown in Fig. 17.2.

For a variable wind speed, the turbine should be controlled in such away to maintain the different variables (C_p, λ, w_t) at their optimal values and to guarantee the safety work of the whole system during the operation, this achieved by deploying the Maximum power point tracking (MPPT) control and controlling the pitch angle, those controls will be discussed in Sect. 17.3.

17.2.2 PMSG Model

Permanent magnet synchronous generator is the main component that converts the mechanical power of turbine into electrical power. It should be noted that, two different types of PMSG exist depending on PM position in rotor which are Surface mounted PM and Inner PM (SPM and IPM respectively). Generally, most turbine with PMSG work with the SPM architecture with a high number of pole pairs,

which guarantee a high efficiency and it can eliminate the gearbox system (Wu et al. 2011c). In this chapter, the PMSG is considered with IPM architecture and with a gearbox system.

The dynamical behavior of PMSG is given in a rotative synchronous dq-frame, where the d-axis is aligned with rotor PM-flux (Yan et al. 2013). Then, the mathematical model of the synchronous generator becomes more simplified as shown for the electrical equations (17.5) and (17.6), and the electromechanical equation (17.7), with the mechanical equation of the equivalent system on (17.8).

$$V_{sd} = -R_s.i_{sd} - L_d\frac{di_d}{dt} + w_e L_q.i_{sq} \tag{17.5}$$

$$V_{sq} = -R_s.i_{sq} - L_q\frac{di_q}{dt} - w_e L_d.i_{sd} + w_e\phi_f \tag{17.6}$$

$$T_e = \frac{3P}{2}\left(\phi_f.i_{sq} + (L_q - L_d)i_{sd}.i_{sq}\right) \tag{17.7}$$

$$J_{eq}\frac{dw_m}{dt} = \frac{T_t}{G} - T_e - f_{eq}w_m \tag{17.8}$$

Where, R_s is the stator resistance, L_{dq} are the stator-inductances in dq-frame, ϕ_f is the PM-flux, P is the pole pairs number, w_e and w_m are electrical and mechanical speed, V_{sdq}, i_{sdq} are the stator voltages and currents components in dq-reference, T_e and T_t are respectively the electromagnetic and turbine torques, J_{eq} and f_{eq} are respectively the equivalent system inertia and viscous damping, and G is the gearbox gain.

17.3 WECS Control Strategies

The new wind turbines operate with variable wind speed, which involve to implement a control strategy for each component of system in order to maximize the extracted power. As mentioned in 17.2, the wind turbine should be controlled in such away to maintain the parameters characteristics at their optimal values regardless of wind speed value as shown in Fig. 17.3.

In this section a control strategy of turbine and PMSG will be presented.

17.3.1 MPPT Control

The purpose of Maximum Power Point Tracking control (MPPT) is to automatically extract maximum power, and it is activated only if the wind speed between the cut-on and rated value. There are three types of MPPT controller:

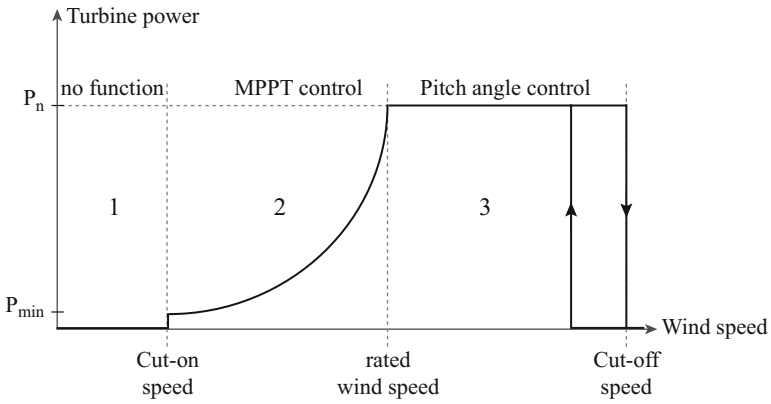

Fig. 17.3 Power turbine evolution with variable wind speed and controls

- MPPT with turbine power profile.
- MPPT with optimal speed ratio.
- MPPT with optimal torque control.

In this chapter, the MPPT with optimal speed ratio is chosen in Fig. 17.4, where the maximum power operation. This is achieved by keeping the tip-speed ratio at their optimal value λ_{opt}. The principle work of this method, is by measuring the wind speed v to produce the reference generator velocity w_{m-ref} according to λ_{opt}. The mechanical generator velocity is controlled to tracks w_{m-ref} in steady-state, at which the MPPT is achieved. When the proposed control is activated, the new expression of power, torque, and turbine speed are expressed as follow:

$$\begin{cases} P_{t-opt} = \dfrac{1}{2}\,\pi\,\rho\,C_{p-max}\,R^5\left(\dfrac{w_{t-opt}}{\lambda_{opt}}\right)^3 \\ w_{t-opt} = \dfrac{v\,\lambda_{opt}}{R} \\ T_{t-opt} = \dfrac{1}{2}\,\pi\,\rho\,C_{p-max}\,R^5\,\dfrac{w_{t-opt}^2}{\lambda_{opt}^3} \end{cases} \tag{17.9}$$

Depending on the wind speed profile, the MPPT regulates the generator velocity, maintaining the turbine at optimal point, and maximize the power capture as shown in the optimal curve of Fig. 17.2.

The MPPT with λ_{opt} was chosen because it guarantees a stale power coefficient and tip speed ratio comparing to others controllers, but it requires a precise measurement of wind speed.

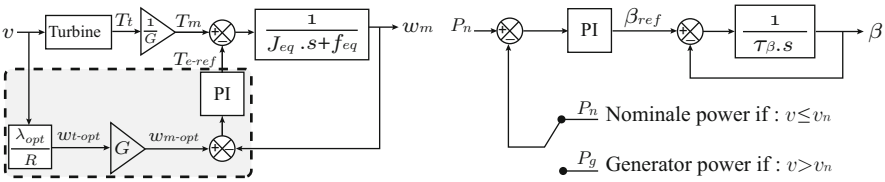

Fig. 17.4 Diagram schemes of the MPPT and pitch angle controllers

17.3.2 Pitch Angle Control

To guarantee a safety work of WECS, the new turbines are equipped with a pitch angle controller to limit the power capture. The Pitch angle control is enabled against the strong wind (the wind speed is between the nominal and cut-off speed). If the wind exceeds the nominal value, and as shown in Fig. 17.2, the pitch angle will vary in such away the power coefficient C_p and tip-speed ratio λ decreased to new optimal values depending on the wind speed which implies that the power turbine P_t will be at their rated value, also the rotor velocity will be limited at the optimal velocity w_{t-opt}. The Pitch controller diagram is shown in Fig. 17.4.

17.3.3 PMSG Control

There are a several methods to control the PM synchronous generator to achieve different objectives (Bose 2009; Wu et al. 2011b). In this chapter, a Field Oriented Control (FOC) is used to maintain the PMSG working in the optimal region. Where, the reference speed will be given by the MPPT controller and the stator current d-axis component, i_{sd}, is controlled to be zero $i_{sd-r} = 0$ (Zero Direct-axis Control: ZDC). The stator current i_s will be equal to its q-axis component (17.10). The electromagnetic torque of the generator derived in (17.7), can be simplified to (17.11).

$$i_s = \sqrt{i_{sd}^2 + i_{sq}^2} = i_{sq} \tag{17.10}$$

$$T_e = \frac{3P}{2}\phi_f . i_{sq} = K_t . i_s \tag{17.11}$$

With a constant PM flux of rotor, the torque presents a linear relationship with stator current, which implies that the behavior will be similar to a DC motor, where the electromagnetic torque is proportional to the armature current.

The current controllers in dq-frame are the PI type, the output of the decoupled controller can be expressed as:

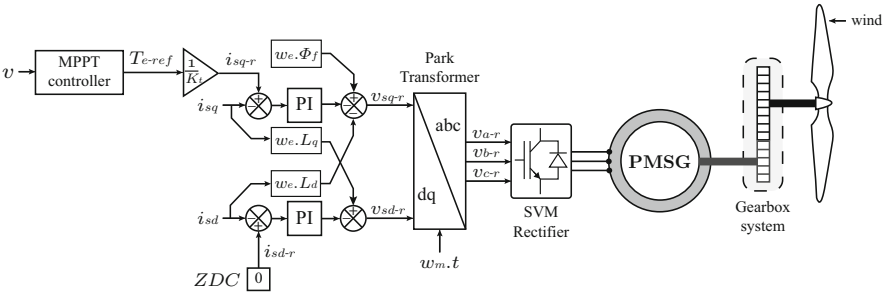

Fig. 17.5 Diagram scheme of PMSG control strategy

$$v_{sd} = -\left(k_{pd} + \frac{K_{id}}{s}\right)(i_{sd-r} - i_{sd}) + w_e.L_q.i_{sq} \tag{17.12}$$

$$v_{sq} = -\left(k_{pq} + \frac{K_{iq}}{s}\right)(i_{sq-r} - i_{sq}) - w_e.L_d.i_{sd} + w_e.\phi_f \tag{17.13}$$

With $\left(K_p + \frac{K_i}{s}\right)$ is the transfer function of PI controller.

As shown in Fig. 17.5, the reference torque T_{e-ref} is given by the MPPT controller. Then, the active power control is realized by dq-current closed-loops. The measured three-phase stator currents i_{sabc} are transformed into dq-frame i_{sdq}. The measured dq-currents are then compared to their references i_{sd-r}, and i_{sq-r} respectively. The comparison errors are sent to PI-current controllers, which generate the dq-axis reference voltage v_{sd-r}, v_{sq-r} for the generator side converter (GSC). An important requirement is that the current controllers must be faster than the speed controller.

To generate the signal gates for the GSC, the reference voltage dq-frame should be transformed into the stationary abc-frame v_{sabc-r}, and sent it to the Space Vector Modulation (SVM) block. Then the generator power will be controlled by adjusting the input GSC voltage v_{abc} to their references.

17.4 Experimental Results and Discussion

17.4.1 Turbine Emulation System

In experimental studies, the turbine will be emulated by a DC motor, it will be controlled in such a way it gives the same mechanical behavior of speed and torque in the output of the gearbox system, then the DC motor will be directly coupled with PMSG (Hardy and Jewell 2011; Ovando et al. 2007).

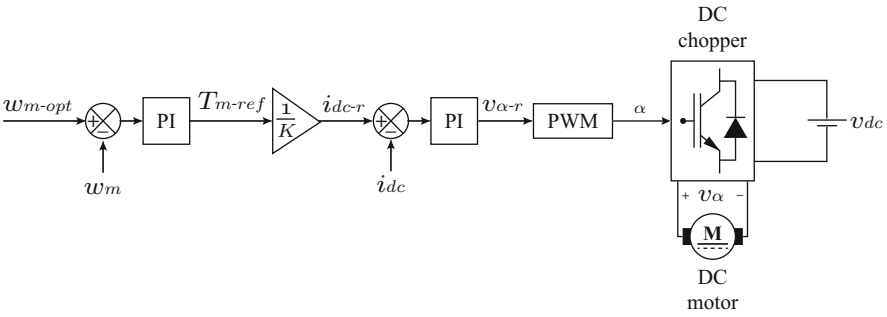

Fig. 17.6 Turbine emulation system by a DC motor controlled by DC chopper

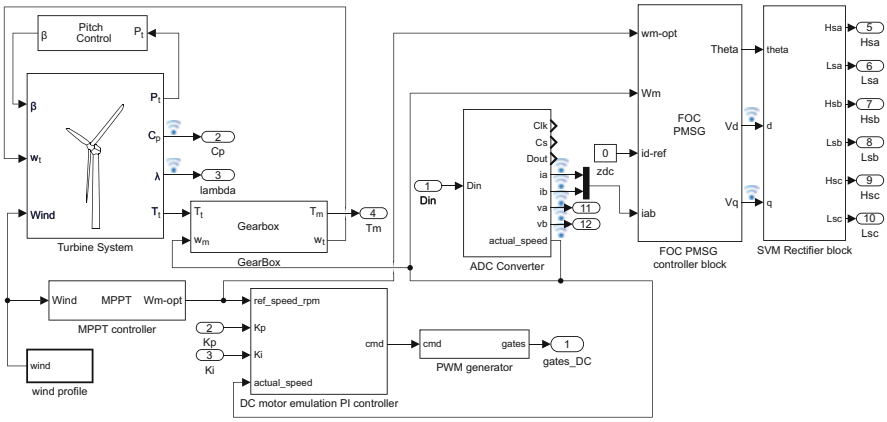

Fig. 17.7 Diagram scheme control model of WECS in simulink

The DC motor was chosen as an emulator drive, due to its simplicity and high torque comparing to AC drives. Also, it will be controlled by a DC-chopper with PWM signal gates from the control block as shown in Fig. 17.6. The DC motor will be controlled by two closed-loops, where the outer-loop will regulate the mechanical speed to its reference given by the MPPT controller, and the inner-loop will regulates the torque to be equal to the mechanical torque in the output of gearbox system by controlling the DC-current i_{dc}. Then, by using the PWM block, the current controller output that represents the control signal will be transformed into a duty cycle signal α of the DC-chopper supplied by a DC supply, which generates a variable DC-voltage v_α to DC motor (Fig. 17.6).

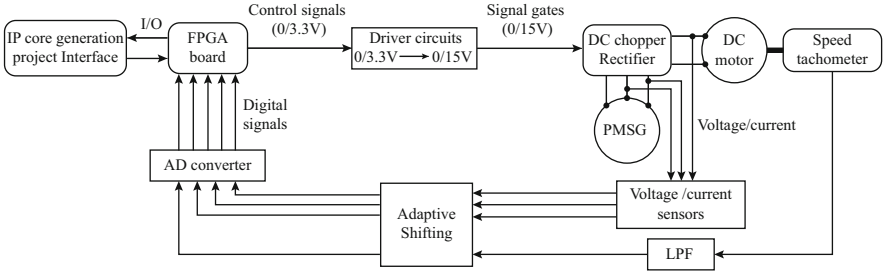

Fig. 17.8 Proposed design flow of the test bench

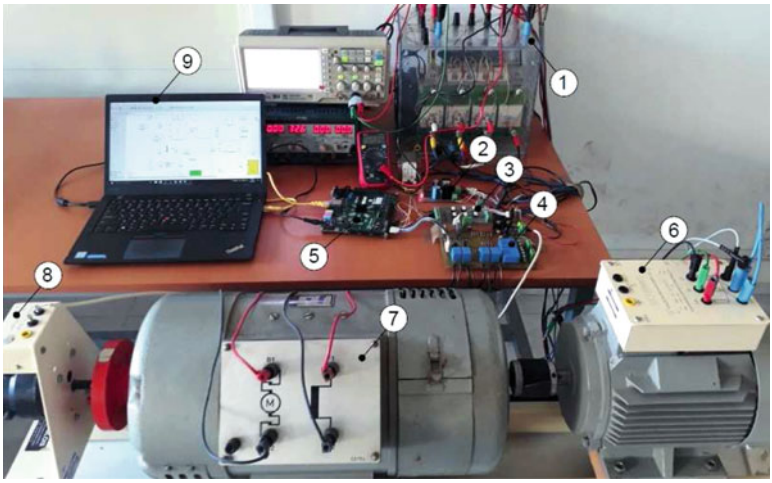

Fig. 17.9 Experimental test bench of WECS based on PMSG with turbine emulator system by a DC motor

17.4.2 Test Bench Description

The experimental test will start by implementing the model control of WECS using the DC motor emulator in FPGA board and generating a project interface. Then, the control signals (3.3 V) generated by the FPGA will be transmitted to the IGBT of DC-chopper and rectifier through a driver circuit from 3.3→15 V. The voltages, currents, and speed informations from the DC motor and PMSG will be taken by the voltage/current sensors and speed tachometer which is directly coupled with DC motor, all informations should be adapted and shifted to signal range 0→3.3 V and convert them by an analog to digital converter (ADC with 12 bits resolution and 8 channels) which is implemented in the data acquisition board and connected to the zedboard by the pmod ports as shown in Figs. 17.8 and 17.9.

17.4.3 Experimental Results

The controllers are implemented using discrete-time domain function, due to their compatibility with HDL Coder toolbox in Simulink for FPGA. Conventional PI controllers with a specific gains are chosen. Also, to account for the inertia effects of the turbine system, a numerical low pass filter was placed on the output speed measurement block to limit the rate at which the controller could request the system response. In order to guarantee the real time function, the sampling time of the interface was fixed in $T_s = 0.0001$ s.

1 Rectifier	**4** Acquisition board	**7** DC motor
2 Adaptive board	**5** Zedboard FPGA	**8** Speed tachometer
3 Driver board	**6** PMSG	**9** Host interface

To validate the experimental results, a simulation was established as shown in Fig. 17.12.

Figure 17.13 shows the experimental results of the PMSG and DC motor control, which are based on wind profile as shown in Fig. 17.10 with rated speed $v_{nom} = 10$ m/s and the parameters of the system are given in Tables 17.1, 17.2 and 17.3. The switching frequency of the DC chopper for motor emulator system control was fixed at 8 kHz, the PMSG was tested with 10 kHz for the rectifier.

To approximate the real dynamic of turbine, the cut-in speed is 3 m/s and cut-off speed is 20 m/s.

The turbine model with MPPT and pitch angle controller was implemented in the zedboard in order to give in real time the turbine behavior to the system emulator by the DC motor.

The turbine controls, was evaluated as shown in Fig. 17.11. The performance of MPPT can be evaluated by Fig. 17.11a, b, where C_p and λ are in their optimal values, and are decreased when the wind speed exceeds the rated speed where the pitch angle is enabled and gives pitch responses as shown in Fig. 17.11c. As discussed previously, the Pitch angle controller limits the generated power at their nominal value as verified in Fig. 17.11d. The Fig. 17.11e, f shows the speed and torque of turbine under the mentioned wind speed profile, it is found that the rated turbine speed is $w_t = 63.43\,\text{rad.s}^{-1}$ and rated turbine torque $T_t = 23.65\,\text{N.m}$.

To verify the performance of the PMSG control, a simulation test has been carried out. In this simulation the PMSG control block received the reference torque from the MPPT controller (Fig. 17.4), then the reference q-axis current is derived from (17.11) and d-axis is chosen to be zero to simplify the control algorithm. As shown in Figs. 17.12a, b shows a good tracking performance of the optimal speed and reference electromagnetic torque given by the MPPT controller block as mentioned before. Figure 17.12c verify the zero direct axis control by maintaining the d-axis current component at zero.The magnitude of the three phase stator currents depends on the q-axis current derived from (17.10), this is shown in Fig. 17.12d with a nominal frequency equal to 50 Hz when the PMSG velocity is maximal ($157\,\text{rad.s}^{-1}$).

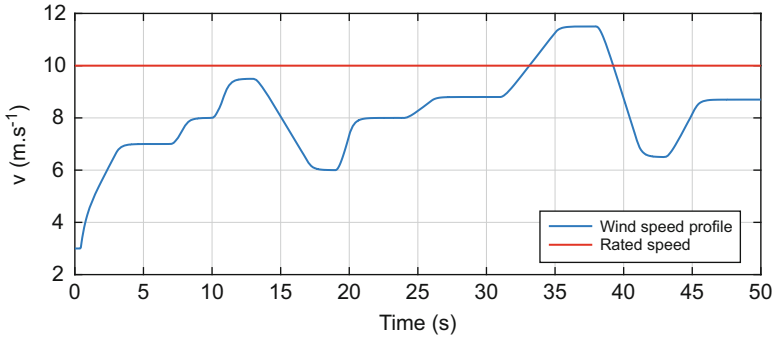

Fig. 17.10 Wind speed v profile

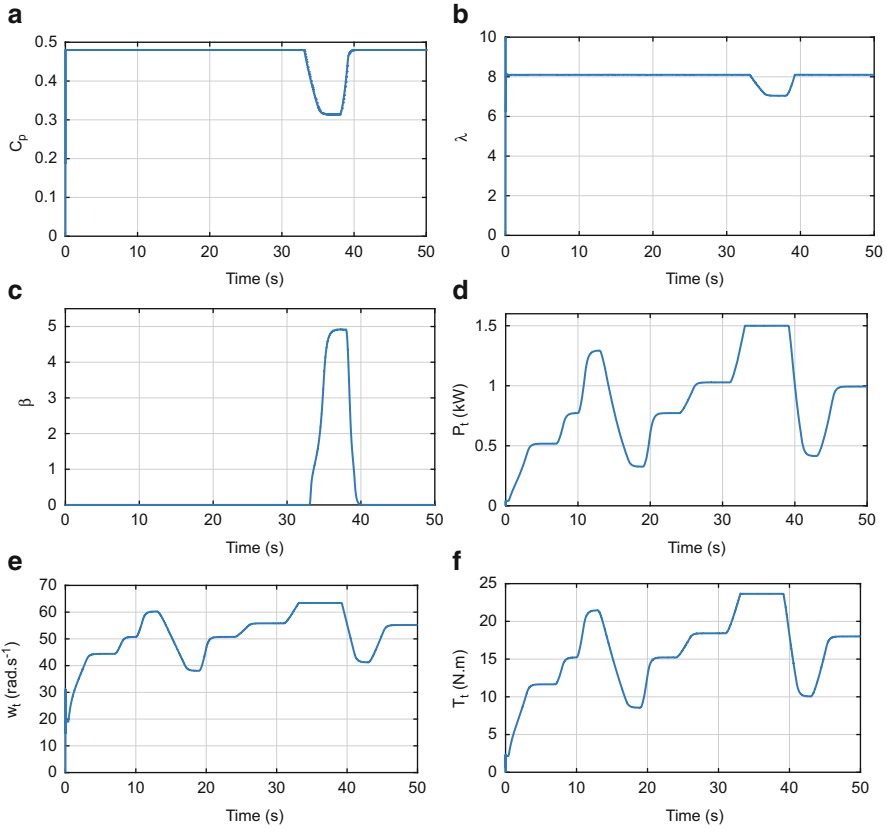

Fig. 17.11 Turbine dynamic performance with MPPT and pitch angle controllers by FPGA. (**a**): Power coefficient C_p. (**b**): Tip speed ratio λ. (**c**): Pitch angle β. (**d**): Turbine power P_t. (**e**): Turbine speed w_t. (**f**): Turbine torque T_t

A prototype system is constructed as shown previously for experimental verification. The prime motor is a DC machine controlled in speed rotating to emulate the turbine and gearbox system, where the reference speed given by the MPPT controller block as discussed before. Figure 17.13a shows a high tracking

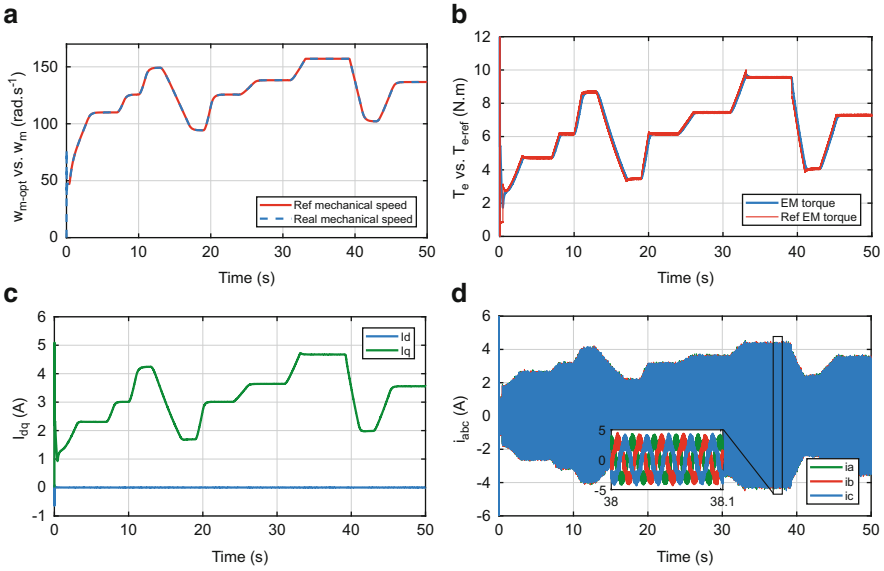

Fig. 17.12 Simulation results: Dynamic performance with the field orientation control. (**a**): Mechanical speed w_m of PMSG. (**b**): Electromagnetic torque T_e. (**c**): Stator currents in dq-frame I_{dq}. (**d**): Three phase stator currents i_{abc}

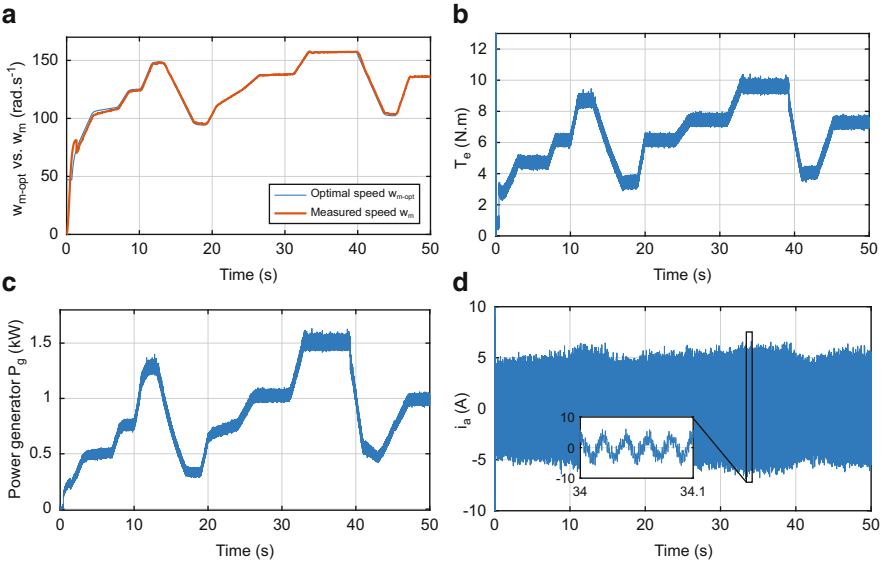

Fig. 17.13 Experimental results: Dynamic performance with the Field Orientation control. (**a**): Measured speed w_m of DC motor. (**b**): Measured electromagnetic torque T_e. (**c**): Measured power from generator P_g. (**d**): Measured stator currents a-component i_a

performance by DC motor for the reference speed with a minimal initial offset due to the mechanical time response of the system.

Figure 17.13b presents the produced electromagnetic torque which is derived from the q-axis current i_{sq}, the nominal torque is 9.8 N.m.

The effectiveness of the pitch angle and MPPT controllers is shown in Fig. 17.13c, where the generated power by PMSG reached the nominal power but is suffers from a high harmonics which comes from the stator current measurement.

Figure 17.13d shows the output current of the PMSG with a high harmonics, in nominal region the magnitude of stator current is stable and equal to 5 A which is consistent with the calculation.

17.5 Conclusion

This chapter provided a comprehensive analysis of various components and control schemes for wind energy conversion systems based on PM synchronous generator. Three controls for the system are analyzed, including maximum power point tracking (MPPT) control, pitch angle control, and generator side converter control for the PMSG. Also, a new system of turbine emulation based on DC motor was presented.

A test bench was constructed based on zedboard zynq-7000 system on chip FPGA to verify and analyze the dynamic performance of the proposed controls and to compare them with simulation results. Experimental results give a high tracking performance comparing to simulation results but it suffers from the harmonics due to current measurement.

Appendix

Table 17.1 Turbine data

Parameter	Value
Rated power P_n	1.5 kW
Rotor radius R	1.277 m
Maximum power coefficient C_{p-max}	0.48
Optimal tip speed ratio λ_{opt}	8.1
Rated wind speed v_{nom}	10 m/s
Speed range [cut-in ; cut-off]	[3 ; 20]

Table 17.2 PMSG data

Parameter	Value
Nominal power P_n	1.5 kW
Stator resistance R_s	2.6
d-inductance L_d	63.77 mH
q-inductance L_q	94.32 mH
PM flux ϕ_f	0.4 Wb
Equivalent inertia J_{eq}	0.0931 N.m.rad^{-1}.s^2
Equivalent viscous damping	0.0153 N.m.rad^{-1}.s
Number of poles pairs P	2
Rated speed w_{nom}	157 rad.s^{-1}
Rated frequency f	50 Hz

Table 17.3 DC motor data

Parameter	Value
Nominal power	3.6 kW
Rated voltage V_{dc}	120 V
Rated current I_{dc}	30 A
Resistance R	0.72 Ω
Motor constant K	0.5

References

Ackermann, T., & Söder, L. (2005). *Wind power in power systems: An introduction* (pp. 25–51). Hoboken: Wiley.

Azzaoui, M. E., Mahmoudi, H., & Ed-dahmani, C. (2016). Backstepping control of the doubly fed induction generator using Xilinx system generator for implementation on FPGA. In *2016 5th International Conference on Multimedia Computing and Systems (ICMCS)*, Marrakech, Morocco (pp. 599–604).

Bakouri, A., Mahmoudi, H., Barara, M., Abbou, A., Bennassar, A., & Moutchou, M. (2015). A complete control strategy of DFIG connected to the grid for wind energy conversion systems. In *2015 3rd International Renewable and Sustainable Energy Conference (IRSEC)*, Marrakech, Morocco (pp. 1–6).

Blaabjerg, F., & Chen, Z. (2006). *Power electronics for modern wind turbines*. San Rafael: Morgan and Claypool.

Blaabjerg, F., & Ma, K. (2013). Future on power electronics for wind turbine systems. *IEEE Journal of Emerging and Selected Topics in Power Electronics, 1*(3), 139–152.

Boldea, I. (2005). *Variable speed generators*. Boca Raton: Taylor & Francis.

Bose, B. K. (2009). Power electronics and motor drives recent progress and perspective. *IEEE Transactions on Industrial Electronics, 56*(2), 581–588.

Busca, C., Stan, A. I., Stanciu, T., & Stroe, D. I. (2010). Control of permanent magnet synchronous generator for large wind turbines. In *2010 IEEE International Symposium on Industrial Electronics*, Bari, Italy (pp. 3871–3876).

Hardy, T., & Jewell, W. (2011). Emulation of a 1.5 MW wind turbine with a DC motor. In *2011 IEEE Power and Energy Society General Meeting*, Detroit, MI, USA (pp. 1–8).

Kocur, M., Kozak, S., & Dvorscak, B. (2014). Design and implementation of FPGA – Digital based PID controller. In *Proceedings of the 2014 15th International Carpathian Control Conference (ICCC)*, Velke Karlovice, Czech Republic (pp. 233–236).

Kung, Y. S., Risfendra, R., Lin, Y. D., & Huang, L. C. (2016). FPGA-based sensorless controller for PMSM drives using sliding mode observer and phase locked loop. In *2016 International Conference on Applied System Innovation (ICASI),* Okinawa, Japan (pp. 1–4).

Mohammadi, D., Daoud, L., Rafla, N., & Ahmed-Zaid, S. (2016). ZYNQ-based SoC implementation of an induction machine control algorithm. In *2016 IEEE 59th International Midwest Symposium on Circuits and Systems (MWSCAS)*, Abu Dhabi, United Arab Emirates (pp. 1–4).

Monmasson, E., Idkhajine, L., Cirstea, M. N., Bahri, I., Tisan, A., & Naouar, M. W. (2011). FPGAs in industrial control applications. *IEEE Transactions on Industrial Informatics, 7*(2), 224–243.

Ovando, R. I., Aguayo, J., & Cotorogea, M. (2007). Emulation of a low power wind turbine with a DC motor in matlab/simulink. In *2007 IEEE Power Electronics Specialists Conference*, Orlando, FL, USA (pp. 859–864).

Pena, R., Círdenas, R., & Asher, G. (2013). Overview of control systems for the operation of DFIGS in wind energy applications. In *IECON 2013 – 39th Annual Conference of the IEEE Industrial Electronics Society*, Vienna, Austria (pp. 88–95).

Polinder, H., Pijl, F. V. D., Vilder, G. D., & Tavner, P. (2006). Comparison of direct-drive and geared generator concepts for wind turbines. *IEEE Transactions on Energy Conversion, 21*, 725–733.

Rogers, P., Kavasseri, R., & Smith, S. C. (2016). An FPGA-based design for joint control and monitoring of permanent magnet synchronous motors. In *2016 International Conference on ReConFigurable Computing and FPGAs (ReConFig)*, Cancun, Mexico (pp. 1–6).

Tormo, D., Idkhajine, L., Monmasson, E., & Blasco-Gimenez, R. (2016). Evaluation of SoC-based embedded real-time simulators for electromechanical systems. In *IECON 2016 – 42nd Annual Conference of the IEEE Industrial Electronics Society*, Florence, Italy (pp. 4772–4777).

Wu, B., Lang, Y., Zargari, N., & Kouro, S. (2011a). An introduction to wind energy conversion systems. In B. Wu, Y. Lang, N. Zargari, & S. Kouro (Eds.), *Power conversion and control of wind energy systems* (pp. 1–23). Oxford/Piscataway: Wiley-IEEE Press.

Wu, B., Lang, Y., Zargari, N., & Kouro, S. (2011b). Variable-speed wind energy systems with synchronous generators. In B. Wu, Y. Lang, N. Zargari, & S. Kouro (Eds.), *Power conversion and control of wind energy systems* (pp. 275–316). Oxford/Piscataway: Wiley/IEEE Press.

Wu, B., Lang, Y., Zargari, N., & Kouro, S. (2011c). Wind generators and modeling. In B. Wu, Y. Lang, N. Zargari, & S. Kouro (Eds.), *Power conversion and control of wind energy systems* (pp. 49–85). Oxford/Piscataway: Wiley-IEEE Press.

Yan, J., Lin, H., Feng, Y., Guo, X., Huang, Y., & Zhu, Z. Q. (2013). Improved sliding mode model reference adaptive system speed observer for fuzzy control of direct-drive permanent magnet synchronous generator wind power generation system. *IET Renewable Power Generation, 7*(1), 28–35.